# Oxidationsverhalten refraktärmetallbasierter Konstruktionswerkstoffe für Hochtemperaturanwendungen

BRONISLAVA GORR

UNIVERSITÄT
SIEGEN

SIEGENER WERKSTOFFKUNDLICHE BERICHTE | BAND 20/2018
HERAUSGEBER: PROF. DR.-ING. HABIL. H.-J. CHRIST

Bronislava Gorr

# Oxidationsverhalten refraktärmetallbasierter Konstruktionswerkstoffe für Hochtemperaturanwendungen

SIEGENER WERKSTOFFKUNDLICHE BERICHTE 2018

Bibliografische Information der Deutschen Nationalbibliothek
Die Deutsche Nationalbibliothek verzeichnet diese Publikation in der Deutschen Nationalbibliografie; detaillierte bibliografische Daten sind im Internet über http://dnb.d-nb.de abrufbar.

Habilitation, Universität Siegen, 2018

Herausgeber:
Prof. Dr.-Ing. habil. H.-J. Christ
Lehrstuhl für Materialkunde und Werkstoffprüfung
Institut für Werkstofftechnik
Paul-Bonatz-Str. 9-11
Universität Siegen
D-57068 Siegen

Als Manuskript gedruckt. Printed in Germany.

URN:nbn:de:hbz:467-14627
ISSN 2193-5114

# Oxidationsverhalten refraktärmetallbasierter Konstruktionswerkstoffe für Hochtemperaturanwendungen

Habilitationsschrift

**Dr.-Ing. Bronislava Gorr**

**Universität Siegen**

**Naturwissenschaftlich-Technische Fakultät**

**August 2016**

# Vorwort

Diese Arbeit ist das Ergebnis meiner Tätigkeit als wissenschaftliche Mitarbeiterin und Leiterin der Arbeitsgruppe Hochtemperaturkorrosion am Lehrstuhl für Materialkunde und Werkstoffprüfung der Universität Siegen. In diesem Zusammenhang gilt mein besonderer herzlicher Dank Herrn Professor Dr.-Ing. habil. Hans-Jürgen Christ, der mir die Möglichkeit gab, diese Arbeit anzufertigen und auf dessen Unterstützung ich stets bauen durfte. Für die unbegrenzten Möglichkeiten der Selbstentwicklung und das stetige Vertrauen danke ich ihm in besonderer Weise. Ebenso möchte ich Herrn Professor Dr.-Ing. Martin Heilmaier für die äußerst angenehme Zusammenarbeit im Rahmen mehrerer Forschungsprojekte, die Begeisterung für neue Themen und darüber hinaus für die Übernahme des zweiten Gutachtens dieser Arbeit danken. Herrn Professor Dr.-Ing. Lorenz Singheiser danke ich ganz aufrichtig für die Übernahme des dritten Gutachtens.

Allen aktuellen und ehemaligen Kollegen, die zum Gelingen dieser Arbeit maßgeblich beigetragen haben, gilt mein besonderer Dank. Hier seien Dr.-Ing. Steffen Burk, M. Sc. Lin Wang, Dr.-Ing. Maria Azim, M. Sc. Franz Müller hervorgehoben. Meinen Kollegen (auch ehemaligen) am Institut für Werkstofftechnik, insbesondere innerhalb der Arbeitsgruppe Hochtemperaturkorrosion, danke ich für die familiäre und freundliche Arbeitsatmosphäre. Den technischen Mitarbeitern am Institut für Werkstofftechnik, insbesondere Dipl.-Ing. Wolfgang Kramer für die professionelle Unterstützung im Hochtemperaturlabor, sei gedankt. Weiterhin danke ich Herrn Ahmad Ismail für seine Zuverlässigkeit und umfangreiche Unterstützung.

Privat gilt mein besonders warmer Dank meiner Familie in Deutschland, in der Ukraine und in den USA.

# Abstrakt

Der anhaltende Bedarf an robusten und leistungsfähigen Hochtemperaturwerkstoffen kommt überwiegend aus der Luft- und Raumfahrtindustrie. Eine Erhöhung der Gaseintritts-temperatur, welche für den Anstieg der thermischen Effizienz von Gasturbinen erforderlich ist, scheint ohne den Einsatz von neuartigen Legierungen schwer realisierbar zu sein. In den letzten Jahren gewinnen refraktärmetallbasierte Legierungen immer mehr an Bedeutung, da diese sehr hohe Schmelztemperaturen und oft gute mechanische Eigenschaften aufweisen. Die Oxidationsbeständigkeit dieser Werkstoffe ist jedoch schwach. Diese Arbeit fasst wesentliche Erkenntnisse mehrerer Forschungsarbeiten zum Thema „Hochtemperaturkorrsionsverhalten refraktärmetallbasierter Werkstoffe“, die am Lehrstuhl für Materialkunde und Werkstoffprüfung des Instituts für Werkstofftechnik an der Universität Siegen durchgeführt wurden, zusammen. Hier werden Ergebnisse zum Hochtemperaturoxidationsverhalten für Molybdänbasislegierungen, deren chemische Zusammensetzung durch Makrolegieren mit Ti im Vergleich zu den recht gut erforschten Mo-Si-B-Legierungen erheblich geändert wurde, sowie für zwei neue Werkstoffsysteme, Co-Re-Basislegierungen und refraktäre Hochentropielegierungen, vorgestellt. Durch gezielte metallurgische Maßnahmen wie Makro- und Mikrolegieren konnte die Oxidationsresistenz von den untersuchten Werkstoffen auf Basis von refraktären Metallen signifikant verbessert werden. Die Ergebnisse zeigen, dass die refraktärmetallbasierten Werkstoffe bei erfolgreicher Weiterentwicklung ein hohes Potenzial für einen zukünftigen Einsatz in Hochtemperaturanwendungen besitzen.

## Inhaltsverzeichnis

1 Einleitung……… 1

2 Untersuchte refraktärmetallbasierte Werkstoffsysteme……… 2

3 Hochtemperatuoxidationsverhalten refraktärmetallbasierter Werkstoffe……… 3

- 3.1 Besonderheiten des Hochtemperaturoxidationsverhaltens refraktärmetallbasierter Legierungen……… 4
- 3.2 Einfluss der Temperatur auf den Oxidationswiderstand……… 6
- 3.3 Effekt des Makrolegierens auf die Mikrostruktur und das Oxidationsverhalten……… 7
- 3.4 Effekt des Mikrolegierens auf die Oxidationsresistenz……… 10

4 Maßnahmen zur Verbesserung der Oxidationsresistenz……… 11

5 Literaturverzeichnis……… 14

6 Anhang……… 19

Manuskript I: B. Gorr, S. Burk, T. Depka, Ch. Somsen, H. Abu-Samra, and H.-J. Christ, G. Eggeler: Effect of Si-addition on the oxidation resistance of Co-Re-Cr-alloys: Recent attainments in the development of novel alloys, International Journal of Material Reseach, 1 (2012) 24-30……… 21

Manuskript II: S. Burk, B. Gorr, H.-J. Christ, D. Schliephake, M. Heilmaier, C. Hochmuth and U. Glatzel: High-temperature oxidation behavior of a single-phase (Mo,Ti)$_5$Si$_3$ (Mo-Si-Ti) alloy, Scripta Materialia, 66 (2012) 223-226……… 31

Manuskript III: S. Majumdar, D. Schliephake, B. Gorr, H.-J. Christ, M. Heilmaier: Effect of yttrium alloying on intermediate to high-temperature oxidation behavior of Mo-Si-B alloys, Metallurgical and Materials Transactions, A 44 (2013) 2013-224……… 37

Manuskript IV: L. Wang, B. Gorr, H.-J. Christ, D. Mukherji, J. Rösler: Optimization of Cr-content for high-temperature oxidation behavior of Co-Re-Si-base alloys, Oxidation of Metals, 80 (2013) 49-59……… 55

Manuskript V: M. Azim, S. Burk, B. Gorr, H.-J. Christ, D. Schliephake, M. Heilmaier R. Bornemann, P.H. Bolivar: Effect of Ti (macro-) alloying on the high-temperature oxidation behavior of ternary Mo-Si-B alloys at 820-1300°C, Oxidation of Metals, 80 (2013) 231-242……… 67

Manuskript VI: B. Gorr, H.-J. Christ, D. Mukherji, J. Rösler: Thermodynamic calculations in the development of high-temperature Co-Re-based alloys, Journal of Alloys and Compounds 582 (2014) 50-58……… 83

Manuskript VII: D. Schliephake, M. Azim, K. von Klinski-Wetzel, B. Gorr, H.-J. Christ, H. Bei, E.P. George, M. Heilmaier: High-temperature creep and oxidation behavior of Mo-Si-B alloys with high Ti contents, Metallurgical and Materials Transactions A, 45A (2014) 1102-1111……… 95

Manuskript VIII: S. Majumdar, B. Gorr, H.-J. Christ, D. Schliephake, M. Heilmaier: Oxidation mechanisms of lanthanum-alloyed Mo-Si-B, Corrosion Science, 88 (2014) 360-371……… 107

Manuskript IX: B. Gorr, L. Wang, S. Burk, M. Azim, S. Majumdar, H.-J. Christ, D. Mukherji, J. Rösler, D. Schliephake, M. Heilmaier: High-temperature oxidation behavior of Mo-Si-B-based and Co-Re-Cr-based alloys, Intermetallics, 48 (2014) 34-43……… 121

Manuskript X: B. Gorr, M. Azim, H.-J. Christ, T. Mueller, D. Schliephake, M. Heilmaier: Phase equilibria, microstructure, and high temperature oxidation resistance of novel refractory high-entropy alloys, Journal of Alloys and Compounds, 624 (2015) 270-278………………………………………………………………… 133

Manuskript XI: L. Wang, B. Gorr, H.-J. Christ, J. Rösler: The effect of alloyed nickel on the short-term high temperature oxidation behaviour of Co-Re-Cr-based alloys, Corrosion Science, 93 (2015) 19-26……………………………………………….. 145

Manuskript XII: L.Wang, B. Gorr, H.-J. Christ, D. Mukherji, J. Rösler: Microstructure and oxidation mechanism evolution of Co-17Re-25Cr-2Si in the temperature range 800-1100°C, Oxidation of Metals, 83 (2015) 465-483…………...................... 155

Manuskript XIII: M. Azim, D. Schliephake, C. Hochmuth, B. Gorr, H.-J. Christ, U. Glatzel, M. Heilmaier: Creep resistance and oxidation behavior of novel Mo-Si-B-Ti alloys, JOM, 67 (2015) 2621-2628…………………………………………………… 177

Manuskript XIV: H. Chen, A. Kauffmann, B. Gorr, D. Schliephake, C. Seemüller, J. N. Wagner, H.-J. Christ, M. Heilmaier.: Microstructure and mechanical properties at elevated temperatures of a new Al-containing refractory high-entropy alloy Nb-Mo-Cr-Ti-Al, Journal of Alloys and Compounds, 661 (2016) 206-215…………………... 187

Manuskript XV: B. Gorr, M. Azim, H.-J. Christ, H. Chen, D.-V. Szaboo, A. Kauffmann, M. Heilmaier: Microstructure evolution in an new refractory high-entropy alloy W-Mo-Cr-Ti-Al, Metallurgical and Materials Transactions A, 47A (2016) 961-970…………………………………………………………………………….. 199

Manuskript XVI: B. Gorr, F. Mueller, H.-J. Christ, T. Mueller, H. Chen, A. Kauffmann, M. Heilmaier, High temperature oxidation behavior of an equimolar refractory metal-based alloy 20Nb-20Mo-20Cr-20Ti-20Al with and without Si addition, Journal of Alloys and Compounds, 688 (2016) 468-477…………………………….. 211

Manuskript XVII: M. Azim, B. Gorr, H.-J. Christ, M. Heilmaier: Characterization of oxidation kinetics of Mo-Si-B-based materials, Oxidation of Metals, 87 (2017) 89-108…………………………………………………………………………….. 223

Manuskript XVIII: B. Gorr, F. Müller, M. Azim, H.-J. Christ, T. Müller, H. Chen, A. Kauffmann, M. Heilmaier: High temperature oxidation behavior of refractory high entropy alloys: Effect of alloy composition, Oxidation of Metals, 88 (2017) 339-349. 245

.

# 1 Einleitung

Der bereits seit Jahrzehnten anhaltende Bedarf an robusten und leistungsfähigen Hochtemperaturwerkstoffen kommt überwiegend aus der Luft- und Raumfahrtindustrie. Nickelbasislegierungen stellen heutzutage die bevorzugt eingesetzten Werkstoffe für hochtemperaturbeanspruchte Bauteile in Gasturbinen dar, da diese Werkstoffe eine vorteilhafte Kombination der geforderten Eigenschaften wie Kriech- und Ermüdungsbeständigkeit, Duktilität bei tiefen Temperaturen und Korrosionsresistenz aufweisen. Da die Einsatztemperatur der Nickelbasislegierungen durch ihre Schmelztemperatur limitiert ist, werden in der Regel komplexe wärmeisolierende Beschichtungssysteme sowie speziell entwickelte Kühltechniken verwendet, um diese Werkstoffe bei Umgebungstemperaturen oberhalb von 1100°C dennoch einsetzen zu können. Allerdings wird der durch eine höhere Gaseintrittstemperatur hervorgerufene Gewinn des thermischen Wirkungsgrades durch die aktive Kühlung der Turbinenschaufeln erheblich herabgesetzt [PER2009]. Der weitere Anstieg der Gaseintrittstemperatur, den der Anstieg der thermischen Effizienz von Gasturbinen erfordert, scheint ohne den Einsatz von neuartigen Legierungen mit einem Potenzial jenseits der Nickelbasissuperlegierungen schwer realisierbar zu sein. Neben Keramiken, intermetallischen Phasen und Verbundwerkstoffen gewinnen refraktärmetallbasierte Legierungen in den letzten Jahren immer mehr an Bedeutung, wobei sowohl bereits relativ gut erforschte Legierungen im Hinblick auf erhöhte Werkstoffanforderungen weiterentwickelt als auch völlig neuartige Legierungssysteme und sogar Legierungskonzepte vorgeschlagen werden.

Der Einsatz von refraktären Metallen in konventionellen Hochtemperaturlegierungen hat eine lange Historie, da diese eine Reihe von besonders günstigen Eigenschaften im Hinblick auf die Hochtemperaturanwendungen besitzen: (i) hoher Schmelzpunkt, (ii) hohes Potential zur Festigkeitssteigerung und (iii) im Vergleich zu reinem Ni oft höherer Elastizitätsmodul. Niedrige Duktilität bei Raumtemperatur (RT), schwache Oxidationsbeständigkeit in Luft und hohe Dichte verhindern jedoch die praktische Implementierung refraktärmetallbasierter Legierungen. Diese ungünstigen Eigenschaften von refraktären Metallen führen dazu, dass diese meistens nur als Legierungselemente in den kommerziellen Hochtemperaturwerkstoffen verwendet werden, beispielsweise um die Kriecheigenschaften zu verbessern. Zu den refraktären Metallen, die einen besonders hohen Stellenwert bei den Hochtemperaturwerkstoffen einnehmen, gehören Cr, Mo, Re, W, Nb und Ta. Diese Metalle, sowie einige ihrer binären und ternären Modelllegierungen, wurden im Hinblick auf ihre physikalischen Werkstoffkennwerte, ihr mechanisches Verhalten und ihre Oxidationsresistenz verhältnismäßig gut erforscht [SYR1961, TIE1965]. Die in Tabelle 1 zusammengefassten Eigenschaften und Werkstoffkennwerte einiger refraktärer Metalle, sowie die Vor- und Nachteile der oben genannten Metalle, begründen die aktuell weltweit aktiv betriebene Grundlagenforschung an Werkstoffen mit hohen Anteilen refraktärer Elemente. Diese Arbeit fasst wesentliche Erkenntnisse mehrerer Forschungsvorhaben zum Thema „Hochtemperaturkorrosionsverhalten refraktärmetallbasierter Legierungen“, die am Lehrstuhl für Materialkunde und Werkstoffprüfung des Instituts für Werkstofftechnik an der Universität Siegen durchgeführt wurden, zusammen und gibt einen Ausblick über zukünftige

Forschungsaktivitäten, die dazu führen können, dass refraktärmetallbasierte Hochtemperaturwerkstoffe in technischen Komponenten eines Flugzeugtriebwerkes eine praktische Anwendung finden.

Tabelle 1: Werkstoffkennwerte und Eigenschaften einiger refraktärer Metalle (nach CAR2008, KLO1969, TIE1965, SYR1961)

| | W | Re | Ta | Mo | Nb | Cr |
|---|---|---|---|---|---|---|
| Gitter | krz | hdp | krz | krz | krz | krz |
| Schmelzpunkt, °C | 3410 | 3180 | 2996 | 2610 | 2468 | 1875 |
| Elastizitätsmodul bei RT, GPa | 399 | 468 | 186 | 330 | 103 | 296 |
| Dichte, g/cm$^3$ | 19,3 | 21,0 | 16,6 | 10,2 | 8,6 | 7,2 |
| Spröd-Duktil-Übergangstemperatur, °C | 340 | existiert nicht | -195 | 30 | -120 | 330 |
| Oxidationsresistenz in Luft | schwach | schwach | schwach | schwach | schwach | gut |

## 2 Untersuchte refraktärmetallbasierte Werkstoffsysteme

Refraktäre Metalle können in verschiedenen Konzentrationen in Hochtemperaturlegierungen vorliegen, meistens werden einem Basiselement allerdings nur einige Atomprozente der refraktären Metalle zulegiert. So beträgt die Konzentration von Re in der Nickelbasissuperlegierung DD32 beispielsweise 3,7 Masse-% [HUA2006]. Viel seltener stellt das refraktäre Metall das Basiselement der jeweiligen Legierungen dar, wie z.B. Nb in den Nb-Si-Basislegierungen [BEW2003]. In dieser Arbeit werden drei Werkstoffsysteme mit unterschiedlichen Anteilen an refraktären Elementen behandelt, wobei das Augenmerk auf die Besonderheiten des Oxidationsverhaltens dieser Werkstoffsysteme gerichtet wird.

Das erste Werkstoffsystem sind die Mo-basierte Legierungen, in denen das refraktäre Metall das Basiselement darstellt. Die sich in dem Mo-reichen Gebiet des Phasendiagramms befindenden ternären Mo-Si-B-Legierungen bestehen aus drei Phasen, dem Mo-Mischkristall (MK) und den Siliziden $Mo_3Si$ und $Mo_5SiB_2$, die eine gute Kombination aus mechanischen Eigenschaften und Korrosionsresistenz sicherstellen, wobei $Mo_5SiB_2$, auch T2 Phase genannt, die Schlüsselrolle bei der Gewährleistung der hervorragenden Oxidationsbeständigkeit dieser Legierungen bei Temperaturen oberhalb von 1000°C spielt [NOV1957, SCH1999, SAK2008]. Als Referenzlegierung für die weitere Legierungsentwicklung dient die chemische Zusammensetzung Mo-9Si-8B (hier und im Folgenden sind alle Angaben in Atom-%) aus dem $Mo_{MK}$-$Mo_3Si$-T2-Phasenfeld mit duktiler MK-Matrix.

Co-Re-Basislegierungen wurden erstmals im Rahmen der von der Deutschen Forschungsgemeinschaft (DFG) geförderten Forschergruppe 727 „Beyond Ni-Base Superalloys“ als neue Hochtemperaturwerkstoffe vorgeschlagen und auf die für Hochtemperaturanwendungen relevanten Eigenschaften wie thermische Stabilität, Kriechwiderstand und Korrosionsresistenz untersucht [RÖS2007, HEI2009, DEP2009, GOR2009]. Da die Co-Re-Cr-Legierungen eine völlig neue Klasse von Hochtemperaturwerkstoffen sind, liegt der Schwerpunkt der Untersuchungen zum Korrosionsverhalten primär in dem Auf-/Ausbau eines Grundlagenverständnisses zu den relevanten Oxidationsmechanismen, die sich in Abhängigkeit von der chemischen Zusammensetzung der Legierungen, der Temperatur und den atmosphärischen Bedingungen erheblich verändern. Die Referenzlegierung mit der chemischen Zusammensetzung Co-17Re-23Cr besteht aus der duktilen hexagonalen Matrix mit relativ spröden Ausscheidungen der σ-Phase vom Typ $Cr_2Re_3$ [BRU2010]. Der Re-Gehalt in der Referenzlegierung beträgt 17 Atom-%, sodass Re ein Legierungselement mit einer relativ hohen Konzentration in dem genannten Referenzwerkstoff darstellt.

Refraktäre High-Entropy Alloys (HEAs) repräsentieren das dritte in dieser Arbeit behandelte Werkstoffsystem. HEAs sind dadurch gekennzeichnet, dass alle Elemente in gleicher Konzentration vorliegen. Das erst im Jahr 2004 von Yeh et al. vorgeschlagene Konzept von HEAs basiert auf dem zweiten Hauptsatz der Thermodynamik und begründet die Ausbildung einfacher, oft einphasiger Werkstoffgefüge mit einer hohen Konfigurationsentropie, die sich nach dem Modell der regulären Lösungen ergibt, wenn die Zahl der Legierungselemente zunimmt und diese gleichzeitig äquimolar vorliegen [Yeh2007]. Neben der einfachen Mikrostruktur [Guo2011] zeichnen sich HEAs häufig durch eine hohe thermische Stabilität infolge verlangsamter Diffusion [YEH2007], eine hohe Festigkeit durch den starken Mischkristallhärtungseffekt [SEN2014] und die Ausbildung extrem kleiner Ausscheidungen [TON2005] sowie eine gute Oxidationsbeständigkeit [DAO2015] aus. Der Anteil der refraktären Metalle in den hier behandelten HEAs ist sehr hoch und beträgt, je nach Werkstoffzusammensetzung, mehr als 50 Atom-%. Als Referenzmaterial wurde die äquimolare Legierung 20W-20Mo-20Cr-20Ti-20Al gewählt.

# 3 Hochtemperaturoxidationsverhalten refraktärmetallbasierter Werkstoffe

Die bedeutsamsten Faktoren, die den Hochtemperaturkorrosionswiderstand eines Werkstoffes bestimmen, sind Temperatur, Legierungszusammensetzung, Werkstoffzustand und die werkstoffumgebende Atmosphäre. Obwohl der letztgenannte Faktor den Einsatz refraktärmetallbasierter Werkstoffe auf Atmosphären mit niedrigen Sauerstoffaktivitäten einschränkt, wird hier auf den Umgebungseinfluss nicht näher eingegangen. Die in dieser Arbeit behandelten Werkstoffe wurden bei den für einen praktischen Einsatz relevanten atmosphärischen Bedingungen, d.h. in Laborluft, untersucht. Andere Faktoren, die das Oxidationsverhalten betreffen, d. h. Temperatur, Legierungszusammensetzung und Werkstoffzustand, werden dagegen detailliert diskutiert.

Das Oxidationsverhalten von Hochtemperaturlegierungen ist extrem stark von der Temperatur abhängig, so dass den Untersuchungen des Temperatureffektes auf den Oxidationswiderstand eine besondere Bedeutung zukommt. In diesem Sinne wurden Mo-Si-B-Legierungen in einem breiten Temperaturintervall von 800-1300°C untersucht, während die Co-Re-Basislegierungen und HEAs zwischen 900°C und 1100°C oxidiert wurden. Sowohl Makro- als auch Mikrolegieren kann die Mikrostruktur maßgeblich beeinflussen und eine starke Veränderung des Oxidationsverhaltens bewirken. Daher wird der Einfluss der Legierungszusammensetzung auf den Oxidationswiderstand einzeln auf die beiden Effekte des Makro- und Mikrolegierens (bis 3 Atom-%) aufgeteilt. Die den entsprechenden Werkstoffsystemen bzw. Referenzlegierungen zulegierten Elemente und deren maximale Konzentrationen sind in der Tabelle 2 zusammengefasst. Der Effekt des durch die legierungstechnischen Maßnahmen veränderten Gefüges auf die Oxidationsresistenz der untersuchten Legierungen wird ebenfalls diskutiert.

Tabelle 2: Makro- und Mikrolegierungselemente in den untersuchten Werkstoffsystemen

| Werkstoffsystem | Mo-Si-B | Co-Re | W-Mo-Cr-Ti-Al |
|---|---|---|---|
| Referenzlegierung (Atom-%) | Mo-9Si-8B | Co-17Re-23Cr | 20W-20Mo-20Cr-20Ti-20Al |
| Makrolegieren: Element (max. Konzentration, Atom-%) | Ti (29) | Cr (30)<br>Ni (15)<br>Al (10) | Nb, Ta (20 / Substitution von W) |
| Mikrolegieren: Element (max. Konzentration, Atom-%) | Y (0.2)<br>La (2) | Si (3) | Si (1) |

## 3.1 Besonderheit des Hochtemperaturoxidationsverhaltens refraktärmetallbasierter Legierungen

Der Oxidationswiderstand von Hochtemperaturlegierungen beruht auf der Ausbildung schützender Deckschichten, die das metallische Substrat von der Atmosphäre trennen und auf diese Weise eine Materialschädigung verhindern. Die betriebssichere Schutzwirkung einer Oxiddeckschicht setzt die schnelle Ausbildung eines dünnen Oxidfilmes auf der Substratoberfläche und das langsame Wachstum der jeweiligen Oxidschicht nach dem parabolischen Zeitgesetz voraus [KOF1988]. Zu den schützenden Oxiden, die die genannten Voraussetzungen erfüllen, gehören $\alpha$-$Al_2O_3$ und $Cr_2O_3$ im kristallinen Zustand sowie amorphes $SiO_2$ [YOU2008]. Speziell in dem System Mo-Si-B bietet die mit B dotierte $SiO_2$-Schicht eine hervorragende Schutzwirkung bei Temperaturen oberhalb von 1000°C [BUR2011, 9]. Der für Hochtemperaturanwendungen erforderliche Oxidationsschutz in dem System Co-Re soll durch die Ausbildung einer dichten $Cr_2O_3$-Schicht gewährleistet werden [1]. Durch die Zugabe von Cr und Al in HEAs wird die Ausbildung zweier hochschützender Oxidschichten, $Cr_2O_3$ und $Al_2O_3$, angestrebt [10].

Wenn die schnelle Ausbildung einer schützenden Deckschicht auf der Oberfläche refraktärmetallbasierter Werkstoffe nicht stattfindet, kann dies (je nach Werkstoff-zusammensetzung und Temperatur) zu einem raschen Zerfall des metallischen Substrats durch die Bildung von schnell wachsenden festen oder volatilen Oxiden führen. Die Oxidationskinetik ist infolge der Bildung volatiler Oxide durch einen starken Masseverlust gekennzeichnet, die Oxidationsart wird als katastrophal bezeichnet. Die in dieser Arbeit untersuchten Werkstoffe enthalten folgende refraktäre Metalle: Mo, Re, W, Nb, Ta und Cr. Mit Ausnahme von Cr weisen diese refraktären Metalle in ihrer reinen Form nur eine schwache Oxidationsbeständigkeit auf. Die relevanten Oxide der oben genannten refraktären

Elemente und ihre Sublimations- bzw. Schmelztemperaturen sind in Tabelle 3 zusammengefasst. Mo und Re bilden niedrigschmelzende Oxide, deren Verdampfung einen schnellen Substratzerfall der Probe zur Folge hat. Zwar verdampfen W-, Nb- und Ta-Oxide bei wesentlich höheren Temperaturen, ihre Oxidationsraten sind dennoch durch die Bildung schnellwachsender Oxide unakzeptabel hoch [TIE1965]. Abbildung 1 zeigt die extrem hohe Werte der Oxidationsraten der reinen refraktären Metalle W, Nb und Ta während der Oxidation an Luft bei Temperaturen zwischen 800°C und 1100°C.

Tabelle 3: Stabilität der refraktären Oxide [nach TIE1965]

| Metall | Oxid | Oxideigenschaften |
|---|---|---|
| Re | $Re_2O_7$ | Verdampft oberhalb 363°C |
| Mo | $MoO_3$ | Verdampft oberhalb 795°C |
| W | $WO_3$ | Verdampft oberhalb 1000°C |
| Nb | $Nb_2O_5$ | Verdampft oberhalb 1370°C |
| Ta | $Ta_2O_5$ | Verdampft oberhalb 1370°C |
| Cr | $Cr_2O_3$ | Schmilzt bei 2440°C |

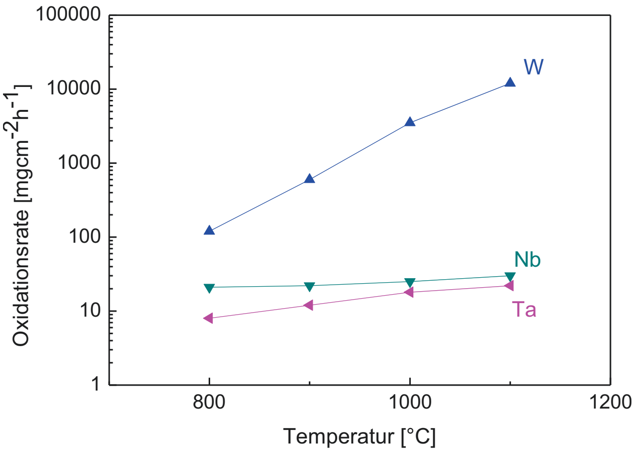

Abbildung 1: Oxidationsraten von W, Nb, und Ta bei verschiedenen Temperaturen in Luft (nach [GEY1961])

Um die Kinetik der Oxidationsprozesse zu bewerten, wird die Masseänderung während der Oxidationsexperimente kontinuierlich in thermogravimetrischen Anlagen (TGA) erfasst. Signifikante Masseverluste infolge der Oxidverdampfung wurden in Mo-Si-B (gasförmiges $MoO_3$ und $B_2O_3$) und Co-Re (gasförmiges $Re_2O_7$) Werkstoffsystemen [9] beobachtet, während das Oxidationsverhalten von HEAs durch eine kontinuierliche Gewichtszunahme geprägt ist [10, 16]. Die aufgenommenen TGA-Kurven von Werkstoffen mit hohen Anteilen refraktärer Metalle müssen allerdings vorsichtig ausgewertet werden, da diese die Summe von gegenläufigen Prozessen darstellen: (i) Massezunahme infolge der Sauerstoffaufnahme und die Ausbildung von festen Oxiden und (ii) Masseabnahme infolge der Verdampfung gasförmiger Oxide. Es wurde eine einfache Methode für das System Mo-Si-B entwickelt, die es erlaubt, einzelne Beiträge quantitativ abzuschätzen [17] und somit die Oxidationsbeständigkeit der jeweiligen Legierung korrekt zu bewerten. Die Abbildung 2 zeigt beispielsweise eine bei 1100°C experimentell ermittelte Masseänderungskurve der Legierung Mo-9Si-8B (schwarze Kurve in Abbildung 2) und die quantitativen Beiträge der unterschiedlichen Oxide zur absoluten Massenänderung: (i) die Massezunahme durch die Ausbildung der adhärenten festen Oxide $SiO_2$ und $MoO_2$ und (ii) die Masseabnahme infolge von volatilen $MoO_3$ und $B_2O_3$. Details der Methode können aus Referenz [17] entnommen werden.

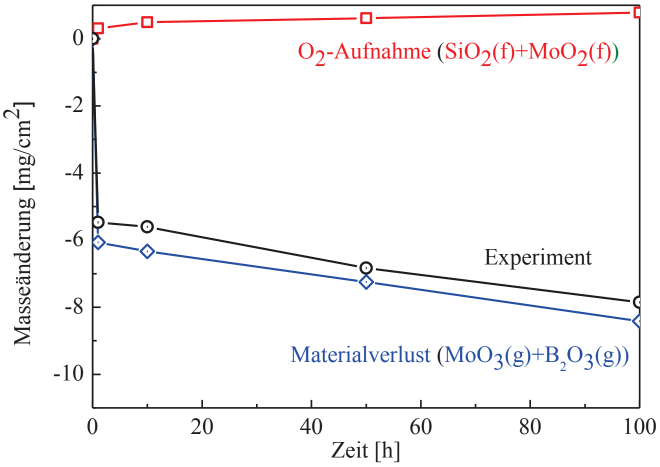

Abbildung 2: Quantitative Beiträge einzelner Oxide zur Massezunahme bzw. Masseabnahme während der Oxidation der Legierung Mo-9Si-8B in Luft bei 1100°C, nach [17]

### 3.2 Einfluss der Temperatur auf den Oxidationswiderstand

Die Oxidationsmechanismen und die daraus resultierenden Oxidationsresistenzen der untersuchten Werkstoffsysteme sind sehr verschieden und hängen von mehreren Faktoren ab. Die Umgebungstemperatur stellt einen äußerst wichtigen Einflussfaktor auf den Oxidationswiderstand von Hochtemperaturlegierungen dar. Eine Erhöhung der Temperatur bringt oft einen grundlegenden Wechsel in den Oxidationsmechanismen mit sich, der sogar eine erhebliche Verbesserung der Oxidationsresistenz von Hochtemperaturlegierungen bewirken kann. So zeigt die Abbildung 3(a), dass die parabolische Oxidationskinetik durch der Ausbildung einer schützenden $Cr_2O_3$-Schicht auf der Legierung Co-17Re-25Cr-2Si erst bei Temperaturen oberhalb von 1000°C beobachtet wird, während eine signifikante Masseabnahme infolge der Ausbildung von porösen Schichten bei Temperaturen unterhalb 1000°C zu verzeichnen ist [12]. In der Legierung Nb-Mo-Cr-Ti-Al zeigt eine Temperaturerhöhung von 900°C auf 1100°C einen ähnlichen positiven Effekt, der sich in der Ausbildung einer quasi-kontinuierlichen $Al_2O_3$-Schicht während der Oxidation der äquimolaren Legierung bei 1100°C äußert [16].

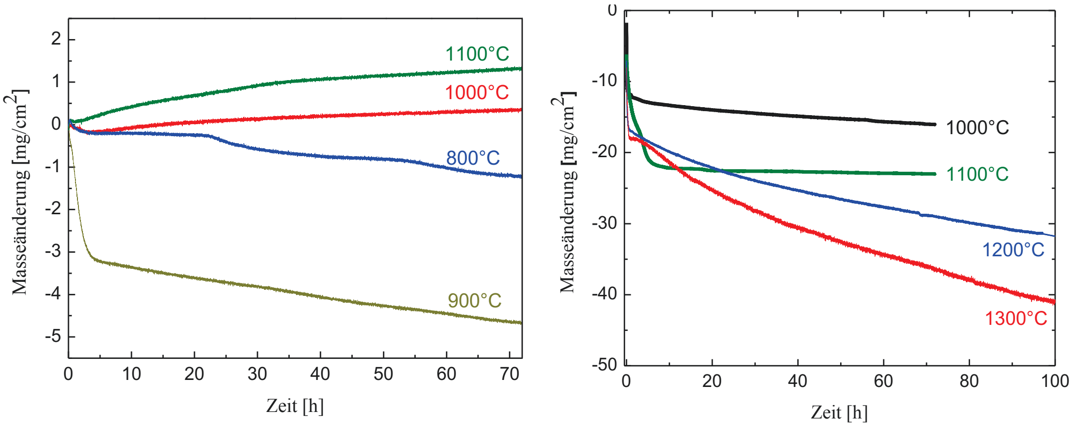

(a) (b)

Abbildung 3: Thermogravimetrische Kurven der Legierungen (a) Co-17Re-25Cr-2Si, nach [12] und (b) Mo-9Si-8B, nach [9] während der Auslagerung in Luft bei verschiedenen Temperaturen

Am stärksten tritt der Temperatureffekt allerdings bei Mo-Si-B-Basislegierungen in Erscheinung und wird daher im Folgenden näher erläutert. Wie oben erwähnt, beruht die Oxidationsresistenz dieses Werkstoffsystems auf der Ausbildung einer Borsilikatschicht. Das Element B verbessert die Flusseigenschaften der Borsilikatschicht bei Temperaturen zwischen 1000°C und 1200°C und ermöglicht eine schnelle Benetzung des metallischen Substrats, was die Verdampfung von $MoO_3$ verhindert [9]. Die Abbildung 3(b) zeigt exemplarisch thermogravimetrische Kurven, die während der Oxidation der Legierung Mo-9Si-8B bei Temperaturen zwischen 1000°C und 1300°C aufgenommen wurden. Nach einer kurzen Phase der Übergangsoxidation, die durch einen starken Masseverlust infolge der Verdampfung von $MoO_3$ von den oberflächennahen Bereichen des Substrats gekennzeichnet ist, beginnt die stationäre Phase der Oxidation, die durch geringe Oxidationsraten geprägt ist. Bei Temperaturen oberhalb von 1200°C findet eine verstärkte Verdampfung von $B_2O_3$ statt, die wiederum signifikante Masseverluste verursacht (s. Abbildung 3(b)). Da die Ausbildung einer schützenden Borsilikatdeckschicht wegen verlangsamter Diffusionsprozesse unterhalb von 1000°C stark gehemmt ist, kann keine wirksame Barriere zwischen dem metallischen Substrat und der Gasphase aufgebaut werden. Dies ermöglicht den ungehinderten kontinuierlichen Zugang des Sauerstoffs zum Metall und somit die chemische Reaktion zwischen Sauerstoff und Molybdän, was wiederum starke Abdampfraten vom gasförmigen $MoO_3$ zur Folge hat. So beläuft sich die absolute Masseabnahme der Legierung Mo-9Si-8B auf den enorm hohen Wert von ~ 95 $mg/cm^2$ nach 72-stündiger Oxidation an Luft bei 820°C [9].

### 3.3 Effekt des Makrolegierens auf die Mikrostruktur und das Oxidationsverhalten

Da die Oxidationsbeständigkeit von Hochtemperaturlegierungen auf der Ausbildung schützender Oxidschichten wie $Cr_2O_3$, $Al_2O_3$ und $SiO_2$ beruht, spielt die Konzentration der oxidschichtbildenden Elemente Cr, Al und Si eine wichtige Rolle. So wurde der Effekt des Cr-Gehalts auf das Oxidationsverhalten von Legierungen Co-17Re-XCr-2Si (X = 23, 25, 27, 30 Atom-%) bei 1000°C und 1100°C untersucht [4, 6]. Es wurde festgestellt, dass eine minimale Cr-Konzentration von 25 Atom-% notwendig ist, um die Ausbildung einer kontinuierlichen $Cr_2O_3$-Schicht bei 1000°C zu ermöglichen (s. Abbildung 4). Das Makrolegieren der Referenzlegierung Co-17Re-23Cr mit Al zielte auf die Ausbildung einer schützenden $Al_2O_3$-Schicht ab [9]. Die experimentellen Ergebnisse zeigen bei 900°C und 1000°C, dass die Zugabe von 10 Atom-% Al die Ausbildung einer hochschützenden Schicht, bestehend aus einer $Cr_2O_3$- und einer darunterliegenden $Al_2O_3$-Schicht, ermöglicht. Bei tieferen und höheren Auslagerungstemperaturen konnte allerdings keine der beiden schützenden Deckschichten beobachtet werden [9]. Die Zugabe von Al zum System Co-Re-Cr hat zudem einen wesentlichen negativen Nebeneffekt. Die in der hexagonal dichtest gepackten (hdp) Matrix eingebettete σ-Phase (helle Phase in der Abbildung 4), die grundsätzlich einen schlechten Oxidationswiderstand aufweist, nimmt mit steigendem Al-Gehalt massiv zu. Grobe Ausscheidungen der σ-Phase beeinträchtigen sowohl die Oxidationsbeständigkeit dieses Legierungssystems als auch die mechanischen Eigenschaften. Aus diesem Grunde wurde die Entwicklung Al-haltiger Co-Re-Basislegierungen nicht weiterverfolgt.

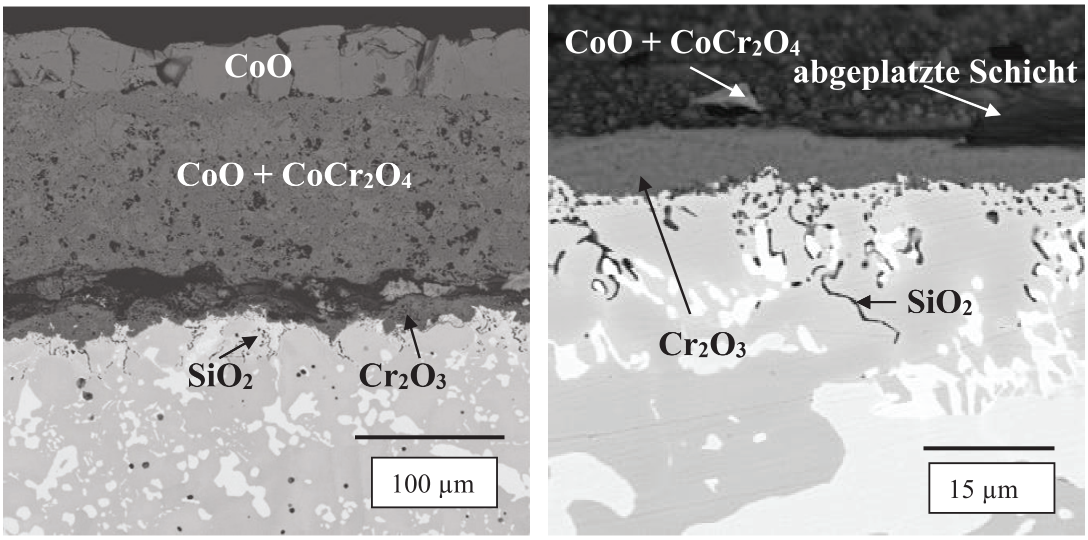

(a) (b)

Abbildung 4: REM-Aufnahmen zum Oxidschichtaufbau der Legierungen (a) Co-17Re-23Cr-2Si und (b) Co-17Re-25Cr-2Si nach der Oxidation an Luft bei 1000°C für 100h, nach [4]

Eine Verfeinerung der σ-Phase in den Co-Re-Basislegierungen konnte durch das Makrolegieren mit Ni erzielt werden. Während die Referenzlegierung Co-17Re-23Cr ein ausgeprägtes zweiphasiges Gefüge, bestehend aus der hdp-Phase und der σ-Phase aufweist, zeigt die Legierung Co-17Re-23Cr-15Ni eine nahezu homogene hdp-Mikrostruktur mit extrem feinen Ausscheidungen an σ-Phase (s. Abbildung 5). Das dramatisch verbesserte Oxidationsverhalten der Ni-haltigen Legierung ist in der homogenen Mikrostruktur, einer höheren Cr-Diffusion in der hdp-Matrix und der daraus resultierenden schnelleren Ausbildung einer $Cr_2O_3$-Deckschicht begründet [11].

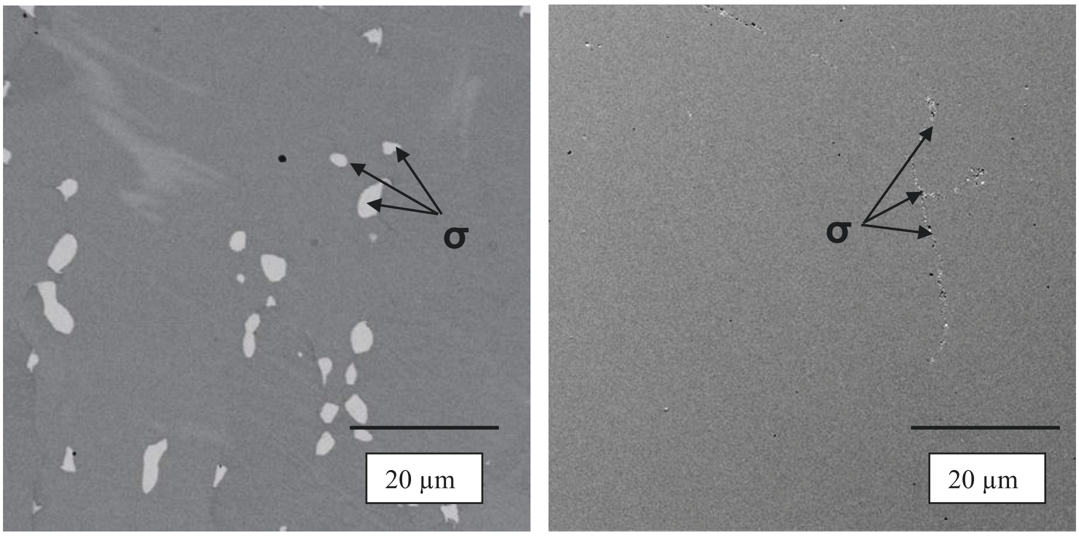

(a) (b)

Abbildung 5: Mikrostruktur der Legierungen (a) Co-17Re-23Cr und (b) Co-17Re-23Cr-15Ni nach dreistufiger Wärmebehandlung (1350°C/5h, 1400/5h, 1450°C/5h), nach [11].

Das Makrolegieren ruft in zwei weiteren Legierungssystemen ebenso signifikante Änderungen in der Legierungsmikrostruktur sowie im Oxidationsverhalten hervor. Eine partielle Substitution von Mo durch Ti in Mo-basierten Legierungen führt zur Stabilisierung der oxidationsresistenten Phase $(Mo,Ti)_5Si_3$ [2] auf Kosten der Si-armen $Mo_3Si$-Phase, die im weiten Temperaturbereich von 820-1300°C ein katastrophales Oxidationsverhalten aufweist [Ros2009]. Experimentell wurde nachgewiesen, dass das Makrolegieren mit Ti eine Verbesserung sowohl der mechanischen Eigenschaften durch die Ausbildung feiner Ti-reicher Silizide, die die Kriechfestigkeit der Legierungen wesentlich erhöhen [7, 13] als auch der Oxidationsresistenz durch die Ausbildung einer Duplexschicht $SiO_2$-$TiO_2$ zur Folge hat [5, 13].

Auch in HEAs verursacht das Makrolegieren gravierende Änderungen in der Mikrostruktur und im Oxidationswiderstand. So führt die Substitution des refraktären Metalls W durch das refraktäre Metall Nb in der äquimolaren Legierung W-Mo-Cr-Ti-Al zu veränderten Mikrostrukturen [14, 15] und Oxidationsmechanismen [10, 16, 18]. Beide Legierungen zeigen eine moderate Oxidationsresistenz bei 1000°C, da sich neben dünnen, relativ schützenden Deckschichten auch dicke und poröse Oxidschichten ausbilden (s. Abbildung 6(a)). Es sei angemerkt, dass die Legierung Nb-Mo-Cr-Ti-Al ein im Vergleich zur W-haltigen Legierung höheres Potential zur Verbesserung der Oxidationsbeständigkeit, z. B. durch Mikrolegieren mit Si, besitzt [16].

Obwohl die refraktären HEAs eine weitgehend neue Werkstoffklasse darstellen, wurden bereits erste bedeutsame Fortschritte hinsichtlich der Verbesserung der Oxidationsbeständigkeit von refraktären HEAs durch das Makrolegieren mit Ta erzielt. So zeigt die Legierung Ta-Mo-Cr-Ti-Al eine parabolische Massezunahme bei 1000°C und 1100°C, die ein

Indiz für die Ausbildung einer schützenden und langsam wachsenden Deckschicht ist [18]. Abbildung 6(b) zeigt Ergebnisse mikrostruktureller Untersuchungen oxidierter Proben der Legierung Ta-Mo-Cr-Ti-Al bei 1000°C, die die Ausbildung einer dünnen kontinuierlichen $Al_2O_3$-Schicht bestätigen [18].

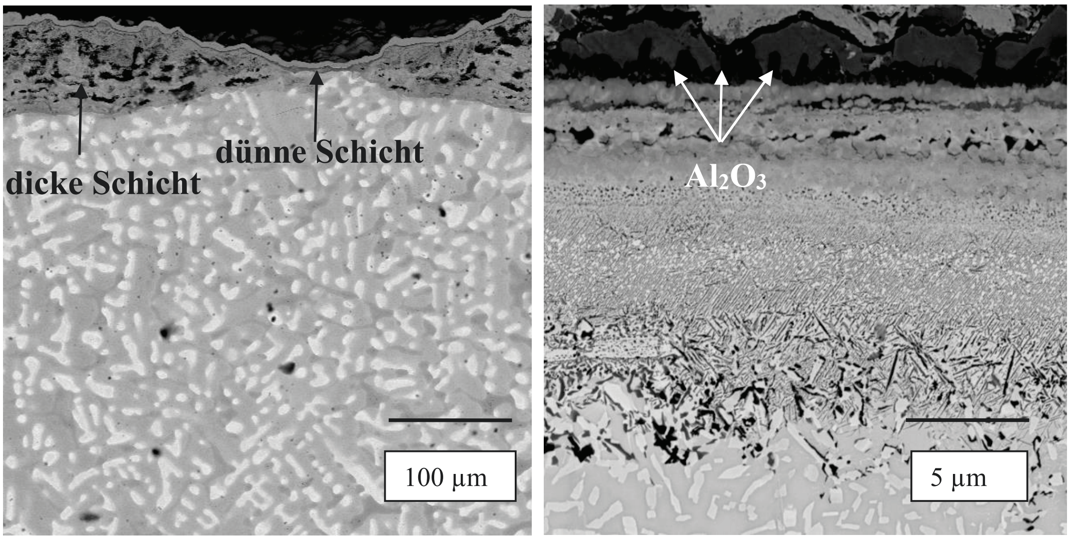

(a) (b)

Abbildung 6: Querschliffaufnahmen oxidierter äquimolarer HEAs nach der Oxidation an Luft bei 1000°C für 48h (a) W-Mo-Cr-Ti-Al und (b) Ta-Mo-Cr-Ti-Al, nach [18]

### 3.4 Effekt des Mikrolegierens auf die Oxidationsresistenz

Es ist allgemein bekannt, dass legierungstechnische Maßnahmen in Form der Zugabe von Si in Konzentrationen bis 3 Atom-% zu einer deutlichen Verbesserung der Oxidationsresistenz in konventionellen Nickelbasislegierungen führen [Li2006]. Chrom und Silizium wirken synergetisch, so dass die Bildung einer $Cr_2O_3$-Schicht bereits bei niedrigen Cr-Konzentrationen erfolgen kann, wenn die Legierung wenige Atom-% Si enthält. Der positive Effekt der Si-Zugabe wurde in zwei untersuchten Systemen experimentell nachgewiesen, nämlich in Co-Re-Basislegierungen und in HEAs. Die Oxidationsresistenz der Mo-Basislegierungen beruht, wie oben erläutert, ausschließlich auf der Ausbildung einer amorphen Borsilikatschicht.

Abbildung 7(a) zeigt tendenziell die positive Wirkung der Si-Zugabe zu der Referenzlegierung Co-17Re-23Cr. Die Abdampfrate nimmt sukzessiv mit dem steigenden Si-Gehalt ab und lässt auf einen klaren positiven Effekt von Si auf die Oxidationskinetik, im Sinne einer Abnahme der Oxidationsgeschwindigkeit, schließen. Mikrostrukturelle Untersuchungen oxidierter Proben zeigten, dass die Ausbildung von kompaktem $Cr_2O_3$ durch die Si-Zugabe begünstigt wird [1]. Einen ähnlichen Effekt der Si-Zugabe zu dem äquimolaren Werkstoff Nb-Mo-Cr-Ti-Al zeigt die Abbildung 7(b) [16]. Während die Si-freie Legierung kontinuierlich nach dem linearen Zeitgesetz bei 1000°C oxidiert, wird bei der Si-haltigen Legierung ein ausgeprägter Bereich der parabolischen Oxidation beobachtet. Die mikrostrukturellen Untersuchungen der Oxidschichten zeigen, dass der Bereich der parabolischen Oxidation auf die Ausbildung einer Al-reichen Oxidschicht zurückzuführen ist [16]. Die auf der Si-freien Legierung Nb-Mo-Cr-Ti-Al ausgebildeten Schichten sind größtenteils dick, porös und bieten dementsprechend einen geringeren Oxidationsschutz.

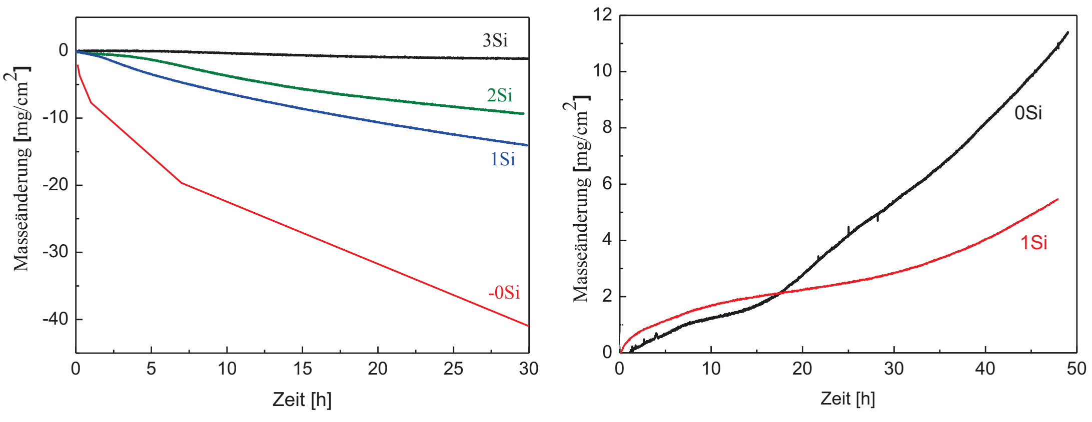

(a) (b)

Abbildung 7: Masseänderung der Legierungen (a) Co-17Re-23Cr-XSi (X=0, 1, 2, 3), nach [1] und (b) Nb-Mo-Cr-Ti-Al-XSi (X=0, 1) nach [16] während der isothermen Oxidation an Luft bei 1000°C

In Molybdänbasislegierungen wurde der Effekt des Mikrolegierens anhand der Zugabe der reaktiven Elemente Y und La untersucht [3, 8]. Es wurde festgestellt, dass das Mikrolegieren mit bis zu 2 Atom-% La die Oxidationsresistenz dieses Legierungssystems in einem beschränkten Temperaturbereich von 750°C-1000°C verbessert [8]. Das Mikrolegieren mit 0.2 Atom-% Y führte zur deutlichen Erhöhung des Oxidationswiderstandes während der Oxidation bei moderaten Temperaturen bis 1000°C. Dies ist primär auf die erhöhte Keimbildungsrate von $SiO_2$ begründet, die im Vergleich zu den Y-freien Mo-Basislegierungen eine schnellere Ausbildung der schützenden Deckschicht ermöglicht [3].

## 4 Maßnahmen zur Verbesserung der Oxidationsresistenz

In dieser Arbeit wurden Forschungsergebnisse zum Thema „Hochtemperaturoxidationsverhalten refraktärmetallbasierter Werkstoffe“ für Molybdänbasislegierungen, deren chemische Zusammensetzung durch Makrolegieren mit Ti im Vergleich zu den recht gut erforschten Mo-Si-B-Legierungen erheblich geändert wurde, sowie für zwei neue Werkstoffsysteme, Co-Re-Basislegierungen und refraktäre HEAs, zusammengefasst. Abbildung 8 zeigt parabolische Oxidationskonstanten der Ta-haltigen HEA im Vergleich zu den Oxidationskonstanten von Nickelbasislegierungen, die $Cr_2O_3$- oder $Al_2O_3$-Schichten bilden. Die Oxidationsraten von Nickelbasissuperlegierungen sind als Zielvorgabe in Abbildung 8 dargestellt. Die dargestellten Ergebnisse zeigen, dass die Oxidationsbeständigkeit der Ta-Mo-Cr-Ti-Al-HEA bereits das Niveau von Nickelbasislegierungen, die eine schützende $Cr_2O_3$-Schicht bilden, erreicht. Es kann daher geschlussfolgert werden, dass die in dieser Arbeit untersuchten refraktärmetallbasierten Werkstoffe ein hohes Potenzial bei erfolgreicher Weiterentwicklung für einen zukünftigen Einsatz in Hochtemperaturanwendungen besitzen.

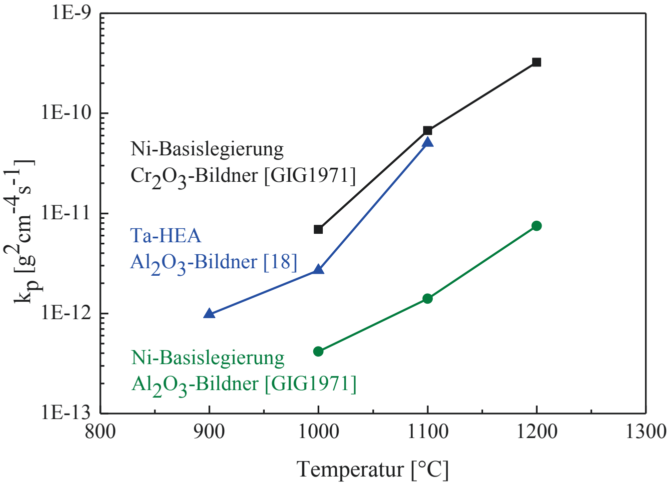

Abbildung 8: Vergleich der parabolischen Oxidationskonstanten von Ta-HEA mit Literaturdaten zu Nickelbasislegierungen.

Das Augenmerk der zukünftigen Forschungsarbeiten sollte auf die interdisziplinäre Grundlagenforschung gerichtet werden, um die beste Kombinationen aus den für die Hochtemperaturanwendungen relevanten Werkstoffeigenschaften wie Kriechfestigkeit, Duktilität bei Raumtemperatur, Oxidationswiderstand etc. zu erzielen. Im Hinblick auf die Erhöhung des Oxidationswiderstands refraktärmetallbasierter Legierungen sollen sowohl extensive experimentelle Untersuchungen, als auch grundlegende theoretische Analysen des Werkstoffes vor und nach einer Oxidation in diversen atmosphärischen Bedingungen durchgeführt werden. Wie die oben dargestellten Ergebnisse zeigen, wird das Oxidationsverhalten durch die chemische Zusammensetzung und die anfängliche Mikrostruktur des Werkstoffes stark beeinflusst. Um die Eigenschaften des Werkstoffes und seine Eignung für den Hochtemperatureinsatz in erster Näherung zu beurteilen, sind thermodynamische Daten zu den relevanten Phasen sowie Diffusionsdaten von metallischen Komponenten und gelösten Gaskomponenten im Werkstoff notwendig. Diese erlauben, die Phasenstabilität und somit die Mikrostrukturentwicklung im technischen Betrieb abzuschätzen. Darüber hinaus sind solche Daten unentbehrlich, um eine gezielte Optimierung der chemischen Zusammensetzung durch Mikro- und Makrolegieren durchzuführen.

Ergebnisse aus den Oxidationsexperimenten liefern die erforderlichen Daten zur Oxidationskinetik und den ausgebildeten Korrosionsprodukten, die umfassend charakterisiert werden müssen. Die systematische Variation der Einflussparameter wie Temperatur, Gaszusammensetzung, Probengeometrie etc. dient dazu, die Oxidationsmechanismen im Detail nachzuvollziehen, um im Weiteren den Oxidationswiderstand durch die gezielte Änderung der Werkstoffzusammensetzung signifikant zu erhöhen. Die sich während der Oxidation ausbildenden Korrosionsprodukte können durch thermodynamische Gleichgewichtsberechnungen hinsichtlich ihrer Stabilität und damit bezüglich der Wahrscheinlichkeit und des Ortes ihres Auftretens vorausgesagt werden.

Da die Betriebszeit vieler technischer Bauteile durch starke Korrosionsangriffe limitiert ist, werden Hochtemperaturoxidationsprozesse oft mit Hilfe numerischer Methoden simuliert.

Dies erfolgt in der Regel durch die numerische Lösung der Diffusionsgleichungen unter Einbeziehung thermodynamischer Daten. Da Oxidationsexperimente, insbesondere die Langzeitversuche, oft mehrere tausend Stunden dauern können, werden numerische Simulationen genutzt, um die Lebensdauer technischer Komponenten abzuschätzen. Die numerischen Simulationen führen zu einer enormen zeitlichen und materiellen Ersparnis, ergänzen sinnvoll die experimentellen Arbeiten und bilden somit die Basis für die erfolgreiche Entwicklung neuartiger Werkstoffe. Das in Abbildung 9 dargestellte Diagramm fasst die oben beschriebenen einzelnen Teilaufgaben zusammen und unterstreicht den starken Zusammenhang zwischen den theoretischen und experimentellen Untersuchungen, die für eine umfassende Charakterisierung des Oxidationsverhaltens und somit für eine erfolgreiche Entwicklung neuartiger rafraktärmetallbasierter Werkstoffe mit einem verbesserten Oxidationswiderstand unentbehrlich sind.

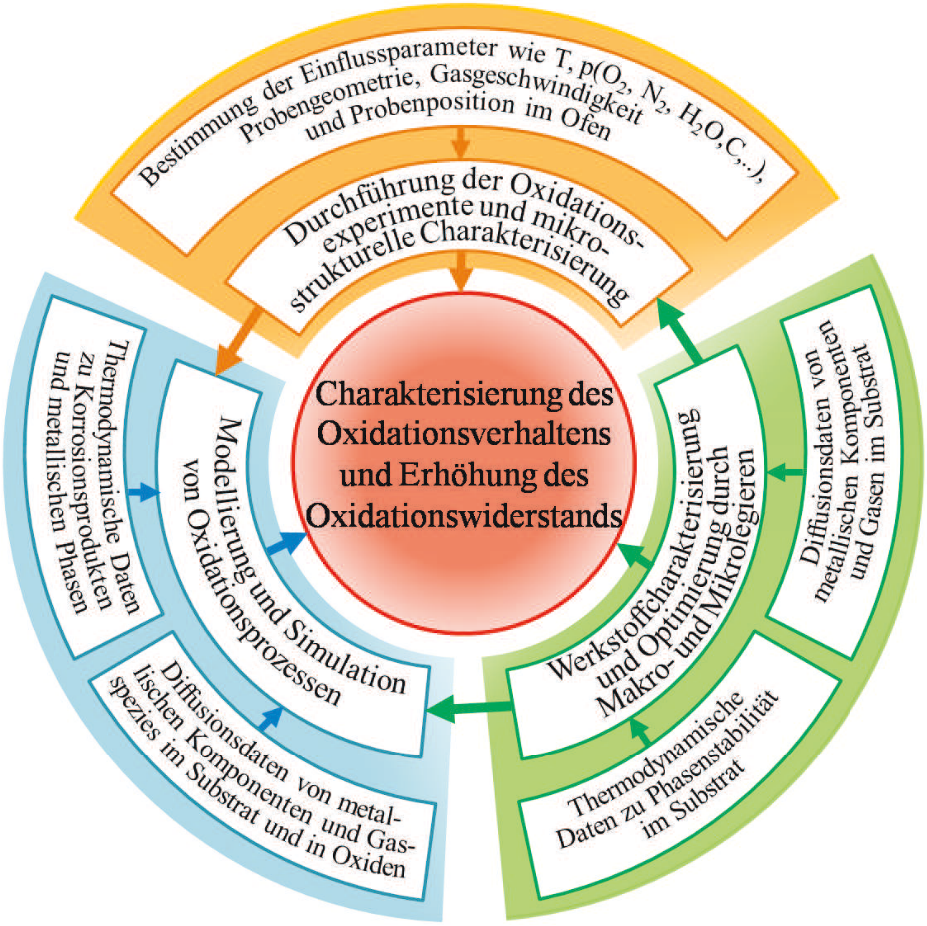

Abbildung 9: Schematische Darstellung einzelner Teilaufgaben zusammen mit erforderlichen Daten für die Charakterisierung des Oxidationsverhaltens neuartiger refraktärer Werkstoffe

# 5 Literaturverzeichnis

[BEW2003] B.P. Bewlay, M.R. Jackson, J.C. Zhao, P.R. Subramanian, M.G. Mendiratta, J.J. Lewandowski: Ultrahigh-temperature Nb-silicide-based composites, Materials Research Society, 28 (2003) 646-653

[BRU2010] M. Brunner, R. Hüttner, M.C. Bölitz, R. Völkl, D. Mukherji, J. Rösler, T. Depka, C. Somsen, G. Eggeler, U. Glatzel: Creep properties beyond 1100°C and microstructure of Co-Re-Cr alloys, Material Science and Engineering A, 528 (2010) 650-656

[BUR2011] S. Burk, Hochtemperaturoxidation Molybdän-basierter Legierungen unter Berücksichtigung von Einflüssen aus Umgebungsatmosphäre und legierungstechnischen Maßnahmen, Dissertation, Siegen, Siegener Werkstoffkundliche Berichte, Band 1/2011

[CAR2008] F. Cardarelli: Materials handbook, Springer-Verlag London Limited, 2008

[DAO2015] H.M. Daoud, A.M. Manzoni, R. Völkl, N. Wanderka, U. Glatzel: Oxidation behavior of Al8Co17Cr17Cu8Fe17Ni33, Al23Co15Cr23Cu8Fe15Ni15, and Al17Co17Cr17Cu17Fe17Ni17 compositionally complex alloys (high-entropy alloys) at elevated temperature in air, Advanced Engineering Materials, 17 (2015) 1134-1141

[DEP2009] T. Depka, C. Somsen, G. Eggeler, D. Mukherji, J. Rösler, M. Krüger, H. Saage, M. Heilmaier: Microstructure of Co-Re-Cr, Mo-Si and Mo-Si-B high-temperature alloys, Materials Science and Engineering A, 510-511 (2009) 337-341

[GEY1961] N.M. Geyer: Protection of refractory metals against atmospheric environments, Directorate of Materials and Processes, ASD, 1961, http://contrails.iit.edu/DigitalCollection/1961/ASDTR61-322article07.pdf. Zugriff am 28.06.2016

[GIG1971] C.S. Giggins and F.S. Pettit: Oxidation of Ni-Cr-Al alloys between 1000°C and 1200°C, Journal of Electrochemical Society: Solid State Science, 118 (1971) 1782-1790

[GOR2009] B. Gorr, V. Trindade, S. Burk, H.-J. Christ, M. Klauke, D. Mukherji, J. Rösler: Oxidation behaviour of model cobalt-rhenium alloys during short-term exposure to laboratory air at elevated temperature, Oxidation of Metals, 71 (2009) 157-172

[GUO2011] S. Guo, C.T. Liu: Phase stability in high entropy alloys: Formation of solid-solution phase or amorphous phase, Progress in Natural Science: Materials International, 21 (2011) 433-446

[HEI2009] M. Heilmaier, M. Krüger, H. Saage, J. Rösler, D. Mukherji, U. Glatzel, R. Völkl, R. Hüttner, G. Eggeler, C. Somson, T. Depka, H.-J. Christ, B. Gorr, S.

Burk: Metallic materials for structural applications beyond nickel-based superalloys, JOM 61 (2009) 61-67

[HUA2006] L. Huang, X.F. Sun, H.R. Guan, Z.Q. Hu: Oxidation behavior of the single-crystal Ni-base superalloy DD32 in air at 900, 1000, and 1100°C, Oxidation of Metals 65, (2006) 391-408

[KLO1969] W. Klopp: Recent development in chromium and chromium alloys, Lewis Research Center Cleveland, Ohio, National Aeronautics and Space Administration, 1969, http://ntrs.nasa.gov/archive/nasa/casi.ntrs.nasa.gov/19690026386.pdf. Zugriff am 28.06.2016

[KOF1988] P. Kofstad: High temperature corrosion, Elsevier Applied Science, London, 1988

[LI2006] B. Li, B. Gleeson: Effects of silicon on the oxidation behavior of Ni-base chromia forming alloys, Oxidation of Metals, 65 (2006) 101-122

[NOV1957] H. Novotny, E. Dimakopoulou, H. Kudielka: Untersuchungen in den Dreistoffsystemen: Molybdän-Silizium-Bor, Wolfram-Silizium-Bor und in dem System $VSi_2$-$TaSi_2$, Monatshefte Chemie 88 (1957) 180-192

[PER2009] J.H. Perepezko: The hotter the engine the better, Science, 326 (2009) 1068-1069

[RÖS2007] J. Rösler, D. Mukherji, T. Baranski: Co-Re-based alloys: A new class of high temperature materials?, Advanced Engineering Materials 9 (2007) 876-881

[ROS2009] I. Rosales, H. Martinez, D. Bahena, J.A. Ruiz, R. Guardian, and J. Colin: Oxidation performance of $Mo_3Si$ with Al additions, Corrosion Science, 51 (2009) 534-38

[SAK2008] R. Sakidja, J.H. Perepezko, S. W. Kim, N. Sekido: Phase stability and structural defects in high-temperature Mo-Si-B alloys, Acta Materialia 56 (2008) 5223-5244

[SCH1999] J.H. Schneibel, C.T. Liu, D.S. Easton, C.A. Carmichael: Microstructure and mechanical properties of Mo-Mo3Si-Mo5SiB2 silicides, Material Science and Engineering A 261 (1999) 78-83

[SEN2014] O.N. Senkov, C. Woodward, D.B. Miracle: Microstructure and properties of aluminium-containing refractory high-entropy alloys, JOM, 66 (2014) 2030-2042

[SYR1961] R. Syre: Niobium, molybdenum, tantalum and tungsten: A summary of their properties with recommendation for research and development, North Atlantic Treaty Organization, Advisory group for aeronautical research and development, 1961, http://www.dtic.mil/dtic/tr/fulltext/u2/274036.pdf , Zugriff am 26.06.2016

[TIE1965] T.E. Tietz, J.W. Wilson: Behavior and properties of refractory metals, Edward Arnold LTD, London, 1965

[TON2005] C.J. Tong, M.R. Chen, S.K. Chen, J.W. Yeh, T.T. Shun, S.J. Lin, S.Y. Chang: Mechanical performance of the AlCoCrCuFeNi high-entropy alloy system with multiprincipal elements, Metallurgical and Materials Transactions A, 36A, (2005) 1263-1271

[YEH2007] J.W. Yeh, Y.L. Chen, S.J. Lin, S.K. Chen: High-entropy alloys – a new era of exploitation, Materials Science Forum, 560 (2007) 1-9

[YOU2008] D. Young: High temperature oxidation and corrosion of metals, Elsevier, Oxford, 2008

## Publikationsliste

[1] B. Gorr, S. Burk, T. Depka, Ch. Somsen, H. Abu-Samra, and H.-J. Christ, G. Eggeler: Effect of Si-addition on the oxidation resistance of Co-Re-Cr-Alloys: Recent attainments in the development of novel alloys, International Journal of Material Reseach*,* 1 (2012) 24-30

[2] S. Burk, B. Gorr, H.-J. Christ, D. Schliephake, M. Heilmaier, C. Hochmuth and U. Glatzel: High-temperature oxidation behavior of a single-phase (Mo,Ti)$_5$Si$_3$ (Mo-Si-Ti) alloy, Scripta Materialia, 66 (2012) 223-226

[3] S. Majumdar, D. Schliephake, B. Gorr, H.-J. Christ, and M. Heilmaier: Effect of yttrium alloying on intermediate to high-temperature oxidation behavior of Mo-Si-B alloys, Metallurgical and Materials Transactions, A 44 (2013) 2013-2243

[4] L. Wang, B. Gorr, H.-J. Christ, D. Mukherji, J. Rösler: Optimization of Cr-content for high-temperature oxidation behavior of Co-Re-Si-base alloys, Oxidation of Metals, 80 (2013) 49-59

[5] M. Azim, S. Burk, B. Gorr, H.-J. Christ, D. Schliephake, M. Heilmaier, R. Bornemann, P.H. Bolivar: Effect of Ti (macro-) alloying on the high-temperature oxidation behavior of ternary Mo-Si-B alloys at 820-1300°C, Oxidation of Metals, 80 (2013) 231-242

[6] B. Gorr, H.-J. Christ, D. Mukherji, J. Rösler: Thermodynamic calculations in the development of high-temperature Co-Re-based alloys, Journal of Alloys and Compounds 582 (2014) 50-58

[7] D. Schliephake, M. Azim, K. von Klinski-Wetzel, B. Gorr, H.-J. Christ, H. Bei, E.P. George, M. Heilmaier: High-temperature creep and oxidation behavior of Mo-Si-B alloys with high Ti contents, Metallurgical and Materials Transactions A, 45A (2014) 1102-1111

[8] S. Majumdar, B. Gorr, H.-J. Christ, D. Schliephake, M. Heilmaier: Oxidation mechanisms of lanthanum-alloyed Mo-Si-B, Corrosion Science, 88 (2014) 360-371

[9] B. Gorr, L. Wang, S. Burk, M. Azim, S. Majumdar, H.-J. Christ, D. Mukherji, J. Rösler, D. Schliephake, M. Heilmaier: High-temperature oxidation behavior of Mo-Si-B-based and Co-Re-Cr-based alloys, Intermetallics, 48 (2014) 34-43

[10] B. Gorr, M. Azim, H.-J. Christ, T. Mueller, D. Schliephake, M. Heilmaier: Phase equilibria, microstructure, and high temperature oxidation resistance of novel refractory high-entropy alloys, Journal of Alloys and Compounds, 624 (2015) 270-278

[11] L. Wang, B. Gorr, H.-J. Christ, J. Rösler: The effect of alloyed nickel on the short-term high temperature oxidation behaviour of Co-Re-Cr-based alloys, Corrosion Science, 93 (2015) 19-26

[12] L.Wang, B. Gorr, H.-J. Christ, D. Mukherji, J. Rösler, Microstructure and oxidation mechanism evolution of Co-17Re-25Cr-2Si in the temperature range 800-1100°C, Oxidation of Metals, 83 (2015) 465-483

[13] M. Azim, D. Schliephake, C. Hochmuth, B. Gorr, H.-J. Christ, U. Glatzel, M. Heilmaier: Creep resistance and oxidation behavior of novel Mo-Si-B-Ti alloys, JOM, 67 (2015) 2621-2628

[14] H. Chen, A. Kauffmann, B. Gorr, D. Schliephake, C. Seemüller, J.N. Wagner, H.-J. Christ, M. Heilmaier.: Microstructure and mechanical properties at elevated temperatures of a new Al-containing refractory high-entropy alloy Nb-Mo-Cr-Ti-Al, Journal of Alloys and Compounds, 661 (2016) 206-215

[15] B. Gorr, M. Azim, H.-J. Christ, H. Chen, D.-V. Szaboo, A. Kauffmann, M. Heilmaier: Microstructure evolution in an new refractory high-entropy alloy W-Mo-Cr-Ti-Al, Metallurgical and Materials Transactions A, 47A (2016) 961-970

[16] B. Gorr, F. Mueller, H.-J. Christ, T. Mueller, H. Chen, A. Kauffmann, M. Heilmaier, High temperature oxidation behavior of an equimolar refractory metal-based alloy 20 Nb-20Mo-20Cr-20Ti-20Al with and without Si addition, Journal of Alloys and Compounds, 688 (2016) 468-477

[17] M. Azim, B. Gorr, H.-J. Christ, M. Heilmaier: Characterization of oxidation kinetics of Mo-Si-B-based materials, eingereicht

[18] B. Gorr, F. Müller, M. Azim, H.-J. Christ, T. Müller, H. Chen, A. Kauffmann, M. Heilmaier: High temperature oxidation behavior of refractory high entropy alloys: Effect of alloy composition, eingereicht

# 6 Anhang

# Manuskript I

## Effect of Si-addition on the oxidation resistance of Co-Re-Cr-alloys: Recent attainments in the development of novel alloys

B. Gorr, S. Burk, T. Depka, Ch. Somsen, H. Abu-Samra, H.-J. Christ, G. Eggeler

International Journal of Material Research, 1 (2012) 24-30

Bronislava Gorr[a], Steffen Burk[a], Timo Depka[b], C. Somsen[b], Hisham Abu-Samra[a], H.-J. Christ[a], G. Eggeler[b]
[a] Institut fuer Werkstofftechnik, University Siegen, Siegen, Germany
[b] Institut fuer Werkstoffe, Ruhr-University Bochum, Bochum, Germany

# Effect of Si addition on the oxidation resistance of Co–Re–Cr-alloys: Recent attainments in the development of novel alloys

*Dedicated to Prof. Dr.-Ing. Christina Berger on the occasion of her 65th birthday*

The influence of silicon on the oxidation behaviour of Co–Re–Cr-alloys has been studied at 1 000 °C and 1 100 °C. Consideration was given to the synergetic effects between chromium and silicon with respect to the development of a protective $Cr_2O_3$ layer. The Si addition to the Co–Re-alloys produces a significant decrease in the evaporation rate of Re oxides. Moreover, the beneficial influence in the transient oxidation period results in a rapid formation of $Cr_2O_3$ scale. While the addition of 1 and 2 at.% Si to the ternary Co-17Re-23Cr alloy was insufficient to form a continuous $Cr_2O_3$ scale, the addition of 3 at.% silicon caused a change in the oxidation mode resulting in the formation of a nearly continuous $Cr_2O_3$ scale. On the oxide/alloy interface of the alloy Co-17Re-30Cr-2Si, a continuous and dense $Cr_2O_3$ scale was observed, which remained stable after 100 h exposure protecting the metallic substrate.

**Keywords:** Co–Re-based alloys; High-temperature oxidation; Evaporation Re-oxides; Alloy development

## 1. Introduction

The experimental Co–Re-based alloys were developed for high-temperature applications for service temperatures beyond 1 200 °C. The development of Co–Re-based alloys has been first proposed by Rösler et al. [1]. The obtained results show great promise for high temperature applications. Mechanical properties, such as creep resistance, were discussed by Brunner et al. [2]. Likewise, high-temperature oxidation resistance of Co–Re-based alloys is essential for applications as high-temperature structural materials. Earlier investigations of Co–Re–Cr model alloys have shown rather poor oxidation resistance during exposure to laboratory air due to evaporation of Re-oxides [3, 4]. Therefore, an important aim of Co–Re alloy development is to derive options for improvement of the oxidation resistance at very high temperatures. The majority of commercially available high-temperature alloys form a chromia scale. For this reason, chromium was added to the base Co–Re system to provide reliable protection against oxidation at intermediate temperatures (below 1 000 °C). However, a semicontinuous $Cr_2O_3$ scale forms on the oxide/alloy interface, which allows the evaporation of Re-oxides. It should be noted that the protective properties of $Cr_2O_3$ are increasingly reduced at temperatures above 1 000 °C because of the accelerated transformation of $Cr_2O_3$ to volatile $CrO_3$ [5]. Consequently, chromium alone will not provide sufficient oxidation protection at very high temperatures. Silicon was added to Co–Re-alloys in order to facilitate the formation of a continuous $SiO_2$ scale.

There are numerous studies on the effect of silicon in the oxidation behaviour of high-temperature alloys, which suggest ideas to explain the positive effect of Si in terms of high-temperature oxidation [6]. One of these generally accepted theories proposes that the presence of a certain Si-content in alloys reduces oxidation through the formation of an amorphous silica layer on the phase boundary alloy/oxide inhibiting the outward diffusion of metal cations to the outer oxide scale as well as the inward diffusion of oxygen anions. Liu et al. reported that a continuous silica sublayer formed at the oxide scale/metal interface on the austenitic matrix, acting as an effective diffusion barrier to metal outward diffusion resulting in a thin and uniform oxide scale [7]. Li and Gleeson investigated the Si effect on the oxidation behaviour of Ni-base chromia forming alloys with 2.7 wt.% silicon and without silicon [8]. It was summarized that Si addition improved the oxidation behaviour of the investigated alloys by forming a continuous $SiO_2$ layer at the alloy/scale interface. It was also found that Si influenced the interdiffusion coefficient of Cr in the alloy, $D_{Cr}^{eff}$ was found to be highest in an alloy that had the highest silicon content. However, there is a large thermal expansion coefficient mismatch between the amorphous silica layer and the metal substrate. During cyclic oxidation, the oxide scale may easily spall off the metal or crack at the oxide/scale interface owing to the brittle character of amorphous silica. Evans et al. investigated stainless steels and found that the extent of scale spallation increased with increasing Si-content [9].

Another popular theory suggests that Si acts as nucleation sites reducing the distance between the $Cr_2O_3$ nuclei and therefore reducing the transient-oxidation stage allowing the quick formation of a continuous protective layer. Baxter et al. [10] reported that silicon promotes formation and maintenance of a continuous $Cr_2O_3$ scale in austenitic Fe – Cr – Ni alloys. It was concluded that due to the low concentration of silicon in the alloy (compared to that of Cr, Fe, and Ni) and the relatively low growth rate of silica, the first formed $SiO_2$ nuclei are quickly overgrown by faster growing oxides, such as $Cr_2O_3$. However, it should be noted that a silicon content of at least 0.8 % reduced the rate of scaling by providing additional sites for the lateral growth of the $Cr_2O_3$ layer, which seems also to be true for the Ni-based systems. An addition of 2 at.% to Ni-10Cr-4Al was sufficient to prevent the growth of external NiO scale, but was insufficient to form external alumina at 1 000 °C. Only a further increase of the Si content was able to form an external $Al_2O_3$ scale as a result of the con-tribution of the internal precipitates of $SiO_2$ in combina-tion with $Al_2O_3$ under a chromia layer to reach the critical volume fraction of internal oxides required to stabilize this oxidation mode [11].

Stott et al. [12] investigated the influence of silicon on the oxidation behaviour of Fe-14Cr and Fe-28Cr with a particular emphasis on the development and nature of the $SiO_2$ layer. The healing $SiO_2$ scale was observed after short time for the alloy Fe-14Cr-10Si, which also showed the lowest growth rate. Examination of the oxidized specimen of the alloy Fe-26Cr-1Si indicated only a very small amount of internal silicon-rich precipitates after short exposure periods. However, the oxidation rate constant for the latter alloy was significantly lower than that for the corresponding binary iron–chromium alloy. Acting as a partial diffusion barrier during short exposure time, internal $SiO_2$-precipitates grew inwards and laterally until they eventually link up to establish a continuous healing layer, when the exposure period was extended beyond 100 h.

For the investigation on the Si effect on the oxidation behaviour of Co – Re-alloys, it is of interest to understand the influence of Si on the oxidation of Co-based alloys. Durham et al. pointed out the high sensitivity to the presence of Si impurities promoting the $Cr_2O_3$ scale formation on Co – Cr alloys during exposure in reduced oxygen partial pressure conditions in silica ampoules, which were considered as a source of Si contamination [13]. In the absence of silicon, chromium was not oxidized selectively, and scales of $CoCr_2O_4$ plus CoO grew relatively fast. When Si was present, chromium was oxidized selectively, leading to protective scales of $Cr_2O_3$ and $CoCr_2O_4$ with much slower reaction rates. Jones and Stringer reported that Si impurities (0.05 wt.%) in a Co-25Cr alloy was sufficient to change the mode of oxidation promoting the formation of the protective $Cr_2O_3$ scale [14].

The aim of the current investigation was to identify the mechanisms for the influence of Si additions on the scaling characteristics of Co – Re-based alloys under isothermal conditions. The experimental results were intended to provide some new insights, which are useful in developing a better material resistant to high-temperature corrosion.

## 2. Experimental procedures

Co – Re-based model alloys with different Si contents were investigated in this study in order to analyze the influence of Si concentration on the oxidation behaviour of these alloys. The chemical compositions of model the Co – Re-alloys are shown in Table 1.

Table 1. Chemical compositions of alloys studied.

| Alloy |
|---|
| Co-17Re-23Cr |
| Co-17Re-23Cr-1Si |
| Co-17Re-23Cr-2Si |
| Co-17Re-23Cr-3Si |
| Co-17Re-30Cr-2Si |

Samples with dimensions of $10 \times 10 \times 2\ mm^3$ with rounded edges to avoid the typical edge effect on oxidation were used for the thermogravimetric study. The samples were ground using SiC paper down to 1 200 grit and were cleaned ultrasonically in ethanol prior to oxidation. A hole of 1 mm diameter was drilled for hanging the samples using a Pt wire suspension. The surface area of each specimen was measured, in order to relate the mass change to this initial surface area. The continuous isothermal oxidation tests were carried out using a Sartorius microbalance with a resolution of $10^{-6}$ g in combination with an alumina tube reaction chamber surrounded by a SiC furnace. The oxidized samples were embedded in epoxy, ground and polished using diamond paste down to 1 μm as the last step of preparation. The morphology and composition of the oxide scales were analysed using scanning electron microscopy (SEM) in combination with energy-dispersive X-ray spectroscopy (EDS). X-ray diffraction (XRD) was used for phase identification. The specimen studied in the transmission electron microscope (TEM) was prepared using focused ion beam target preparation.

## 3. Results

Figure 1 compares the mass changes of the alloys based on Co-17Re-23Cr with different Si contents after 30 h exposure at 1 000 °C. The kinetics of these alloys is extensively influenced by volatilization of Re oxides. This phenomenon is typical for refractory alloys and also affected the kinetics of Co – Re-based alloys, which were investigated in previous studies [3, 4]. The addition of 1 at.% Si to the ternary alloy Co-17Re-23Cr produced a significant decrease in the mass loss by a factor of about 3, while increasing the Si

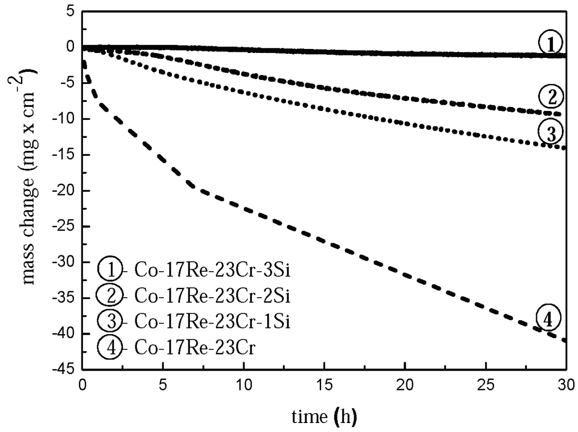

Fig. 1. Effect of Si addition to the system Co-17Re-23Cr-*x*Si on the mass change during oxidation in laboratory air for 30 h at 1 000 °C.

content to 2 and 3 at.% caused further decrease in the mass loss by a factor of about 1.5 for Co-17Re-23Cr-2Si and 7.8 for Co-17Re-23Cr-3Si.

Figure 2 shows the cross-sections of alloys Co-17Re-23Cr-1Si, Co-17Re-23Cr-2Si, and Co-17Re-23Cr-3Si after 7 h exposure to air at 1 100 °C. The oxide scale formed on the alloy Co-17Re-23Cr-1Si consists of outmost CoO with a coarse grain structure, porous Co – Cr-, and thin and semi-continuous Cr oxide on the oxide/substrate interface. This oxide structure was also detected in some areas on the surface of the alloy Co-17Re-23Cr-2Si, while other parts of the surface were covered by $Cr_2O_3$. A completely different oxide structure was found on the surface of the alloy Co-17Re-23Cr-3Si. The oxide scale consists of an outer Co – Cr-rich oxide and an inner Cr-rich oxide, the latter is nearly continuous. Internal precipitates of Si-rich oxide were found in all oxidized alloys. Obviously, the amount of internal precipitates increases with increasing Si content. Values of the amount of the linear density, which was proposed by Exner and Hougardy, were calculated and summarized in Table 2 [15].

Figure 3 shows the cross-section of a sample of the alloy Co-17Re-23Cr-3Si oxidized for 48 h. Characteristically for this exposure time is the formation of an inhomogeneous oxide scale on the surface. A part of the sample surface seems to be covered with a $Cr_2O_3$ scale, which is marked in Fig. 3. Some areas with completely different oxide structure were also found in the cross-section of the samples.

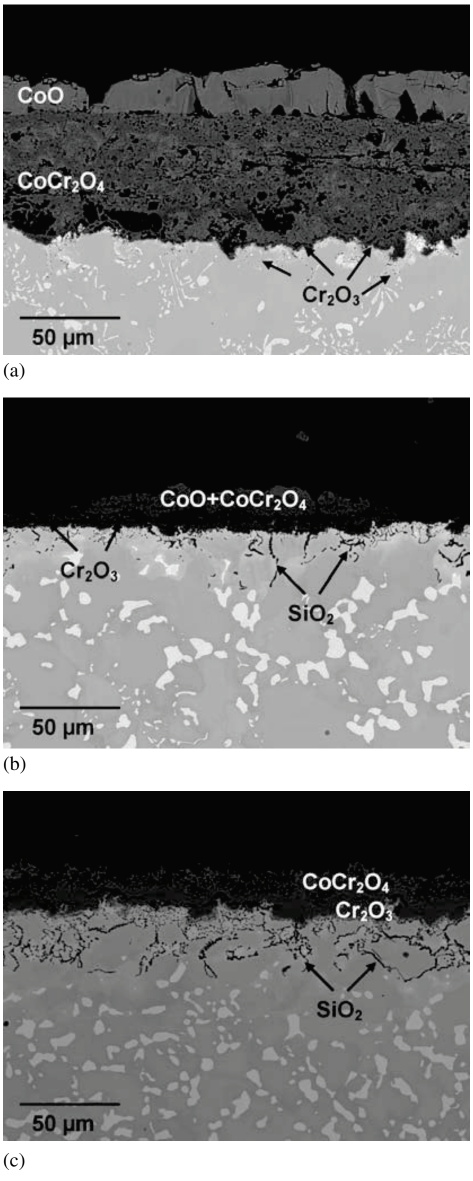

(a)

(b)

(c)

Fig. 2. Oxidation behaviour of model Co – Re-based alloys after 7 h exposure at 1 100 °C; (a) alloy Co-17Re-23Cr-1Si, (b) alloy 17Re-23Cr-2Si, and (c) alloy 17Re-23Cr-3Si.

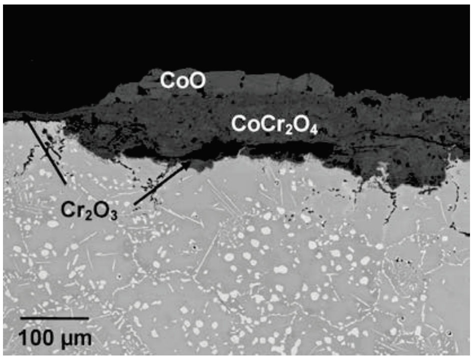

Fig. 3. Degradation of the $Cr_2O_3$ scale formed on the alloy Co-17Re-23Cr-3Si after 48 h exposure to air at 1 100 °C.

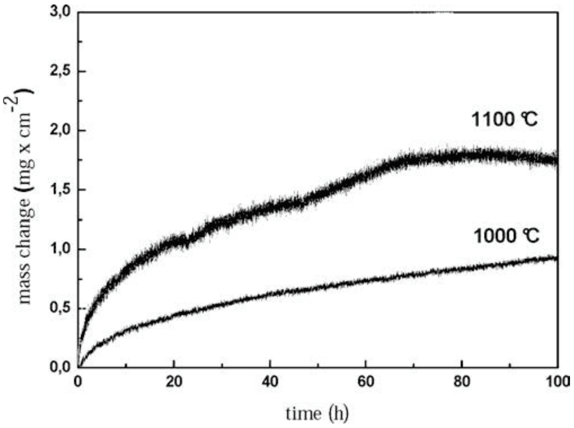

Fig. 4. Mass change of alloy Co-17Re-30Cr-2Si during exposure to laboratory air for 100 h at 1 000 °C and 1 100 °C.

Table 2. Amount of linear density of Si-rich internal precipitates measured in alloys with different Si contents.

| Alloy | Co-17Re-23Cr-1Si | Co-17Re-23Cr-2Si | Co-17Re-23Cr-3Si |
|---|---|---|---|
| Amount of linear density $N_L$ ($\mu m^{-1}$) | 0.025 | 0.07 | 0.2 |

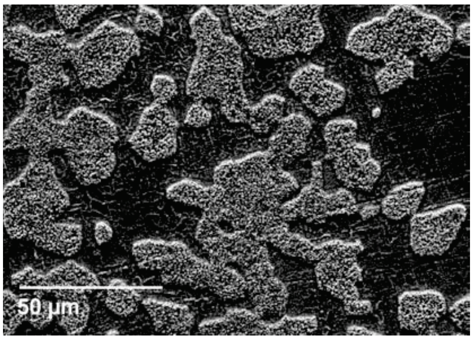

Fig. 5. Oxidized surface of the alloy Co-17Re-30Cr-2Si after 15 min exposure to air at 1 100 °C showing different oxides.

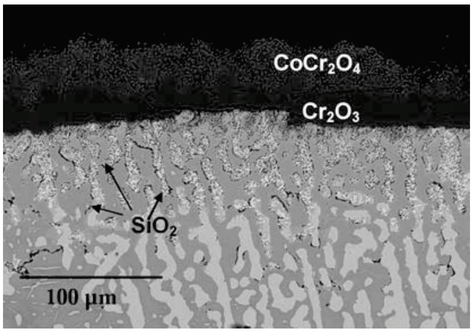

Fig. 6. Cross-section of the oxidized alloy Co-17Re-30Cr-2Si after 72 h exposure to air at 1 000 °C.

The morphology of these regions yielded an outmost CoO layer above a thick and porous Co – Cr oxide, which itself covers a semicontinuous Cr oxide film. Compared to the cross-section of the alloy Co-17Re-23Cr-3Si after 7 h exposure shown in Fig. 2c, it is clear that the $Cr_2O_3$ scale does not remain stable but degrades with increasing exposure time at 1 100 °C.

As a result of the increase in the chromium content in the alloy Co-17Re-*x*Cr-2Si from 23 at.% to 30 at.%, a slight mass gain was detected after exposure of this alloy to laboratory air for 100 h at 1 000 °C and 1 100 °C (see Fig. 4). The oxidation kinetics of the alloy Co-17Re-30Cr-2Si at 1 000 °C obeys the parabolic rate law, which indicates the formation of a protective oxide scale. Also, the oxidation kinetics at 1 100 °C shows a near-parabolic dependence.

The oxidized surfaces of the alloys studied yielded an inhomogeneous oxide structure indicating the formation of different oxide phases. Figure 5 shows representatively the oxidized surface of the alloy Co-17Re-30Cr-2Si after 15 min exposure at 1 100 °C. In order to identify the devel-

Table 3. Phases detected on the oxidized surface of the alloy Co-17Re-30Cr-2Si using XRD analysis.

| Exposure time | Phases |
|---|---|
| 7 min | CoO, $Co_3O_4$, $CoCr_2O_4$, $Cr_2O_3$ |
| 15 min | CoO, $Co_3O_4$, $CoCr_2O_4$, $Cr_2O_3$ |
| 30 min | CoO, $Co_3O_4$, $CoCr_2O_4$, $Cr_2O_3$ |
| 48 h | $CoCr_2O_4$, $Cr_2O_3$ |

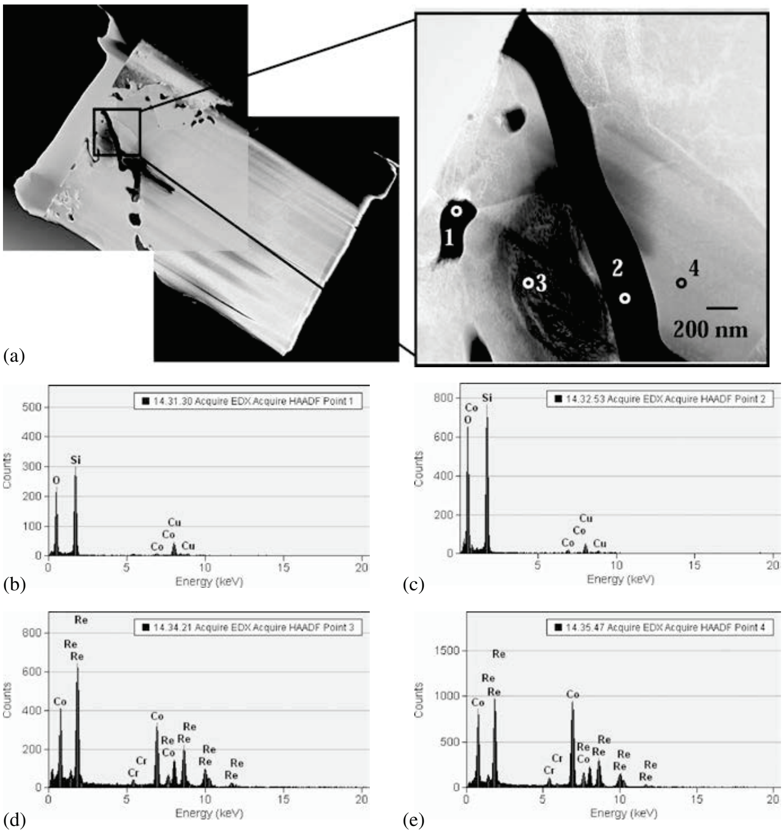

Fig. 7. TEM-analysis of the alloy Co-17Re-30Cr-2Si after 30 h exposure to air at 1 000 °C; (a) a lamella from the region of internal precipitates, (b) – (e) EDX analysis.

opment of the oxide scale, the oxides formed on the surface of the alloy Co-17Re-30Cr-2Si after different exposure times at 1 000 °C were analyzed using X-ray diffraction. The results are presented in Table 3.

Four different oxides, namely CoO, $Co_3O_4$, $CoCr_2O_4$ and $Cr_2O_3$, were detected on the oxidized surface of this alloy after short exposure periods (up to 30 min), while two oxides, $CoCr_2O_4$ and $Cr_2O_3$ were found after 48 h exposure. It is concluded that apart from transient Co-oxides, $Cr_2O_3$ and $CoCr_2O_4$ are the main oxides formed on the surface of the alloy Co-17Re-30Cr-2Si after prolonged exposure to air at 1 000 °C.

Based on the results of cross-section SEM micrographs of the alloy Co-17Re-30Cr-2Si it was confirmed that the $Cr_2O_3$ layer forms adjacent to the scale/metal interface, whereas $CoCr_2O_4$ forms the outer layer (see Fig. 6). A zone of internal precipitates exists underneath the $Cr_2O_3$ outer layer. It should be mentioned that the microstructure of this alloy exposed at 1 100 °C is very similar to that after exposure at 1 000 °C. However, the zone of internal precipitates was found to be slightly thicker at 1 100 °C. In order to identify the nature of internal precipitates, a lamella was cut from the oxidized specimen using focused ion beam and was analyzed in the transmission electron microscope (see Fig. 7).

Figure 7a shows the cut lamella with the marked region, which was analyzed in the transmission electron microscope, by means of EDX (Fig. 7b–e) of different points marked in Fig. 7a. It was found that points 1 and 2 reflect elements Si and O (small peaks of Cu related to the TEM Cu-grid), while points 3 and 4 reflect the main matrix elements.

## 4. Discussion

It is well-known that certain conditions, such as extremely high temperatures, presence of water vapour or high velocity of the flowing gas may interfere with the stability of oxide scales. Berthod investigated the volatilization of the external chromia layer formed by oxidation of an Ni-30Cr alloy at 1 000, 1 100, 1 200, and 1 300 °C [5]. It has been reported that volatile $CrO_3$ forms above 1 000 °C through the following reaction:

$$^1/_2\,Cr_2O_3(s) + {}^3/_4\,O_2(g) \leftrightarrow CrO_3(g) \qquad (1)$$

Numerous studies confirm that $Cr_2O_3$ evaporates at temperatures above 1 000 °C especially in the presence of water vapour [16, 17]. At high-temperatures, silica can also decompose into gaseous oxide, namely SiO, through the reaction

$$2\,SiO_2(s) \leftrightarrow 2\,SiO(g) + O_2(g) \qquad (2)$$

Figure 8 shows the calculated partial pressures of $CrO_3$ above $Cr_2O_3$ and SiO above $SiO_2$ at different temperatures. It is seen that the partial pressure of SiO is negligible compared to the partial pressure of gaseous $CrO_3$ in the whole temperature range. The presented comparison, i. e., thermodynamic stability of chromia and silica, explains the attempts to replace $Cr_2O_3$ through $SiO_2$ in Co–Re-based alloys, which were developed for service temperatures beyond 1 100 °C.

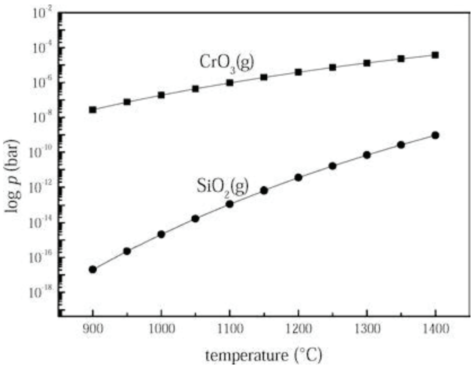

Fig. 8. Calculated partial pressure of $CrO_3$ above $Cr_2O_3$ and SiO above $SiO_2$ at different temperatures (calculated with FactSage).

Even though chromia evaporates at temperatures above 1 000 °C, chromium plays a very important role for Co–Re-based alloys in terms of high-temperature oxidation protection at moderate temperatures. Usually, high-temperature alloys for usage at temperatures below 1 100 °C contain high amounts (typically 18–30 wt.%) of the oxide-forming element Cr to protect the materials against rapid oxidation through the formation of a protective chromia scale. It is well-known that Cr and Si act synergetically. This implies that a lower content of Cr may be sufficient to produce a continuous $Cr_2O_3$ if the alloy contains sufficient Si. Kumar and Douglass studied the oxidation behaviour of austenitic Fe-14Cr-14Ni steels containing up to 4 wt.% Si [18]. The alloy without Si-addition formed a scale comprised of Fe- and Ni-rich oxides and internal precipitates of spinel oxides, while a continuous chromia layer formed on the surface of the alloy with 4 wt.% Si. This seems also to be the case for Co–Re–Cr alloys. Based on weight change measurements as well as cross-section SEM micrographs it is concluded that the Si addition causes a general change in the oxide scale microstructure and therefore in the oxidation mechanism. The alloys without or with a low Si content (1–2 at.%) and 23 at.% Cr form a scale including non-protective CoO and Co–Cr oxides as well as a discontinuous $Cr_2O_3$ layer, while a nearly continuous $Cr_2O_3$ scale was observed on the surface of the alloy Co-17Re-23Cr-3Si in the early phase of oxidation. However, the steady-state oxidation of this alloy yields the fast growth of CoO and $CoCr_2O_4$, which does not prevent the evaporation of Re oxides resulting in the rapid consumption of the base material. The damage mechanism of the $Cr_2O_3$ scale formed on the surface of the Co–Re–Cr alloys during exposure to an atmosphere with a low oxygen partial pressure was discussed previously [4].

The results obtained in this work allow us to state that the ratio Cr/Si plays a crucial role on the general change of the high-temperature oxidation behaviour in Co–Re-based alloys. In contrast to alloys with 23 at.% Cr and different Si concentrations, on the surface of the alloy Co-17Re-30Cr-2Si a continuous chromia layer was detected, which remains protective after 100 h exposure to air at 1 000 °C and therefore reliably protects the material preventing the evaporation of Re oxides. Development of the scale on Co-17Re-30Cr-2Si alloys involves an initial, transient stage of oxidation during which CoO, $CoCr_2O_4$, $SiO_2$ and $Cr_2O_3$ are able to nucleate and grow on the alloy surface, followed by establishment of a $Cr_2O_3$ layer on the metallic surface. The steady-state scale consists of an outer $CoCr_2O_4$ layer, an inner $Cr_2O_3$ scale, and internal precipitates of $SiO_2$.

As mentioned above, silica was only found as internal precipitates, which definitely retard the outward diffusion of metallic constituents as well as inward oxygen flux, but they do not certainly prevent the evaporation of Re-oxides. Since none of the alloys studied forms a continuous silica layer on the oxide/alloy interface, which would protect the metallic substrate and consequently prevent the evaporation of Re oxides, it could be concluded that Si act as nucleation sites, therefore reducing the transient-oxidation stage allowing the quick formation of a continuous $Cr_2O_3$ layer. Due to the low Si concentration, Co – Re-alloys containing 1 and 2 at.% Si obviously do not provide sufficient nucleation sites. Thus, more rapidly growing Co oxides were able to nucleate and grow on the exposed alloy. For the alloy Co-17Re-23Cr-3Si, a nearly continuous $Cr_2O_3$ was detected on the scale/alloy interface in the early period of oxidation, supporting the theory that high Si availability on the alloy surface provides the required amount of nucleation sites to enable a rapid formation of a continuous $Cr_2O_3$ layer. As expected, a development of a continuous $Cr_2O_3$ layer occurs most quickly for the alloy Co-17Re-30Cr-2Si not only because of sufficient nucleation sites but also because of the higher chromium concentration.

Li and Gleeson found an interesting dependence of the interdiffusion coefficient of Cr in Ni-based chromia forming on the Si-content, $D_{Cr}^{eff}$ was found to be highest in an alloy that had the highest silicon content [8]. They pointed out that two factors may influence the movement of atoms: bond strength and space for movement. The melting point of a solid is indicative for its bond strength, while space for movement is directly related to the lattice parameter of the host crystal. Strong metallic bonding and a small lattice parameter would contribute to restricting atom movement, and thus result in a lower diffusivity [8]. Figure 9 shows calculated equilibrium temperatures for the liquid-phase formation during heating of the Co-17Re-23Cr-*x*Si alloys with different Si concentrations. The calculations were performed using the thermodynamic program FactSage. It is clear that the higher Si-content yields the lower equilibrium temperature for the liquid-phase. It could be deduced that an increase in the Si content weakens the metallic bonds in Co – Re – Cr-alloys, probably resulting in an enhanced $D_{Cr}^{eff}$, which, on the one hand, could be considered as beneficial regarding the oxidation resistance of Co – Re-based alloys. On the other hand, the decrease in the equilibrium temperature for the liquid-phase with increasing Si content reduces the field of applications for Co – Re based alloys drastically.

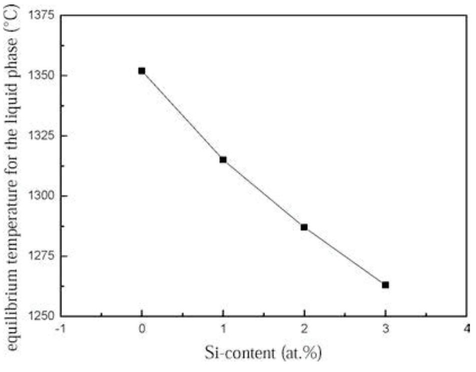

Fig. 9. Calculated minimum equilibrium temperatures for liquid phase formation in Co-17Re-23Cr-alloys.

This study provides a first insight into the oxidation behaviour of Si-containing Co – Re – Cr alloys. Although the presence of a continuous layer of $SiO_2$ can give increased protection to the Co – Re – Cr alloys by suppressing cation transport through the $Cr_2O_3$ scale, poor spallation characteristics of such scales have been reported, particularly if the $SiO_2$ layer is continuous. Recent studies have indicated that implanted reactive-element additions (yttrium, lanthanum) can be beneficial. Baxter et al. found that yttrium improved scale adhesion of the chromia layer on austenitic Fe – Cr – Ni alloys [10]. Paul et al. [6] reported that lanthanum, which was surface deposited by means of ionic exchange, enhanced the formation of a silica layer by a change in the diffusion mechanism through the scale. The reactive element also changed the expansion coefficient at the scale/alloy interface, increasing the adherence of the oxide layer to the metal. The method of reactive element addition is also intended to be applied for Co – Re – Cr alloys containing Si, assuming that a continuous silica layer will be formed at the oxide/alloy interface of newly developed Co – Re – Cr alloys.

Two other concepts to increase the high-temperature oxidation resistance of Co – Re-based alloys are (i) alloying with Si + B and (ii) alloying with Al. In the case of Mo – Si – B-based alloys, boron is usually added in order to form a continuous borosilica layer ($SiO_2$ and $B_2O_3$). This is because boron reduces the viscosity of the glassy silica scale that forms on Mo – Si – B alloys during exposure to air. The low viscosity helps to maintain a continuous protective scale [19]. The B/Si ratio was found to be very important in adjusting the quality of the silica layer. Lowering the B/Si ratio results in a decrease in the high-temperature oxidation resistance because silica forms at a low rate at moderate temperatures [20]. The concept of the formation of a protective borosilica layer will be applied to the Co – Re – Cr alloys as one of the next steps in the development of this alloy system.

Another concept to increase the high-temperature oxidation resistance of Co – Re-based alloys is alloying with Al. Many Ni-based superalloys, the intermetallic β-NiAl and ferritic FeCrAl alloys are typical alumina formers. These materials have good oxidation resistance due to their ability to form scales which are exclusively $Al_2O_3$ [16]. Oxidation of alumina-forming alloys at temperatures below about 1 200 °C often leads initially to the formation of transient, metastable alumina scales. This is significant, because the metastable aluminas grow much more rapidly than protective $\alpha$-$Al_2O_3$. Alloying additions such as Cr, Pt or Ni accelerate the transformation from poor protective metastable aluminas to highly stable $Al_2O_3$.

Figure 10 summarizes the development of Co – Re-based alloys in the last years and shows the promising progress attained with respect to oxidation resistance. The newly proposed Co – Re-based system, consisting of a set of binary, ternary and quaternary alloys, has been systematically investigated during last few years [3, 4]. Figure 10 shows selective results of some Co – Re-based alloys, which are representative for the development of this alloy system. The data for the alloy Co-17Re and Co-17Re-30Cr were taken

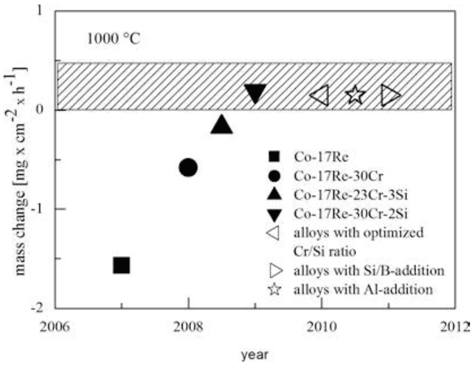

Fig. 10. Development of Co – Re-based alloys in terms of high-temperature oxidation resistance (full symbols indicate alloys studied, blank symbols imply alloys which will be investigated, shaded area indicates acceptable high-temperature oxidation resistance.

from the reference [3]. Though significant progress has been achieved regarding improvement of the oxidation behaviour of Co – Re-based alloys, it is clear that there are a lot of open questions and a high demand for further investigations on these materials to make them competitive among well-established high-temperature alloys.

## 5. Conclusions

Experiments were carried out in order to investigate the influence of Si content on the oxidation resistance of Co – Re – Cr-alloys. The main factors can be summarized as follows:

1. It has been found that Si improves the oxidation resistance of all Si-containing Co – Re – Cr-based alloys resulting in a significant decrease in the evaporation rate of Re-oxides during exposure to air at 1 000 °C and 1 100 °C.
2. Silicon acts as nucleation sites which reduce the transient-oxidation stage and can promote the formation of a continuous $Cr_2O_3$ layer.
3. While the addition of 1 and 2 at.% Si to the ternary Co-17Re-23Cr alloy was insufficient to form a continuous $Cr_2O_3$ scale on the oxide/alloy interface, the addition of 3 at.% silicon seems to change the oxidation mode from the non-protective $CoO – CoCr_2O_4 – Cr_2O_3$ scale structure with a semicontinuous $Cr_2O_3$ scale to a protective $CoCr_2O_4 – Cr_2O_3$ structure containing a dense and continuous $Cr_2O_3$ layer in the oxide/alloy interface. However, the protectiveness of the oxide layer $CoCr_2O_4 – Cr_2O_3$ in the alloy Co-17Re-23Cr-3Si decreases with prolonged exposure time.
4. On the oxide/alloy interface of the alloy Co-17Re-30Cr-2Si, a continuous and dense $Cr_2O_3$ scale was observed, which remains stable even after 100 h exposure and therefore can be considered as reliably protective for isothermal conditions at temperature below 1 100 °C.
5. Other concepts to improve the oxidation resistance of this class of materials were discussed, such as the formation of a borosilicate layer or a protective $Al_2O_3$ scale on the substrate surface.

Financial support of Deutsche Forschungsgemeinschaft (DFG) in the framework of the Research Group "Beyond Ni-Base Superalloys" is gratefully acknowledged. We are grateful to Dr. D. Mukherji and Prof. Dr. J. Rösler (University of Braunschweig, Germany) for providing the material used in this study.

### References

[1] J. Rösler, D. Muckherji, T. Baranski: Adv. Eng. Mater. 9 (2007) 876. DOI:10.1002/adem.200700132
[2] M. Brunner, R. Hüttner, M.C. Bölitz, R. Völkl, D. Mukherji, J. Rösler, T. Depka, C. Somsen, G. Eggeler, U. Glatzel: Mater. Sci. Eng. 528 (2010) 650. DOI:10.1016/j.msea.2010.09.035
[3] B. Gorr, V. Trindade, S. Burk, H.-J. Christ, M. Klauke, D. Mukherji, J. Rösler: Oxid. Met. 71 (2009)157. DOI:10.1007/s11085-008-9133-y
[4] B. Gorr, S. Burk, V. Trindade, H.-J. Christ: Oxid. Met. 74 (2010) 239. DOI:10.1007/s11085-010-9213-7
[5] P. Berthod: Oxid. Met. 64 (2005) 235. DOI:10.1007/s11085-005-6562-8
[6] A. Paul, R. Sanchez, O.M. Montes, J.A. Odriozola: Oxid. Met. 67 (2007) 87. DOI:10.1007/s11085-006-9046-6
[7] Y. Liu, W. Wei, L. Benum, M. Oballa, M. Gyorffy, W. Chen: Oxid. Met. 73 (2010) 207. DOI:10.1007/s11085-009-9172-z
[8] B. Li, B. Gleeson: Oxid. Met. 65 (2006) 101. DOI:10.1007/s11085-006-9003-4
[9] H.E. Evans, D.A. Hilton, R.A. Holm, S.J. Webster: Oxid. Met. 19 (1983) 1. DOI:10.1007/BF00656225
[10] D.J. Baxter, R.T. Derricott, R.C. Hurst: Werkst. Korros. 34 (1983) 446. DOI:10.1002/maco.19830340904
[11] S. Wang, Y. Wu, F. Gesmundo, Y. Niu: Oxid. Met. 69 (2008) 299. DOI:10.1007/s11085-008-9103-4
[12] F.H. Stott, G.J. Gabriel, F.I. Wei, G.C. Wood: Werkst. Korros. 38 (1987) 521. DOI:10.1002/maco.19870380910
[13] R. Durham, B. Gleeson, D.J. Young: Mat. Corros. 49 (1998) 855. DOI:10.1002/(SICI)1521-4176(199812)49:12<855::AID-MACO855>3.0.CO;2-5
[14] D.E. Jones, J. Stringer: Oxid. Met. 9 (1975) 409. DOI:10.1007/BF00611689
[15] H.E. Exner, H.P. Hougardy: Einführung in die Quantitative Gefügeanalyse, DGM-Informationsgesellschaft Verlag, Oberursel (1986).
[16] D.J. Young, B.A. Pint: Oxid. Met. 66 (2006) 137. DOI:10.1007/s11085-006-9030-1
[17] H. Asteman, J.-E. Svensson, L.-G. Johansson, M. Norell: Oxid. Met. 52 (1999) 95. DOI:10.1023/A:1018875024306
[18] A. Kumar andD.L. Douglass: Oxid. Met. 10 (1976) 1 DOI:10.1007/BF00611695
[19] J.H. Schneibel, J.J. Kruzic, R.O. Ritchie: Mo – Si – B Alloy Development, information on http://www.ms.ornl.gov/fossil/pdf/APR/FY04/Materials/Schneibel.pdf
[20] F.A. Rioult, S.D. Imhoff, R. Sakidja, J.H. Perepezko: Acta Mat. 57 (2009) 4600. DOI:10.1016/j.actamat.2009.06.036

(Received March 31, 2011; accepted October 20, 2011)

### Bibliography

DOI 10.3139/146.110626
Int. J. Mat. Res. (formerly Z. Metallkd.)
103 (2012) 1; page 24 – 30

ISSN 1862-5282

### Correspondence address

Bronislava Gorr
Institut für Werkstofftechnik, Paul-Bonatz-Str. 9 – 11
D-57068 University Siegen, Germany
Tel.: +49 271 740 4653
Fax: +49 271 740 2545
E-mail: gorr@ifwt.mb.uni-siegen.de

You will find the article and additional material by entering the document number **MK110626** on our website at *www.ijmr.de*

# Manuskript II

## High-temperature oxidation behavior of a single-phase $(Mo,Ti)_5Si_3$ (Mo-Si-Ti) alloy

S. Burk, B. Gorr, H.-J. Christ, D. Schliephake, M. Heilmaier, C. Hochmuth and U. Glatzel

Scripta Materialia, 66 (2012) 223-226

ELSEVIER

Available online at www.sciencedirect.com

SciVerse ScienceDirect

Scripta Materialia 66 (2012)

Scripta MATERIALIA

www.elsevier.com/locate/scriptamat

# High-temperature oxidation behaviour of a single-phase $(Mo,Ti)_5Si_3$ (Mo–Si–Ti) alloy

Steffen Burk,[a,*] Bronislava Gorr,[a] Hans-Jürgen Christ,[a] Daniel Schliephake,[b]
Martin Heilmaier,[b] Christian Hochmuth[c] and Uwe Glatzel[c]

[a] *Lehrstuhl für Materialkunde und Werkstoffprüfung, Universität Siegen, Paul-Bonatz-Str. 9-11, 57068 Siegen, Germany*
[b] *Physikalische Metallkunde, Technische Universität Darmstadt, Petersenstr. 23, 64287 Darmstadt, Germany*
[c] *Lehrstuhl Metallische Werkstoffe, Universität Bayreuth, Ludwig-Thoma-Str. 36b, 95440 Bayreuth, Germany*

Received 8 August 2011; revised 24 October 2011; accepted 25 October 2011

The alloy composition Mo–37Si–40Ti (at.%) was synthesized by arc melting in order to obtain nearly single-phase $(Mo,Ti)_5Si_3$. At 750–1300 °C, the intermetallic compound was found to be superior to both single-phase $Mo_5Si_3$ and single-phase $Ti_5Si_3$ with regard to oxidation resistance. Upon oxidation, formation of a protective $SiO_2$–$TiO_2$ duplex scale was observed, which dramatically reduces outward diffusion of Ti. The results indicate that Ti alloying is a promising concept to further improve oxidation resistance of Mo-based alloys such as Mo–Si–B.

*Keywords:* Intermetallic phases; Silicides; High temperature oxidation; Mo–Si–B alloys

Systematic examinations of refractory metal-rich silicide phases have revealed their outstanding structural features [1]. Recently, it was found by thermodynamic modeling with coupled experiments that (macro)alloying of Ti to the Mo–Si–B system stabilizes/extends the three-phase equilibrium Mo_ss–$Mo_3Si$–$Mo_5SiB_2$, where Mo_ss is the body-centered cubic Mo solid-solution phase. Moreover, if Ti is added in sufficiently high concentration, instead of the $Mo_3Si$ phase, $Mo_5Si_3$ with Ti in solid solution is stabilized (in the following denoted as $(Mo,Ti)_5Si_3$) resulting in a Mo_ss–$(Mo,Ti)_5Si_3$–$Mo_5SiB_2$ alloy [2]. Here, Ti substitutes Mo, while the concentrations of Si or B in the existing phases are either unaffected or remain negligibly small [3]. Ti alloying may be important in the further design of three phase Mo–Si–B alloys for ultrahigh-temperature applications due to the following reasons: (i) (partially) substituting Mo by Ti will lead to a significant reduction in the alloy density (which is 9.6 g $cm^{-3}$ for a typical composition of Mo–9 at.% Si–8 at.% B [4]), yielding a strong increase of turbine efficiency; (ii) in terms of oxidation resistance, replacing $Mo_3Si$ by the $(Mo,Ti)_5Si_3$ in Mo–Si–B alloys may improve the overall high-temperature oxidation resistance of the alloy due to a significantly higher Si concentration [5].

It is well known that both $Mo_3Si$ and $Mo_5Si_3$ in single-phase condition are only oxidation resistant at ultrahigh temperatures beyond 1600 °C due to a highly porous silica scale which forms as a consequence of the evaporation of $MoO_3$ [6]. Ti as a major alloying element might have a positive effect. The oxidation behaviour of single-phase $Ti_5Si_3$ as reference material has been previously investigated by Williams and Akinc [7] as well as by Mitra and Rao [8], and provides a basis for understanding the fundamental oxidation behaviour of $(Mo,Ti)_5Si_3$ too.

To the best of our knowledge, no data on the oxidation behaviour of the Mo–Si–Ti system has been reported. Hence, in this paper we investigate the oxidation behaviour of the alloy Mo–37Si–40Ti in the nearly single-phase $(Mo,Ti)_5Si_3$ condition in the temperature range between 750 and 1300 °C.

Guided by thermodynamic modeling [2], a molybdenum silicide alloy with the composition Mo–37Si–40Ti (at.%) was prepared from elemental powder mixtures of Mo, Si and Ti of 99.95%, 99.9% and 99.5% purity by an arc-melting process route. After drop casting the alloy, annealing under $H_2$ atmosphere was carried out at 1550 °C for 100 h followed by a subsequent

---

* Corresponding author. Tel.: +49 271740 4660; fax: +49 271740 2545; e-mail: steffen.burk@uni-siegen.de

homogenization treatment in Ar atmosphere at 1600 °C for 100 h, yielding the microstructure given in Figure 1. The alloy is (nearly) single-phase and comprises a Mo-rich $(Mo,Ti)_5Si_3$ phase with traces of Ti-rich $Ti(Mo)_5Si_3$, possibly due to fact that thermodynamic equilibrium was not achieved completely during the homogenization treatment.

The oxidation kinetics was studied under isothermal testing conditions by using continuous thermogravimetric analysis (TGA) in static laboratory air. The tailor-made system comprises a Rubotherm high-resolution magnetic suspension balance ($10^{-5}$ g) equipped with automatic electronic drift compensation. Surface and cross-sectional scanning electron microscopy (SEM) in secondary-electron (SE) and backscattered-electron (BSE) mode was applied using a Helios Nanolab 600 FE-SEM (FEI) as well as energy-dispersive X-ray spectroscopy (EDS) to qualitatively determine the elements present in the scale with an Apollo XL silicon drift detector (EDAX) ensuring high count rates even for lightweight elements, e.g. O. Oxidation samples having the dimensions $10 \times 4 \times 3$ mm$^3$ were machined using a slow-cutting diamond saw. Prior to oxidation, the samples were ground and polished with SiC paper down to 1200 grit and ultrasonically cleaned in ethanol. For kinetics examination, TGA measurements were carried out up to 100 h with the samples hanging on an alumina hook connected contactlessly to the microbalance via a permanent magnet at the reaction chamber side as well as an electromagnet at the microbalance side. Oxidation experiments were performed in the temperature range 750–1300 °C.

The specific weight change vs. time for the alloy $(Mo,Ti)_5Si_3$ at 750, 820, 1100 and 1300 °C is shown in Figure 2. At all temperatures, continuous weight gaining kinetics with the oxidation rate increasing disproportionally with temperature is observed. At 1100 and 1300 °C, a strong linear oxidation relationship dominates the oxidation kinetics within the first hour of oxidation. This is in good agreement with the oxidation behaviour of elemental Ti at temperatures above 900 °C, which was reported by Kubaschewski [9].

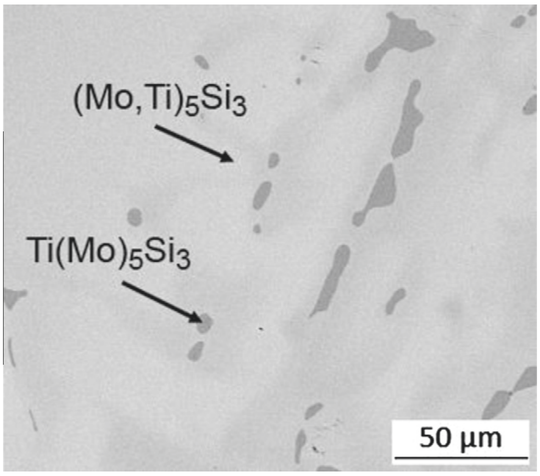

**Figure 1.** SEM microstructure of the arc melted alloy Mo–37Si–40Ti (SEM, BSE mode).

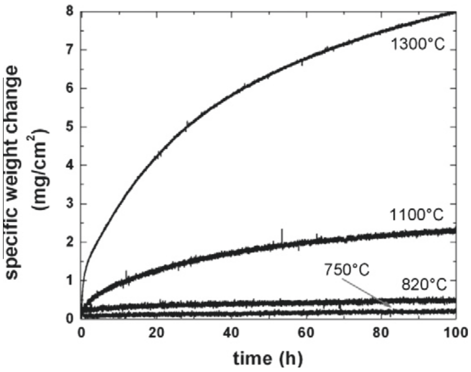

**Figure 2.** Specific weight change vs. time for the alloy Mo–37Si–40Ti oxidized in air at temperatures between 750 and 1300 °C.

Figure 3 shows the SEM microstructures (surface and cross-section views) of oxidized near single-phase $(Mo,Ti)_5Si_3$ after oxidation at 750 °C (surface, top left), 1100 °C (cross-section, top middle) and 1300 °C (surface, top right) for 100 h including the main features of oxide scale evolution. At 750 °C but also at 820 °C (not shown in the figure), nanometer-sized $TiO_2$ particles are found randomly distributed at the oxide/air interface without visible formation of a compact titania scale. In between and below the particle gaps, $SiO_2$ is detected. Continuous $TiO_2$ scale formation is observed at 1100 and 1300 °C. The structure of the $TiO_2$ grains exhibits a rather sharply edged structure. In this context, the relatively wide spacing of the $TiO_2$ grain boundaries at very high temperatures (see Fig. 3 (top right)) needs to be mentioned. It is assumed that the oxygen readily permeates through this open structure.

Based on the oxidized alloy cross-section after oxidation exposure at 1100 °C for 100 h given in Figure 3 (top middle), the oxide morphology can be subdivided into three major regions. (i) The outermost layer at the oxide/air interface consists of a single-phase and continuous $TiO_2$ scale exhibiting an average thickness of 4–8 µm at 1100 °C after 100 h. (ii) Below the titania layer, a duplex layer containing $SiO_2$ as well as $TiO_2$ is observed. Since $TiO_2$ exists as discontinuous and embedded particles within this scale, continuous $SiO_2$ is considered as the matrix or skeleton phase of this layer. (iii) At the duplex-layer/substrate interface, internal oxidation of Si is observed, but the presence of Ti was not confirmed. The $SiO_2$ particles are embedded within a Mo-rich matrix. EDS analyses underline the depletion of Ti within the internal oxidation zone. At 1300 °C, the oxide morphology cross-section is rather similar to the one found for 1100 °C, although the $TiO_2$ layer exhibits an average thickness of 80 µm. At the lower temperatures of 750 and 820 °C, the oxide layers are comparably thinner, exhibiting an identical morphological structure. The external $TiO_2$ scale possesses an average thickness of 200 nm, whereas the thickness of the duplex layer lies in the 500 nm range. The internal oxidation depth after 100 h is in the range of 1–2 µm.

In the following, the main factors determining oxidation kinetics are discussed briefly. The mechanisms

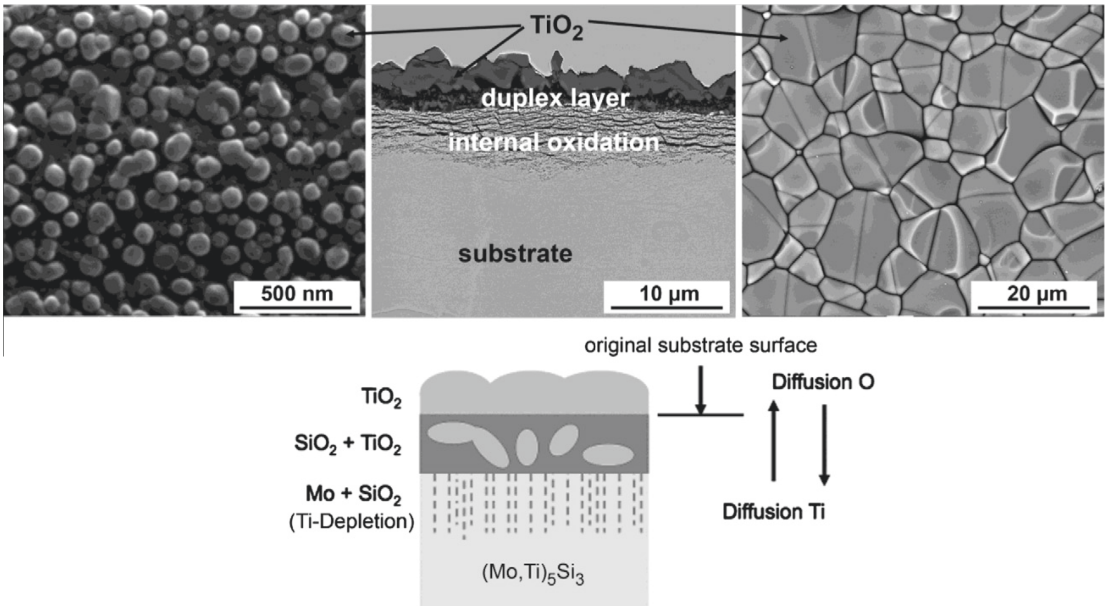

**Figure 3.** SEM microstructures of (Mo,Ti)$_5$Si$_3$ oxidized in air for 100 h at 750 °C (top left, surface, SE mode), 1100 °C (top middle, cross-section, BSE mode) and 1300 °C (top right, surface, BSE mode), and proposed oxidation schematic in cross-section view (bottom).

are also summarized schematically in Figure 3 (bottom). It is assumed that external growth of the TiO$_2$ layer originates from the substrate surface, since Ti diffusion becomes oxidation rate controlling at temperatures beyond 900 °C [9]. The SiO$_2$–TiO$_2$ duplex layer underneath is believed to grow mainly by inward diffusion of oxygen as confirmed by Melsheimer et al. using Pt marker experiments [10]. With increasing time and/or temperature, rapid outward diffusion of Ti leads to its depletion within the internal oxidation zone.

The continuous oxidation experiments (see Fig. 2) show good oxidation resistance for the (Mo,Ti)$_5$Si$_3$ phase in the temperature range of 750–1300 °C through protective oxide scale formation. Extensive EDS analyses at the titania scale/air as well as at the titania/duplex scale interface did not confirm the presence of Mo, and hence it is assumed that volatile MoO$_3$ formation is not an issue for this alloy during long-term oxidation. The oxygen partial pressure at the duplex-scale/substrate interface is concluded to be below the dissociation pressure of any Mo-oxide formation. However, a combined oxidation behaviour of evaporation of MoO$_3$ (weight loss) and formation of silica and titania (weight gain) during the initial stage of oxidation cannot be excluded entirely, although the typical condensed Mo-oxide-rich reaction products which are usually located at the reaction chamber walls of the TGA system as a consequence of an evaporation–condensation reaction were not observed.

The advantage of the (Mo,Ti)$_5$Si$_3$ is most clearly understood by directly comparing its oxidation characteristics with those of single-phase Mo$_5$Si$_3$ and Ti$_5$Si$_3$. Mo$_5$Si$_3$ exhibits no oxidation resistance at temperatures below 1400 °C due to the formation of a highly porous SiO$_2$ scale which allows oxygen to permeate readily through the scale [6,11,12]. The (Mo,Ti)$_5$Si$_3$ phase is superior to Mo$_5$Si$_3$ with regard to oxidation resistance, and moreover it exhibits a lower density. Furthermore, the (Mo,Ti)$_5$Si$_3$ phase shows far better oxidation resistance as compared to stoichiometric Ti$_5$Si$_3$. Breakaway oxidation, which was observed for this phase at temperatures beyond 1000 °C [13,14], is not observed if Mo is present in the alloy. For stoichiometric Ti$_5$Si$_3$, Williams and Akinc assume almost identical Gibbs free energy values for silica and titania, allowing SiO$_2$ as well as TiO$_2$ nuclei to form simultaneously on the surface in the initial oxidation stage. With increasing oxidation time, the oxidation behaviour shifts to a breakaway behaviour [7]. The reason is believed to lie in atmospheric nitrogen allowing the formation of a metastable TiN transient layer at the substrate interface, facilitating

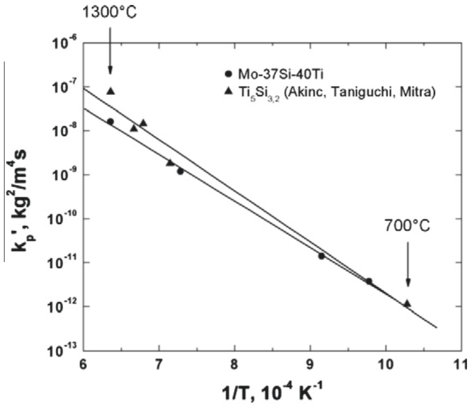

**Figure 4.** Calculated values of the parabolic oxidation rate constant $k_p'$ of the alloy Mo–37Si–40Ti at temperatures of 700–1300 °C compared to the available literature data for Ti$_5$Si$_{3.2}$ [10–12].

continuous formation of $TiO_2$ [14]. The formation of TiN may additionally be enhanced by high diffusivities of nitrogen in $TiO_2$ [9]. A durable improvement of the oxidation behaviour of $Ti_5Si_3$ was achieved by adding small amounts of C to the alloy system. It is thought that C reduces oxygen diffusion in the interstitial lattice.

The same effect was achieved by shifting the chemical composition of the alloy to an excess of Si ($Ti_5Si_{3.2}$). Both strategies result in the formation of a $SiO_2$–$TiO_2$ duplex layer with $SiO_2$ as matrix phase, which is also the case for the $(Mo,Ti)_5Si_3$ phase as presented in this work. If the duplex-layer exhibits a $TiO_2$ matrix, which is the case for the conventional $Ti_5Si_3$ phase, breakaway oxidation is observed [7].

Figure 4 shows the calculated values of the weight change based parabolic oxidation rate constant $k_p$' for the alloy composition Mo–37Si–40Ti compared to the available literature data of the $Ti_5Si_{3.2}$ phase, which also oxidizes according to a parabolic relationship. The calculated values of $k_p'$ are similar to the literature values, although $k_p'$ for the $(Mo,Ti)_5Si_3$ phase at 1300 °C is almost one order of magnitude lower than the reference values, underlining its superior oxidation resistance especially at ultra-high temperatures.

The aim of the present investigation was to gain an initial understanding of the oxidation behaviour of the bulk monolithic $(Mo,Ti)_5Si_3$ phase. The main conclusions can be summarized as follows. Study of the alloy with composition Mo–37Si–40Ti shows that beneath a superficial $TiO_2$ scale a duplex layer containing a mixture of $SiO_2$ and $TiO_2$ is formed. It appears to be very important that $SiO_2$ forms the matrix of this $SiO_2$–$TiO_2$ duplex layer. As a consequence an effective oxidation barrier which reduces the continuous growth of an outer $TiO_2$ layer and inhibits the formation and evaporation of volatile Mo oxide exists. Hence, the intermetallic phase is superior with regard to oxidation resistance compared to both monolithic $Mo_5Si_3$ and monolithic $Ti_5Si_3$. Additional studies on the stability of the oxide scales during cyclic oxidation are necessary to provide further clarification of the applicability of the observed oxide scale formation mechanism to severe service conditions.

The research was sponsored by Deutsche Forschungsgemeinschaft (DFG) within the framework of the research unit 727 “Beyond Ni-Base Superalloys”.

[1] R. Sakidja, J.H. Perepezko, S. Kim, N. Sekido, Acta Mater. 56 (2008) 5223.

[2] Y. Yang, H. Bei, S. Chen, E.P. George, J. Tiley, Y.A. Chang, Acta Mater. 58 (2010) 541.

[3] Y. Yang, Y.A. Chang, L. Tan, Y. Du, Mater. Sci. Eng. A 362 (2003) 281.

[4] P. Jéhanno, M. Heilmaier, H. Kestler, Intermetallics 12 (2004) 1005.

[5] M.G. Mendiratta, T.A. Parthasarathy, D.M. Dimiduk, Intermetallics 10 (2002) 225.

[6] J.B. Berkowitz-Mattuck, R.R. Dils, J. Electrochem. Soc. 112 (1965) 583.

[7] J.J. Williams, M. Akinc, Oxid. Met. 58 (2002) 57.

[8] R. Mitra, V.V.R. Rao, Metall. Mater. Trans. A 29 (1998) 1665.

[9] O. Kubaschweski, Oxidation of Metals and Alloys, second ed., Butterworths, London, 1967.

[10] S. Melsheimer, M. Fietzek, V. Kolarik, A. Rahmel, M. Schütze, Oxid. Met. 47 (1997) 139.

[11] M. Meyer, M. Kramer, M. Akinc, Adv. Mater. 8 (1996) 85.

[12] R.W. Bartlett, J.W. McCamont, P.R. Gage, J. Am. Ceram. Soc. 48 (1965) 551.

[13] S. Taniguchi, T. Minamida, T. Shibata, Mater. Sci. Forum 251–254 (1997) 227.

[14] Z. Tang, J.J. Williams, A.J. Thom, M. Akinc, Intermetallics 16 (2008) 1118.

# Manuskript III

## Effect of yttrium alloying on intermediate to high-temperature oxidation behavior of Mo-Si-B alloys

S. Majumdar, D. Schliephake, B. Gorr, H.-J. Christ, and M. Heilmaier

Metallurgical and Materials Transactions, A 44 (2013) 2013-2243

# Effect of Yttrium Alloying on Intermediate to High-Temperature Oxidation Behavior of Mo-Si-B Alloys

S. MAJUMDAR, D. SCHLIEPHAKE, B. GORR, H.-J. CHRIST, and M. HEILMAIER

The oxidation behavior of 0.2 Y-alloyed Mo-9Si-8B (at. pct) was investigated in a wide temperature range from 923 K to 1673 K (650 °C to 1400 °C). Formation of a thin yttrium-silicate scale at the outer layer along with the thick silica-rich inner layer containing Y-rich oxide inclusions was detected beyond 1573 K (1300 °C). A substantial improvement in the oxidation resistance of the alloy could be realized at 1073 K to 1273 K (800 °C to 1000 °C) with the addition of yttrium. The formation of a viscous silica-rich protective scale could prevent the permeation of $MoO_3$ at the initial stages of oxidation at this temperature regime. The growth of the internal oxidation zone followed a parabolic rate at 1273 K to 1673 K (1000 °C to 1400 °C), and the activation energy values calculated for both the outer oxide scale and internal oxidation zone formation indicated the inward diffusion of oxygen as the dominant rate controlling mechanism. The microstructural and kinetic data obtained for internal and external oxidation indicate that yttrium-silicate scale reduces the inward diffusion of oxygen, thereby improving the oxidation resistance of the alloy at high temperatures in any oxidizing environment.

DOI: 10.1007/s11661-012-1589-3

## I. INTRODUCTION

DESIGN and development of new materials suitable for service for application temperatures beyond those of nickel-based super alloys (>1423 K) have been the key focus of interest for energy and aero-space industries. Molybdenum and niobium silicide-based composites are considered among the most promising candidates due to their favorable mechanical properties and oxidation resistance at higher temperatures.[1–6] The key technological challenge is to design a material which possesses good creep properties, adequate oxidation resistance beyond 1473 K (1200 °C), and improved manufacturability. Alloys within the ternary Mo-Si-B system have shown attractive properties with respect to high-temperature creep and oxidation resistance.[7–11] A suitable alloy is composed of a tough and potentially ductile molybdenum solid solution ($Mo_{ss}$) matrix with uniform distribution of $Mo_5SiB_2$ (T2) and $Mo_3Si$ (A15) intermediate phases. The volume fraction of these three phases depends upon the alloy composition, and Mo-9Si-8B (at. pct) shows a reasonable combination of phases, leading to balanced mechanical and oxidation properties.[7,8] The detailed oxidation behavior of Mo-Si-B alloys in different temperature regimes has been studied and is well documented in the literature.[12–17] The alloy possesses excellent oxidation resistance in the range of 1373 K to 1573 K (1100 °C to 1300 °C) due to the formation of an amorphous and low viscosity borosilicate, which flows over the surface producing a protective scale. However, the alloy shows an inferior oxidation behavior at intermediate temperatures starting from 923 K to 1223 K (650 °C to 950 °C). During the oxidation of Mo-Si-B in 923 K to 1023 K (650 °C to 750 °C), a porous scale forms and $MoO_3$ vapor flows out through the pores/channels of the oxide layer. Beyond 1073 K (800 °C), the viscosity of the developed oxide scale is reduced and it is composed of Si-B-Mo-O. An optimum concentration of $B_2O_3$ is required to produce a protective borosilicate scale.[13] The $B_2O_3$ to $SiO_2$ ratio is high until 1223 K (950 °C), and a low viscosity scale is formed in this intermediate temperature regime. The B-rich low viscosity scale allows $MoO_3$ to permeate by bubbling through the scale and inward diffusion of oxygen is enhanced, which leads to the faster growth of the silica scale at 1073 K to 1223 K (800 °C to 950 °C).[13] Beyond 1373 K (1100 °C), the evaporation rate of boron is increased and the required $B_2O_3$ to $SiO_2$ ratio is reached to form a higher viscosity scale sufficient to cover the surface and to prevent $MoO_3$ bubbling, providing protection against oxidation.[13,15]

It has been already established that microalloying addition of Y drastically improves the oxidation behavior of NiCoCrAlY and MCrAlY alloy coatings.[18–27] This element segregates along the alloy grain/phase boundaries[24] and oxidizes simultaneously along with the major alloying element (Al) forming the oxide ($Y_2O_3$) inclusions in the protective scale ($Al_2O_3$). The parabolic growth rate constant of the protective scale is reduced[23] and, in some cases, these rare earth oxides

---

S. MAJUMDAR, Scientific Officer, is with the Materials Processing Division, Bhabha Atomic Research Centre, Mumbai 400085, India, and also Visiting Researcher with the Institut für Werkstofftechnik, Universität Siegen, Paul-Bonatz-Str. 9-11, 57068 Siegen, Germany. Contact e-mail: sanjib731@gmail.com D. SCHLIEPHAKE, Ph.D. Candidate, and M. HEILMAIER, Professor, are with Institut für Angewandte Materialien-Werkstoffkunde (IAM-WK), Karlsruhe Institute of Technology (KIT), Engelbert-Arnold-Str. 4, 76131 Karlsruhe, Germany. B. GORR, Research Group Leader, and H.-J. CHRIST, Professor, are with the Institut für Werkstofftechnik, Universität Siegen.

Manuscript submitted September 3, 2012.

improve the spallation resistance of the scale, while cooled from high temperature by developing protrusions (also called pegs) along the metal/oxide interface.[25] The change in microstructure[26] and improvement of adhesion[27] of the oxide scale are observed with the addition of these reactive elements.

Silicon-based ceramic (SiC) composite materials are being developed for high-temperature structural components in aeronautic application, which forms a protective silica scale on high-temperature oxidation in dry air. However, in moist atmosphere, the material suffers from a high rate of recession due to active oxidation of silica by forming a more volatile compound $Si(OH)_4$ beyond 1473 K (1200 °C).[28,29] Due to the superior oxidation resistance in both dry and wet atmosphere, yttrium silicates ($Y_2SiO_5$ and $Y_2Si_2O_7$) are used as coatings on these SiC composites.[30–33] The effect of Y on the properties of the borosilicate scale formed during oxidation of Mo-Si-B alloys has not been reported earlier. Therefore, in the current approach, a detailed investigation has been carried out to study the oxidation behavior of Mo-9Si-8B alloy with the addition of 0.2 at. pct yttrium. Isothermal oxidation kinetics was studied in a wide temperature range from 923 K to 1673 K (650 °C to 1400 °C). The oxidation mechanisms at different temperature regimes were interpreted from the observations using XRD, SEM, EDS, EBSD, FIB-SEM, and TEM.

## II. EXPERIMENTAL

The alloy composition comprising of Mo-9Si-8B-0.2Y (at. pct) was produced using mechanical alloying of the elemental powder mixtures of Mo, Si, B, and Y of 99.95, 99.9, 99.6, and 99.9 pct purity, respectively. At the initial stage, the proper quantities of Mo, Si, B, and Y powder were manually mixed inside a glove box containing argon atmosphere. The powder mix along with the tungsten carbide (WC) balls was filled in the WC-lined stainless steel pots followed by tightening of the top cover with the pots using rubber gaskets inside the glove box. The ball to powder weight ratio (BPR) was maintained at 12:1, and planetary ball milling (Retsch PM 400) was conducted for 10 hours. The mechanically alloyed powder was subsequently consolidated using field assisted sintering (FAST). The temperature of the powder compact was initially increased to 1373 K (1100 °C) at a heating rate of 100 K/minutes (100 °C/minutes) and the compact was kept at this temperature for 15 minutes for removing gaseous species trapped inside the compact. The final sintering was conducted at 1873 K (1600 °C) for 0.25 hours applying a pressure of 50 MPa through graphite rods. The sintered material was cooled to room temperature at a very fast rate (150 K/minutes), and a final stage of grinding treatment was given to remove the carbon layers from the surfaces.

The as-consolidated alloys were characterized using density measurement, X-ray diffraction (XRD), scanning electron microscopy (SEM), energy dispersive spectrometry (EDS), and electron back-scattered diffraction (EBSD) to evaluate the compositions, microstructures, and phase formations. For oxidation tests, the specimens of dimensions 5 mm × 4 mm × 3 mm were prepared from the sintered alloy using diamond wheel cutting. The specimens were ground and polished with SiC paper up to 500 grit and ultrasonically cleaned in ethanol. The oxidation behavior was studied under isothermal conditions by continuous thermogravimetric analysis (TGA) and also discontinuous weight change measurement. TGA was carried out in static laboratory air at temperatures from 923 K to 1673 K (650 °C to 1400 °C) for up to 100 hours using a Rubotherm tailor-made magnetic suspension balance with a resolution of 1 $\mu$g and automatic electronic drift compensation. The specimens were hung up by a platinum wire on an alumina hook in a reaction chamber and connected without contact via a permanent magnet to the microbalance located inside a separated measuring chamber. The reaction chamber of the TGA was comprised of an alumina tube of 50 mm diameter with the sample hanging in the middle and the distance between the specimen and inner wall of the tube sufficiently high to avoid Mo-oxide contamination through condensation directly affecting the TGA measurements.

For studying the kinetics of growth of the outer oxide layers and also the internal oxidation zone, separate oxidation experiments were conducted inside the resistance heating muffle-type furnaces in static air. Specimens of the same dimensions were placed in the alumina trays, which were subsequently placed on magnesia bricks inside the furnace. These experiments were conducted at four different temperatures between 1373 K and 1673 K (1100 °C and 1400 °C) with different exposure times of 2, 5, 25, and 50 hours. The specimens obtained from the oxidation tests at each time interval at the particular temperature were analyzed for their weight change, and cross-sectional SEM analysis was conducted for measuring the thickness of the oxide scale as well as the internal oxidation zone very accurately.

The surface of the oxidized specimens was characterized using XRD, SEM, and EDS. The cross section of the oxide scale was analyzed using SE and BSE imaging coupled with EDS measurements and also EBSD for identifying the distribution of phases, especially at the oxide/metal interface. For EBSD measurement, the samples were prepared by metallographic polishing followed by electro-polishing using the electrolyte comprised of 12.5 vol pct methanol-87.5 vol pct $H_2SO_4$. Electro-polishing was carried out using LectroPol 5 (Struers), maintaining a bath temperature of 275 K (2 °C) with the applied potential of 20 V for 20 seconds. Suitable cross-sectional specimens for EBSD were also prepared by focused ion beam (FIB) milling in a duel beam SEM of type Helios Nanolab 600 FE-SEM (FEI). FIB was also used for preparing thin specimens suitable for transmission electron microscopic (TEM) observation taken from the metal/oxide interface of the oxidized specimens. Finally, the TEM analysis of the specimens obtained from FIB milling was carried out using a Hitachi (Model-8100) microscope equipped with $LaB_6$ cathode.

## III. RESULTS AND DISCUSSION

### A. *Alloy Microstructure*

Figure 1 represents the electro-polished microstructures of a 0.2 at. pct Y-alloyed Mo-9Si-8B specimen prepared by field assisted sintering. The presence of three distinct phases $Mo_{ss}$, $Mo_5SiB_2$ (T2), and $Mo_3Si$ (A15) along with very fine bright precipitates is clearly visible (Figure 1(a)). EDS analysis revealed that these precipitates are enriched with Y. The composition of these fine particles (<100 nm) could not be detected accurately using EDS; however, the oxygen concentration of these precipitates was found to be higher compared to the surrounding matrix, which could be due to the minor amount of oxygen pick-up by the particles during the electro-polishing stage. Mo-Y binary phase diagram[34] suggests that the solubility of Y in Mo is very low, being of the order of 0.03 to 0.065 at. pct at 1723 K (1450 °C). The formation of the Y-rich precipitates in the alloy (Figure 1(a)) indicated that the solubility of Y was also very low in T2 and A15 phases. The bright appearance of the precipitates in the back-scattered electron image (Figure 1(a)) and EDS analysis indicates that the precipitates mainly consist of elemental yttrium. A partial oxidation of Y during the milling stage could not be avoided, and the oxide particles of $Y_2O_3$ could also be present (black particles) in the microstructure. As the density of the sintered Mo-9Si-8B-0.2Y specimens was of the order of 91 to 92 pct of theoretic value ($\rho_{th}$ = 9.6 g/cc), very fine pores were observed along the grain/phase boundaries (Figure 1(a)). EBSD maps obtained from the same electro-polished

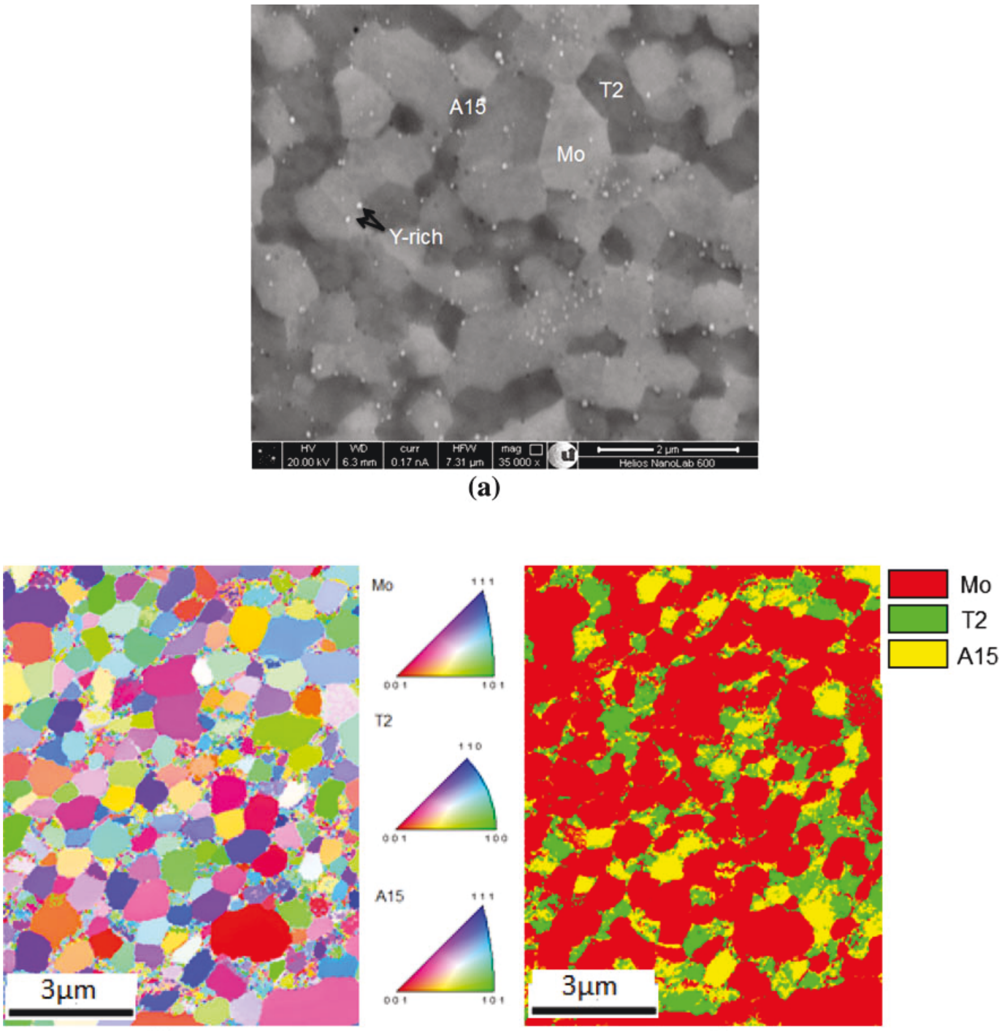

(a)

(b)

(c)

Fig. 1—Microstructures of an electro-polished surface of the sintered Mo-9Si-8B-0.2Y alloy; (*a*) BSE image, (*b*) EBSD map indicating orientation image with inverse pole figures (*inset*), and (*c*) corresponding phase map showing three color codes for three phases.

Manuskript III

Mo-9Si-8B-0.2Y alloy specimen are presented in Figures 1(b) and (c). Grain size distribution combined with grain orientation (Figure 1(b)) and phase (Figure 1(c)) mapping was done for $Mo_{ss}$, T2, and A15 phases. The fine size Y-rich particles were not indexed during mapping. However, the disturbances stemming from these particles during the electron beam scanning could be observed in the grain orientation map (Figure 1(b)) showing the small dots present throughout the microstructure. The presence of the three-phase $Mo_{ss}$-T2-A15 microstructure with the continuous $Mo_{ss}$ phase is visible in Figure 1(c). The average grain size of these phases was calculated to vary between 400 and 600 nm. The EBSD analysis gives the area fractions of 54.8 pct $Mo_{ss}$, 26 pct T2, and 19.2 pct A15, which are very close to the reported values.[35] The presence of fine precipitates and the application of a relatively lower sintering temperature (1873 K) are the main reasons for the formation of such fine-grained structure in molybdenum-based alloys.[36,37]

### B. *Oxidation at High Temperatures: 1573 K to 1673 K (1300 °C to 1400 °C)*

The isothermal oxidation kinetic data for Mo-9Si-8B-0.2Y alloy obtained from thermo-gravimetric experiments conducted at 1573 K and 1673 K (1300 °C and 1400 °C) are presented in Figure 2. The experimental data were compared with the reported data[13] for a reference Mo-12Si-12B alloy. The alloy showed an initial transient weight loss due to the higher evaporation rate of $MoO_3$ and subsequent slower rate of weight loss with increasing time. The hump observed in the TGA curve 1 in Figure 2 could be due to the formation of some localized cracks through which evaporation loss was detected at 87 hours; however, the steady state was again reached after 90 hours. The kinetic behavior during the isothermal oxidation of Mo-9Si-8B-0.2Y alloy in static air was found to be very similar to that reported for the reference alloy.[13] However, a different type of oxide scale formation was detected for 0.2 at. pct Y-alloyed specimens during oxidation in this high-temperature regime. Figure 3 shows the surface morphology of the specimen oxidized at 1573 K (1300 °C) for 100 hours. Formation of a viscous layer enriched with Y (Figure 3, Y L map) was detected. XRD analysis identified the presence of yttrium-silicate ($Y_2Si_2O_7$) phase on the oxidized surface. The cross-sectional image of the same specimen with EDS maps is presented in Figure 4, which indicates that a thin outer oxide layer rich in Y (Figure 4 YL map) was formed during oxidation at 1573 K (1300 °C). Therefore, the outer oxide layer mainly consists of yttrium-silicate phase, whereas the inner oxide layer is composed of amorphous borosilicate compound. The presence of a thick internal oxidation zone (IOZ) was observed between the alloy substrate and the oxide scale. A very thin layer rich in Mo along with its oxide ($MoO_2$) was also present between the borosilicate scale and IOZ. Thin yttrium-silicate scale formation at the outer layer of the oxide scale was observed even at shorter times of oxidation at 1673 K (1400 °C). The continuous outward diffusion of Y through the borosilicate scale leads to increase in the thickness of the yttrium-silicate layer as shown in Figure 5. The thickness of the yttrium-silicate layer was found to be about 6-8 $\mu$m after 2 hours of oxidation at 1673 K (1400 °C) (Figure 5). Localized Y-enrichments in the inner borosilicate layer closer to the outer layer (Figure 5) indicate the outwardly diffusion of Y.

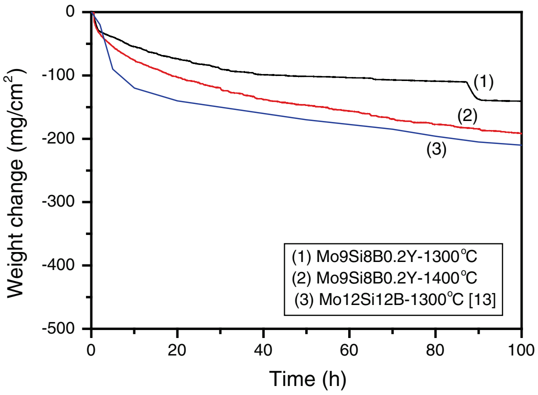

Fig. 2—TGA plots showing the isothermal oxidation behavior of Mo-9Si-8B-0.2Y alloy at 1573 K and 1673 K (1300 °C and 1400 °C).

Formation of such a thin yttrium-silicate scale could further improve the oxidation resistance of Mo-Si-B alloy in the atmosphere containing moisture. This outer scale could prevent the active oxidation of silica scale in the moisture environment at services beyond 1523 K (1250 °C).[31] Yttrium silicate was also reported to have good erosion resistance and less permeability for oxygen diffusion.[38] Therefore, a proper quantity of Y addition in Mo-Si-B could improve the oxidation resistance of the alloy in both dry and wet environments during exposure at high temperatures.

### C. *Oxidation at 1273 K to 1473 K (1000 °C to 1200 °C)*

The results obtained from the isothermal oxidation tests conducted in laboratory static air at 1273 K to 1473 K (1000 °C to 1200 °C) are presented in Figure 6. The kinetic data obtained from Mo-9Si-8B-0.2Y alloy specimens were compared with those observed for the reference Mo-9Si-8B alloy also prepared by field assisted sintering. Isothermal weight change data indicate that both the reference and 0.2 at. pct Y-alloyed materials had similar oxidation behavior at 1373 K and 1473 K (1100 °C and 1200 °C). Both the materials show a transient weight loss at initial stages, followed by loss of weight at a much slower and steady rate. Figure 7 shows the surface morphology (Figure 7(a)) and cross-sectional (Figure 7(b)) SEM images obtained from a representative specimen oxidized at 1473 K (1200 °C). The oxidized surface is comprised of a continuous silica-rich phase with some localized increase in concentration of $Y_2O_3$-$SiO_2$ (Figure 7(a)). All the specimens oxidized between 1273 K and 1473 K (1000 °C and 1200 °C) showed similar surface morphology. No separate yttrium silicate layer was observed in this temperature regime. Instead, the $Y_2O_3$-$SiO_2$ type of precipitates

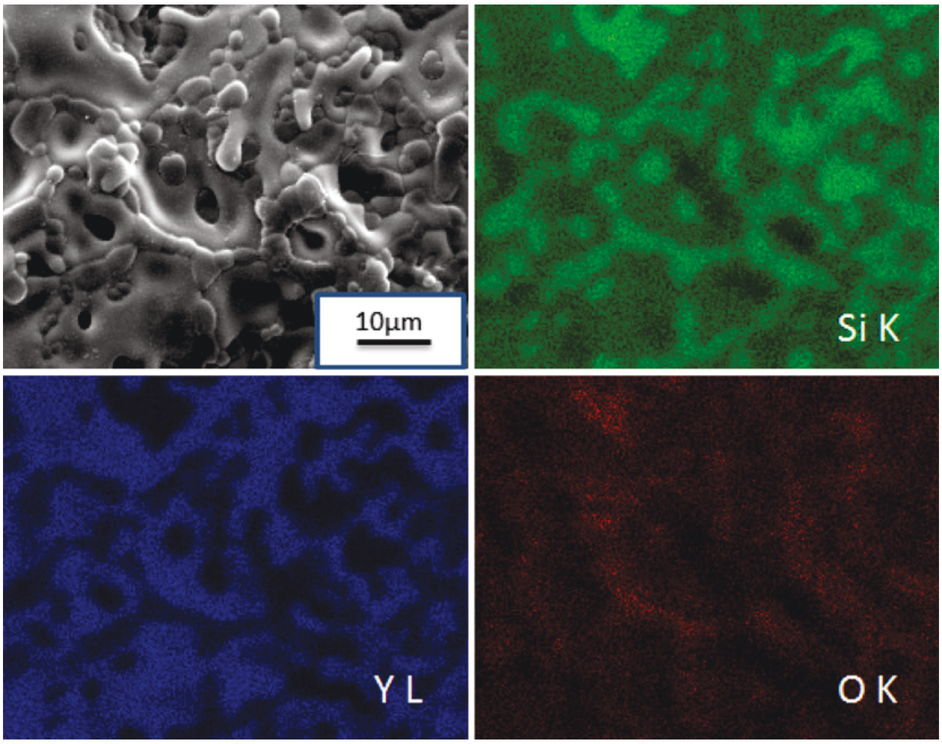

Fig. 3—SE image of Mo-9Si-8B-0.2Y alloy surface oxidized at 1573 K (1300 °C) for 100 h and the corresponding EDS maps indicating Y-enrichment in the silicate scale.

are present as second-phase inclusions in the continuous borosilicate phase. The cross-sectional image (Figure 7(b)) indicates the formation of a continuous and adherent borosilicate scale forming the outer layer, and also the presence of an internal oxidation zone near the substrate. The small yttrium-rich oxide precipitates were also observed along the cross section of the oxide scale.

At 1273 K (1000 °C), a superior oxidation behavior was noted for the Mo-9Si-8B-0.2Y alloy compared to the reference Mo-9Si-8B material; compare curves 1 and 2 in Figure 6. The cross-sectional SEM micrograph and EDS maps for the elements along the cross section of the oxide scale formed on Mo-9Si-8B-0.2Y alloy oxidized at 1273 K (1000 °C) for 100 hours are presented in Figure 8. The enrichment of Y was detected beneath the outer oxide layer (Figure 8, Y L map) at the interface between the outer oxide scale and the substrate. The localized enrichment of Y was also detected along the cross section of the silica-rich oxide scale as observed at 1473 K (1200 °C). These observations indicate that Y ions diffuse outward and get simultaneously oxidized with Si and B. However, the scale formation at 1273 K (1000 °C) suggests that the presence of Y in the scale increases the viscosity to such an extent that the scale becomes protective in nature. The segregation of Y at the scale/metal interface could reduce the diffusion of oxygen further. Compared to 1473 K (1200 °C), the rate of evaporation of B is still low at 1273 K (1000 °C) and the loss of B increases with increasing time. This has a significant effect on the oxidation behavior of the reference material (Mo-9Si-8B) at 1273 K (1000 °C). Therefore, the Y-enrichment at the silica scale improves the oxidation resistance at 1273 K (1000 °C), especially at the early stages.

An attempt was made to prepare a TEM specimen using focused ion beam milling and subsequent thinning to study the structure of the interface between the substrate and the oxide scale formed at 1273 K (1000 °C) for 100 hours. As presented in Figure 9(a), a thin slice was cut perpendicular to the cross section revealing the substrate and the oxide scale. A pore could be detected inside the oxide scale. The magnified image (Figure 9(b)) captured from the surface of the thin specimen indicates the formation of a very thin (~2 $\mu$m) internal oxidation zone penetrating the substrate followed by a layer rich in Mo, and the subsequent outer layer is formed by $MoO_2$ and a borosilicate scale. Clearly, the fine grain structure could be identified in the substrate (Figure 9(b)), and a preferential oxidation along some of the grains was observed in the internal oxidation zone. After lift out and final thinning, the TEM investigation was carried out. Figure 10(a) shows the microstructure obtained from the bulk material indicating the presence of a fine grain (400 to 500 nm) structure. The grain size of the A15 grains was found to be the smallest and Y-rich fine particles were also detected. Figure 10(b) represents a micrograph obtained

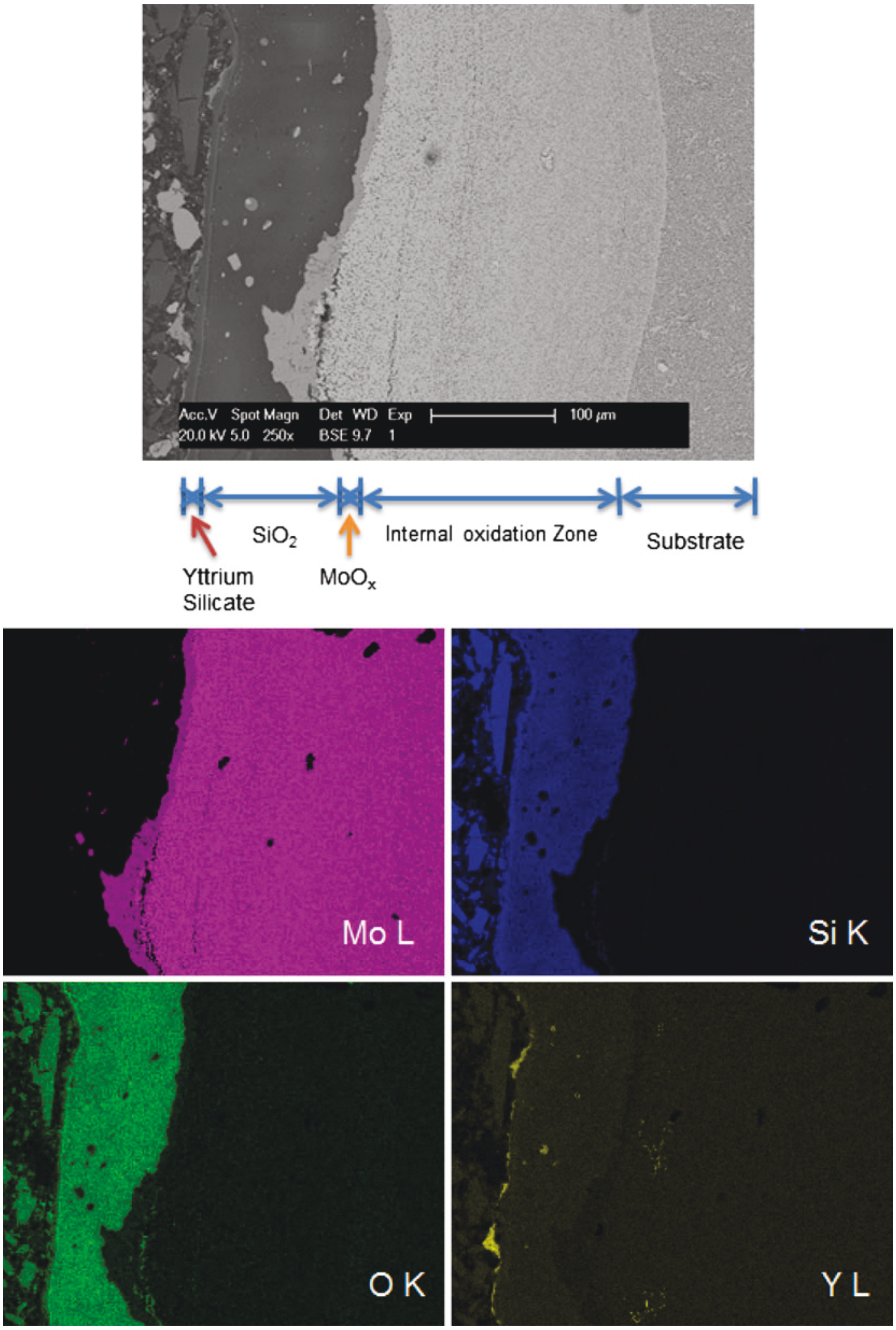

Fig. 4—Cross-sectional micrograph and elemental distribution maps for Mo-9Si-8B-0.2Y specimen oxidized at 1573 K (1300 °C) for 100 h.

near the interface between the oxide scale and the substrate. The presence of very fine (nanosize) precipitates was detected inside the oxide matrix. The selected area diffraction analysis produced a number of concentric rings (inset in Figure 10(b)). These diffraction patterns can be interpreted as stemming from molybdenum solid solution. Amorphous diffraction spot patterns were also observed for the borosilicate oxide scale.

This finding indicated that the thin layer formed just above the internal oxidation zone (marked as Mo-rich layer in Figure 9(b)) actually comprises a very fine Mo grain structure inside the amorphous silicate scale.

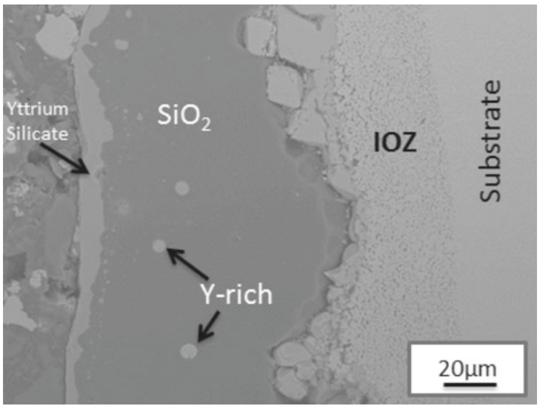

Fig. 5—Cross-sectional BSE image of Mo-9Si-8B-0.2Y alloy oxidized at 1673 K (1400 °C) for 2 h showing the formation of an outer yttrium-silicate layer.

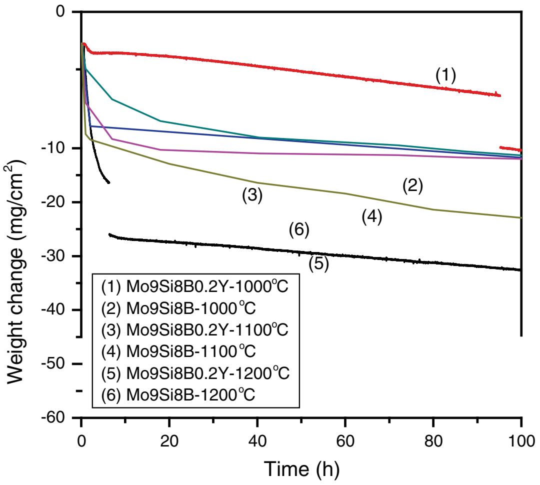

Fig. 6—TGA plots showing isothermal oxidation kinetics of the alloys at 1273 K to 1473 K (1000 °C to 1200 °C).

### D. *Oxidation at Intermediate Temperatures: 923 K to 1173 K (650 °C to 900 °C)*

Although Mo-Si-B alloys have proven good oxidation resistance beyond 1373 K (1100 °C) due to the formation of the protective borosilicate scale,[13–15,17] the alloys usually show inferior oxidation behavior in the intermediate temperature 923 K to 1173 K (650 °C to 900 °C) regime. This is due to the formation and easy evaporation of $MoO_3$ through the porous and non-protective oxide scale[39] with the rate of vaporization increasing with increasing temperature. At 923 K to 1023 K (650 °C to 750 °C), the viscous scale does not form, and $MoO_3$ evaporates out through the porous oxide scale. The melting point of $MoO_3$ is 1068 K (795 °C),[40] and a low viscosity B-rich scale is formed above this temperature. However, the scale is still non-protective up to 1173 K to 1223 K (900 °C to 950 °C) due to the lower evaporation rate of boron. The intermediate temperature regime can therefore be split into two regimes, *i.e.*, oxidation (1) at 1073 K to 1173 K (800 °C to 900 °C) and (2) at 923 K to 1023 K (650 °C to 750 °C). The detailed oxidation behavior observed for Y-alloyed Mo-Si-B in these two regimes is presented in the following sections.

#### 1. *At 1073 K to 1173 K (800 °C to 900 °C)*

The isothermal oxidation kinetic results obtained from Mo-9Si-8B-0.2Y alloy oxidized at 1073 K, 1093 K, and 1173 K (800 °C, 820 °C, 900 °C) are plotted in Figure 11. The results were compared with those obtained on the reference alloy without Y reported in the literature.[13,17] It can be clearly seen from Figure 11 (curves 4 and 5) that the reference alloys show a continuous higher rate of weight loss with increasing time of oxidation at 1073 K and 1173 K (800 °C and 900 °C). In other words, the 0.2 at. pct Y-alloyed Mo-Si-B alloys exhibit an improved oxidation resistance in this temperature regime. Even a gradual weight gain at the initial periods of oxidation was noted for all three tested temperatures (curves 1, 2, and 3 in Figure 11). At 1073 K (800 °C) (curve 1, Figure 11), the gain in weight continued until about 60 hours of oxidation, followed by a gradual loss of weight for some time and a subsequent low rate of weight loss.

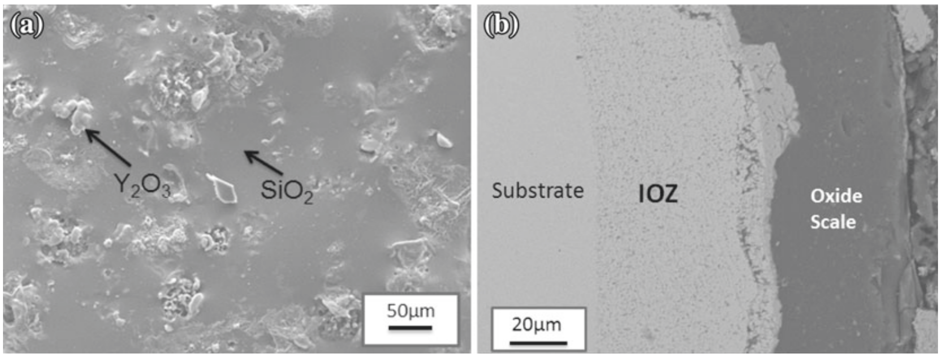

Fig. 7—Mo-9Si-8B-0.2Y alloy oxidized at 1473 K (1200 °C) for 100 h; (*a*) surface morphology and (*b*) cross-sectional image.

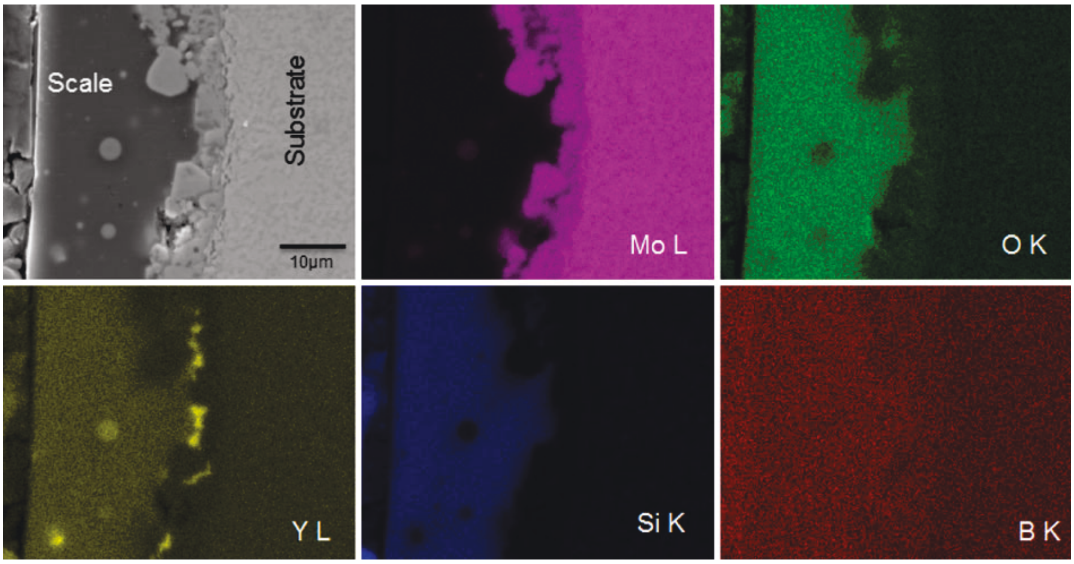

Fig. 8—Cross-sectional SEM image and elemental distribution maps obtained from a specimen oxidized at 1273 K (1000 °C) for 100 h.

A similar trend in change of weight was observed at 1093 K and 1173 K (820 °C and 900 °C) (curves 2 and 3, Figure 11) with the difference of the initiation of weight loss toward the lower time of oxidation as the temperature was increased. For identifying possible reasons for the improved oxidation behavior of the alloy in this temperature regime, cross sections of oxide layers were studied by oxidizing the specimens for different time intervals at 1073 K (800 °C). Figure 12 represents the cross section of the oxide layers formed at 1, 4, 24, and 48 hours of oxidation at 1073 K (800 °C). The presence of a continuous silicate scale was observed in all the specimens. A separate $MoO_2$ layer was present between the outer silicate scale and the substrate. The presence of some $MoO_3$ whiskers was also detected in this layer. The thickness of both the layers increased with increasing time. The growth kinetics of the outer silicate scale and the inner $MoO_2$ layer is presented in Figure 13. Although the outer scale shows a transition from linear to parabolic growth, the thickness of the inner $MoO_2$ layer increases linearly. Therefore, the linear weight gain observed in the TGA plots (curve 1, Figure 11) was mainly due to the simultaneous oxidation of Mo and Si and also other elements such as B and Y. EDS analysis indicated that the elemental Y concentration corresponding to 2.2 mol pct $Y_2O_3$ was present in the silicate scale formed after 1 hour of oxidation at 1073 K (800 °C). The concentration of $Y_2O_3$ would increase with time of oxidation as more amount of Y diffuses toward the oxide scale. The presence of a reactive element like Y reduces the rate of formation of $MoO_3$ at the initial stages leading to the formation of a silica and B-rich oxide. The $Y_2O_3$ inclusions act as the nucleation sites for silica and thereby increase the rate of nucleation of silica. The incorporation of $Y_2O_3$ in the B-rich silica scale could also increase the viscosity of the scale, preventing the $MoO_3$ bubbling, as observed, in the case of the reference material (Mo-Si-B). However, with increasing time, the scale gets enriched with boron, and oxygen ions can penetrate continuously through the defects formed in such a complex oxide (Si-B-Mo-Y-O) structure. Hence, the formation of molybdenum oxides takes place continuously and a time is reached when the vapor pressure of $MoO_3$ is high enough to bubble through the low viscosity scale by forming cracks. The presence of bigger size pores could be observed at the outer scale and Mo-oxide interface after 48 hours of oxidation at 1073 K (800 °C) (Figure 12). These pores grew to a larger size with increasing time, generating stresses on the outer layer and finally leading to the formation of cracks in the outer scale. The loss of weight of the specimens observed (Figure 11) at a higher time was due to the evaporation of $MoO_3$ through these cracks formed in the scale. However, the scale has the tendency of self-healing once the internal stress is reduced after escape of the $MoO_3$ formed at the earlier stages. The zigzag shape of the curves 2 and 3 in Figure 11 could be due to simultaneous crack formation and self-healing of the scale. This self-healing nature of the silicate scale can also be deduced from the reduced rate of loss of weight observed in TGA curves at higher time periods (Figure 11).

### 2. *At 923 K to 1023 K (650 °C to 750 °C)*

Figure 14 shows the isothermal oxidation kinetics of the specimens at 1023 K (750 °C). Mo-9Si-8B-0.2Y alloy exhibited a very similar oxidation behavior as observed for the reference samples reported in the literatures.[13,17] The 0.2 at. pct Y-alloyed specimen experienced (curve 1 in Figure 14) a drastic weight loss with the increase in time of oxidation. The scale was found to be porous and 0.2 at. pct Y could not play any major role in enhancing the growth of the silica scale formation. Evaporation of $MoO_3$ along the porous scale

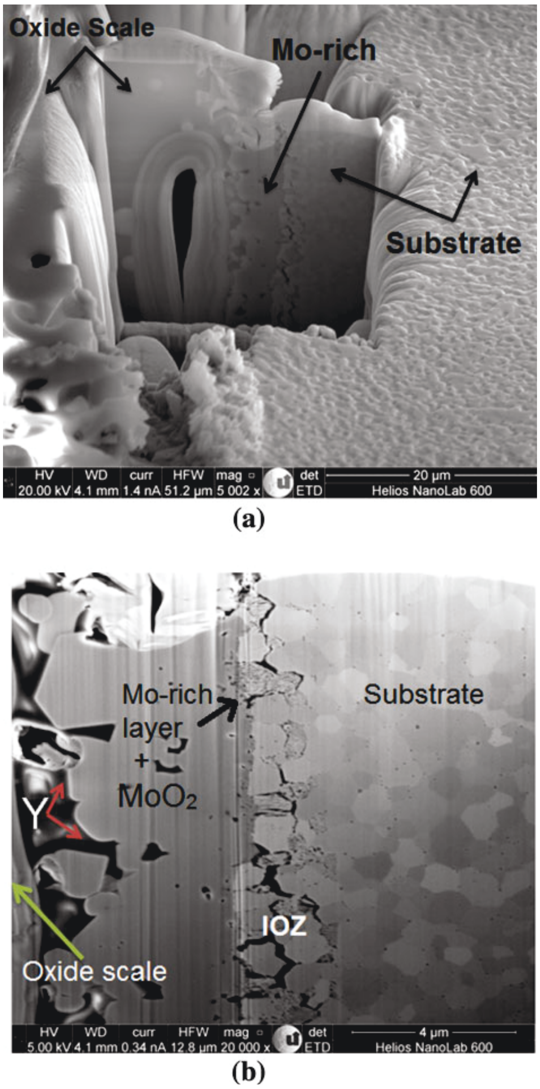

Fig. 9—(*a*) Thin specimen cut perpendicular to the cross section at the metal/oxide interface (from Mo-9Si-8B-0.2Y specimen oxidized at 1273 K (1000 °C) for 100 h) using focused ion beam (FIB) milling and (*b*) SE image showing the microstructure of the thin specimen along the perpendicular direction.

led to catastrophic oxidation. The alloy specimen was completely oxidized, leaving powder residue after 40 hours.

The oxidation behavior of 0.2 at. pct Y-alloyed material was found to be similar to the behavior of the unalloyed Mo-Si-B alloys at 923 K (650 °C) presented in Figure 15. The continuous loss of weight was observed with increasing time after a small initial weight gain. At this low temperature, $MoO_3$ begins to evapo-rate, and the silicate scale growth rate is very low, forming a powdery scale. However, the rate of evapo-ration loss was found to be much lower at this temperature.

An attempt was made to study the oxidation behavior of Mo-9Si-8B-0.2Y alloy at 1023 K (750 °C) after giving pre-oxidation treatment at higher temperatures. Figure 16 shows the weight change behavior obtained from thermogravimetric analysis carried out by designing a cyclic heat treatment schedule. Firstly, the alloy specimen was isothermally oxidized at 1273 K (1000 °C) for 3 hours. An initial weight loss was followed by a steady state scale formation. The specimen was subsequently heated to 1573 K (1300 °C) at a very fast rate followed by isothermal oxidation at 1573 K (1300 °C) for 9 hours. This duration was selected to reach the steady state scale formation stage after the initial transient evaporation stage. The pre-oxidized specimen was cooled to 1023 K (750 °C) and an isothermal oxidation test was carried out at 1023 K (750 °C). The isothermal oxidation plot at 1023 K (750 °C) shows marginal continuous weight gain with increasing time. Therefore, the oxide scale formed during the two-stage pre-oxidation treatments was capable of preventing evaporation loss of $MoO_3$ from the alloy at 1023 K (750 °C). However, the scale could remain protective for a definite period of time because more amount of B diffusion in the scale from the substrate with increasing time would reduce its viscosity, thereby making it non-protective.

### E. *Internal Oxidation*

The selective oxidation of solute elements of an alloy due to the reaction between the inwardly diffusing oxidizing species and the alloying elements of the material is termed "internal oxidation." The classical model of internal oxidation of binary alloys was developed by Wagner,[41] who assumed the solubility product of the internal oxide ($BO_v$) to be very small so that the concentrations of oxygen and solute atom (B) at the oxidation front may be neglected. This model leads to an analytical expression for the parabolic rate constant of internal oxidation. However, the oxidation mechanisms for ternary system like Mo-Si-B are more complex as compared to binary systems such as Ni-Al,[42] Ag-Cd,[43] etc., studied as model systems for predicting the kinetic phenomenon of internal oxidation. The occurrence of an internal oxidation zone in Mo-9Si-8B-0.2Y alloy oxidized at 1273 K to 1673 K (1000 °C to 1400 °C) has been presented earlier (Figures 4, 5, 7, 9). The separate layer of internal oxidation zone forms below the outer protective silicate scale. Figure 17 shows the cross-sectional image of electrolytically polished surface presenting the interface between the internal oxidation zone (IOZ) and Mo-9Si-8B-0.2Y substrate oxidized at 1373 K (1100 °C) for 100 hours. The microstructure of the IOZ looked entirely different from that of the substrate (Figure 17). Both T2 and A15 phases reacted with the oxygen and formed oxides. The presence of porosities, oxide particles, and unreacted molybdenum grains could be seen in the IOZ. For identifying the structures formed in IOZ, the attempt was made to prepare the interface by polishing with focused ion beam (FIB) and running the EBSD measurements subsequently. Figure 18 shows the result of this analysis. The most interesting result

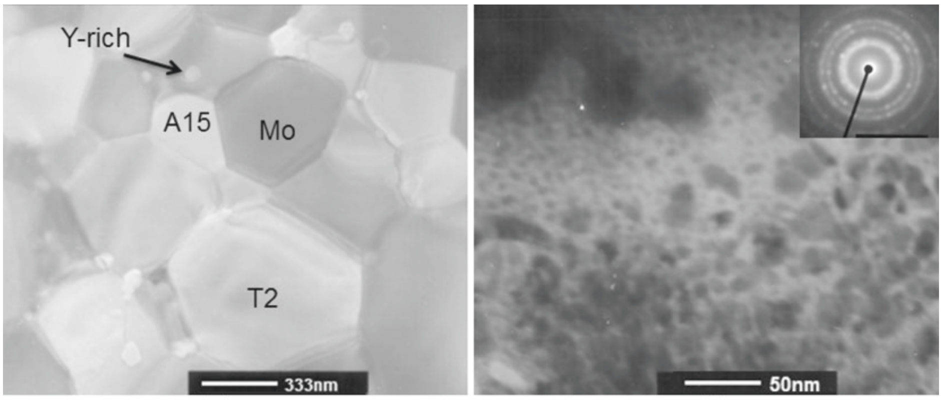

(a) (b)

Fig. 10—TEM micrographs; (*a*) substrate and (*b*) at the oxide scale/substrate interface indicating the presence of nanosized particles of molybdenum inside the amorphous oxide scale; inset: SAD ring patterns for Mo (110), (200), (211), and (220) diffractions correspondingly from lower to higher diameter rings.

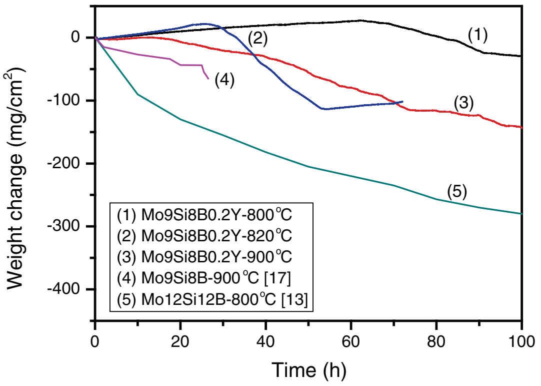

Fig. 11—TGA plots showing isothermal oxidation kinetics of the Y-alloyed and the reference alloy at 1073 K to 1173 K (800 °C to 900 °C).

obtained from this analysis is the identification of very fine-sized (nanograins) molybdenum grains in the IOZ (Figure 18(a)). The area near and beneath the IOZ was completely transformed to molybdenum phase as indicated by the phase map (Figure 18(c)) obtained from the specimen. The possible oxidation reactions occurring in the IOZ can therefore be written as

$$2Mo_5SiB_2 + 5O_2 = 10Mo + 2SiO_2 + 2B_2O_3 \qquad [1]$$

$$Mo_3Si + O_2 = 3Mo + SiO_2 \qquad [2]$$

The presence of Mo nanoparticles in the oxide scale near the scale/substrate interface formed at 1273 K (1000 °C) was also detected by means of the TEM examination. With increasing temperature, the particles grew near the substrate (IOZ) and they were also consumed by the preexisting molybdenum grains. The increase in size of the preexisting Mo grains could be identified near the IOZ (Figure 18(a)). Therefore, the internal oxidation zone is composed of Mo grains and the oxide particles such as $SiO_2$, $B_2O_3$, and also $Y_2O_3$. A small amount of $MoO_2$ could also be present as the subsequent layer beneath the borosilica scale consists mainly of $MoO_2$.

According to Wagner's theory of internal oxidation, the rate of penetration of the internal oxide front into the alloy is a parabolic function of time. To understand the penetration rate of the internal oxidation front in Mo-9Si-8B-0.2Y alloy, a series of oxidation tests was conducted in furnace air at 1373 K, 1473 K, 1573 K, and 1673 K (1100 °C, 1200 °C, 1300 °C, 1400 °C) for different time intervals such as 2, 5, 25, and 50 hours. As there is a formation of thick silicate scale in the outer layer at all the selected temperatures, the change in the thickness ($h$) of the IOZ with time at different temperatures was measured using cross-sectional SEM imaging. Applying Wagner's theory, the kinetic equation for growth of the internal oxidation zone may be written as the following:

$$h = 2\gamma(D_0 t)^{1/2} \qquad [3]$$

where $D_0$ is the diffusivity of oxygen in the base material and $\gamma$ is a dimensionless parameter dependent on the relative contribution of the diffusion of the components (O, Si, B, etc.) involved in the formation of the internal oxidation zone. The thickness data for the IOZ formed during oxidation of Mo-9Si-8B-0.2Y alloy are plotted against time (in logarithmic scale) in Figure 19(a) for the four different temperatures studied. The growth rate exponents ($n$) at different temperatures were calculated by fitting linear plots for ln($h$) *vs* ln($t$) data points. It can be seen from Figure 19(a) that the growth of the IOZ followed a parabolic ($n \approx 0.5$) relationship with time, as predicted by Eq. [3]. A slightly higher value for $n$ (~0.68) was calculated at 1473 K (1200 °C). The most significant result from Figure 19(a) is that the thickness of

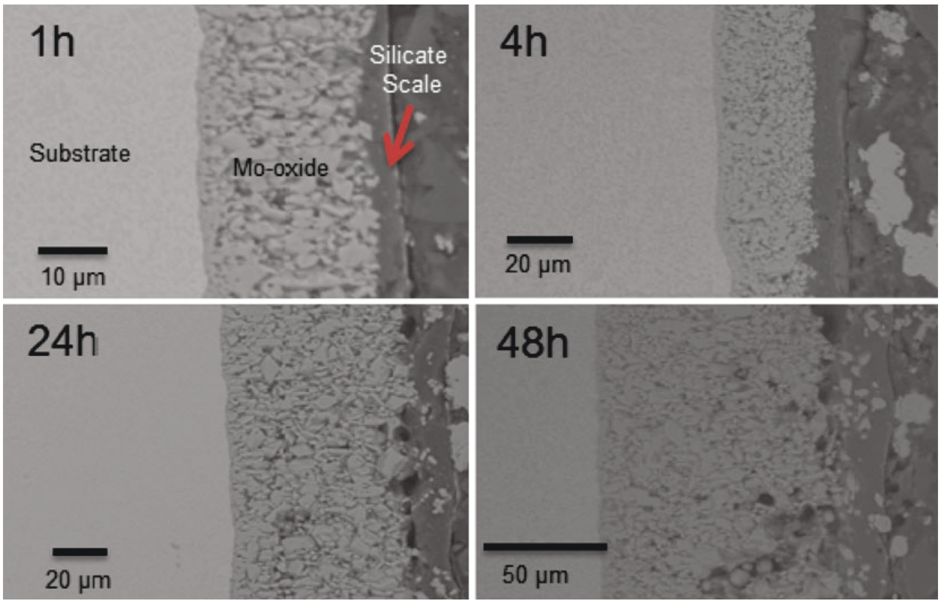

Fig. 12—Cross-sectional microstructures of Mo-9Si-8B-0.2Y specimens oxidized at 1073 K (800 °C) for different time intervals.

IOZ formed at 1573 K and 1673 K (1300 °C and 1400 °C) was almost identical. This behavior indicates that the effect of temperature activation was nullified by the occurrence of some other mechanism at 1673 K (1400 °C).

From Wagner's analysis, the expression for the kinetic parameter $\gamma$ in Eq. [3] can be expressed as

$$\gamma = \left( \frac{N_O^{(s)}}{2\nu N_B^{(o)}} \right)^{1/2} \qquad [4]$$

where $N_O^{(s)}$ and $N_B^{(o)}$ are the atomic fractions of dissolved oxygen at the alloy (AB) surface and the initial concentration of B in the bulk alloy, respectively. Equation [4] is valid when the solute atom (B) diffuses out at a much slower rate compared to the inward diffusing species oxygen and when the solubility of oxygen is very small with respect to the solutes' content of the alloy. However, in the case of the Mo-Si-B system, the solute atoms (Si and B) oxidize both externally and internally, which was observed by the simultaneous increase in thickness of the outer oxide scale and of the IOZ with time at the same oxidation temperature. Therefore, the fraction of oxygen atoms diffusing through the external oxide scale contributes to the internal oxide formation.

Böhm and Kahlweit[43] proposed that internal oxide ($BO_\nu$) precipitation does not occur along a well-defined front (as proposed by Wagner), but rather within a region of small but finite width where the concentration profiles of oxygen and solute atom change with time as new oxide particles nucleate and grow. The expression for the kinetic parameter derived by analyzing this model was found to be

$$\gamma = \frac{N_O^{(s)}}{2\nu(N_B^{(o)} - N_B^{'})}\Bigg)^{1/2} \qquad [5]$$

where $N_B^{'}$ is the finite solute atom fraction at the internal oxidation front. A comparison of Eqs. [4] and [5] shows that a greater growth rate of the IOZ is predicted by Böhm and Kahlweit compared to Wagner's model. Böhm and Kahlweit were also able to calculate the number density ($f_N$) of the oxide precipitates with spherical morphology at a finite diffusion distance ($X_i$). They were able to arrive at the following relationship for a continuous nucleation and growth process.

$$f_N(X_i) = \mathrm{Constant}p_{O_2}^{n} \qquad [6]$$

Therefore, as per Eq. [6], the number of oxides formed in the IOZ is directly proportional to the atom fraction of oxygen ($((N_O^{(s)})^m)$) or the partial pressure of oxygen beneath the external oxide scale, where the exponents $n$ and $m$ are dependent upon the stoichiometry of the oxide. Now, the kinetic data for internal oxidation for the Mo-9Si-8B-0.2Y alloy at 1573 K and 1673 K (1300 °C and 1400 °C) (Figure 19(a)) revealed that the thickness of the IOZ does not increase from 1573 K to 1673 K (1300 °C to 1400 °C) for the same oxidation times. The cross-sectional analysis of the oxidized specimen (Figure 5) indicated that a thin yttrium silicate layer forms at 1673 K (1400 °C) within a shorter oxidation time. This yttrium silicate layer could reduce the diffusivity of oxygen, thereby reducing the fraction of oxygen atoms below the silicate scale. Reduced oxygen partial pressure ($N_O^{(s)}$ or $p_{O_2}^{n}$) at the scale/IOZ interface would lead to the reduction in rate of forma-

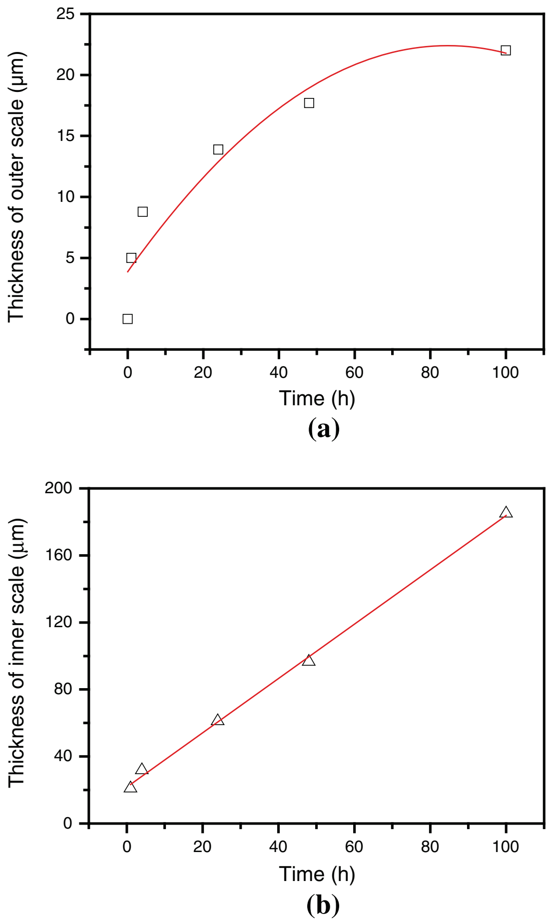

Fig. 13—Growth kinetics of the oxide layers on Mo-9Si-8B-0.2Y alloy at 1073 K (800 °C); (*a*) outer silicate scale and (*b*) inner Mo-oxide layer.

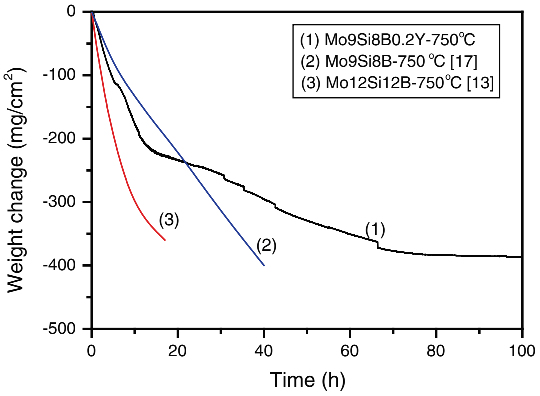

Fig. 14—TGA plots showing isothermal oxidation kinetics at 1023 K (750 °C).

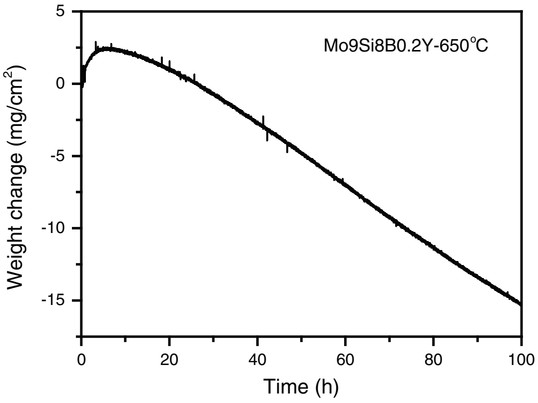

Fig. 15—TGA plots showing isothermal oxidation kinetics at 923 K (650 °C).

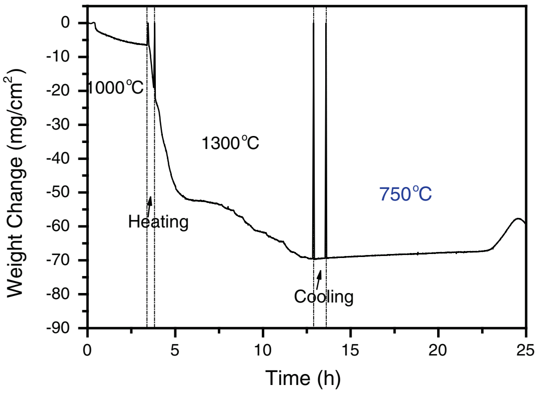

Fig. 16—TGA plot for Mo-9Si-8B-0.2 Y alloy pre-oxidized at 1273 K (1000 °C) followed by at 1573 K (1300 °C) and subsequently oxidized isothermally at 1023 K (750 °C).

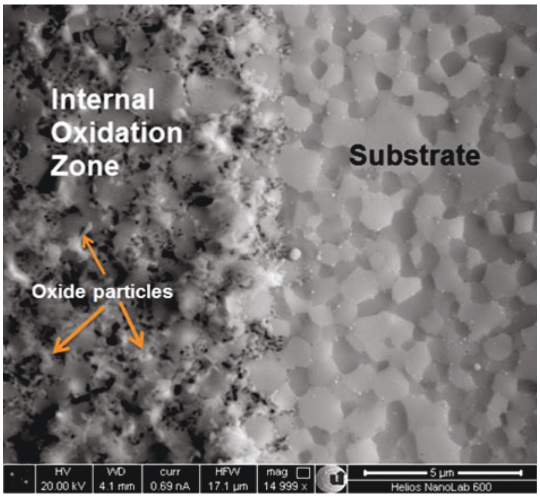

Fig. 17—SEM image showing the interface between the substrate and internal oxidation zone (IOZ) formed during oxidation of Mo-9Si-8B-0.2Y alloy at 1373 K (1100 °C) for 100 h.

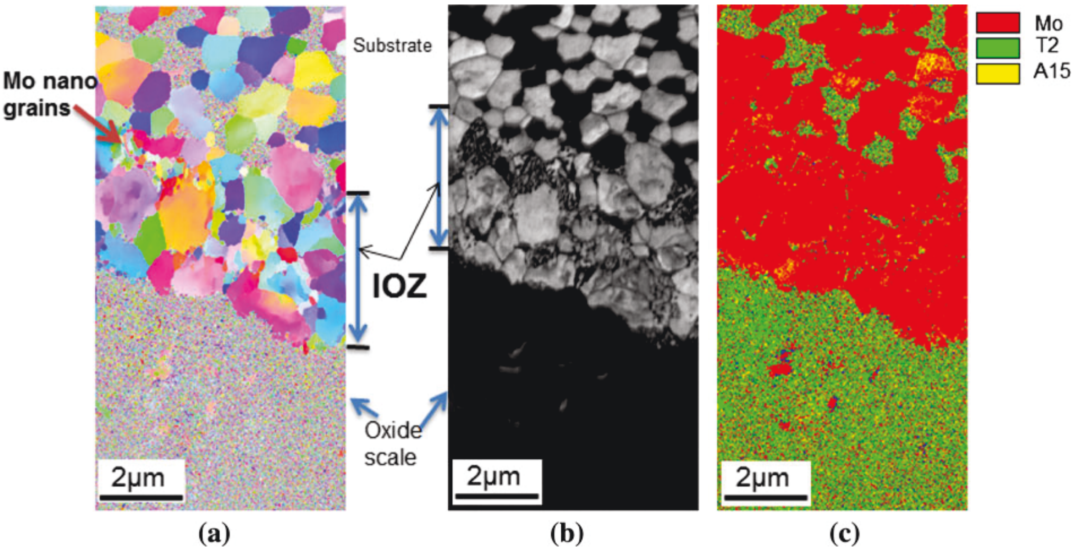

Fig. 18—EBSD maps showing interface between the IOZ and the substrate (Mo-9Si-8B-0.2Y) oxidized at 1373 K (1100 °C) for 2 h. Specimen was prepared using focused ion beam milling and polishing. (*a*) Orientation map, (*b*) image quality map, and (*c*) phase map.

tion of the internal oxidation zone or the fraction of internal oxides as predicted by Eqs. [4] through [6].

Figure 19(b) shows the Arrhenius plot for the thickness data against temperature for both the outer borosilicate oxide scale and the IOZ formed during oxidation of Mo-9Si-8B-0.2Y alloy. The data obtained for the IOZ were plotted for 1273 K to 1573 K (1000 °C to 1300 °C) because the thickness data for 1573 K and 1673 K (1300 °C and 1400 °C) were identical. For the outer borosilicate-rich oxide scale, the data points were plotted for 1273 K to 1673 K (1000 °C to 1400 °C). The thickness of the thin yttrium-silicate layer formed at the outer surface at 1573 K and 1673 K (1300 °C and 1400 °C) was not considered for these calculations. The linear plots obtained for the IOZ at different times were almost parallel, which indicated that there should be no significant change in mechanism for the IOZ formation with increasing time. The activation energy for the IOZ formation was calculated to be 248 kJ/mol. This value gives a qualitative indication for thermal activation required for diffusion of oxygen along the interphase boundaries between Mo, and T2 and A15. The linear plot obtained for the outer borosilicate scale formed after 100 hours of oxidation at different temperatures showed a much shallower slope (Figure 19(b)) com-pared to that for the IOZ. The activation energy for the growth of the silicate scale was found to be 118.6 kJ/mol (28.4 kcal/mol), which is very close to the reported value (29 kcal/mol)[44] of activation energy for diffusion of oxygen in fused silica at 1373 K to 1523 K (1100 °C to 1250 °C). This result confirms that yttrium-silicate slows the oxygen diffusion at higher temperatures.

## IV. SUMMARY AND CONCLUSIONS

The detailed oxidation studies conducted with 0.2 at. pct Y-alloyed Mo-9Si-8B in the wide temperature range from 923 K to 1673 K (650 °C to 1400 °C) indicated that Y plays a key role in the formation of the oxide scale. Beyond 1573 K (1300 °C), formation of two separate oxide layers was identified. The outer thin layer was composed of an yttrium-silicate phase, and the inner thick layer was composed of borosilica. At 1273 K to 1473 K (1000 °C to 1200 °C), the scale consisted of only one layer of silica-rich oxide, and fine particles of Y-rich oxides were distributed inside the scale. The oxidation resistance of Y-alloyed material was found to be comparable with that of the reference (Mo-9Si-8B) material at 1373 K to 1673 K (1100 °C to 1400 °C). An improvement in the oxidation resistance of the Y-alloyed material was detected at 1273 K (1000 °C).

In the intermediate temperature regime 923 K to 1173 K (650 °C to 900 °C), the 0.2 at. pct Y-alloyed material showed a much more different and improved oxidation behavior compared to the reference alloy (Mo-Si-B), especially at 1073 K to 1173 K (800 °C to 900 °C). Based on the compositional analysis of the oxide scale, it could be revealed that the formation of a silica-rich scale containing some quantities of $Y_2O_3$-$SiO_2$ as dispersed particles is capable of preventing the permeation of $MoO_3$ for a sufficiently long time. The isothermal oxidation data showed a systematic gain in weight at the initial stages of oxidation of Y-alloyed material, whereas the unalloyed reference material shows a drastic weight loss during this period. At 923 K to 1023 K (650 °C to 750 °C), no major difference in the oxidation behavior between the reference

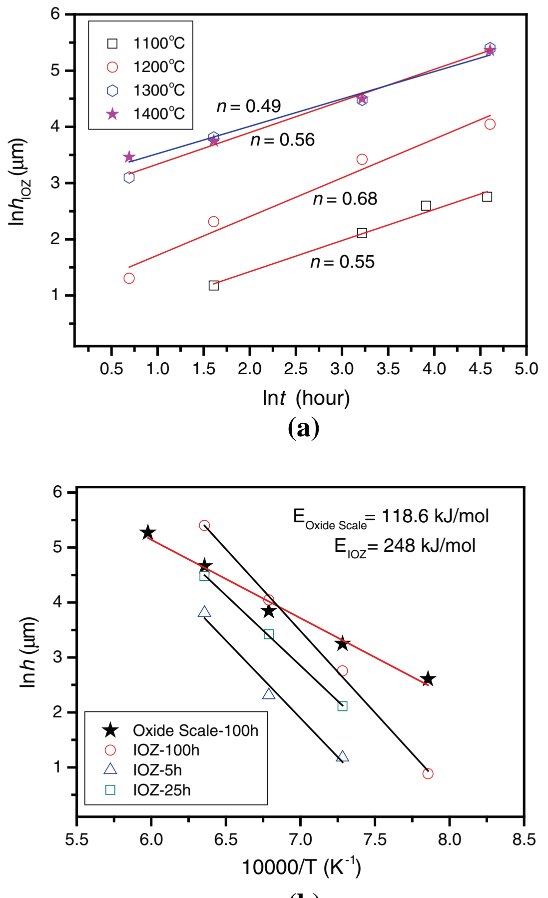

**(a)**

**(b)**

Fig. 19—(*a*) Growth kinetics plots for internal oxidation zone (IOZ) formed on Mo-9Si-8B-0.2Y alloy at different temperatures 1373 K to 1673 K (1100 °C to 1400 °C) and (*b*) Arrhenius plots showing the temperature dependence of growth of the outer borosilicate oxide scale and of the IOZ during oxidation of Mo-9Si-8B-0.2Y alloy in static air at different time intervals between 1273 K to 1673 K (1000 °C to 1400 °C).

material and Y-alloyed material was observed. However, a much superior oxidation resistance of Mo-9Si-8B-0.2Y alloy was detected at 1023 K (750 °C) after giving a two-stage pre-oxidation treatment at 1273 K and 1573 K (1000 °C and 1300 °C).

More in-depth microstructural investigations and kinetic analysis of the internal oxidation zone formed on Mo-9Si-8B-0.2Y alloy at 1273 K to 1673 K (1000 °C to 1400 °C) resulted in new observations and conclusions. The oxygen ions diffusing inward through the oxide scale react mainly with T2 ($Mo_5SiB_2$) and A15 ($Mo_3Si$) phases forming $SiO_2$ and $B_2O_3$ particles in the inner oxidation layer. The formation of fine-grained (nanosize) Mo structure and the growth of the preexisting Mo grains were detected at the inner oxidation zone. The inner oxidation layer showed parabolic growth kinetics at all temperatures from 1373 K to 1673 K (1100 °C to 1400 °C). The thicknesses of the inner oxidation layer formed at 1573 K and 1673 K (1300 °C and 1400 °C) were found to be identical. This phenomenon was attributed to the formation of an outer layer comprising yttrium-silicate phase, which reduces the inward diffusion rate of oxygen.

Further investigations are being carried out to study the oxidation behavior of Mo-Si-B with varying concentrations of Y. The results of these investigations will be presented later. One major limitation of this work is that the fraction of $B_2O_3$ present in the oxide scale could not be measured accurately using EDS analysis. The interaction of $B_2O_3$ with $Y_2O_3$-$SiO_2$ and the possible effect on the scale structure needs to be understood. Finally, a suitable silicide-based coating has to be designed for Mo-Si-B-Y system for its final application as structural components.

## ACKNOWLEDGMENTS

S. Majumdar wishes to thank the Alexander von Humboldt foundation, Bonn, for financial support of the research stay at Siegen. The research support by the Deutsche Forschungsgemeinschaft (DFG) within the framework of the research unit 727 "Beyond Ni-Base Superalloys" is gratefully acknowledged.

## REFERENCES

1. J.H. Perepezko: *Science*, 2009, vol. 20, pp. 1068–69.
2. M. Heilmaier, M. Kruger, H. Saage, J. Rosler, D. Mukherji, U. Glatzel, R. Volkl, R. Huttner, G. Eggeler, Ch. Somsen, T. Depka, H.-J. Christ, B. Gorr, and S. Burk: *J. Met.*, 2009, vol. 67, pp. 61–67.
3. E.W. Lee, J. Cook, A. Khan, R. Mahapatra, and J. Waldman: *J. Met.*, 1991, vol. 43, pp. 54–57.
4. J. Cook, A. Khan, E.W. Lee, and R. Mahapatra: *Mater. Sci. Eng., A*, 1992, vol. 155, pp. 183–98.
5. P.J. Meschter: *Metall. Trans. A*, 1992, vol. 23A, pp. 1763–72.
6. A.K. Vasudevan and J.J. Petrovic: *Mater. Sci. Eng., A*, 1992, vol. 155, pp. 1–17.
7. D.M. Berczik: U.S. Patent No. 5.693.156, 1997.
8. D.M. Berczik: U.S. Patent No. 5.695.616, 1997.
9. M.K. Meyer and M. Akinc: *J. Am. Ceram. Soc.*, 1996, vol. 79, pp. 2763–66.
10. M.K. Meyer and M. Akinc: *J. Am. Ceram. Soc.*, 1996, vol. 79, pp. 938–45.
11. M.K. Meyer, A.J. Thom, and M. Akinc: *Intermetallics*, 1999, vol. 7, pp. 153–62.
12. V. Supatarawanich, D.R. Johnson, and C.T. Liu: *Mater. Sci. Eng., A*, 2003, vol. 344, pp. 328–39.
13. T.A. Parthasarathy, M.G. Mendiratta, and D.M. Dimiduk: *Acta Mater.*, 2002, vol. 50, pp. 1857–68.
14. V. Supatarawanich, D.R. Johnson, and C.T. Liu: *Intermetallics*, 2004, vol. 12, pp. 721–25.
15. M.G. Mendiratta, T.A. Parthasarathy, and D.M. Dimiduk: *Intermetallics*, 2002, vol. 10, pp. 225–32.
16. P. Sharma, R. Mitra, and S.K. Roy: *Intermetallics*, 2007, vol. 15, pp. 1217–27.
17. S. Burk, B. Gorr, V.B. Trindade, and H.-J. Christ: *Oxid. Met.*, 2010, vol. 73, pp. 163–81.
18. J.M. Francis and W.H. Whitlow: *Corros. Sci.*, 1965, vol. 5, pp. 701–10.
19. J.K. Tien and F.S. Petit: *Metall. Trans. A*, 1972, vol. 3A, pp. 1587–99.
20. A. Kumar, M. Nasrallah, and D.L. Douglass: *Oxid. Met.*, 1974, vol. 8, pp. 227–63.

21. B.A. Pint: *Oxid. Met.*, 1998, vol. 49, pp. 531–60.
22. N. Hiramatsu and F.H. Stott: *Oxid. Met.*, 1999, vol. 51, pp. 479–94.
23. B.A. Pint: *J. Am. Ceram. Soc.*, 2003, vol. 86, pp. 686–95.
24. B.A. Pint: *Oxid. Met.*, 1996, vol. 45, pp. 1–37.
25. T.J. Nijdam and W.G. Sloof: *Acta Mater.*, 2007, vol. 55, pp. 5980–87.
26. D. Naumenko, B. Gleeson, E. Wessel, L. Singheiser, and W.J. Quadakkers: *Metall. Mater. Trans. A*, 2007, vol. 38A, pp. 2974–83.
27. D.P. Whittle and J. Stringer: *Philos. Trans. R. Soc. Lond.*, 1980, vol. 295, pp. 309–29.
28. E.J. Opila: *J. Am. Ceram. Soc.*, 1999, vol. 82, pp. 625–36.
29. E.J. Opila, J.L. Smialek, R.C. Robinson, D.S. Fox, and J.S. Jacobson: *J. Am. Ceram. Soc.*, 1999, vol. 82, pp. 1826–34.
30. J. Schneider, K. Biswas, G. Rixecker, and F. Aldinger: *J. Am. Ceram. Soc.*, 2003, vol. 86, pp. 501–07.
31. Y.Q. Wang, J.F. Huang, Z.H. Chen, and L.Y. Cao: *J. Compos. Mater.*, 2012, vol. 46, pp. 371–82.
32. J.F. Huang, H.J. Li, X.R. Zeng, K.Z. Li, X.B. Xiong, and M. Huang: *Carbon*, 2004, vol. 42, pp. 2356–59.
33. J.F. Huang, H.J. Li, X.R. Zeng, and K.Z. Li: *Ceram. Int.*, 2006, vol. 32, pp. 417–21.
34. W. Chan, M.C. Gao, Ö.N. Dogan, and P. King: *J. Phase Equilb. Diff.*, 2010, vol. 31, pp. 414–20.
35. P. Jehanno, M. Heilmaier, and H. Kestler: *Intermetallics*, 2004, vol. 12, pp. 1005–09.
36. S. Majumdar, S. Raveendra, I. Samajdar, P. Bhargava, and I.G. Sharma: *Acta Mater.*, 2009, vol. 57, pp. 4158–68.
37. P. Jehanno, M. Heilmaier, H. Saage, H. Heyse, M. Böning H. Kestler, and J.H. Schneibel: *Scripta Mater.*, 2006, vol. 55, pp. 525–28.
38. P.D. Sarkisov, L.A. Orlova, N.V. Popovich, and Yu.E. Ananeva: *Glass Ceram.*, 2007, vol. 64, pp. 1–6.
39. D.M. Dimiduk and J.H. Perepezko: *MRS Bull.*, 2003, pp. 639-45.
40. G.R. Smolik, D.A. Petti, and S.T. Schuetz: *J. Nucl. Mater.*, 2000, vols. 283–287, pp. 1458–62.
41. C. Wagner: *Z. Elekrochem.*, 1959, vol. 63, pp. 772–80.
42. D.P. Whittle, Y. Shida, G.C. Wood, F.H. Stott, and B.D. Bastow: *Phil. Mag. A*, 1982, vol. 46, pp. 931–49.
43. G. Böhm and M. Kahlweit: *Acta Metall.*, 1964, vol. 12, pp. 641–48.
44. E.L.Williams: *J. Am. Ceram. Soc.*, 1965, vol. 48, pp. 190–94.

# Manuskript IV

# Optimization of Cr-content for high-temperature oxidation behavior of Co-Re-Si-base alloys

L. Wang, B. Gorr, H.-J. Christ, D. Mukherji, J. Rösler

Oxidation of Metals, 80 (2013) 49-59

Oxid Met (2013) 80
DOI 10.1007/s11085-013-9369-z

ORIGINAL PAPER

# Optimization of Cr-Content for High-Temperature Oxidation Behavior of Co–Re–Si-Base Alloys

**Lin Wang · Bronislava Gorr · Hans-Jürgen Christ · Debashis Mukherji · Joachim Rösler**

Received: 4 July 2012 / Published online: 7 February 2013

**Abstract** The oxidation behavior of Co-17Re-xCr-2Si alloys containing 23, 25, 27 and 30 at.% chromium at 1,000 and 1,100 °C were investigated. Alloy Co–17Re–23Cr–2Si showed a poor oxidation resistance during exposure to laboratory air forming a two-layer external scale and a very thin discontinuous $Cr_2O_3$ layer at the oxide/substrate interface. The outer layer of the oxide scale consisted of CoO, whereas the inner layer was a porous mixture of $CoCr_2O_4$ spinel particles in a CoO matrix. The oxide scale was found to be non-protective in nature as the vaporization of Re-oxide took place during oxidation. An increase of chromium content from 23 at.% to 25 at.% improved significantly the alloy oxidation resistance; a compact protective $Cr_2O_3$-scale formed and prevented the rhenium oxide evaporation. The oxidation behavior of alloys containing 27 at.% and 30 at.% chromium were quite similar to that of Co–17Re–25Cr–2Si. The oxidation mechanism for Co–17Re–25Cr–2Si alloy was established and the subsurface microstructural changes were investigated by means of EBSD characterization.

**Keywords** Co–Re-base alloys · $Cr_2O_3$-scale · Re-oxide vaporization · EBSD

---

L. Wang (✉) · B. Gorr · H.-J. Christ
Institut für Werkstofftechnik, Universität Siegen, Paul-Bonatz-Straße 9-11, 57068 Siegen, Germany
e-mail: lin.wang@uni-siegen.de

B. Gorr
e-mail: bronislava.gorr@uni-siegen.de

H.-J. Christ
e-mail: christ@ifwt.mb.uni-siegen.de

D. Mukherji · J. Rösler
Institut für Werkstoffe, TU Braunschweig, Langer Kamp 8, 38106 Braunschweig, Germany
e-mail: d.mukherji@tu-bs.de

J. Rösler
e-mail: j.roesler@tu-braunschweig.de

## Introduction

Alloys used for high-temperature applications such as power plants, gas turbines etc., require to possess both superior high-temperature corrosion resistance and excellent high-temperature mechanical properties. Nowadays, Ni-based superalloys are the dominating class of materials for applications in the hot section of gas turbines. However, their application is increasingly restricted if substrate material temperature exceeds 1,000 °C, since the strengthening $\gamma$'-phase in Ni-based alloys begins to dissolve at these temperatures [1]. Moreover, the melting point around 1,300 °C of this alloy system is also restricting its further development at extreme high temperature. Therefore, a new class of alloys, namely Co–Re-base model alloys, has been recently developed for high-temperature applications beyond 1,100 °C [2]. Because of the high melting point of Re (3,182 °C), the addition of Re in cobalt increases the melting point and the strength of the material while forming a continuous solid solution with Co.

Regarding the aspect of oxidation resistance, alloys used for high-temperature usually need to form a slow growing protective oxide scale, which are mostly chromia, alumina, or silica scales. The first generation of chromium containing Co–Re-base alloys for the high-temperature oxidation study has been developed by Rösler et al. [3] in order to form a $Cr_2O_3$-scale for intermediate temperature applications. However, the firstly studied Co-17Re-base alloys, which contained 23 at.% and 30 at.% chromium showed rather poor oxidation resistance after exposure to laboratory air. The porous and non-protective nature of the formed oxide scale resulted in a heavy mass loss due to evaporation of Re-oxide during oxidation. Gorr et al. [4] reported that Co–17Re–xCr alloys normally contain two phases at room temperature if the Cr-content is exceeded 20 at.%. One is the Cr–Re-rich sigma phase and the other one is the hexagonal closed packed (hcp) Co solid solution matrix. They also pointed out that the sigma phase fraction is increased with increasing Cr-content. The detailed microstructure of Co–Re–Cr alloys was reported by Depka et al. [5] elsewhere. Further, the brittle behavior of the sigma phase and its negative effect on the mechanical properties are well-known and were reported by many authors [6, 7].

There are numerous studies indicating that a silicon addition can significantly improve the oxidation resistance of Co-Cr-base alloys [8–10]. It was found by Gorr et al. [11] that the oxidation resistance of Co–17Re–23Cr can be enhanced by increasing the Si-content from 1 at.% to 3 at.%. A quasi-continuous chromia layer was formed on Co–17Re–23Cr–3Si after exposure to air at 1,100 °C for 7 h. However, this layer was still insufficient to avoid the evaporation of Re-oxide. On the other hand, higher silicon content strongly reduces the melting point of the alloys, which restricts their applications at elevated temperatures. For this reason, the Si-content in the Co–Re–Cr-alloys has been fixed to 2 at.%. Thus, there are two contradictory requirements: (i) a relatively high Cr-concentration is needed to facilitate the formation of a compact $Cr_2O_3$-scale; (ii) the high Cr-content should be avoided to restrict the volume fraction of the sigma phase, which is detrimental for the mechanical properties. Therefore, the aim of this work is to optimize the Cr-content in the Co–17Re–xCr–2Si alloy system to achieve favorable mechanical properties and superior oxidation resistance.

**Table 1** Chemical compositions of the alloys studied (in at.%)

| Model alloy | Co | Re | Cr | Si | Volume fraction of sigma phase (%) |
|---|---|---|---|---|---|
| Co–17Re–23Cr–2Si | bal. | 17 | 23 | 2 | 14.0 |
| Co–17Re–25Cr–2Si | bal. | 17 | 25 | 2 | 25.5 |
| Co–17Re–27Cr–2Si | bal. | 17 | 27 | 2 | 36.6 |
| Co–17Re–30Cr–2Si | bal. | 17 | 30 | 2 | 43.6 |

## Materials and Experimental Procedures

A series of Co–Re-base alloys containing 2 at.% Si and different concentrations of Cr were studied in this work, see Table 1. High purity metals were used as raw materials for alloying by means of arc-melting. Alloys were then homogenized by a three-step heat treatment (1,350 °C/5 h, 1,400 °C/5 h, 1,450 °C/5 h) followed by argon quenching in a vacuum furnace.

A typical microstructure of the homogenized Co–17Re–25Cr–2Si sample is shown in Fig. 1a showing the Cr–Re-rich sigma phase (bright) and the hcp matrix (dark). The volume fraction of the sigma phase for each alloy was measured using automated image analysis applying software Image J®, see Fig. 1b. Five microstructure images were taken from different areas of each sample in order to obtain the average volume fraction; the results are listed in Table 1.

Oxidation samples of approximate dimension of 10 × 10 × 2 mm$^3$ were cut from the homogenized alloys. Their surface were ground using SiC paper down to 1,200 grit and ultrasonically cleaned in acetone and ethanol immediately before use. Discontinuous isothermal oxidation tests were carried out at 1,000 and 1,100 °C in laboratory air for different times to study the scale growth mechanism. Specimens were directly taken out from the furnace after isothermal oxidation and cooled in air. Continuous thermogravimetric analysis (TGA) was also carried out to determine isothermal oxidation kinetics of alloys.

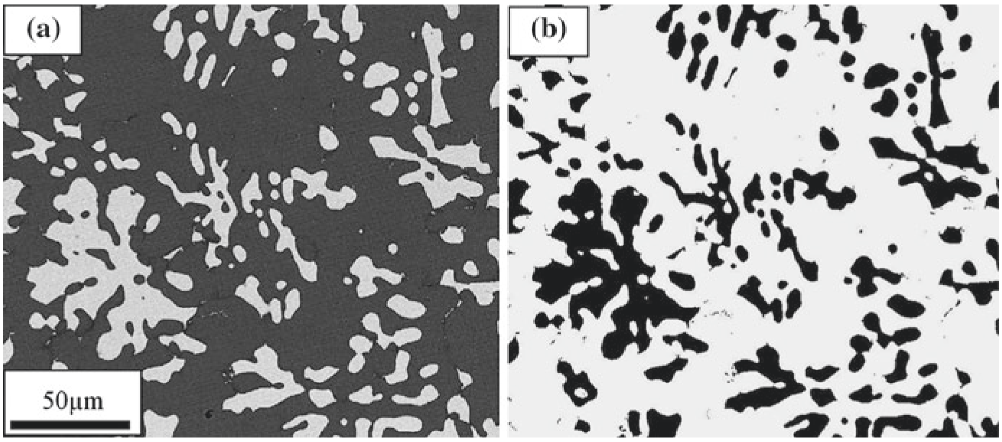

**Fig. 1** **a** Back-scattered electron image of polished Co–17Re–25Cr–2Si alloy, **b** adjusted image by program IMAGE J for phase volume fraction calculation

X-ray diffractometry (XRD) was used to identify the phases of untreated specimens as well as the oxide scale formed after oxidation tests. The surfaces and cross-section of oxidized samples were examined by scanning electron microscopy (SEM) in combination with energy dispersive X-ray spectroscopy (EDS). For cross-sectional studies, oxidized specimens were firstly coated with Nickel by electro deposition and then prepared using standard metallographic techniques. Electron back-scattered diffraction (EBSD) measurements were also carried out to study the microstructural changes of the alloy subsurface during oxidation.

## Results

### Kinetics

The thermogravimetric curves shown in Fig. 2a indicate two distinct types of oxidation behavior of the alloys as the Cr-content was varied from 23 at.% to 27 at.%. A weight gain was observed for Co–17Re–25Cr–2Si and Co–17Re–27Cr–2Si following a parabolic manner. On the contrary, a relative heavy mass loss was observed for Co–17Re–23Cr–2Si alloy. Moreover, the thickness of $Cr_2O_3$-scale formed on Co–17Re–25Cr–2Si as a function of exposure time at 1,100 °C shown in Fig. 2b follows a parabolic growth manner as well.

### Oxide Scale Morphology

The oxide scale that forms on Co–17Re–23Cr–2Si at 1,000 °C, shown in Fig. 3a, can be essentially identified as a 3 layer structure. With the aid of XRD and EDS analysis, the outer layer was identified as pure coarse-grained CoO layer; the middle layer is a mixture of spinel $CoCr_2O_4$ and CoO, which is very porous and is also the thickest of all the layers. At the scale/alloy interface, a thin and discontinuous $Cr_2O_3$ layer is formed. Besides these 3 oxide layers, $SiO_2$ was observed as internal

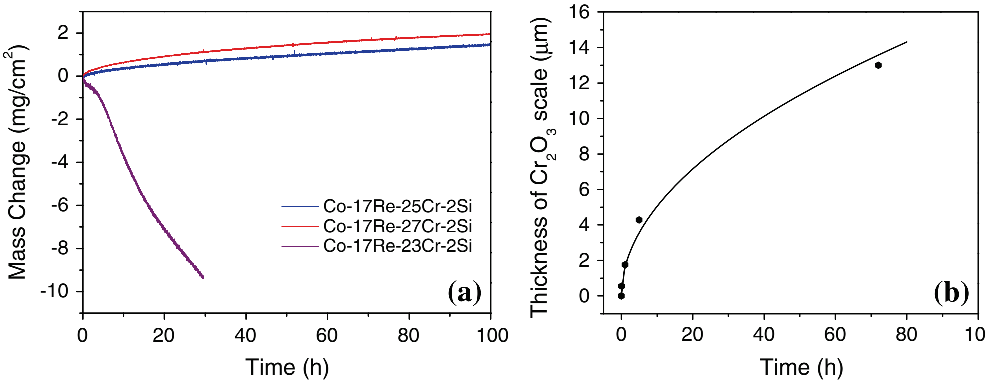

**Fig. 2** **a** Thermogravimetric data from oxidation tests conducted in air at 1,000 °C on Co–17Re–xCr–2Si alloys containing different Cr-content, **b** thickness of $Cr_2O_3$-scale formed on Co–17Re–25Cr–2Si as a function of exposure time in laboratory air at 1,100 °C

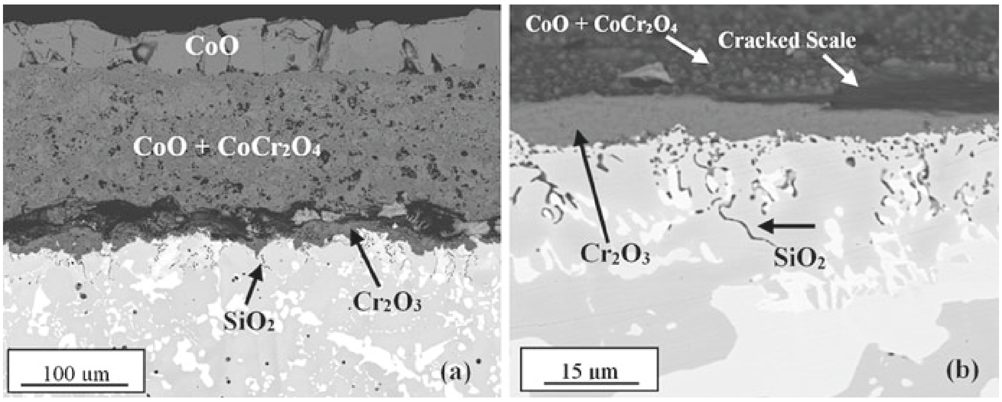

**Fig. 3** Back-scattered electron images of cross-sections of alloys after exposure in air at 1,000 °C for 100 h: **a** Co–17Re–23Cr–2Si, **b** Co–17Re–25Cr–2Si (combined with surface view on the *top*)

precipitates. The scales grown on Co–17Re–25Cr–2Si, Co–17Re–27Cr–2Si and Co–17Re–30Cr–2Si are all rather similar. A typical cross-section in combination with the surface morphology of Co–17Re–25Cr–2Si is shown in Fig. 3b. A thick compact protective $Cr_2O_3$ oxide layer is formed under an extreme thin outer oxide layer, which is identified as a mixture of CoO and $CoCr_2O_4$ by means of XRD and EDS analysis. Underneath the $Cr_2O_3$ layer, $SiO_2$ inner oxides were formed and mostly distributed at the location where the primary sigma phase has been dissolved.

Discontinuous oxidation tests were carried out in order to study the scale growth mechanism. Figure 4a–c shows the surface morphology of oxide scales formed on Co–17Re–25Cr–2Si oxidized at 1,100 °C for 1, 5 and 72 h, respectively. Figure 4e–f shows the corresponding cross-sections. At the early stage of oxidation, different kinds of oxide products form on the two different bulk phases. The outer coarse oxide formed on the sigma phase shown in Fig. 4a was identified as CoO, whereas the one formed on the hcp solid solution matrix was found to be $Cr_2O_3$ covered by an extreme thin layer of the $CoCr_2O_4$ spinel phase. From the cross-sectional image, Fig. 4d, it is seen that a relatively thick compact $Cr_2O_3$-layer forms on both the sigma phase and the solid solution matrix, despite the fact that the outer oxide layers differ. It is noteworthy that the outer oxide layer can hardly be observed in the cross-sectional image even after 72 h of oxidation (Fig. 4f) while the thickness of the $Cr_2O_3$-scale has significantly grown with extending exposure period (from about 2 μm after 1 h to about 13 μm after 72 h). The detailed growth kinetics of $Cr_2O_3$-scale is shown in Fig. 2b.

## Alloy Microstructure Changes

As mentioned above, part of the primary sigma phase in the subsurface region was dissolved after the exposure of the alloy Co–17Re–25Cr–2Si in air at 1,000 °C for 100 h. The reason of this phenomenon is suggested to be the consumption of chromium in this region, which had stabilized the primary sigma phase before. This phenomenon can be more clearly observed in the alloy oxidized at 1,100 °C.

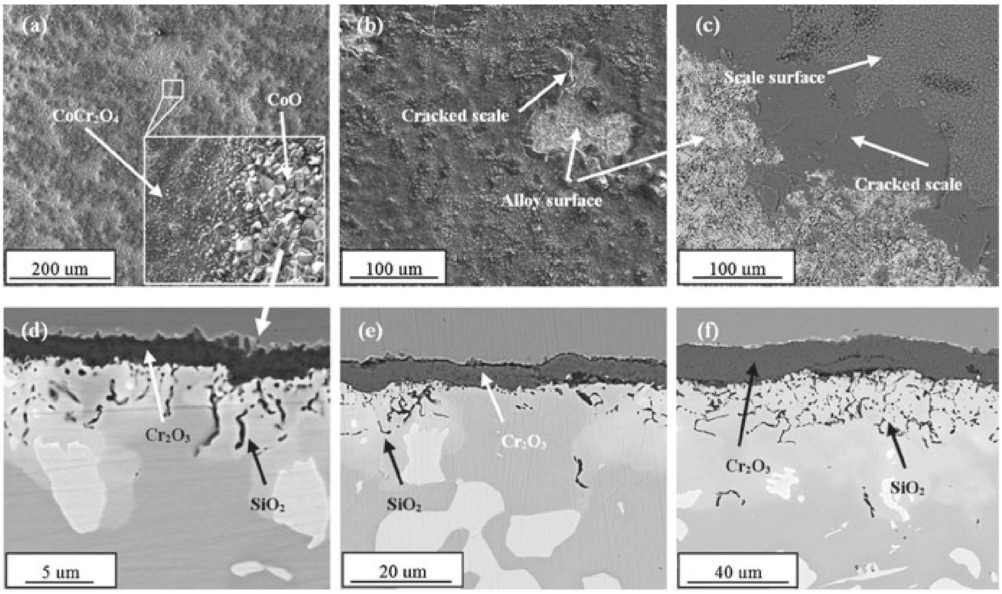

**Fig. 4** Surface (**a**–**c**) and cross-section (**e**–**f**) back-scattered electron microscopy images of Co–17Re–25Cr–2Si alloy after exposing at 1,100 °C for different times, **a** 1 h, **b** 5 h, **c** 72 h, **d** 1 h, **e** 5 h, **f** 72 h

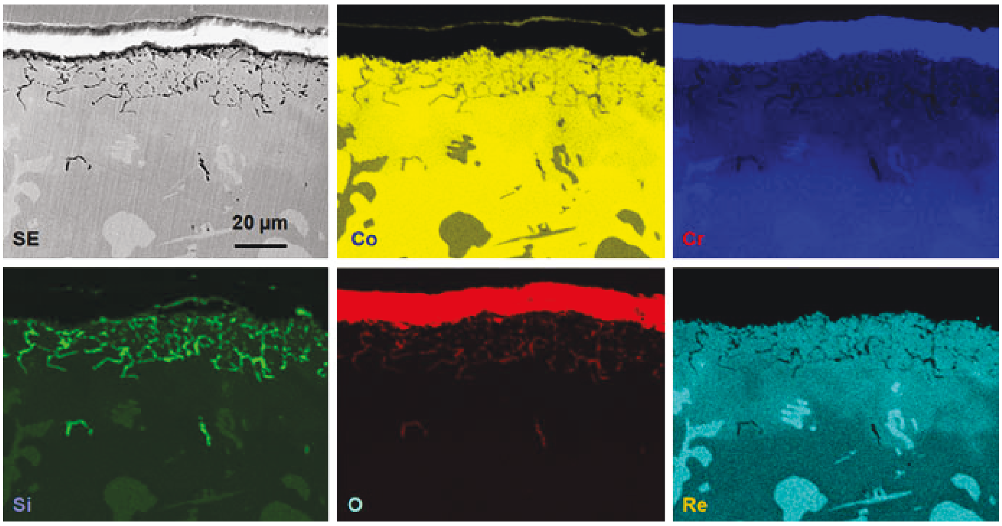

**Fig. 5** The element distribution maps of cross-section of Co–17Re–25Cr–2Si alloy after exposure in air at 1,100 °C for 72 h

Figure 5 shows an EDS mapping of an alloy cross-section from a sample oxidized at 1,100 °C. The elemental distribution of chromium indicates an approximately 50 µm deep Cr depletion zone underneath the $Cr_2O_3$-layer. The primary sigma phase in this zone is completely dissolved, forming a relatively Re-rich subsurface. The enrichment of Re at the subsurface also implies the protective nature of the scales avoiding the formation and evaporation of rhenium oxide. Moreover, the diffusion of Co from the original hcp matrix into the region of dissolved sigma phase at the subsurface is observed.

Besides the dissolution of the primary sigma phase below the surface of the Co–17Re–25Cr–2Si alloy, $SiO_2$ particles distributed as network-like structure was formed both at 1,000 and 1,100 °C. However, the distributions of these oxides were different. For samples oxidized at 1,000 °C for 72 h, $SiO_2$ mostly forms in the region where the primary sigma phase dissolved and quite few of them are formed in the hcp matrix (Fig. 3b). The same $SiO_2$ distribution is also observed in Co–17Re–25Cr–2Si oxidized at 1,100 °C for a short period (Fig. 4e). However, after a long exposure period at 1,100 °C, the $SiO_2$ particles are homogeneously distributed underneath the $Cr_2O_3$-scale, as shown in Fig. 4f.

Figure 6 shows the EBSD maps of the subsurface cross-section of the Co–17Re–25Cr–2Si alloy oxidized at 1,000 °C for 26 h. The formed oxide layer in the measured area was completely removed before sample was coated by Nickel. Figure 6a represents the grain distribution and grain orientations. Obviously many small grains with a mean size of about 3 μm have formed in the region where an original sigma particle has almost completely dissolved during oxidation. The phase map shown in Fig. 6b confirms that the newly formed fine grains are of the hcp phase, the same as the original matrix. This is not surprising, since the sigma phase stabilizer, Cr, in the original sigma phase is consumed due to the growth of $Cr_2O_3$-scale during oxidation. However, it is important to point out that after such an oxidation period almost all of the formed $SiO_2$ particles concentrates in the original sigma phase region and are mainly located at the grain boundaries. This can be seen in the image quality map shown in Fig. 6c. The dark black particles in the former sigma region represent $SiO_2$, because of its weak diffraction behavior. This has also been confirmed by EDS analysis.

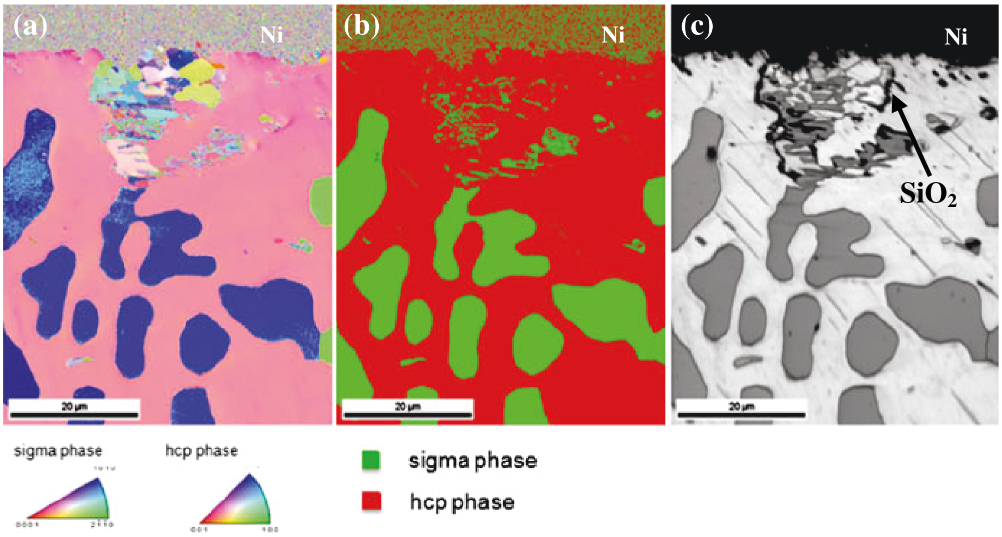

**Fig. 6** Subsurface cross-sectional EBSD map of Co–17Re–25Cr–2Si oxidized in air at 1,000 °C for 26 h, **a** orientation map, **b** phase map, **c** image quality map

## Discussion

Wright and Wood [12] studied in detail the oxidation behavior of Co-Cr binary alloys with different amount of Cr content (0–30 wt%, 0–32.7 at.%) at 1,000 °C. The morphology and composition of the oxide scale in the alloy Co–17Re–23Cr–2Si are quite similar to that in the Co-Cr binary alloy with 20–30 wt% Cr. The formed $Cr_2O_3$ layers at the alloy/scale interface in their study are all discontinuous and therefore did not protect the alloy from further oxidation in almost all cases. However, the $Cr_2O_3$ layer became more continuous with increasing Cr content in the base metal. Gorr et al. [11] recently also mentioned that a continuous and protective $Cr_2O_3$ layer was obtained on Co–17Re–30Cr–2Si after exposure of this alloy to laboratory air for 100 h at 1,000 and 1,100 °C.

The increase of Cr in the Co–Re alloy system raises the amount of the sigma phase. The volume fraction of the sigma phase in the alloys Co–17Re–xCr–2Si containing 23 at.%, 25 at.%, 27 at.% and 30 at.% Cr has been determined experimentally based on the SEM image analysis. The results are listed in Table 1 and show that the sigma phase volume fraction increases significantly from 14 % in Co–17Re–23Cr–2Si to 43.6 % in Co–17Re–30Cr–2Si. This agrees reasonably to the thermodynamic calculation for the Co–17Re–xCr alloy system at 1,000 °C [4], see Fig. 7. It is important to point out that regarding the high-temperature oxidation resistance both alloys, namely Co–17Re–25Cr–2Si and Co–17Re–30Cr–2Si form a continuous protective $Cr_2O_3$-scale, while the volume fraction of the sigma phase in Co–17Re–25Cr–2Si is almost half of that in Cr–17Re–30Cr–2Si. This sigma phase reduction is certainly beneficial in terms of mechanical properties.

As the results shown above document, the increase of the chromium content from 23 at.% to 25 at.% has significantly improved the oxidation behavior of the alloy by the formation of a dense and protective $Cr_2O_3$ layer both at 1,000 and 1,100 °C. The parabolic mass gain kinetics of the oxidation of Co–17Re–25Cr–2Si at 1,000 °C shown in Fig. 2a as well as the parabolic growth manner of the $Cr_2O_3$-scale on Co–17Re–25Cr–2Si oxidized at 1,100 °C shown in Fig. 2b suggests that the oxidation proceeds through solid state diffusion.

The oxidation kinetics of Co–17Re–25Cr–2Si and Co–17Re–27Cr–2Si at 1,000 °C can be described by a parabolic rate equation:

**Fig. 7** Phase distribution in the Co–17Re–xCr system depending on Cr-concentration calculated by the commercial software FactSage® [4]

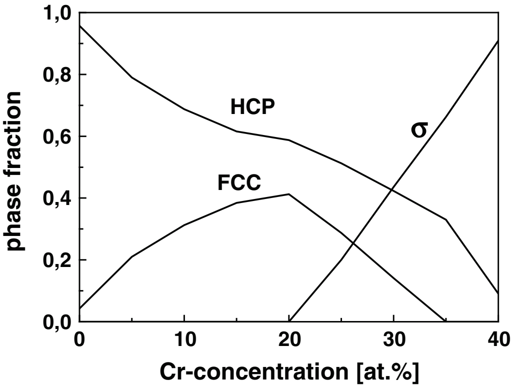

$$\left(\frac{\Delta m}{A}\right)^2 = 2k_p t \qquad (1)$$

where $\Delta m$ represents the mass change, $A$ is the total surface area of the specimen, $k_p$ is the parabolic rate constant and $t$ is the oxidation time.

The calculated parabolic oxidation rates of these two alloys oxidized at 1,000 °C in air are compared with the literature data reported by Gorr et al. [4] in Table 2. The calculated parabolic constants of Co–17Re–25Cr–2Si and Co–17Re–27Cr–2Si in air are in a good agreement with that of Co–17Re–30Cr obtained under low oxygen partial pressure, where only Cr is oxidized by selective oxidation. This result also indicates the good oxidation resistance of Co–17Re–25Cr–2Si and Co–17Re–27Cr–2Si, since the oxidation rates of them are dominated by the growth of the protective $Cr_2O_3$-scales.

A comparison of the oxidation results of the Co–17Re–xCr–2Si alloys with different Cr-content shows that there are two different oxidation mechanisms both at 1,000 °C and 1,100 °C. As a result, two different kinds of oxide scale morphology were observed, which are schematically presented in Fig. 8. The porous non-protective scales formed on Co–17Re–23Cr–2Si allows fast transport of oxygen from the gas phase to the scale/metal interface, bringing about rhenium oxidation and its evaporation at such high temperature, as shown in Fig. 8a.

According to the oxide scale morphology and the EBSD in combination with EDS analysis of subsurface microstructural changes, the oxidation mechanism of Co–17Re–25Cr–2Si, Co–17Re–27Cr–2Si and Co–17Re–30Cr–2Si at both 1,000 and 1,100 °C in laboratory air can be considered to take place in the following steps: (i) at the very early oxidation stage, a mixture of all oxides is formed on the fresh

**Table 2** Comparison of the measured values of the parabolic rate constant $k_p$ with literature data

| Alloy | Oxidation condition | $k_p$ ($g^2/cm^4/s^1$) |
|---|---|---|
| Co–17Re–25Cr–2Si | 1,000 °C, laboratory air | $2.04 \times 10^{-12}$ |
| Co–17Re–27Cr–2Si | 1,000 °C, laboratory air | $2.72 \times 10^{-12}$ |
| Co–17Re–30Cr [4] | 1,000 °C, $p(O_2) = 1 \times 10^{-16}$ bar | $4.70 \times 10^{-12}$ |

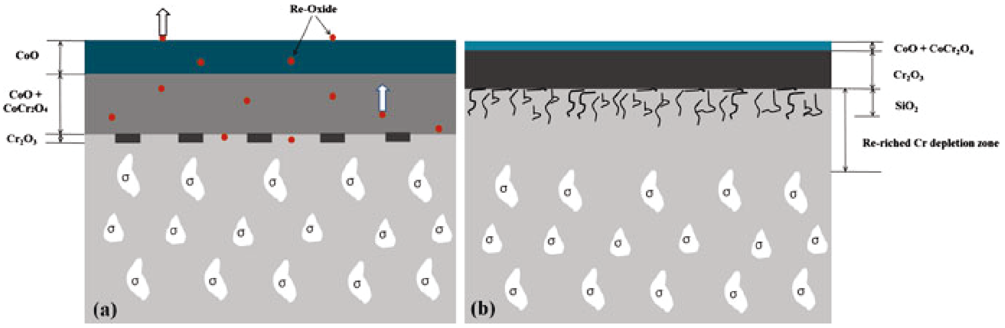

**Fig. 8** Schematic illustration of oxidation mechanism for the alloy conducted in air at 1,000 and 1,100 °C, **a** Co–17Re–23Cr–2Si, **b** Co–17Re–25/27/30Cr–2Si

alloy surface; (ii) the synergetic effects between Cr and Si as well as the sufficient Cr-content of the base alloy leads to a reduction of the transient oxidation period and results in a rapid formation of a protective $Cr_2O_3$-scale. The oxidation rate of the alloys is then controlled by the growth of the $Cr_2O_3$-layer; (iii) the growth of the $Cr_2O_3$-layer can be attributed to the predominant outward diffusion of Cr. As the consequence of Cr consumption in the subsurface, the Cr-stabilized sigma phase becomes thermodynamically unstable. Nucleation and growth of new hcp phase takes place within the sigma phase and therefore increases local grain boundary density in the former sigma phase region, which accelerates the outwards diffusion of Cr by grain boundary diffusion and further promotes the formation a protective $Cr_2O_3$-scale; (iv) once a continuous $Cr_2O_3$-scale covers the surface of the alloy, it can be assumed that local equilibrium is achieved at the interface between $Cr_2O_3$ and the alloy. From a thermodynamic point of view, Si is the only element that can be oxidized underneath the compact $Cr_2O_3$-layer. $SiO_2$-precipitates as small separate particles were observed after short exposure time. As oxidation period extends, the $SiO_2$-precipitatation zone grows inwards and laterally until the particles eventually link up to establish a nearly continuous network that act as a partial barrier to metal outward diffusion, as shown in Fig. 8b. A detailed study of the inner $SiO_2$ growth and the accompanying alloy subsurface microstructural changes is currently in progress. Supplementary experiments and their results will be published in a separate paper.

It is also important to point out that even though a significant improvement of the isothermal oxidation behavior has been achieved by increasing the Cr concentration from 23 to 25 at.%, the relatively massive spallation of formed $Cr_2O_3$-scale during cooling of Co–17Re–25Cr–2Si (Fig. 4c) had to be observed. Hence, accompanied Cr consumption at the subsurface might lead to a reduction in stability of the protective chromia layer under cyclic oxidation condition. Thus, a closer consideration of the $Cr_2O_3$-scale adhesion behavior is required in the future investigation.

## Conclusions

Experiments were carried out in order to investigate the influence of Cr-content on the oxidation behavior of Co–17Re–xCr–2Si alloys. Results indicate that 23 at.% Cr-content is insufficient for the alloy to form a protective $Cr_2O_3$-scale in air at 1,000 and 1,100 °C, but an increase of the Cr-content from 23 at.% to 25 at.% significantly enhances the oxidation resistance by the formation of a compact and protective $Cr_2O_3$-scale. The volume fraction of the sigma phase in Co–17Re–25Cr–2Si alloy is 25.5 %, which is almost half of that in Co–17Re–30Cr–2Si. The oxidation kinetics of Co–17Re–25Cr–2Si both at 1,000 and 1,100 °C followed a parabolic rate law. Cr diffusion towards the oxide/gas interface causes the dissolution of the sigma phase and the formation of a Re-rich zone underneath the $Cr_2O_3$-scale.

**Acknowledgments** Financial support of Deutsche Forschungsgemeinschaft (DFG) in the framework of Research Group “Beyond Ni-Base Superalloys” is gratefully acknowledged.

## References

1. C. R. Brooks, *Heat Treatment, Structure and Properties of Nonferrous Alloys*, (American Society for Metals, Ohio, 1984).
2. J. Rösler, D. Mukherji and T. Baranski, *Advanced Engineering Materials* **9**, 2007 (876–881).
3. B. Gorr, V. Trindade, S. Burk, H.-J. Christ, M. Klauke, D. Mukherjid and J. Rösler, *Oxidation of Metals.* **71**, 2009 (157–172).
4. B. Gorr, S. Burk, V. B. Trindade and H–. J. Christ, *Materials and Corrosion* **60**, 2010 (741–747).
5. T. Depka, Ch Somsen, G. Eggeler, D. Mukherji, J. Rösler, M. Krüger, H. Saage and M. Heilmaier, *Materials Science and Engineering* **A510–511**, 2009 (337–341).
6. M. Heilmaier, M. Krüger, H. Saage, J. Rösler, D. Mukherji, U. Glatzel, R. Völkl, R. Hüttner, G. Eggeler, Ch Somsen, T. Depka, H. Christ, B. Gorr and S. Burk, *JOM Journal of the Minerals, Metals and Materials Society* **61**, 2009 (61–67).
7. K. D. Adams, J. N. Dupont and A. R. Marder, *Journal of Materials Engineering and Performance* **16**, 2007 (123).
8. D. E. Jones and J. Stringer, *Oxidation of Metals* **9**, 1975 (409–413).
9. P. Y. Hou and J. Stringer, *Oxidation of Metals* **33**, 1990 (357–369).
10. R. Durham, B. Gleeson and D. J. Young, *Materials and Corrosion* **49**, 1998 (855–863).
11. B. Gorr, S. Burk, T. Depka, C. Somsen, H. Abu-Samra, H. J. Christ and G. Eggeler, *International Journal of Materials Research* **103**, 2012 (24–30).
12. I. G. Wright and G. C. Wood, *Oxidation of Metals* **11**, 1977 (163–191).

# Manuskript V

# Effect of Ti (macro-) alloying on the high-temperature oxidation behavior of ternary Mo-Si-B alloys at 820-1300°C

M. Azim, S. Burk, B. Gorr, H.-J. Christ, D. Schliephake, M. Heilmaier, R. Bornemann, P.H. Bolivar

Oxidation of Metals, 80 (2013) 231-242

Oxid Met (2013) 80
DOI 10.1007/s11085-013-9375-1

ORIGINAL PAPER

# Effect of Ti (Macro-) Alloying on the High-Temperature Oxidation Behavior of Ternary Mo–Si–B Alloys at 820–1,300 °C

**Maria Azimovna Azim · Steffen Burk · Bronislava Gorr · Hans-Jürgen Christ · Daniel Schliephake · Martin Heilmaier · Rainer Bornemann · Peter Haring Bolívar**

Received: 19 June 2012 / Published online: 9 February 2013

**Abstract** The aim of the present investigation was to gain an initial understanding of the effect of (macro-) alloying with Ti on the oxidation behavior of Mo–Si–B alloys in the ternary phase region of Mo_ss–$Mo_3Si$–$Mo_5SiB_2$ at 820–1,300 °C. Motivated by recent studies and thermodynamic calculations, the alloy compositions Mo–9Si–8B–29Ti (at.%) and Mo–12.5Si–8.5B–27.5Ti (at.%) were selected and synthesized by arc-melting. Compared to the reference alloy Mo–9Si–8B, superior initial oxidation rates at 1,100–1,300 °C as well as a significant density reduction by nearly 18 % were observed. Due to enhanced initial evaporation of

---

M. Azimovna Azim (✉) · S. Burk · B. Gorr · H.-J. Christ
Institut für Werkstofftechnik, Universität Siegen, Paul-Bonatz-Str. 9-11, 57068 Siegen, Germany
e-mail: maria.azim@uni-siegen.de

S. Burk
e-mail: steffen.burk@gmx.net

B. Gorr
e-mail: bronislava.gorr@uni-siegen.de

H.-J. Christ
e-mail: christ@ifwt.mb.uni-siegen.de

D. Schliephake · M. Heilmaier
Institut für Angewandte Materialien-Werkstoffkunde (IAM-WK), Karlsruher Institut für Technologie (KIT), Engelbert-Arnold-Str. 4, 76131 Karlsruhe, Germany
e-mail: daniel.schliephake@kit.edu

M. Heilmaier
e-mail: martin.heilmaier@kit.edu

R. Bornemann · P. H. Bolívar
Institut für Höchstfrequenztechnik und Quantenelektronik, Universität Siegen, Hölderlinstr. 3, 57076 Siegen, Germany
e-mail: rainer.bornemann@zess.uni-siegen.de

P. H. Bolívar
e-mail: peter.haring@uni-siegen.de

$MoO_3$ and mainly inward diffusion of oxygen, a borosilicate-rutile duplex scale with a continuous $TiO_2$ phase had formed. Detailed investigations of the oxidation mechanism by SEM, EDX, XRD and confocal micro-Raman spectroscopy indicated that Ti alloying is promising with regard to further improvement of the oxidation resistance as well as the strength-to-weight ratio of Mo–Si–B alloys.

**Keywords** Ultra-high temperature materials · Mo–Si–B alloys · Titania · Silica

## Introduction

Considering increasing energy prices and globalization as well as scarcity of resources at the same time, it is necessary to improve the turbine propulsion efficiency by the design of materials with properties exceeding those of Ni-base superalloys. Mo–Si–B-based multiphase alloys in the ternary phase region of Mo_ss–$Mo_3Si$–$Mo_5SiB_2$ (T2) are promising with regard to structural applications in ultra high-temperature environments due to their melting point of the order of 2,000 °C and their attractive combination of mechanical properties as well as good oxidation resistance [1]. While the ductile body centered cubic Mo in solid solution (Mo_ss) provides high fracture toughness, the brittle intermetallic compounds $Mo_3Si$ (chrystal structure A15) as well as $Mo_5SiB_2$ (T2) are responsible for the oxidation resistance and strength durability. Showing a promising balance between mechanical properties and oxidation resistance due to an appropriate volume fraction of intermetallic compounds and the α-Mo solid solution phase [1], Mo–9Si–8B was selected to serve as starting point for further improvement of the oxidation behavior and strength to weight ratio [2].

Taking into consideration the valence electron concentration and atomic size factor, Sakidja et al. [3] showed that Ti acts as stabilizer for the BCC, T2 and $Mo_5Si_3$ phase with the $D8_8$—crystal structure in Mo–Si–B alloys. Yang et al. [4] observed that Ti partially substitutes Mo in the intermetallic phases and leaves the metalloid concentrations of Si and B, needed for the formation of a protective borosilicate layer, unaffected. Due to a density of 4.50 g $cm^{-3}$ Ti has the potential of a significant increase of the strength to weight ratio. Supplementary thermodynamic calculations indicated that (macro-) alloying with Ti stabilizes the Si-rich and therefore more oxidation resistant $(Mo,Ti)_5Si_3$-phase by suppressing the A15-phase [5]. As a result, the alloy composition comprises the phases Mo_ss, $(Mo,Ti)_5Si_3$ and T2 [5].

Why the stabilization of these phases is advantageous can be deducted from several investigations carried out at elevated temperatures. Yoshimi et al. [6] showed that T2-phase based alloys revealed passive oxidation after sealing the substrate with $SiO_2$-glass. It is well-known, that B, as a constituent of the T2-phase, facilitates the formation of a protective borosilicate layer by decreasing its viscosity [2]. On the other hand, both binary single phases $Mo_3Si$ and $Mo_5Si_3$ (T1) are oxidation resistant at temperatures only beyond 1,600 °C. Below 1,600 °C they develop a highly porous silica scale which is attributed to the evaporation of $MoO_3$ and the lack of B [7–9]. However, investigations on the oxidation behavior of

Mo–37Si–40Ti at temperatures ranging from 750 to 1,300 °C revealed excellent oxidation resistance especially at intermediate temperatures at which the reference alloy Mo–9Si–8B tends to catastrophic oxidation [2]. As Mo–37Si–40Ti consists of nearly single-phase $(Mo,Ti)_5Si_3$, it is apparent, that Ti addition can improve the oxidation resistance drastically. Investigations on quaternary Mo–Si–B–Ti alloys started with thermogravimetric analyses on Mo–9Si–8B–35Ti [8], comprising Mo_ss, Ti_ss (11.21 vol%) and T2 (27.3 vol%), and indicated passivation at 1,100–1,300 °C. However, the evaporation rates were much higher than those for the reference alloy. This is in agreement with the investigations on Ti–Si–B-systems, indicating increasing oxidation rates with increasing content of Ti_ss [10].

It is obvious that the oxidation resistance of quaternary Mo–Si–B–Ti alloys can drastically be improved by stabilizing the $(Mo,Ti)_5Si_3$ phase and suppressing Ti_ss. Thus, in the present study we continued to analyze the oxidation behavior of Mo–9Si–8B–29Ti as well as Mo–12.5Si–8.5B–27.5Ti in order to reveal the underlying oxidation mechanisms in comparison to Mo–37Si–40Ti.

## Experimental Procedures

Two quaternary Mo–Si–B–Ti alloys with the compositions Mo–9Si–8B–29Ti and Mo–12.5Si–8.5B–27.5Ti were arc-melted in Oak Ridge National Laboratory (ORNL) in ≈0.7 atm of argon from the same elemental powder mixtures as used by Yang et al. [5] and heat-treated at 1,600 °C for 150 h in vacuum. Oxidation specimens with dimensions of 10 × 4 × 3 mm were machined using a slow-cutting diamond saw. Afterwards, the samples were ground and polished with SiC paper down to 1,200 grit and ultrasonically cleaned in ethanol.

The oxidation behavior was studied under isothermal conditions by continuous thermogravimetric analysis (TGA) and discontinuous weight change measurement. The last one aimed at avoiding measuring faults attributed to accumulations of the cooled and condensed evaporated molybdenum oxide on the span wire below 1,000 °C and analyzing the microstructure at different exposure times. TGA were carried out in static laboratory air at temperatures from 1,100 to 1,300 °C for 100 h using a Rubotherm tailor made magnetic suspension balance with a resolution of $10^{-6}$ g and automatic electronic drift compensation. The specimens were hanged up by a platinum wire on an alumina hook in a reaction chamber and connected contactless via permanent magnet to the microbalance located inside a separated measuring chamber. At 820 and 1,000 °C discontinuous oxidation experiments were conducted using a box furnace. For short-term (5 min, 15 min, 1 h, 5 h) and long-term discontinuous tests (100 h) carried out to study the oxide microstructure at different states of oxidation, the specimens were placed on platinum wires fixed on alumina crucibles in such a way that there was no contact with the alumina. The oxidation temperatures were selected according to the oxidation isotherms estimated by Burk for the reference alloy [2]. No oxidation testing was carried out below the sublimation point of $MoO_3$ (795 °C) as fully degradation of the substrate was expected [2]. To determine the relevant diffusion mechanisms marker experiments were carried out. For not to influence the diffusion process during the oxidation, the samples were sputtered with a porous, 300 nm thin Pt layer. All compositions are denoted in at.%.

Crystalline corrosion products were examined by X-ray diffraction (XRD) with Cu-Kα radiation. Surface and cross-sectional scanning electron microscopy (SEM) in secondary-electron (SE) and backscattered-electron (BSE) mode was conducted by a Helios Nanolab 600 FE-SEM (FEI). The relevant elements as well as their distribution were determined qualitatively using energy-dispersive X-ray spectroscopy (EDX) with an Apollo X silicon drift detector (EDAX) that enables high count rates even for lightweight elements. Upon oxidation Raman spectra were collected by a confocal Raman microspectrometer with laser excitation of 532 nm and 500 mW from a diode pumped solid state (DPSS) laser to identify the modifications of molybdenum oxide. After filtering by band-pass filter, images were recorded with a step resolution of 1 μm using a motorized scanning stage.

## Results

Using XRD and SEM it could be determined that both investigated alloys consist of Mo_ss, T2 and the Ti-rich, hexagonal $(Ti,Mo)_5Si_3$ phase. Mo–12.5Si–8.5B–27.5Ti contains an additional forth phase—cubic $Mo_3Si$—resulting in a fine-grained structure. Table 1 lists the different phases of the investigated alloy compositions as identified via EDX and XRD, the volume fractions calculated using an image processing program and the densities. Ti addition lowers the density of both alloys by nearly 18 % in comparison to the reference alloy. In the contrary to the thermodynamic calculations carried out by Yang et al. [5] no $(Mo,Ti)_5Si_3$ could be detected in both alloys received from ORNL. As the elemental bulk material composition was the same and the $Ti_5Si_3$ phase is stabilized first during the sintering process it can be assumed that no $(Mo,Ti)_5Si_3$-phase precipitates due to insufficient diffusion kinetics.

Isothermal oxidation weight change curves for selected temperatures between 820 and 1,300 °C are summarized in Fig. 1. In this context it should be noted that discontinuously determined curves are highlighted with dotted lines and symbols at the discrete data points. For a better overview of the obtained data, a scale break from −270 to −150 and −280 and −70 is applied for the weight change axis in Fig. 1a and b, respectively. Above 1,000 °C the oxidation isotherms reveal increasing evaporation rates with increasing temperature as well as decreasing weight loss with a higher volume fraction of intermetallic phases. At 1,100 °C the absolute mass loss after 100 h exposure time can be decreased from ≈23.5 to 20.6 mg $cm^{-2}$ compared to the reference alloy. Below 1,000 °C linear weight loss

**Table 1** Approximate volume fractions of the phases in the investigated alloy compositions

| Alloy composition | $Mo_{\_SS}$ | $Mo_3Si$ | $Mo_5SiB_2$ | $(Ti,Mo)_5Si_3$ | Density (g $cm^{-3}$) |
|---|---|---|---|---|---|
| Mo–9Si–8B–29Ti | 63.3 ± 2.9 | – | 27.7 ± 2.3 | 9.1 ± 1.2 | 7.71 |
| Mo–12.5Si–8.5B–27.5Ti | 39.8 ± 1.9 | 24.5 ± 3.1 | 27.3 ± 1.4 | 7.1 ± 1.9 | 7.78 |

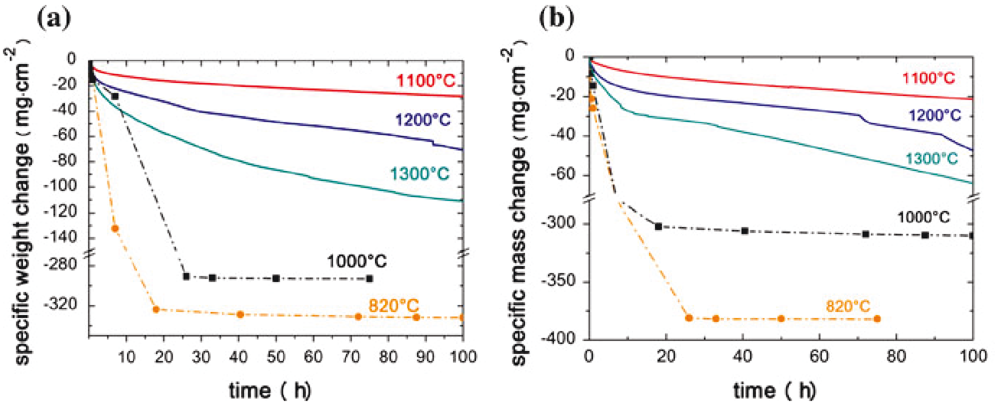

**Fig. 1** Specific weight change versus time for the alloy compositions **a** Mo–9Si–8B–29Ti and **b** Mo–12.5Si–8.5B–27.5Ti oxidized in air at 820–1,300 °C

leads to fully sample degradation. Thus, at 1,000 °C the substrate is completely oxidized after 18 h (resp. 26 h) with an absolute mass loss of 331.78 and 381.87 mg cm$^{-2}$ at 1,000 °C for the alloys with 29 at.% and 27.5 at.% Ti, respectively.

Both alloys oxidized in air at 820 °C reveal enhanced evaporation of $MoO_3$ during the first 30 min and a similar surface structure. Figure 2a shows the SE image for Mo–9Si–8B–29Ti oxidized in air for 5 min. Using EDX and XRD the bright blobs on the surface were determined as Mo oxide. Underneath, a scale mainly consisting of rutile ($TiO_2$) was identified in agreement with the $SiO_2$–$TiO_2$ phase diagram. As $SiO_2$ transforms from α- to β-quartz at 573 °C in atmospheric air pressure [11], β-quartz with semi-crystalline structure was also detected on the surface. One peak at the position 42.3° indicates the presence of TiN. Figure 2b shows that after 15 min only rutile and weak $MoO_3$ peaks appear indicating that the sample surface is completely covered with $TiO_2$. After prolonged time, a rough, fissured and porous surface as well as a high volume expansion is observed visually for both alloys. The substrate is completely transformed to $TiO_2$ and $B_2O_3{\cdot}SiO_2$ as represented by the oxidation isotherms. The samples oxidized for 100 h at 1,000 °C

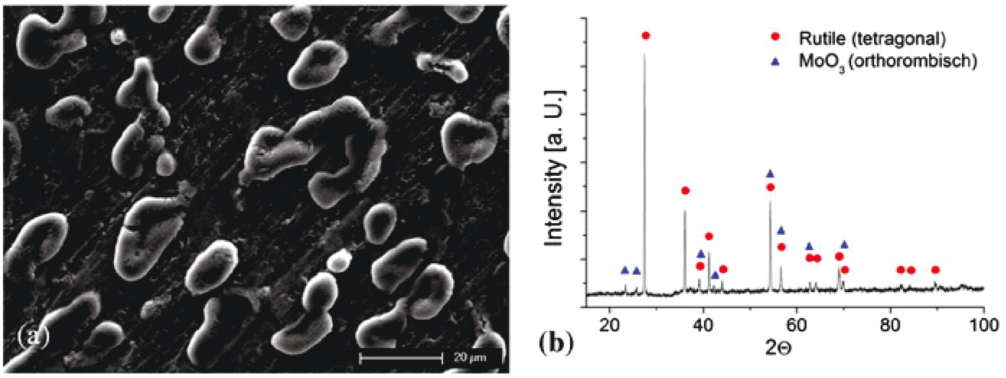

**Fig. 2** Secondary electron image of the surface of Mo–9Si–8B–29Ti oxidized in air at 820 °C **a** for 5 min and **b** X-ray pattern after 15 min exposure time

reveal the same rough and highly fissured surface with dense circular particles with diameters up to 2 µm in places surrounded by a highly porous silica layer.

In the initial states of oxidation (<15 min) the specimens of both the alloys oxidized at 1,100 °C exhibit a dark grey surface with silvery sparkling dots. SEM images of Mo–9Si–8B–29Ti evince the different phases densely covered with round rutile particles with diameters up to 1 µm within a borosilicate layer. XRD analyses show no distinct $SiO_2$ peak besides a weak one for tetragonal α-cristobalite at the angular position of 22.00°. As the instable high-temperature phase, β-cristobalite, easily converts to α-cristobalite at lower temperatures, this feature agrees to the $SiO_2$–$TiO_2$ phase diagram calculated by Ricker and Hummel [12]. Significantly higher intensities for rutile and only small peaks for the Mo oxides as well as a very weak α-cristobalite peak can be observed after 100 h. Only at this temperature and composition, spheres with diameters of 5-200 µm appear at the boundary areas (Fig. 3b). In these regions the rutile particles are dense and sharp-edged with lengths of 4–20 µm whereby in further distance of the boundary areas the grains become smaller with lengths of 1–10 µm and rounded down (Fig. 3a). Near those spheres with diameters >100 µm cracks emerge.

At 1,200 °C the surface reveals a similar morphology with the difference of increasing porosity within and between the rutile particles (Fig. 3c) attributed to accelerated evaporation of $MoO_3$. All rutile grains are rounded down with the size of 0.5–20 µm and the rutile diffraction peaks have a higher intensity.

At 1,300 °C no silica can be observed between the rutile grains after 100 h. As the surface is covered with a dense rutile layer, XRD reveal only rutile peaks. The rutile grains are of the order of 2–20 µm.

The alloy Mo–12.5Si–8.5B–27.5Ti shows a similar surface appearance with the difference of smaller rutile grain formation indicating a reduced growth rate of $TiO_2$.

Backscattered electron images of the investigated alloys reveal different oxidation resistance for the different existing phases. Looking at Fig. 4a which shows the cross section of Mo–9Si–8B–29Ti oxidized in air for 5 min at 1,100 °C, it becomes obvious that $(Ti,Mo)_5Si_3$ oxidizes first while the T2 phase remains unoxidized. Figure 4b in combination with EDX mapping confirms that the oxide morphology, formed gradually, can be subdivided into the following major regions:

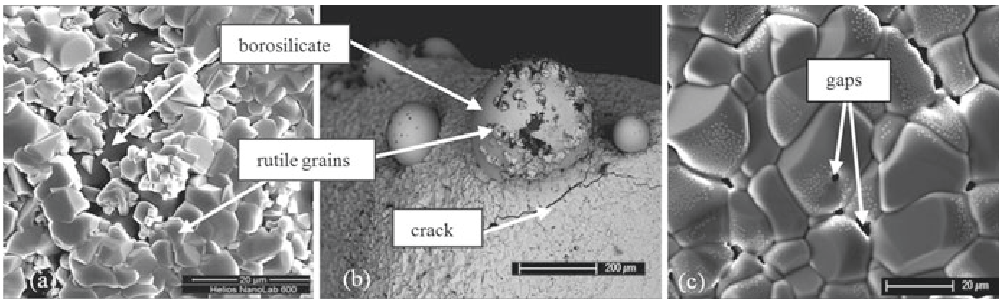

**Fig. 3** Scanning electron microscopy images of the surfaces of **a** an intermediate area of Mo–9Si–8B–29Ti for 100 h at 1,000 °C, **b** an edge area of Mo–9Si–8B–29Ti oxidized for 100 h in air at 1,100 °C and **c** Mo–9Si–8B–29Ti oxidized at 1,200 °C

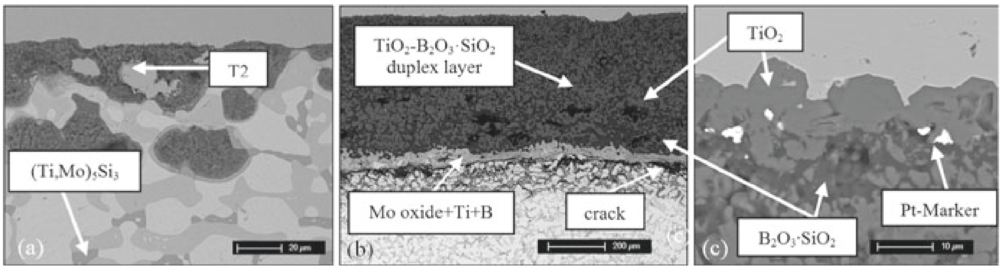

**Fig. 4** Backscattered electron images of **a** Mo–9Si–8B–29Ti oxidized at 1,100 °C for 5 min, **b** Mo–12.5Si–8.5B–27.5Ti oxidized for 100 h at 1,300 °C and **c** Mo–9Si–8B–29Ti with sputtered Pt markers after 100 h exposure time at 1,100 °C

(i) an outermost, predominantly continuous $TiO_2$ layer at the oxide/air interface with less amounts of borosilicate filling the space between the rutile particles (Fig. 4c). (ii) Below this titania scale, a layer comprising amorphous silica and rutile is formed. In the contrary to the nearly single phase $(Mo,Ti)_5Si_3$ alloy, $B_2O_3{\cdot}SiO_2$ particles are embedded in a continuous $TiO_2$ matrix with numerous pores growing with increasing exposure time and temperature. Figure 4c shows that Pt markers are observed at the titania/duplex layer interface. (iii) Underneath the oxide scale, a zone of inner oxidation is observed after 100 h exposure time. (iv) Due to enhanced inward diffusion of oxygen through numerous pores and channels of the duplex scale, another interlayer mainly consisting of $MoO_2$ as well as less amounts of Ti emerges beneath the duplex layer (Fig. 4b) and reaches a thickness up to 50 µm at 1,300 °C. In this $MoO_2$-intermediate layer the amount of Ti increases with the increasing distance from the inner oxidation zone.

By means of Raman spectroscopy it was possible to identify corrosion products formed during oxidation, as the qualitative distribution of $MoO_3$, $MoO_2$ and $TiO_2$ could be analyzed. As shown in Fig. 5, sharp Raman bands at the wavenumbers 609, 819 and 739 $cm^{-1}$ could be found indicating the presence of $TiO_2$, $MoO_3$ but also $MoO_2$ [13]. The Raman band at 996 $cm^{-1}$ is attributed to the hygroscopic behavior of $MoO_3$ (Fig. 5).

A detailed overview of the measured average oxide scale thickness versus temperature for both the alloys is given in Fig. 6a. This representation indicates minor oxide scale thicknesses for the alloy with the composition Mo–12.5Si–8.5B–27.5Ti. Cross sectional analyses of Mo–12.5Si–8.5B–27.5Ti show that even at

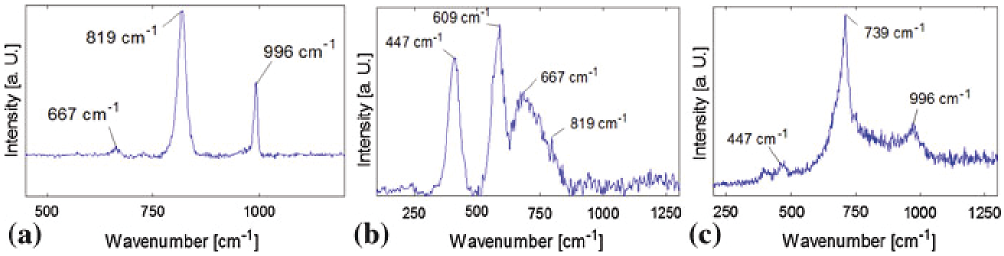

**Fig. 5** Representative Raman spectra of **a** $MoO_3$, **b** rutile superposed with $MoO_3{\cdot}2H_20$ and **c** $MoO_2$ with $MoO_3$ excited at 532 nm on the cross-section of Mo–9Si–8B–29Ti after oxidation for 100 h at 1,100 °C

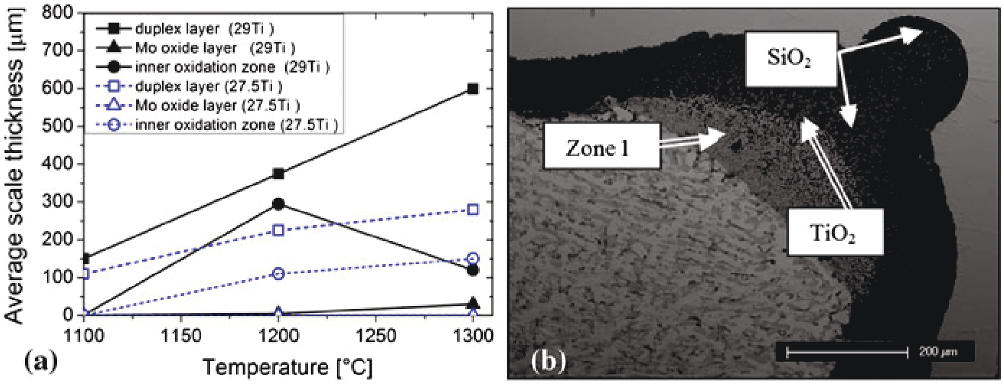

**Fig. 6** **a** Average oxide scale thicknesses for the investigated alloys and **b** backscattered electron image of the cross section of Mo–9Si–8B–29Ti after exposure time of 100 h and 1,100 °C

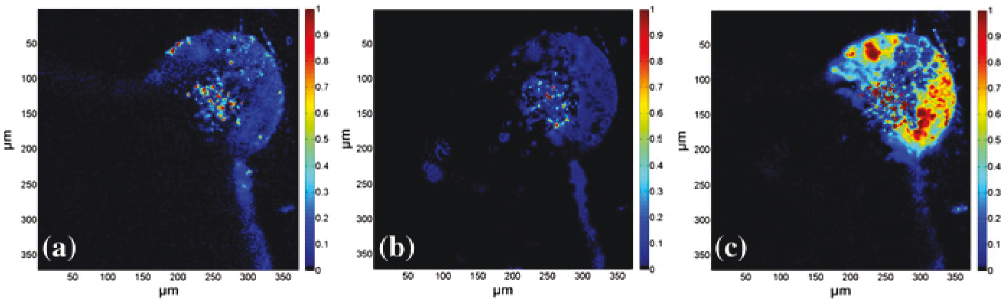

**Fig. 7** Raman-spectroscopy images (size 512 × 512 µm) after broad-band subtraction of background emission by MATLAB® of **a** $MoO_3$, **b** $MoO_3{\cdot}2H_2O$ and **c** $MoO_2$ (Color figure online)

1,300 °C no Mo oxide interlayer is formed due to a more protective duplex scale attributed to the higher content of intermetallic phases.

Based on results gained by EDX analyses of the cross section of a sphere, illustrated in Fig. 6b, it can be assumed that the spheres comprise amorphous silica and rutile surrounded by a homogeneous dense borosilicate layer. Under this silica-titania duplex layer a clear enrichment of O, Mo, B and depletion of Si and Ti are observed. Raman images in Fig. 7 show the integrated intensities at the center positions 819, 739, 996 $cm^{-1}$ with ±30 $cm^{-1}$ indicating the presence of $MoO_3$, $MoO_2$ and $MoO_3{\cdot}2H_2O$ beneath and in the spheres after broad band background subtraction by MATLAB® performed on the basis of [14]. In addition small particles oozing out of the spheres can be observed and via EDX identified as $TiO_2$ (Fig. 3b).

## Discussion

Regarding the oxidation kinetics, a significant reduction of the initial evaporation rates of $MoO_3$ was observed for both investigated alloys beyond 1,000 °C compared to the reference alloy Mo–9Si–8B studied by Burk [2]. That makes apparent, that passivation occurs immediately. However, due to the volatilization of $B_2O_3$ at higher temperatures [15] and evaporation of $MoO_3$ through numerous pores, mass loss was observed for all temperatures.

By comparison with Mo–9Si–8B–35Ti, a better oxidation behavior was found even for Mo–9Si–8B–29Ti due to the absence of Ti_ss. A further decrease of Ti-concentration and simultaneous increase of Si- and B-content, implemented in Mo–12.5Si–8.5B–27.5Ti, stabilizes the $Mo_3Si$ phase at the expense of Mo_ss and the intermetallic compound $Ti_5Si_3$, resulting in a fine grain structure and a better oxidation resistance. Attributed to a higher volume fraction of intermetallic phases and therefore shorter diffusion paths, a better oxidation behavior is observed at 1,100–1,300 °C for Mo–12.5Si–8.5–27.5Ti compared to Mo–9Si–8B–29Ti. For stoichiometric $Ti_5Si_3$, mass gain and poor corrosion resistance above 850 °C were reported due to the formation of nitride subscales beneath the $SiO_2$–$TiO_2$ oxide layer and the inability to establish a protective, continuous silica layer [16]. For the samples of the investigated alloys oxidized at 820 and 1,100 °C, sharp XRD peaks indicating TiN were only observed during the first 15 min. With increasing exposure time (>1 h) and increasing temperature the TiN peaks disappear as a denser rutile layer is formed.

Derived from the experimental results, the relevant oxidation mechanisms are summarized schematically in Fig. 8. The oxidation starts with accelerated evaporation of $MoO_3$. As Mo has an unlimited solubility for Ti, i.e. Ti substitutes Mo, Mo_ss/$Mo_3Si$/$Mo_5SiB_2$ comprise up to 24.5/29.9/29 at.% Ti [5]. Thus rutile nuclei form all over the surface, especially above the Ti-rich $(Ti,Mo)_5Si_3$ phase. While the $TiO_2$ particles grow fast and in all directions, borosilicate forms due to volatilization of $MoO_3$ out of $Mo_3Si$ and T2. However, its viscosity is insufficient to fill all the gaps between the fast and inhomogeneous growing Ti grains. This leads to an unavoidable volatilization of $MoO_3$, since the sealing of the surface by an effective oxidation barrier becomes impossible.

Pt markers which were originally located at the surface are shifted inside the interface rutile/duplex layer (Fig. 4b) indicating that inward diffusion of oxygen is the dominant diffusion mechanism. Indeed, the diffusion of O in $TiO_2$ at 1,100 °C is significantly faster than through $SiO_2$ [15, 17]. With increasing exposure time and temperature the outermost rutile layer is also growing, though to a minor degree, pointing out outward diffusion of Ti. After oxidation for 5 min at temperatures beyond 1,100 °C, different oxidation resistance for the different phases becomes obvious. Ti-rich $(Ti,Mo)_5Si_3$ oxidizes much faster than T2 or $Mo_3Si$ because of

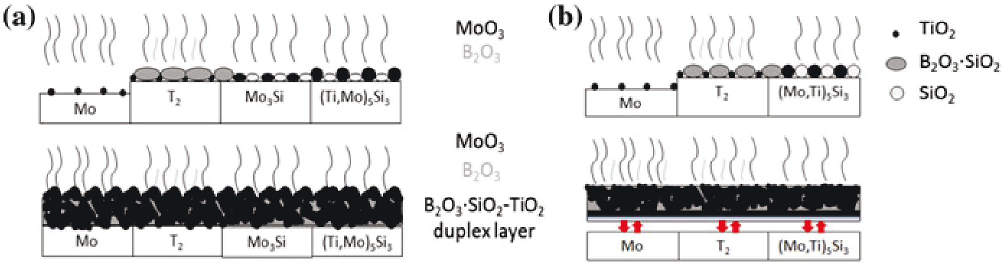

**Fig. 8** Proposed oxidation schematic for **a** Mo–12.5Si–8.5B–27.5Ti and **b** Mo–9Si–8B–29Ti above 1,000 °C

accelerated diffusion of O into the phase. The accelerated growing rate of $TiO_2$, the high volume fraction of Ti and the different thermal expansion coefficients for $TiO_2$ and $SiO_2$ are the reason for the development of a highly porous duplex layer mainly consisting of rutile. That is the main difference to the oxide scale with $SiO_2$ as matrix phase observed on Mo–37Si–40Ti [2]. As the protective borosilicate layer only fills the space between the inhomogeneous growing rutile particles, an effective barrier to oxidation cannot be formed. That affirms the assumption established by Burk that a duplex scale with a continuous $B_2O_3 \cdot SiO_2$ layer is required for good oxidation resistance [2]. Due to outward diffusion of Ti indicated by a depletion of Ti at the interface duplex layer/inner oxidation zone and the growth of a rutile layer above the platinum marker from ≈1 μm (1 h) up to ≈9 μm (100 h) a dense outermost $TiO_2$ layer is formed.

At higher temperatures, the diffusion increases drastically and the duplex layer becomes thicker and more porous. Because of proceeding inward diffusion of O through $TiO_2$, an interlayer mainly comprising $MoO_2$ and boron oxides is formed beneath the duplex layer. $MoO_3$ can only evaporate through pores, but neither through $TiO_2$ nor $B_2O_3 \cdot SiO_2$. That feature induces high volume expansion and therefore internal stresses indicated by the red arrows in Fig. 8b. After exceeding a critical limit these growth stresses cause local spalling above the internal oxidation zone and thick continuous cracks appear, as clearly shown in Fig. 4c. This effect does not occur for Mo–12.5Si–8.5B–27.5 Ti as the higher amount of intermetallic phases and the fine-grained structure provide shorter diffusion paths and facilitates the formation of borosilicate. The higher amount of $B_2O_3 \cdot SiO_2$ within the duplex layer forms a better barrier to further oxidation.

At temperatures below 1,000 °C the formation of $B_2O_3 \cdot SiO_2$ on both the investigated alloys is too slow to protect them from further oxidation resulting in linear mass loss. XRD results show that even after 15 min the surfaces of both alloy compositions are completely covered with rutile. The accelerated inward oxide growth and the different thermal expansion coefficients of $SiO_2$ and $TiO_2$ cause a very thick and porous oxide layer. In other words, a protective oxidation barrier cannot be formed as the penetration of O to the substrate is facilitated by numerous pores and channels in the silica-rutile layer resulting in fully consumption of the material after few hours.

The mechanism proposed before for the oxidation behavior can be confirmed by analyzing the spheres in detail. The enrichment of O, Mo, B and the depletion of Si and Ti underneath the duplex layer not only affirm the duplex layer being a barrier to Mo as well as boron oxides, but also indicate that at the edges of the specimen initially enhanced inward diffusion of oxygen takes place and therefore accelerates the formation of Mo, Si and B oxides. The determination of Raman bands around 819 and 739 $cm^{-1}$ indicating $MoO_3$ and $MoO_2$ [13], respectively, prove the presence of both Mo oxides within the duplex layer. The depletion of Si and Ti beneath the duplex scale confirms enhanced outward diffusion of Si and Ti which oxidize to amorphous $SiO_2$ and rutile. In those regions, where T2 lies on the surface, a continuous viscous borosilicate layer could develop initially (see Fig. 3b). Due to inward diffusion of oxygen through the less protective rutile in near vicinity of those regions covered with a protective $B_2O_3 \cdot SiO_2$, diverse oxides are built. That results in a high volume expansion beneath the protective oxide layer and is the reason for the cracks in the oxide scale, which are observed in those regions, where the internal stresses are stronger indicated by bigger and frequent spheres. Owing to a sufficient viscosity the borosilicate layer could withstand this high external compression strength. A compromise could be found in the spheres structure, as spheres have a maximum volume and a minimum surface at the same time. With increasing exposure time and thus increasing evaporation of $B_2O_3$ the viscosity of the borosilicate layer is increased and micropores as well as fissures develop on the layer. At these places rutile structures appear on the homogeneous protective oxide layer and the spheres crack (Fig. 3b).

## Conclusions

The intention of the present investigation was to gain a detailed understanding of the oxidation behavior of Mo–9Si–8B–29Ti as well as Mo–12.5Si–8.5B–27.5Ti and reveal the underlying oxidation mechanisms in comparison to Mo–37Si–40Ti. From the results described above it can be concluded that the rutile-silica duplex layer exhibits an effective oxidation barrier only, when $B_2O_3 \cdot SiO_2$ is the matrix phase. It was proved that the $B_2O_3 \cdot SiO_2$–$TiO_2$ duplex layer formed on the investigated alloys mainly grows by inward diffusion of oxygen through rutile. Thus, a thick and porous duplex layer with rutile as matrix phase is formed, which is the reason for the declined oxidation resistance in contrary to Mo–37Si–40Ti. Due to volatilization of $B_2O_3$ and evaporation of $MoO_3$ the samples experience mass loss. For a deeper understanding of the oxidation mechanism and the oxidation components oxidation tests in different atmospheres and TEM analyses are needed.

This study provides the significant conclusion that the stabilization of $(Mo,Ti)_5Si_3$ is required for the development of a protective oxide layer, as $(Ti,Mo)_5Si_3$ oxidized too fast not giving the borosilicate layer the possibility to seal the surface. If the stabilization of the $Mo_{ss} + T_1 + T_2$ phase field becomes possible, not only the oxidation behavior, but also the strength to weight ratio will be improved significantly with regard to the reference alloy of the ternary phase region of Mo_ss–$Mo_3Si$–$Mo_5SiB_2$.

**Acknowledgments** Financial support by Deutsche Forschungsgemeinschaft (DFG) within the framework of the research unit 727 “Beyond Ni-Base Superalloys” is gratefully acknowledged. The authors would like to thank E. P. George and H. Bei for the preparation of the alloys in ORNL.

## References

1. D. M. Berczik, US Patent No. 5,693,156 (1997).
2. S. Burk, “High temperature oxidation of Mo-based alloys considering the influence of surrounding atmosphere and alloying methods” PhD Thesis, Institut für Werkstofftechnik, Universität Siegen, 2011.
3. R. Sakidja, J. H. Perepezko, S. Kim and N. Sekido, *Acta Materialia* **56**, 2008 (5223).
4. Y. Yang, Y. A. Chang, L. Tan and Y. Du, *Material Science and Engineering A* **362**, 2003 (281).
5. Y. Yang, H. Bei, S. Chen, E. P. George, J. Tiley and Y. Austin Chang, *Acta Materialia* **58**, 2010 (541).

6. K. Yoshimi, S. Nakatani, T. Suda, S. Hanada and H. Habazaki, *Intermetallics* **10**, 2002 (407).
7. M. K. Meyer and M. Akinc, *Journal of the American Ceramic Society* **79**, 1996 (938).
8. M. K. Meyer, A. J. Thom and M. Akinc, *Intermetallics* **7**, 1999 (153).
9. J. B. Berkowitz-Mattuck and R. R. Dils, *Journal of the Electrochemical Society* **112**, 1965 (583).
10. E. C. T. Ramos, G. Silva, A. S. Ramos, C. A. Nunes and C. A. R. P. Baptista, *Material Science and Engineering A* **363**, 2003 (297).
11. J. D. Axe and G. Shirane, *Physical Review B* **1**, 1970 (342).
12. R. W. Ricker and R. A. Hummel, *Journal of the American Ceramic Society* **34**, 1951 (27).
13. Website http://rruff.info/. Accessed Mar 2012.
14. P. H. C. Eilers and H. F. M. Boelens, *Baseline Correction with Asymmetric Least Square Smoothing*, Report (Leiden University Medical Centre, 2005).
15. S. Melsheimer, M. Fietzek, V. Kolarik, A. Rahmel and M. Schütze, *Oxidation of Metals* **47**, 1996 (139).
16. A. J. Thom, Y. Kim and M. Akinc, *Material Research Society Symposium Proceedings* **288**, 1992 (1037).
17. P. Kofstad, *Nonstoichiometry, Diffusion, and Electrical Conductivity in Binary Metal Oxide*, (Wiley, New York, 1972).

# Manuskript VI

## Thermodynamic calculations in the development of high-temperature Co-Re-based alloys

B. Gorr, H.-J. Christ, D. Mukherji, J. Rösler

Journal of Alloys and Compounds 582 (2014) 50-58

Journal of Alloys and Compounds 582 (2014)

Contents lists available at SciVerse ScienceDirect

Journal of Alloys and Compounds

journal homepage: www.elsevier.com/locate/jalcom

# Thermodynamic calculations in the development of high-temperature Co–Re-based alloys

Bronislava Gorr [a],*, Hans-Jürgen Christ [a], Debashis Mukherji [b], Joachim Rösler [b]

[a] *University of Siegen, Institut für Werkstofftechnik, Siegen, Germany*
[b] *TU Braunschweig, Institut für Werkstoffe, Braunschweig, Germany*

ARTICLE INFO

*Article history:*
Received 21 March 2013
Received in revised form 18 June 2013
Accepted 8 July 2013
Available online 16 July 2013

*Keywords:*
Thermodynamic calculations
Composition optimization
High-temperature alloys development
Co–Re-based alloys

ABSTRACT

The experimental Co–Re-based alloys are being developed for high-temperature applications for service temperatures beyond 1100 °C. One of the main tasks of this research is to find the optimal chemical composition. Thermodynamic calculations are very helpful for composition selection and optimization. In this study, thermodynamic calculations were used to identify potential alloying elements and to determine suitable concentration ranges to improve properties, such as strength and oxidation resistance that are essential for high-temperature structural materials. The calculated ternary phase diagram of the Co–Re–Cr system was used to design the reference model alloy. Corrosion products formed under different atmospheric conditions were reliably predicted for a number of model Co–Re-based alloys. Pre-oxidation treatment, a common method used to improve the oxidation resistance of alloys in aggressive atmosphere, was successfully designed based on thermodynamic considerations.

## 1. Introduction

Ni-based superalloys are the most widely used materials for high-temperature applications such as in gas turbines. In order to achieve higher efficiency of gas turbines, the gas inlet temperature needs to be increased. However, the use of Ni-based alloys is increasingly restricted if service temperature exceeds 1000 °C, since these temperatures are very close to the melting point of these alloys. Therefore, for substantial improvement of thermodynamic efficiency, novel metallic materials with higher melting points, increased intrinsic strength, and good high-temperature corrosion resistance are needed [1,2]. Rösler et al. [3] first pointed out that Re addition to Co increases the melting point in Co alloys due to the high melting temperature of Re (the third highest amongst all elements in the periodic table). Moreover, Re dissolves readily in the Co-matrix and has a complete miscibility with Co, in contrast to the Ni-based alloys, where brittle phases start to form on addition of Re in high amounts. It is therefore possible to continuously increase the melting temperature of binary Co–Re alloys with the addition of Re, opening the unique possibility to steadily elevate the melting range in the Co–Re system, changing the character of the material from that of a contemporary Co-based alloy to that of a high-temperature material [4].

In addition to the high melting point, materials used in the hot section of gas turbine must provide good mechanical and creep strength at high temperature as well as maintain high-temperature corrosion resistance in the aggressive environment. Frequently, these both requirements yield a contradiction in terms. The conflicting property requirements are also observed in nickel-based superalloys and the solution for this complex problem is provided by a corrosion-resistant coating on Ni superalloys with an alloy composition optimized for high-temperature strength [5]. It seems to be very probable that such coatings are also to be developed in Co–Re-based alloys.

In the case of Co–Re-based alloys, chromium additions are detrimental to their creep properties at the levels required to enable chromia scale formation in order to protect the base alloy when exposed to high-temperatures in air. Furthermore, the refractory metal Re suffers from severe oxidation due to the formation of volatile Re oxides [6]. However, in Co–Re-based alloys, Re also takes the important role of a solid–solution strengthening element and it is worth to note that Re is well-known as a potential solid solution hardener in several alloys [7]. Therefore, it is important to find a suitable balance in the alloy compositions of Co–Re-based alloys considering the need for strength, toughness, ductility, and corrosion resistance.

In 2007, the Co–Re-based alloy system was firstly proposed, and subsequently development started within the framework of the research group "Beyond Ni-base Superalloys" supported by the German Research Foundation (DFG). The aim was to develop a new generation of high-temperature alloys for the use at 100 °C above the service temperature of present single-crystal Ni-superalloys. A trial-and-error development of new alloys is not only quite expensive but also a time-consuming process. Since Co–Re-based

---

* Corresponding author. Address: Paul-Bonatz-Str., 9-11, 57068 Siegen, Germany. Tel.: +49 (0) 271740 4653.
*E-mail address:* gorr@ifwt.mb.uni-siegen.de (B. Gorr).

0925-8388/$ - see front matter © 2013 Elsevier B.V. All rights reserved.
http://dx.doi.org/10.1016/j.jallcom.2013.07.055

alloys represent a completely novel material class, it was considered indispensable to combine theoretical evaluations by means of thermodynamic calculations with detailed analysis of experimentally gained knowledge in order to design potential technical alloys which will fulfil all the above requirements. One of the limitations of the equilibrium thermodynamic calculations results from the fact that they take into account only phases in thermodynamic equilibrium. A second limitation is due to the available database and this is particularly the case for the Co–Re system where only limited data exist. Therefore, large deviation of the calculated phase compositions from the reality is anticipated in materials that are far from the thermodynamic equilibrium [8]. However, the reliability of the thermodynamic calculations can considerably be improved if it is accompanied by experimental methods [9].

This paper explores the potential of thermodynamic calculations for alloy design and composition optimization of high-temperature corrosion-resistant Co–Re-based alloys. In the first part of this study, the basic features of thermochemical software FactSage will be introduced. In the second part, alloy development strategy regarding mechanical properties, particularly the main hardening mechanisms, will be discussed. The capability of the combination of thermodynamic calculations and microstructure analyse will be illustrated by means of examples. The third part will focus on the development effort aiming at an improvement of the high-temperature oxidation behaviour of Co–Re-based alloys.

### 2. Experimental

The Co–Re-based alloys were melted in a vacuum arc furnace using elementary substances with high purity (>99.98%) and subsequently cast in bar form. The cast Co–Re, Co–Re–Cr, Co–Re–Cr–C, and Co–Re–Cr–Si alloys were solution heat treated in three steps (1350 °C/5 h, 1400 °C/5 h, 1450 °C/5 h in a vacuum furnace. All of the heat treated specimens were directly quenched by argon flow within the vacuum furnace.

For oxidation tests, the Co–Re-based alloy specimens of dimension of approximately 10 mm × 10 mm × 2 mm were cut from the heat-treated bar and polished up to 1200 grit. All specimens were ultrasonically cleaned in ethanol directly before testing. The morphology and composition of the substrate materials as well as the corrosion products were analysed by means of standard experimental techniques such as XRD, SEM, EDS, and TEM.

### 3. Thermochemical software

Thermodynamic calculations presented in this study were carried out using the software FactSage (V5.4.1) in conjunction with a commercial database which includes the following elements: Co, Re, Cr, C, Si, O. The thermochemical software FactSage permits the calculation of stoichiometric reactions, complex equilibria and phase diagrams. In addition, the behaviour of different phases, i.e. phase amounts and phase internal composition as well as species activities can be calculated. The essential theoretical background, practical assignments as well as guided instruction are given in FactSage-Teach [10].

### 4. Development strategy – strengthening mechanisms

For the Co–Re-based alloys three hardening mechanisms are considered to be promising:

- Solid solution strengthening through large Re atoms.
- Composite strengthening by the particles of the second phase.
- Precipitate strengthening by carbides.

The ternary Co–Re–Cr system was selected to explore the potential of both solid–solution hardening through Re atoms and a composite strengthening through the second hard phase, namely $\sigma$ phase. Each element in this ternary alloy system plays the following role. Co represents the main component and provides for the ductile matrix. Re is a very effective solid-solution strengthener due to its atomic size. Further, in addition to the very high melting temperature mentioned above (see also Fig. 1(d)), it is a major constituent of the hardening $\sigma$-phase having the stoichiometry $Cr_2Re_3$. Cr has multiple roles: (i) it serves as a solid–solution strengthener, (ii) it is involved in the $\sigma$ phase formation, (iii) it forms carbides in alloys which contain C, and (iv) it plays a significant role in oxidation resistance by forming the protective $Cr_2O_3$ scale.

Re is a potential solid–solution strengthening element even in Ni-based superalloys. However, brittle topologically closed packed (TCP) phases occur after long exposure time if Re content exceeds about 6 wt.%. In contrast, the Re solubility in Co is unlimited and a rather high Re-amount may be added to the Co matrix in order to raise the high-temperature strength. For example, the hardness of the binary Co–Re alloys is increased from about 320HV to 360HV if the Re-concentration is enhanced from 17 at.% to 25 at.%, which indicates clearly the solid–solution strengthening by Re [11]. However, Re in association with Cr forms $\sigma$ phase in Co–Re–Cr alloys. It has been reported previously how $\sigma$-phase in Co–Re–Cr–Ni alloys can be exploited for alloy strengthening [12]. Also it should be noted that high Re content is critical, since Re yields poor oxidation resistance as well as it possesses a very high density.

Fig. 2(a and b) reveal that the $\sigma$ phase becomes stable in the Co–17Re–Cr system if the Cr content exceeds 20 at.%. According to the thermodynamic calculations, the amount of the $\sigma$-phase in the ternary Co–17Re–Cr system increases significantly with increasing Cr content above 20 at.% (Fig. 2(b)). Microstructure analysis of two ternary Co–Re–Cr alloys, namely Co–17Re–23Cr and Co–17Re–30Cr, confirms this tendency (Fig. 3(a–d)). The hard $\sigma$ phase appears as a bright phase in the hcp matrix. Using the program Image J, it was possible to use the contrast differences between the Co matrix (hcp) and the $\sigma$ phase and in order to quantify the volume fraction of the $\sigma$ phase in the two alloys of different Cr content. Results show that the $\sigma$ phase volume fraction increases from 3.7% and 30.5% with the increase in Cr-content from 23 at.% to 30 at.%. The corresponding values obtained from the thermodynamic calculations are 12 vol.% and 43 vol.% for the alloys Co–17Re–23Cr and Co–17Re–30Cr, respectively. The volume fraction estimated from microscopic images is truly the area fraction and only if the particles are randomly distributed, the area fraction is equivalent to the volume fraction. Further, the alloys studied may not be in the equilibrium conditions. Considering these factors, the difference in the calculated and measured $\sigma$-phase vol-

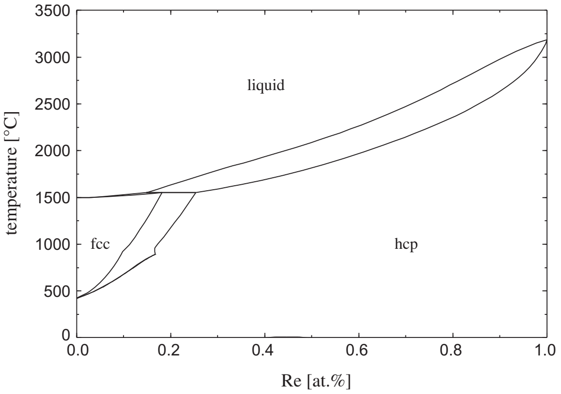

**Fig. 1.** Co–Re phase diagram.

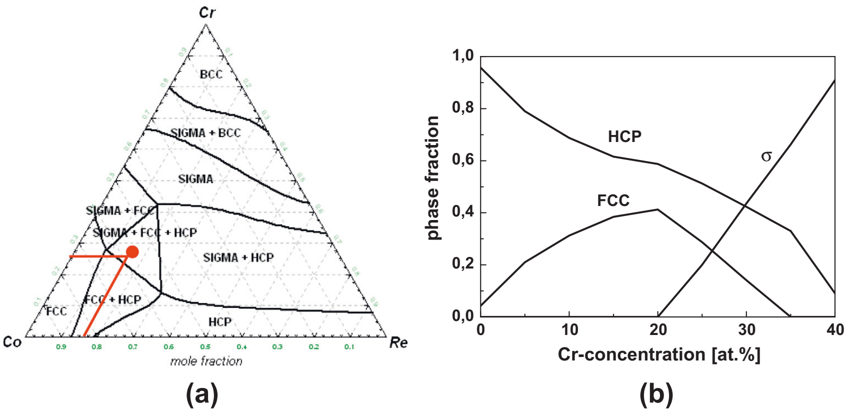

**Fig. 2.** (a) Ternary phase diagram Co–Re–Cr at 1100 °C (the reference alloy Co–17Re–23Cr is marked by the red dot), (b) phase distribution in the alloy Co–17Re–Cr at 1000 °C.

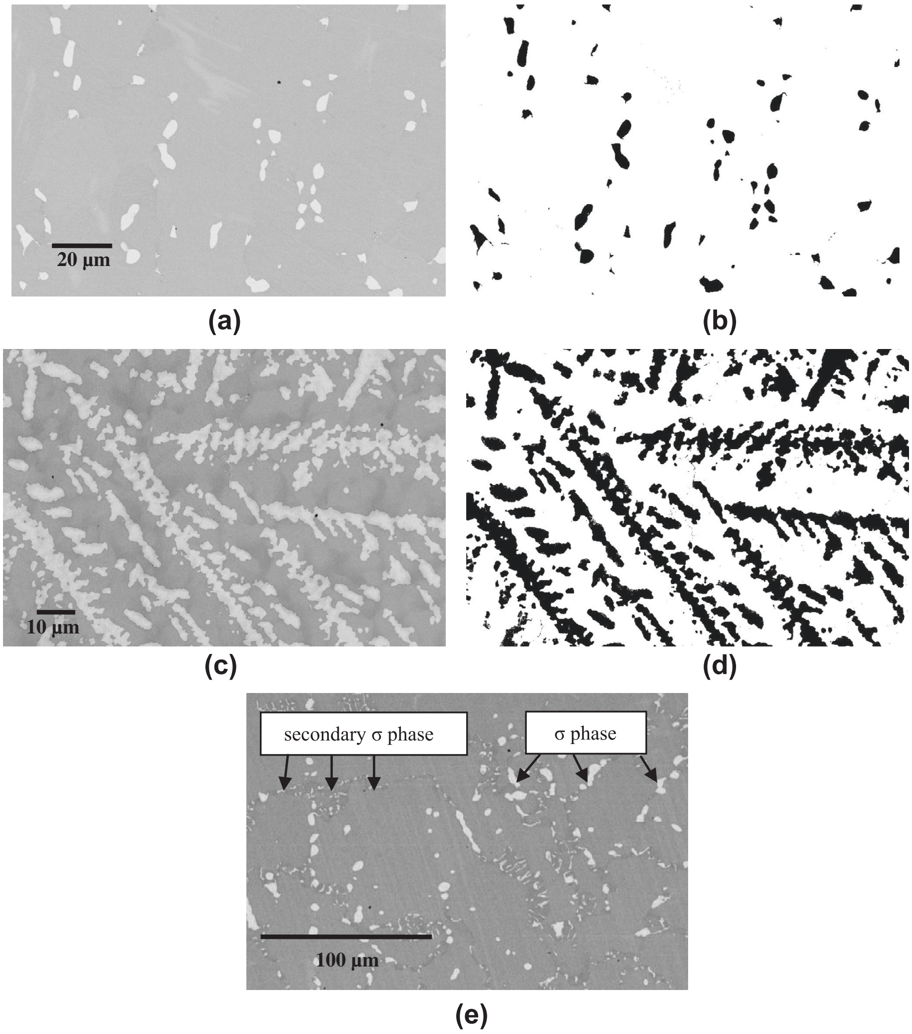

**Fig. 3.** (a) Microstructure of the alloy Co–17Re–23Cr, (b) microstructure of the alloy Co–17Re–23Cr collected by Image J to determine the volume fracture of the σ phase, (c) microstructure of the alloy Co–17Re–30Cr, (d) microstructure of the alloy Co–17Re–30Cr collected by Image J, and (e) microstructure of the alloy Co–17Re–23Cr with the secondary σ phase.

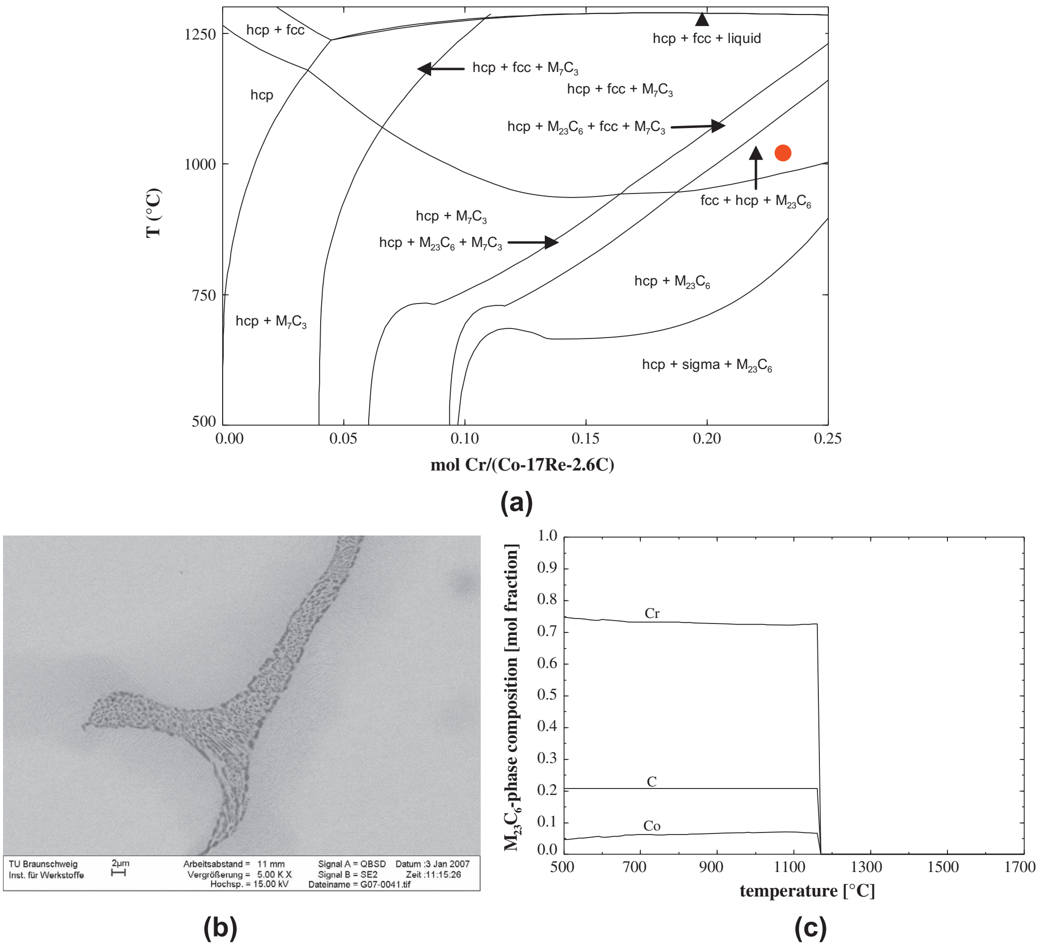

**Fig. 4.** (a) Phase diagram Co–17Re–Cr–2.6C with stability regions of $M_{23}C_6$ and $M_7C_3$ at 1000 °C (the alloy Co–17Re–23Cr–2.6C is indicated by the red dot), (b) the microstructure of the $M_{23}C_6$ carbides at the grain boundaries, and (c) element distribution in $M_{23}C_6$.

ume fraction is reasonable. The microstructure in Fig. 3(e) was taken from the substrate of the alloy Co–17Re–23Cr after an oxidation test and reveals the formation of new small particles of the σ-phase, the so-called secondary σ phase, which strengthens the assumption of the metastable state in the alloys. Finely dispersed secondary σ phase particles were also reported in the alloys Co–17Re–23Cr and Co–17Re–23Cr–2.6C after creep tests at 1100 °C [13].

The σ phase particles in Co–Re–Cr alloys have a very high hardness (∼1500HV) that increases the strength of these alloys, but they are also very brittle, which can adversely affect the mechanical behaviour [4]. The detrimental effect of the σ phase on the mechanical properties of Ni- and Fe-based alloys as a consequence of their high brittleness is well-known and has been reported in the literature [14]. Mukherji et al. reported that large σ phase particles in Co–17Re–23Cr alloy develop cracks on deformation [4]. However, the σ phase particles in this alloy are isolated and the cracks do not propagate through the Co matrix suggesting that Co–Re-based alloys are not inherently brittle due to the presence of the σ phase. Mukherji et al. further showed that when the σ phase particles are finely dispersed, as in Co–17Re–23Cr–15Ni, they are no longer brittle [12]. Nevertheless, a very high Cr concentration is unfavourable in most Co–Re–Cr alloys due to the presence of a high volume fraction of σ phase and should be avoided. Although, a sufficiently high Cr content (>25 at.%) can provide an improved oxidation resistance [15].

A suitable balance in the chemical composition of the ternary Co–Re–Cr system needs to be found, which will fulfil the following requirements: (i) the concentration of Cr and Re should allow the formation of the σ phase but not in large volume fraction, (ii) the Re content should not be too high, and (iii) the Cr concentration should only slightly exceed the concentration needed to facilitate the formation of the $Cr_2O_3$ scale. Analysing the ternary phase diagram (Fig. 2(a)) and putting above considerations together, the reference alloy with the composition Co–17Re–23Cr (indicated as red dot in Fig. 2(a)) has been selected as the base alloy for further development.

Similar to the conventional Co-based alloys, the strength of the Co–Re-based alloys may be significantly improved by carbide precipitations due to Cr and C additions. Thermodynamic calculations shown in Fig. 4(a) reveal that, in addition to fcc and hcp phase, $M_{23}C_6$ carbide may form in the quaternary Co–17Re–Cr–2.6C alloy at 1000 °C. In fact, $M_{23}C_6$ type was detected by microstructure analysis [14]. Mukherji et al. carried out a study on the high-tem-

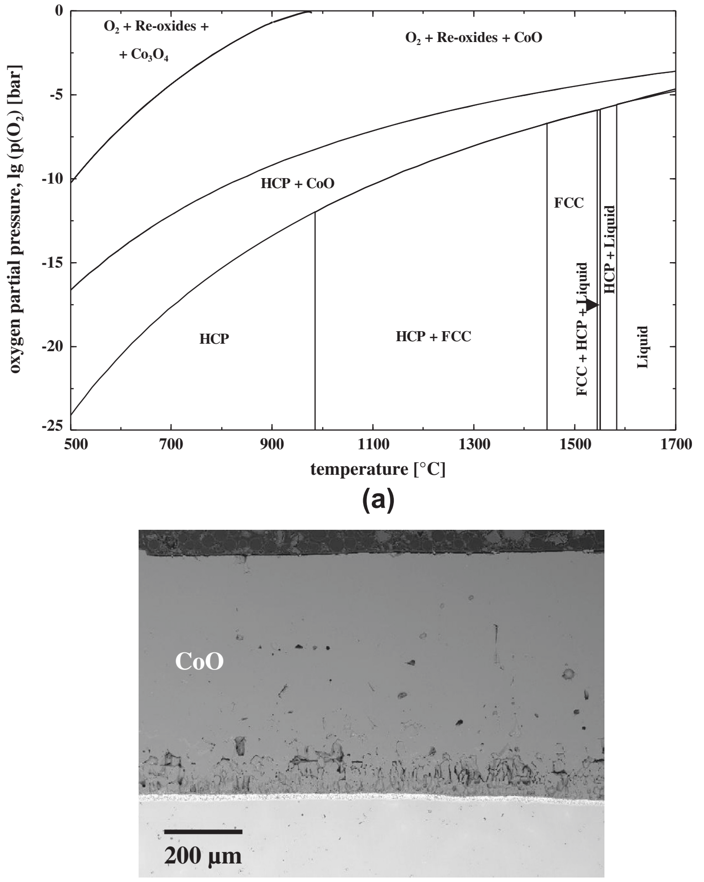

(a)

(b)

**Fig. 5.** (a) Phase diagram Co–17Re–O and (b) cross-section of the oxidised alloy Co–17Re, 1000 °C, 72 h, air.

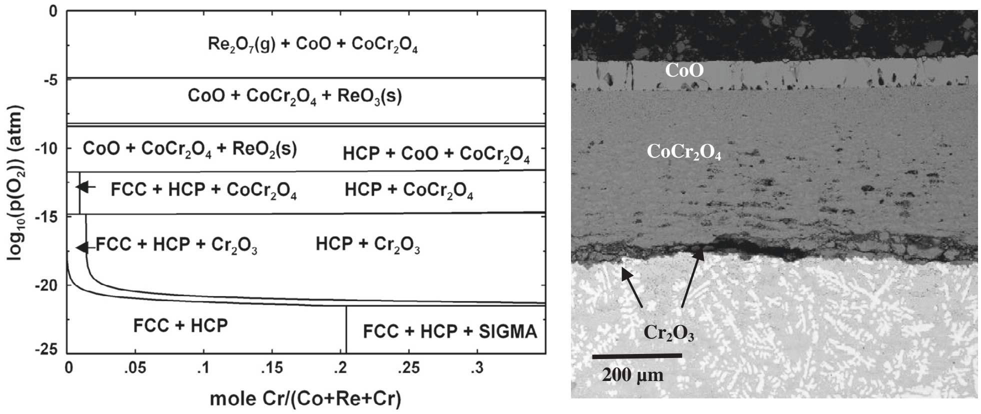

(a)

(b)

**Fig. 6.** (a) Phase diagram Co–17Re–Cr–O at 1000 °C and (b) cross-section of the oxidised alloy Co–17Re–30Cr, 1000 °C, 72 h, air.

perature stability of the $M_{23}C_6$ type chromium carbides in the alloy Co–17Re–23Cr–2.6C. In this alloy, fine lamellae in the Co matrix with a thickness of the order of 40 nm and an inter-plate distance varying between 200 and 500 nm were identified in TEM as $Cr_{23}C_6$ carbides in solution treated condition [16]. Blocky carbides were also found in the grain interior. In addition, eutectic-like structure of $M_{23}C_6$ carbides can also be seen at the grain boundaries (see Fig. 4(b)). However, the carbides present in the alloy after the solu-tion heat treatment are unstable at high temperatures and start to dissolve or coarsen on exposure at temperatures above 1000 ° C. Recent investigations showed that not all the $M_{23}C_6$ carbides dis-solve completely, only a partial dissolution of $M_{23}C_6$ carbides was detected [17]. This was also supported by the microstructural investigations using SEM on long-term annealed samples [18]. Fur-ther, thermodynamic calculation show that Cr is the main partici-pant in the formation of the $M_{23}C_6$ carbides (see Fig. 4(c)). This knowledge is also important because it documents which elements is dissolved in the matrix if the dissolution of $M_{23}C_6$ carbides oc-curs. The measurements by means of neutron diffraction clearly showed that the $M_{23}C_6$ carbides dissolution leads to the precipita-tion of σ phase [17]. This is not surprising since the formation of the σ phase is very sensitive to the Cr concentration (see Fig. 2(b)).

The experimental results document that the proper ratio of Cr and Re addition to produce the σ phase of the right amount to achieve optimal mechanical properties at high-temperatures could be identified by thermodynamic calculations. Also, the formation of carbides can be predicted by means of thermodynamic analysis. An alternative strategy for further alloy development is to add elements like Ta to promote MC-type carbide formation, which are more stable at high temperatures than the $Cr_{23}C_6$ carbides. Depka et al. experimentally proved that the addition of Ta results in the formation of homogeneously distributed globular precipitates of type TaC [19].

## 5. Development strategy – oxidation

The oxidation resistance of high-temperature materials is largely based on the formation of a protective oxide scale. The formation of a compact, dense, and slow-growing oxide scale can be provided by (i) the alloying with suitable elements such as Cr and/or (ii) the application of appropriate pre-treatment methods. Both paths are promising for providing oxidation resistance to Co–Re-based alloys and were explored in this study.

With respect to the improvement of the high-temperature oxidation resistance, on the one hand, thermodynamic analysis aims at the prediction of the identity of corrosion products. On the other hand, diffusion investigations seek to determine the mass transfer in the alloy and oxide scales, therefore enabling an assessment of the material life. The diffusion-controlled scale growth can be accurately calculated by the well-known Wagner theory when certain conditions are fulfilled [20]. Unfortunately, the Wagner theory can hardly be applied to scales grown on alloys of practical interest. In his outstanding work, Young [21] states that the rates of alloy consumption for most high-temperature alloys are so slow as to be seldom of any concern in the case of structural components, excepting they are alloy foils. More important, high-temperature alloys should be designed in such a way that the rapid formation of the desired slow-growing scales and their continuous stability is ensured.

In the case of the binary Co–17Re alloy, two cobalt oxides, CoO and $Co_3O_4$, can be formed depending on the temperature and the oxygen partial pressure (see Fig. 5(a)). At 1000 °C, the CoO is the only stable oxide during oxidation in air. This was experimentally confirmed by means of the XRD-measurements. However, CoO grows too fast to be effective as protective scale. The CoO layer shown in Fig. 5(b) is about 600 μm thick after 72 h of exposure to air at 1000 °C. In addition, the CoO scale contains porosity and microchannels which permit inward transport of oxygen as well as outward transport of volatile Re oxides.

For the reasons discussed above, Co–Re-based alloys need additional elements to form a slow-growing oxide, such as $Cr_2O_3$, $SiO_2$, or $Al_2O_3$. For this reason, Cr was added to the binary Co–17Re alloy to promote the formation of a protective $Cr_2O_3$ scale. Thermodynamic calculations shown in Fig. 6(a) reveal that $Cr_2O_3$ is the most stable oxide among all oxides that can be formed in the Co–17Re–Cr–O system at 1000 °C. Moreover, $Cr_2O_3$ can exist even at a very low Cr content in this alloy system. However, from the thermodynamic calculations along it is impossible to state whether $Cr_2O_3$ forms as an external oxide scale or as internal precipitates in the Co solid–solution matrix. Furthermore, no conclusions regarding the oxide scale density and its compactness can be drawn from the thermodynamic analysis. The SEM micrograph in Fig. 6(b) shows the oxide scale formed on the Co–17Re–23Cr alloy after exposure to air at 1000 °C. From the composition determined by energy dispersive X-ray spectroscopic (EDS) analysis (and from the morphology of the scale) became evident that the scale consists of three layers: an outermost CoO scale, a porous $CoCr_2O_4$ layer and a very thin, discontinuous $Cr_2O_3$ film adhering to the base metal. It should be noted that the arrangement of the layered structure in the oxide scale basically reflects the sequence of the oxide stability as a function of the oxygen partial pressure shown in the corresponding phase diagram (Fig. 6(a)). Consequently, thermodynamic calculations can be successfully applied not only to determine the corrosion products, but also predict their possible location. However, the later point may be viewed critically, as ki-

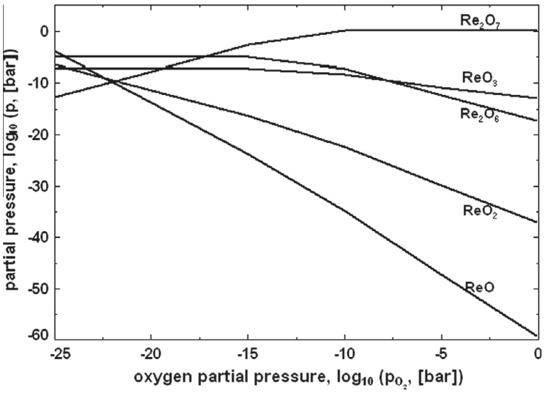

**Fig. 7.** Partial pressure of Re oxides as a function of oxygen partial pressure at 1000 °C and a total pressure of 1 atm.

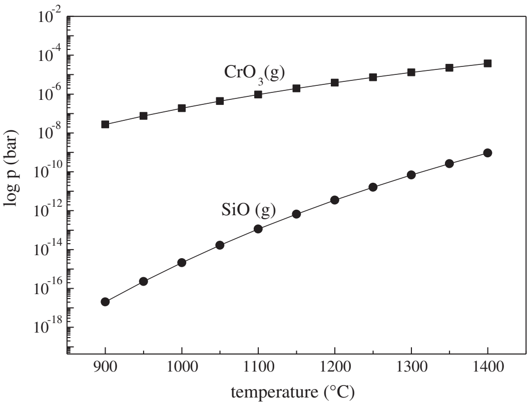

**Fig. 8.** Calculated partial pressure of $CrO_3$ above $Cr_2O_3$ and SiO above $SiO_2$ at different temperatures.

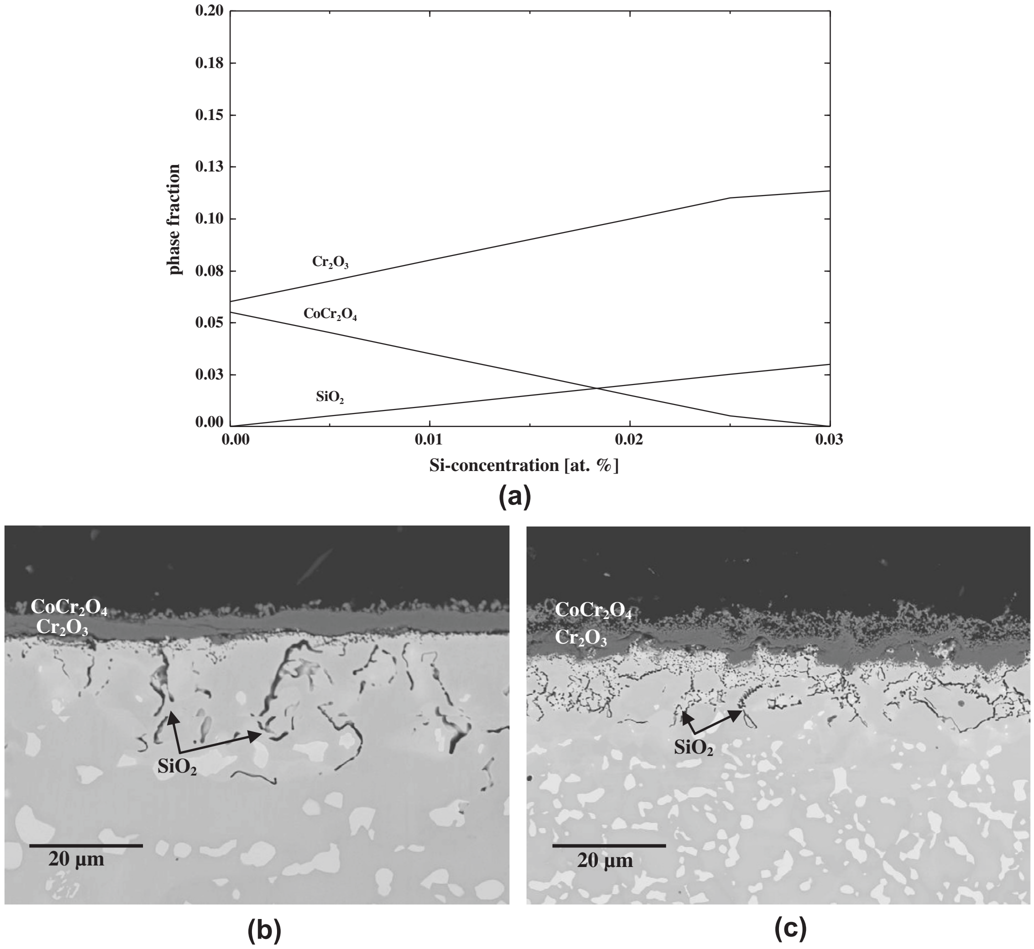

**Fig. 9.** (a) Phase fraction of oxides formed in the alloy system Co–17Re–23Cr–*x*Si, (b) cross-section of the oxidised alloy Co–17Re–23Cr–1Si, 1100 °C, 7 h, air and (c) cross-section of the oxidised alloy Co–17Re–23Cr–3Si, 1100 °C, 7 h, air.

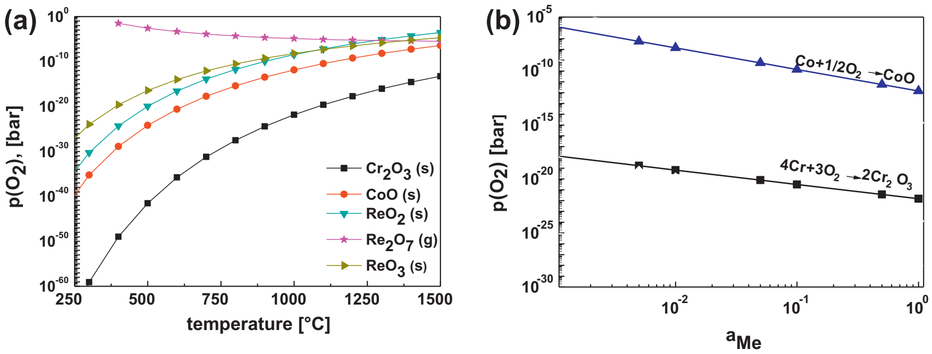

**Fig. 10.** (a) Temperature dependence of equilibrium oxygen partial pressure for the formation of various oxides and (b) relation between metal activity and oxygen activity for the equilibrium of oxide formation at 1000 °C.

netic considerations must be taken into account also. In the initial stage of oxidation, the oxidation of alloy components will follow the behaviour predicted by thermodynamic stability of the respective oxides. The subsequent development of scale morphology depends on the competition between fast growing, but less stable oxides such as CoO and $CoCr_2O_4$ and slow growing, but more stable ones such as $Cr_2O_3$. While thermodynamic analysis supports the determination of oxidation mechanisms and basically contributes to the alloy development, alloy design in general and the expecta-tion regarding high-temperature oxidation behaviour in particular should be supplemented by empirical knowledge gained from experiments. The high-temperature oxidation behaviour of several model Co–Re-based alloys in air and at low oxygen partial pressure was investigated and the corresponding results are available in lit-erature (see Refs. [18,22] for details).

Mass loss due to the evaporation of Re oxides was observed during exposure of Co–Re-based alloys at high-temperatures in air [18]. Experimentally, it is difficult to determine the nature of gaseous species (in this case, the particular Re oxides), but thermodynamic calculations can provide a plausible answer. The calculated partial pressure of various Re-oxides as a function of oxygen partial pressure at 1000 °C is represented in Fig. 7 indicating that the loss of Re most probably occurs by the formation of the gaseous rhenium oxide of the type $Re_2O_7$. This type of oxide is not predicted for the total equilibrium condition at low oxygen partial pressures, where the solid Re oxides $ReO_3$ and $ReO_2$ prevail (see Fig. 6(a)). $Re_2O_7$ may however form by the reaction of $ReO_3$ with oxygen. The result of thermodynamic calculations for the system $ReO_3$–$O_2$, as shown in Fig. 7, thus represents a first approach in predicting the local situation at the gas/$ReO_3$ interface. $Re_2O_7$ is clearly the oxide with the highest partial pressure among all gaseous Re-oxides that can be formed.

As mentioned above, during the exposure of Co–Re–Cr alloys to high-temperatures at around 1000 °C in air, a non-protective semi-continuous $Cr_2O_3$ scale forms on the oxide/alloy interface (see also Fig. 6(b)), which allows continuous oxidation of Re in the base metal and the evaporation of Re oxides. Depletion of the heavy metal Re from the alloy through oxidation results in a significant mass loss and this was observed in experiments [18]. Furthermore, it is well-known that $Cr_2O_3$ also evaporates at temperatures above 1000 °C [e.g. 23]. In the literature, several useful methods have been proposed to evaluate evaporation rates of $Cr_2O_3$ in dry air [24] and in flowing gases containing water vapour [25]. Despite the evaporation of chromia at temperatures above 1000 °C, chromium plays a very important role for Co–Re-based alloys in terms of high-temperature oxidation protection at moderate temperatures.

Si was added to the Co–Re–Cr alloys in order to facilitate the formation of a protective $SiO_2$ scale. However, silica can also decompose into gaseous oxide, namely SiO. Fig. 8 shows the calculated partial pressures of $CrO_3$ above $Cr_2O_3$ and SiO above $SiO_2$ at different temperatures. It is seen that the partial pressure of SiO is significantly lower compared to the partial pressure of gaseous $CrO_3$ in the whole temperature range. The presented comparison, i.e., thermodynamic stability of chromia and silica, explains the attempts to replace $Cr_2O_3$ by $SiO_2$ in Co–Re-based alloys, which were developed for service temperatures beyond 1100 °C. Thermodynamic calculations shown in Fig. 9(a) reveal that the volume fraction of $SiO_2$ clearly increases with increasing Si content. However, $SiO_2$ was only found as internal precipitates in Co–17Re–23Cr–*x*Si alloys using EDS analysis in TEM (see Fig. 9(b and c)). Experimental investigations confirm that the volume fraction of internal precipitates of $SiO_2$ increases with increasing Si content. In the alloy Co–17Re–23Cr–3Si, $SiO_2$ precipitates as a semi-continuous net, which definitely retards the outward diffusion of metallic constituents as well as inward oxygen flux, improving the oxidation behaviour of Co–Re-based alloys significantly (see Fig. 9(c)).

Literature survey shows that a pre-oxidation treatment is widely applied to improve the oxidation behaviour in many high-temperature alloys [e.g. 26]. In most cases, this is accomplished by the formation of a slow-growing protective oxide layer. The pre-oxidation of Co–Re–Cr alloys at low oxygen pressure aims at the selective oxidation of only the highly reactive element in the alloy, namely Cr, but not the oxidation of Co and Re. In this respect, the knowledge of the equilibrium partial pressure $p(O_2)$ of the corresponding oxides at given temperature is needed. Fig. 10(a) shows the dependence of the equilibrium oxygen pressure on the temperature of the oxide formation. From the thermodynamic point of view, all considered oxides are stable in the reaction of the alloy with air ($p(O_2) = 0.21$ bar) at high-temperatures. At low oxygen partial pressure (e.g., $p(O_2) = 10^{-16}$ bar at 1000 °C), $Cr_2O_3$ is the only oxide that can be formed in the Co–Re–Cr alloys, while the oxidation of Co and Re is inhibited. The dependence of the equilibrium partial pressure $p(O_2)$ of pure oxides on the metal activity of Co and Cr is shown in Fig. 10(b). The relatively small slope at given temperature (which is simply determined by the ratio of the stoichiometric coefficients) allows the use of a partial pressure value at which the oxidation of Co and Re does not occur but the formation of $Cr_2O_3$ is possible, even if depletion of the element (Cr in this case) takes place in the alloy near the surface. The sole formation of a $Cr_2O_3$ scale on four model Co–Re–Cr alloys at 1000 °C as a consequence of exposure to an atmosphere with the oxygen partial pressure of about $10^{-16}$ bar was successfully verified by corresponding oxidation experiments [22]. The formation of $Cr_2O_3$ scale on the top of the alloy Co–17Re–30Cr is shown in Fig. 11.

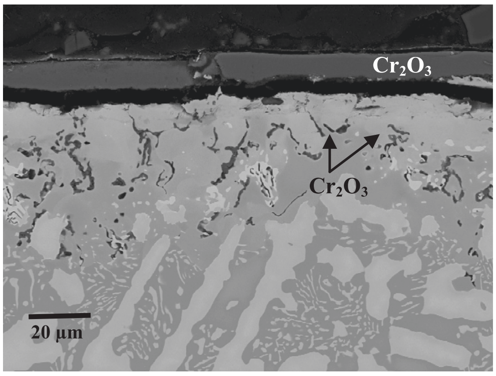

**Fig. 11.** The sole formation of $Cr_2O_3$ scale on the model alloy Co–17Re–30Cr alloys after exposure to an atmosphere with low oxygen partial pressure ($p(O_2) = 10^{-16}$ -bar) at 1000 °C for 100 h.

## 6. Conclusions

In this paper, the use of computational thermodynamics for research/development of Co–Re-based alloys regarding the improvement of high-temperature strength and corrosion resistance was presented. In view of high-temperature strength, the search for optimal compositions of Co–Re-based alloys was directed applying the following criteria: (i) solid–solution hardening by large Re-atoms, (ii) precipitate strengthening by fine dispersions of carbides, and (iii) composite strengthening through a hard second phase, i.e. the σ phase. The phase diagram of the ternary Co–Re–Cr system was calculated and used to choose the reference model alloy Co–17Re–23Cr. The role of the additions of 17 at.% Re, 23 at.% Cr, and 2.6 at.% C to the main element Co is discussed in detail in this contribution with respect to the improvement of high-temperature strength. In addition, the assessment of the phase fractions and phase element fractions enhances the understanding of materials chemistry and heterogeneous equilibria.

In the present stage of alloy development, a major effort of the research activities is directed towards the improvement of oxidation resistance of Co–Re-based alloys, concentrating on finding suitable concentrations of elements such as Cr and Si, which facilitate the thermal growth of protective oxide scales on the metallic substrate. The volatilisation phenomenon of $Cr_2O_3$ and $SiO_2$ was discussed. It was concluded that the partial pressure of SiO is negligible in comparison with the partial pressure of $CrO_3$ at high temperatures. Therefore, $SiO_2$ is more protective compared to $Cr_2O_3$ at very high temperatures and this fact explains the efforts to facilitate the formation of a $SiO_2$ scale.

Pre-oxidation treatment, as a common method used to improve the oxidation resistance of alloys used in aggressive atmosphere, was applied on several Co–Re–Cr alloys. Equilibrium oxygen partial pressures for the expected Co, Cr, and Re oxides were calculated. The dependence of the oxygen partial pressure on temperature and metal activity for the oxides considered and its relevance for the respective alloy chemical compositions and atmospheric conditions was discussed in this study.

Using Co–Re-based alloys as an example of a newly developed alloy system, it was shown that the combination of the thermodynamic calculations and experimental investigations has enormous benefits in alloy design.

## Acknowledgments

Financial support of Deutsche Forschungsgemeinschaft (DFG) in the framework of the Research Group ‘‘Beyond Ni-Base Superalloys’’ is gratefully acknowledged.

## References

[1] B.A. Pint, JOM 61 (2009) 42–43.
[2] J.C. Zhao, J.H. Westbrook, MRS 28 (2003) 622–630.
[3] J. Rösler, D. Mukherji, T. Baranski, Adv. Eng. Mater. 9 (2007) 876–881.
[4] D. Mukherji, J. Rösler, P. Strunz, R. Gilles, G. Schumacher, S. Piegert, Int. J. Mat. Res. 102 (2011) 1125–1132.
[5] W.J. Quadakkers, V. Shemet, D. Sebold, R. Anton, E. Wessel, L. Singheiser, Surf. Coat. Tech. 199 (2005) 77–82.
[6] C. Durez, Oxid. Met. 61 (2004) 49–67.
[7] L. Huang, X.F. Sun, H.R. Guan, Z.Q. Hu, Surf. Coat. Tech. 200 (2006) 6863–6870.
[8] M. Born, J. Korb, D. Rafaja, M. Dopita, R.W. Schülein, Mater. Corros. 58 (2007) 673–680.
[9] P. Waldner, E. Königsberger, H. Gamsjäger, J. Alloys Comp. 220 (1995) 148–151.
[10] K. Hack, FactSage-teach, A selftuition package on computational thermochemistry (2005). Version 1.0.
[11] M. Heilmaier, Project Report of the Research Group ‘‘Beyond Ni-Base Superalloys’’, 2009.
[12] D. Mukherji, J. Rösler, T. Fricke, S. Piegert, F. Schmitz, in: Proceedings of the 9th Liege Conference: Materials for Advance Power Engineering 2010 Energy and Environment, 2010.
[13] M. Brunner, R. Hüttner, M. Bölitz, R. Völkl, D. Mukherji, J. Rösler, T. Depka, C. Somsen, G. Eggeler, U. Glatzel, Mater. Sci. Eng. 528 (2010) 650–656.
[14] K.D. Adams, J.N. DuPont, A.R. Marder, J. Mater. Eng. Perform. 16 (2007) 123–130.
[15] W. Betteridge, Cobalt and its Alloys, Ellis Horwood Ltd., Chichester, 1982.
[16] D. Mukherji, M. Klauke, P. Strunz, I. Zizak, G. Schumacher, A. Weidenmann, J. Rösler, Int. J. Mat. Res. 101 (2010) 340–348.
[17] D. Mukherji, J. Rösler, P. Strunz, R. Gilles, G. Schumacher, S. Pieger, Int. J. Mat. Res. 102 (2011) 1125–1132.
[18] B. Gorr, V. Trindade, S. Burk, H.-J. Christ, M. Klauke, D. Mukherji, J. Rösler, Oxid. Met. 71 (2009) 157–172.
[19] D. Mukherji, J. Rösler, J. Wehrs, P. Strunz, P. Beran, R. Gilles, M. Hoffmann, M. Hoelzel, H. Eckerlebe, L. Szentmiklosi, Z. Macsik, Metall. Mat. Trans. A 44 (2013) 22–30.
[20] N. Birks, G.H. Meier, Introduction to High Temperature Oxidation of Metals, Edward Arnold Ltd., London, 1983.
[21] D. Young, High Temperature Oxidation and Corrosion of Metals, Elsevier, Oxford, 2008.
[22] B. Gorr, S. Burk, V. Trindade, H.-J. Christ, Mater. Corros. 61 (2010) 741–747.
[23] K.P. Lillerud, P. Kofstad, Oxid. Met. 17 (1982) 195–276.
[24] F. Zamoum, T. Benlaharche, N. David, R. Podor, M. Vilasi, Intermetallics 16 (2008) 498–507.
[25] D.J. Young, B.A. Pint, Oxid. Met. 66 (2006) 137–153.
[26] O. Altin, S. Eser, Oxid. Met. 65 (2006) 75–99.

# Manuskript VII

# High-temperature creep and oxidation behavior of Mo-Si-B alloys with high Ti contents

D. Schliephake, M. Azim, K. von Klinski-Wetzel, B. Gorr, H.-J. Christ, H. Bei, E.P. George, M. Heilmaier

Metallurgical and Materials Transactions A, 45A (2014) 1102-1111

# High-Temperature Creep and Oxidation Behavior of Mo-Si-B Alloys with High Ti Contents

DANIEL SCHLIEPHAKE, MARIA AZIM, KATHARINA VON KLINSKI-WETZEL,
BRONISLAVA GORR, HANS-JÜRGEN CHRIST, HONGBIN BEI, EASO P. GEORGE,
and MARTIN HEILMAIER

Multiphase alloys in the Mo-Si-B system are potential high-temperature structural materials due to their good oxidation and creep resistance. Since they suffer from relatively high densities, the current study focuses on the influence of density-reducing Ti additions on creep and oxidation behavior at temperatures above 1273 K (1000 °C). Two alloys with compositions of Mo-12.5Si-8.5B-27.5Ti and Mo-9Si-8B-29Ti (in at. pct) were synthesized by arc melting and then homogenized by annealing in vacuum for 150 hours at 1873 K (1600 °C). Both alloys show similar creep behavior at stresses of 100 to 300 MPa and temperatures of 1473 K and 1573 K (1200 °C and 1300 °C), although they possess different intermetallic volume fractions. They exhibit superior creep resistance and lower density than a state-of-the-art Ni-base superalloy (single-crystalline CMSX-4) as well as other Mo-Si-B alloys. Solid solution strengthening due to Ti was confirmed by Vickers hardness measurements and is believed to be the reason for the significant increase in creep resistance compared to Mo-Si-B alloys without Ti, but with comparable microstructural length scales. The addition of Ti degrades oxidation resistance relative to a Mo-9Si-8B reference alloy due to the formation of a relatively porous duplex layer with titania matrix enabling easy inward diffusion of oxygen.

DOI: 10.1007/s11661-013-1944-z

## I. INTRODUCTION

INCREASING the efficiency of turbines for aerospace and power generation applications by operating them at higher temperatures has been of interest in both academia and industry over the past several decades. Currently used Ni-base superalloys are capable of functioning at temperatures approaching 1423 K (1150 °C). As this temperature is close to their melting point, it limits their further development.[1]

At present, several other metallic systems (*e.g.*, $\gamma'$-strengthened Co-based superalloys,[2] multiphase Nb-Si alloys[3,4]) have the potential of operating at temperatures higher than Ni-base superalloys. Three-phase Mo-Si-B alloys, consisting of Mo solid solution (bcc) and the intermetallic phases $Mo_3Si$ (A15) and $Mo_5SiB_2$ ($T_2$), are also of interest as new high-temperature structural materials because of their favorable combination of properties such as good oxidation resistance, excellent creep resistance, and strength at ultrahigh temperatures.[1,5–8] However, for application in aero-engines, current Mo-Si-B alloys suffer from one major problem (besides their low room temperature fracture toughness), namely, a relatively high density of around 9.5 g/cm$^3$[9] compared to Ni-base superalloys which typically have densities <9 g/cm$^3$.[10] This problem may be solved by additions of light elements such as Ti. However, a high concentration of titanium would be needed to lower the density of Mo-Si-B alloys substantially. Also, its impact on mechanical properties and oxidation resistance is likely to be significant, since Ti is soluble in both Mo and its several silicide phases.[11] As an example, Sakidja *et al.*[12] prepared Mo-20Si-10B-50Ti and Mo-20Si-10B-35Ti alloys (all concentrations in this paper are in at. pct if not stated otherwise) by arc melting and confirmed that densities were reduced to 6.5 and 7.6 g/cm$^3$, respectively. However, the mechanical and oxidation behaviors at elevated temperatures of Mo-Si-B alloys containing high levels of Ti have not yet been studied in detail.

Recently, Yang *et al.*[13] investigated the effect of Ti content on the microstructure of a three-phase Mo-12.5Si-8.5B alloy. For thermodynamic calculations, they used the commercially available software package Pandat®, which is based on the Calphad method, to calculate phase stability at different Ti contents and temperatures. The database for the Mo-Si-B-Ti system was determined by Yang and colleagues[11,14,15] in several previous investigations. In their studies, they found that higher concentrations of titanium, *e.g.*, 27 to

---

DANIEL SCHLIEPHAKE and KATHARINA VON KLINSKI-WETZEL, Scientists, and MARTIN HEILMAIER, Professor, are with the Institute for Applied Materials, Karlsruhe Institute of Technology, 76128 Karlsruhe, Germany. Contact email: daniel.schliephake@kit.edu MARIA AZIM, Scientist, BRONISLAVA GORR, Research Staff Member, and HANS-JÜRGEN CHRIST, Professor, are with the Institute for Materials Engineering, University of Siegen, 57068 Siegen, Germany. HONGBIN BEI, Research Staff Member, is with the Materials Science and Technology Division, Oak Ridge National Laboratory, Oak Ridge, TN 37831. EASO P. GEORGE, Distinguished Research Staff Member, is with the Materials Science and Technology Division, Oak Ridge National Laboratory, and also Professor with the Department of Materials Science and Engineering, University of Tennessee, Knoxville, TN 37996.

Manuscript submitted January 18, 2013.

29 at. pct in a Mo-12.5Si-8-5B base alloy, lead to the substitution of the $Mo_3Si$ phase by $Mo_5Si_3$ ($T_1$). From the literature, it is known that $Mo_5Si_3$ shows superior oxidation resistance compared to $Mo_3Si$. Although the oxidation resistance of these silicides is considered to be still rather poor, it can be considerably improved by alloying with boron.[16,17] Likewise, the high-temperature strength of $Mo_5Si_3$ is known to be superior to that of $Mo_3Si$.[17,18] Hence, a three-phase Mo-Si-B alloy consisting of Mo solid solution and the intermetallic phases $Mo_5SiB_2$ and $Mo_5Si_3$ (instead of the $Mo_3Si$ phase) may yield improved high-temperature performance as compared to the above-mentioned alloys.[1,4–9]

Therefore, it was the goal of the present study to assess the high-temperature behavior of quaternary Mo-Si-B-Ti alloys for the first time. In particular, this work aims to understand the effect of titanium on the creep and oxidation behavior of two different Mo-Si-B alloy systems. The first is the Ti-containing Mo-12.5Si-8.5B-27.5Ti alloy of Yang *et al*.[13] which was inspired by investigations of Schneibel *et al*.[19] on a ternary alloy with the same Si and B content, but without the Ti. As indicated by the results of thermodynamic calculations shown in Figure 1(a), the quaternary composition should result in a four-phase alloy consisting of Mo solid solution, $Mo_3Si$, $Mo_5SiB_2$, and $Mo_5Si_3$, plus a fifth phase, namely, $Ti_5Si_3$, if the thermodynamic calculations of Yang *et al*.[13] hold true. Utilizing the same database as Yang *et al*.,[13] it was decided to synthesize a second alloy based on the ternary composition Mo-9Si-8B pioneered by Berczik.[6] In this case, the titanium content was chosen to be 29 at. pct, which should result in a three-phase alloy consisting of Mo solid solution, $Mo_5SiB_2$, and $Mo_5Si_3$, as shown by the thermodynamic calculations in Figure 1(b).

## II. EXPERIMENTAL

Two alloys with compositions of Mo-12.5Si-8.5B-27.5Ti and Mo-9Si-8B-29Ti (at. pct) were prepared from elemental bulk materials by arc melting in ~0.7 atm argon. The initial shape and purities of the starting materials are listed in Table I. Buttons with a mass of ~50 g were arc melted in a water-chilled copper hearth. To insure homogenization, the buttons were turned over and remelted five times. Afterward, both alloys were annealed at 1873 K (1600 °C) for 150 hours in vacuum ($10^{-3}$ Pa) to promote the formation of equilibrium phases and thus facilitate comparison of their microstructures with the thermodynamic predictions (Figure 1). The densities of both alloys were determined using the Archimedes principle.

Microstructures were investigated using X-ray diffraction (XRD, Bruker D8) with Cu $K_\alpha$ radiation and scanning electron microscopy (SEM) in the back-scattered electron mode (BSE) in a DSM 962 (Zeiss). Samples for SEM investigation were polished with oxide polishing suspension (OPS) and colloidal silica suspension. The composition of each observed phase was analyzed by wavelength-dispersive spectroscopy (WDS) in a JEOL JXA 8530F. The accuracies of the measured Mo, Si, and Ti contents lie typically within 0.2 at. pct. Since B is a light element and its $K_\alpha$ peak interferes with the Mo $M_\gamma$ peak, accurate determination of its concentration is very difficult. Because of this, and its negligible solubility in the Mo solid solution,[20] $Mo(Ti)_3Si$, and $Ti(Mo)_5Si_3$ phases,[13] being less than 1 at. pct at 2073 K (1800 °C),[21] the boron content was assumed to be zero in these phases.

**Table I. Raw Materials Used for the Arc Melting**

| Element | Form | Purity (Wt Pct) |
|---|---|---|
| Mo | plate | 99.95 |
| Si | lump | 99.999 |
| B | lump | 99.5 |
| Ti | plate | 99.95 |

Purities are based only on metallic impurities, *i.e.*, non-metallics such as C, S, P are not considered.

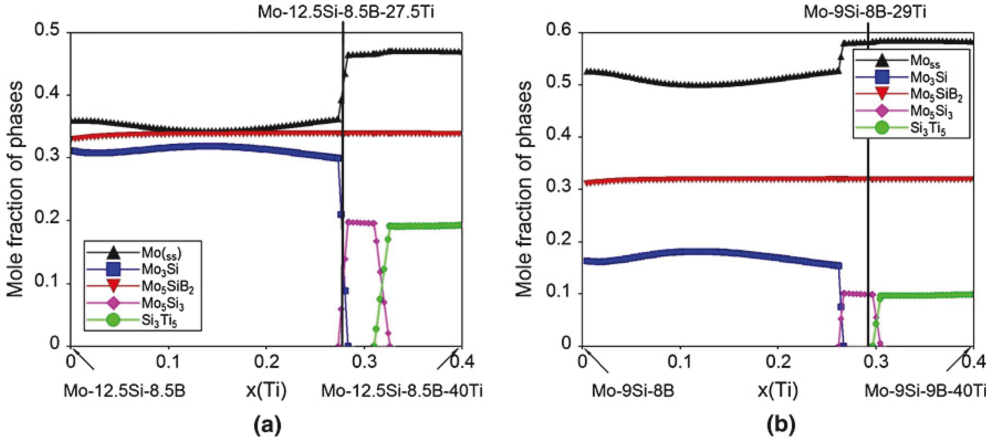

Fig. 1—Calculated mole fractions of phases in (*a*) Mo-12.5Si-8.5B (modified from Ref. [13]) and (*b*) Mo-9Si-8B as a function of Ti content at 1873 K (1600 °C).

To investigate the high-temperature oxidation behavior, samples with dimensions of 10 × 4 × 3 $mm^3$ were machined using a slow-cutting diamond saw. Oxidation tests were carried out under isothermal conditions in laboratory air by both continuous thermogravimetric analysis and discontinuous weight change measurements. A more detailed description of the experimental setup is given elsewhere.[22,23]

Compressive creep behavior was determined using electro-discharge machined specimens with dimensions of 5 mm height and 3 × 3 $mm^2$ cross section. Top and bottom surfaces were ground and polished to insure planar-parallel loading. All creep tests were carried out under constant true stresses at temperatures of 1473 K and 1573 K (1200 °C and 1300 °C) in a Zwick universal testing device equipped with a Maytec vacuum furnace ($<10^{-4}$ Pa). Creep strain was continuously monitored by a couple of inductive displacement transducers at the upper and lower punch. This signal was converted into true strain utilizing a self-written Matlab routine running on the personal computer used for data acquisition assuming constant sample volume. Likewise, true stress was calculated and kept constant through closed loop control of the testing device. Vickers microhardness measurements were made with a Q10A+ (Qness GmbH) hardness tester using loads of 500 g and 1 kg.

## III. RESULTS AND DISCUSSION

### A. *Microstructure and Density*

Representative microstructures of the investigated alloys are shown in Figure 2. Using XRD (Figure 3), it was proven that both alloys consist of Mo solid solution ($Mo_{ss}$), $Mo(Ti)_5SiB_2$, and $Ti(Mo)_5Si_3$ ($D8_8$), where the elements in parentheses partly substitute for the preceding major phase constituent. However, the Mo-12.5Si-8.5B-27.5Ti alloy contains an additional $Mo(Ti)_3Si$ phase, which partially replaces the Mo solid solution and, thus, increases both the volume fraction of the intermetallic phases and the interface density (Table II). Therefore, the microstructure of this alloy was found to be finer than that of the Mo-9Si-8B-29Ti alloy. Phase distributions before and after creep, as well as interface density, were determined using the linear intercept method in an image processing program (Table II). The analyzed phase compositions are presented in Table III. Contrary to the investigations and thermodynamic predictions of Yang *et al.*,[13] and our own thermodynamic calculations, no tetragonal $Mo(Ti)_5Si_3$ was found by either XRD (Figure 3) or WDS analysis (not shown here). The reason for this is not clear yet: Even the homogenization heat treatment for 150 hours at 1873 K (1600 °C) did not lead to the predicted formation of $Mo(Ti)_5Si_3$. This finding could be due to the strong thermal stability of the hexagonal $Ti(Mo)_5Si_3$ phase as confirmed by Figure 3 or due to segregation effects. These aspects will be investigated in future studies.

Sakidja *et al.*[12,24] determined the influence of different alloying elements on phase formation and stability in Mo-Si-B alloys. They classified titanium as a $D8_8$ stabilizer and niobium, tungsten, and tantalum as

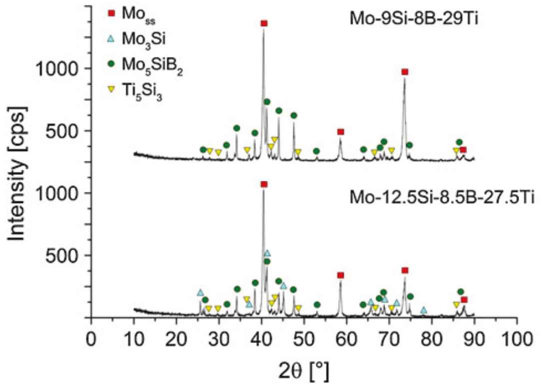

Fig. 3—X-ray diffraction patterns showing the phases present after annealing at 1873 K (1600 °C) for 150 h.

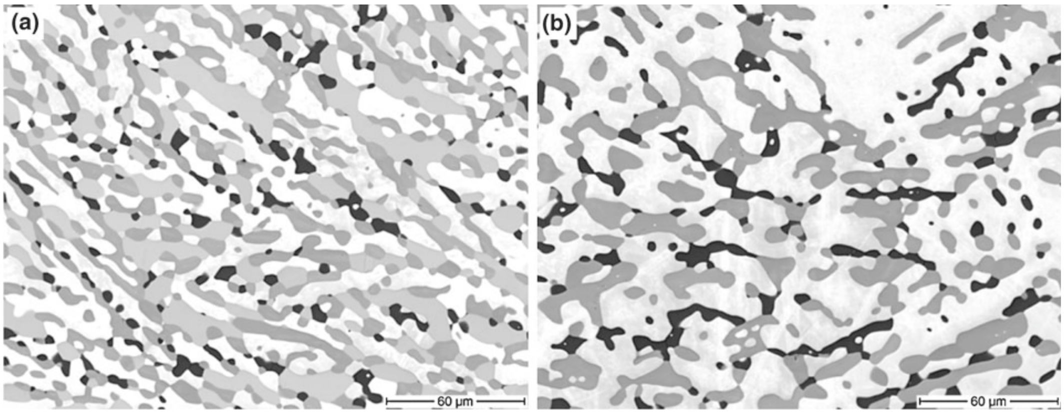

Fig. 2—Microstructures of (*a*) Mo-12.5Si-8.5B-27.5Ti and (*b*) Mo-9Si-8B-29Ti in BSE contrast showing Mo solid solution (bright), $Mo(Ti)_3Si$ (gray), $Mo(Ti)_5SiB_2$ (darker gray), and $Ti(Mo)_5Si_3$ (black).

**Table II. Phase Distributions Before and After Creep and Interface Densities of the Investigated Alloys (Standard Deviation in Parentheses)**

| Alloy Composition | $Mo_{ss}$ | $Mo(Ti)_3Si$ | $Mo(Ti)_5SiB_2$ | $Ti(Mo)_5Si_3$ | Interface Density ($\mu m^{-1}$) |
|---|---|---|---|---|---|
| Before creep | | | | | |
| Mo-12.5Si-8.5B-27.5Ti | 37.9 (±2.8) | 26.2 (±3.8) | 27.6 (±1.7) | 7.1 (±1.6) | 0.353 |
| Mo-9Si-8B-29Ti | 61.1 (±3.1) | — | 29.2 (±2.3) | 9.4 (±1.0) | 0.175 |
| After creep | | | | | |
| Mo-12.5Si-8.5B-27.5Ti | 36.6 (±1.1) | 28.2(±0.6) | 28.8 (±0.3) | 6.3 (±0.4) | 0.373 |
| Mo-9Si-8B-29Ti | 60.5 (±2.2) | — | 30.2 (±1.8) | 8.6 (±1.2) | 0.174 |

**Table III. Compositions of the Phases Present in the Two Alloys as Determined by WDS**

| Phase | Components | Mo-12.5Si-8.5B-27.5Ti (At. Pct) | Mo-9Si-8B-29Ti (At. Pct) |
|---|---|---|---|
| $Mo_{ss}$ | Mo | 71.7 | 71.5 |
| | Si | 2.5 | 2.27 |
| | B | 0 | 0 |
| | Ti | 25.76 | 26.11 |
| $Mo(Ti)_3Si$ | Mo | 47.13 | — |
| | Si | 22.98 | — |
| | B | 0 | — |
| | Ti | 29.86 | — |
| $Mo(Ti)_5SiB_2$ | Mo | 34.17 | 33.52 |
| | Si | 13.72 | 13.94 |
| | B | 23.70 | 23.53 |
| | Ti | 28.41 | 28.99 |
| $Ti(Mo)_5Si_3$ | Mo | 16.91 | 13.96 |
| | Si | 37.41 | 38 |
| | B | 0 | 0 |
| | Ti | 45.66 | 48.01 |

$T_1$-stabilizing elements. W and Ta may be excluded from consideration as alloying elements based on their high densities. Similarly, taking into account the known poor oxidation resistance of niobium, a Mo-Nb-Si-B alloy containing high Nb levels might also not be suitable for high-temperature applications without additional coating protection to improve oxidation resistance.[25] Also, the density reduction due to niobium is not as marked as it is for titanium.[12] The observed solubility of Ti in every phase here leads to a density reduction of nearly 18 pct as compared to a reference Mo-Si-B alloy with a density of 9.6 g/cm$^3$.[9] At 7.7 and 7.8 g/cm$^3$ for Mo-12.5Si-8.5B-27.5Ti and Mo-9Si-8B-29Ti, respectively, they are even lower than the densities of currently used Re-containing Ni-base single-crystalline superalloys.[10]

### B. *Oxidation Behavior*

Ti additions are expected to have a strong influence on the oxidation behavior of Mo-Si-B alloys as a consequence of the presence of the hexagonal $Ti(Mo)_5Si_3$ phase (Figure 3 as well as the corresponding explanation) and because of the high Ti solubility of 26, 30, 28, and 48 at. pct in the phases $Mo_{ss}$, $Mo(Ti)_3Si$, $Mo(Ti)_5SiB_2$, and $Ti(Mo)_5Si_3$, respectively (Table III). In order to reveal the influence of Ti alloying on the oxidation resistance of the Mo-Si-B system, the oxidation kinetics as well as oxide morphology of two quaternary Mo-Si-B-Ti alloys will be presented and finally compared with the corresponding results of the reference alloy Mo-9Si-8B consisting of the three phases $Mo_{ss}$, $Mo_3Si$, and $Mo_5SiB_2$.[23]

Figure 4(a) shows the specific weight change *vs* time for the alloy Mo-12.5Si-8.5B-27.5Ti. For the sake of illustration, Figure 4(b) presents the oxidation curves of one of our Ti-containing alloys, Mo-9Si-8B-29Ti, and those of the reference alloy without Ti, Mo-9Si-8B, at 1373 K to 1573 K (1100 °C to 1300 °C). To facilitate a comparison, both figures are scaled in the same manner. The heavy initial weight loss due to $MoO_3$ evaporation during the first few hours, which is typical of Mo-9Si-8B at higher temperatures, was not observed for both Mo-Si-B-Ti alloys studied at 1373 K (1100 °C), indicating that passivation and, thus, diffusion-controlled oxidation kinetics are operative from the beginning. However, the TGA results of the Ti-containing alloys reveal increasing weight loss with increasing temperature in general accordance with the oxidation behavior of Mo-9Si-8B. Specifically, the weight loss of the reference alloy approaches zero for longer exposure times, while this weight loss is still pronounced in the case of the Ti-containing silicide alloys, indicating continuing evaporation of $MoO_3$. Furthermore, the comparison of the TGA curves of the two Mo-Si-B-Ti alloys generally shows a slightly reduced weight loss rate for Mo-12.5Si-8.5B-27.5Ti which may be qualitatively rationalized by the higher volume fraction of intermetallic phases present due to the higher Si content (Table II). Below 1273 K (1000 °C) (not shown here), the investigated Mo-Si-B-Ti alloys experience rapid linear weight loss (“pesting”) which is typical of Mo-Si-B alloys.[22]

Figures 5(a) and (b) shows the SEM BSE cross section and surface of Mo-9Si-8B-29Ti oxidized for 100 hours at 1373 K (1100 °C). For the sake of comparison, the cross section of Mo-9Si-8B after 72 hours of oxidation at 1373 K (1100 °C) is shown in Figure 5(d). The reasonable oxidation resistance of Mo-9Si-8B at 1373 K (1100 °C) is a consequence of the formation of an outer continuous and thus protective amorphous borosilicate layer with an average thickness of ≈13 $\mu$m.[23] Underneath this layer, a zone of internal oxidation consisting of silica precipitates within a $Mo_{ss}$ matrix develops. Compared to the reference alloy, the oxide morphology of the Mo-Si-B-Ti alloys is completely different. Considering the phase diagrams of Ti-Si-O,[26] $B_2O_3$-$SiO_2$,[27] and Mo-9Si-8B-$O_2$[28] as well as the results of XRD investigations of the oxide surface in conjunction with detailed cross-sectional

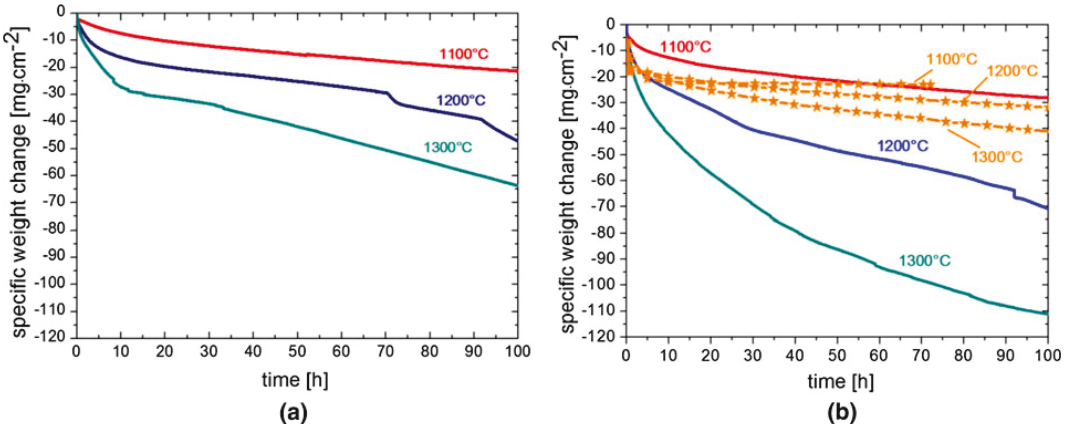

Fig. 4—Specific weight change *vs* time for the alloys (*a*) Mo-12.5Si-8.5B-27.5Ti and (*b*) Mo-9Si-8B-29Ti (indicated by continuous lines) along with Mo-9Si-8B (indicated by broken lines with symbols) oxidized in air at temperatures ranging between 1373 K and 1573 K (1100 °C and 1300 °C).

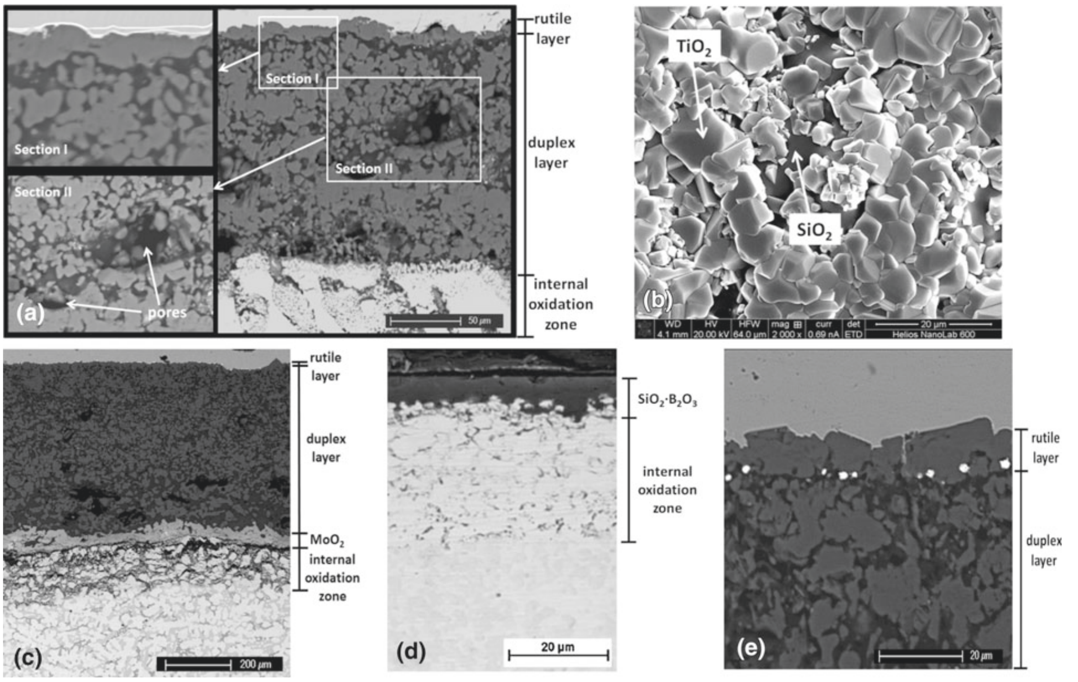

Fig. 5—SEM images of (*a*) Mo-9Si-8B-29Ti oxidized for 100 h at 1373 K (1100 °C) with magnified sections of the rutile layer (Section I) and the titania/silica-duplex scale (Section II), whereby rutile is displayed in bright gray and silica in dark gray BSE-phase contrast, (*b*) the oxidized surface of Mo-9Si-8B-29Ti [1373 K (1100 °C), 100 h], (*c*) Mo-9Si-8B-29Ti oxidized for 100 h at 1573 K (1300 °C), (*d*) the reference alloy Mo-9Si-8B oxidized at 1373 K (1100 °C) for 72 h (from Ref. [22]), and (*e*) Mo-9Si-8B-29Ti oxidized for 100 h at 1373 K (1100 °C) with Pt markers located at the rutile/duplex layer interface.

analyses *via* SEM and EDX, the oxide scale can be divided into two major regions as demonstrated in Figure 5(a) using the example of Mo-9Si-8B-29Ti: (i) an outermost, predominantly continuous rutile layer at the oxide/air interface and (ii) a thick and porous duplex layer, comprising titania and silica.

The outermost rutile layer possesses an average thickness of 15 $\mu$m after 100 hours of oxidation at 1373 K (1100 °C) and is especially visible on the magnified BSE cross section in picture-excerpt I in Figure 5(a). The spaces between the rutile particles are filled with small amounts of an amorphous phase, in which Si, O, and small amounts of B can be detected *via* EDX (Figure 5(b)). In the experimental part, the difficulty of detecting B in the alloy composition investigated was already mentioned. However, according to thermodynamic calculations and the literature survey on the oxidation behavior of Mo-Si-B alloys, it can be stated that a certain amount of $B_2O_3$ is dissolved in $SiO_2$ in the initial state of oxidation at high temperatures. It is well known that $B_2O_3$ reduces the viscosity of silica drastically,[29,30] facilitating the sealing of the substrate in the initial period of oxidation by a protective oxide layer[17] as long as the viscosity of the silica layer remains above the glass transition ($10^{13}$ Pa s), which is only the case for very low B concentrations.[29] However, Yoshimi *et al.*[29] estimated in this context that the concentration of B in the $SiO_2$ glass scale formed on $Mo_5SiB_2$ after 24 hours of oxidation at 1473 K (1200 °C) is under a detectable limit of EPMA and TEM-EDS, even though this phase has a (B/Si) ratio of 2. That confirmed that $B_2O_3$ evaporates at higher temperatures. Extrapolating the data obtained from Cofer and Economy,[30] Burk *et al.*[23] determined a volatilization rate of $B_2O_3$ of 1 and 5 mg $cm^{-2}$ $h^{-1}$ at 1373 K and 1573 K (1100 °C and 1300 °C), respectively. Thus, it can be assumed that the borosilicate is partially depleted in $B_2O_3$ at 1373 K (1100 °C), whereas it consists of nearly sole $SiO_2$ above 1473 K (1200 °C). Underneath the rutile scale, a thick, porous duplex layer forms (see image section II in Figure 5(a)) that mainly consists of rutile and amorphous silica with an expected depletion of B due to the evaporation of $B_2O_3$ through several pores and channels. Using the image processing program ImageJ, it was possible to use the contrast differences between the titania and silica in order to quantify the volume fractions of both phases in the duplex layer. The average value of 20 BSE micrographs with a typical magnification as in Figure 5(a) was used for this. After 100 hours of oxidation at 1373 K (1100 °C), the volume fractions of titania and silica are about 62 and 38 pct, respectively. After the same exposure time and temperature, the amount of titania and silica in the alloy Mo-12.5Si-8.5B-27.5Ti with a higher amount of intermetallic phases is changed to 52 and 48 pct, respectively, in other words less titania and more silica are present. It is noteworthy that at 1373 K (1100 °C), the thickness of the duplex layer varies from 70 to 110 $\mu$m and is, thus, partially up to eight times thicker than the protective borosilicate layer formed on Mo-9Si-8B after 72 hours of exposure time (Figure 5(c) and (d)). With prolonged oxidation time and/or increasing temperature, the duplex layer formed on the Ti-containing silicide alloys becomes thicker and more porous. After 100 hours of oxidation at 1573 K (1300 °C) (Figure 5(c)), the duplex layer on Mo-9Si-8B-29Ti even reaches a thickness of 360 to 420 $\mu$m. Samples sputtered with a porous, 300-nm thin Pt layer before the oxidation revealed that the Pt marker is located at the borderline between the outermost rutile layer and the duplex layer (Figure 5(e)), indicating that the rutile layer grows through the outward diffusion of Ti cations, whereas the duplex layer expands through enhanced inward diffusion of oxygen.

Underneath the duplex layer, an interlayer mainly consisting of $MoO_2$ is formed only on Mo-9Si-8B-29Ti at 1573 K (1300 °C) presumably because of the inward transport of oxygen (Figure 5(c)). No formation of a $MoO_2$ layer was observed after oxidation of the reference alloy at 1573 K (1300 °C).[23] For Mo-9Si-8B-29Ti, this interlayer yields local thicknesses of 50 $\mu$m after 100 hours of oxidation at 1573 K (1300 °C), and is distinctly visible in Figure 5(c). At high temperatures, a zone of internal oxidation forms beneath the oxide layer, where Si and B in the intermetallic phases $Mo(Ti)_5SiB_2$ and $Mo(Ti)_3Si$ oxidize due to the high affinity to oxygen, which diffuses through the entire oxide layer.

The analysis of the oxide morphology indicates that the porous duplex layer, which mainly consists of $TiO_2$, does not serve as an effective barrier to oxidation. The main reason of the insufficient protectiveness of the oxide scale formed on Ti-containing Mo-Si-B alloys is that (rapid) inward transport of oxygen can occur through channels and pores in the scale. In the case of the formation of a protective borosilicate layer during the oxidation of Mo-9Si-8B above 1173 K (900 °C), the growth of the oxide scale may only proceed through solid-state diffusion through the oxide layer. In Ti-containing Mo-Si-B alloys, oxygen can easily penetrate through the rutile particles as the mobility of oxygen in $TiO_2$ is significantly higher than in $SiO_2$.[31] That, in turn, results in an increasing volume fraction of $TiO_2$ within the duplex layer with increasing time and/or temperature, leading to an accelerated inward transport of oxygen, the formation of new $TiO_2$ particles, and consequently pores through which oxygen can reach the substrate easily, allowing the evaporation of gaseous $MoO_3$. At the same time, the outward transport of cations increases, resulting in a thicker outermost rutile layer as well as in a high amount of $TiO_2$ in a duplex layer. At temperatures below 1273 K (1000 °C), the formation of $B_2O_3{\cdot}SiO_2$ is too slow and the viscosity of the borosilicate layer is too high to seal the gaps between the fast-growing $TiO_2$ particles.

Recently, a study by some of the present authors of a nearly single-phase $(Mo,Ti)_5Si_3$ model material revealed excellent oxidation resistance in a broad temperature range of 1023 K to 1573 K (750 °C to 1300 °C).[32] In that case, an oxide layer forms that exhibits a continuous silica matrix in which rutile particles are embedded. It should be pointed out that the oxide composition of the duplex layer seems to play a crucial role on the oxidation resistance of Mo-Si-B-Ti alloys. Obviously, the scale morphology with a continuous silica matrix and embedded rutile particles served as an effective barrier to oxidation. Thus, the existence of $TiO_2$ does not necessarily preclude the formation of an oxide layer that provides sufficient oxidation protection. Rather, what is needed for a duplex layer to serve as an effective oxidation barrier is that borosilicate forms the matrix phase.

### C. *Compressive Creep Behavior*

Figure 6 shows selected compressive creep curves of the two investigated alloys as log strain rate *vs* true strain. Minimum creep rates, marked by filled circles on

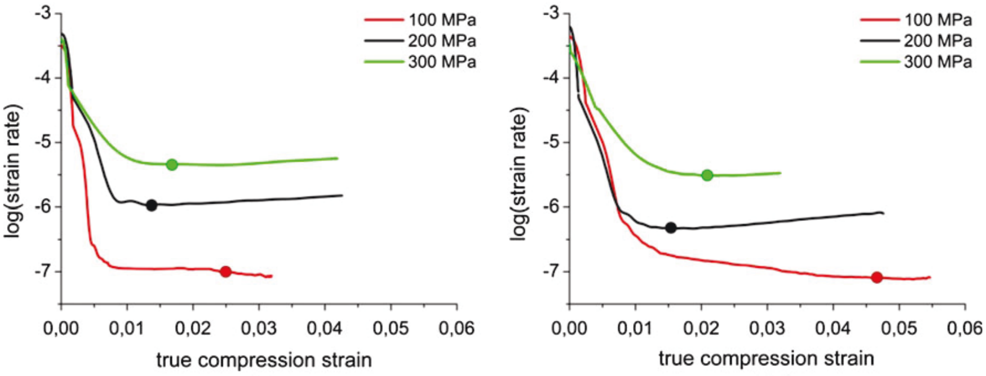

(a) (b)

Fig. 6—Logarithmic strain rate *vs* true strain at 1573 K (1300 °C) for (*a*) Mo-12.5Si-8.5B-27.5Ti and (*b*) Mo-9Si-8B-29Ti. Filled circles indicate the points at which the minimum strain rates were determined for further evaluation in Figs. 7 and 9.

the curves, were determined for each test condition and are plotted as a function of the applied stresses in Figure 7. Typically, minimum creep rates in Figure 6 were attained after a substantial drop in creep rate during the primary transient at strains >0.02. Thereafter, only little strain rate acceleration (less than a factor of two) takes place up to the maximum recorded strain of about 5 pct. Especially when compared to single-crystalline Nickel-base superalloys with their pronounced microstructural changes during creep such as rafting,[33] this indicates a relatively stable microstructure of the present alloys and close to steady-state creep conditions.

Furthermore, both alloys show comparable creep resistance at the two investigated temperatures of 1473 K and 1573 K (1200 °C and 1300 °C). This finding was somewhat unexpected, since Mo-9Si-8B-29Ti has a much lower content of intermetallic phases and only a slightly coarser microstructure. Assuming power law creep, the creep behavior of most metals is dominated by the dislocation density established in the steady-state creep regime, rather than by the grain size.[34] As the Mo solid solution is known to be the phase with the lowest creep resistance,[18,34,35] it is assumed to be the main carrier of high-temperature plastic deformation. Thus, one may expect the creep behavior to depend strongly on the volume fraction of intermetallic phases, which is, however, not the case here. Additionally, Meyer *et al.*[18] reported that, at temperatures ranging from 1493 K to 1593 K (1220 °C to 1320 °C), $Mo_3Si$ shows a high dislocation density as compared to the intermetallic phases $T_1$ and $T_2$ in their investigated alloy. The observed polygonization in $Mo_3Si$ was interpreted as evidence for a dislocation climb-controlled deformation mechanism. Rosales and Schneibel[36] measured the 0.2 pct offset yield strength of single-phase $Mo_3Si$ and found it to be approximately 100 MPa at a temperature of 1673 K (1400 °C) and strain rate of $10^{-5}$ $s^{-1}$. For all the above reasons, we believe that the $Mo(Ti)_3Si$ phase also participates in the plastic deformation process.

The creep behavior of $T_2$ single crystals was investigated by Ito *et al.*[37] They reported a very low (measurable) strain rate of $10^{-9}$ $s^{-1}$ for the most easily deformed orientation ([021] with slip on [001](010)) at a temperature of 1773 K (1500 °C) and a stress of 300 MPa. These experimental conditions (temperature and stress) are much higher than the highest ones investigated in the present study. Therefore, the $Mo(Ti)_5SiB_2$ phase in the present alloys should not deform during creep, particularly if there is additional strengthening due to titanium in this phase compared to the Ti-free $T_2$ phase of Ito *et al.*[37]

The strain rate of monolithic $Ti_5Si_3$ at 1473 K (1200 °C) was reported to be approximately $10^{-6}$ $s^{-1}$ at 100 MPa and, assuming power law creep, the stress exponent $n = \Delta\log\dot{\varepsilon}/\Delta\log\sigma$ was found to be 3.[38] Hence, the strain rate of pure $Ti_5Si_3$ is two orders of magnitude higher than the strain rate of both alloys investigated here. Therefore, the $Ti(Mo)_5Si_3$ phase is believed to participate in the creep process.

In Figure 7(a), the stress exponent $n$ was determined to be between 3 and 3.5, indicating a dislocation climb-controlling creep mechanism in both alloys. Taking this observation and the above-discussed deformability of $Mo(Ti)_3Si$ and $Ti(Mo)_5Si_3$ at these temperatures into account, a plausible reason for why the two alloys show comparable creep behavior can be inferred. For Mo-12.5Si-8.5B-27.5Ti and Mo-9Si-8B-29Ti, the volume fractions of Mo solid solution are around 38 and 61 pct, respectively, while the volume fraction of $Ti(Mo)_5Si_3$ is nearly identical in both alloys. Since the Mo-12.5Si-8.5B-27.5Ti alloy also contains the $Mo(Ti)_3Si$ phase, the volume fractions of the deformable phases at the creep temperatures, namely, Mo solid solution, $Mo(Ti)_3Si$, and $Ti(Mo)_5Si_3$, are virtually the same in both alloys, as seen in Table II.

To verify the above-stated microstructural stability during creep, the microstructures and respective phase distributions were determined after creep and are tabulated in Table II. Moreover, Figure 8 represents a SEM micrograph of Mo-12.5Si-8.5B-27.5Ti after 15 pct strain at 1573 K (1300 °C) and 300 MPa. There was no evidence of significant microstructural coarsening or of a change in the phase distribution confirming the

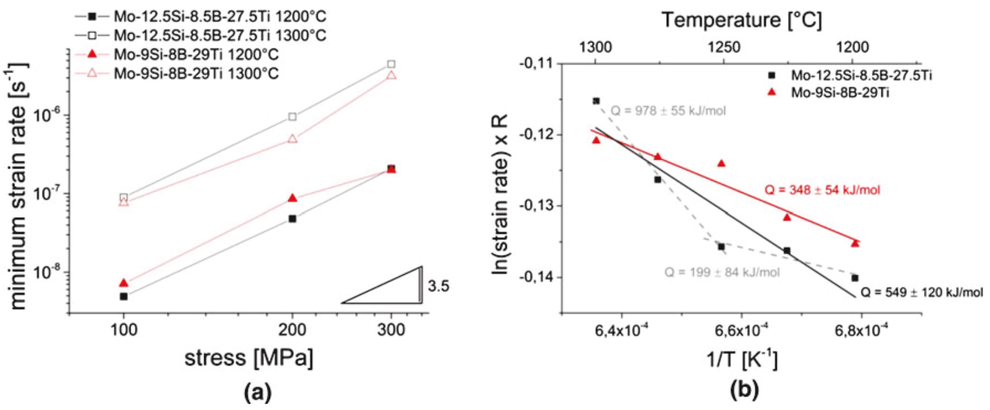

Fig. 7—(*a*) Double logarithmic plot of minimum strain rate *vs* applied stress at 1473 K and 1573 K (1200 °C and 1300 °C) and (*b*) Arrhenius plot at 200 MPa.

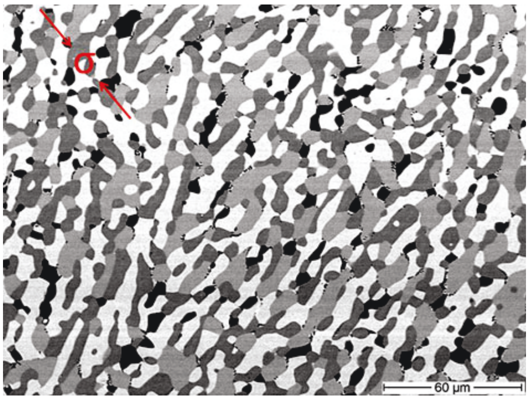

Fig. 8—SEM BSE micrograph of Mo-12.5Si.8.5B-27.5Ti after 15 pct compressive creep strain at 1573 K (1300 °C) and 300 MPa.

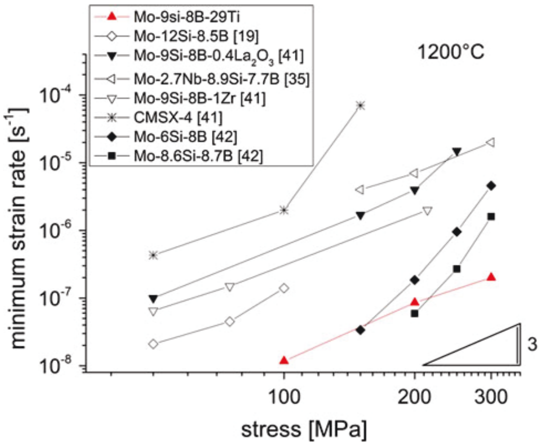

Fig. 9—Double logarithmic plot of minimum strain rate *vs* applied stress at 1473 K (1200 °C) for Mo-9Si-8B-29Ti compared to other Mo-Si-B alloys and the single-crystalline Ni-base superalloy CMSX-4.

assumption of microstructural stability due to sluggish diffusion. This is also in accord with earlier findings of Sakidja *et al*.[34] and Jéhanno *et al*.[39]

Finally, activation energies for creep were determined at a stress of 200 MPa using the slope of the Arrhenius plot, presented in Figure 7(b). Values of 549 ± 120 kJ/mol for Mo-12.5Si-8.5B-27.5Ti (square symbols) and 348 ± 54 kJ/mol for Mo-9Si-8B-29Ti (triangles) were obtained if a single deformation mechanism was assumed to operate in the investigated temperature region. The activation energy of Mo-9Si-8B-29Ti is not that different from the activation energy for Mo self-diffusion, $Q_{\mathrm{sd}}$ = 405 kJ/mol,[40] indicating that bulk diffusion of Mo atoms in the Mo solid solution matrix might play the major role in creep deformation of this alloy. A similar behavior was observed by Jéhanno *et al*.[35] in an ultrafine grained Mo-Nb-Si-B alloy. The high value for Mo-12.5Si-8.5B.27.5Ti may be consistent with the assumption of multiphase deformation in this four-phase alloy, because its activation energy, while significantly exceeding the activation energy for Mo self-diffusion (405 kJ/mol[40]), is much lower than that of a $T_2$ single crystal (740 kJ/mol[37]). However, the course of the squared data points may alternatively suggest a change in deformation mechanism at around 1523 K (1250 °C) with a low temperature branch exhibiting similar activation energy than that obtained for the other alloy and a high-temperature branch for which the slope would come close to the activation energy of the $T_2$ phase. Detailed future TEM investigations on creep-deformed samples will be needed to shed light on this open issue.

In Figure 9, the creep behavior of the Mo-9Si-8B-29Ti alloy at 1473 K (1200 °C) is compared to differently processed two- and three-phase Mo-Si-B alloys and a Ni-base single-crystalline superalloy CMSX-4. It is noteworthy that CMSX-4 has inferior creep resistance compared to all the Mo-Si-B alloys, but not surprising because the chosen creep temperature of 1473 K (1200 °C) is close to the solvus temperature of the $\gamma'$ phase in CMSX-4. Hence, a substantial decrease in the volume fraction of $\gamma'$ phase occurs, leading to accelerated creep. The Mo-Si-B alloys with a slightly better creep resistance than CMSX-4 were all processed by powder metallurgy,[35,41] typically resulting in very fine microstructures. In those cases, the grain and phase sizes have been found to lie between 0.7 and 7 $\mu$m.[35,41] The best performance (*i.e.*, lowest minimum creep rates) is shown by the Ti-rich alloys investigated here and by the gas-atomized alloys of Jain and Kumar.[42] Since the latter ones posses much larger grain and phase sizes typically ranging between 20 and 25 $\mu$m, they also exhibit larger stress exponents than their PM counterparts. At any given creep stress level, the Ti-rich alloys yield minimum strain rates that are more than one order of magnitude lower than those of the similarly processed Mo-12Si-8.5B alloy with a comparable microstructure in terms of volume fraction of Mo solid solution, and grain and phase sizes.[19]

We believe that the enhanced creep resistance is due to solid solution strengthening by the dissolved titanium (Table III) plus the additional effect of dissolved Si in Mo which is known to cause substantial strengthening.[35] Sturm *et al.*[43] measured Vickers hardness numbers (VHN) of Mo-Si solid solutions containing 1.69 and 3.34 at. pct dissolved Si (using a load of 1 kg) and obtained values of 316 and 413, respectively. The solid solution strengthening of Mo by simultaneous alloying with Si and B in a two-phase Mo-Si-B alloy was examined by Alur *et al.*[44] using microhardness measurements with a load of 500 g. They obtained VHN values of 375 and 474 in well-annealed and as-forged conditions, respectively. Here, for the Mo solid solution phase of our Ti-containing alloys, VHN values of 515 and 583 were obtained using loads of 1 kg and 500 g, respectively. These hardness values are substantially higher than any of the former. Thus, we confirm that the dissolved titanium in Mo leads to additional solid solution strengthening at room temperature. If this mechanism persists at high temperatures, it may be responsible for the high creep resistance of our Ti-containing alloys.

## IV. SUMMARY AND CONCLUSIONS

The high-temperature creep behavior of two arc-melted quaternary Mo-Si-B-Ti alloys (Mo-12.5Si-8.5B-27.5Ti and Mo-9Si-8B-29Ti) was investigated in this study for the first time. The $\mathrm{Mo(Ti)_5Si_3}$ phase predicted by thermodynamic CALPHAD calculations was not found; instead, significant amounts of the $\mathrm{Ti(Mo)_5Si_3}$ phase were found experimentally, even though the alloys were annealed for 150 hours at 1873 K (1600 °C) to homogenize them. While the reason for this discrepancy remains unclear, our alloys show extraordinary microstructural stability at creep temperatures of 1473 K and 1573 K (1200 °C and 1300 °C). Due to solid solution strengthening by Ti, the creep resistance of our alloys is far superior to that of a state-of-the-art Ni-base superalloy CMSX-4. They are also one order of magnitude better in terms of minimum strain rate when compared to a reference alloy without Ti, namely, Mo-12Si-8.5B alloy. Combined with the beneficial density reduction of around 18 pct relative to the reference alloy without Ti, to values even below those of Ni-base superalloys, the high-temperature properties measured so far are encouraging and motivate further investigations into (i) mechanical behavior, *e.g.*, ambient temperature fracture toughness and deformability, and (ii) oxidation resistance at elevated temperatures if it is possible to suppress the hexagonal $\mathrm{Ti(Mo)_5Si}$ phase responsible for the formation of a relatively porous duplex layer with titania matrix.

## ACKNOWLEDGMENTS

The financial support by the Deutsche Forschungsgemeinschaft (DFG) within the framework of the research unit 727 "Beyond Ni-base Superalloys" is gratefully acknowledged. HB and EPG were supported by the U.S. Department of Energy, Office of Fossil Energy, Advanced Turbine Systems Program. The authors would also like to thank Dr. T. Gietzelt and U. Gerhards from the Institute for Micro Process Engineering at the Karlsruhe Institute of Technology for help with electron microprobe wavelength-dispersive spectroscopy measurements.

## REFERENCES

1. D.M. Dimiduk and J.H. Perepezko: *MRS Bull.*, 2003, vol. 28, pp. 639–45.
2. J. Sato, T. Omori, K. Oikawa, I. Ohnuma, R. Kainuma, and K. Ishida: *Science*, 2006, vol. 312, pp. 90–91.
3. B.P. Bewlay, M.R. Jackson, J.-C. Zhao, P.R. Subramanian, M.G. Mendiratta, and J.J. Lewandowski: *MRS Bull.*, 2003, vol. 28, pp. 646–53.
4. P. Jéhanno, M. Heilmaier, H. Kestler, M. Böning, A. Venskutonis, B. Bewlay, and M. Jackson: *Metall. Mater. Trans. A*, 2005, vol. 36A, pp. 515–23.
5. J.H. Schneibel, C.T. Liu, D.S. Easton, and C.A. Carmichael: *Mater. Sci. Eng. A*, 1999, vol. 261, pp. 78–83.
6. D.M. Berczik: US Patents 5,595,616 and 5,693156, 1997.
7. H. Choe, D. Chen, J.H. Schneibel, and R.O. Ritchie: *Intermetallics*, 2001, vol. 9, pp. 319–29.
8. T.A. Parthasarathy, M.G. Mendiratta, and D.M. Dimiduk: *Acta Mater.*, 2002, vol. 50, pp. 1857–68.
9. P. Jéhanno, M. Heilmaier, and H. Kestler: *Intermetallics*, 2004, vol. 12, pp. 1005–09.
10. G. Erickson: *JOM*, 1995, vol. 47, pp. 36–39.
11. Y. Yang, Y.A. Chang, L. Tan, and W. Cao: *Acta Mater.*, 2005, vol. 53, pp. 1711–20.
12. R. Sakidja and J.H. Perepezko: *J. Nucl. Mater.*, 2007, vol. 366, pp. 407–16.
13. Y. Yang, H. Bei, S. Chen, E.P. George, J. Tiley, and Y.A. Chang: *Acta Mater.*, 2010, vol. 58, pp. 541–48.
14. Y. Yang, Y.A. Chang, L. Tan, and Y. Du: *Mater. Sci. Eng. A*, 2003, vol. 361, pp. 281–93.
15. Y. Yang and Y.A. Chang: *Intermetallics*, 2005, vol. 13, pp. 121–28.
16. I. Rosales, H. Martinez, D. Bahena, J.A. Ruiz, R. Guardian, and J. Colin: *Corros. Sci.*, 2009, vol. 51, pp. 534–38.
17. M.K. Meyer, M.J. Kramer, and M. Aknic: *Adv. Mater.*, 1996, vol. 8, pp. 85–88.
18. M.K. Meyer, M.J. Kramer, and M. Akinca: *Intermetallics*, 1996, vol. 4, pp. 273–81.
19. J.H. Schneibel, P.F. Tortorelli, R.O. Ritchie, and J.J. Kruzic: *Metall. Mater. Trans. A*, 2005, vol. 36A, pp. 525–31.
20. R. Mitra: *Int. Mater. Rev.*, 2006, vol. 51, pp. 13–64.

21. S.-H. Haa, K. Yoshimia, K. Maruyamaa, R. Tub, and T. Goto: *Mater. Sci. Eng. A*, 2012, vol. 552, pp. 179–88.
22. M. Azim, S. Burk, B. Gorr, H.-J. Christ, D. Schliephake, M. Heilmaier, R. Bornemann, and P. Haring Bolivar: *Oxid. Met.* DOI: 10.1007/s11085-013-9375-1.
23. S. Burk, B. Gorr, V.B. Trindade, and H.-J. Christ: *Oxid. Met.*, 2009, vol. 73, pp. 163–81.
24. R. Sakidja, J.H. Perepezko, S. Kim, and N. Sekido: *Acta Mater.*, 2008, vol. 56 (18), pp. 5223–44.
25. Y. Liu, M.J. Kramer, A.J. Thom, and M. Akinc: *Metall. Mater. Trans. A*, 2005, vol. 36A, pp. 601–07.
26. R.W. Ricker and R.A. Hummel: *J. Am. Ceram. Soc.*, 1951, vol. 34, pp. 271–79.
27. T.K. Gupta and J.H. Jean: *J. Mater. Res.*, 1994, vol. 9, pp. 999–1009.
28. S. Burk, B. Gorr, and H.-J. Christ: *Acta Mater.*, 2010, vol. 58, pp. 6154–65.
29. K. Yoshimia, S. Nakatanic, T. Sudac, S. Hanadaa, and H. Habazakid: *Intermetallics*, 2002, vol. 10, pp. 407–14.
30. N.P. Bansal and R.H. Doremus: *Handbook of Glass Properties*, Academic Press, New York, 1986.
31. P. Kopfstad: *Nonstoichiometry, Diffusion, and Electrical Conductivity in Binary Metal Oxide*, Wiley, New York, 1972.
32. S. Burk, B. Gorr, H.-J. Christ, D. Schliephake, M. Heilmaier, C. Hochmuth, and U. Glatzel: *Scripta Mater.*, 2012, vol. 66, pp. 223–26.
33. H. Mughrabi: *Mater. Sci. Technol.*, 2009, vol. 25, pp. 191–204.
34. R. Sakidja, H. Sieber, and J.H. Perepezko: *Philos. Mag. Lett.*, 1999, vol. 79, pp. 351–57.
35. P. Jéhanno, M. Heilmaier, H. Saage, M. Böning, H. Kestler, J. Freudenberger, and S. Drawin: *Mater. Sci. Eng. A*, 2007, vol. 463, pp. 216–23.
36. I. Rosales and J.H. Schneibel: *Intermetallics*, 2000, vol. 8, pp. 885–89.
37. K. Ito, K. Ihara, K. Tanaka, M. Fujikura, and M. Yamaguchi: *Intermetallics*, 2001, vol. 9, pp. 591–602.
38. R. Rosenkranz, G. Frommeyer, and W. Smarsly: *Mater. Sci. Eng. A*, 1992, vol. 152, pp. 288–94.
39. P. Jéhanno, M. Heilmaier, H. Saage, H. Heyse, M. Böning, H. Kestler, and J.H. Schneibel: *Scripta Mater.*, 2006, vol. 55, pp. 525–28.
40. H.J. Frost and M.F. Ashby: *Deformation-Mechanism Maps: The Plasticity and Creep of Metals and Ceramics*, Pergamon Press, Oxford, 1982.
41. M. Heilmaier, M. Krüger, H. Saage, J. Rösler, D. Mukherji, U. Glatzel, R. Völkl, R. Hüttner, G. Eggeler, C. Somsen, T. Depka, H.-J. Christ, B. Gorr, and S. Burk: *JOM*, 2009, vol. 61, pp. 61–67.
42. P. Jain and K.S. Kumar: *Acta Mater.*, 2010, vol. 58, pp. 2124–42.
43. D. Sturm, M. Heilmaier, J.H. Schneibel, P. Jéhanno, B. Skrotzki, and H. Saage: *Mater. Sci. Eng. A*, 2007, vol. 463, pp. 107–14.
44. A.P. Alur, N. Chollacoop, and K.S. Kumar: *Acta Mater.*, 2004, vol. 52, pp. 5571–87.

# Manuskript VIII

# Oxidation mechanisms of lanthanum-alloyed Mo-Si-B

S. Majumdar, B. Gorr, H.-J. Christ, D. Schliephake, M. Heilmaier

Corrosion Science, 88 (2014) 360-371

Corrosion Science 88 (2014)

Contents lists available at ScienceDirect

Corrosion Science

journal homepage: www.elsevier.com/locate/corsci

# Oxidation mechanisms of lanthanum-alloyed Mo–Si–B

Sanjib Majumdar [a,b,*], Bronislava Gorr [a], Hans-Jürgen Christ [a], Daniel Schliephake [c], Martin Heilmaier [c]

[a] Institut für Werkstofftechnik, Universität Siegen, Paul-Bonatz-Str. 9-11, 57068 Siegen, Germany
[b] Materials Processing Division, Bhabha Atomic Research Centre, Trombay, Mumbai 400085, India
[c] Institut für Angewandte Materialien – Werkstoffkunde (IAM-WK), Karlsruhe Institute of Technology (KIT), Engelbert-Arnold-Str. 4, D-76131 Karlsruhe, Germany

ARTICLE INFO

*Article history:*
Received 26 March 2014
Accepted 26 July 2014
Available online 12 August 2014

*Keywords:*
A. Rare earth elements
B. SEM
B. TEM
C. Oxidation
C. High temperature corrosion

ABSTRACT

High temperature oxidation behavior of a Mo–9Si–8B (at.%) alloy containing 0.2 and 2 at.% La was studied between 750 and 1400 °C in static air. Isothermal thermogravimetric analysis for up to 72 h indicated a significant improvement in the oxidation resistance of the 2La-alloyed material in the 750–1000 °C temperature range. The oxide layers characterized by XRD, SEM, EDS, and FIB-TEM revealed the formation of more stable lanthanum–molybdates ($x\mathrm{La_2O_3}\cdot y\mathrm{MoO_3}$), which reduces the evaporation of $MoO_3$ below 1000 °C. The thickness data obtained for the external scale and the inner oxidation layers indicated a reduction of inward diffusion of oxygen with higher La concentrations.

## 1. Introduction

The research activities for developing new materials suitable for application temperatures (>1200 °C) beyond the capability limit of nickel-based superalloys are pursued worldwide. The refractory metal (Nb, Ta, Mo, W, and Re) based materials became the obvious choice as these metals possess high melting temperatures, greater than 2400 °C. However, the pure refractory metals suffer from insufficient creep strength and catastrophic oxidation at high temperatures. The efforts to improve the high temperature creep properties and fracture toughness of the material led to the development of alloys such as Nb–1Zr, Nb–1Zr–0.1C (PWC-11), Nb–10Hf–1Ti (C-103), Mo–0.5Ti–0.1Zr–0.02C (TZM), Mo–30W, Ta–10W and W–3Re [1–3]. These alloys exhibit favorable mechanical properties, and good compatibility with acidic medium, alkaline metals, and other liquid metals [1,4–7]. However, they have very poor oxidation resistance at higher temperatures due the non-protective nature of the oxide scales. Silicides of Nb and Mo show the most attractive behavior with respect to high temperature oxidation resistance, and therefore, these materials are studied intensively [8–25]. Amongst these materials, the Mo–Si–B alloy [12–25] is the most promising candidate comprising of a three phase $Mo_{ss}$ (molybdenum solid solution) – $Mo_5SiB_2$ (T2) – $Mo_3Si$ (A15) microstructure, which is stable up to temperatures of about 1600 °C in non-oxidizing environment. The volume fraction of the individual phase in the alloy is dependent on the composition and hence the properties of interest. The Mo–9Si–8B (at.%) alloy consists of about 55% $Mo_{ss}$, 26% T2 and 19% A15 phases and exhibits balanced mechanical and oxidation properties at high temperatures [26,27].

The oxidation mechanisms of Mo–Si–B alloy at different temperature regimes are well documented in the open literature [28–32]. The alloy shows a good oxidation resistance beyond 1050 °C. A protective borosilica scale forms on the alloy surface in this temperature regime, and the thermogravimetric analysis indicate a transient weight loss in the initial period of oxidation due to the spontaneous evaporation of $MoO_3$ followed by a steady state with marginal rate of weight loss [28–31]. The viscous sintering of the oxide scale closes the pores formed due to the evaporation of $MoO_3$ at the transient stage, and forms a passive layer. The addition of a sufficient quantity of boron (B) in molybdenum silicide leads to such a protective scale development. B-addition has also been proved to eliminate catastrophic failure of molybdenum silicides ($Mo_5Si_3$) due to pest oxidation at 800 °C [33]. In the case of the Mo–9Si–8B alloy, the concentration of Si is much lower compared to the stoichiometric $Mo_5Si_3$ and $MoSi_2$ compounds. The presence of boron is reported to enhance the growth kinetics of silica at the transient stage of oxidation at 1100 °C [32]. However, the slower reaction kinetics for silica on the Mo–9Si–8B alloy leads to the development of a boron (or $B_2O_3$)-rich silica scale formation, which possesses a very low viscosity at 800–950 °C [28]. Consequently, a higher permeation rate of oxygen causes the formation and the volatilization of $MoO_3$ by bubbling or channeling through the low viscosity oxide scale. The oxidation resistance of the

---

* Corresponding author at: Materials Processing Division, Bhabha Atomic Research Centre, Trombay, Mumbai 400085, India.

*E-mail addresses:* sanjib@barc.gov.in, sanjib731@gmail.com (S. Majumdar).

http://dx.doi.org/10.1016/j.corsci.2014.07.058
0010-938X/© 2014 Elsevier Ltd. All rights reserved.

Mo–Si–B alloys is the worst at 650–750 °C, where the evaporation of $MoO_3$ is initiated and a silica layer does not yet form [16].

The alloying of reactive and rare earth elements such as Ti, Zr, Hf, La, Ce and Y in proper quantities proves to enhance the oxidation resistance of alumina scale forming alloys such as Fe–Al [34–38] and Ni–Al [39–41]. These elements oxidize simultaneously along with the base element (Al). As a consequence, the growth rate of the protective alumina scale is reduced, and an improvement in the scale adhesion is also reported [42]. The effect of these elements on silica scale forming alloys is not well understood, which could be due to the complex molecular structure of the thermally grown amorphous silica layer. Niobium silicide based systems containing the elements like Ti, Hf are studied for their mechanical behavior and oxidation performance [43–45]. The oxidation behavior Ti alloyed Mo–Si–B was reported elsewhere [46,47]. Our earlier studies [27,48] indicated that the addition of Y could improve the oxidation resistance of Mo–Si–B at 750–950 °C. Doping of $La_2O_3$ in Mo–Si–B showed encouraging results with respect to the oxidation resistance in 800–1000 °C [46]. In the present investigation, attempts were made to study the oxidation behavior of the Mo–9Si–8B alloy with the addition of 0.2 and 2 at.% La at the selected temperatures between 750 and 1400 °C. The oxide scales were characterized to understand the mechanisms, supported by thermodynamic considerations.

## 2. Experimental procedure

Two alloy compositions comprising of Mo–9Si–8B–0.2La and Mo–9Si–8B–2La (at.%) were produced using mechanical alloying of the elemental powder mixtures of Mo, Si, B, and La of 99.95%, 99.9%, 99.6% and 99.89% purity (Alfa Aesar make), respectively. The initial manual mixing of the elemental powder was done inside a glove box containing inert argon atmosphere. To minimize the contamination from oxygen, the filling-up of the powder mix inside the WC lined stainless steel pots, and the subsequent fixing of the top cover of the pots were carried out inside the glove box. WC-ball to powder weight ratio (BPR) was maintained at 12:1, and planetary ball milling was conducted for 10 h using a Retsch PM 400 machine. Spark plasma sintering (SPS) schedule was optimized for consolidation of the alloy powder to obtain a high density product. The first step of heating of the alloy powder inside a graphite die was carried out at 1100 °C applying a heating rate of 100 °C/min, and the compact was soaked at this temperature for 15 min to remove gaseous impurities. The final stage of sintering was conducted at 1600 °C for 15 min applying a pressure of 50 MPa through graphite rods. Sintered material was cooled to room temperature at a very fast rate (150 °C/min), and a final stage of grinding treatment was applied to remove the carbon layers from the surfaces.

The sintered alloys were characterized using density measurement, X-ray diffraction (XRD), scanning electron microscopy (SEM), energy dispersive spectrometry (EDS), and electron back scattered diffraction (EBSD) to evaluate the compositions, the microstructures, and the phase formation. The samples were prepared by metallographic polishing followed by electro-polishing using the electrolyte comprised of 12.5 vol% methanol–87.5 vol.% $H_2SO_4$. Electro-polishing was carried out using LectroPol 5 (Struers) maintaining a bath temperature of 1 °C with the applied potential of 20 V for 20 s. For oxidation tests, the specimens of dimensions 5 mm × 3 mm × 2 mm were prepared using diamond wheel. The specimens were ground to 500-grit size SiC embedded paper and cleaned in ethanol. The oxidation behavior was studied under isothermal conditions applying continuous thermogravimetric analysis (TGA). TGA was carried out in static laboratory air at selected temperatures between 750 and 1300 °C for up to 72 h using a Rubotherm tailor-made magnetic suspension balance with a resolution of 1 μg and automatic electronic drift compensation. For confirming the weight change data of TGA and characterizing the oxide scale at intermediate exposure times, the separate isothermal oxidation experiments were also conducted using the resistance heating muffle type furnaces in static air at selected temperatures.

The surface of the oxidized specimens was characterized using XRD, SEM and EDS. The cross-section of the oxide scale was studied using SE and BSE imaging coupled with EDS analysis. Before observing the cross-section of the oxide layers, the samples were coated with pure nickel using electrolytic deposition technique. The nickel coating was provided to avoid the possible damage of the outer oxide layers during metallographic grinding and polishing stages. For understanding the oxidation mechanisms at the initial stages of oxidation, suitable TEM samples were prepared from the oxidized specimens using focused ion beam (FIB) milling in a dual beam SEM of the type Helios Nanolab 600 FE-SEM (FEI). TEM (Hitachi 8100) analysis of the FIB thinned specimens was carried out to observe the interface between the oxide scale and the substrate alloy.

## 3. Results

### 3.1. Microstructures

Fig. 1(a) and (b) shows the SEM images obtained from the electro-polished surfaces of the sintered Mo–9Si–8B–0.2La and Mo–9Si–8B–2La alloys. The faster heating and cooling rates applied in SPS process produced fine-grained microstructures for both materials. The BSE microstructure (Fig. 1a) of Mo–9Si–8B–0.2La alloy indicates the presence of $Mo_{ss}$ (bright contrast) grains along with T2 (black contrast) and A15 (grey contrast) grains. The detailed EBSD analysis with the different phase mapping is presented elsewhere [49]. The average grain size varies between 0.6 and 0.7 μm. The fine La-rich precipitates are distributed at the grain/phase boundaries as well as in grain interiors. Fig. 1(b) represents the BSE image of electro-polished Mo–9Si–8B–2La alloy surface. Coarsening of the lanthanum rich phase in the three phase $Mo_{ss}$–T2–A15 microstructure is observed. The average grain size of this material is found to be 1.5–2 μm. The size of the pores appeared as black dots/areas is much higher for the 2La-alloyed materials (Fig. 1b) as compared to the 0.2La-added alloy (Fig. 1a). Although, the electrolytic polishing step could generate more pores at the interphase boundaries near the existing pores, the density of 2La-alloyed material was found to be lower compared to that of 0.2La alloy. For studying the microstructure of the 2La-alloyed material more effectively, a thin specimen was milled out from the mechanically polished surface using focused ion beam milling. Fig. 1(c) shows the cross-section of the FIB milled surface, with the deposited platinum on the top and copper grid at the bottom. The magnified SE microstructure after a further ion beam polishing of the sample is presented in Fig. 1(d). $Mo_{ss}$ grains have the highest grain-size, whereas the A15 phase has the lowest grain size. A variable size of the La-rich areas could be observed in Fig. 1(d). The detailed EDS analysis indicates the presence of a higher amount of oxygen in these La-rich areas. However, Mo and Si were not found to be present in these regions. Therefore, these areas might consist of La and $La_2O_3$ phases. La has a very low solubility (~0.07 at.%) in Mo [50], and the segregation or partitioning of La-rich phase indicates a low solubility limit of La in other two phases (T2 and A15), too. The formation of complex oxides such as lanthanum silicate could not be denied, which needs further investigations using advanced characterization techniques.

### 3.2. Isothermal oxidation

The oxidation tests were carried out under isothermal conditions at five different temperatures between 750 and 1300 °C in

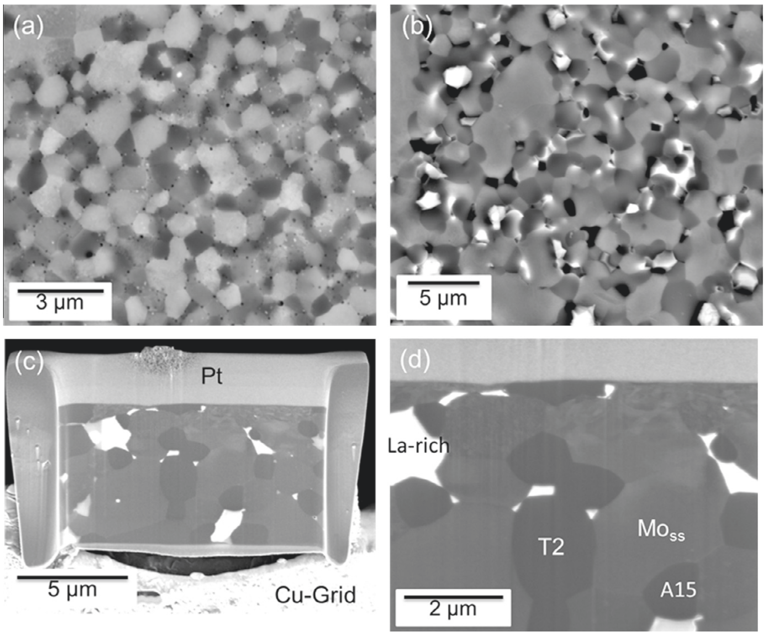

**Fig. 1.** Back scattered electron images of electrolytically polished (a) Mo–9Si–8B–0.2La and (b) Mo–9Si–8B–2La samples showing three phase $Mo_{ss}$–T2–A15 microstructure with dispersed La-rich phase particles, (c) a lamella milled out from Mo–9Si–8B–2La sample surface using FIB and fixed on a Cu-grid, and (d) a magnified SE image of the ion beam thinned specimen showing bright La-rich areas in the three phase alloy.

static laboratory air. The isothermal weight change data plotted from the TGA measurements are presented in Fig. 2. At 750 °C, the 0.2La-alloyed material shows a drastic weight loss like the reference alloy (Mo–9Si–8B) from the initial period of exposure. However, the Mo–9Si–8B–2La alloy experiences a different kind of oxidation behavior at 750 °C. The alloy shows a transient weight loss for the initial 3 h (inset at 750 °C in Fig. 2) followed by a weight gain until 27 h and a subsequent gradual loss of the weight (curve 2 at 750 °C). This result indicates that 2La-alloyed material possesses a much improved oxidation resistance at 750 °C for about 27 h. The transient weight loss is due to the spontaneous evaporation of $MoO_3$. The subsequent weight gain indicates that a protective silica-based oxide scale forms on the surface of the material, which prevents the further loss of material. The weight gain behavior of the rare earth element alloyed Mo–9Si–8B in 750–900 °C was also observed earlier [27], which was caused by the linear growth rate of the inner $MoO_2$ layer. The gradual drop of the weight of the 2La-alloyed material at 750 °C after 27 h can be attributed to the change in the outer scale structure (presented in the next section), which leads to the permeation and evaporation of $MoO_3$ through the scale. At 900 °C, 0.2La-alloyed material (curve 1) shows a superior oxidation performance compared to the reference alloy (curve 3) for the initial 8 h, beyond which a gradual loss of weight is observed. A drastic improvement in the weight change behavior (curve 2) of 2La-alloyed Mo–9Si–8B is observed at 900 °C. The weight change curve reaches the steady state after a transient weight loss for the initial 4 h. This behavior indicates the formation of a protective scale on the Mo–9Si–8B–2La alloy at 900 °C during longer exposure times.

At 1000 °C, both 0.2La and 2La-alloyed materials experience less amount of transient weight loss as compared to the reference alloy. The TGA curves show a minimal weight loss rate of about 0.05 and 0.17 $mg/cm^2$ h for 2La and 0.2La alloys, respectively, at the steady state condition. Both the La-added materials indicate superior oxidation resistance compared to the reference alloy at 1000 °C. The weight change behavior of 0.2La-alloyed material is found to be identical with that of the reference material at 1100 °C. A transient weight loss due to $MoO_3$ volatilization followed a steady state oxidation for longer exposure times. Slightly higher mass loss rate is observed for the 0.2La-alloyed material compared to the reference material at steady state. The 2La-alloyed material experiences a higher amount of weight loss compared to the other two alloys after 72 h, although it exhibits less weight loss for the initial 25 h of oxidation at this temperature (1100 °C). At 1300 °C, the TGA curve for 2La-alloyed material shows a drastic drop in weight (curve 2, at 1300 °C in Fig. 2) from the initial stages. This could be attributed to the presence of a higher porosity in the as received sintered Mo–9Si–8B–2La alloy. However, the 0.2La-alloyed material shows a transient weight loss (at 1300 °C) and eventually a steady state behavior is reached as in observed for the reference Mo–9Si–8B alloy. The amount of transient weight loss for the 0.2La alloy is higher compared to that for the reference alloy. However, both the materials show a comparable weight loss rate ($\sim$0.1 $mg/cm^2$ h) during the steady state at 1300 °C after 72 h.

### 3.3. Oxide scale

At 750 °C, no oxide scale formation was observed for the 0.2La-alloyed material. Only powder oxide residue was obtained after 72 h of exposure of the material at this temperature. A similar oxidation behavior was reported for the reference material [28,29]. Fig. 3(a) represents the image of the Mo–9Si–8B–2La alloy specimen after 72 h of exposure at 750 °C. The alloy specimen could not retain the outer rectangular shape, and the visual observation indicates that the scale formed at the outer surface had a very low viscosity, which led to the run-over (like a liquid) of the top oxide on the entire surface. The arrow in Fig. 3(a) indicates the mark (line) left by the platinum wire, which was used to tie the specimen before the test. The platinum wire seems to be penetrated into the sample due to the formation of voluminous

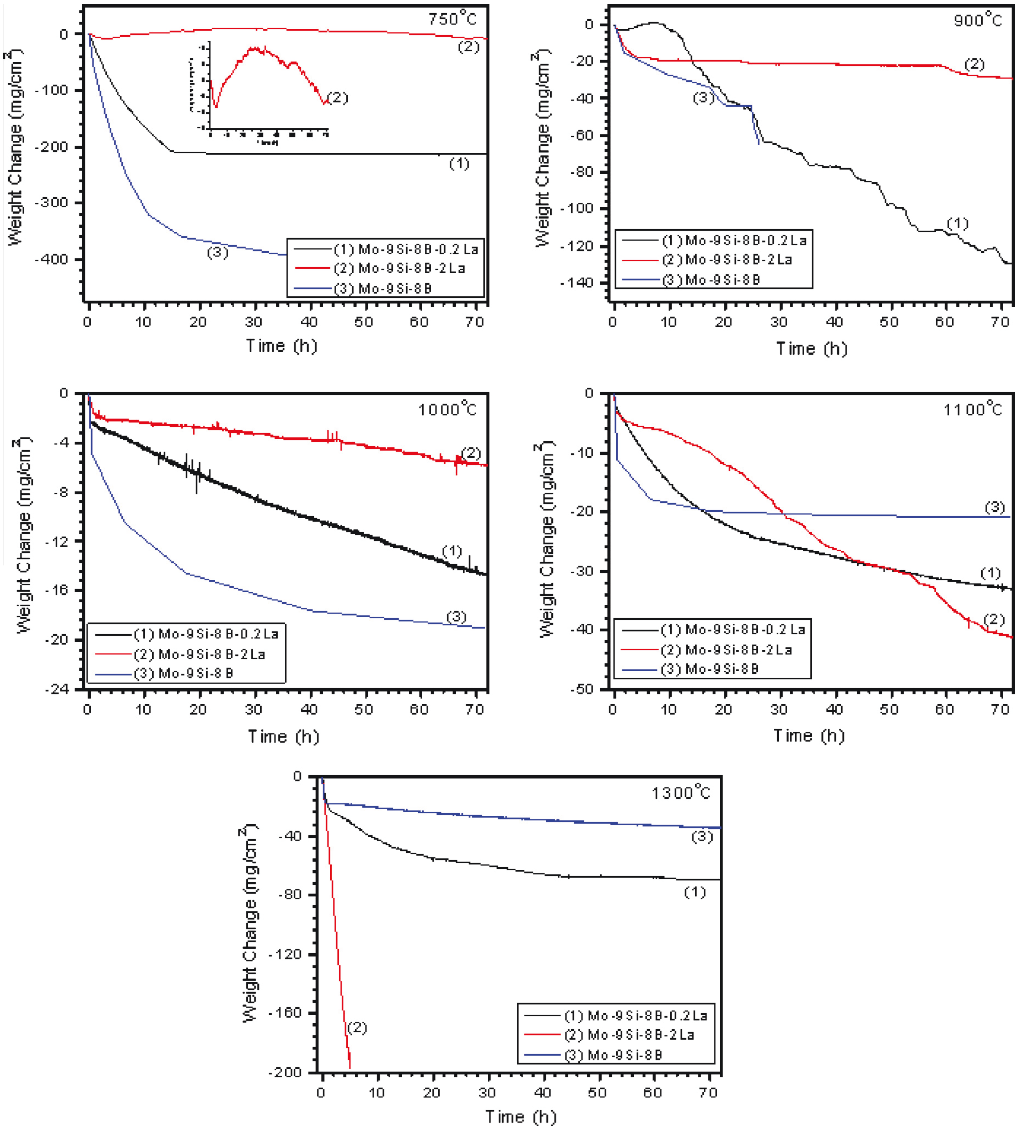

**Fig. 2.** TGA plots showing the isothermal weight change behavior of La-alloyed Mo–9Si–8B during oxidation in static air. The weight change data for reference Mo–9Si–8B alloy are also plotted for comparisons [27].

corrosion products inside and a low viscosity scale on the surface. Other cavities observed on the surface (Fig. 3a) were probably generated during the removal of the platinum wire. EDS analysis reveals that the outer scale consists primarily of silica based composition. The distribution of many bright oxide particles enriched with Mo (~48 at.%) and La (~22 at.%) was observed (Fig. 3a, analyzed at higher magnification) on the silica surface. The low viscosity scale flowed over the surface, which led to the change in shape of the 0.2La alloyed material after 72 h of isothermal oxidation at 900 °C (Fig. 3b). The arrow in Fig. 3(b) indicates the mark of the platinum wire trapped inside the scale. The corners of the specimen got rounded off due the higher rate of evaporation loss of $MoO_3$ from these regions. 2La-alloyed Mo–9Si–8B shows a drastic improvement at 900 °C even after 72 h of exposure in air. The sample retains its original shape, and the cross-sectional BSE image of the specimen is presented in Fig. 4(a). The discontinuous outermost brighter phase marked as ‘1’ in Fig. 4(a) consists of a La (~23 at.%) and Mo (35 at.%) based oxide. The subsequent continuous layer (marked as ‘2’) is identified as a silica rich oxide, which is mainly responsible for the superior oxidation resistance of the Mo–9Si–8B–2La alloy at 900 °C. The innermost layer (marked as ‘3’) is composed mainly of $MoO_2$, which is further confirmed by the XRD analysis. Presence of a Ni layer outside of the oxide layers could be found in most of the cross-sectional micrographs. Fig. 5 shows the elemental distribution of Mo, Si, La, and O along the cross-section of the 2La-alloyed specimen oxidized at 900 °C. Presence of La could be observed in the outermost discontinuous layer and also at the interface between the inner $MoO_2$ layer near and the $SiO_2$ layer. La-rich oxide shows a needle-like structure located near the interface between $MoO_2$ and $SiO_2$ (Fig. 5).

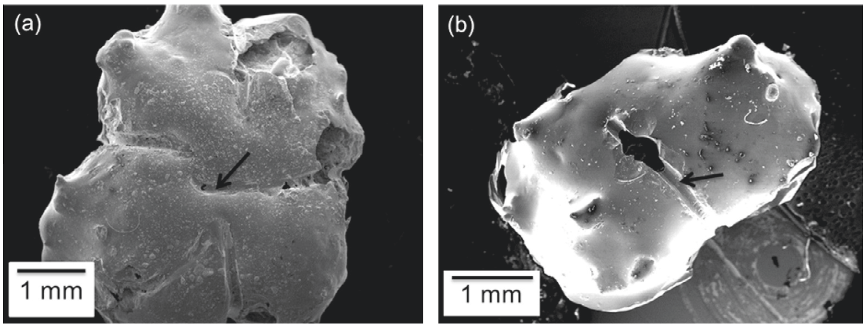

**Fig. 3.** (a) SE image showing the outlook of a Mo–9Si–8B–2La sample oxidized at 750 °C for 72 h, and (b) SE image showing the outlook of a Mo–9Si–8B–0.2La sample oxidized at 900 °C for 72 h in static air. The arrows indicate the impression of the platinum wire moved inside the surface due to the formation of the low-viscosity boron-rich oxides.

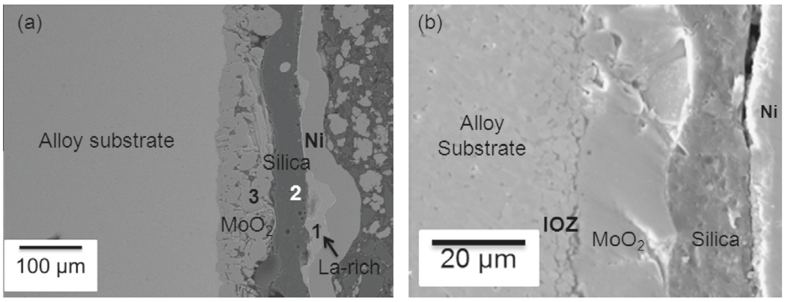

**Fig. 4.** Cross-sectional BSE image showing the interface of different oxide layers with the Mo–9Si–8B–2La alloy substrate isothermally oxidized at (a) 900 °C for 72 h and (b) 1000 °C for 72 h.

Internally oxidized $SiO_2$-rich particles are also observed in the inner $MoO_2$-rich layer.

Fig. 4(b) represents the cross-sectional BSE image of a 2La-alloyed Mo–9Si–8B specimen tested for oxidation at 1000 °C for 72 h. A thin and continuous silica phase at the outer scale followed by a thick $MoO_2$ layer is detected. A separate layer marked as the internal oxidation zone (IOZ) is also formed between the alloy substrate and the $MoO_2$ rich layer. The detailed elemental diffusion obtained by EDS mapping along the interface is presented in Fig. 6. The La ions mostly diffuse towards the interface between the outer scale and the $MoO_2$-rich layer. The fine size oxide precipitates rich in La are present in the outer silica-rich scale. The $LaL_\alpha$ map in Fig. 6 clearly shows the distribution of La in the substrate (Mo–9Si–8B–2La) alloy, too. Internally oxidized silica-rich particles are found to be present in the $MoO_2$ layer and IOZ (Figs. 4b and 6). It should be noted here that the thickness of the silica-rich scale formed at 1000 °C (Fig. 4b) is much thinner compared to that observed at 900 °C (Fig. 4a) for the identical period of exposure in air. This indicates a change in the mechanisms of oxidation between 900 °C and 1000 °C, which is discussed in the next section. The thicknesses of the different layers observed after oxidation tests of the two alloys at selected temperatures are presented in Table 1.

No protective scale is formed on the Mo–9Si–8B–0.2La alloy at 750 and 900 °C for longer exposure times in air. However, the alloy shows a superior oxidation behavior beyond 1000 °C. Fig. 7(a) and (b) shows the representative cross-sectional BSE images of 0.2La-alloyed specimens oxidized at 1000 °C and 1300 °C. The outer layer, consisting of a silica-rich scale and a thin $MoO_2$ intermediate layer followed by an IOZ, is observed at 1000–1300 °C. The individual layer thicknesses are tabulated in Table 1. Although the X-ray peaks for boron was observed, EDS analysis is unable to detect the boron content of the outer scale accurately. It is well-known that evaporation of boron starts from 950 °C [28]. Therefore, the amount of boron in the outer scale is reduced drastically at higher temperatures. However, considering the presence of boron in the outer layer, it is named as either silica-rich or borosilica. It could be noticed from Table 1 that the thickness of the outer scale for the 0.2La-alloy is much higher than that of the 2La-alloy at 1000 and 1100 °C for 72 h of exposure in air. On the contrary, the thicknesses of the subsequent inner layers are reversed for these two materials. At 1300 °C, a thick (~100 μm) outer silica-rich layer (Fig. 7b) is formed after 72 h of exposure, and the thickness of the IOZ is also found to be relatively high. The distribution of the elements near the outer scale of Mo–9Si–8B–0.2La at 1300 °C is presented in Fig. 8, which shows an enrichment of La-containing oxide particles at a very thin region of the outer silica-rich layer. The consequence of La diffusion is also detected at the interfaces of the IOZ/$MoO_2$. Fig. 9 shows a representative SE image of the oxidized surface of Mo–9Si–8B–0.2La alloy formed at 1000–1200 °C. The surface shows the formation of a smooth silica layer with embedded La-rich dispersed oxide particles (bright). Fig. 10(a) shows the surface morphology of the oxides formed on the Mo–9Si–8B–2La alloy at 900 °C after 72 h. EDS analysis reveals that the brighter phase is composed of a lanthanum–molybdate phase and the darker matrix phase is silica-rich. This discontinuous bright phase is also detected in the cross-sectional analysis (Figs. 4a and 5). A similar surface morphological characteristic is observed at 1300 °C (Fig. 10b) on the Mo–9Si–8B–0.2La alloy. However, the brighter oxide formed at 1300 °C is identified

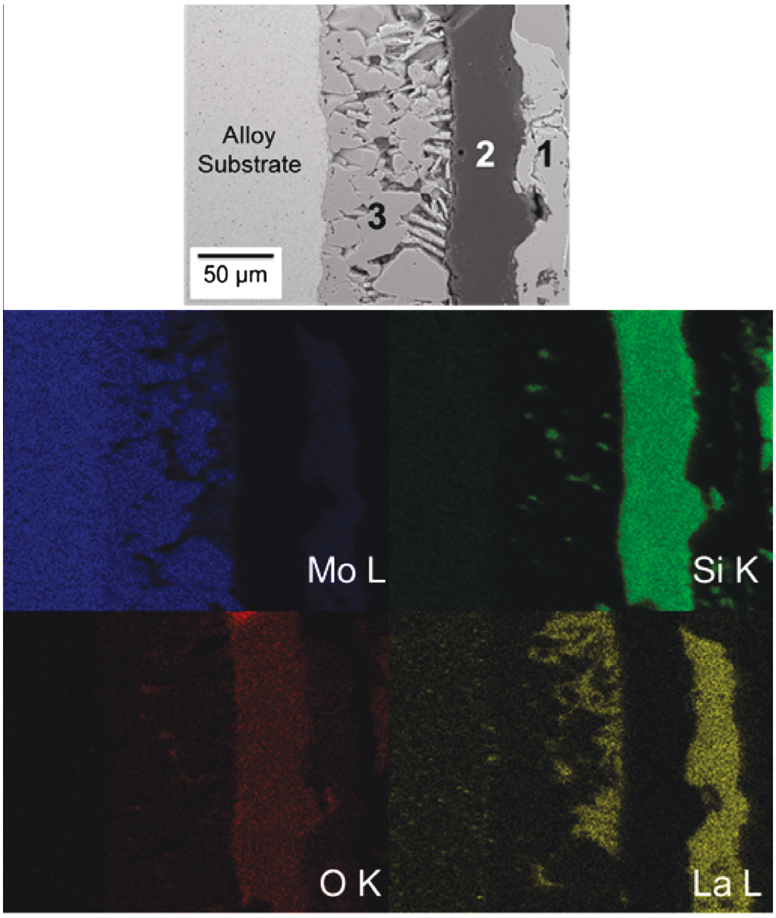

**Fig. 5.** SE image and the corresponding area X-ray (EDS) maps for different elements distributed along the cross-section of the Mo–9Si–8B–2La specimen oxidized at 900 °C for 72 h.

as a lanthanum–silicate phase. The darker phase consists of silica-rich layer. The entirely different morphologies of the bright oxide phases formed at 900 °C and 1300 °C (Fig. 10a and b) also indicate the formation of two different oxides, namely lanthanum–molybdate and lanthanum–silicate, respectively. As shown above, the alloy Mo–9Si–8B–2La suffers a drastic weight loss at 1300 °C. Fig. 11(a) showing the surface morphology of a 2La alloy oxidized at 1300 °C for 23 h indicates the formation of cracks and holes on the oxide surface, which act as channels for the evaporation of $MoO_3$. A higher amount of Mo was detected in the bright oxide phase floated on the surface (Fig. 11a). The cross-sectional microstructure of a Mo–9Si–8B–2La alloy oxidized at 1200 °C for 2 h is presented in Fig. 11(b), which shows the presence of pores in the outer oxide scale. The outer silica-rich (black) scale is not continuous, and a partition or phase separation is observed between the silica and the bright oxide phase consisting of Mo and La. The mismatch of thermal expansion coefficient between these oxide phases leads to the development of cracks during cooling. The Mo–9Si–8B–0.2La alloy, however, shows a good oxidation resistance in the high temperature regime. Formation of an outer silica-rich protective scale can be observed even at 1400 °C (Fig 12). Fine lanthanum–silicate particles are present near the outer surface of the silica scale, and the formation of a $MoO_2$ inner layer and the IOZ is also observed at this temperature.

## 4. Discussion

The oxidation mechanisms operating in the Mo–9Si–8B alloy in different temperature regimes are understood to a significant extent [17,18,27–33]. The T2 ($Mo_5SiB_2$) phase is mainly responsible for the formation of a protective silica scale beyond 1050 °C, and it also prevents pest oxidation of molybdenum silicide at intermediate temperatures of around 800 °C. The probable reactions which could occur at the surface of the Mo–9Si–8B–La alloy during its exposure in an oxidizing environment at high temperatures are listed below.

$$Mo_5SiB_2 + 10O_2 \rightarrow 5MoO_3 + SiO_2 + B_2O_3 \tag{1}$$

$$2Mo_5SiB_2 + 15O_2 \rightarrow 10MoO_2 + 2SiO_2 + 2B_2O_3 \tag{2}$$

$$2Mo_5SiB_2 + 5O_2 \rightarrow 10Mo + 2SiO_2 + 2B_2O_3 \tag{3}$$

$$2Mo_3Si + 11O_2 \rightarrow 6MoO_3 + 2SiO_2 \tag{4}$$

$$Mo + O_2 \rightarrow MoO_2 \tag{5}$$

$$2MoO_2 + O_2 \rightarrow 2MoO_3 \tag{6}$$

$$4La + 3O_2 \rightarrow 2La_2O_3 \tag{7}$$

$$La_2O_3 + SiO_2 \rightarrow La_2SiO_5 \tag{8}$$

$$xLa_2O_3 + yMoO_3 \rightarrow xLa_2O_3.yMoO_3 \tag{9}$$

$$La_2O_3 + B_2O_3 \rightarrow 2LaBO_3 \tag{10}$$

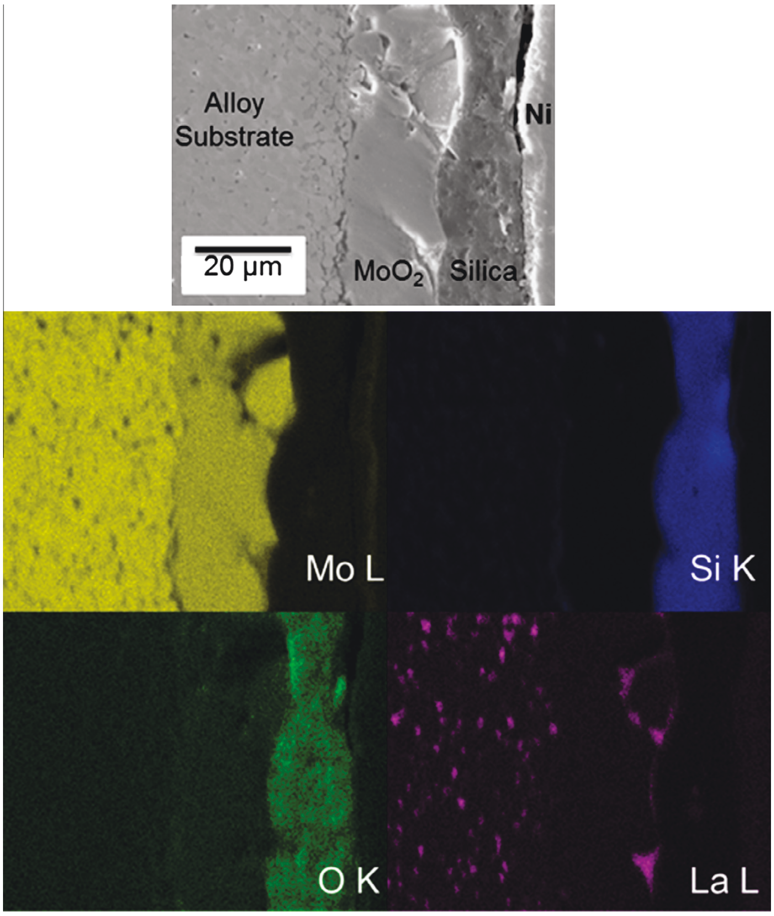

**Fig. 6.** SE image and the corresponding area X-ray maps for different elements distributed along the cross-section of the Mo–9Si–8B–2La specimen oxidized at 1000 °C for 72 h.

**Table 1**
Experimentally measured thickness of different layers formed on the La-alloyed Mo–Si–B samples after isothermal oxidation at selected temperatures.

| Alloy | Temperature of oxidation (°C) | Time (h) | Thicknesses (in µm) of oxidation layers | | |
|---|---|---|---|---|---|
| | | | Outer Silica based layer | Inner $MoO_2$ layer | Inner oxidation zone (IOZ) |
| Mo–9Si–8B–2La | 900 | 72 | 44 | 79.6 | 0.5 |
| | 1000 | 72 | 2.4 | 61 | 11.7 |
| | 1100 | 72 | 5 | 72.6 | 27 |
| Mo–9Si–8B–0.2La | 1000 | 72 | 20.5 | 12.6 | 5.2 |
| | 1100 | 72 | 40.3 | 22.5 | 11.2 |
| | 1300 | 72 | 101 | 24.1 | 86.3 |

The standard free energy change values for the formation of all the elemental oxides at standard oxygen partial pressure are calculated between 600 °C and 1400 °C using Factsage software and plotted in Fig. 13. The values for the other rare earth (RE) element yttrium (Y) are also presented for comparison. The oxide with higher to lower thermodynamic stability is sequenced as $Y_2O_3 > La_2O_3 > SiO_2 > B_2O_3 > MoO_2 > MoO_3$. However, the actual concentration of the element in the alloy system as well as the diffusion aspects determines the growth kinetics of the individual oxides. Due to higher concentration of silicon and more favorable free energy of formation, the silica phase is formed first. Subsequently, the continuous diffusion of oxygen through the outer silica layer leads to the formation of $MoO_2$ inner layer as the activity of Mo is very high at the interface. The partial pressure of oxygen is reduced further at the interface between the substrate and the inner $MoO_2$ layer. The more active element silicon gets internally oxidized at the substrate and $MoO_2$ interface due to very low oxygen partial pressure, thereby forming an internal oxidation zone (IOZ). Thermally grown silica undergoes a structural transition between 950 and 975 °C [51], and the growth kinetics of the silica scale is inherently slow below this temperature. In the case of the Mo–9Si–8B alloy, a thin silica layer is formed at the initial stage due to the presence of boron oxide which is reported to enhance the growth rate of silica at 800–900 °C. However, as the exposure time increases, the scale gets

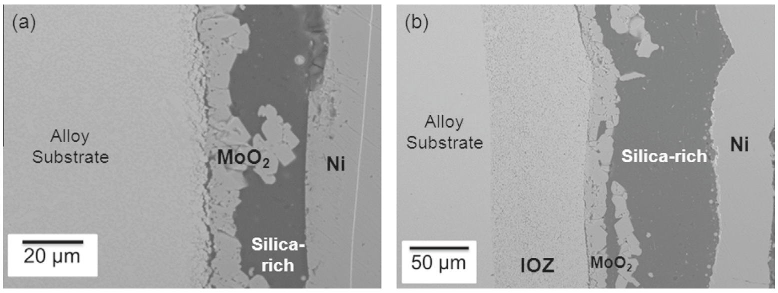

**Fig. 7.** Cross sectional BSE images obtained from Mo–9Si–8B–0.2La alloy oxidized isothermally at (a) 1000 °C for 72 h and (b) 1300 °C for 72 h.

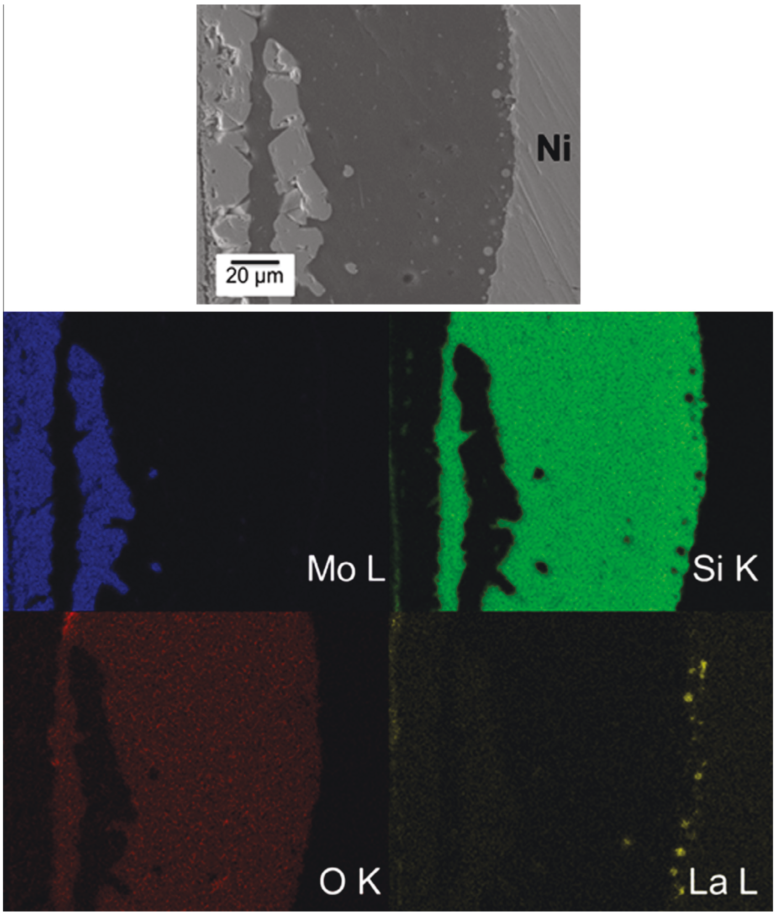

**Fig. 8.** SE image near the outer oxide scale and the corresponding area X-ray maps for different elements distributed along the cross-section of the Mo–9Si–8B–0.2La specimen oxidized at 1300 °C for 72 h.

enriched with more amount of boron oxide, thereby reducing the viscosity of the scale to such an extent that the scale runs over the surface. The inward diffusion of oxygen is also increased which leads to the formation and evaporation of $MoO_3$ (as per reactions 1, 4 and 6), which bubbles through the low viscosity scale. The specimen loses its original shape and, after a longer time of exposure, appears as shown in Fig. 3. The 0.2La-alloyed specimen shows an improvement at the initial stages at 900 °C, however, the La concentration could be too low (0.2 at.%) to cause any significant improvement in the protective scale formation for a longer period of oxidation. The 2La-alloyed material shows a drastic improvement in oxidation resistance at 900 °C (TGA curve 2 at 900 °C in Fig. 2). For a better understanding of the mechanism at the early stage of oxidation, the Mo–9Si–8B–2La alloy specimen was oxidized at 900 °C for 15 min, and a thin sample was milled perpendicular to the oxidized surface using FIB (Fig. 14a). The cross-sectional SEM

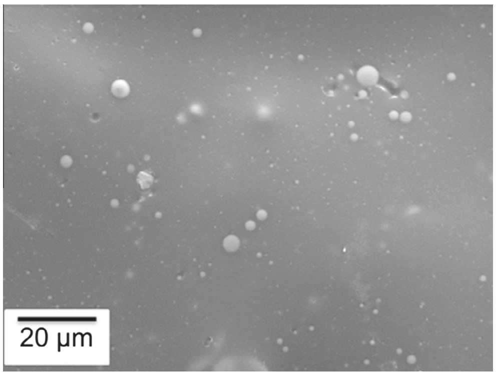

**Fig. 9.** SE image showing a typical oxidized surface observed on the Mo–9Si–8B–0.2La alloy at 1000–1200 °C.

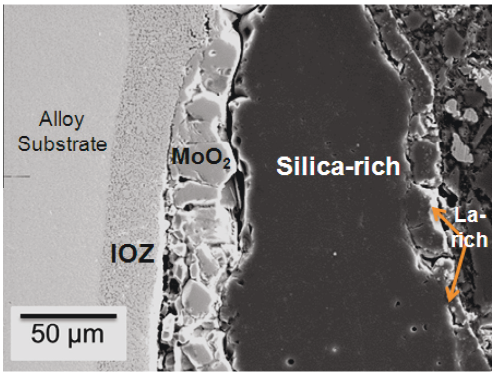

**Fig. 12.** BSE image indicating the cross-section of a Mo–9Si–8B–0.2La alloy oxidized at 1400 °C for 2 h in static air.

image of the specimen after performing some stages of ion beam polishing is presented in Fig. 14(b), which clearly indicates the formation of a thin continuous scale on the top followed by an inner oxidation area and the substrate grains. Fig. 15(a) shows a bright field TEM micrograph of the overall cross-section. The outermost layer appearing as bright phase was found to be composed of an amorphous silica-rich phase. The area of the outer layer showing fine particle (appearing dark) has been magnified (marked by arrow) and presented in Fig. 15(b). The selected area diffraction pattern obtained from the point marked as ‘1’ in Fig. 15(b) is presented in Fig. 15(d). The big bright spot at the center of the diffraction pattern indicates the presence of an amorphous matrix, whereas the analysis of the other fine diffraction spots confirms the existence of a cubic $La_6MoO_{12}$ ($3La_2O_3{\cdot}MoO_3$) oxide phase appearing as dark particles in the silica matrix. The inner oxidation area is found to be composed of the grains (or phases) with different contrasts (Fig. 15a). The diffraction pattern (Fig. 15e) obtained from the fine dark grains located at point ‘2’ in Fig. 15(a) indicate a hexagonal $La_2O_3$ phase. The SAD pattern (Fig. 15f) at point ‘3’ (in Fig. 15a) confirms the formation of monoclinic $MoO_2$ grains beneath the outer silica-rich scale. Fig. 15(c) is a magnified area of Fig. 15(a), which clearly shows the boundary line (marked by two arrows in Fig. 15c) between the inner oxide (mainly $MoO_2$) phase and the substrate alloy grains of $Mo_{ss}$–T2–A15. The boundary line (in Fig. 15c)

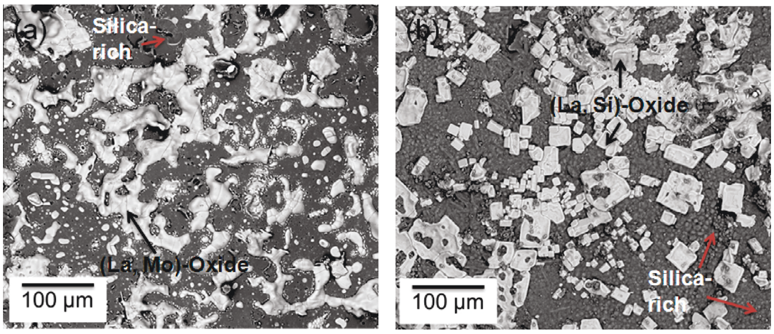

**Fig. 10.** SE images showing the different morphologies of the surface oxides formed (a) on the alloy Mo–9Si–8B–2La after 72 h oxidation at 900 °C, and (b) on the alloy Mo–9Si–8B–0.2La alloy after 72 h oxidation at 1300 °C.

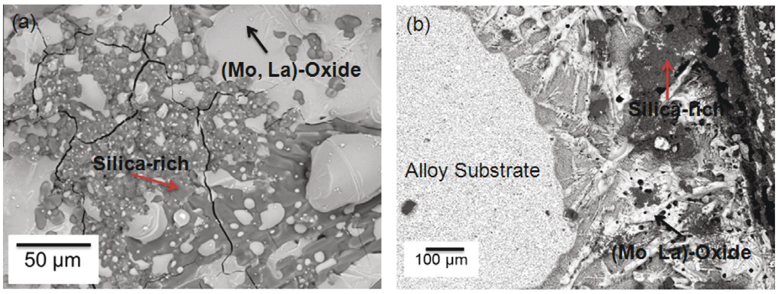

**Fig. 11.** (a) SE image showing the oxidized surface of a Mo–9Si–8B–2La specimen at 1300 °C for 23 h, and (b) cross-sectional BSE image indicating a porous oxide scale formation on the same material at 1200 °C for 2 h of oxidation.

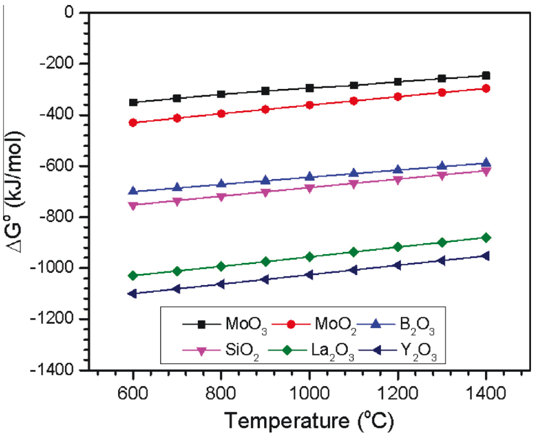

**Fig. 13.** Calculated standard free energy change values for the formation of different oxides (e.g. 4/3La + $O_2$ = 2/3$La_2O_3$) for Mo–Si–B–La/Y systems at different oxidation temperatures.

is analogous to an oxidation front which moves inwardly by consuming the grains of the parent alloy, and therefore, the inter-phase boundary between the alloy grains disappears gradually. The bright region present in the inner oxidation area is found to be an internally oxidized amorphous silica-rich phase, which is also present at the grain/phase boundaries of the alloy substrate near the interface. The formation of the bright particles leading to an increase of the width or splitting of the grain/phase boundaries (Fig. 15a and c) near the inner oxidation zone indicates that the grain/phase boundaries are the preferred path for diffusion processes in the multiphase Mo–9Si–8B–2La alloy.

The oxide phases $MoO_2$ (PCPDF No. 781072), $La_2O_3$ (PCPDF No. 831355) and $La_6MoO_{12}$ (PCPDF No. 241087) identified by selected area diffraction analysis in TEM were also observed by X-ray diffraction experiments carried out on the surface of the Mo–9Si–8B–2La alloy specimen oxidized at 900 °C for 15 min (Fig. 16). The XRD peaks from the parent Mo phase are observed because the thickness of the oxide layers is small for such a short oxidation time. The presence of $B_2O_3$ (PCPDF No. 731550), $LaBO_3$ (PCPDF No. 761389), $La_2Mo_3O_{12}$ ($La_2O_3$. $3MoO_3$, PCPDF No. 260821) and $La_{10}Mo_2O_{21}$ ($5La_2O_3.2MoO_3$, PCPDF No. 341018) oxide phases was detected at 900 °C (15 min) by XRD analysis. Some of these oxide phases are present after a longer exposure time (72 h) at 1000 °C (Fig. 16). The binary oxide phase diagram of $MoO_3$–$La_2O_3$ [52] suggests that a number of compounds may form at different molar ratios of $La_2O_3$ and $MoO_3$ e.g. 1:3, 1:2, 3:1 etc., as described by reaction 9. The $La_2O_3$-rich oxides such as $5La_2O_3{\cdot}2MoO_3$ ($La_{10}Mo_2O_{21}$) and $3La_2O_3{\cdot}MoO_3$ ($La_6MoO_{12}$) have cubic structure and possess melting temperatures beyond 1500 °C. The monoclinic $La_2O_3{\cdot}3MoO_3$ ($La_2Mo_3O_{12}$) phase is also stable up to 1020 °C. The La-rich oxides form at a much faster rate as compared to $MoO_3$. Therefore, the formation of more stable lanthanum molybdates ($xLa_2O_3{\cdot}yMoO_3$) strongly reduces the formation and vaporization of $MoO_3$ from the Mo–9Si–8B–2La alloy at oxidation temperatures below 1000 °C. The amount of boron released from these reactions could lead to the formation of $LaBO_3$ phase as per reaction 10. Fine oxide ($La_2O_3$, $La_6MoO_{12}$ etc.) particles act as nucleation sites for silica, and therefore enhance the formation tendency of the protective silica-rich scale at the initial stages of oxidation of Mo–9Si–8B–2La alloy. Formation of stable (La, Mo)-rich oxides releases more amount of silicon for the outer silica-rich scale, and therefore enhances the growth of the outer layer. These combined effects cause the improvement of the oxidation resistance of La-alloyed Mo–9Si–8B at 750–900 °C. A lesser transient weight loss was also detected for both the La-alloyed Mo–9Si–8B at 1000 °C. It may be concluded from Table 1 that the thickness of the outer silica layer formed on the Mo–9Si–8B–2La alloy at 900 °C is higher than that formed at 1000 °C. This behavior is also explained using the TGA curves (Fig. 2), which show a higher transient weight loss at 900 °C (curve 2) compared to 1000 °C (curve 2). The inherent sluggish growth rate and defect structure [51] of thermally grown silica formed below 950 °C causes evaporation of $MoO_3$ particularly at the initial stages, which leads to the release of more quantity of silicon from T2 and A15 phases. The simultaneous reactions involving the formation of $xLa_2O_3{\cdot}yMoO_3$ phases also push the excess silicon (and boron) to the oxide scale, thereby forming a much thicker silica-rich scale at 900 °C.

Beyond 1000 °C, the whole oxidation mechanism is changed due to the faster kinetics of the silica formation, and defect-free structure of silica [51]. The rate of boron evaporation is also increased beyond 1000 °C, and the oxide scale attends a higher viscosity which becomes sufficient to cover the whole surface of the alloy making it more protective. Presence of silica (cristobalite) phase is detected from the XRD peaks (Fig. 16) of Mo–9Si–8B–2La oxidized at 1100 °C for 72 h. The 2La-alloyed material, however, showed a drastic weight loss beyond 1200 °C. There are two reasons behind this behavior: (1) the dissociation of $La_2O_3{\cdot}3MoO_3$ at higher temperatures leading to evaporation loss of $MoO_3$, and (2) the higher amount of porosity present in the sintered alloy creating cracks in the outer scale due to larger volume expansion at the pores at higher temperatures. The 0.2La-alloyed

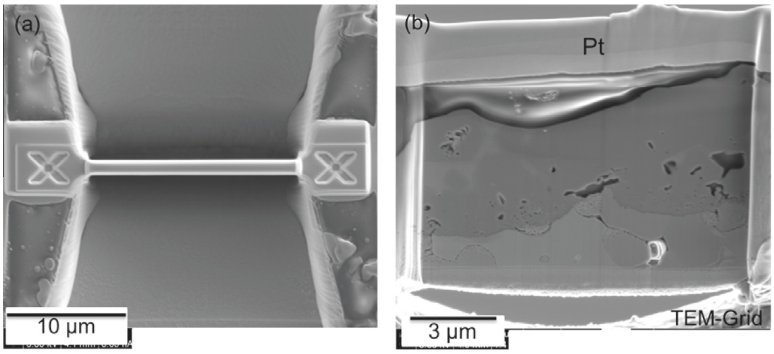

**Fig. 14.** (a) SE image showing the top view of a thin specimen just-milled using FIB on the surface oxidized at 900 °C for 15 min for a Mo–9Si–8B–2La specimen, and (b) the cross-section of the ion beam milled specimen showing formation of different oxidation zones for the short time of exposure.

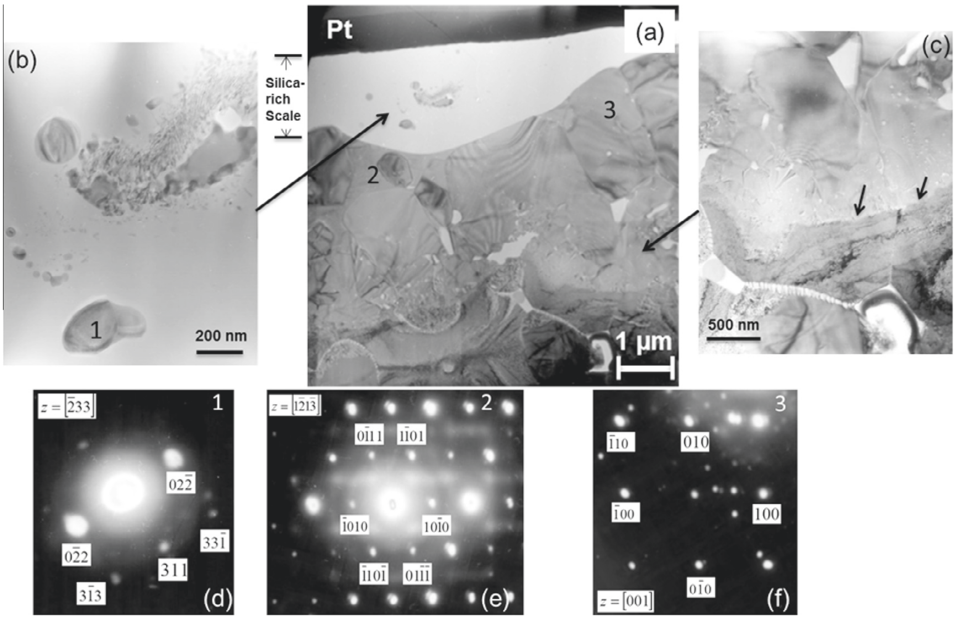

**Fig. 15.** (a) TEM bright field image of the FIB thinned (Fig. 14b) specimen indicating the outer oxide scale followed by the inner oxidation zone and substrate grains, (b) magnified area in the outer scale showing the presence of fine precipitates in the amorphous oxide, (c) a magnified area near the substrate in which the arrows indicate the line of the oxidation front, and (d), (e) and (f) selected area diffraction patterns corresponding to the areas indicated as 1, 2, and 3, respectively.

Mo–9Si–8B showed acceptable oxidation resistance from 1100 °C until 1400 °C. The outer scale mainly consists of a protective silica-rich amorphous scale. It was studied earlier [53] that $La_2O_3$ promotes the formation of amorphous $SiO_2$, and no phase separation is observed unlike in $HfO_2$–$SiO_2$ or $ZrO_2$–$SiO_2$ systems [53]. At high temperatures, lanthanum–silicate ($La_2SiO_5$ or $La_2Si_2O_7$) is formed, which is observed at 1300 °C after 72 h of oxidation of the Mo–9Si–8B–0.2La alloy (Figs. 8, 10b). The lanthanum–silicate oxide particles are found to be distributed in the outer silica-rich layer, and no separate continuous lanthanum–silicate layer is detected, as observed earlier for yttrium-containing Mo–9Si–8B [27]. The activation energies for the growth of the outer silica-rich layer in 1000–1300 °C calculated from the slope of thickness vs $1/T$ plots (Fig. 17) are obtained as 109.8 kJ/mole and 87.9 kJ/mole for Mo–9Si–8B–2La and Mo–9Si–8B–0.2La, respectively. These values are close to the reported activation energy value (~122 kJ/mole) for the diffusion of oxygen in fused silica at 850–1250 °C [54]. From the thickness data (Table 1), it is concluded that a higher amount of La reduces the growth rate of the externally oxidized protective silica layer beyond 1000 °C either by reducing the outward diffusion of silicon or by reducing the inward diffusion of oxygen. The formation of La–Si–O precipitates is not observed in the internal oxidation zone or at the interfaces, and therefore, the outward diffusion of silicon should not be affected. This indicates that the higher La-content reduces the inward diffusion rate of oxygen during the process of oxidation of the Mo–Si–B–La alloy.

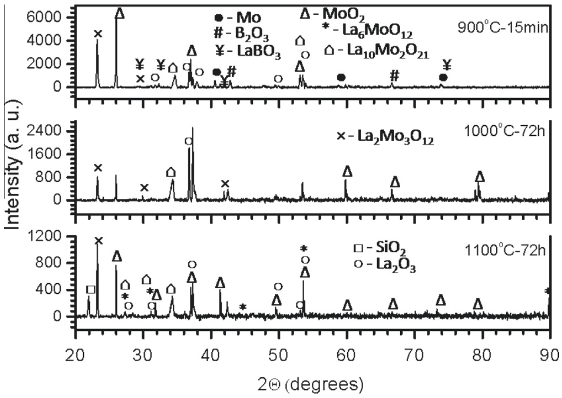

**Fig. 16.** XRD peaks obtained from the surface of Mo–9Si–8B–2La alloy specimens tested for oxidation at different conditions.

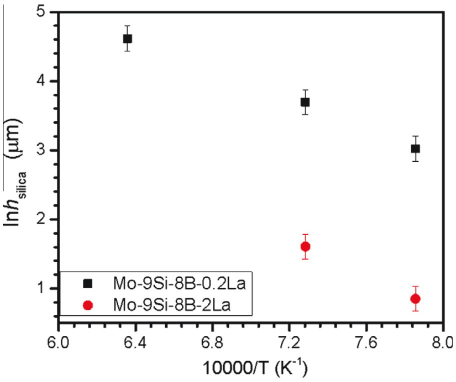

**Fig. 17.** Temperature dependence of growth of the outer silica-rich oxide scale after isothermal oxidation of Mo–9Si–8B–0.2La and Mo–9Si–8B–2La alloys for 72 h in static air between 1000 and 1300 °C.

## 5. Concluding remarks

The detailed oxidation mechanisms of 0.2 and 2 at.% La-containing Mo–9Si–8B alloys studied at selected temperatures between 750 and 1400 °C in laboratory air indicate that La significantly influences the oxide layer formations. Three layers consisting of an outer silica-rich layer followed by an inner $MoO_2$ layer, and a subsequent internal oxidation zone (IOZ) comprised of solute oxide precipitates (e.g. $SiO_2$) are observed after isothermal oxidation tests. At 750–900 °C, the formation of La-containing stable oxides such as $La_2O_3$, $La_2O_3{\cdot}3MoO_3$ and $3La_2O_3{\cdot}MoO_3$ near the outer oxide layer reduces the formation and evaporation loss of $MoO_3$ from the Mo–9Si–8B–2La alloy. A protective silica-rich scale is formed in this alloy after a transient stage below 950 °C. The oxidation performance of 0.2La-alloyed material is found to be comparable with the reference (Mo–9Si–8B) alloy at 1100–1300 °C. Lanthanum-silicate particles are found to be distributed discontinuously in the outer silica scale formed on the Mo–9Si–8B–0.2La alloy oxidized at 1300 °C for 72 h. The 2La-alloy shows inferior oxidation performance beyond 1200 °C probably due to the presence of a high amount of porosity in the as-sintered microstructure. The thickness data of the oxide layers indicates that the inward diffusion of oxygen through the outer scale is reduced due to the presence of La. Further investigation needs to be carried out to optimize the concentration of La for maximizing the benefit of processing difficulties and optimizing the oxidation resistance in the wide temperature regime.

## Acknowledgements

S. Majumdar wishes to thank the Alexander von Humboldt Foundation, Bonn, Germany for financial support of the research stay at Siegen. The research support by Deutsche Forschungsgemeinschaft (DFG) within the framework of the research unit 727 “Beyond Ni-Base Superalloys” is gratefully acknowledged.

## References

[1] M.S. El-Genk, J.M. Tournier, J. Nucl. Mater. 340 (2005) 93–112.
[2] Y. Kubota, S. Masuzaki, T. Morisaki, K. Tokunaga, N. Noda, Fusion Eng. Des. 75–79 (2005) 297–301.
[3] D.G. Cepraga, E. Menapace, G. Cambi, S. Ciattaglia, L. Petrizzi, G. Cavallone, M. Costa, U. Broccoli, J. Nucl. Mater. 212–215 (1994) 644–648.
[4] S. Majumdar, R. Kapoor, S. Raveendra, H. Sinha, I. Samajdar, P. Bhargava, J.K. Chakravartty, I.G. Sharma, A.K. Suri, J. Nucl. Mater. 385 (2009) 545–551.
[5] S.A. Beske, Y. Arikawa, R.N. Andrews, W. Lundbald, J. Cryst. Grow. 137 (1994) 102–106.
[6] J.J. Park, D.P. Butt, C.A. Beard, Nucl. Eng. Des. 196 (2000) 315–325.
[7] J.V. Cathcart, W.D. Manly, Corrosion 12 (1956) 43–47.
[8] S. Mathieu, S. Knittel, M. Francois, L. Portebois, S. Mathieu, M. Vilasi, Corros. Sci. 79 (2014) 119–127.
[9] S. Binbin, F. Peizhong, W. Jianzhong, G. Yuan, W. Guangzhi, W. Xiaohong, A. Farid, Corros. Sci. 85 (2014) 311–317.
[10] Ping Zhang, Xiping Guo, Corros. Sci. 71 (2013) 10–19.
[11] Wan Wang, Bifei Yuan, Chungen Zhou, Corros. Sci. 80 (2014) 164–168.
[12] B. Roy, J. Das, R. Mitra, Corros. Sci. 68 (2013) 231–237.
[13] A. Lange, R. Braun, Corros. Sci. 84 (2014) 74–84.
[14] Yu-L. Zhang, He-J. Li, Zhi-X. Hu, Jin-C. Ren, Ke-Z. Li, Corros. Sci. 72 (2013) 150–155.
[15] J.H. Perepezko, Science 20 (2009) 1068–1069.
[16] D.M. Dimiduk, J.H. Perepezko, MRS Bull. 28 (2003) 639–645.
[17] M. Meyer, M. Kramer, M. Akinc, Adv. Mater. 8 (1996) 85–88.
[18] M.K. Meyer, M. Akinc, J. Am. Cer. Soc. 79 (1996) 2763–2766.
[19] M. Akinc, M.K. Meyer, M.J. Kramer, A.J. Thom, J.J. Huebsch, B. Cook, Mater. Sci. Eng. A261 (1999) 16–23.
[20] M.K. Meyer, A.J. Thom, M. Akinc, Intermetall 7 (1999) 153–162.
[21] D. Berczik, U.S. Patent Number 5,595-616 (1997).
[22] D. Berczik, U.S. Patent Number 5,693-156 (1997).
[23] A.P. Alur, K.S. Kumar, Acta Mater. 54 (2006) 385–400.
[24] M. Krüger, S. Franz, H. Saage, M. Heilmaier, J.H. Schneibel, P. Jéhanno, Intermetall 16 (2008) 933–941.
[25] P. Jain, A.P. Alur, K.S. Kumar, Scrip. Mater. 54 (2006) 13–17.
[26] M. Krüger, D. Schliephake, P. Jain, K.S. Kumar, G. Schumacher, M. Heilmaier, JOM 65 (2013) 301–306.
[27] S. Majumdar, D. Schliephake, B. Gorr, H.-J. Christ, M. Heilmaier, Metall. Mater. Trans. A 44 (2013) 2243–2257.
[28] T.A. Parthasarathy, M.G. Mendiratta, D.M. Dimiduk, Acta Mater. 50 (2002) 1857–1868.
[29] M.G. Mendiratta, T.A. Parthasarathy, D.M. Dimiduk, Intermetall 10 (2002) 225–232.
[30] V. Supatarawanich, D.R. Johnson, C.T. Liu, Mater. Sci. Eng. A344 (2003) 328–339.
[31] V. Supatarawanich, D.R. Johnson, C.T. Liu, Intermetall 12 (2004) 721–725.
[32] F.A. Rioult, S.D. Imhoff, R. Sakidja, J.H. Perepezko, Acta Mater. 57 (2009) 4600–4613.
[33] M.K. Meyer, M. Akinc, J. Am. Ceram. Soc. 79 (1996) 938–944.
[34] T.A. Ramanarayanan, R. Ayer, R. Petkovic-Luton, D.P. Leta, Oxid. Met. 29 (1988) 445–472.
[35] J.M. Francis, W.H. Whitlow, Corros. Sci. 5 (1965) 701–710.
[36] J.K. Tien, F.S. Petit, Metall. Trans. A 3 (1972) 1587–1599.
[37] N. Hiramatsu, F.H. Stott, Oxid. Met. 51 (1999) 479–494.
[38] D. Naumenko, B. Gleeson, E. Wessel, L. Singheiser, W.J. Quadakkers, Metall. Mater. Trans. A 38 (2007) 2974–2983.
[39] A. Kumar, M. Nasrallah, D.L. Douglass, Oxid. Met. 8 (1974) 227–263.
[40] B.A. Pint, Oxid. Met. 49 (1998) 531–560.
[41] B.A. Pint, J. Am. Cer. Soc. 86 (2003) 686–695.
[42] T.J. Nijdam, W.G. Sloof, Acta Mater. 55 (2007) 5980–5987.
[43] I. Grammenos, P. Tsakiropoulos, Intermetall 18 (2010) 242–253.
[44] S. Mathieu, S. Knittel, P. Berthod, S. Mathieu, M. Vilasi, Corros. Sci. 60 (2012) 181–192.
[45] I. Grammenos, P. Tsakiropoulos, Intermetall 19 (2011) 1612–1621.
[46] S. Majumdar, S. Burk, D. Schliephake, M. Krüger, H.-J. Christ, M. Heilmaier, Oxid. Met. 80 (2013) 219–230.
[47] M. Azim, S. Burk, B. Gorr, H.-J. Christ, D. Schliephake, M. Heilmaier, R. Bornemann, P. Haring Bolivar, Oxid. Met. 80 (2013) 231–242.
[48] S. Majumdar, D. Schliephake, B. Gorr, H.-J. Christ, M. Heilmaier, Oxidation Mechanisms in Yttrium-alloyed Mo–Si–B, An ECI conference on Beyond Nickel-Based Superalloys, Bad Berneck, Germany, 2013. May 13–17.
[49] S. Majumdar, A. Kumar, D. Schliephake, H.-J. Christ, X. Jiang, M. Heilmaier, Mater. Sci. Eng., A 573 (2013) 257–263.
[50] C.P. Wang, J. Wang, X.J. Liu, I. Ohnuma, R. Kainuma, K. Ishida, J Alloys. Compd. 453 (2008) 174–179.
[51] E.P. EerNisse, Appl. Phys. Lett. 35 (1979) 8–10.
[52] J.P. Fournier, J. Fournier, R. Kohlmuller, Bull. Soc. Chim. France 12 (1970) 4278.
[53] J.-P. Maria, D. Wickaksana, J. Parrette, A.I. Kingon, J. Mater. Res. 17 (2002) 1571–1579.
[54] E.L. Williams, J. Am. Cer. Soc. 48 (1965) 190–194.

# Manuskript IX

# High-temperature oxidation behavior of Mo-Si-B-based and Co-Re-Cr-based alloys

B. Gorr, L. Wang, S. Burk, M. Azim, S. Majumdar, H.-J. Christ, D. Mukherji, J. Rösler,
D. Schliephake, M. Heilmaier

Intermetallics, 48 (2014) 34-43

Intermetallics 48 (2014)

Contents lists available at ScienceDirect

Intermetallics

journal homepage: www.elsevier.com/locate/intermet

# High-temperature oxidation behavior of Mo–Si–B-based and Co–Re–Cr-based alloys

B. Gorr [a], [*], L. Wang [a], S. Burk [a], M. Azim [a], S. Majumdar [a], H.-J. Christ [a], D. Mukherji [b], J. Rösler [b], D. Schliephake [c], M. Heilmaier [c]

[a] *Institut für Werkstofftechnik, Universität Siegen, Paul-Bonatz-Straße 9-11, 57078 Siegen, Germany*
[b] *Institut für Werkstoffe, Technische Universität Braunschweig, 38023 Braunschweig, Germany*
[c] *Institut für Angewandte Materialien – Werkstoffkunde, Karlsruher Institut für Technologie, 76128 Karlsruhe, Germany*

ARTICLE INFO

*Article history:*
Received 17 June 2013
Received in revised form
8 October 2013
Accepted 10 October 2013
Available online 31 October 2013

*Keywords:*
A. Molybdenum silicides
A. Multiphase intermetallics
B. Oxidation
G. Aero-engine components

ABSTRACT

Improving the efficiency of aerospace gas turbine engines requires materials that can be used at increasingly higher temperatures in aggressive environments. This paper summarizes the current stage of alloy development of Mo–Si–B-based and Co–Re–Cr-based alloys regarding the high-temperature oxidation resistance. Since refractory metals, such as Mo and Re, suffer from catastrophic oxidation, the main task of research is to find alloying elements that improve the oxidation behavior of these alloys. For Mo–Si–B-based alloys, it was observed that an addition of Zr has a significant positive influence on the oxidation resistance by reducing the time necessary for the formation of a protective borosilicate layer. An addition of 0.2 at.% Y improves the viscous properties of the borosilicate increasing the protectiveness of the oxide scale. Macroalloying with Ti yields a strong positive effect on the oxidation behavior and, in addition, notably reduces the density of Mo–Si–B-based alloys. In Co–Re–Cr-based alloys, Cr is included to achieve favorable mechanical properties and to form a protective chromia layer during oxidation. As a consequence of the synergetic effect of Cr and Si, an addition of 2 at.% Si significantly improves the oxidation behavior of the alloy. Al addition further promotes the formation of the protective chromia layer at intermediate temperatures and exhibits the potential of the formation of a protective alumina scale suitable for applications at very high temperatures. The critical evaluation of the complex oxidation behavior of both metallic systems in a broad temperature range gives insight into the underlying fundamental mechanisms, reveals the potentials of particular alloying elements and, thus, guides future development of these material classes.

## 1. Introduction

Research to increase the gas inlet temperature with the aim to enhance the efficiency of gas turbines has been pursued worldwide for several decades. The need to reduce $CO_2$ emission has recently provided an additional incentive to increase turbine efficiency. Gas temperatures of the most efficient gas turbines are now at around 1400 °C, which represents an increase of about 100 °C within 30 years [1]. It is expected that gas temperatures will rise further in the future [2,3]. The need for metallic materials capable of reliable applicability at even higher temperatures has created great interest in high-melting alloys represented by the group of refractory metals such as Nb, Ta, Mo, W. This interest has been lingering for some decades leading to extensive research in order to develop high-melting materials which should possess both good high-temperature mechanical properties and high-temperature corrosion resistance. In the framework of the German Research Unit "Beyond Nickel-Base Superalloys" [4], the Mo–Si–B-system and Co–Re–Cr-system were proposed as promising in-situ metal composites for further development as potential materials for high-temperature structural applications.

It is a striking negative feature of refractory metals that they suffer from a poor oxidation resistance, which strongly restricts their extensive use in oxidizing atmosphere at high-temperatures. In contrast to the overwhelming majority of non-refractory metals, which form solid oxides as corrosion products, refractory metals such as Mo, W and Re oxidize by forming liquid or gaseous oxide phases. If an alloy substrate is not covered by a protective oxide scale, the refractory metal as alloying constituent may oxidize and subsequently evaporate from the bulk leading to catastrophic

---

[*] Corresponding author. Tel.: +49 271 740 4653; fax: +49 271 740 2545.
*E-mail address:* gorr@ifwt.mb.uni-siegen.de (B. Gorr).

0966-9795/$ – see front matter © 2013 Elsevier Ltd. All rights reserved.
http://dx.doi.org/10.1016/j.intermet.2013.10.008

oxidation. As a result, excessively fast oxidation and disintegration of the alloys occurs. Well-known examples of catastrophic oxidation are found in oxidation of refractory metals and other elements forming volatile oxides, such as $MoO_3$, $Re_2O_7$, $V_2O_5$, $Bi_2O_3$, $WO_3$, etc. [5,6].

Besides coatings, which are not in the focus of this study, a metal may be protected from oxidation at high-temperatures in oxidizing environment in several ways: (i) alloying, (ii) pre-treatment, and (iii) surface modification. In either case the purpose is to form and establish a layer on the metal surface which acts as a barrier separating the reacting gas and the underlying metal, thus, inhibiting the reaction between the reaction partners. Hence, the purpose of the most studies on alloy oxidation is to improve the oxidation resistance of alloys. Specifically, many of these studies aim at compact, well-adhering oxide scales with low rates of diffusion for the reacting species [4].

The high potential of the alloy system Mo–Si–B for structural applications at higher temperatures due to the fast formation of a dense, adherent, and thus protective borosilicate glass scale was discovered and intensively studied by Berczik in the 1990s [7]. He found that a Mo–Si–B alloy with a reasonable combination of high-temperature strength and high-temperature corrosion resistance should lie in the three phase field containing the following phases: (i) Mo solid solution, (ii) $Mo_3Si$, and (iii) $Mo_5SiB_2$ (T2 phase). For our investigations, the reference alloy with the composition Mo–9Si–8B (in at.%) has been selected as the base alloy for further development. This alloy constitution should be favorable for both, the mechanical properties and oxidation resistance. The continuous Mo solid-solution matrix is required for sufficient low-temperature toughness, whereas both the Si-rich $Mo_3Si$ and the T2 phase should provide oxidation resistance.

Co–Re–Cr-based model alloys have been recently developed for high-temperature applications beyond 1200 °C [8]. Although the development activities of conventional Co-based alloys have been nearly stopped few decades ago due to the lack of precipitation strengthening alike the strengthening by the $\gamma'$ phase in Ni-based superalloys, Co-based alloys still play an important role in turbines because of their excellent thermal shock resistance and the ease of manufacturing [9]. While the solubility of Re in Ni is limited, the complete miscibility in the Co–Re system opens a unique possibility to change the application temperature range of Co-based alloys from intermediate to very high operation temperatures by Re alloying. In addition, the complete miscibility of the Co–Re system reveals a good chance to find a suitable balance between the need for toughness and ductility on the one hand and strength at temperatures beyond the capability of Ni-based superalloys on the other hand. The current focus of the study on this rather unknown alloy system is still very basic and the fundamental trying to elucidate the relevant oxidation mechanisms and to develop strategies for an improvement of the oxidation resistance.

In this work, the current stage of alloy development regarding high-temperature oxidation resistance of the two alloy systems will be summarized. It should be kept in mind that improved oxidation resistance should not be obtained at the expense of desirable mechanical properties. Hence, all alloys presented in this study were either already explored regarding their high-temperature mechanical properties or they are currently under investigation [10–14].

## 2. Experimental

The reference alloy Mo–9Si–8B as well as the alloy Mo–9Si–8B–1Zr were prepared from elemental powder mixtures of Mo, Si, and B of 99.95%, 99.9%, 99.6% purity, respectively, using a mechanical alloying (MA) route. In the case of the alloy Mo–9Si–8B–1Zr, about 1 wt.% $ZrH_2$ powder, which is reduced to about 1 at.% Zr upon sintering, was added. After cold isostatic pressing, a homogenization process followed in a $H_2$-atmosphere at 1500 °C. The further compaction of the sintered material was applied by hot-isostatic pressing at 1500 °C followed by annealing at 1700 °C [15]. The alloy Mo–9Si–8B–0.2Y was produced using MA of the elemental powder mixtures of Mo, Si, B, and Y of 99.95%, 99.9%, 99.96%, and 99.9% purity, respectively. Unlike above, this mechanically alloyed powder was subsequently consolidated using field assisted sintering technique. For details see Ref. [16]. The alloy Mo–37Si–40Ti was prepared from Mo, Si, and Ti of 99.95%, 99.9%, and 99.5% purity, respectively, by an arc-melting process route. Annealing under $H_2$ atmosphere was carried out at 1550 °C for 100 h followed by a subsequent homogenization treatment in Ar atmosphere at 1600 °C for 100 h [17].

The Co–Re-based alloys were melted in a vacuum arc furnace using elementary substances with high purity (>99.98%), and subsequently casted in bar form. The casted Co–Re, Co–Re–Cr, Co–Re–Cr–Si alloys were then solution heat treated in three-steps (1350 °C/5 h, 1400 °C/5 h, 1450 °C/5 h), while the Co–Re–Cr–C and the Co–Re–Cr–Al alloys were heat treated applying only two-steps (1350 °C/7.5 h, 1400 °C/7.5 h) in a vacuum furnace [18]. All heat treated specimens were directly quenched by argon flow within the vacuum furnace.

For oxidation tests, the Mo–Si–B-based alloy specimens were cut from the material bar in dimensions of approximately 5 mm × 4 mm × 3 mm and polished with SiC paper down to grit 500, while the Co–Re-based alloy specimens were cut from heat treated bar in dimensions of approximately 10 mm × 10 mm × 2 mm and polished down to grit 1200. All specimens were ultrasonically cleaned in ethanol directly before use. The oxidation behavior of all alloys was studied by continuous thermogravimetric analysis in a thermobalance with accuracy of 1 µg as well as by discontinuous weight change measurements. The oxidized samples were embedded in epoxy (some of them were coated by Ni before embedding in order to protect the oxide scale formed), ground, and polished for cross-sectional investigations. The morphology and composition of the corrosion products were analyzed by means of standard experimental techniques such as XRD, SEM, EDS.

## 3. Results obtained on the Mo–Si–B-system

### 3.1. *Mo–9Si–8B*

It is well understood that high-temperature oxidation protection of Mo–Si–B alloys is provided through the formation of a dense and well-adherent borosilicate layer. However, the initial transient state of oxidation is usually accompanied by the severe formation of volatile $MoO_3$ in the near-surface region and consequently results in a certain material consumption and decrease of sample weight. In this region, remaining Si and B oxidize simultaneously forming the borosilicate scale. Thus, the initial mass loss exhibits an unavoidable step leading to the formation of a protective borosilicate layer. Its protective properties are dependent on the oxidation temperature as well as the B content, determining the fluidity and, in turn, the protectiveness of the oxide scale [19]. Once, the continuous borosilicate seals the metallic surface, separating the bulk material from the corrosive environment, steady-state oxidation takes place. The growth of the $SiO_2$–$B_2O_3$ scale during steady-state oxidation proceeds predominantly through the solid-state inward diffusion of oxygen. The rate of the initial transient oxidation and consequently the following steady-state oxidation process is strongly dependent on the temperature applied and the alloy microstructure. Below 900 °C, the reference alloy Mo–9Si–8B shows a rather poor oxidation resistance due to the formation of gaseous Mo oxides resulting in a continuous mass loss and causing a fast material damage. Two distinct oxide layers, $MoO_2$ at the substrate/oxide interface covered with a continuous $SiO_2$—$B_2O_3$ scale, are formed during exposure to air below 900 °C [19]. However, the viscosity of the $SiO_2$—$B_2O_3$ scale seems to be too low due to the high $B_2O_3$ to $SiO_2$ ratio, allowing significant oxygen diffusion, permeation and evaporation of $MoO_3$ through the borosilicate layer. The formation of a protective $SiO_2$—$B_2O_3$ scale could not be observed at the critical temperatures below 900 °C, representing the process of catastrophic oxidation mentioned above.

A protective borosilicate layer is observed in the temperature range between 1000 °C and 1300 °C. At these temperatures, the $SiO_2$—$B_2O_3$ layer exists as a continuous outer scale [19]. Fig. 1(a) shows results of continuous TGA experiments carried out at 1000—1300 °C for 72 h. The oxidation curves displayed in Fig. 1(a) reveal that oxidation rates of the alloy Mo—9Si—8B during exposure to laboratory air are extremely susceptible to the oxidation test temperature. At 1300 °C, a significant continuous weight loss is observed during exposure to air, indicating that the oxide scale is not reliably protective. The relatively severe mass loss at 1300 °C is caused by the volatilization of $B_2O_3$. Fig. 1(b) shows the cross-section of the alloy Mo—9Si—8B after 72 h at 1300 °C. Borosilicate exists as a continuous outer scale, whereas underneath $SiO_2$ precipitates form an internal oxidation zone in the Mo-matrix [19]. Despite the evaporation of Mo and B oxides, a dense and continuous silica scale can be observed on the alloy Mo—9Si—8B, which certainly represents an effective barrier against severe corrosion attack at this very high temperature. At 1200 °C, a continuous slight mass loss is detected, whereas a negligible weight change is found after a short period of the transient oxidation at 1000 °C and 1100 °C indicating that the metallic substrate is reliably protected against oxidation (see Fig. 1(a)).

### 3.2. *Mo—9Si—8B—1Zr*

Aiming at an enhancement of the mechanical properties, small amounts of Zr were added to the reference alloy [14,20]. The alloy Mo—9Si—8B—1Zr exhibits a significantly finer microstructure compared to the reference alloy Mo—9Si—8B. Moreover, it is suggested that Zr segregates at grain boundaries as Zr oxide formed during the mechanical alloying process and sintering [14,20]. Since $ZrO_2$ exhibits a very high thermodynamic stability, processing related oxygen impurities may lead to the very fast oxidation of Zr during material preparation.

Due to the finer phase distribution, it could be expected that the period of the transient oxidation may be reduced, resulting in a faster formation of a protective oxide scale. Similar to the reference alloy Mo—9Si—8B, the formation of a continuous and protective silica layer is not observed at temperatures below 900 °C. The oxide layer formed on the alloy Mo—9Si—8B—1Zr at these temperatures exhibits a non-protective porous multi-scale structure, consisting of $SiO_2$, $MoO_2$ and $MoO_3$ [15]. Fig. 2(a) summarizes TGA results for Mo—9Si—8B—1Zr at temperatures between 1000 °C and 1300 °C. Severe mass loss due to the heavy volatilization of $MoO_3$ is observed at 1300 °C. The damage of the silica formed within the first few minutes can be attributed to $ZrO_2$, which is present in the silica scale as a consequence of the initial evaporation of $MoO_3$ during formation of the silica layer on the alloy surface. $ZrO_2$ experiences a phase transformation from a monoclinic to a tetragonal crystallographic structure when heating to temperatures above 1150 °C [21]. Unfortunately, this phase transformation is accompanied by a substantial volume decrease leading to the formation of open pores in the silica layer. With increasing exposure time, the diameter of the pores enlarges allowing the evaporation of $MoO_3$ [15]. Then, damage of the silica layer, heavy volatilization of $MoO_3$, and disintegration of an entire sample occurs at a relatively fast rate. At 1200 °C, a slight continuous weight loss is detected during exposure to air for 100 h. In the temperature range 1000—1100 °C, passivation and steady-state oxidation occurs after few hours of exposure to air resulting in the formation of a protective oxide scale. After prolonged exposure time (about 72 h) at 1100 °C, the second phase particles of $ZrO_2$ (see Fig. 2(b)) were detected in the outer silica layer, whereas the oxide surface of the Zr-free reference alloy Mo—9Si—8B is single-phase silica [15]. The comparison of the TGA-curves at 1100 °C for the reference alloy (see Fig. 1(a)) and the alloy Mo—9Si—8B—1Zr (see Fig. 2(a)) reveals that the passivation occurs significantly earlier for the alloy Mo—9Si—8B—1Zr due to its finer microstructure. This leads to notably lower values of the absolute mass loss after the same exposure time clearly indicating the better oxidation resistance of the alloy Mo—9Si—8B—1Zr at 1100 °C.

### 3.3. *Mo—9Si—8B—0.2Y*

It is well-known that Y substantially improves the oxidation behavior of many alloys as well as alloy coatings. In general, Y segregates along oxide grain boundaries and consequently inhibits grain boundary diffusion of metal cations and/or oxygen anions [22,23]. Apparently, grain boundary diffusion flux is higher compared to the lattice diffusion, especially at intermediate and low temperatures, thus, Y can affect the growth rate of the oxide scale significantly [5]. Besides, small additions of Y improve the adhesion of oxide layers formed on different high-temperature alloys [24,25].

The results of thermogravimetric experiments conducted in air in the temperature range 1000—1200 °C are shown in Fig. 3(a). The comparison of these oxidation curves with kinetic data of the reference alloy (Fig. 1(a)) reveals that both, the alloy Mo—9Si—8B

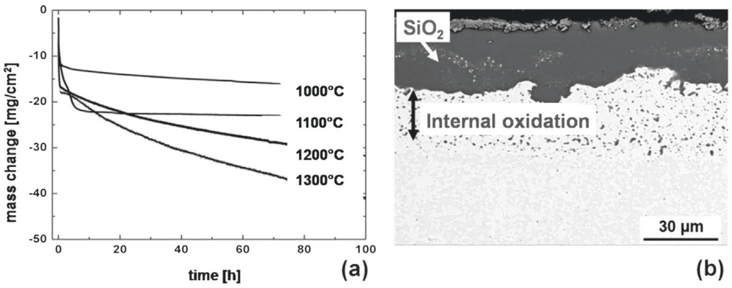

**Fig. 1.** Oxidation behavior of the alloy Mo—9Si—8B; (a) TGA results at 1000—1300 °C and (b) cross-section (back scattered signal) of the alloy after oxidation at 1300 °C in air for 72 h. The dark $SiO_2$ particles form a zone of internal oxidation in the bright metallic matrix.

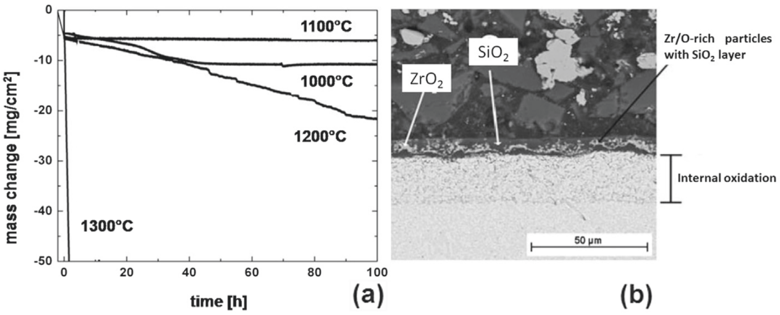

**Fig. 2.** Oxidation behavior of the alloy Mo—9Si—8B—1Zr; (a) TGA results at 1000—1300 °C and (b) cross-section (back scattered signal) of the alloy after oxidation at 1100 °C in air for 72 h. The dark $SiO_2$ particles precipitate internally in the bright metallic matrix underneath the $SiO_2$ scale with $ZrO_2$ inclusions.

and Mo—9Si—9B—0.2Y, exhibit similar oxidation behavior in this temperature range. Both alloys show a transient and notable weight loss in the first stage of oxidation followed by steady state oxidation characterized by a very slight mass loss. Fig. 3(b) shows a cross-section of the alloy Mo—9Si—9B—0.2Y oxidized at 1100 °C for 72 h. A thin and compact borosilicate containing finely distributed precipitates of the $Y_2O_3$—$SiO_2$ type is observed. A relatively thin zone of internal oxidation is detected underneath the $MoO_2$ layer. The presence of Y-rich inclusions in the borosilicate layer positively affects the viscosity of the borosilicate. The flow ability of the outer layer seems to be significantly improved, especially at 1100 °C and even stronger at 1000 °C (compare Figs. 1(a) and 3(a)). At 1200 °C, the initial mass loss of the alloy Mo—9Si—9B—0.2Y is slightly higher compared to the reference alloy, however, the following steady state oxidation exhibits a lower weight loss rate.

As mentioned above, Mo—Si—B alloys have proven very good oxidation resistance in the temperature range from 1000 °C to 1300 °C due to the formation of a protective borosilicate. These alloys usually show inferior oxidation resistance at temperatures below 900 °C. Majumdar et al. studied the oxidation behavior of Y-containing Mo—Si—B alloys at the intermediate temperatures below 900 °C. They found that the alloy Mo—9Si—9B—0.2Y shows a continuous lower rate of weight loss at 800 °C and 900 °C compared to the reference alloy. Even a gradual weight gain during the initial periods of oxidation was detected at these temperatures [16]. A continuous outer silicate scale was detected above a separate $MoO_2$ layer, containing some $MoO_3$ whiskers. Majumdar concluded that due to the presence of $Y_2O_3$ in the silica, the oxide scale becomes less viscous and can flow easier over the pores preventing high evaporation rates of gaseous $MoO_3$, which are typical of the oxidation characteristics of the reference alloy at 800—900 °C. Moreover, a self-healing nature of the silicate scale is noted for the alloy Mo—9Si—9B—0.2Y. For details of the effect of Y alloying on the oxidation behavior of Mo—Si—B alloys see Ref. [16].

### *3.4. Mo—37Si—40Ti*

An addition of Ti to both, the binary Mo—Si and the ternary Mo—Si—B alloy system, represents a new concept in alloy development of this material class. Macroalloying with Ti is suggested to aim at a simultaneous improvement of (i) the high-temperature oxidation resistance and (ii) the strength/density ratio by a significant reduction of the alloy density over a wide temperature range. Yang et al. [26] recently found that Ti extends the three-phase equilibrium region of Mo_ss—$Mo_5Si_3$—$Mo_5SiB_2$ described earlier. According to their thermodynamic calculations, if the Ti concentration exceeds 27.5 at.% in the quaternary alloy Mo—9Si—8B—*x*Ti, $Mo_5Si_3$ phase with Ti in solid-solution, i.e. $(Mo,Ti)_5Si_3$, will form instead of the $Mo_3Si$ phase. The substitution of Mo through Ti in the $(Mo,Ti)_5Si_3$ phase to a significant extent may lead to a considerable improvement of the oxidation resistance of the Mo—Si-based alloys.

In order to get a first understanding of the high-temperature oxidation behavior of Ti-containing Mo—Si-based alloys, the alloy with an overall composition of Mo—37Si—40Ti (at.%), constituting a nearly $(Mo,Ti)_5Si_3$ single-phase, was used in high-temperature oxidation investigations. Thermogravimetric curves for the alloy Mo—37Si—40Ti at 820 °C, 1000 °C, 1100 °C, and 1200 °C are shown in Fig. 4(a). At all temperatures, continuous mass gain was observed during exposure to laboratory air for the alloy studied. Only at 1000 °C, a negligibly small mass loss was detected during

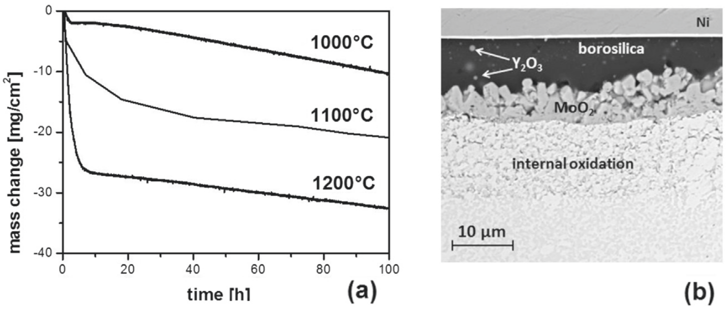

**Fig. 3.** Oxidation behavior of the alloy Mo—9Si—8B—0.2Y; (a) TGA results at 1000—1200 °C and (b) cross-section (back scattered signal) of the alloy after oxidation at 1100 °C in air for 72 h. The dark $SiO_2$ particles form a zone of internal oxidation in the bright metallic matrix.

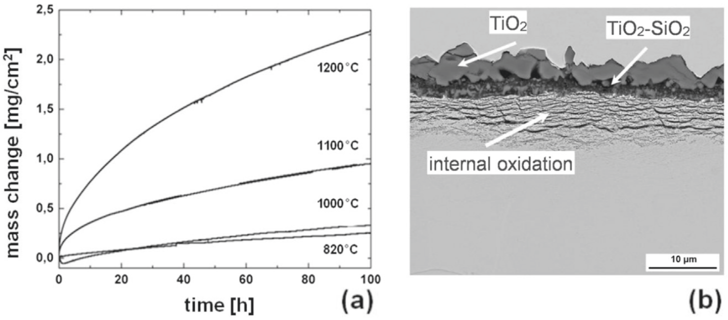

**Fig. 4.** Oxidation behavior of the alloy Mo—37Si—40Ti; (a) TGA results at 820—1200 °C and (b) cross-section (back scattered signal) of the alloy after oxidation at 1100 °C in air for 100 h. The dark $SiO_2$ particles form a zone of internal oxidation in the light gray $(Mo,Ti)_5Si_3$ phase.

the first hours of exposure. The thermogravimetric curves obtained from the oxidation tests follow the parabolic rate law, which is common for the oxidation behavior of highly oxidation resistant high-temperature materials and which indicates the formation of a protective oxide scale. Even at the critical temperature of 820 °C, a parabolic mass gain is detected for the alloy Mo—37Si—40Ti characterized by a very low oxidation rate. The cross-sectional micrograph shown in Fig. 4(b) reveals the formation of a duplex oxide layer consisting of an outmost $TiO_2$ scale above the $SiO_2$ layer at 1100 °C. The last one includes separate $TiO_2$ particles incorporated in the $SiO_2$ matrix, which provides the protectiveness of the entire oxide layer. Below the interface oxide/substrate, a relatively thin zone of internal precipitates of $SiO_2$ in the Mo matrix is observed. Burk et al. reported that the oxide scales formed on the alloy Mo—37Si—40Ti at 1000 °C and 1200 °C possess similar structure, whereas small particles of $TiO_2$ were found on the top of a single $SiO_2$ scale at 820 °C, which also remained protective during the complete oxidation time [17]. The oxidation resistances of the single phases $Mo_5Si_3$ and $Ti_5Si_3$ have been investigated earlier [27,28]. Both phases showed insufficient high-temperature oxidation resistances, since a porous $SiO_2$ layer formed on the single-phase $Mo_5Si_3$ below 1400 °C, whereas a TiN transient layer developed on stoichiometric $Ti_5Si_3$ beyond 1000 °C. On the contrary, the single $(Mo,Ti)_5Si_3$ phase presented in this study exhibited a clearly superior oxidation behavior most probably because of the continuous $SiO_2$ matrix of the scale in which $TiO_2$ particles are embedded [17].

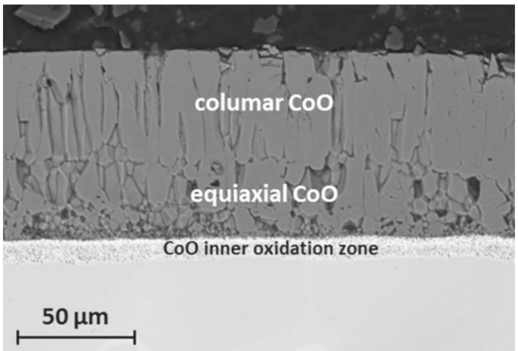

**Fig. 5.** Cross-sectional microstructure (back scattered signal) of the model alloy Co—17Re after exposure to laboratory air at 1000 °C for 1 h.

## 4. Results obtained on the Co—Re—Cr-system

### 4.1. Co—Re—(Cr—C)

Although the Co—Re—Cr-based alloys possess a high melting point and the potential to achieve good mechanical properties at high temperatures, one of the important issues of the development of these alloys concerns the oxidation resistance [8]. The binary alloy Co—17Re shows a catastrophic oxidation behavior during exposure to laboratory air at 1000 °C [18]. The cross-sectional micrograph of an oxidized specimen is shown in Fig. 5 presenting the constitution of the CoO scale, which consists of two sublayers with different morphologies due to different diffusion mechanisms. However, none of these oxide scales is protective. The oxidation of rhenium followed by the evaporation of its oxides resulted in massive mass loss during oxidation despite the significant uptake of oxygen through the formation of Co-oxides.

Chromium is generally added to alloys such as stainless steels, Ni-based superalloys as well as Co-based superalloys to enhance their oxidation resistance by the formation of a slow growing $Cr_2O_3$ scale [29—31]. Similarly, Cr was added to the Co—Re system not only to provide for the formation of a dense and protective chromia layer but also to achieve favorable mechanical properties [8]. Fig. 6(a) shows the Co—Re—Cr ternary phase diagram for 1100 °C. An addition of 23 at.% chromium to Co—17Re promotes the precipitation of the hard intermetallic $Cr_2Re_3$-type sigma phase, which may strengthen the alloy by composite hardening. A typical microstructure of the ternary alloy Co—17Re—23Cr is shown in Fig. 6(b). Further, carbon addition may also enhance the creep resistance of the alloy system through the formation of carbides and their subsequent interaction with dislocation during creep deformation [8]. However, the ternary alloy Co—17Re—23Cr shows an even poorer oxidation resistance compared to the binary Co—17Re alloy, forming a more porous $CoCr_2O_4$ spinel layer underneath the CoO layer [18]. A discontinuous $Cr_2O_3$ scale underneath the $CoCr_2O_4$ layer does not protect the metallic substrate against severe corrosion attacks. A similar oxide scale constitution with the consequent weight loss kinetics was also observed on Co—17Re—30Cr, although the $CoCr_2O_4$ layer contains less porosity. Short time oxidation tests indicate that the sigma phase is preferentially attacked during oxidation as compared to the hcp matrix. The addition of C to ternary alloys of Co—17Re—23/30Cr for improving mechanical properties does not play a significant role on the oxidation behavior. A slower oxidation rate along grain boundaries as compared to the grain interior is only observed in a short oxidation period for the quaternary alloy Co—17Re—23Cr—2.6C. This phenomenon disappears with increasing time of oxidation [18].

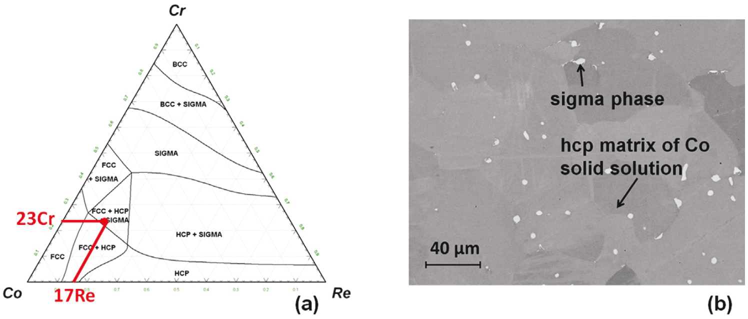

**Fig. 6.** Co—Re—Cr ternary alloy system; (a) phase diagram of Co—Re—Cr at 1100 °C and (b) a typical microstructure (back scattered signal) of Co—17Re—23Cr after the homogenization.

### *4.2. Co—17Re—23Cr—xSi*

There are numerous studies indicating that a small amount of silicon addition can significantly improve the oxidation resistance of Co—Cr-based alloys, since a low content of Cr is efficient to produce a continuous protective $Cr_2O_3$ layer [32—34]. One of the generally accepted theories to this phenomenon proposes that Si or initially formed silica acts as nucleation sites reducing the distance between $Cr_2O_3$ nuclei and therefore promoting the fast formation of a continuous protective chromia layer. Some other authors also reported that the addition of silicon improves the oxidation resistance of alloys through the formation of an amorphous silica layer between the outer oxide layer and the alloy substrate, inhibiting the outward diffusion of metal cations to the outer oxide scale as well as the inward diffusion of oxygen anions [35]. Thus, it is of great interest to investigate the influence of Si on the oxidation behavior of Co—Re—Cr-based alloys.

Fig. 7(a) represents the weight change of a series of alloys of type Co—17Re—23Cr—*x*Si with different amounts of Si content during exposure to laboratory air at 1000 °C for 30 h [36]. Oxidation kinetics of these alloys is still extensively affected by the evaporation of Re oxides. The weight loss of Co—17Re—23Cr alloy is strongly and progressively decreased by the addition of 1 at.% to 3 at.% Si. The weight loss of alloy Co—17Re—23Cr—1Si is less than that of the ternary alloy Co—17Re—23Cr by a factor of about 3, while increasing the Si content to 2 and 3 at.% causes further decrease of the weight loss by factors of about 1.5 for Co—17Re—23Cr—2Si and 7.8 for Co—17Re—23Cr—3Si [36].

From a microstructural point of view, the oxide scale formed on the alloy Co—17Re—23Cr—1Si consists of an outermost CoO layer, followed by a porous $CoCr_2O_4$ layer and a thin discontinuous inner $Cr_2O_3$ layer. Similar constitution of the oxide scale was detected in some areas of Co—17Re—23Cr—2Si, while other parts of the alloy are covered by $Cr_2O_3$. A completely different oxide structure, which consists of an outer $CoCr_2O_4$ layer and a relatively thick inner $Cr_2O_3$ layer, is found on the alloy Co—17Re—23Cr—3Si, see Fig. 7(b). The $Cr_2O_3$ layer formed on Co—17Re—23Cr—3Si is nearly continuous. $SiO_2$ precipitates in inner oxidation zone were found in all Si-containing alloys. The amount of $SiO_2$ precipitates increases with increasing Si content [36].

### *4.3. Co—17Re—xCr—2Si*

As mentioned above, a quasi-continuous $Cr_2O_3$ layer was found underneath the thin spinel $CoCr_2O_4$ layer on Co—17Re—23Cr—3Si after oxidation at 1000 °C. However, a slight weight loss was still observed, indicating the lingering evaporation of Re oxides. Moreover, a high Si content strongly reduces the melting point of the alloy negatively affecting the mechanical properties. Regarding high temperature oxidation resistance, the high Si content causes heavy spallation of the scales formed. On this account, a further increase of the Si content in Co—17Re—23Cr—*x*Si would not lead to the superior combination of desired mechanical properties and reliable corrosion resistance. Rather, it seems that a higher Cr content is required to facilitate the formation of a compact and continuous $Cr_2O_3$ layer on the quaternary Co—Re—Cr—Si alloy system. For this reason, another series of alloys of type Co—17Re—*x*Cr—2Si ($x = 23, 25, 27, 30$) with a moderate amount of Si and different Cr contents was investigated.

The weight changes of Co—17Re—*x*Cr—2Si during oxidation at 1000 °C are shown in Fig. 8(a). As mentioned above, a relatively high weight loss of Co—17Re—23Cr—2Si is observed due to the lack of a continuous protective oxide layer, allowing the evaporation of Re oxides. In contrary, parabolic weight gain kinetics is observed on Co—17Re—25Cr—2Si and Co—17Re—27Cr—2Si, which contain higher Cr contents [37]. The cross-sectional micrograph of Co—17Re—25Cr—2Si after exposure to air at 1000 °C for 72 h, shown in Fig. 8(b), indicates that the alloy surface is completely covered by a compact $Cr_2O_3$ layer. $SiO_2$ particles are found underneath the $Cr_2O_3$ layer as internally oxidized precipitates and are mostly located in the sigma phase region. A very thin outermost $CoCr_2O_4$ layer, which thickness is almost constant during the entire oxidation period, seems to be a product from the transient oxidation period. The growth of the thickness of the formed $Cr_2O_3$ layer as a function of oxidation time, as identified by discontinuous oxidation tests, follows a parabolic manner as well. Thus, one can conclude that the oxidation rate of the alloy is controlled by the growth of the protective chromia layer. The consumption of Cr at the alloy subsurface causes the dissolution of the sigma phase and the formation of a Re-enriched zone underneath the $Cr_2O_3$ scale. The evaporation of Re oxides is prevented [37]. The oxide scale formed on Co—17Re—25Cr—2Si in the temperature range from 800 °C to 1100 °C was found to be a compact $Cr_2O_3$ layer which evolves from a non-protective multi-layer indicating the important role of diffusion kinetics of Cr on the oxidation behavior of the alloy.

The constitution of the oxide scales formed on Co—17Re—27Cr—2Si and Co—17Re—30Cr—2Si is quite similar to that formed on Co—17Re—25Cr—2Si. However, the volume fraction of the sigma phase in the alloys Co—17Re—*x*Cr—2Si, determined experimentally after homogenization heat treatment, increases significantly from 14% in Co—17Re—23Cr—2Si to 43.6% in Co—17Re—30Cr—2Si [35]. This is in agreement with the thermodynamic calculation for the Co—17Re—*x*Cr alloy system at 1000 °C [38]. Apart from the weak oxidation resistance of the sigma phase, many authors also reported on the

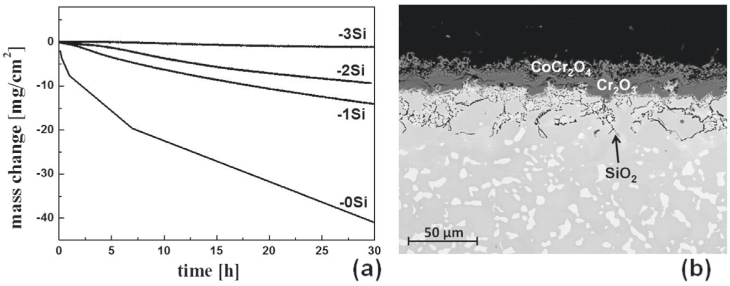

**Fig. 7.** Oxidation behavior of the alloy Co—17Re—23Cr—*x*Si; (a) TGA results at 1000 °C and (b) cross-section (back scattered signal) of the alloy Co—17Re—23Cr—3Si after oxidation at 1000 °C in air for 7 h. In the metallic substrate, sigma phase appears as a bright phase in the gray hcp matrix.

brittle behavior of the sigma phase and its negative effect on the mechanical properties [39,40]. The formation of the sigma phase in Co—Re-based alloys, its volume fraction, size, and distribution in the alloy matrix represents an ambiguous and often controversially discussed issue regarding mechanical properties and corrosion resistance. Thus, although a high Cr content is beneficial for the oxidation behavior of the alloys, it should also be kept in mind that improved oxidation resistance should not be obtained at the expense of favorable mechanical properties.

### *4.4. Co—17Re—23Cr—xAl*

It is well-known that $Cr_2O_3$ evaporates through oxidation as volatile $CrO_3$ at temperatures above 1000 °C [41,42]. For applications at even higher temperatures, the formation of a slow growing $SiO_2$ or $Al_2O_3$ scale is normally aimed at in the case of conventional superalloys. As mentioned above, no continuous $SiO_2$ layer forms on the quaternary alloy Co—17Re—23Cr—*x*Si even with 3 at.% Si addition, but an internal oxidation zone of $SiO_2$ precipitates was found underneath the chromia layer. In order to preserve the high melting point of the alloy system, a higher silicon addition should be avoided. Against this background, the addition of Al in Co—Re—Cr-based alloys was studied to investigate the oxidation behavior and the nature of oxide scale formation.

The oxidation behavior of two alloys Co—17Re—23Cr—5/10Al with different amounts of Al was examined at temperatures in the range from 800 °C to 1300 °C. Fig. 9(a) shows some of the mass change curves of both alloys during exposure to laboratory air. At 900 °C, the oxide scale formed on Co—17Re—23Cr—5Al consists of an outer Co oxide layer and a porous inner $Co(Al,Cr)_2O_4$ scale, resulting in a continuous mass loss through the evaporation of Re oxides. As temperature increases, the thermogravimetric curve of the alloy Co—17Re—23Cr—5Al follows a parabolic behavior at 1000—1100 °C. The oxide scale consists of a thin external $CoCr_2O_4$ layer and a protective $Cr_2O_3$ layer. $Al_2O_3$ internal oxide and AlN precipitates formed underneath the $Cr_2O_3$ layer. At 1200—1300 °C, however, neither $Cr_2O_3$ nor $Al_2O_3$ seems to establish a protective layer. The oxide scale consists of an outermost CoO and a thick porous inner oxide layer, where the $Co(Cr,Al)_2O_4$ is embedded in a CoO matrix. As a consequence of the lack of a protective oxide layer, a strong mass loss was obtained, see Fig. 9(a).

With higher Al content, the alloy Co—17Re—23Cr—10Al exhibits a completely different oxidation behavior. The higher Al addition stimulates the formation of big sigma phase particles. At 800—1000 °C, a slight weight loss was observed during the initial stage of the test due to the fast oxidation of the exposed Re-rich sigma phase, following by the quick evaporation of Re-oxides. After this transient oxidation period, the TGA curve tends to become flat. A parabolically slow growing oxidation manifests itself in the weight change curve obtained at 1000 °C. The time of the transient period becomes shorter as the temperature increases. The oxide scale formed on the alloy matrix at 1000 °C consists an outer $Cr_2O_3$ layer and a continuous inner $Al_2O_3$ layer. Few AlN particles were observed under the oxide scale, see Fig. 9(b). A similar constitution of the oxide scales except of the existence of AlN was observed at 900 °C. As temperature increases to above 1100 °C, the formation of $Al_2O_3$ takes place internally. However, a protective $Cr_2O_3$ layer underneath a thin $CoCr_2O_4$ layer still formed at 1100—1200 °C, retarding the formation and evaporation of Re oxides. Unlike the simultaneous internal oxidation and nitridation behavior of Ni—Cr—Al alloys reported by Han [43], no $Cr_2N$ was detected in Co—17Re—23Cr—5Al and Co—17Re—23Cr—10Al after exposure to air at 900—1200 °C.

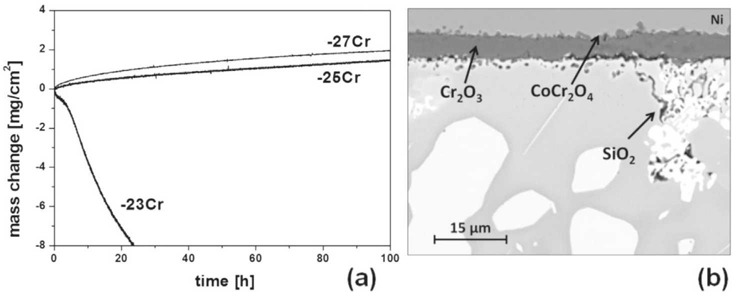

**Fig. 8.** Oxidation behavior of the alloy Co—17Re—*x*Cr—2Si; (a) TGA results at 1000 °C and (b) cross-section (back scattered signal) of the alloy Co—17Re—25Cr—2Si after oxidation at 1000 °C in air for 72 h. In the metallic substrate, sigma phase appears as a bright phase in the gray hcp matrix.

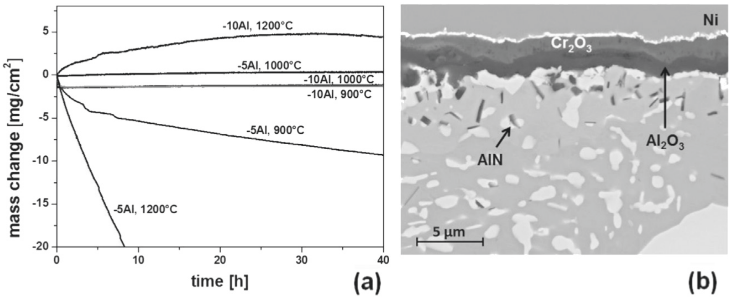

**Fig. 9.** Oxidation behavior of the alloy Co—17Re—23Cr—5/10Al; (a) TGA results and (b) cross-section (back scattered signal) of the alloy Co—17Re—23Cr—10Al after oxidation at 1000 °C in air for 72 h. In the metallic substrate, sigma phase appears as a bright phase in the gray hcp matrix.

## 5. Comparison of the alloy systems

Fig. 10 summarizes the oxidation behavior of different Mo—Si- and Co—Re-based alloys starting with their reference alloys, Mo—9Si—8B and Co—17Re—23Cr. On the one hand, Fig. 10 reveals the qualitative progress in alloy development, on the other hand, the strong potentials of both alloy systems are documented. As outlined above, the oxidation behavior of Mo—Si-based alloys and most Co—Re-based alloys can be subdivided into two stages: (i) transient oxidation which indicates that the surface and reaction processes are rate-determining and (ii) steady-state oxidation which signifies that the diffusion processes are rate-determining. In the case of the Mo—Si-based alloys, the mass change for the transient period was taken as values after 5 h of oxidation and the value for the steady-state oxidation refers to the TGA curves after 72 h of exposure to air. For Co—Re-based alloys, the values for the transient and steady-state oxidation represent the mass change after 3 and 30 h of oxidation, respectively.

As mentioned above, the oxidation resistance of the Mo—Si-based alloys is very sensitive to the alloy composition as well as the oxidation temperature. At high temperatures, Mo—Si-based alloys generally show a fast passivation and consequently better oxidation resistance. At intermediate temperatures, a protective borosilicate layer does not form on these alloys, which leads to the fast damage of the entire material. In fact, the Mo—Si-based alloys are prone to show an inferior high-temperature oxidation resistance at 820 °C, whereas they offer their best performance at 1100 °C. For the sake of illustration and a critical evaluation of the extensive oxidation behavior in a wide temperature range, the oxidation rates for Mo—Si-based alloys studied are compared in Fig. 10(a) and (b) at these two temperatures. The alloy Mo—9Si—8B—1Zr clearly shows a superior oxidation resistance only at 1100 °C. It should be pointed out that steady-state oxidation does not occur for the reference alloy as well as for the Mo—9Si—8B—1Zr at 820 °C. In the case of the Y-addition, a slight improvement is detected at 820 °C, whereas at 1100 °C, a notably reduced oxidation rate is observed. The alloy Mo—37Si—40Ti, containing a significantly higher Si-concentration compared to other alloys, shows an excellent oxidation resistance at both temperatures encouraging to further investigations of Ti-containing Mo—Si-based alloys.

Fig. 10(c) and (d) summarizes the progress in the development of the novel Co—Re-based alloys regarding the high temperature oxidation resistance. In fact, Cr-addition is beneficial for the oxidation resistance of the Co—Re-based alloys, particularly in combination with ignoble elements such as Si and Al. Since Co—Re—Cr—Si alloys may form a protective chromia scale, they can, therefore, be used in oxidizing atmospheres at temperatures up to 1000 °C, whereas alumina forming Co—Re—Cr—Al alloys may maintain their oxidation resistance at temperatures significantly higher than 1000 °C due to the very stable $Al_2O_3$.

Fig. 10(c) shows that the oxidation behavior of quaternary Co—Re—Cr—Si alloys strongly depends on the alloy composition. With the optimized Cr/Si content, alloy Co—17Re—25Cr—2Si exhibits a favorable oxidation resistance at intermediate temperatures. The formation of a continuous compact $Cr_2O_3$ scale successfully prevents the evaporation the Re oxides for this alloy. In the case of the Co—Re—Cr—Al system (Fig. 10(d)), the addition of 10 at.% Al significantly improves the oxidation resistance of the reference alloy Co—17Re—23Cr in a wide temperature range by either forming a protective $Al_2O_3$ layer at 800°—1000 °C, or by promoting the formation of a compact and protective $Cr_2O_3$ scale which is covered by a thin $CoCr_2O_4$ layer at 1100—1200 °C that also retards the evaporation of Re oxides.

Although Fig. 10 allows a rather qualitative assessment of the oxidation behavior of Mo—Si and Co—Re-based alloys, it is evident that a clear progress in the oxidation resistance has been developed for both alloy systems. However, there are still many critical points and open questions that need elucidation, e.g. the formation of the $SiO_2$ matrix in the $SiO_2$—$TiO_2$ duplex oxide layer in Mo—Si—Ti alloys or the optimization of the chemical composition of Co—Re—Cr—Al alloys to facilitate the formation of $Al_2O_3$ scale in a broad temperature range. These interesting aspects as well as the achievements obtained so far encourage further investigations of Mo—Si- and Co—Re-based alloys.

## 6. Summary and conclusions

As pointed out above, the aim of most high temperature oxidation studies is to facilitate the formation of a protective oxide scale with the following characteristics: (i) compactness and continuousness, (ii) good adherence, (iii) low rates of diffusion of the reacting species, and (iv) fast formation. In the case of systems containing refractory metals, the last point becomes particularly important since the refractory metals oxidize forming gaseous oxides. Both material groups studied, Mo—Si—B- and Co—Re—Cr-based alloys, suffer from severe catastrophic oxidation if the material surface is not covered by a sustainably protective oxide scale. The exploratory activities regarding the improvement of the oxidation protectiveness of these alloys were concentrated on: (i) enabling of the quick formation of protective oxide scales through additions of suitable alloying elements and (ii) investigation of the oxide scale stability in different environmental conditions. It should be pointed out that the focus of our studies was on exploring and improving the inherent properties regarding high temperature oxidation resistance of both alloy systems. Hence, the effect of coatings was beyond the scope of this investigation.

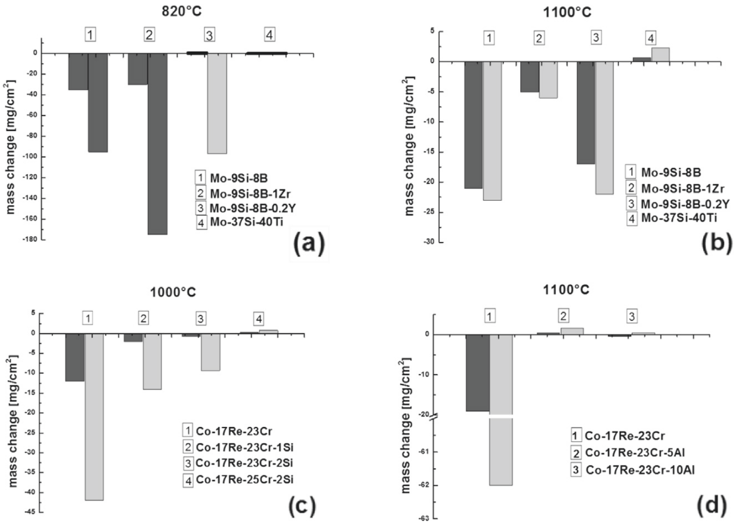

**Fig. 10.** Comparison of the oxidation behavior of Mo–Si- and Co–Re-based alloys: (a) Mo–Si-based alloys at 820 °C, (b) Mo–Si-based alloys at 1100 °C, (c) Co–Re–Cr–Si-based alloys at 1000 °C, and (d) Co–Re–Cr–Al-based alloys at 1100 °C (■: transient oxidation, □: steady-state oxidation).

The results presented above reveal that the oxidation resistance of Mo–Si–B- and Co–Re–Cr-based alloys is very sensitive to the alloy composition. Further, such characteristic alloy features such as microstructure, i.e. phase volume fraction, phase distribution and stability at high temperatures, affect the oxidation behavior significantly. Moreover, material defects presented in the alloys such as porosity, cracks and inhomogeneity may influence the oxidation resistance of the alloys detrimentally.

The most significant characteristics of Mo–Si–B- and Co–Re–Cr-based alloys regarding the high temperature oxidation behavior can be summarized as follows:

1. The reference alloy Mo–9Si–8B exhibits an excellent oxidation resistance in the temperature range of 1100–1300 °C due to the formation of a low viscosity borosilicate layer. Below 900 °C, the reference alloy suffers from catastrophic oxidation because the borosilicate scale formed on the alloy surface is porous allowing the evaporation of gaseous $MoO_3$.
2. Oxidation studies conducted on the alloy Mo–9Si–8B–1Zr reveal a very strong dependence of the oxidation behavior on the oxidation temperature. At temperatures below 900 °C, the oxidation resistance of this alloy is very poor due to the heavy evaporation of $MoO_3$. At 1000 °C and especially at 1100 °C, it was observed that the addition of Zr improves the oxidation behavior substantially, reducing the time necessary for the formation of a protective oxide scale. At 1300 °C, the borosilicate layer becomes unstable due to the phase transformation of $ZrO_2$ taking place above 1150 °C.
3. The oxidation behavior of the alloy Mo–9Si–8B–0.2Y shows, in general, superior characteristics compared to the reference alloy Mo–9Si–8B. This alloy forms a protective borosilicate containing $Y_2O_3$ inclusions during exposure to air at temperatures from 800 °C up to 1200 °C. $Y_2O_3$-particles improve the viscous properties of a borosilicate layer, which becomes more protective.
4. The investigation of the alloy Mo–37Si–40Ti reveal a strong beneficial effect of Ti in the formation of nearly single phase $(Mo,Ti)_5Si_3$, which possesses an excellent oxidation resistance at all temperatures, from 820 °C up to 1200 °C, due to the formation of a protective oxide scale. It seems to be very important that the duplex layer, which forms underneath the outer $TiO_2$ scale, consists of a $SiO_2$ matrix, i.e., the $TiO_2$ particles are embedded in $SiO_2$. This kind of oxide scale formation should ensure the long-term protectiveness of the Mo–Si–Ti-based alloys.
5. The binary Co–17Re reference alloy shows a poor oxidation resistance at 1000 °C/1100 °C. The non-protective CoO scale formed on the alloy allows the evaporation of Re-oxides, resulting in catastrophic oxidation kinetics.
6. The addition of 23 at.% Cr to Co–17Re does not improve the oxidation resistance significantly at 1000°/1100 °C. Rather strong volatilization of Re-oxides through the formation of a more porous inner $CoCr_2O_4$ layer underneath the outermost CoO layer was found. A weaker oxidation resistance of the sigma phase compared to the hcp matrix is observed.
7. Additions of Si from 1 at.% to 3 at.% to the alloy Co–17Re–23Cr significantly improves the oxidation behavior by promoting the formation of protective $Cr_2O_3$ layer at 1000 °C/1100 °C. However, a slight mass loss caused by Re oxides evaporation was still observed in Co–17Re–23Cr–3Si during oxidation at 1000 °C. $SiO_2$ particles were found as internal oxide precipitates underneath the oxide scales in all silicon containing Co–17Re–23Cr alloys.
8. The increase of the Cr content from 23 at.% to 25 at.% in Co–17Re–*x*Cr–2Si significantly enhances the oxidation resistance by the formation of a compact and protective $Cr_2O_3$ scale at 1000 °C/1100 °C. The enrichment of Re at the alloy subsurface and the parabolic weight gain kinetics indicate the retardation of Re oxides evaporation.
9. Although no continuous $Al_2O_3$ layer forms on alloy Co–17Re–23Cr–5Al at the entire temperature range 800–1300 °C, the addition of 5 at.% Al demonstrates a strong positive influence on the oxidation behavior of the alloy, promoting the formation of a compact $Cr_2O_3$ scale at 1000 °C and 1100 °C. Alloy Co–17Re–23Cr–10Al exhibits excellent oxidation resistance at 800–1000 °C, forming a continuous protective $Al_2O_3$ layer. At 1100–1200 °C, the external oxide scale, which consists of a continuous compact $Cr_2O_3$ layer and a thin outermost $CoCr_2O_4$ layer,

preserves its protective nature, preventing the volatilization of the Re oxides.

## Acknowledgments

Financial support of Deutsche Forschungsgemeinschaft (DFG) in the framework of the Research Unit "Beyond Ni-Base Superalloys" is gratefully acknowledged.

## References

[1] Huenecke K. Jet engines: fundamentals of theory, design and operation. Shrewsbury: Airlife Publishing Ltd; 1997.

[2] Zhao JC, Westbrook JH. Ultrahigh-temperature materials for jet engines. Mater Res Soc 2003;28:622.

[3] Deodeshmukh VP, Srivastava SK. The oxidation performance of modern high-temperature alloys. JOM J Min Met Mat Soc 2009;61:56–9.

[4] http://www.iam.kit.edu/wk/1051.php [accessed 28.05.13].

[5] Kofstad PK. High temperature corrosion. London: Elsevier Applied Schience; 1988.

[6] Young D. High temperature oxidation and corrosion of metals. Oxford: Elsevier; 2008.

[7] Berczik DM. Method for enhancing the oxidation resistance of a molybdenum alloy, and a method of making a molybdenum alloy, United States Patent 5.595.616, 1997.

[8] Rösler J, Mukherji D, Baranski T. Co-Re-based alloys: a new class of high temperature materials? Adv Eng Mater 2007;9:876–81.

[9] Sato J, Omori T, Oikawa K, Ohnuma I, Kainuma R, Ishida K. Cobalt-base high-temperature alloys. Science 2006;312:90–1.

[10] Azim M, Burk S, Gorr B, Christ H-J, Schliphake D, Heilmaier M, et al. Effect of Ti (macro-)alloying on the high-temperature oxidation behavior of ternary Mo-Si-B alloy at 820-1300 °C. Oxid Met 2013. http://dx.doi.org/10.1007/s11085-013-9375-1.

[11] Krüger M. Pulvermetallurgische Herstellung und Charakterisiereung von oxidationsbeständigen Molybdänbasislegierungen für Hochtemperaturanwendungen. Ph.D thesis. Magdeburg: Universität Magdeburg; 2010.

[12] Brunner M, Hüttner R, Bölitz M-C, Völkl R, Mukherji D, Rösler J, et al. Creep properties beyond 1100 °C and microstructure of Co-Re-Cr alloys. Mater Sci Eng A 2010;528:650–6.

[13] Krüger M, Franz S, Saage H, Heilmaier M, Schneibel JH, Jéhanno P, et al. Mechanically alloyed Mo-Si-B alloys with a continuous $\alpha$-Mo matrix and improved mechanical properties. Intermetallics 2008;16:933–41.

[14] Saage H, Krüger M, Sturm D, Heilmaier M, Schneibel JH, George E, et al. Ductilization of Mo-Si solid solutions manufactured by powder metallurgy. Acta Mater 2009;57:3895–901.

[15] Burk S, Gorr B, Trindade VB, Christ H-J. Effect of Zr addition on the high-temperature oxidation behaviour of Mo-Si-B alloys. Oxid Met 2009;73:163–81.

[16] Majumdar S, Schliephake D, Gorr B, Christ H-J, Heilmaier M. Effect of yttrium alloying on intermediate to high-temperature oxidation behavior of Mo-Si-B alloys. Metall Mater Trans A 2013. http://dx.doi.org/10.1007/s11661-012-1589-3.

[17] Burk S, Gorr B, Christ H-J, Schliephake D, Heilmaier M, Hochmuth C, et al. High-temperature oxidation behaviour of a single-phase $(Mo, Ti)_5Si_3$ (Mo-Si-Ti) alloy. Scr Mater 2012;66:223–6.

[18] Gorr B, Trindade V, Burk S, Christ H-J, Klauke M, Mukherji D, et al. Oxidation behaviour of model cobalt-rhenium alloys during short-term exposure to laboratory air at elevated temperature. Oxid Met 2009;71:157–72.

[19] Burk S. Hochtemperaturoxidation molybdän-basierter Legierungen unter Berücksichtigung von Einfüssen aus Umgebungsatmosphäre und legierungstechnischen Maßnahmen. Ph.D thesis. Siegen: Universität Siegen; 2011.

[20] Mousa M, Wanderka N, Timpel M, Singh S, Kruger M, Heilmaier M, et al. Modification of Mo-Si alloy microstructure by small additions of Zr. Ultramicroscopy 2011;111:706–10.

[21] Poulton DJ, Smeltzer WW. Oxygen diffusion in monoclinic zirconia. J Electrochem Soc 1970;117:378–81.

[22] Fujikawa H, Morimoto T, Nishiyama Y, Newcomb SB. The effects of small additions of yttrium on the high-temperature oxidation resistance of a Si-containing austenitic stainless steel. Oxid Met 2003;59:23–40.

[23] Liu Z, Gao W, He Y. Modeling of oxidation kinetics of Y-doped Fe-Cr-Al alloys. Oxid Met 2000;53:341–50.

[24] Pérez FJ, Cristóbal MJ, Hierro MP, Arnau G, Botella J. Corrosion protection of low-nickel austenitic stainless steel by yttrium and erbium-ion implantation against isothermal oxidation. Oxid Met 2000;54:87–101.

[25] Wu Y, Umakoshi Y, Li XW, Narita T. Isotherma oxidation behavior of Ti-50Al alloy with Y additions at 800 and 900 °C. Oxid Met 2006;66:321–48.

[26] Yang Y, Bei H, Chen S, George EP, Tiley J, Chang YA. Effects of Ti, Zr, and Hf on the phase stability of Mo_ss + $Mo_3Si$ + $Mo_5SiB_2$ alloys at 1600 °C. Acta Mater 2010;58:541–8.

[27] Berkowitz-Mattuck JB, Dils RR. High-temperature oxidation: II. Molybdenum silicides. J Electrochem Soc 1965;112:583–9.

[28] Bartlett RW, McCamont JW, Gage PR. Structure and chemistry of oxide films thermally grown on molybdenum silicides. J Am Ceram Soc 1965;48:551–8.

[29] Li B, Gleeson B. Effects of silicon on the oxidation behavior of Ni-base chromia-forming alloys. Oxid Met 2006;65:101–22.

[30] Przybylski K, Szwagierczak D. Kinetics and mechanism of high-temperature oxidation of dilute cobalt-chromium alloys. Oxid Met 1982;17:267–95.

[31] Evans HE, Donaldson AT, Gilmour TC. Mechanisms of breakaway oxidation and application to a chromia-forming steel. Oxid Met 1999;52:379–402.

[32] Durham R, Gleeson B, Young DJ. Silicon contamination effects in the oxidation of carbide-containing cobalt-chromium alloys. Mater Corros 1998;49:855–63.

[33] Hou PY, Stringer J. Effect of internal oxidation pretreatments and Si contamination on oxide-scale growth and spalling. Oxid Met 1990;33:357–69.

[34] Jones DE, Stringer J. The effect of small amounts of silicon on the oxidation of high-purity Co-25 wt. % Cr at elevated temperatures. Oxid Met 1975;9:409–13.

[35] Liu Y, Wei W, Benum L, Oballa M, Gyorffy M, Chen W. Oxidation behavior of Ni-Cr-Fe-based alloys: effect of alloy microstructure and silicon content. Oxid Met 2009;73:207–18.

[36] Gorr B, Burk S, Depka T, Somsen C, Abu-Samra H, Christ H-J, et al. Effect of Si addition on the oxidation resistance of Co-Re-Cr-alloys: recent attainments in the development of novel alloys. Int J Mater Res 2012;2012:24–30.

[37] Wang L, Gorr B, Christ H-J, Mukherji D, Rösler J. Optimization of Cr-content for high-temperature oxidation behavior of Co-Re-Si-base alloys. Oxid Met 2013. http://dx.doi.org/10.1007/s11085-013-9369-z.

[38] Gorr B, Burk S, Trindade V, Christ H-J. The effect of pre-oxidation treatment on the high-temperature oxidation of Co-Re-Cr model alloys at laboratory air. Oxid Met 2010;74:239–53.

[39] Heilmaier M, Krüger M, Saage H, Rösler J, Mukherji D, Glatzel U, et al. Metallic materials for structural applications beyond nickel-based superalloys. JOM J Min Met Mat Soc 2009;61:61–7.

[40] Ping DH, Cui CY, Gu YF, Harada H. Microstructure of a newly developed gamma′ strengthened Co-base superalloy. Ultramicroscopy 2007;107:791–5.

[41] Berthod P. Kinetics of high temperature oxidation and chromia volatilization for a binary Ni-Cr alloy. Oxid Met 2005;64:235–52.

[42] Kofstad P, Lillerud KP. Chromium transport through $Cr_2O_3$ scales I. On lattice diffusion of chromium. Oxid Met 1982;17:177–94.

[43] Han S, Young DJ. Simultaneous internal oxidation and nitridation of Ni-Cr-Al alloys. Oxid Met 2001;55:223–42.

# Manuskript X

## Phase equilibria, microstructure, and high temperature oxidation resistance of novel refractory high-entropy alloys

B. Gorr, M. Azim, H.-J. Christ, T. Mueller, D. Schliephake, M. Heilmaier

Journal of Alloys and Compounds, 624 (2015) 270-278

Journal of Alloys and Compounds 624 (2015)

Contents lists available at ScienceDirect

Journal of Alloys and Compounds

journal homepage: www.elsevier.com/locate/jalcom

# Phase equilibria, microstructure, and high temperature oxidation resistance of novel refractory high-entropy alloys

B. Gorr [a,*], M. Azim [a], H.-J. Christ [a], T. Mueller [b], D. Schliephake [c], M. Heilmaier [c]

[a] *Institut für Werkstofftechnik, Universität Siegen, Paul-Bonatz-Str. 9-11, 57068 Siegen, Germany*
[b] *Institut für Bau- und Werkstoffchemie, Universität Siegen, Paul-Bonatz-Str. 9-11, 57068 Siegen, Germany*
[c] *Institut für Angewandte Materialien – Werkstoffkunde (IAM-WK), Karlsruhe Institute of Technology (KIT), Engelbert-Arnold-Str. 4, D-76131 Karlsruhe, Germany*

ARTICLE INFO

*Article history:*
Received 8 October 2014
Received in revised form 30 October 2014
Accepted 1 November 2014
Available online 8 November 2014

*Keywords:*
High temperature material
High entropy alloy
Refractory element
Microstructure

ABSTRACT

A new refractory high-entropy alloy system Mo–W–Al–Cr–x is proposed as a family of candidate materials for structural applications at high temperatures. Thermodynamic assessment was used to set the chemical composition of the first alloy as 20Mo–20W–20Al–20Cr–20Ti (at.%) with a calculated melting temperature of about 1700 °C. A single disordered BCC phase should be stable at high temperatures between 1077 °C and 1700 °C. Microstructural examination and XRD results clearly show that the alloy in the as-cast condition exhibits a non-homogeneous microstructure with pronounced dendritic and interdendritic regions. Heat treatment processes, however, reveal a strong tendency of the alloy 20Mo–20W–20Al–20Cr–20Ti to homogenize. While possessing a high hardness of around 800HV, the crack-free indents allow the assumption that the alloy studied may be intrinsically ductile at room temperature. Despite the fact that the alloy possesses 40 at.% of refractory elements, high temperature oxidation tests show a surprisingly good oxidation resistance. Strategies to enhance the long-term stability of the disordered BCC phase aiming at achieving the required mechanical properties as well as optimizing the alloy's chemical composition in terms of high temperature oxidation resistance are discussed.

## 1. Introduction

A new alloying concept, originally proposed by Yeh et al., induced the development of various high-entropy alloys (HEAs) [1]. For these materials, a single-phase solid solution strengthened microstructure is targeted. So far, the international activities to design, characterize, and optimize HEAs are mainly focused on the alloy system Fe–Co–Ni–Cr–x (x = Mn, Cu, Al, Ti, etc.) which crystallizes in a face centered cubic (FCC) structure. For this alloy system, extensive investigations on microstructure of polycrystals as well as single crystals, phase stability, identification of hardening mechanisms, and mechanical properties at room temperature as well as at elevated temperatures have been carried out [2–7]. The second distinctive alloy family of HEAs is nearly exclusively based on refractory metals (RM), such as W, Mo, Nb, Ta, typically crystallizing in body centered cubic (BCC) structure. Due to the well-known high melting point of RM, alloys manufactured from these elements seem to be very promising for applications at very high service temperatures [8]. Outstanding values were reported for yield strength of Nb–Mo–Ta–W and V–Nb–Mo–Ta–W alloys at temperatures of up to 1600 °C [9]. To reduce the strikingly high alloy density, some heavy refractory elements were substituted by lighter elements, such as Zr and Ti [10].

In the present work, along the line of the second alloy system approach, we aim for a new high-entropy alloy system containing refractory elements. The prime incentive of this study is to develop novel high temperature materials, the alloying concept of which is generally based on alloy design principles of HEAs. The alloy system containing refractory elements should possess the following property combination: (i) a melting point exceeding those of Ni-based superalloys by at least 200 K, (ii) a good long-term high temperature strength, (iii) oxidation protectiveness at temperatures of at least 1000 °C, and (iv) a density <10 g/cm$^3$. In the first part of this paper, the alloy design concept will be presented. Following, the microstructure of the alloy in the as-cast condition as well as the microstructure after heat treatments will be discussed. Next, results of hardness measurements will be shown to give first insights into the ductility of the alloy at room temperature. Finally, results of oxidation experiments will be presented to allow a concise characterization of high temperature oxidation protectiveness.

---

* Corresponding author. Tel.: +49 2717404653.
*E-mail address:* gorr@ifwt.mb.uni-siegen.de (B. Gorr).

http://dx.doi.org/10.1016/j.jallcom.2014.11.012
0925-8388/© 2014 Elsevier B.V. All rights reserved.

## 2. Alloy design concept

The presented approach here is rather simple: four main elements will be set, building a core alloy system which may be expanded gradually by adding further alloying elements to fulfill the requirements mentioned above. Firstly, the majority of these elements should exhibit a high melting point. Secondly, most of the elements composing the HEAs to be developed should possess the same lattice structure, at least at the anticipated high temperatures, to facilitate the formation of a single-phase solid solution. With respect to these two constraints, it seems reasonable that Mo and W, both BCC, can be considered as prime candidates for the new alloy system. Due to their chemical similitude, they form a continuous solid solution [11]. Unfortunately, both, Mo and W, show a very poor high temperature oxidation resistance, so-called catastrophic oxidation, due to the formation of gaseous oxides [12]. In order to potentially enable the formation of a protective oxide scale on the metallic surface and, consequently, to ensure the alloy protectiveness, Al and Cr will be added to the core alloy system. The addition of both elements, Al and Cr, is essentially aimed at the formation of an alumina layer that maintains its highly protective properties also at temperatures above 1000 °C [13]. In terms of high temperature oxidation, Cr effectively supports the formation of a continuous alumina scale in many alumina forming high temperature alloys [13]. While Cr also fulfills the requirement of having the same BCC structure as W and Mo, Al possesses the FCC lattice structure. However, it was found not only in other HEA systems such as $Al_x$CoCrFeNi, but also in steels that Al acts as a strong BCC stabilizer [6,14]. Thus, it may be expected that Al addition to new refractory HEAs might not deteriorate the formation of a single phase BCC structure.

Most refractory elements exhibit a rather high density. This feature is undesirable and, consequently, confining for many practical applications. In order to reduce the density of the new alloy system further, Ti may be added. In addition, Ti possesses the BCC lattice at temperatures above 882 °C. Therefore, it may be assumed that Ti additions would also in our alloy support the formation of a single BCC phase, at least at targeted temperatures beyond about 1000 °C. Thus, the first equimolar refractory high-entropy alloy proposed within the core alloy system determined previously consists of 20Mo–20W–20Al–20Cr–20Ti.

Since the alloy 20Mo–20W–20Al–20Cr–20Ti represents the first candidate from the new material family Mo–W–Al–Cr–x, it was considered indispensable to combine experimental investigations with theoretical evaluations, which use thermodynamic calculations. Table 1 shows phases which can form in the corresponding binary, ternary, quaternary, and quinary systems at 1100 °C. Thermodynamic calculations were carried out using the software FactSage V6.4 in conjunction with a commercial database which includes the following elements: Mo, W, Al, Cr, Ti, O Results of these calculations clearly show that except two binary systems, Al–Ti and Mo–Al, the BCC phase is the solid-solution phase forming in all investigated combinations. In the binary Cr–Ti system, the ordered Laves phase (C15 crystal structure) can form along with the BCC phase, while two ternary systems, W–Cr–Al and Mo–Al–Ti, exhibit additional solid solution phases, designated B2B and CUB_A15, respectively. It is obvious that all binary systems containing Al and the majority of ternary alloys with Al form intermetallic compounds, predominantly TiAl (see Table 1). Furthermore, all ternary systems containing the two elements, Ti and Al, as well as the majority of quaternary systems which include Ti and Al may form the well known TiAl intermetallic compound. It is obvious that this intermetallic compound may exhibit a very high thermodynamic stability. However, in the quinary alloy, TiAl seems to become rather unstable from a thermodynamic point of view and the BCC phase is the only phase which can form at 1100 °C.

**Table 1**
Phases in the equimolar metallic systems.

| Systems | Solid-solution phases | Intermetallic compounds |
|---|---|---|
| Mo–W | BCC | |
| Mo–Cr | BCC | |
| Mo–Ti | BCC | |
| W–Cr | BCC | |
| W–Ti | BCC | |
| Cr–Ti | BCC + LAVES_C15 | |
| Al–Ti | | TiAl |
| Mo–Al | | $Mo_3Al + Mo_3Al_8$ |
| W–Al | BCC | $WAl_4$ |
| Cr–Al | BCC | $Cr_5Al_8$ |
| Mo–W–Cr | BCC | |
| Mo–W–Ti | BCC | |
| Mo–Cr–Al | BCC | |
| Mo–Cr–Ti | BCC | |
| W–Cr–Ti | BCC | |
| W–Cr–Al | BCC + B2B | |
| W–Al–Ti | BCC | TiAl |
| Cr–Al–Ti | BCC | TiAl |
| Mo–Al–Ti | BCC + CUB_A15 | TiAl |
| Mo–W–Al | BCC | $Mo_3Al_8$ |
| Mo–W–Cr–Al | BCC | |
| Mo–W–Cr–Ti | BCC | |
| Mo–Cr–Al–Ti | BCC | |
| Mo–W–Cr–Ti | BCC | |
| Mo–W–Al–Ti | BCC | TiAl |
| W–Cr–Al–Ti | BCC | TiAl |
| Mo–W–Al–Cr–Ti | BCC | |

Fig. 1 shows fraction of phases which may be formed under equilibrium conditions in the alloy 20Mo–20W–20Al–20Cr–20Ti in the wide temperature range from 200 °C to 2000 °C. One intermetallic compound, TiAl, and four solid-solution phases, i.e. BCC, B2B, CUB, and sigma, can be formed below the melting temperature. It is worth noting that the BCC phase is the only phase that is stable between 1077 °C and the melting point, while the intermetallic compound is only stable within a very narrow temperature range from 935 °C to 1077 °C, the CUB phase becomes thermodynamically unstable above 780 °C, and both, the sigma and B2B phases seem to transform into the BCC phase above 1000 °C. Most importantly, the chosen alloy has a melting point of $T_m$ = 1700 °C that is considerably higher (at least 250 K) than those of commercial Ni-based alloys.

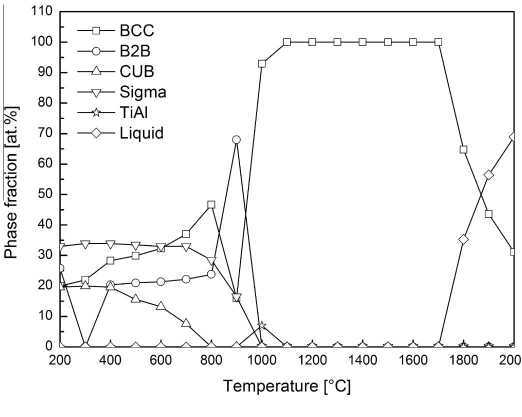

**Fig. 1.** Equilibrium phase distribution in the alloy 20Mo–20W–20Al–20Cr–20Ti (calculated by FactSage).

Further, it is of interest to know the elemental partitioning between the phases possibly present in the alloy as shown in Fig. 1. This knowledge will be useful for further alloy development, since an undesirable phase may be eliminated by lowering the concentration of the corresponding element or even by its complete substitution by another element. Fig. 2 shows the elemental distribution in the respective phases as displayed in Fig. 1 at 700 °C. Thermodynamic calculations clearly reveal that the disordered BCC phase is rich in W and Mo at this temperature, while the ordered cubic B2B phase is primarily rich in Cr. Al and Ti are the main elements present in the sigma phase, whereas the CUB phase with the ordered A15 crystal structure, generally exhibits the composition $(Mo,Ti)_3Al$, however, being enriched in Mo.

### 3. Experimental

The alloy 20Mo–20W–20Al–20Cr–20Ti was produced from elemental bulk aterials by arc-melting in ~0.6 atm of argon utilizing an arc-melter AM 0.5 by Edmund Bühler GmbH. The purities of the starting materials Mo, W, Al, Cr and Ti were 99.9%, 99.96%, 99.9%, 99% and 99.8%, respectively. Gaseous impurities such as oxygen and nitrogen were generally found to be on a very low level, with the used titanium being of significantly higher purity than commercial Ti grade 1 in particular. The prepared buttons had a mass of ~25 g and were flipped over and remelted more than five times in a water-chilled copper mold to ensure homogenization of the alloying elements. Heat treatments were carried out in protective Ar atmosphere using a tube furnace (Gero GmbH) at temperatures up to 1200 °C.

The microstructure of the samples in the as-cast condition as well as after heat treatment processes was analyzed using a FIB-SEM DualBeam System of type FEI Helios Nanolab 600 equipped with BSE and EDS detector. The crystal structure was identified by using of the Panalytical X′Pert pro MPD X-ray diffractometer applying Cu Kα radiation. Vickers microhardness was measured on polished cross-sectional surfaces using a 136° Vickers diamond pyramid with a load of 100 g applied for 12s (Struers Duramin-1/-2 device). For the oxidation test, one specimen of dimension of approximately 10 mm × 10 mm × 10 mm was cut from the bar in the as-cast condition and polished up to 1000 grit. The specimen was ultrasonically cleaned in ethanol directly before testing in a Rubotherm thermogravimetric system. The morphology and composition of corrosion products was analyzed using the same experimental techniques as mentioned above.

## 4. Results

### 4.1. Microstructure

One of the severe limitations of the thermodynamic calculations results from the fact that they assume thermodynamic equilibrium. However, this assumption is often not fulfilled, since kinetics plays an important role in the development of the microstructure and, consequently, in determining the alloy properties. For this reason, experimental investigations on the material microstructure in different conditions, i.e. in the as-cast condition and after heat treatments, were carried out. Fig. 3 shows the microstructure of the alloy 20Mo–20W–20Al–20Cr–20Ti in the as-cast condition. The alloy exhibits a dendritic microstructure which is typical of many HEAs [15]. The dendrites are slightly branched and rather rounded in shape. The EDX analysis reveals that preferentially W and partially Mo segregate to the dendrite arms, while the interdendritic regions are rich in the lighter elements Al, Cr, Ti, and, to a minor extent, in Mo (see Fig. 4). Hence, it can be assumed that the alloy in the as-cast condition either forms two phases with different crystal structures, or both dendritic and interdendritic regions possess the same crystal structure, but different chemical compositions due to segregation effects of the heavy and high melting elements, W and Mo. To clarify the last point, the cast alloy 20Mo–20W–20Al–20Cr–20Ti was solution heat treated for 20 h and 40 h at 1200 °C, respectively.

Fig. 5 shows the microstructure of the alloy 20Mo–20W–20Al–20Cr–20Ti after solution heat treatments at 1200 °C for 20 h and

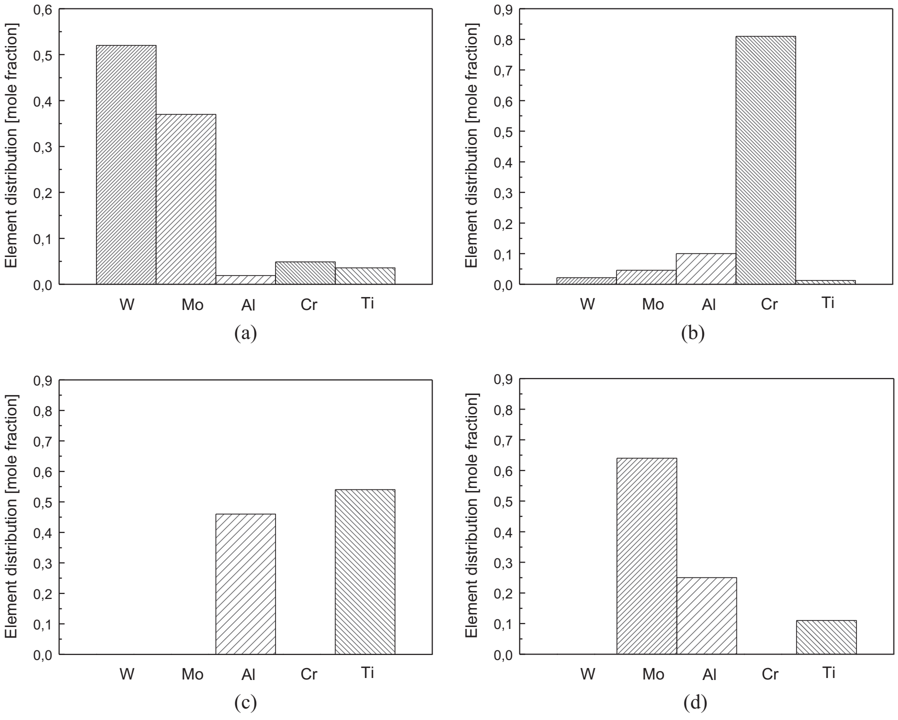

**Fig. 2.** Element distribution in the phases of the alloy 20Mo–20W–20Al–20Cr–20Ti at 700 °C; (a) BCC phase, (b) B2B phase, (c) sigma phase, and (d) CUB phase.

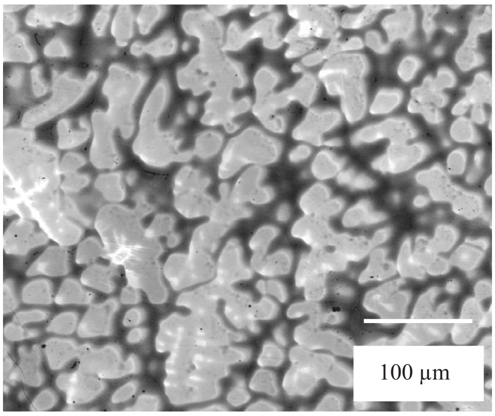

**Fig. 3.** Microstructure of the alloy 20Mo–20W–20Al–20Cr–20Ti in the as-cast condition (SEM BSE mode).

40 h (Fig. 5(a)) and 40 h (Fig. 5(b), respectively). It is obvious that the annealing at 1200 °C leads to a pronounced homogenization of the alloy microstructure. After 20 h only some small separate islands rich in W and Mo (former dendrites) are visible, with their size being substantially decreased compared to that formed in the as-cast condition (compare Figs. 3 and 5(a)). After 40 h of annealing at 1200 °C the alloy microstructure appears to be nearly homogeneous. Small black dots were identified as contaminations arising from the manufacturing process.

In order to characterize the development of the alloy microstructure further, X-ray diffraction (XRD) measurements were carried out on two samples, in the as-cast condition and after 40 h of heat treatment at 1200 °C, see Fig. 6. Both XRD plots have been corrected for background noise and the measured intensities are plotted in a linear fashion. The analyses on both samples show five strong peaks in the $2\theta$-range from 15° to 120°. However, higher magnifications reveal ambiguous shoulder peaks on the left side of all diffraction peaks with high intensity (see the insertion with the higher magnification, Fig. 6). To fit the peak shape, the insertion of an additional peak arranged extremely close to the main peak was necessary, indicating that the alloy in the as-cast condition as well as after the heat treatment apparently comprises two different BCC phases. One of these two BCC phases in the sample in the as-cast condition possesses a derived lattice constant of 3.1033 Å, while the second BCC phase reveals a lattice parameter of 3.116 Å. The corresponding lattice parameters determined on the sample after 40 h of heat treatment at 1200 °C are 3.0934 Å and 3.1015 Å for

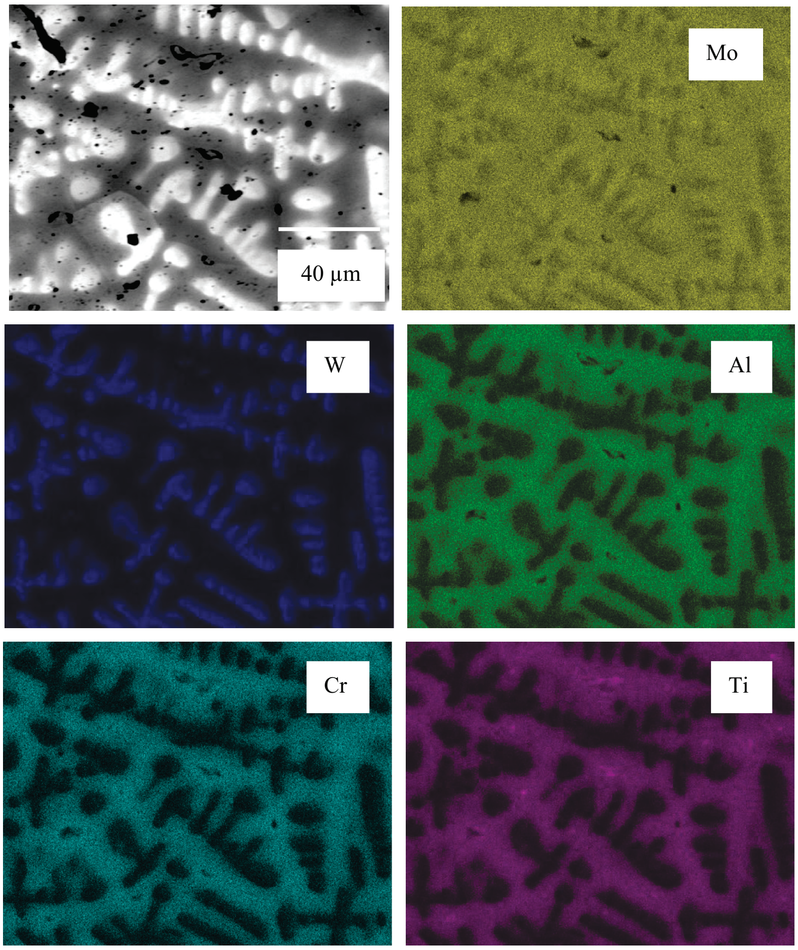

**Fig. 4.** Element distribution in the alloy 20Mo–20W–20Al–20Cr–20Ti in the as-cast condition.

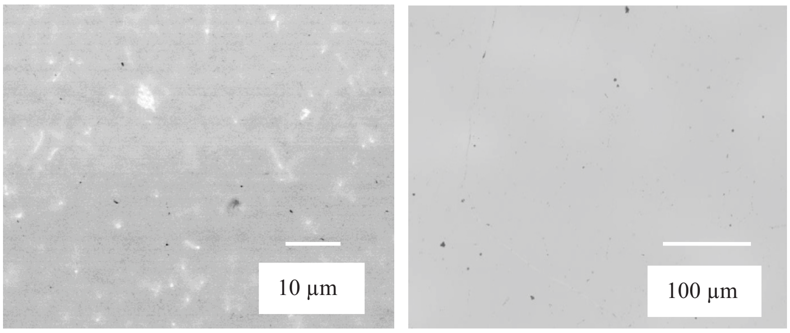

(a) (b)

**Fig. 5.** Effect of heat treatment processes on the microstructure of the alloy 20Mo–20W–20Al–20Cr–20Ti; (a) microstructure after 20 h of heat treatment at 1200 °C, (b) microstructure after 40 h of heat treatment at 1200 °C, both SEM BSE mode.

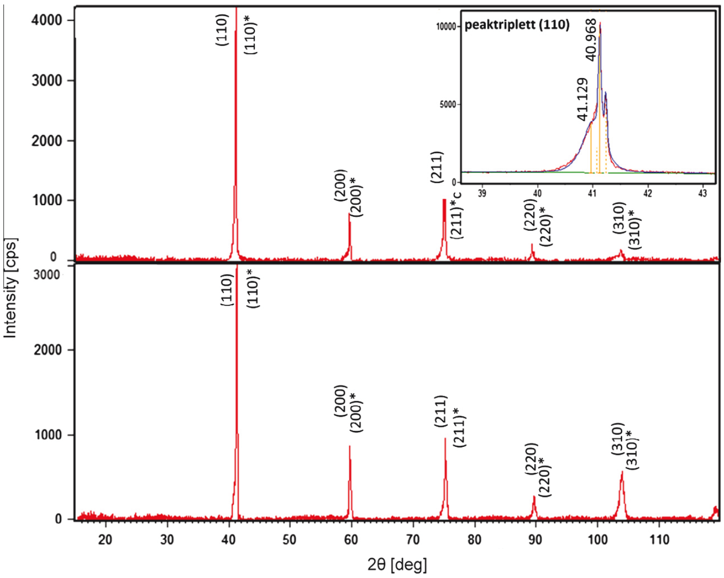

**Fig. 6.** XRD patterns of the alloy 20Mo–20W–20Al–20Cr–20Ti: (top) in the as-cast condition and (bottom) after 40 h of heat treatment at 1200 °C.

the first BCC phase and the second BCC phase, respectively. It is obvious that the marginal difference in the lattice constants between two BCC phases detected on the sample in the as-cast condition decreases further for the sample after heat treatment supporting the conclusion drawn from the thermodynamic calculations that a single BCC phase prevails after complete homogenization. The sole presence of disordered BCC phase(s) was also confirmed by additional inspection of the measured intensities in the XRD patterns by plotting on a logarithmic scale (not shown here): no additional peaks due to further phases could be detected.

### *4.2. Hardness measurement*

Hardness measurements should provide first insights into the mechanical properties of the alloy at room temperature. The hardness indentation in Fig. 7(a) exemplarily carried out on the as-cast sample clearly demonstrates the ductile nature of the alloy since cracks were neither detected in the dendrites nor in the interdendritic areas. As expected, the W- and Mo-rich dendrites exhibit much higher hardness values compared to the interdendritic areas and the spread of the hardness values is substantial. Clearly, these values can be grouped into two categories in terms of the dendritic and the interdendritic regions, respectively, as shown in Fig. 7(b). The mean hardness value of the dendrites is about 685 HV, while the corresponding value for the interdendritic regions is about 330 HV. By contrast, the hardness values measured on the sample after 40 h annealing at 1200 °C lie with 802 ± 10 HV0.1 very close together (see Fig. 7(c)) indicating a significantly more homogeneous microstructure. These results are in good agreement with the microstructural analysis shown above.

### *4.3. Oxidation behavior*

As mentioned above, the oxidation behavior is a crucial feature for alloys containing refractory metals. Since the alloy 20Mo–20W–20Al–20Cr–20Ti contains 40 at.% of refractory elements (20 at.% Mo and W each), it is of interest to explore the potential of this alloy regarding the high temperature oxidation resistance.

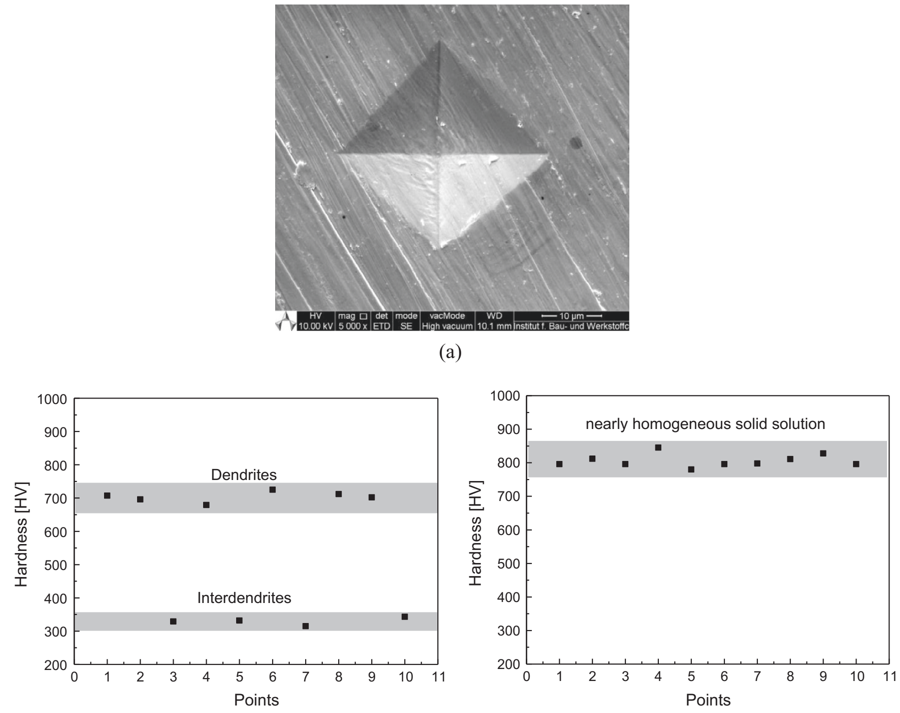

(a)

(b)

(c)

**Fig. 7.** Hardness measurement; (a) top view of a hardness indent, (b) hardness values of the alloy 20Mo–20W–20Al–20Cr–20Ti in the as-cast condition, and (c) hardness values of the alloy 20Mo–20W–20Al–20Cr–20Ti after 40 h of heat treatment at 1200 °C.

Fig. 8 shows the mass change of the alloy 20Mo–20W–20Al–20Cr–20Ti in the as-cast condition during 40 h of exposure to laboratory air at 1000 °C. The kinetic curve obviously obeys the parabolic rate law indicating that the growth of the oxide scale proceeds through solid state diffusion. Further, considering the position of the thermogravimetric curve at positive values and its positive slop, it can be assumed that the evaporation of Mo and W oxides during the oxidation process is either negligibly small or entirely inhibited by the oxide layer formed on the metallic substrate. However, it should be pointed out that despite the parabolic trend of the kinetic curve the mass gain after 40 h of exposure is significant compared to state-of-the-art Ni-based superalloys [13].

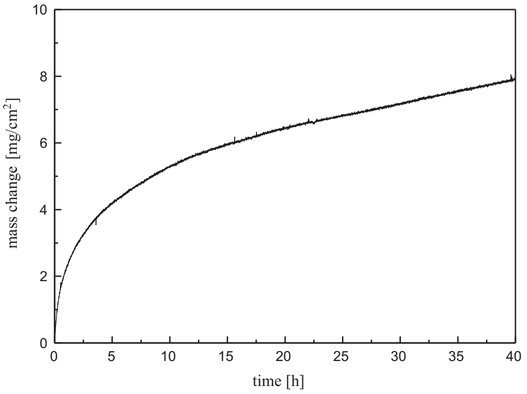

**Fig. 8.** Mass change of the alloy 20Mo–20W–20Al–20Cr–20Ti during exposure to laboratory air at 1000 °C.

Fig. 9 shows micrographs of a cross-section as well as the EDX element distributions of the alloy 20Mo–20W–20Al–20Cr–20Ti after 40 h exposure to air at 1000 °C. The formation of a rather inhomogeneous and porous oxide scale on the surface is characteristic of the alloy. The metallic substrate is covered by a mixed oxide which primarily consists of Al, Cr, and Ti oxides. In addition, this oxide layer exhibits a slight tendency to spalling. Despite the fact that the scale formed on the surface consists of a mixed oxide, several prospective features can be found. Firstly, the thickness of the oxide scale is rather moderate (about 23 µm), indicating the relatively slow diffusion rates in the oxide scale. Secondly, EDX element distribution micrographs clearly show that a semi-continuous $Cr_2O_3$ scale forms on the interface oxide/substrate, underpinning the potential ability of the alloy to form a protective oxide scale. Thirdly, the EDX analysis evidently indicates that only negligibly small amounts of Mo and W were detected in the oxide scale, suggesting that the alloy does not suffer from catastrophic oxidation.

## 5. Discussion

The concept of HEAs postulates the preferential formation of a disordered, ideally single-phase, solid solution microstructure in equimolar HEAs, while the formation of brittle intermetallic compounds should be inhibited in consequence of thermodynamic driving forces [1]. In reality, in addition to disordered solid solutions, HEAs quite often form other phases, such as ordered solid solutions, amorphous phases and even intermetallic compounds [4]. This may indicate that in many cases the simple HEA concept is at least debatable. The development of the alloy

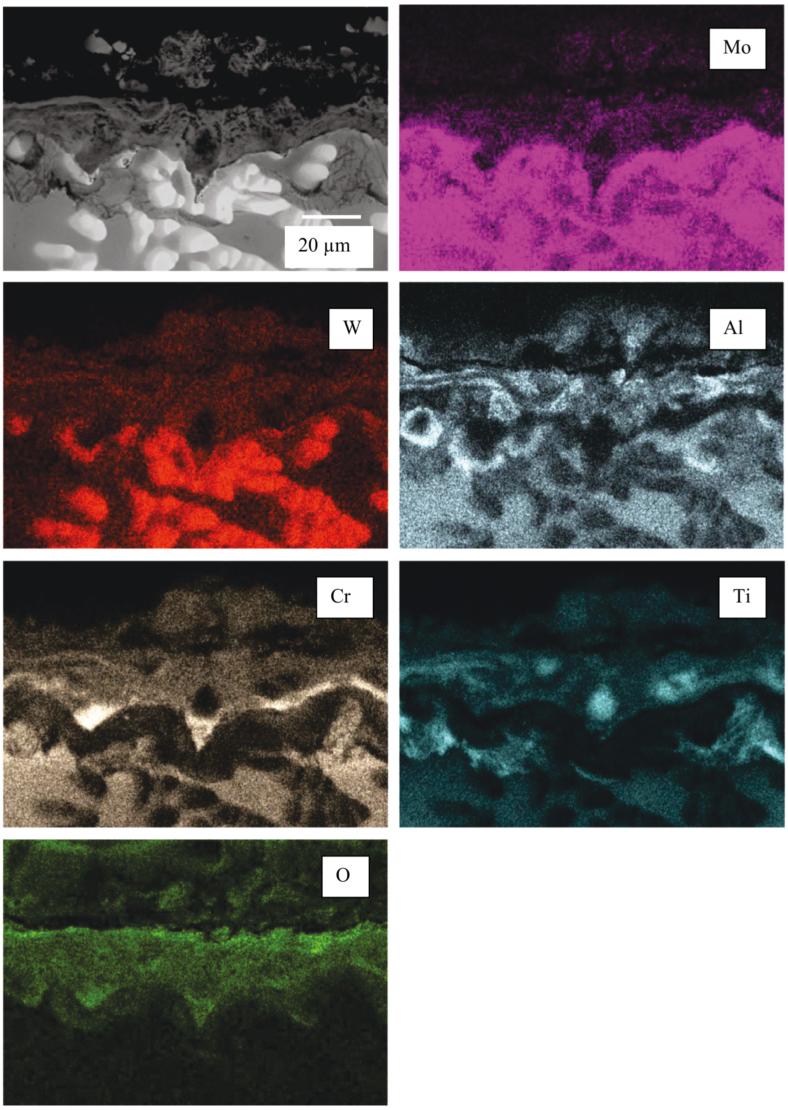

**Fig. 9.** Cross-section and corresponding EDX element distribution micrographs of the alloy 20Mo–20W–20Al–20Cr–20Ti after exposure to laboratory air at 1000 °C for 40 h.

20Mo–20W–20Al–20Cr–20Ti also aimed at the formation of a simple-single phase microstructure. The results of the microstructural analysis shown above reveal that our alloy obviously tends to form a disordered body centered cubic crystal structure at high temperatures upon annealing. XRD measurements clearly show that the difference in lattice constant between two crystal structures diminishes for the sample after the heat treatment supporting the conclusion from the thermodynamic calculations that only one BCC phase should form in the alloy after appropriate heat treatment. After the applied heat treatment of 40 h at 1200 °C, however, the alloy still reveals inhomogeneity in the chemical composition on atomic scale due to insufficient intermixing of the atoms with substantially different radii. This can either cause locally varying lattice distortions within a single BCC phase or the presence of two BCC phases with only slightly different lattice constants. Hence, the assumed incomplete homogenization leaves potential for further optimization in order to achieve a truly single-phase and, hence, homogeneous microstructure. In this regard, further heat treatments as well as extensive microstructural investigations will be carried out in future work.

Although the alloy 20Mo–20W–20Al–20Cr–20Ti tends to possess a rather simple microstructure consisting of the two BCC phases, the thermodynamic calculations shown in Fig. 1 reveal that the formation of a small amount (about 7 at.%) of an intermetallic compound TiAl is possible within the temperature range from 935 °C to 1077 °C. To clarify whether TiAl forms in the alloy at 1000 °C, further XRD measurements were carried out on a sample annealed for 24 h at 1000 °C. However, no TiAl was detected utilizing XRD which is assumed to be caused by the sluggish kinetics in this alloy at 1000 °C as well as due to the relatively short time of the annealing process. Thus, the formation of the TiAl phase in the alloy seems to be inhibited.

In order to identify the critical concentration of Al that must be deceeded to suppress the intermetallic compound TiAl in the alloy

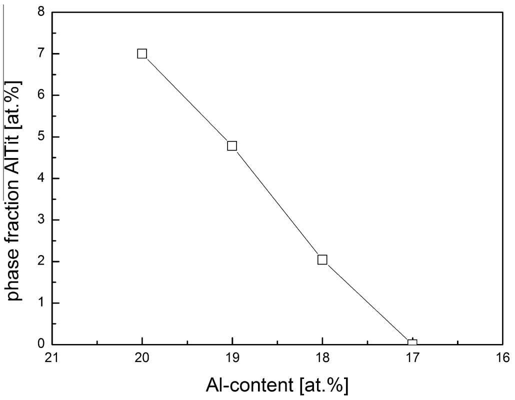

**Fig. 10.** Change of the phase fraction of the intermetallic compound TiAl with decreasing Al content in the alloy system Mo–W–Al–Cr–Ti at 1000 °C.

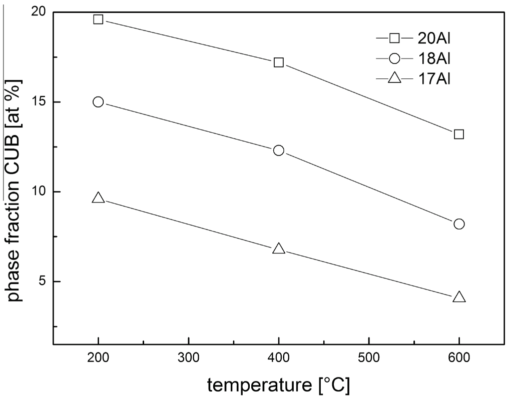

**Fig. 11.** Effect of Al content on the phase fraction of the CUB phase in the alloy system Mo–W–Al–Cr–Ti at different temperatures.

20Mo–20W–20Al–20Cr–20Ti, additional thermodynamic calculations were carried out. In these calculations, the amount of Al was varied, while the concentrations of all other elements in the alloy were kept equal and calculated as $(100 - c^{Al})/4$. Fig. 10 proofs that the formation of the intermetallic compound TiAl can be avoided completely if the Al concentration in the alloy is set to 17 at.%.

Likewise, Al plays an important role for the formation of the ordered CUB phase, which is found in the thermodynamic calculations to be stable in the alloy 20Mo–20W–20Al–20Cr–20Ti in the temperature range from room temperature up to 800 °C. Fig. 11 shows that a slight reduction of the Al content from 20 down to 17 at.% also yields a significant decrease of the phase fraction of the CUB phase, e.g. at 600 °C from roughly 13 to 4 at.%. Additionally, lowering of the Al concentration in this alloy system causes a shrinkage of the field of thermodynamic stability for the CUB phase leading to a shift to lower temperatures. Since the diffusion processes are very slow at such low temperatures, the formation of the CUB phase seems to be strongly inhibited. This explains, why the phase was not observed in this study.

On the one hand, the results of thermodynamic calculations regarding the Al effect on the phase stability in the alloy system Mo–W–Al–Cr–Ti indicate that lowering the Al concentration may be beneficial in terms of the alloy microstructure since the amount of the TiAl and CUB phases can be reduced significantly or their formation can even be suppressed. On the other hand, besides the suppression of some ordered phases, the formation of the disordered BCC solid solution was of paramount importance. Fig. 12 shows the effect of the Al content on the Gibbs free energy of the BCC phase within the temperature range from 200 to 1700 °C. Clearly, the calculated increase of the Gibbs free energy with decreasing Al concentration is marginal. Thus, it can be assumed that lowering of the Al content in the alloy system Mo–W–Al–Cr–Ti, at least from 20 to 17 at.%, will cause no significant change of the thermodynamic stability of the disordered BCC phase.

High temperature oxidation experiments displayed that though the oxidation kinetics follows the parabolic rate law, the oxidation rate is rather high. In fact, the high temperature oxidation resistance of the alloy 20Mo–20W–20Al–20Cr–20Ti may be improved by the formation of a dense and continuous oxide layer, either $Al_2O_3$ or $Cr_2O_3$. The cross-sectional analysis of an oxidized sample

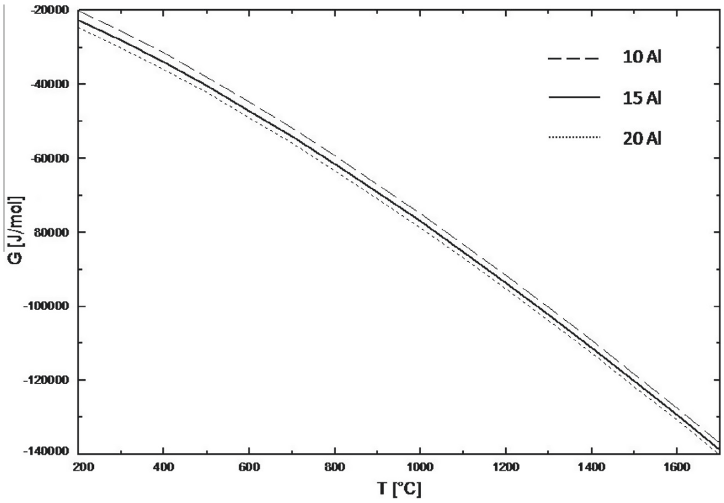

**Fig. 12.** Effect of Al content on the Gibbs energy of the BCC phase in the alloy system Mo–W–Al–Cr–Ti at different temperatures.

(Fig. 9) clearly reveals that no protective oxide scale, neither $Al_2O_3$ nor $Cr_2O_3$, is formed on the metallic surface. While a discontinuous layer of $Cr_2O_3$ is clearly visible at the interface oxide/substrate, $Al_2O_3$ was only found as a constituent of the thick oxide scale that represents a mixture of diverse oxides, such as $TiO_2$, $Al_2O_3$, $Cr_2O_3$ and $WO_3$. Numerous studies on high temperature oxidation behavior of different alloys concluded that the formation of a highly protective oxide layer consisting of a single oxide is substantially impeded if oxides form, which exhibit similar thermodynamic stabilities. It is, for example, surprising that TiAl alloys containing high Al concentrations from 35 at.% to 50 at.% do not form a protective $Al_2O_3$ scale. Instead, a thick and porous oxide layer consisting of a mixture of $Al_2O_3$ and $TiO_2$ forms on the metallic surface leading to high oxidation rates [16]. Here, both oxides, $Al_2O_3$ and $TiO_2$, show very similar thermodynamic stabilities and, thus, the same behavior prevails in the alloy 20Mo–20W–20Al–20Cr–20Ti.

Becker et al. investigated the effect of different additional elements on the oxidation protectiveness of TiAl alloys. It was found that only Nb containing alloys formed a long-lasting, protective $Al_2O_3$ layer [16]. Stroosnijder et al. reported the strong beneficial effect of Nb ion implantation on the high temperature oxidation resistance of the $\gamma$-TiAl-based alloy Ti–48Al–2Cr [17]. This process facilitates the formation of a $Al_2O_3$ scale notably enhancing the oxidation protectiveness of the alloy. One can speculate whether Nb has the same positive effect on the oxidation behavior of the alloy 20Mo–20W–20Al–20Cr–20Ti. In addition, Nb exhibits a BCC crystal structure as most of the elements in the alloy 20Mo–20W–20Al–20Cr–20Ti. Thus, it can be supposed that no additional complex phases form in the alloy. Further, thermodynamic assessments as well as ensuing experiments will be needed to verify these hypotheses.

## 6. Conclusions

In this paper, a new refractory high-entropy alloy system Mo–W–Al–Cr–x was proposed as a perspective candidate for applications at high temperatures. Neither thermodynamic nor experimental data have been published yet on this system. The alloy 20Mo–20W–20Al–20Cr–20Ti from this system was investigated with respect to phase stability, alloy microstructure, mechanical properties at room temperature, and high temperature oxidation behavior. The following characteristics of this alloy can be summarized:

1. Thermodynamic calculations were used as a powerful means to define and confirm the suitable chemical composition of the alloy 20Mo–20W–20Al–20Cr–20Ti. The calculated melting temperature of the alloy is about 1700 °C. According to the results of the thermodynamic calculations, the BCC phase is the only phase which is stable at temperatures above 1100 °C. Three solid solutions and the intermetallic compound TiAl possibly form at lower temperatures. A reduction of the Al content in the alloy down to 17 at.% would, however, entirely prevent the formation of the intermetallic compound TiAl. Additionally, the reduction of the Al concentration may induce a significant decrease of the phase fraction of the ordered CUB phase. Concurrently, the thermodynamic stability of the solid-solution BCC phase seems to remain nearly unaffected.
2. The alloy exhibits a dendritic microstructure in the as-cast condition which is typical of many HEAs. Microstructural analysis reveals that preferentially W and partially Mo segregate to dendrites, while the interdendritic regions are rich in Al, Cr, Ti, and, to some extent, in Mo. The corresponding heat treatments lead to a homogenization of the alloy. XRD measurements show that either two BCC phases with slightly different lattice constants or even one BCC phase with a fluctuating lattice distortion form in the alloy in the as-cast conditions as well as after homogenization. This can probably be attributed to the incomplete homogenization of the alloy after annealing. Further investigations are needed to solve this issue.
3. Hardness measurements of the sample in the as-cast condition show a bifurcation of the hardness values depending on whether dendritic or interdendritic regions were probed, while the hardness values of the sample after annealing are constant with 802 ± 10 HV. In addition, the hardness indentations reveal no cracks in both, the dendritic and interdendritic areas, indicating the potentially ductile behavior of the alloy at room temperature.
4. Although many materials containing refractory metals suffer from severe oxidation, the alloy already reveals a surprisingly good high temperature oxidation resistance. The mass change of the alloy during 40 h of exposure to air at 1000 °C follows the parabolic rate law indicating that the growth of the oxide scale proceeds through solid state diffusion. The evaporation of oxides of refractory elements Mo and W seems to be either negligibly small or entirely inhibited by the oxide layer formed on the alloy. Nevertheless, the oxidation rate is still relatively high. A substitution of Ti by Nb in the alloy may facilitate the formation of a protective $Al_2O_3$ on the metallic substrate, improving the oxidation resistance notably.

## References

[1] J.W. Yeh, S.K. Chen, S.J. Lin, J.Y. Gan, T.S. Chin, T.T. Shun, C.H. Tsau, S.Y. Chang, Nanostructured high-entropy alloys with multiple principal elements, novel alloy design, conceptes and outcomes, Adv. Eng. Mater. 6 (2004) 299–303.

[2] M.R. Chen, S.J. Lin, J.W. Yeh, S.K. Chen, Y.S. Huang, C.P. Tu, Microstructure and properties of $Al_{0.5}CoCrCuFeNiTi_x$ ($x = 0-2.0$) high-entropy alloys, Mater. Trans. 47 (2006) 1395–1401.

[3] S.G. Ma, S.F. Zhang, M.C. Gao, P.K. Liaw, Y. Zhang, A successful synthesis of the $CoCrFeNiAl_{0.3}$ single-crystal, high-entropy alloy by Bridgman solidification, JOM 65 (2013) 1751–1757.

[4] S. Guo, C.T. Liu, Phase stability in high entropy alloys: formation of solid-solution phase or amorphous phase, Prog. Nat. Sci. 21 (2011) 433–446.

[5] Y.J. Zhou, Y. Zhang, Y.L. Wang, G.L. Chen, Microstructure and compressive properties of multicomponent $Al_x(TiVCrMnFeCoNiCu)_{100-x}$ high-entropy alloys, Mater. Sci. Eng. A 454–455 (2007) 260–265.

[6] C. Zhang, F. Zhang, S. Chen, W. Cao, Computational thermodynamics aided high-entropy alloy design, JOM 64 (2012) 839–845.

[7] C.J. Tong, M.R. Chen, S.K. Chen, J.W. Yeh, T.T. Shun, S.J. Lin, S.Y. Chang, Mechanical performance of the $Al_xCoCrCuFeNi$ high-entropy system with multicomponent elements, Metall. Mater. Trans. A 36A (2005) 1263–1271.

[8] O.N. Senkov, G.B. Wilks, D.B. Miracle, C.P. Chuang, P.K. Liaw, Refractory high-entropy alloys, Intermetallics 18 (2010) 1758–1765.

[9] O.N. Senkov, G.B. Wilks, J.M. Scott, D.B. Miracle, Mechanical properties of $Nb_{25}Mo_{25}Ta_{25}W_{25}$ and $V_{20}Nb_{20}Mo_{20}Ta_{20}W_{20}$ refractory high entropy alloys, Intermetallics 19 (2011) 698–706.

[10] O.N. Senkov, J.M. Scott, S.V. Senkova, D.B. Miracle, C.F. Woodward, Microstructure and room temperature properties of a high-entropy TaNbHf ZrTi alloy, J. Alloys Comp. 509 (2011) 6043–6048.

[11] Landolt-Börnstein, Binary Systems Form Mn–Mo to Y–Zr. Phase Diagrams, Phase Transition Data, Integral and Partial Quantities of Alloys, Springer, Berlin, Heidelberg, 2006 (Part 4).

[12] P. Kofstad, High Temperature Oxidation of Metals, John Wiley and Sons Inc., New York, USA, 1966.

[13] D.J. Young, High Temperature Oxidation and Corrosion of Metals, Elsevier, New York, 2010.

[14] Z. Tang, M.C. Gao, H. Diao, T. Yang, J. Liu, T. Zuo, Y. Zhang, Z. Lu, Y. Cheng, Y. Zhang, K.A. Dahmen, P.K. Liaw, T. Egami, Aluminium alloying effects on lattice types, microstructures, and mechanical behavior of high-entropy alloys systems, JOM 65 (2013) 1848–1858.

[15] B. Cantor, I.T.H. Chang, P. Knight, A.J.B. Vincent, Microstructural development in equiatomic multicomponent alloys, Mater. Sci. Eng. A 375–377 (2004) 213–218.

[16] S. Becker, A. Rahmel, M. Schorr, M. Schütze, Mechanism of isothermal oxidation of the intermetallic TiAl and of TiAl alloys, Oxid. Met. 38 (1992) 425–464.

[17] M.F. Stroosnijder, N. Zheng, W.J. Quadakkers, R. Hofman, A. Gil, F. Lanza, The effect of niobium ion implantation on the oxidation behavior of a $\gamma$-TiAl-based intermetallics, Oxid. Met. 46 (1996) 19–35.

# Manuskript XI

## The effect of alloyed nickel on the short-term high temperature oxidation behaviour of Co-Re-Cr-based alloys

L. Wang, B. Gorr, H.-J. Christ, J. Rösler

Corrosion Science, 93 (2015) 19-26

Corrosion Science 93 (2015)

Contents lists available at ScienceDirect

Corrosion Science

journal homepage: www.elsevier.com/locate/corsci

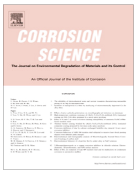

# The effect of alloyed nickel on the short-term high temperature oxidation behaviour of Co–Re–Cr-based alloys

L. Wang [a,*], B. Gorr [a], H.-J. Christ [a], D. Mukherji [b], J. Rösler [b]

[a] *Institut für Werkstofftechnik, Universität Siegen, Paul-Bonatz-Str. 9-11, 57068 Siegen, Germany*
[b] *Institut für Werkstoffe, TU Braunschweig, Langer Kamp 8, 38106 Braunschweig, Germany*

ARTICLE INFO

*Article history:*
Received 28 August 2014
Accepted 1 January 2015
Available online 9 January 2015

*Keywords:*
A. Superalloys
B. SEM
B. XRD
C. High temperature corrosion

ABSTRACT

The effect of Ni on the oxidation behaviour of the alloy Co–17Re–23Cr (at.%) is studied. The results show that the alloying of 15 at.% Ni improves the alloy oxidation resistance significantly by promoting the formation of a protective $Cr_2O_3$ layer. This effect can be attributed at least partially to the enhancement of Cr diffusion by Ni in the metallic Co–Re–Cr–Ni matrix. Moreover, the formation of relatively slow growing Co(Ni)O solid–solution in the transient stage supports the lateral growth of $Cr_2O_3$ nuclei and thus accelerates the establishment of the compact chromia layer.

## 1. Introduction

Based on thermodynamic data suggesting the complete miscibility of Co and Re, Co–Re-based alloys with melting points well beyond that of the commercial Ni-based superalloys have been recently proposed as a potential material class for high temperature structural applications [1]. Similar to the conventional Co-based superalloys, Cr is added to the Co–Re alloy system, aiming to improve both the mechanical properties through solid–solution strengthening and the oxidation resistance through the formation of a protective $Cr_2O_3$ scale. The alloy Co–17Re–23Cr (at.%) is designed as reference alloy for the successive development of the Co–Re–Cr system by means of further alloying additions (e.g., B, C, Si, Ta, etc.) to provide sufficient strength and oxidation resistance at elevated temperatures [2–6]. The microstructure of the reference alloy Co–17Re–23Cr consists of a hexagonal close-packed (hcp) Co-based solid–solution matrix in which the Cr-stabilised composite-strengthening sigma ($\sigma$) phase is embedded [7], see Fig. 1(a). A slightly detrimental effect of the hard (1500 HV) but brittle $\sigma$ phase both on mechanical properties and oxidation resistance in the Co–Re–Cr-based alloys has been reported before [2,3]. Nevertheless, the morphology and volume fraction of the sigma phase can be considerably adjusted by proper control of the chemical composition and thermal treatment [8]. Mukherji et al. report [9,10] that the alloying of 15 at.% Ni to the alloy Co–17Re–23Cr significantly refines the particle size of the sigma phase down to a size of about 100 nm, enhancing the intrinsic ductility of the alloy without weakening its strength. Such a microstructure is also very beneficial for high temperature creep resistance. Therefore, the effect of alloyed Ni on the oxidation behaviour of the Co–Re–Cr-based alloys is of great interest and has been the main driving force to conduct this study.

## 2. Materials and experimental procedure

The materials used in this work, the alloy Co–17Re–23Cr–15Ni, Co–17Re–23Cr–15Ni–ANN (see Table 1 for denotation) as well as the reference alloy Co–17Re–23Cr, have been produced by arc melting using elementary substances with high purity (>99.98%). After drop casting the alloys, a three-step solid–solution heat treatment (1350 °C/5 h, 1400 °C/5 h, 1450 °C/5 h) has been carried out in a high vacuum furnace followed by argon quenching. The microstructure of the solution heat treated Co–17Re–23Cr–15Ni is shown in Fig. 1(b). In addition, a part of the solution heat treated Co–17Re–23Cr–15Ni has been subsequently further annealed at 1050 °C for 4 h to achieve the fine sigma precipitates, see Fig. 1(c). Obviously, the alloy Co–17Re–23Cr–15Ni is almost free of sigma phase, whereas the volume fraction of the sigma phase in the reference alloy Co–17Re–23Cr and the annealed alloy Co–17Re–23Cr–15Ni–ANN is 2.3% and 38.3%, respectively. The chemical compositions and heat treatment conditions of all alloys used in this study are presented in Table 1.

Thermogravimetric analyses (TGA) were carried out under isothermal testing conditions in laboratory air to study the oxidation kinetics. Specimens having dimensions of $10 \times 5 \times 2\ \mathrm{mm}^3$ were

---

[*] Corresponding author.
*E-mail addresses:* linwang.ycy@gmail.com, lin.wang@uni-siegen.de (L. Wang).

http://dx.doi.org/10.1016/j.corsci.2015.01.004
0010-938X/

ground using SiC paper down to 1200 grit and ultrasonically cleaned in ethanol prior to oxidation. X-ray diffractometry (XRD) measurements were performed to identify the phase of oxides formed. Surface and cross-sectional scanning electron microscopy (SEM) in combination with energy-dispersive X-ray spectroscopy (EDS) was applied to study the oxide morphology and constitution. Oxidised specimens for cross-sectional examinations have been Au-sputtered and coated with Ni by electrolytic deposition to protect the oxide scale during sample preparation.

## 3. Results

### 3.1. Oxidation kinetics

The specific weight changes vs. time for the alloys exposed to laboratory air at 1000 °C are shown in Fig. 2(a). Continuous weight loss kinetics is observed for the alloy Co–17Re–23Cr due to the evaporation of Re oxides, referring to the non-protective nature of the oxide scale formed. The detailed oxidation mechanism of the alloy Co–17Re–23Cr has been reported by Gorr et al. elsewhere [3]. Compared to the reference alloy Co–17Re–23Cr, a significant improvement in oxidation performance are demonstrated by both Ni containing alloys, showing extremely small weight changes during oxidation at 1000 °C for 24 h. Fig. 2(b) shows a comparison of the TGA curves of both Ni containing alloys in a high resolution of the mass change. It is evident that a kind of semi-parabolic rate law is obeyed during the oxidation of the alloy Co–17Re–23Cr–15Ni–ANN in air at 1000 °C from the beginning, whereas the alloy Co–17Re–23Cr–15Ni exhibits a transient mass loss before a steady-state weight-gain kinetics is achieved.

### 3.2. Scale morphology and constitution

Fig. 3 shows the surface and cross-sectional microstructures of the alloys Co–17Re–23Cr, Co–17Re–23Cr–15Ni and Co–17Re–23Cr–15Ni–ANN after exposure to laboratory air at 1000 °C for 72 h. The outermost oxide scale formed on the reference alloy Co–17Re–23Cr is much coarser compared to that formed on both Ni-containing alloys. Chemical analysis was performed on the oxide surfaces through EDS. Results shown in Fig. 4 demonstrate that the outermost oxide layer formed on the reference alloy Co–17Re–23Cr consists of pure cobalt-oxide, while both Ni and Cr were additionally detected through the surface EDS analysis on the Ni-containing alloys. In addition, high Cr intensity was obtained on the alloy Co–17Re–23Cr–15Ni–ANN. To determine the lattice structure of the oxide scales formed, XRD measurements were carried out directly on the surfaces of the oxidised alloys, and the results are shown in Fig. 5. The outermost oxide layer formed on the reference alloy was determined to be CoO with preferential growth orientation. The peak positions of the spectrum obtained from the alloy Co–17Re–23Cr–15Ni match reasonably with those of pure CoO. Slight shifts of all peaks to larger $2\theta$ direction, which indicates a smaller lattice parameter compared to pure CoO according to Bragg's law, was observed (Fig. 5b). Combining these results with the EDS analysis, it can be concluded that the outermost oxide layer formed on the alloy Co–17Re–23Cr–15Ni is the Co(Ni)O solid–solution monoxide. However, the oxide formed on the alloy Co–17Re–23Cr–15Ni–ANN was identified by XRD to consist mainly of $Cr_2O_3$ and $CoCr_2O_4$.

The cross-sectional micrographs (Fig. 3d–f) shows the multi-layered structure of the oxide scales and demonstrate that the total thickness of the oxide scale formed on the alloy Co–17Re–23Cr–15Ni is about 50 times smaller than that formed on the alloy Co–17Re–23Cr. In contrast to the typical non-protective CoO/$CoCr_2O_4$ scales formed on the reference alloy, a compact and protective chromia layer is formed on the alloy Co–17Re–23Cr–15Ni underneath an outermost Co(Ni)O monoxide solid–solution layer as well as a Ni-doped $CoCr_2O_4$ spinel intermediate layer. Obviously, the $Cr_2O_3$ scale prevents the alloy from oxidation of Re and consequently from the evaporation of Re oxides. The Ni content detected by EDS analysis in the Co(Ni)O layer and the intermediate $CoCr_2O_4$ spinel layer is 19.3% and 2.3% (in atomic percent), respectively. On the alloy Co–17Re–23Cr–15Ni–ANN, an oxide layer forms, which mainly consists of pure $Cr_2O_3$. Only an extremely thin spinel layer, which allows the electron beam to penetrate into the subsurface $Cr_2O_3$ and, hence, leads to a high Cr intensity of the surface EDS analysis, was observed above the compact and protective $Cr_2O_3$ layer.

### 3.3. Discontinuous oxidation

In order to fundamentally study the cause of the distinct oxidation kinetics of the two Ni-containing alloys at the initial stage of oxidation, discontinuous isothermal oxidation tests for different exposure times were carried out. A single specimen was used for each test. As shown in Fig. 6(a) and (b), a compact and continuous $Cr_2O_3$ layer is quickly formed on the alloy Co–17Re–23Cr–15Ni–ANN after exposure to air already during 10 min, and the oxidation of Re and the subsequent evaporation of its oxides are almost completely prevented. The later oxidation of the alloy is then controlled by the growth of the protective chromia layer, resulting in a parabolic weight-gain kinetics. On account of the continuous chromium consumption at the alloy subsurface by the growth of the chromia layer, the Cr- and Re-stabilised sigma phase dissolves

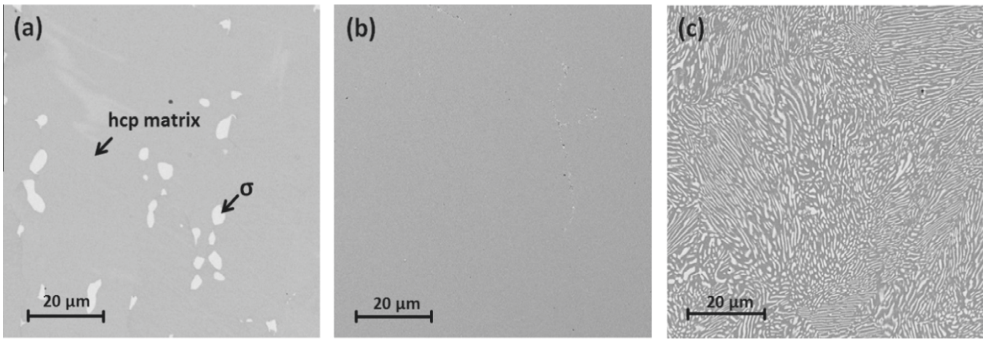

**Fig. 1.** Microstructures of the alloys after heat treatment (SEM, BSE mode): (a) Co–17Re–23Cr; (b) Co–17Re–23Cr–15Ni; and (c) Co–17Re–23Cr–15Ni–ANN (see text and Table 1 for details on heat treatment).

**Table 1**
Alloy heat-treatment conditions and phase compositions measured by EDS.

| Alloy | Heat treatment | Matrix composition (at.%) | | | | Sigma phase composition (at.%) | | | |
|---|---|---|---|---|---|---|---|---|---|
| | | Co | Re | Cr | Ni | Co | Re | Cr | Ni |
| Co–17Re–23Cr | ST[a] | 58.2 | 19.2 | 22.6 | – | 33.4 | 38.3 | 28.3 | – |
| Co–17Re–23Cr–15Ni | ST[a] | 43.4 | 18.2 | 22.6 | 15.8 | – | – | – | – |
| Co–17Re–23Cr–15Ni–ANN | ST[a] + AT[a] | 48.1 | 12.6 | 21.0 | 18.3 | 29.3 | 33.5 | 28.2 | 9.0 |

[a] ST for solid solution heat treatment (1350 °C/5 h, 1400 °C/5 h, 1450 °C/5 h); AT for annealing heat treatment (1050 °C/4 h).

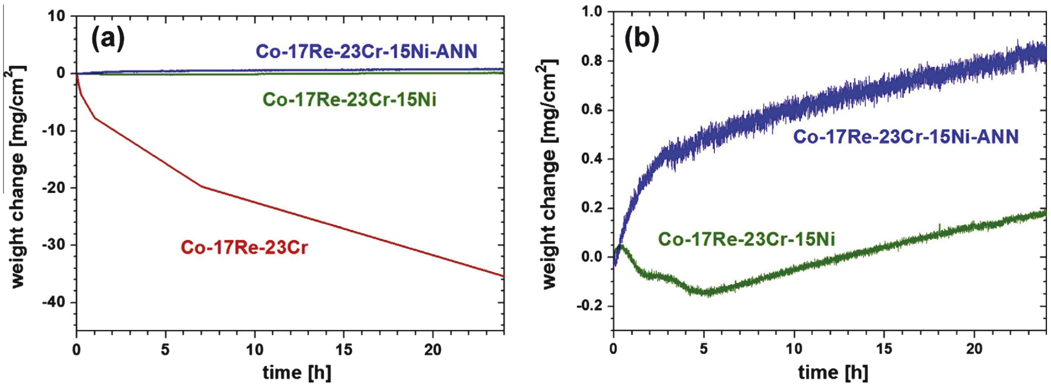

**Fig. 2.** (a) Specific weight change vs. time for the investigated alloys oxidised in air at 1000 °C; and (b) high resolution representation for the Ni-containing alloys.

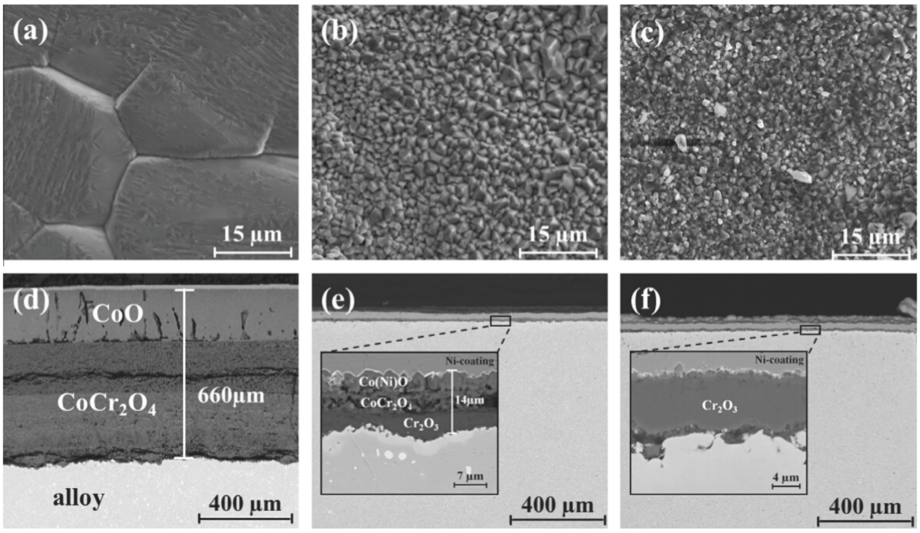

**Fig. 3.** SEM images of the alloy surfaces (top, SE mode) and cross-sections (bottom, BSE mode) after exposure to air at 1000 °C for 72 h: (a and d) Co–17Re–23Cr; (b and e) Co–17Re–23Cr–15Ni; (c and f) Co–17Re–23Cr–15Ni–ANN.

and results in a Re-riched layer underneath the chromia layer. The transient oxidation period of the alloy Co–17Re–23Cr–15Ni–ANN is quite short and negligible, retaining a very thin $CoCr_2O_4$ layer over the chromia layer. On the alloy Co–17Re–23Cr–15Ni, an outermost column-grained Co(Ni)O layer and an inner porous Ni-doped $CoCr_2O_4$ layer were observed after exposure to air at 1000 °C for 10 min, as shown in Fig. 6(c). A similar structure of the oxide scale was found after 1 h (Fig. 6(d)). The thickness of each oxide layer is increased from about 3.5 µm to 5.7 µm, indicating that the scaling process on the alloy Co–17Re–23Cr–15Ni in the transient oxidation period is governed by the growth of both oxide layers, i.e. the Co(Ni)O and the spinel phase. Despite the obvious oxygen uptake through the formation of the oxide scale, the oxidation curve shows weight loss during the first 5 h indicating an evaporation of Re in the form of volatile oxide(s) due to the lack of a protective chromia layer. However, it is important to point out that a semi-continuous $Cr_2O_3$ scale is established at the spinel/alloy interface after exposure for 1 h. The EDS line scan, which

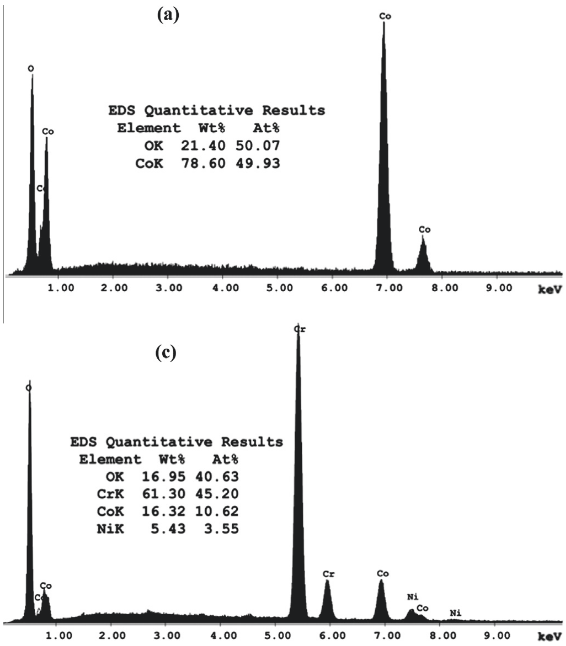

(a) EDS Quantitative Results

| Element | Wt% | At% |
|---|---|---|
| OK | 21.40 | 50.07 |
| CoK | 78.60 | 49.93 |

(b) EDS Quantitative Results

| Element | Wt% | At% |
|---|---|---|
| OK | 18.79 | 45.91 |
| CrK | 1.84 | 1.39 |
| CoK | 54.19 | 35.94 |
| NiK | 25.18 | 16.76 |

(c) EDS Quantitative Results

| Element | Wt% | At% |
|---|---|---|
| OK | 16.95 | 40.63 |
| CrK | 61.30 | 45.20 |
| CoK | 16.32 | 10.62 |
| NiK | 5.43 | 3.55 |

**Fig. 4.** Comparison of the EDS spectra obtained on the surface of the oxide scales formed on the studied alloys after oxidation at 1000 °C: (a) Co–17Re–23Cr; (b) Co–17Re–23Cr–15Ni; and (c) Co–17Re–23Cr–15Ni–ANN.

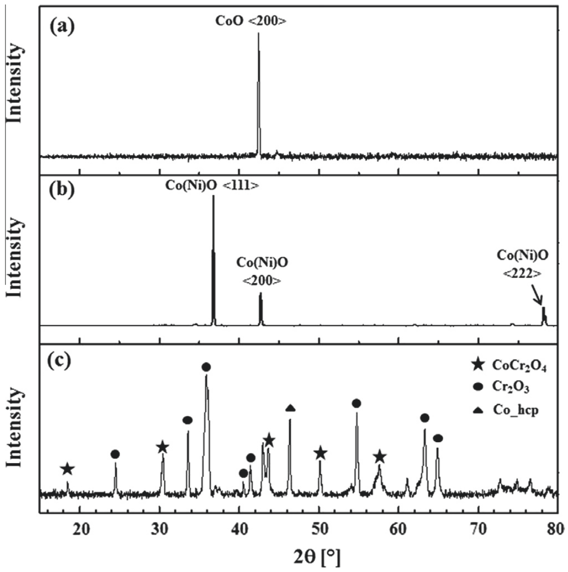

**Fig. 5.** Comparison of the XRD spectra of alloy surfaces (oxides) after oxidation at 1000 °C: (a) Co–17Re–23Cr; (b) Co–17Re–23Cr–15Ni; and (c) Co–17Re–23Cr–15Ni–ANN.

was run from the oxide scale to the alloy, shows a sharp increase of the Cr intensity at the spinel/alloy interface, see Fig. 7. Moreover, few $Cr_2O_3$ internal precipitates were found just underneath the oxide scale.

## 4. Discussion

Upon initial exposure of the alloy Co–17Re–23Cr–15Ni to air at 1000 °C, the oxides of the transient oxidation such as CoO, NiO, $Cr_2O_3$, and probably the spinel phase rapidly nucleate on the surface. Similar to the alloy Co–17Re–23Cr, Re oxidises and its oxides evaporate simultaneously. At this temperature, the CoO and the NiO nuclei grow simultaneously, forming the solid–solution Co(Ni)O oxide. $Cr_2O_3$ particles probably react preferably with adjacent CoO to form the $CoCr_2O_4$ spinel phase not only because of the higher amount of cobalt in the bulk material, which produce more CoO on the alloy surface, but also as a consequence of thermodynamic stabilities, since the Gibbs' free energy reduction of the $CoCr_2O_4$ formation reaction is almost 4 times higher than that of $NiCr_2O_4$ formation:

$$NiO + Cr_2O_3 = NiCr_2O_4 \quad \Delta G^0 = -12.571\ \text{kJ mol}^{-1} \quad (T = 1000\ ^\circ\text{C}) \tag{1}$$

$$CoO + Cr_2O_3 = CoCr_2O_4 \quad \Delta G^0 = -46.551\ \text{kJ mol}^{-1} \quad (T = 1000\ ^\circ\text{C}) \tag{2}$$

Here $\Delta G^0$ is the standard Gibbs' free energy change of the corresponding reaction. It should be noted that all thermodynamic calculations in this work were conducted by means of the commercial software FactSage using the "FRAN" database.

Since CoO and NiO grow much more rapidly than $Cr_2O_3$ [11], a significant amount of Co(Ni)O can overgrow the transient nuclei, establishing an outermost Co(Ni)O layer on the alloy. From the point of view of the resulting oxidation protectiveness it is important that the slower-growing $Cr_2O_3$ nuclei grow laterally fast enough to form a continuous protective $Cr_2O_3$ layer, rather than propagate as oxide islands, and then react with Co(Ni)O to form the spinel phase. Thus, the nucleation rate of $Cr_2O_3$ and the necessary/sufficient supply of Cr for the growth of the $Cr_2O_3$ kernels at the oxide/alloy interface are a key issue. Based on this principle, different efforts were conducted by many authors to facilitate the

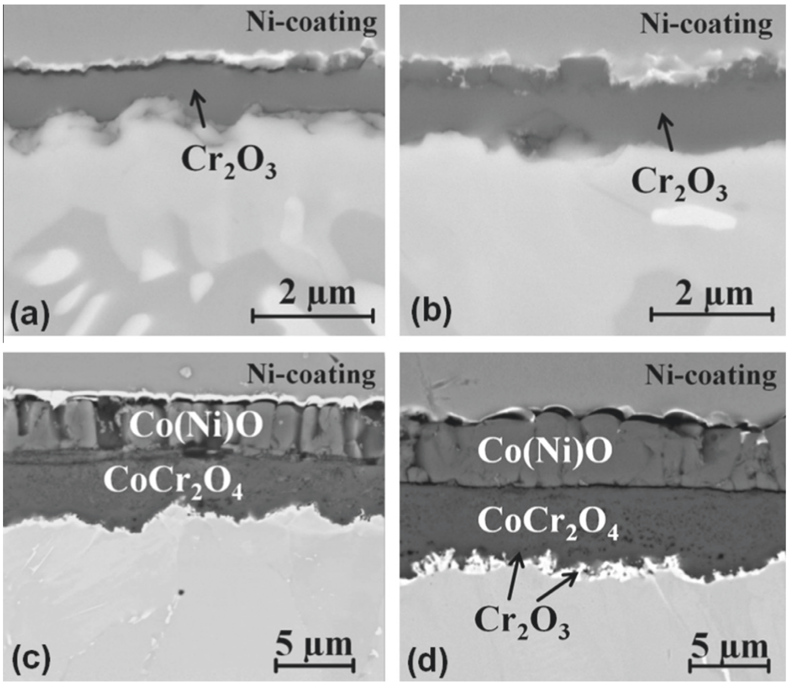

**Fig. 6.** Cross-sentional images (BSE) of the Ni-containing alloys oxidised in air at 1000 °C Co–17Re–23Cr–15Ni–ANN (a and b) and the alloy Co–17Re–23Cr–15Ni (c and d) after oxidation for 10 min (a and c) and 1 h (b and d).

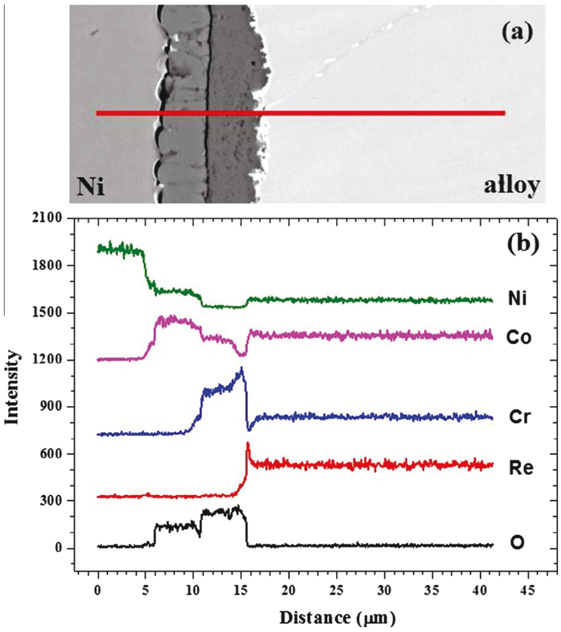

**Fig. 7.** EDX line scan through the oxide scale formed on Co–17Re–23Cr–15Ni after exposure to air at 1000 °C for 1 h: (a) SEM micrograph (BSE); and (b) elemental intensity courses along the red line in (a). (For interpretation of the references to colour in this figure legend, the reader is referred to the web version of this article.)

formation of the protective chromia scale on alloys with low Cr-content, such as adding elements with higher oxygen affinity to promote the nucleation of $Cr_2O_3$ by selective oxidation [6,12], increasing the diffusivity of Cr from the substrate to the alloy surface by decreasing the alloy grain size [13,14], or shot-peening treatment of the alloy surface [15,16].

From the thermodynamic point of view, the calculated Gibbs' free energy change of the NiO formation reaction is even lower in absolute values than that of CoO formation at 1000 °C, while the Gibbs' free energy reduction of $Cr_2O_3$ formation is about twice as high as that of CoO formation, as shown in the following equations:

$$2\ \mathrm{Ni} + \mathrm{O_2} = 2\ \mathrm{NiO} \quad \Delta G^0 = -252.270\ \mathrm{kJ\ mol^{-1}O_2} \quad (T = 1000\ ^\circ\mathrm{C}) \tag{3}$$

$$2\ \mathrm{Co} + \mathrm{O_2} = 2\ \mathrm{CoO} \quad \Delta G^0 = -290.125\ \mathrm{kJ\ mol^{-1}O_2} \quad (T = 1000\ ^\circ\mathrm{C}) \tag{4}$$

$$4/3\ \mathrm{Cr} + \mathrm{O_2} = 2/3\ \mathrm{Cr_2O_3}$$
$$\Delta G^0 = -532.483\ \mathrm{kJ\ mol^{-1}O_2} \quad (T = 1000\ ^\circ\mathrm{C}) \tag{5}$$

Consequently, it is impossible for Ni to promote the nucleation of $Cr_2O_3$ by means of the so-called reactive element effect, where the reactive element involved exhibits normally higher oxygen affinity than the scale former [17]. Therefore, the significant improvement of the oxidation behaviour of the Ni-containing alloy Co–17Re–23Cr–15Ni seems to be connected to changes in the diffusion kinetics. Fig. 8 indicates that the average grain size of the matrix in the alloy Co–17Re–23Cr–15Ni (200 µm) is about 4 times bigger than that in the alloy Co–17Re–23Cr (50 µm). This is in principle disadvantageous for a high Cr flux resulting from diffusion along grain boundaries towards the alloy surface. However, it has been reported by Chattopadhyay and Wood [11] that the alloy interdiffusion coefficient in binary Co–*x*Cr (*x*: 0–40 wt.%) alloys is between $3 \cdot 10^{-16}$ and $6 \cdot 10^{-16}\,m^2\,s^{-1}$ at 1000 °C, while that in binary Ni–*x*Cr (*x*: 0–30 wt.%) alloys lies between $1 \cdot 10^{-15}$ and $4 \cdot 10^{-15}\,m^2\,s^{-1}$, which is about an order of magnitude higher, referring to a faster diffusion of Cr in the Ni–Cr alloys than in the Co–Cr alloys. In addition, the value of the critical concentration of Cr required for developing a protective external $Cr_2O_3$ scale on Ni–Cr-based alloys was commonly observed to be lower than that for the Co–Cr-based alloys due to the faster diffusion of Cr [18]. All these evidences indicate that the alloyed Ni may accelerate the lattice diffusivity of Cr in the alloy Co–17Re–23Cr.

In order to assess the effect of Ni on the diffusivity of Cr in the Co–Re–Cr–Ni system, in a first approach the ternary system Co–Cr–Ni was considered and the interdiffusion coefficient of chromium, $D_{CrCr}$, was expressed following the treatment given in Ref. [19] as a function of the tracer diffusion coefficients $D^*_{CrCr}, D^*_{NiNi}$, and $D^*_{CoCo}$, the thermodynamic factors $g_{CrCr}$, $g_{NiNi}$, and $g_{NiCr}$, and the mole fractions $x_{Cr}$ and $x_{Ni}$. As shown in detail in the Appendix, the following equation can be deduced:

$$D_{CrCr} = (1 - x_{Cr}) g_{CrCr} D^*_{CrCr} - x_{Ni} g_{NiCr} D^*_{NiNi} + (x_{Cr} g_{CrCr} + x_{Ni} g_{NiCr}) D^*_{CoCo} \qquad (6)$$

Obviously, the diffusivity of Cr in the Co–Cr–(Ni) system is dependent not only on the composition but also on the related thermodynamic factors. The values of $g_{CrCr}$ and $g_{NiCr}$ as a function of both $x_{Cr}$ and $x_{Ni}$ in a fcc Co–Cr–(Ni) solid–solution at 1000 °C were calculated by means of FactSage using the "FRAN" database and the results obtained are shown in Fig. 9. The values of the tracer diffusion coefficients $D^*_{CrCr}, D^*_{NiNi}, D^*_{CoCo}$ at 1000 °C were taken from the literature [20,21] as $5.22 \cdot 10^{-16}\,m^2/s$, $3.07 \cdot 10^{-16}\,m^2/s$ and $2.82 \cdot 10^{-16}\,m^2/s$, respectively. Finally, $D_{CrCr}$ was calculated and the results are plotted in Fig. 10. It must be noticed that $D^*_{NiNi}$ and $D^*_{CoCo}$ were directly taken from experimental results on $Ni^{63}$ impurity diffusion in fcc Co and the tracer diffusion coefficient of $Co^{60}$ in fcc Co [20], respectively, whereas $D^*_{CrCr}$ refers to experimental interdiffusion results in Co–Cr alloys with relatively low Cr concentration [21], since there is no published data for Cr impurity diffusion in fcc Co available to the best knowledge of the authors.

The calculated values shown in Fig. 10 indicate that interdiffusion coefficient $D_{CrCr}$ increases slightly with increasing Ni content. This result is in good agreement with the experimental observation obtained by Minamino et al. [22], who demonstrated that $D_{CrCr}$ shows a slight increase with increasing Ni concentration for the alloys Co–(15–30)Ni–15Cr at 1200 °C. However, in the calculation given above, the influence of Re is not considered. Therefore, additional studies taking Re into account are necessary to provide further clarification, whether the alloyed Ni accelerates the lattice diffusion of Cr in the quaternary Co–Re–Cr–Ni alloys towards the alloy surface, promoting the formation of a compact chromia layer.

In the alloy Co–17Re–23Cr–15Ni–ANN, many fine sigma particles are distributed homogeneously in the matrix grains. The high density of phase boundaries between the sigma particles and the matrix, which are considered as fast diffusion paths, supports the formation of a compact and continuous $Cr_2O_3$ layer further.

Wood et al. [23] reported that the parabolic rate constant of NiO growth on pure Ni ($2.9 \cdot 10^{-10}\,g^2\,cm^{-4}\,s^{-1}$) in oxygen at 1000 °C is about two orders of magnitude lower than that of CoO growth on pure Co ($2.1 \cdot 10^{-8}\,g^2\,cm^{-4}\,s^{-1}$) under the same conditions. The large difference of the oxidation rates is suggested to be caused by the fact that the cation vacancy concentration of NiO formed under these conditions is much lower than that of CoO (0.07% compared to 0.86%), leading to a slower outwards transport of the Ni cations to the oxidation front, i.e. the scale/gas interface [23]. In addition, Stiglich et al. [24] studied the interdiffusion in Co(Ni)O solid–solution and reported that the isothermal values of the interdiffusion coefficients in CoO–NiO system increase exponentially with the CoO concentration.

In the present study, marker experiments indicated that the growth of both the CoO layer on the reference alloy Co–17Re–23Cr and the Co(Ni)O layer on the alloy Co–17Re–23Cr–15Ni is dominated by the outward transport of the metal cations from the alloy to the oxide/air interface, whereas the spinel phase on both alloys grows inwardly. As discussed above, the growth of the outermost pure CoO layer on the alloy Co–17Re–23Cr is quite rapid as compared to that of the Co(Ni)O layer formed on the alloy Co–17Re–23Cr–15Ni at 1000 °C. This fast outward transport of Co as cations from the alloy to the oxide/gas interface is connected with a high formation rate of vacancies and vacancy clusters in the alloy, eventually leading to the formation of voids at the oxide/alloy interface. Although the diffusion coefficient of oxygen anions in CoO is well-known to be several orders of magnitude lower than that of Co cations at 1000 °C, oxygen can still penetrate the CoO layer through pores between the coarse CoO grains. The voids formed at the alloy/oxide phase boundary increase the specific surface of the alloy. This makes it more difficult to form a continuous chromia layer by lateral growth of the $Cr_2O_3$ nuclei. Rather it is easier to enclose the $Cr_2O_3$ particles by CoO forming the $CoCr_2O_4$ spinel phase. Re oxidises at the oxide/alloy interface and its oxides evaporate continuously, also raising the porosity of the $CoCr_2O_4$ spinel layer formed and giving the gaseous oxygen access to the alloy.

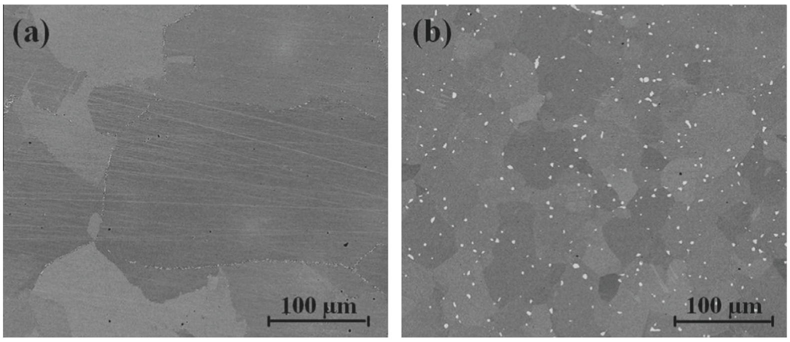

**Fig. 8.** High contrast SEM images (BSE signal) of alloy: (a) Co–17Re–23Cr–15Ni; and (b) Co–17Re–23Cr.

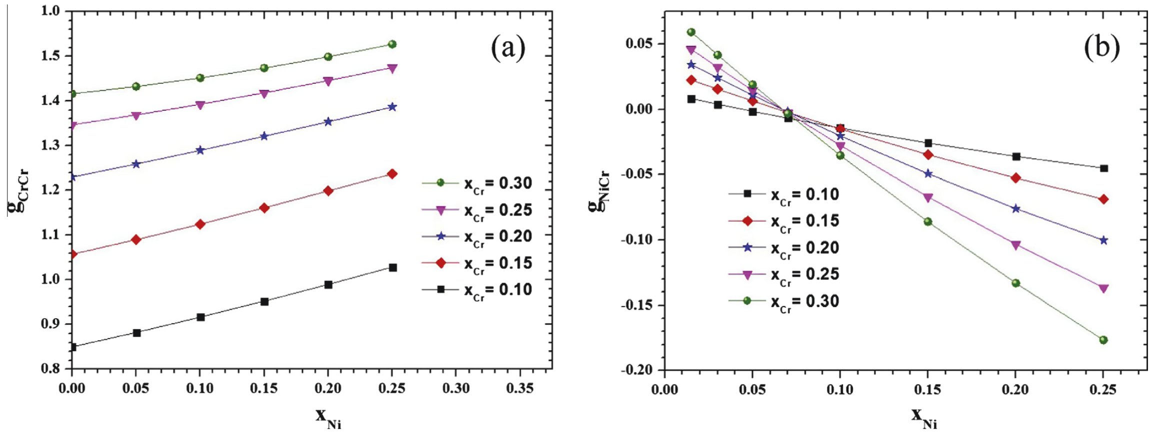

**Fig. 9.** The thermodynamic factors as a function of composition in ternary Co–Cr–Ni fcc solid solution: (a) $g_{CrCr}$; and (b) $g_{NiCr}$.

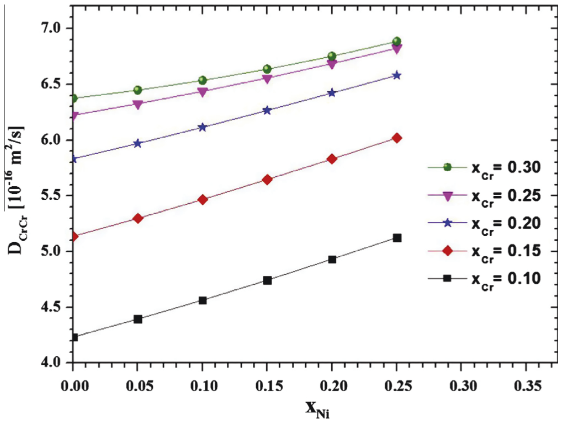

**Fig. 10.** Concentration dependence of interdiffusion coefficient $D_{CrCr}$ in ternary Co–Cr–Ni system at 1000 °C.

The outermost oxide layer formed on the alloy Co–17Re–23Cr–15Ni is a solid–solution of CoO and NiO and the growth rate is reasonably smaller than that of the CoO on the reference alloy Co–17Re–23Cr. Consequently, the spinel phase formed on the Co–17Re–23Cr–15Ni is much denser compared to that formed on Co–17Re–23Cr. Thus, the inward transport of oxygen through the spinel layer tends to be diffusion-controlled. The effective oxygen potential at the alloy/oxide interface is now low enough so that only $Cr_2O_3$ can form because of thermodynamic reasons. Once a continuous $Cr_2O_3$ layer exists at the oxide/alloy interface, the further oxidation of the alloy is dominated by the solid-state diffusion in the chromia layer.

## 5. Conclusion

It was shown in this study that alloying of 15 at.% Ni to the reference alloy Co–17Re–23Cr improves the alloy oxidation resistance significantly. Regardless of the existence or distribution of the sigma phase, a continuous protective $Cr_2O_3$ layer is formed on both Ni-containing alloys studied. The oxidation of Re and consequently the evaporation of its oxides are therefore strongly retarded. The alloy Co–17Re–23Cr–15Ni–ANN which exhibits fine sigma precipitates provides the best oxidation behaviour after a very short transient oxidation period. The alloying of Ni to the alloy is assumed to accelerate the bulk diffusion of Cr in the alloy towards the oxidation reaction front. A relatively slow growth of the outermost Co(Ni)O solid–solution layer results in the formation of a dense spinel layer in the transient oxidation period, facilitating the selective oxidation of Cr at the oxide/alloy interface. Consequently, this promotes the formation of the continuous and protective chromia layer, which controls the further oxidation kinetics.

## Acknowledgement

Financial support of Deutsche Forschungsgemeinschaft (DFG) in the framework of the Research Group FOR727 “Beyond Ni-Base Superalloys” is gratefully acknowledged.

## Appendix A. Calculation of an interdiffusion coefficient in a ternary system from the tracer diffusion coefficients

Generally, the fundamental driving forces for isothermal diffusion are chemical potential gradients. According to Kirkaldy, the one dimensional isotherm diffusion flux $J_i$ of component $i$ in an $n$-component system can be described by the equation [19]:

$$J_i = -\sum_{j=1}^{n} L_{ij} \frac{\partial \mu_j}{\partial x} \quad (i = 1, 2, \ldots n) \tag{A1}$$

where $L_{ij}$ are the phenomenological coefficient matrix and $\mu_j$ is the chemical potential of component $j$. The equation above indicates that the flux of any particular component is related to the chemical potential gradients of all components. Since the chemical potentials of the n components must fulfil the Gibbs–Duhem equation of thermodynamics, there are $(n - 1)$ independent chemical potential gradients. Eq. (A1) is generally rewritten on the basis of Onsager formalism of Fick’s law as following:

$$J_i = -\sum_{j=1}^{n-1} D_{ij} \frac{\partial C_j}{\partial x} \quad (i = 1, 2, \ldots n) \tag{A2}$$

where $C_j$ is the concentration and $D_{ij}$ is the interdiffusion coefficient, which is a function of $L_{ij}$ and also reflects the dependence of the chemical potentials on composition. Generally, the $D_{ij}$ $(i \neq j)$ are cross-coefficients and can often be neglected because of the small values, yielding:

$$J_i = -D_{ii}\frac{\partial C_i}{\partial x} \tag{A3}$$

In a ternary system consisting of components $i, j$ (solute) and $k$ (solvent), the interdiffusion coefficient of solute $i$, $D_{ii}$, can be expressed as follows:

$$D_{ii} = D^k_{ii} - x_i\left(D^k_{ii} + D^k_{ji} + D^k_{ki}\right) \tag{A4}$$

where $x_i$ is the mole fraction and $D^k_{ii}, D^k_{ji}, D^k_{ki}$ are the intrinsic diffusion coefficients. The evaluation of the intrinsic diffusion coefficients can be obtained from the tracer diffusion coefficients $D^*_{ii}, D^*_{jj}$, and $D^*_{kk}$ on the one hand and thermodynamic factors $g_{ii}$, $g_{jj}$, and $g_{ji}$ on the other hand:

$$\frac{\partial \mu_i}{\partial x_i} = \frac{\partial(\mu_i^0 + RT\ln a_i)}{\partial x_i} = RT\frac{\partial \ln a_i}{\partial x_i} = \frac{RT}{x_i}\frac{\partial \ln a_i}{\partial \ln x_i} \tag{A5}$$

$$D^k_{ii} = \frac{x_i D^*_{ii}}{RT}\frac{\partial \mu_i}{\partial x_i} = D^*_{ii}g_{ii} \tag{A6}$$

$$D^k_{jj} = \frac{x_j D^*_{jj}}{RT}\frac{\partial \mu_j}{\partial x_j} = D^*_{jj}g_{jj} \tag{A7}$$

$$D^k_{ji} = \frac{x_j D^*_{jj}}{RT}\frac{\partial \mu_j}{\partial x_i} = \frac{x_j}{x_i}D^*_{jj}g_{ji} \tag{A8}$$

$$D^k_{ji}/D^k_{jj} = \frac{\partial \mu_j}{\partial x_i}\bigg/\frac{\partial \mu_j}{\partial x_j} = \frac{x_j}{x_i}\frac{g_{ji}}{g_{jj}} \tag{A9}$$

$$D^k_{ki} = -\frac{D^*_{kk}}{RT}\left(x_i\frac{\partial \mu_i}{\partial x_i} + x_j\frac{\partial \mu_j}{\partial x_i}\right) = -D^*_{kk}\left(g_{ii} + \frac{x_j}{x_i}g_{ji}\right) \tag{A10}$$

where $D^*_{ii}, D^*_{jj}, D^*_{kk}$ are the tracer/self diffusion coefficients of components $i$, $j$, and $k$. $R$ is the gas constant, $T$ is temperature, and $a_i$ represents the activity of component $i$. $g$ denotes the thermodynamic factor and is defined as:

$$g_{ii} = \left(\frac{\partial \ln a_i}{\partial \ln x_i}\right)_{x_j} \tag{A11}$$

$$g_{ji} = \left(\frac{\partial \ln a_j}{\partial \ln x_i}\right)_{x_j} \tag{A12}$$

Inserting Eqs. (A6), (A8) and (A10) in Eq. (A4), yields:

$$D_{ii} = (1 - x_i)g_{ii}D^*_{ii} - x_j g_{ji}D^*_{jj} + (x_i g_{ii} + x_j g_{ji})D^*_{kk} \tag{A13}$$

Application of this equation to the ternary system Co–Cr–Ni using the indices $i$ for Cr, $j$ for Ni and $k$ for Co leads to the expression (A14) for the interdiffusion coefficient of Cr in the alloy.

$$\begin{aligned} D_{\mathrm{CrCr}} &= (1 - x_{\mathrm{Cr}})g_{\mathrm{CrCr}}D^*_{\mathrm{CrCr}} - x_{\mathrm{Ni}}g_{\mathrm{NiCr}}D^*_{\mathrm{NiNi}} \\ &\quad + (x_{\mathrm{Cr}}g_{\mathrm{CrCr}} + x_{\mathrm{Ni}}g_{\mathrm{NiCr}})D^*_{\mathrm{CoCo}} \end{aligned} \tag{A14}$$

## Appendix A. Supplementary material

Supplementary data associated with this article can be found, in the online version, at http://dx.doi.org/10.1016/j.corsci.2015.01.004.

## References

[1] J. Rösler, D. Mukherji, T. Baranski, Co–Re-based alloys: a new class of high temperature materials?, Adv Eng. Mater. 9 (2007) 876–881.

[2] M. Heilmaier, M. Krüger, H. Saage, J. Rösler, D. Mukherji, U. Glatzel, R. Völkl, R. Hüttner, G. Eggeler, C. Somsen, T. Depka, H.-J. Christ, B. Gorr, S. Burk, Metallic materials for structural applications beyond nickel-based superalloys, JOM – J. Min. Met. Mat. S. 61 (2009) 61–67.

[3] B. Gorr, V. Trindade, S. Burk, H.-J. Christ, M. Klauke, D. Mukherji, J. Rösler, Oxidation behaviour of model cobalt–rhenium alloys during short-term exposure to laboratory air at elevated temperature, Oxid. Met. 71 (2009) 157–172.

[4] L. Wang, B. Gorr, H.-J. Christ, D. Mukherji, J. Rösler, Optimization of Cr-content for high-temperature oxidation behavior of Co–Re–Si-base alloys, Oxid. Met. 80 (2013) 49–59.

[5] M. Brunner, R. Hüttner, M.-C. Bölitz, R. Völkl, D. Mukherji, J. Rösler, T. Depka, C. Somsen, G. Eggeler, U. Glatzel, Creep properties beyond 1100 °C and microstructure of Co–Re–Cr alloys, Mater. Sci. Eng. A 528 (2010) 650–656.

[6] B. Gorr, S. Burk, T. Depka, C. Somsen, H. Abu-Samra, H.-J. Christ, G. Eggeler, Effect of Si addition on the oxidation resistance of Co–Re–Cr-alloys: recent attainments in the development of novel alloys, Int. J. Mater. Res. 103 (2012) 24–30.

[7] T. Depka, C. Somsen, G. Eggeler, D. Mukherji, J. Rösler, M. Krüger, H. Saage, M. Heilmaier, Microstructures of Co–Re–Cr, Mo–Si and Mo–Si–B high-temperature alloys, Mater. Sci. Eng. A 510–511 (2009) 337–341.

[8] B. Gorr, H.-J. Christ, D. Mukherji, J. Rosler, Thermodynamic calculations in the development of high-temperature Co–Re-based alloys, J. Alloy Compd. 582 (2013) 50–58.

[9] D. Mukherji, J. Rösler, P. Strunz, R. Grilles, G. Schumacher, S. Piegert, Beyond Ni-based superalloys: development of CoRe-based alloys for gas turbine application at very high temperatures, Int. J. Mater. Res. 102 (2011) 1125–1132.

[10] D. Mukherji, J. Rösler, Co–Re-based alloys for high temperature applications: design considerations and strengthening mechanisms, J. Phys. Conf. Ser. 240 (2010) 012066.

[11] B. Chattopadhyay, G.C. Wood, The transient oxidation of alloys, Oxid. Met. 2 (1970) 373–399.

[12] D.P. Whittle, M.E. El-Dahshan, J. Stringer, The oxidation behaviour of cobalt-base alloys containing dispersed oxides formed by internal oxidation, Corros. Sci. 17 (1977) 879–891.

[13] H.J. Grabke, E.M. Muller-Lorenz, S. Strauss, E. Pippel, J. Woltersdorf, Effects of grain size, cold working, and surface finish on the metal-dusting resistance of steels, Oxid. Met. 50 (1998) 241–254.

[14] H.Z. Zheng, S.Q. Lu, Y. Huang, Influence of grain size on the oxidation behavior of $NbCr_2$ alloys at 950–1200 °C, Corros. Sci. 51 (2009) 434–438.

[15] R. Naraparaju, H.-J. Christ, F.U. Renner, A. Kostka, Effect of shot-peening on the oxidation behaviour of boiler steels, Oxid. Met. 76 (2011) 233–245.

[16] L. Tan, X. Ren, K. Sridharan, T.R. Allen, Effect of shot-peening on the oxidation of alloy 800H exposed to supercritical water and cyclic oxidation, Corros. Sci. 50 (2008) 2040–2046.

[17] D.P. Whittle, J. Stringer, Improvements in high temperature oxidation resistance by additions of reactive elements or oxide dispersions, Philos. Trans. R. Soc. A 295 (1980) 309–329.

[18] N. Birks, G.H. Meier, F.S. Pettit, Introduction to the High Temperature Oxidation of Metals, Cambridge University Press, New York, 2006.

[19] J.S. Kirkaldy, D.J. Young, Diffusion in the Condensed State, Institute of Metals, London, 1987.

[20] K.I. Hirano, R.P. Agarwala, B.L. Averbach, M. Cohen, Diffusion in cobalt–nickle alloys, J. Appl. Phys. 33 (1962) 3049–3054.

[21] A. Green, D.P. Whittle, J. Stringer, N. Swindells, Interdiffusion in the cobalt–chromium system, Scr. Metall. 7 (1973) 1079–1082.

[22] Y. Minamino, Y. Koizumi, N. Tsuji, T. Yamada, T. Takahashi, Interdiffusion in Co solid solutions of Co–Al–Cr–Ni system at 1423 K, Mater. Trans. 44 (2003) 63–71.

[23] G.C. Wood, I.G. Wright, T. Hodgkiess, D.P. Whittle, A comparison of the oxidation of Fe–Cr, Ni–Cr and Co–Cr alloys in oxygen and water vapour, Mater. Corros. 21 (1970) 900–910.

[24] J.J. Stiglich, J.B. Cohen, D.H. Whitmore, Interdiffusion in CoO–NiO solid solutions, J. Am. Ceram. Soc. 56 (1973) 119–126.

# Manuskript XII

# Microstructure and oxidation mechanism evolution of Co-17Re-25Cr-2Si in the temperature range 800-1100°C

L.Wang, B. Gorr, H.-J. Christ, D. Mukherji, J. Rösler

Oxidation of Metals, 83 (2015) 465-483

Oxid Met (2015)
DOI 10.1007/s11085-014-9515-2

ORIGINAL PAPER

# Microstructure and Oxidation Mechanism Evolution of Co–17Re–25Cr–2Si in the Temperature Range 800–1,100 °C

**L. Wang · B. Gorr · H.-J. Christ ·**
**D. Mukherji · J. Rösler**

Received: 1 October 2014 / Revised: 13 November 2014 / Published online: 22 February 2015

**Abstract** The oxidation behavior of the newly developed Co–Re–Cr-based alloy Co–17Re–25Cr–2Si (at.%) has been studied in laboratory air at 800–1,100 °C. A transition of oxidation mechanism was observed in the alloy within this temperature range. At 800 and 900 °C, the oxide scale mainly consists of an outermost Co-oxide layer and an inner spinel $CoCr_2O_4$ layer. Few $SiO_2$ particles were found in the inner oxide layer. Re oxidizes and then evaporates during the exposure to air since both of these two layers are not protective. Above 1,000 °C, the main oxide product is a continuous compact $Cr_2O_3$ layer. $SiO_2$ was found as inner oxides particles underneath the $Cr_2O_3$ layer. Thus, the evaporation of Re-oxide is strongly retarded. Due to the outward diffusion of Cr during the formation of the $Cr_2O_3$ scale, the original Cr-rich sigma ($\sigma$) phase at the subsurface dissolves. Furthermore, the hcp Co solid-solution matrix supersaturated in Cr an Re brings about the precipitation of the secondary $\sigma$ phase in the substrate during oxidation test.

**Keywords** Co–Re-based alloy · Temperature dependence · Oxidation mechanism evolution · Microstructure change

## Introduction

The development of the intrinsic properties of the Ni-based superalloys as well as the successive improvement in the turbine blade design in the last few decades has allowed a steady increase in engine operating temperatures. However, these

L. Wang (✉) · B. Gorr · H.-J. Christ
Institut für Werkstofftechnik, Universität Siegen, Paul-Bonatz-Str. 9-11, 57068 Siegen, Germany
e-mail: linwang.ycy@gmail.com; lin.wang@uni-siegen.de

D. Mukherji · J. Rösler
Institut für Werkstoffe, TU Braunschweig, Langer Kamp 8, 38106 Brunswick, Germany

operating temperatures are now reaching the limits posed by the melting temperature of these materials [1]. Therefore, design and development of new materials suitable for applications at service temperatures beyond those of Ni-based superalloys have become one of the key interests for the turbine industry. Molybdenum and niobium silicide-based alloys as alternative systems are now being widely investigated due to their promising high temperatures properties [2–5]. Co–Re-based alloys have recently been proposed by Rösler et al. [6] as materials for applications at temperatures beyond 1,200 °C. These alloys seem to be very promising due to their high melting point and acceptable mechanical properties at high temperatures.

One of the open issues at the very early stage of these alloys' development pertains to their oxidation resistance. Gorr et al. [7] reported that Co–17Re (all numbers in composition are in atomic percent) exhibits a very poor oxidation behavior due to the formation of a porous, non-protective Co-oxide layer, resulting in the evaporation of rhenium oxides.

Similar to conventional Co-based superalloys, the addition of chromium to the Co–Re alloy system may improve both, the mechanical properties and the oxidation resistance of the alloys [6]. Figure 1 shows an isothermal section (at 1,100 °C) of the Co–Re–Cr ternary phase diagram. An addition of 23 at.% chromium to the alloy Co–17Re promotes the precipitation of the harder $Cr_2Re_3$-type sigma phase, the particles of which increase the material strength by composite hardening [6]. Studies on the microstructure and mechanical properties of the Co–Re–Cr-based alloys have been reported by Depka and coworkers [8] and Brunner et al. [9] elsewhere, respectively. Furthermore, Gorr et al. [7] reported that the addition of 23

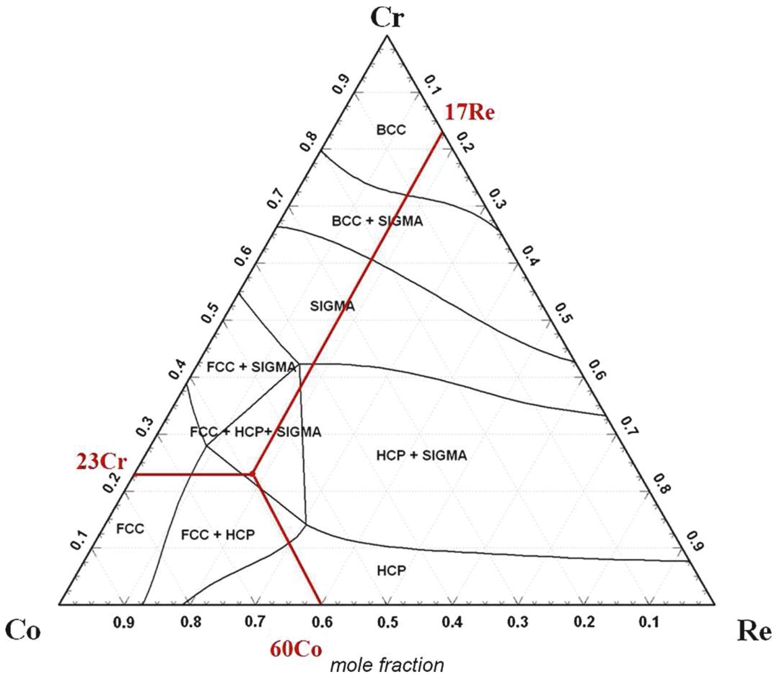

**Fig. 1** Co–Re–Cr ternary phase diagram at 1,100 °C calculated by FactSage program

at.% chromium to the binary alloy Co–17Re does not improve the oxidation behavior, but results in a higher evaporation rate of Re oxides caused by the formation of a more porous $CoCr_2O_4$ spinel phase. Nevertheless, a better oxidation resistance has been found for the alloy with a higher chromium content Co–17Re–30Cr since a semi-continuous $Cr_2O_3$ layer forms underneath the spinel phase. Due to the synergetic effect of Si and Cr, the oxidation resistance of the alloys Co–17Re–23Cr–*x*Si ($x = 1, 2, 3$) becomes significantly enhanced. A quasi-continuous chromia layer forms on the alloy Co–17Re–23Cr–3Si surface with $SiO_2$ as internal precipitates [10]. In all of these alloys, a compact and protective $Cr_2O_3$ oxide layer has never been observed. Considering that higher silicon content may strongly diminish the melting point of the alloy, we have studied the influence of the Cr content on the oxidation behavior of the Co–17Re–*x*Cr–2Si system. Results showed that an increase of the Cr content from 23 to 25 at.% dramatically enhances the oxidation resistance of the alloy due to the formation of a compact $Cr_2O_3$ layer at 1,000 and 1,100 °C [11].

However, most of the previous investigations on the oxidation behavior of the Co–Re–Cr-based alloys devoted to the composition optimization to facilitate the formation of a protective oxide layer were carried out at 1,000 and 1,100 °C. In these investigations, insufficient consideration has been given to the temperature effect on the oxidation behavior of Co–Re–Cr-based alloys, which could lead to an incomprehensive understanding of the alloy mechanisms and may restrict the further design/development of the alloy system. The present paper describes a systematic study of the oxidation behavior of the alloy Co–17Re–25Cr–2Si at various temperatures from 800 to 1,100 °C in air. Particular emphasis is placed on the investigation of the oxidation mechanism evolution of the alloy in the temperature range 800–1,100 °C. A study of the microstructural changes of the alloy subsurface and the substrate during oxidation is also presented.

## Material and Experimental Methods

The alloy of the composition Co–17Re–25Cr–2Si was produced by arc-melting using elementary substances with high purity (>99.98 %) and cast in bar form ($11 \times 11 \times 50$ mm$^3$). The cast bar was then annealed in a vacuum furnace for 3-step homogenization (1,350 °C/5 h, 1,400 °C/5 h, and 1,450 °C/5 h). At the end of the annealing time, the bar was quenched by argon flow within the vacuum furnace.

Oxidation specimens with dimensions of $5 \times 10 \times 2$ mm$^3$ were cut from the bar by wire cut electrical discharge machining. The surface of specimens was subsequently ground using SiC paper down to 1,200 grit. Rounded edges were specially prepared to avoid typical edge effects on oxidation. Prior to oxidation, all specimens were thoroughly cleaned in ethanol in an ultrasonic bath and finally dried.

Thermogravimetric experiments were carried out to examine the weight changes of the alloy during exposure to laboratory air at different temperatures: 800, 900, 1,000, and 1,100 ° C. Discontinuous isothermal oxidation experiments at these temperatures for different times were also performed to study the microstructural evaluation of oxides formed on the alloy. Separate specimen was used for each exposure time. X-ray diffraction (XRD) and scanning electron microscopy (SEM) in combination with energy-dispersive X-ray spectroscopy (EDS) and wavelength-dispersive spectroscopy (WDS) were used to characterize the alloy microstructure and the constitution of oxides formed. Oxidized samples were Au-spattered and coated with Nickel by electrolytic deposition for cross-sectional study. In addition, electron backscatter diffraction (EBSD) measurements were conducted before and after oxidation tests to study the microstructural change of the alloy.

## Results

### Alloy Microstructure

The typical microstructure of the alloy Co–17Re–25Cr–2Si before oxidation is presented in Fig. 2a. The alloy consists of two phases, which are the hexagonal-closed-packed (hcp) matrix of Co solid solution and the σ phase. The existence of the fcc phase as demonstrated in Fig. 1 for the ternary Co–Re–Cr system at 1,100 °C was not observed in the alloy Co–17Re–25Cr–2Si at room temperature. The reason could be that the fcc phase is only stable at high temperatures and were transformed to hcp phase during cooling from the solution treatment temperature. Mukherji et al. [12] studied the hcp/fcc transition in the Co–Re–Cr-based alloys by in situ neutron diffraction and found that this transformation has a large hysteresis (about 100 °C) depending on the thermal history. By heating the alloy Co–17Re–23Cr–2.6C and the alloy Co–17Re–23Cr–1.2Ta–2.6C from room temperature, the transition temperature of hcp to fcc in both alloys were determined to be above 1,100 °C. An EBSD measurement of the alloy reveals that the σ-phase particles are situated not only along the grain boundaries of the hcp-matrix but also within the matrix grains, see Fig. 2b, c. Since some single σ particles near each other in Fig. 2c show the same crystal orientation in Fig. 2b, it can be presumed that these

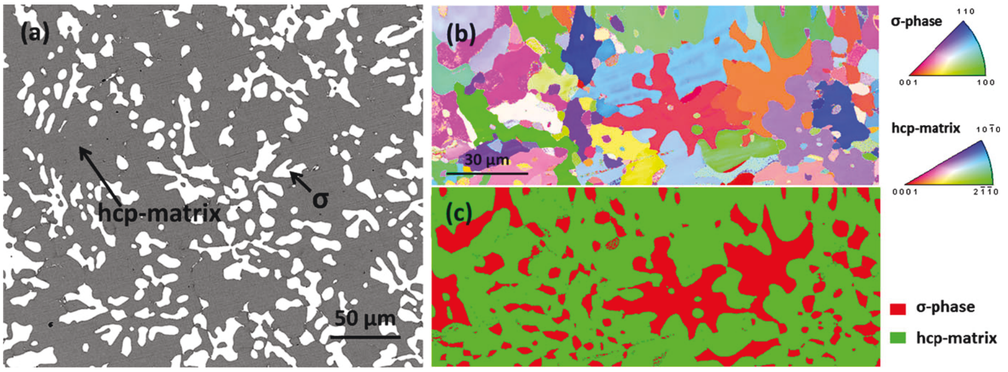

**Fig. 2** Microstructure of the alloy Co–17Re–25Cr–2Si before oxidation: **a** backscattered electron image (BSE); **b** grain distribution and orientation map gained by EBSD, **c** corresponding phase map of (**b**)

separated particles in the two-dimensional view of the cross-section are actually connected spatially forming octopus-shaped σ grains. The volume fraction of the σ phase in the alloy was determined using automated image analysis applying software Image J® to be 24.0 % ± 1.0. The chemical composition in both phases were measured by WDS analysis and listed in Table 1.

## Isothermal Oxidation Kinetics

In Fig. 3, the continuous weight changes of the alloy Co–17Re–25Cr–2Si during exposure to air at various temperatures from 800–1,100 °C are plotted versus time. At 800 °C, a small positive weight change caused by the initial oxygen uptake was only observed at the very initial stage of the test. After this extreme short period, the weight change curve tends towards negative direction, demonstrating the non-protective nature of the oxide scale formed. The evaporation of Re oxides is not prevented. The weight loss rate is, however, reduces after about 5 h. Similarly, negative weight change behavior of the alloy was also observed at 900 °C. However, the weight loss rate in the first few hours is high and follows an almost linear rate law. After a turning point around 5 h, the weight loss rate is mightily slowed down.

In contrast, the TGA data obtained at 1,000 and 1,100 °C shows a significant different feature. Despite the fact that a slight negative weight change occurs in the initial period at 1,000 °C, both TGA curves seem to exhibit a weight gaining behavior for long-term oxidation. Furthermore, the weight gain increase, especially at 1,100 °C, it follows a parabolic time law.

## Scale Morphology and Constitution

The surface morphology of the oxide scale formed on the Co–17Re–25Cr–2Si alloy after exposure in air for 72 h at different temperatures in the range from 800 to 1,100 °C, is presented in Fig. 4. The external oxide layer formed at 800 °C is porous and fine-grained, while that formed at 900 °C is dense with relatively larger grains. Both of these two scales appear to be quite uniform. The outer layers formed at both temperatures were identified as pure Co-oxide by the EDS analysis (see Table 2). The external scale formed at 1,000 °C is not homogeneous. Significant differences were found at lower magnification (see Fig. 4c), showing darker areas, the distribution of which resembles the distribution of the sigma phase in the Co–Re–Cr matrix. The oxide grain size in the darker areas is slightly bigger than that in the brighter areas. Both types of areas reveal a high Cr content, but the darker area contains more cobalt than the brighter area, as listed in Table 2. At 1,100 °C, the

**Table 1** Chemical composition analysis applying WDS in the alloy Co–17Re–25Cr–2Si

| | Co (at.%) | Re (at.%) | Cr (at.%) | Si (at.%) |
|---|---|---|---|---|
| hcp matrix | 63.1 | 12.2 | 22.8 | 1.95 |
| σ phase | 43.9 | 22.8 | 31.9 | 1.4 |

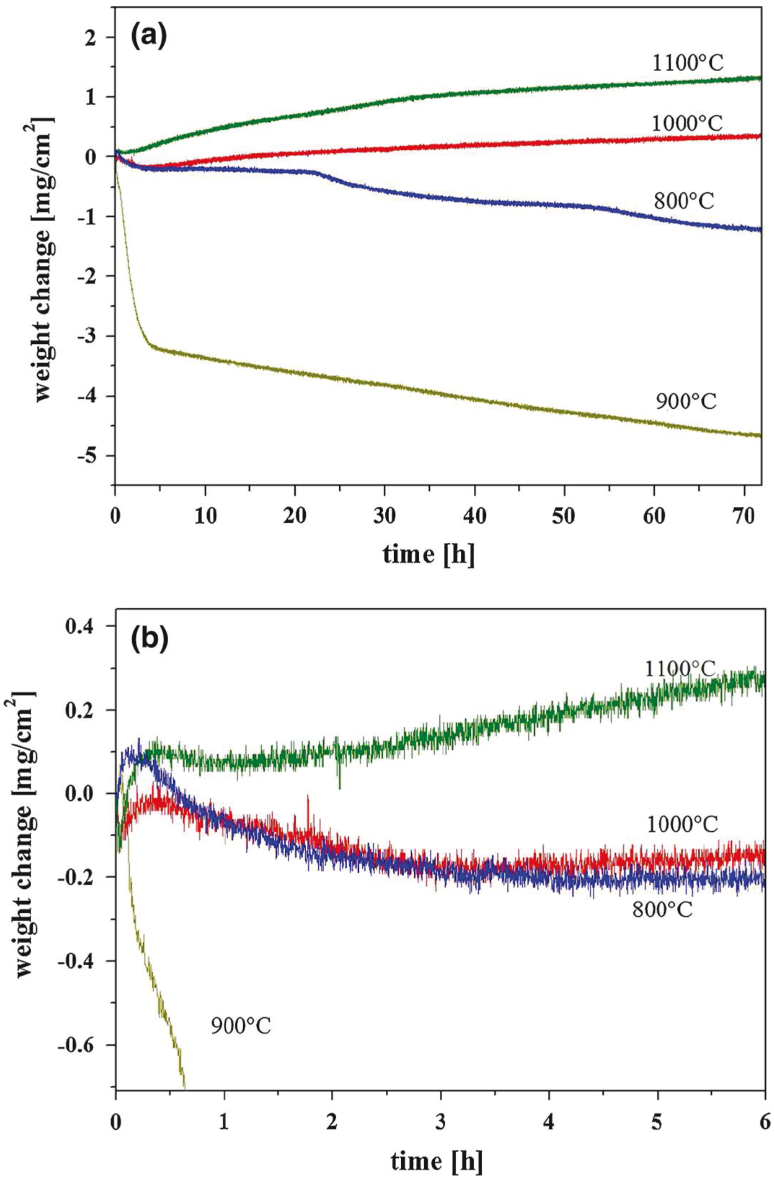

**Fig. 3** **a** Thermogravimetric data of the alloy Co–17Re–25Cr–2Si during exposure to laboratory air at different temperatures; **b** high resolution for the initial stages

surface of the oxide is quite homogeneous and appears similar to that formed in the brighter area at 1,000 °C. The grain size of the external scales formed at 1,000 and 1,100 °C are also very fine compared to those formed at 900 °C. In addition, the oxide scales formed at 1,000 and 1,100 °C appear to be denser.

In order to precisely characterize the structure of the oxide scales, microscopic and chemical examinations were conducted on the cross-sections of oxidized specimens. As shown in Fig. 5, both of the scales formed at 800 and 900 °C possess two distinct oxide layers. XRD measurements, which were carried out over the sample surfaces directly after oxidation, reveal that the outermost Co oxide layer

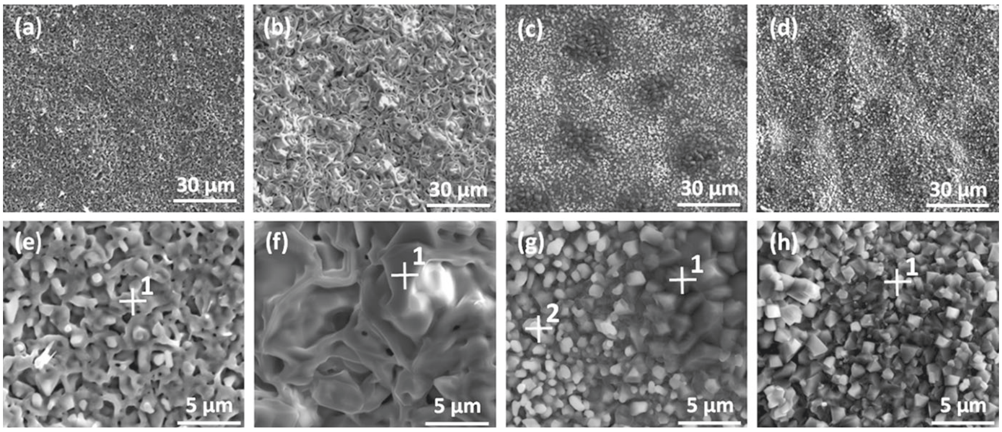

**Fig. 4** Topview (SEM/SE) of the external surfaces of the alloy Co–17Re–25Cr–2Si after exposure to air for 72 h at different temperatures: **a**, **e** 800 °C; **b**, **f** 900 °C; **c**, **g** 1,000 °C; **d**, **h** 1,100 °C

**Table 2** EDS analysis of the external scale formed on the alloy Co–17Re–25Cr–2Si

| EDS position (Fig. 4) | Co (at.%) | Cr (at.%) | O (at.%) |
|---|---|---|---|
| e-1 | 49.7 | – | 50.3 |
| f-1 | 48.9 | – | 51.1 |
| g-1 | 7.9 | 33.7 | 58.4 |
| g-2 | 1.2 | 39.3 | 59.5 |
| h-1 | 1.3 | 39.7 | 59.0 |

formed at 800 °C is pure $Co_3O_4$, while the one formed at 900 °C consists of both CoO and $Co_3O_4$ (Table 3). This is not surprising since $Co_3O_4$ is thermodynamically more stable than CoO in air at temperatures below 880 °C (see Fig. 6). A $CoCr_2O_4$ spinel layer, in which few $SiO_2$ particles were found to be embedded, forms underneath the Co oxide layer at both 800 and 900 °C. However, the spinel layer formed at 800 °C is more porous than that formed at 900 °C. A higher Cr intensity at 800 and 900 °C in combination with a reduced Co concentration was found at the oxide/alloy interface. A relatively semi-continuous and thin layer of $Cr_2O_3$ forms at alloy/oxide interface beneath the double-layered scale. Relatively few internal oxide $SiO_2$ particles were found underneath the spinel layer.

The oxide scales formed at higher temperatures are distinct from those formed at lower temperatures. EDX line scans reveal that the scales formed at 1,000 and 1,100 °C consist mainly of a single-phase layer, which is clearly identified as $Cr_2O_3$ by both EDS and XRD analysis. Only an extremely thin $CoCr_2O_4$ layer forms at the scale/air interface. A large amount of $SiO_2$ particles was also found as a result of internal oxidation underneath the chromia scale for both temperatures.

A comparison of the cross-section microstructure of the samples oxidized for 72 h at different temperatures, which include the oxidation products as well as the metallic substrate below the oxide scale is shown in Fig. 7. The detailed structure of the oxide scales formed at these temperatures is summarized and presented in

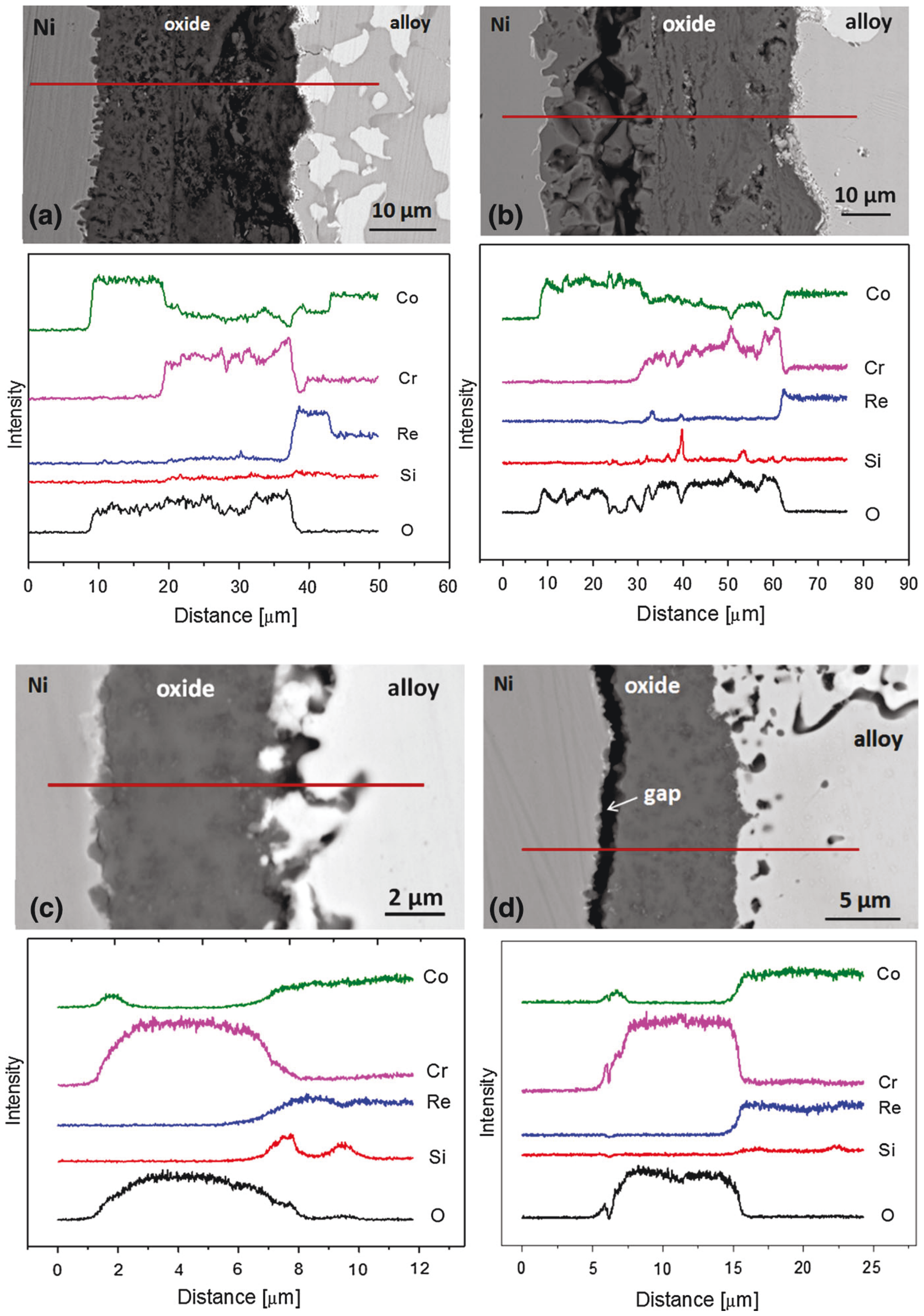

**Fig. 5** Cross-sectional images (BSE) combined with EDS line scan of the alloy Co–17Re–25Cr–2Si after exposure to laboratory air for 72 h at 800–1,000 °C: **a** 800 °C; **b** 900 °C; **c** 1,000 °C; **d** 1,100 °C

Table 4. Even though the structure of the oxide scales formed at 1,000 and 1,100 °C are similar, the $Cr_2O_3$ scale formed at 1,100 °C is about twice as thick as that formed at 1,000 °C. In addition, the amount of $SiO_2$ internal precipitation

**Table 3** XRD determination of the type of oxides formed on the alloy Co–17Re–25Cr–2Si at 800–1,100 °C

| Temperature (°C) | Detected oxides |
|---|---|
| 800 | $Co_3O_4$ |
| 900 | $Co_3O_4$, CoO |
| 1000 | $Cr_2O_3$ (major phase), $CoCr_2O_4$ (minor phase) |
| 1100 | $Cr_2O_3$ (major phase), $CoCr_2O_4$ (minor phase) |

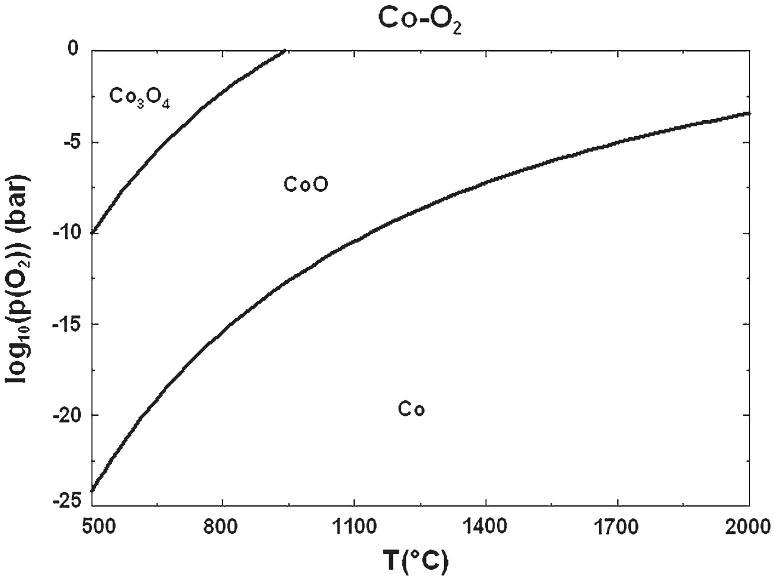

**Fig. 6** Co–$O_2$ phase diagram calculated by FactSage

underneath the oxide scale increases with increasing oxidation temperature. At 1,000 °C, most of the internal oxidation particles are formed in the sigma phase. In contrast, the $SiO_2$ precipitates formed at 1,100 °C are much more homogeneously distributed in the alloy subsurface.

## Microstructural Change of the Substrate

The cross-sectional micrographs of the alloy Co–17Re–25Cr–2Si shown in Fig. 7a–d demonstrate the precipitation of the secondary sigma phase in the alloy substrate during isothermal oxidation test at 800–1,100 °C. The amount, morphology, and distribution of the secondary sigma particles are, however, different after oxidation tests at different temperatures. The aggregate volume fraction of the sigma phase in the alloy substrate were determined by statistical analysis of microstructures after oxidation tests and are summarized in Table 4. Considering the volume fraction of the primary sigma phase in the unoxidized alloy being about 24 %, only 4 vol.% is additionally precipitated as secondary sigma phase along the grain boundaries of the hcp matrix at 800 °C. At 900 °C, the secondary sigma phase precipitates can also be

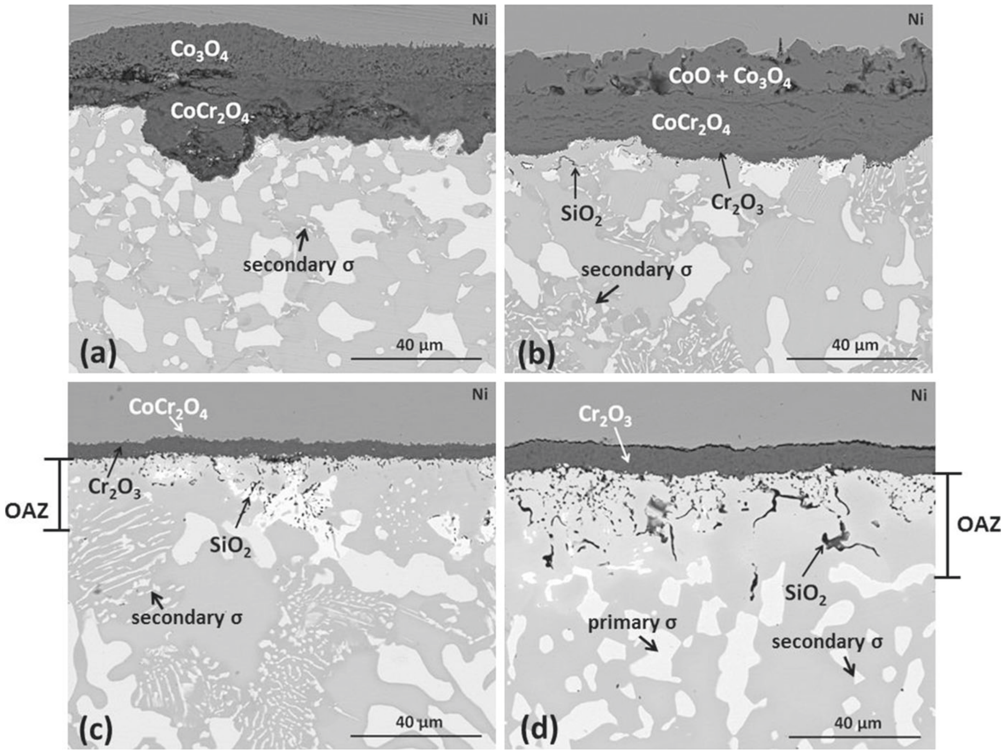

**Fig. 7** The cross-sectional micrographs (BSE) of the alloy Co–17Re–25Cr–2Si after exposure to air for 72 h at different temperatures indicating the oxidation-affected zone (OAZ): **a** 800 °C; **b** 900 °C; **c** 1,000 °C; **d** 1,100 °C

found in certain hcp matrix grains, where the volume fraction of this phase increases up to 10 %. The distribution of the secondary sigma phase formed at 1,000 °C is similar to that formed at 900 °C, but a high increase of the volume fraction of the sigma phase of 13.8 % was detected. At 1,100 °C, the amount of the additionally precipitated sigma phase is almost the same as that measured at 1,000 °C. Furthermore, the secondary sigma phase exhibits different shapes from lamellar arrangements or tiny particles at lower temperatures to relatively coarse and spheroidal particles after oxidation at 1,100 °C.

## Oxidation-Induced Phase Transformation

It has been proved that chromium stabilizes the sigma phase in Co–Re–Cr-based alloys [11]. At 800 and 900 °C, no significant microstructural change was found in the alloy subsurface except for the precipitation of the secondary sigma phase. At temperatures above 1,000 °C, Cr is continuously consumed from the alloy subsurface, particularly from the primary sigma particles, due to the growth of a protective chromia scale, leading to the dissolution of the primary sigma phase. In Fig. 7c, one can see that the sigma phase directly underneath the chromia scale is dissolved and results in a slightly brighter contrast in this region. EDS analysis indicates a high intensity of Re. In certain areas of the same sample, the sigma phase

**Table 4** Characterization of the cross-section of the alloy Co–17Re–25Cr–2Si after exposure to air for 72 h at 800–1,100 °C

| Temperature (°C) | Structure of oxide scale (from air/scale interface to scale/alloy interface) | Scale thickness (μm) | Depth of the inner oxidation zone (μm) | σ phase volume fraction in the matrix (%) |
|---|---|---|---|---|
| 800 | $Co_3O_4$, Co–Cr–O spinel | 30 | – | 28.6 ± 1.4 |
| 900 | $Co_3O_4$ + CoO, Co–Cr–O spinel | 55 | 5 | 34.0 ± 2.1 |
| 1000 | $CoCr_2O_4$, $Cr_2O_3$ | 6 | 26 | 37.8 ± 2.1 |
| 1100 | $CoCr_2O_4$, $Cr_2O_3$ | 11 | 40 | 36.9 ± 3.0 |

is completely dissolved (see Fig. 8a), and instead, more $SiO_2$ particles are formed. EBSD scans in theses areas reveal that a fine-grained hcp phase region is newly formed underneath the oxide scale after oxidation, which indicate recrystallization of the alloy subsurface, see Fig. 8b. The element distribution obtained by EDS mapping, shown in Fig. 9, exhibits a noteworthy difference of chemical composition between the newly formed hcp phase and the original hcp phase in the alloy. Lower Cr and Co but higher Re contents are found in the new hcp grains. A joint analyse of Figs. 8 and 9 indicates that most of the $SiO_2$ particles form along the grain boundaries between the new grains.

## Discussion

### Transition of the Oxidation Mode

A large amount of studies on the high temperature oxidation behavior of binary Co–Cr alloys and Co–Cr-based alloys had been carried out by various authors in the last decades (e.g. [13–19]). Most of these studies were conducted at temperatures around 1,000 °C. At these temperatures, it is a common observation that a non-protective double-layered oxide scale, which consists of an outer CoO layer and an inner mixture of $Cr_2O_3$ and $CoCr_2O_4$ particles in a CoO matrix, forms on alloys containing Cr less than the critical concentration required for the formation of a closed $Cr_2O_3$ layer. If a Co–Cr alloy possesses sufficient Cr-concentration, a densely packed $Cr_2O_3$ layer usually develops with an associated reduction in oxidation rate. However, the critical concentration of Cr for the formation of a protective $Cr_2O_3$ scale is markedly reduced by adding oxygen ‘‘getter’’ elements or rare-earth oxides such as Si or $Y_2O_3$, respectively [20, 21]. In addition to the variation of the Cr-content and the effect of additional elements, Kofstad and Hed [22] have reported that the transition from the non-protective to the protective oxidation products also depends sensitively on the oxygen partial pressure. Nevertheless, there are quite limited reports on the temperature effect on the oxidation mechanism, especially on the oxide product transition of Co-Cr-based alloys.

In spite of the possibility of Re oxidation and the consequent volatilization of its oxides, scales formed on Co–Re–Cr-based alloys are generally similar to that formed on conventional Co–Cr-based alloys at 1,000 and 1,100 °C [7, 11, 23, 24]. The results shown above clearly reveal that a transition of the oxidation products on the alloy Co–17Re–25Cr–2Si from non-protective double layers to a dense and slowly growing $Cr_2O_3$ external layer occurs as the temperature of oxidation is changed from 800 to 1,100 °C. Figure 10 plots the equilibrium dissociation oxygen partial pressures of most oxides, which could form in the Co–Re–Cr-Si alloy system, as a function of temperature. It is clear that $Cr_2O_3$ is always thermodynamically much more stable than CoO in the temperature range from 800 to 1,100 °C. Hence, it can be assumed that the intense temperature dependence of the type of oxidation products on alloy Co–17Re–25Cr–2Si is a consequence of changes in kinetics. In this respect, the Cr diffusion plays the key role.

During the very initial stage of exposure to air, all elements present in the Co–17Re–25Cr–2Si are oxidized on the alloy surface. However, the nucleation and growth of chromia is preferred as discussed above. The difference in Cr concentration at the alloy surface and within the substrate that arised due to the formation of $Cr_2O_3$ drives a diffusion flux of Cr towards the alloy surface. A compact $Cr_2O_3$ layer can quickly form in the case where sufficient Cr is continuously supplied to the reaction front. Otherwise, prior formed $Cr_2O_3$ kernels can easily be engulfed by the fast growing cobalt oxide and the spinel phase formation follows. The Arrhenius plot of the Cr diffusion coefficient D in the binary Co–Cr alloy system [25] shown in Fig. 11 indicates that the diffusion coefficient of Cr in Co–Cr alloys increases almost by three orders of magnitude when the temperature increases from 800 °C to 1,100 °C. The accelerated diffusion flux of Cr at higher temperature facilitates the formation of a continuous chromia layer on the alloy surface.

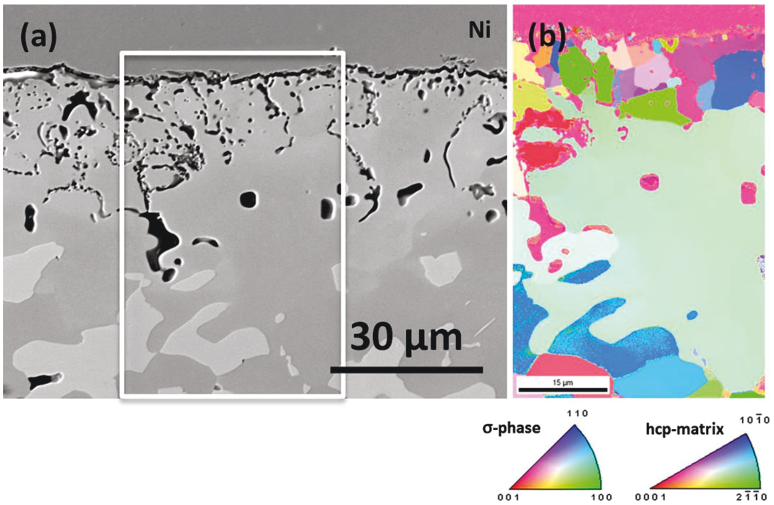

**Fig. 8** Results of a EBSD measurement of the cross-section of Co–17Re–25Cr–2Si after exposure to air at 1,000 °C for 72 h (the external oxide scale is completely spalled): **a** BSE micrograph; **b** grain orientation map of the frame indicated area in (**a**)

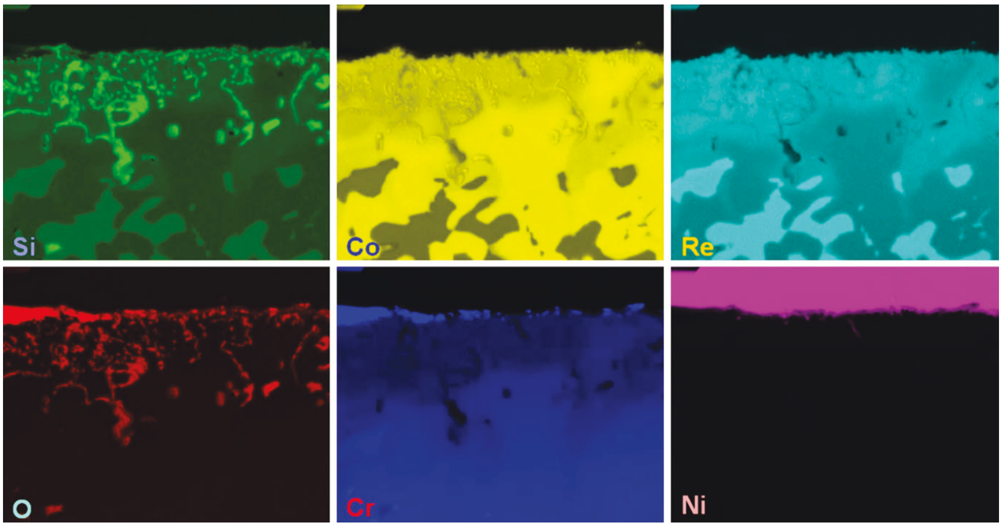

**Fig. 9** Element distribution of the subsurface of Co–17Re–25Cr–2Si after oxidation in air for 72 h; Fig. 8**a** shows the corresponding position

Figure 12 shows the oxides formed on Co–17Re–25Cr–2Si after short exposure to air in different conditions. At all the three temperatures, namely 800, 1,000 and 1,100 °C, a thin $Cr_2O_3$ layer is quickly formed on the top of the hcp phase in the early oxidation stage. However, the oxides formed on the sigma phase are quite different from each other. Even though sigma phase contains more Cr than the hcp phase, no protective $Cr_2O_3$ layer is formed on the sigma phase at 800 °C. Instead, a thick, porous Co-oxide/spinel-oxide double-layer is obtained (see Fig. 12a). When the temperature increases to 1,000 °C, sufficient supply of Cr results from the

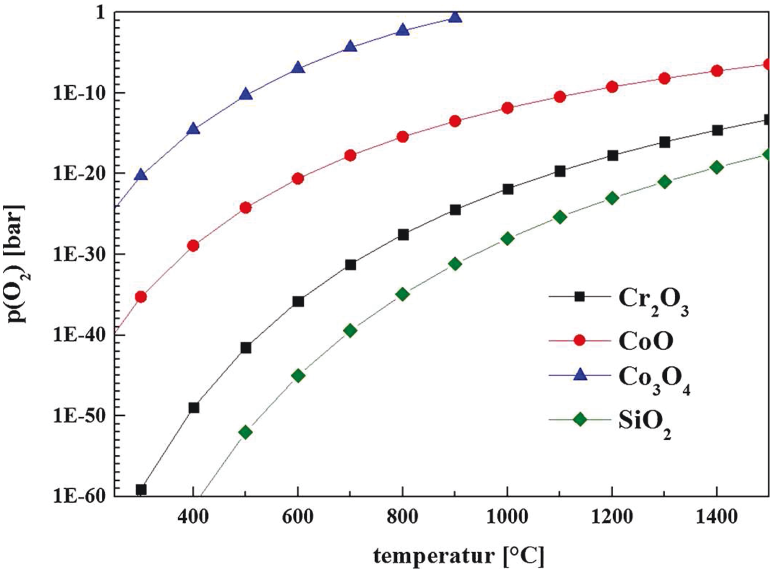

**Fig. 10** Equilibrium dissociation oxygen partial pressures of different oxides

accelerated Cr diffusion in the sigma phase also and promotes the formation of a dense and semi-continuous $Cr_2O_3$ layer at the scale/alloy interface. This layer is established after only 20 min, as shown in Fig. 12b. The non-protective nature of the oxide scale formed during the transient oxidation period leads to the oxidation of Re and consequently the evaporation of its oxides, which corresponds to the initial negative weight change appearing in the TGA curve shown in Fig. 3. Once a complete continuous $Cr_2O_3$ layer exists, the evaporation of volatile Re-oxides is stopped, resulting in continuous weight gain from oxide scale growth. At 1,100 °C, a compact protective $Cr_2O_3$ layer forms on the sigma phase almost as quickly as it forms on the hcp Co matrix phase. The oxidation of Re and the evaporation of its oxides is restricted to the very initial stage of oxidation only (Fig. 12c).

### Oxide Scale Growth Mechanism

In order to determine the growth mechanism of the oxide scales formed, marker experiments were carried out. Gold markers, placed on the alloy surface before oxidation, were found at the spinel/Co-oxide interface after exposure to air at 900 °C for 2 h (Fig. 13a). A similar result was obtained at 800 °C. The presence of the Au markers at the boundary between the outer and the inner oxide layer of the scale implies that the outer layer grows by the outward migration of cobalt cations and the inner spinel layer grows by inward migration of oxygen. However, at 1,000 °C/1,100 °C, no gold marker was found at the scale/alloy interface or scale/air interface using the same experimental method. In order to avoid the confusion caused by the standard sample preparation in this work, where the oxidized specimens for cross-sectional examination are normally gold sputtered before Ni-coating, and by the low melting point of Au (1,064 °C), platinum markers were used

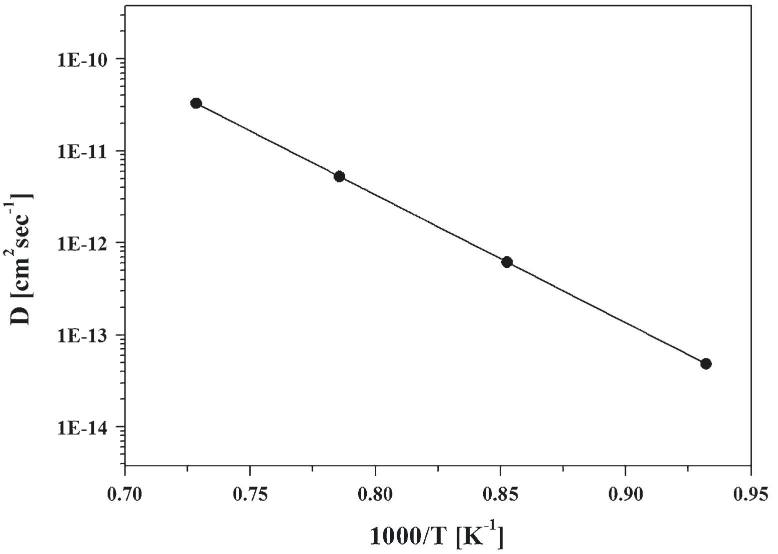

**Fig. 11** Arrhenius plot of the Cr diffusion coefficient in binary Co–Cr alloys (0–40 at.%) in temperature range 800–1,100 °C

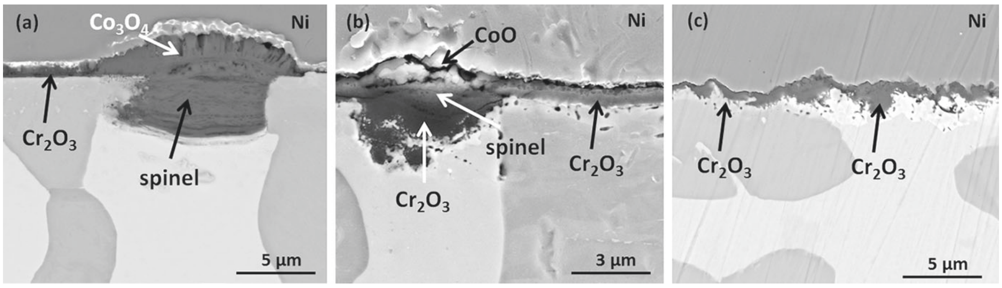

**Fig. 12** Cross-section view (BSE) of oxide scales formed on alloy Co–17Re–25Cr–2Si: **a** 800 °C for 2 h; **b** 1,000 °C for 20 min; **c** 1,100 °C for 5 min

for experiments carried out at temperatures above 1,000 °C. A specimen oxidized at 1,100 °C was directly investigated after exposure without Ni-coating, as shown in Fig. 13b, c. Since the spinel phase, as a transient product, does not form a continuous dense outer oxide layer, platinum markers were found on the top of the oxide scale as well as at the spinel/$Cr_2O_3$ interface (Fig. 13b, c). This observation suggests that the $Cr_2O_3$ scale grows predominantly due to the oxygen transport through the $Cr_2O_3$ scale being in contrast to most of the $Cr_2O_3$ scale forming alloys [26]. The marker is mostly reported to remain at the oxide/alloy interface, indicating that the $Cr_2O_3$ scale grows through outward diffusion of Cr.

However, similar observations on the alternation of the growth mechanism of the $Cr_2O_3$ scale from cation outward to anion inward transport have also been reported in the literature for alloys containing reactive elements [27, 28]. According to Whittle and Stringer [29], almost any element which has a higher affinity for oxygen than the scale-forming element may be beneficial in terms of the ''reactive element effect (REE)''. The Si-effect in the alloy Co–17Re–25Cr–2Si can thus be considered as the REE, since $SiO_2$ is thermodynamically more stable than $Cr_2O_3$. Two feasible explanations of the phenomena have been extensively reviewed and discussed by Hou and Stringer [30]. The first hypothesis suggests that the reactive element accumulates at the grain boundary of the $Cr_2O_3$ scale, greatly retarding the cation outward transport through the scale, and consequently, resulting in an anion inward transport dominated scale growth. However, it has been pointed out by Hou

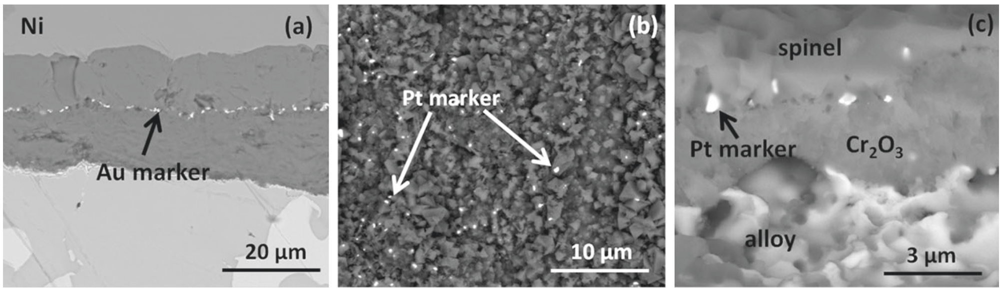

**Fig. 13** *Markers* in the oxidized alloy Co–17Re–25Cr–2Si: **a** cross-sectional BSE picture after exposure at 900 °C for 2 h; **b** top view (BSE) of the sample surface after exposure at 1,100 °C for 8 h; **c** cross-sectional view of the cracked oxide scale shown in (**b**)

and Stringer [30] that the preferential path of anion transport through $Cr_2O_3$ at temperatures around 800 °C is also grain boundaries. Thus, it is difficult to envisage how the presence of a RE could prohibit the transport of cations but at the same time allows the transport of anions. The other hypothesis is so called ‘‘interface poisoning mode’’, where the reactive elements are considered to segregate at the scale/alloy interface and block dislocations from climbing due to their large size, and, therefore, stop the vacancy annihilation process. Hence, the cation transport through the scale is greatly retarded, resulting in scale growth mainly due to the inward diffusion of oxygen anions through the scale.

At 1,000 °C/1,100 °C, the rapid transient oxidation produces an thin spinel oxide layer which then stops growing, as a protective chromia layer forms underneath. As the further oxidation of the alloy is then governed by the growth of the $Cr_2O_3$ layer, chromium is continuously transported from the alloy subsurface to the scale/alloy interface, resulting in a Cr depletion zone, and accordingly in a Re enriched zone, directly underneath the $Cr_2O_3$ scale (see Fig. 9). It is well-known that Re-based alloys act as an effective diffusion barrier at high temperatures in Re-based diffusion barrier coating systems on Ni-based superalloys [31]. Probably, the Re-enriched zone underneath the $Cr_2O_3$ scale formed on the alloy Co–17Re–25Cr–2Si has a similar effect, slowing down the outward transport of Cr.

### Substrate Microstructural Evolution

As shown above, the precipitation of the secondary sigma phase takes place at all oxidation temperatures from 800 to 1,100 °C due to the supersaturation of Cr and Re in the hcp matrix. Since the homogenized specimens are quenched by argon from 1,450 °C to room temperature, the precipitation of further sigma phase during cooling is strongly retarded. The coarse and spheroidal shaped secondary sigma phase particles precipitated in the alloy Co–17Re–25Cr–2Si after exposure to air at 1,100 °C for 72 h (see Fig. 7) indicate that the supersaturated Cr and Re in the hcp matrix is completely precipitated as secondary sigma phase and the coarsening process of the precipitates has been initiated.

The formation of small new grains in the hcp matrix in the outermost part of the alloy subsurface may be attributed to the classical recrystallization phenomenon, since the material in the near surface region exhibits a relatively high dislocations density as a result of the polishing process prior to oxidation testing and, consequently, is in a relatively high strain energy state. However, it should be kept in mind that the process of the sigma phase transformation into the hcp phase may lead to the accumulation of excessive chemical energy, which may facilitate the formation of the new hcp grains. In order to specify, whether the microstructural changes are driven by the strain energy stored in the dislocations or the chemical energy which resulted from the phase transformation, the alloy Co–17Re–25Cr–2Si has been ground down to 1,200 grit and exposed to an atmosphere with very low oxygen partial pressure at 1,000 ° C for 72 h. These conditions should primarily prevent the oxidation of Cr, the formation of the chromia layer and, most important, the dissolution of the sigma phase. Figure 14 shows the cross-section of the specimen exposed to the atmosphere with very low oxygen partial pressure

($10^{-19}$ bar). Although the oxidation of Cr could not be prevented completely, the dissolution of the sigma phase has largely been retarded. New small grains as seen in Fig. 8b did not form at the alloy subsurface, except for few tiny hcp Co grains newly formed mainly in the sigma phase. Since the sample surface has been prepared in exactly the same way as in the case of the sample showing the formation of small grains, one can conclude that this microstructural change is probably induced by the chemical energy caused by the transformation of the sigma phase into the hcp phase. Further, nucleation processes, in general, often take place on defects in the material such as coarse particles. Since the new small grains have not been observed at the silica particles, it could be assumed that the nucleation of the new small grains occurs at partially dissolved sigma phase particles.

## Outlook

Since the diffusivity of Cr plays such an important role on the oxidation behavior of the alloy Co–17Re–25Cr–2Si, an interesting question is, whether a pre-treatment such as shot-peening could enhance the oxidation resistance of the alloy at low temperatures through higher dislocation density in the alloy subsurface, i.e. generating paths for fast Cr diffusion and supporting the establishment of a compact external $Cr_2O_3$ scale. An investigation is presently underway, and the results will be published in future. Furthermore, the results shown above also indicate that the sigma phase exhibits a much worse oxidation resistance than the hcp phase and plays a detrimental role in the formation of an external chromia scale. Thus, a reduction of the volume fraction and/or the mean particle size of the sigma phase could also be beneficial for the oxidation resistance of Co–Re–Cr-based alloys.

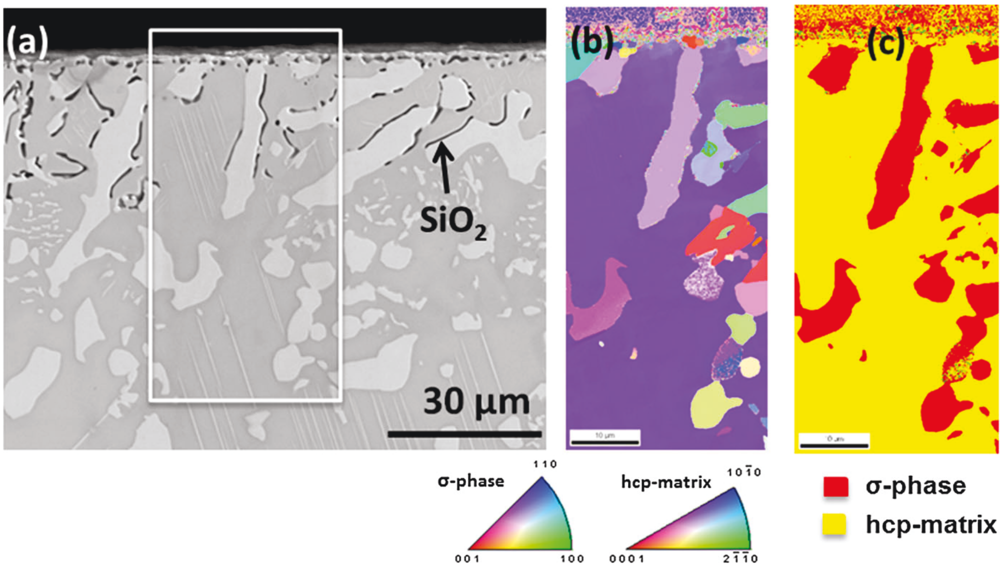

**Fig. 14** Results of the EBSD measurement of the cross-section of the alloy Co–17Re–25Cr–2Si after exposure to Ar–$H_2$/$H_2O$ atmosphere ($p(O_2) = 10^{-19}$ bar) at 1,000 °C for 72 h: **a** BSE micrograph; **b** grain orientation map of the framed area indicated in (**a**); **c** phase map

## Conclusions

The oxidation mechanism of the alloy Co–17Re–25Cr–2Si is strongly dependent on temperature in the temperature range 800–1,100 °C. Poor oxidation resistance of the alloy was found at 800 and 900 °C due to the insufficient supply of Cr to the reaction front to form a continuous and compact $Cr_2O_3$ layer mainly due to the low diffusivity of Cr. The non-protective nature of the scale formed results in a material loss through the evaporation of Re oxides. At temperatures above 1,000 °C, accelerated Cr diffusion/transport flux in the alloy promotes the formation of a protective $Cr_2O_3$ layer. Marker experiments indicate that the growth of the $Cr_2O_3$ layer takes mainly place via inward transport of oxygen This observation is in accordance with the REE and can be attributed to silicon. The depletion of Cr at the alloy subsurface leads to the dissolution of sigma phase. Apart from the subsurface microstructural change, secondary sigma phase precipitation takes place in the alloy substrate during oxidation at different temperatures.

**Acknowledgments** Financial support of Deutsche Forschungsgemeinschaft (DFG) in the framework of Research Group DFG-FOR727 ‘‘Beyond Ni-Base Superalloys’’ is gratefully acknowledged.

## References

1. J. H. Perepezko, *Science* **326**, 1068 (2009).
2. B. P. Bewlay, M. R. Jackson, P. R. Subramanian and J. C. Zhao, *Metallurgical and Materials Transactions A* **34**, 2043 (2003).
3. S. Burk, B. Gorr, V. B. Trindade and H.-J. Christ, *Oxidation of Metals* **73**, 163 (2009).
4. S. Majumdar, A. Kumar, D. Schliephake, H. J. Christ, X. Jiang and M. Heilmaier, *Materials Science and Engineering A* **573**, 257 (2013).
5. M. Azimovna Azim, S. Burk, B. Gorr, H.-J. Christ, D. Schliephake, M. Heilmaier, R. Bornemann and P. Bolívar, *Oxidation of Metals* **80**, 231 (2013).
6. J. Rösler, D. Mukherji and T. Baranski, *Advanced Engineering Materials* **9**, 876 (2007).
7. B. Gorr, V. Trindade, S. Burk, H.-J. Christ, M. Klauke, D. Mukherji and J. Rösler, *Oxidation of Metals* **71**, 157 (2009).
8. T. Depka, C. Somsen, G. Eggeler, D. Mukherji, J. Rösler, M. Krüger, H. Saage and M. Heilmaier, *Materials Science and Engineering A* **510–511**, 337 (2009).
9. M. Brunner, R. Hüttner, M.-C. Bölitz, R. Völkl, D. Mukherji, J. Rösler, T. Depka, C. Somsen, G. Eggeler and U. Glatzel, *Materials Science and Engineering A* **528**, 650 (2010).
10. B. Gorr, S. Burk, T. Depka, C. Somsen, H. Abu-Samra, H.-J. Christ and G. Eggeler, *International Journal of Materials Research* **103**, 24 (2012).
11. L. Wang, B. Gorr, H.-J. Christ, D. Mukherji and J. Rösler, *Oxidation of Metals* **80**, 49 (2013).
12. D. Mukherji, P. Strunz, S. Piegert, R. Gilles, M. Hofmann, M. Holzel and J. Rosler, *Metallurgical and Materials Transactions A* **43A**, 1834 (2012).
13. P. Y. Hou and J. Stringer, *Oxidation of Metals* **29**, 45 (1988).
14. E. M. Fryt, G. C. Wood, F. H. Stott and D. P. Whittle, *Oxidation of Metals* **23**, 77 (1985).
15. S. Espevik, R. A. Rapp, P. L. Daniel and J. P. Hirth, *Oxidation of Metals* **20**, 37 (1983).
16. K. Przybylski and D. Szwagierczak, *Oxidation of Metals* **17**, 267 (1982).
17. C. A. Barrett and C. E. Lowell, *Oxidation of Metals* **12**, 293 (1978).
18. I. G. Wright and G. C. Wood, *Oxidation of Metals* **11**, 163 (1977).
19. P. K. Kofstad and A. Z. Hed, *Oxidation of Metals* **2**, 101 (1970).
20. J. Stringer and I. G. Wright, *Oxidation of Metals* **5**, 59 (1972).
21. D. E. Jones and J. Stringer, *Oxidation of Metals* **9**, 409 (1975).
22. P. K. Kofstad and A. Z. Hed, *Materials and Corrosion* **21**, 894 (1970).
23. B. Gorr, S. Burk, V. B. Trindade and H.-J. Christ, *Materials and Corrosion* **61**, 741 (2010).

24. B. Gorr, S. Burk, V. Trindade and H.-J. Christ, *Oxidation of Metals* **74**, 239 (2010).
25. J. W. Weeton, *Diffusion of Chromium in Alpha Cobalt-Chromium Solid Solutions*, (U. S. Goverment Printing Office, Ohio, 1951).
26. M. Skeldon, J. M. Calvert and D. G. Lees, *Oxidation Of Metals* **28**, 109 (1987).
27. J. Stringer, B. A. Wilcox and R. I. Jaffee, *Oxidation of Metals* **5**, 11 (1972).
28. I.G. Wright, J. Stringer, B.A. Wilcox, and R.I. Jaffee, *Oxidation and hot corrosion of Ni-Cr- and Co-Cr-base alloys containing rare earth oxide dispersions*, Defense Technical Information Center, 1971.
29. D. P. Whittle and J. Stringer, *Physical and Engineering Sciences* **295**, 309 (1980).
30. P. Y. Hou and J. Stringer, *Materials Science and Engineering: A* **202**, 1 (1995).
31. D. Sumoyama, K. Z. Thosin, T. Nishimoto, T. Yoshioka, T. Izumi, S. Hayashi and T. Narita, *Oxidation of Metals* **68**, 313 (2007).

# Manuskript XIII

## Creep resistance and oxidation behavior of novel Mo-Si-B-Ti alloys

M. Azim, D. Schliephake, C. Hochmuth, B. Gorr, H.-J. Christ, U. Glatzel, M. Heilmaier

JOM, 67 (2015) 2621-2628

JOM, Vol. 67, No. 11, 2015
DOI: 10.1007/s11837-015-1560-z

# Creep Resistance and Oxidation Behavior of Novel Mo-Si-B-Ti Alloys

M.A. AZIM,[1,4] D. SCHLIEPHAKE,[2] C. HOCHMUTH,[3] B. GORR,[1]
H.-J. CHRIST,[1] U. GLATZEL,[3] and M. HEILMAIER[2]

1.—Institut für Werkstofftechnik, Universität Siegen, Paul-Bonatz-Str. 9-11, 57068 Siegen, Germany. 2.—Institut für Angewandte Materialien, Karlsruher Institut für Technologie, Engelbert-Arnold-Straße 4, 76131 Karlsruhe, Germany. 3.—Metallische Werkstoffe, Universität Bayreuth, Ludwig-Thoma-Str. 36b, 95447 Bayreuth, Germany. 4.—e-mail: maria.azim@uni-siegen.de

Mo-Si-B-alloys are promising materials for high-temperature applications because of their high melting point, excellent phase stability, large alloying capabilities, and reasonable mechanical as well as oxidative properties. A continuing alloy development is, however, required because of the catastrophic oxidation taking place at intermediate temperatures and the rather high density. The addition of Ti stabilizes a new ternary phase field including the $Mo_5Si_3$ (T1) phase instead of the $Mo_3Si$ (A15) phase. Alloys comprising the phases $Mo_{ss}$, T1 and $Mo_5SiB_2$ (T2) show very high creep resistance, improved oxidation behavior and significantly reduced density. The new T1 phase seems to play a crucial role in the improved oxidation resistance of these new materials, since this phase exhibits excellent oxidation behavior at intermediate and high temperatures. The 4-component alloys possess superior creep behavior compared to Mo-Si-B alloys with the same microstructural phase arrangement and size or to the single crystal Ni-base superalloy CMSX-4. The main reason was found to be the formation of Ti-rich silicide precipitates during processing.

## INTRODUCTION

New high-temperature materials required for applications in highly efficient combustion engines in the field of power generation or transportation have to fulfill a number of demanding requirements. Compared to other novel alloying concepts, such as Nb-[1] and Pt-based alloys,[2] Mo-Si-B alloys designed within the three-phase field $Mo_{ss}$ (molybdenum-based solid solution)-$Mo_3Si$-$Mo_5SiB_2$ represent very promising materials regarding (1) high melting point and phase stability, (2) multiphase options and alloying capabilities, (3) high temperature oxidation resistance, (4) high temperature strength and creep resistance and (5) economic viability.[3–6] Despite the already high level of mechanical properties, the implementation of these alloys is hampered because of the lack of oxidation resistance at intermediate temperatures. In addition, Mo-Si-B alloys possess a relatively high density (9.6 g/cm$^3$).[7]

Numerous alloying strategies, such as macroalloying with Cr, Al, Ti, Zr, Ce and microalloying with reactive elements, such as Y, La and their dispersoids, have already been investigated by researchers from the United States and Japan[3,8–13] and have also been examined in detail in the framework of the Research Unit “Beyond Ni-based alloys” funded by the German Science Foundation (DFG). The application of Ti as an alloying element in the Mo-Si-B system was triggered by thermodynamic calculations carried out by Yang et al.[12] indicating that Ti causes the formation of a new ternary phase field consisting of $Mo_{ss}$, $T_1$ and $T_2$ phases. From all the alloying approaches mentioned above, only macroalloying with Ti seems to suppress the formation of $Mo_3Si$, which does not exhibit any oxidation resistance, and stabilizes a new phase field consisting of a ductile $Mo_{ss}$ matrix together with the two intermetallic compounds, $Mo_5SiB_2$ (T2) and Si-rich $Mo_5Si_3$ (T1).[12] Ti addition to the T1 phase obviously does not improve the oxidation resistance of $Mo_3Si$, but suppresses catastrophic oxidation as well as the so-called “pesting” in the temperature range 400–700°C[14,15] of the $Mo_5Si_3$ phase. Regarding mechanical properties, the beneficial effect of Ti addition in Mo-based alloys is already known for TZM (Ti-Zr-Mo) alloys. In the Mo-Si-B system, it is expected that the substitution of Mo by Ti increases the strength of $Mo_{ss}$.

Due to the high solubility of Ti in the different phases of Mo-Si-B-Ti alloys, where Ti atoms exclusively substitutes Mo atoms on their respective lattice sites, improved mechanical and oxidative properties of these alloys are presumed. Additionally, a beneficial density reduction is received as an important positive side effect (e.g., 7.7 g/cm$^3$ for Mo-12.5Si-8.5B-27.5Ti).[16]

However, in contrast to the thermodynamic predictions by Yang,[12] the arc-melted composite material Mo-12.5Si-8.5B-27.5Ti (all compositions are denoted in at.%) additionally contained 7% $Ti_5Si_3$ and 26% $Mo_3Si$ (A15).[16] This was primarily attributed to the manufacturing difficulties because of the extremely narrow phase field encompassing the required three phases (see Fig. 1a). However, recent thermodynamic calculations revealed that this ternary phase field can be considerably broadened by minor additions of Fe (see Fig. 1b).

This study summarizes the effects of macroalloying with Ti on creep and oxidation resistance of Mo-Si-B-Ti(-Fe) composite alloys. As a basis of comparison, the behavior of the respective constituting single phases has also been studied and is dealt with in this paper.

## MATERIALS AND EXPERIMENTAL PROCEDURE

The compositions, processing routes and phase fractions of the monolithic intermetallic compounds and of the composites investigated in this study are summarized in Table I.

For the monolithic intermetallic compounds (alloys B–D) as well as for the two-phase alloy (alloys A and E), a powder metallurgical (PM) processing route was applied. For this purpose, elemental powder mixtures of Mo, Si, Ti and B of 99.95%, 99.9%, 99.5% and 99.4% purity, respectively, were used for mechanical alloying (MA). MA was carried out under Ar atmosphere in a planetary ball mill (Retsch PM 400) with 200 rpm and a powder to ball weight ratio of 1:13. Afterwards, the material was compacted by field assisted sintering technique (FAST) at 1600°C applying 50 MPa uniaxial pressure. The powder was heated up with 100 K/min and held for 15 min at the maximum temperature. Finally, the material was hot isostatically pressed at 1400°C and 150 MPa to reduce its porosity. The homogenization treatment was carried out at 1600°C for 100 h in Ar atmospheres. By contrast, alloy B (T1 with 40 at.% Ti) and the composite materials F, G and H were prepared by arc melting. A detailed description of the processing routes of the arc melted materials is presented in.[15,16]

Oxidation samples with dimension of 10 × 4 × 3 mm were machined using a slow-cutting diamond saw, ground down to a surface finish of 1200 grit, slightly rounded at the edges and ultrasonically

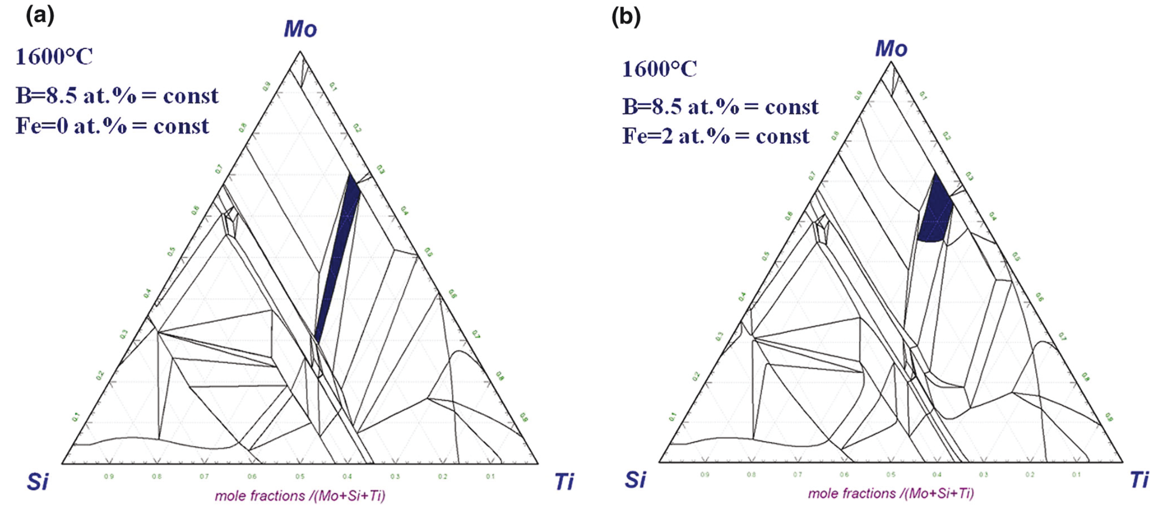

Fig. 1. Isothermal section at 1600°C of (a) Mo-Si-Ti-8.5B-0Fe compared with (b) Mo-Si-Ti-8.5B-2Fe; calculated using FactSage with a specifically developed database predominantly based on the parameters published by Yang et al.[12] The desired ternary phase field is highlighted in black.

**Table I. Alloys studied with the corresponding chemical composition, processing route (*PA* powder metallurgical, *AM* arc melted) and phase fractions**

| Alloy | Chemical composition | Processing route | Phase fractions |
|---|---|---|---|
| A | Mo-23Si-30Ti | PM | 77% A15 + 22% T1 + 1% contamination |
| B | Mo-37.5Si-40Ti | AM | Nearly monolithic T1 with traces of $Ti_5Si_3$ |
| C | Mo-37.5Si-20Ti | PM | Monolithic T1 |
| D | Mo-11Si-25B-25Ti | PM | 92% T2, 7% $Mo_{ss}$, 1% contamination |
| E | Mo-13.8Si-23.6B-28.7Ti | PM | 19% T1 + 79% T2 + 2% contamination |
| F | Mo-12.5Si-8.5B-27.5Ti | AM | 26% A15 + 28% T2 + 38% $Mo_{ss}$ + 7% $Ti_5Si_3$ |
| G | Mo-12.5Si-8.5B-27.5Ti-2Fe | AM | 31% T1 + 23% T2 + 39% $Mo_{ss}$ + 1% $Ti_5Si_3$ |
| H | Mo-9Si-8B-29Ti | AM | 61% $Mo_{ss}$ + 29% T2 + 10% $Ti_5Si_3$ |

cleaned in ethanol. Oxidation kinetics was studied under isothermal testing conditions for 100 h in static laboratory air using a tailor-made Rubotherm magnetic suspension balance with a resolution of $10^{-5}$ g equipped with automatic electronic drift compensation. For cross-section analyses, the oxidized samples were first nickel-coated, then embedded in epoxy and ground down to 4000 grit. Material microstructure and corrosion products were characterized by scanning electron microscopy (SEM; Helios Nanolab 600) in secondary-electron (SE) and backscattered-electron (BSE) mode supplemented by energy-dispersive x-ray spectroscopy (EDS; Apollo XL). Phase identification was performed by room temperature x-ray diffraction analysis (XRD) using Cu $K_\alpha$ radiation (45 kV/ 40 mA/$\lambda$ = 0.15406 nm), a step size of 0.01° and a count time of 100 s/step. Furthermore, spatially resolved phase analysis was carried out using electron backscattered diffraction (EBSD; TSL-EDAX).

Compression creep tests were performed at temperatures ranging from 1100°C to 1300°C in vacuum better than $10^{-5}$ hPa. Samples were prepared by electro-discharge machining with dimensions of 5 × 3 × 3 mm and ground at the pressure-loaded area down to 600 grit. The applied true stresses were calculated (and kept constant in close loop control) during the creep tests by $\sigma_{\text{true}} = \sigma(1 + \varepsilon)$, while the strain $\varepsilon$ was measured by an extensometer attached to the upper and lower pushrod close to the compression sample. TEM samples of crept alloy F were prepared by mechanical grinding and polishing to foils of about 100 $\mu$m thicknesses. Then, these foils were twin jet polished using a solution of 13 vol.% sulfuric acid at –35°C. The microstructure of the crept samples was analyzed using a ZEISS Libra 200FE with a field emission gun operated at an acceleration voltage of 200 kV.

## RESULTS AND DISCUSSION

### Oxidation Resistance in Air

This section concentrates on the description of the oxidative properties of the nearly monolithic intermetallic phases and the composite with Ti as additional alloying element, comparing those materials to the corresponding alloys without Ti. First, the necessity to substitute the $Mo_3Si$ phase is presented based on the oxidative properties of alloy A. Then, the oxidation behavior of monolithic T1 as well as the nearly single-phase T2 and the effect of a reinforcement of T2 by means of 19% T1 is discussed. For selected alloys, the effect of $N_2$ known for Ti-based silicides as a consequence of exposure to air is shown. Finally, the oxidation kinetics and oxide morphology of the composite material are illustrated.

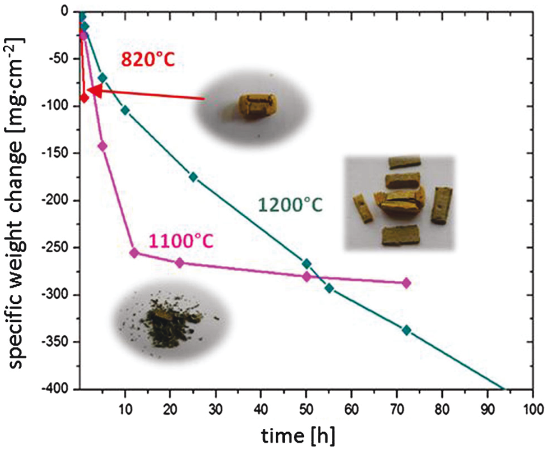

Fig. 2. Oxidation isotherms of the alloy A ($Mo_3Si$ with 22% T1) oxidized in air for 100 h at 820–1200°C.

$Mo_3Si$ does not exhibit any oxidation resistance upon exposure to air due to the high Mo content.[17] Figure 2 shows that even the addition of 22% T1, which shows high oxidation resistance, to $Mo_3Si$ results in fully material degradation at 820–1200°C. It becomes obvious that Ti addition cannot sufficiently increase the Si activity and decrease the Mo activity to enable the formation of a continuous/adherent oxide layer and suppress pesting.

Pure $Mo_5Si_3$ exhibits pest disintegration at 800°C and a lack of oxidation resistance in air below 1650°C because of the formation of porous oxide layers.[18,19] This insufficient oxidation protection can be attributed to the low activity of $SiO_2$.[18,19]

According to thermodynamics, 40 at.% Ti leads to the transformation of the tetragonal Mo-rich Mo(Ti)$_5$Si$_3$ to hexagonal Ti-rich Ti(Mo)$_5$Si$_3$. Stoichiometric Ti$_5$Si$_3$ oxidizes in air, forming a mixed TiO$_2$-SiO$_2$ rutile layer above a TiN subscale[20] at temperatures beyond 1000°C.[21]

Figure 3a shows the oxidation kinetics of monolithic T1 with 20 at.% and 40 at.% Ti, alloys B and C, respectively. At intermediate temperatures, full passivation of both alloys occurs after only a few minutes due to the formation of a continuous SiO$_2$ layer, which contains embedded TiO$_2$ particles (Fig. 3b). At higher temperatures, transient and steady-state oxidation stages are clearly observed. Passivation also occurs for both alloys, but the courses of oxidation isotherms are different depending on the Ti concentration. The alloy B (with 40% Ti) reveals continuous weight gain kinetics while alloy C (with 20% Ti), possessing a substantially higher Mo content, shows negative kinetics. Here, the initial mass loss due to evaporating MoO$_3$ overcompensates the mass gain resulting from oxygen uptake for the formation of different oxides, i.e. SiO$_2$ and TiO$_2$. The oxide morphology of the alloy B (see Fig. 3c) can be subdivided into (1) an outermost rutile layer formed due to the outward diffusion of Ti,[22] followed by (2) a protective duplex layer mainly consisting of silica and (3) a zone of inner oxidation and nitridation caused by air nitrogen. In this region, the substrate decomposes to Ti-depleted tetragonal Mo$_5$Si$_3$ with SiO$_2$ and TiO$_2$ inbetween. Interestingly, if the alloy with 40% Ti is exposed to an Ar-20%O$_2$ atmosphere, the oxide layer becomes extremely thin compared to that formed in air (compare Fig. 3c and d). This difference indicates that N$_2$ strongly influences the formation of both the external oxide scale and the zone with internal precipitates. After exposure to the N$_2$ free environment, the zone of internal oxidation consists of a Mo$_3$Si matrix containing SiO$_2$ precipitates.

A comparison of the results obtained in this study on Ti-containing T1 samples with those observed on the Ti-free T1 phase reported in the literature[18,19] shows that Ti significantly improves the oxidation behavior of Mo$_5$Si$_3$. Possible reasons for this behavior are (1) the higher affinity of Ti to O as compared to Si, (2) a fast outward diffusion rate of Ti and (3) a fast growth kinetics of TiO$_2$. The fast outward diffusion rate of Ti and, on the contrary, the slow outward diffusion of Si results in a depletion of Ti in the subscale region during the oxidation process enhancing the Si activity there. In the Ti-Si-O system, as reported by Wakelkamp, the activity ratio $a_{\mathrm{Si}}/a_{\mathrm{Ti}}$ increases by more than 12 orders of magnitude when the concentration of Si increases from 35.7 (Ti$_5$Si$_{2.77}$) to 39 at.% (Ti$_5$Si$_{3.20}$) across the Ti$_5$Si$_3$ homogeneity range.[23] As a result, SiO$_2$ becomes more stable than Ti oxides in a wide range of oxygen activity. Consequently, SiO$_2$ can cover the substrate by lateral growth in the further stages of oxidation beneath the TiO$_2$ layer and, further, enables reliable oxidation protection. Additional experimental results and a detailed description of the underlying mechanisms of the oxidation behavior of the T1 phase will be described in more detail elsewhere.

Earlier investigations by Yoshimi et al.[24] indicated that the oxidation resistance of Mo$_5$SiB$_2$(T$_2$)-based alloys might be even worse than that of B-doped Mo$_5$Si$_3$ because of the initially lower viscosity of silicate formed onto Mo$_5$SiB$_2$ and the high evaporation rates of B$_2$O$_3$ at higher temperatures. Figure 4a shows discontinuously measured oxidation isotherms of nearly monolithic (Mo,Ti)$_5$SiB$_2$ (alloy D) and of (Mo,Ti)$_5$SiB$_2$ with 19% T1 (alloy E). The transient stage of all curves is characterized by mass gain indicating enhanced formation of solid oxides. Alloy D initially exhibits weight gain kinetics that turns into negative kinetics after 6–7 h of oxidation suggesting that the evaporation of MoO$_3$ and B$_2$O$_3$ becomes dominant. After 10 h of oxidation, the nearly linear weight loss changes into diffusion controlled behavior characterized by insignificant mass changes (see Fig. 4 a). It should be emphasized that the oxidation rates of the T2 phase investigated in this study during the steady-state period are significantly lower than those of the T2 phase without Ti.[24] The absolute mass loss after 100 h of exposure to air is less than 3 mg cm$^{-2}$ for the Ti-containing T2, while pure Mo$_5$SiB$_2$ exhibits a

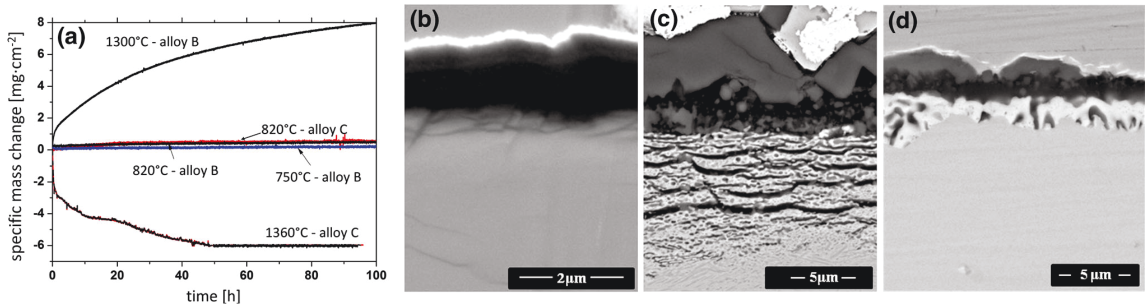

Fig. 3. (a) Oxidation isotherms of alloy B and C oxidized in air for 100 h at 820–1360°C. Cross-sections of alloy B oxidized for 100 h (b) at 820°C, (c) 1100°C and (d) 1100°C in Ar-20%O$_2$.

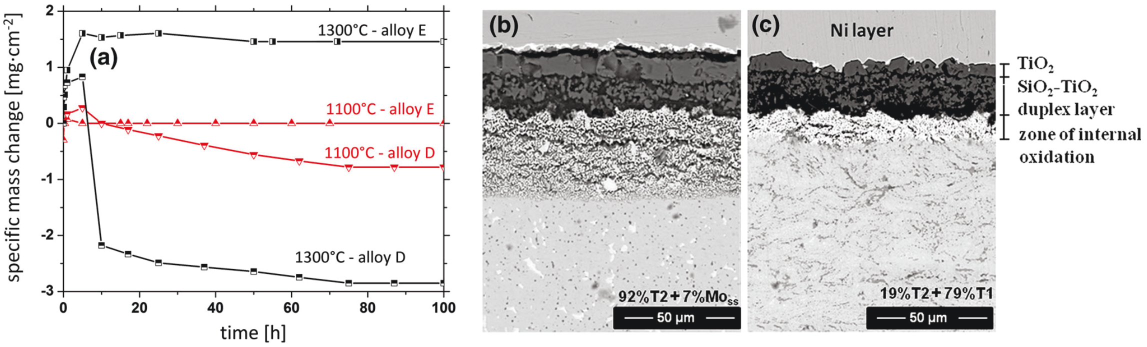

Fig. 4. (a) Specific weight change versus time for alloy D and E oxidized in air for 100 h at 1100°C and 1200°C; (b) BSE-SEM micrograph of the cross-sections of T2 (alloy D) oxidized for 100 h at 1100°C and (c) alloy E oxidized for 100 h at 1100°C.

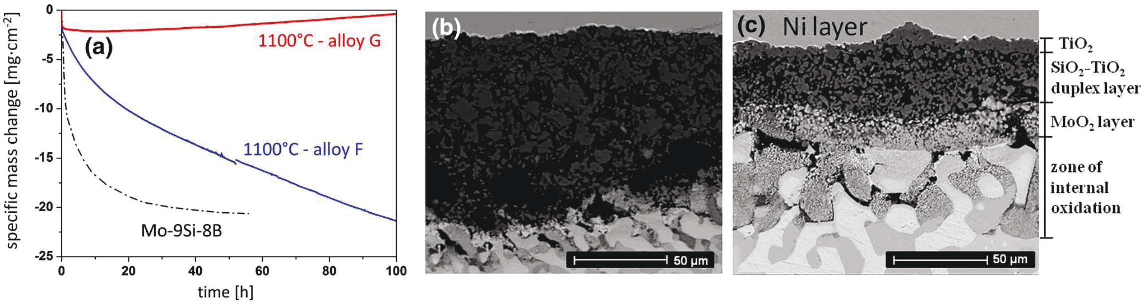

Fig. 5. (a) Overview of oxidation isotherms of alloy F and G at 1100°C in comparison with the Mo-9Si-8B alloy,[17] (b) BSE-SEM cross-section micrograph of alloy F oxidized in air at 1100°C for 100 h and (c) BSE-SEM cross-section micrograph of alloy G oxidized in air at 1100°C for 100 h.

value of 18 mg cm$^{-2}$. As can be seen in Fig. 4b, in the case of alloy D, an outermost rutile layer (≈11 $\mu$m thickness) is formed with a subjacent duplex layer (∼17 $\mu$m) consisting of a $SiO_2$ matrix. The $SiO_2$ amount increases towards the substrate. Below the outer oxidation scale, a zone of internal oxidation of ∼65 $\mu$m thickness arises. The addition of 19% T1 to the T2 phase significantly improves the oxidation resistance. This is clearly represented by the horizontal course of oxidation isotherms of alloy E. As compared to the plain T2 phase, the alloy is covered by a thinner oxide layer and the zone of internal oxidation is reduced by a factor of 4 (see Fig. 4c). These observations demonstrate the significance of the T1 phase. At lower temperatures, however, catastrophic oxidation occurs, as the Si activity is not high enough for the formation of a protective oxide scale.

The oxidation kinetics of the composite materials F and G was compared with that of the base alloy Mo-9Si-8B, which consists of the three phases $Mo_{ss}$, $Mo_3Si$, and T2. The results are illustrated in Fig. 5a. The alloy F consisting of $Mo_{ss}$, $Mo_3Si$, T2 and $Ti_5Si_3$ shows an almost linear mass loss during oxidation at 1100°C because of the formation of a porous $SiO_2$-$TiO_2$ duplex layer (see Fig. 5b).[22] The addition of only 2 at.% Fe stabilizes the T1 phase at the expense of the unwanted $Mo_3Si$ causing a considerable reduction of the oxidation rate compared to that of alloy F. Analyses of the oxide morphology show that 2% Fe significantly enhance the fraction of $SiO_2$ in the duplex layer resulting in an improved protection and, consequently, in a thinner oxide layer (see Fig. 5c). During oxidation at intermediate temperatures, the composite material still shows linear mass loss despite the presence of the T1 phase. Further attempts to improve the oxidation resistance of these alloys will, therefore, concentrate on increasing the $SiO_2$ fraction in the duplex surface layer in such a way that it is sufficient to provide reliable oxidation protection of the composite materials at all temperatures of interest.

## Creep Resistance

Figure 6a represents a typical creep curve in strain versus time representation of the Ti-containing Mo-Si-B alloy F. After 500 h of testing at 1100°C and 200 MPa, the sample reaches a plastic deformation of only about 1.6%. After strain hardening within the primary transient stage lasting up to around 200 h and 1% of total strain, the sample approaches steady-state creep with a determined minimum strain rate of $5.5 \times 10^{-9}$ $s^{-1}$. This is more than two orders of magnitude lower than for a single-crystalline CMSX-4 under the same testing conditions.[3] Both multi-phase Mo-Si-B-Ti alloys F and H show a comparable creep behavior, as illustrated in Fig. 6b, and the stress exponent n was determined to be between 3 and 4, indicating a dislocation climb-controlled creep mechanism. It is known from the literature that the Mo solid solution should be the main carrier for high-temperature plastic deformation in Mo-Si-B alloys.[25–27] Since the content of 61% versus 38% of $Mo_{ss}$ is different in both alloys (see Table I), their comparable creep behavior is somewhat unexpected. In a previous paper, our hypothesis was that the intermetallic phases A15 and $Ti_5Si_3$ might also deform during creep.[16] This was assumed because literature data for A15 by Meyer et al. [27] and Rosales and Schneibel,[28] as well as for $Ti_5Si_3$ by Rosenkranz et al.[29] indicate possible plastic deformation at temperatures above 1200°C. Ito et al.[30] investigated the creep behavior of $T_2$ single crystals and reported a very low measurable strain rate of $10^{-9}$ $s^{-1}$ at 1500°C and 300 MPa for the most easily deformable orientation ([021] with slip on [001](010)). Therefore, the $T_2$ phase should not creep at our testing conditions, especially when taking additional strengthening due to the Ti present in this phase into account. Considering all this, the deformable phase fraction in both alloys should then be nearly the same (about 70%).

To prove our first assumption, the alloy F was investigated by TEM after 15% of compressive strain at a testing temperature of 1300°C and 200 MPa applied stress. In Fig. 7, dark field images of the $Mo_{ss}$ and A15 phases are presented. Together with the $Ti_5Si_3$ phase (not shown here), all three phases possess many dislocations after deformation. In conjunction with the determined stress exponent n of around 3.5, it is clear that all these phases participate in the creep deformation, which is believed to be the reason for the same creep behavior of alloy F and alloy H. Furthermore, dislocations seem to be pinned at particles within the $Mo_{ss}$ phase (see Fig. 7a). EDS analysis indicates

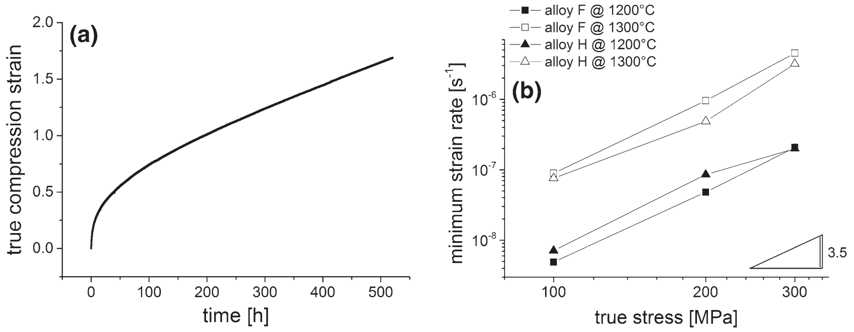

Fig. 6. (a) True compression strain versus time for alloy F at 1100°C and 200 MPa applied true stress and (b) double logarithmic plot of minimum strain rate versus true stress for alloy F and alloy H.

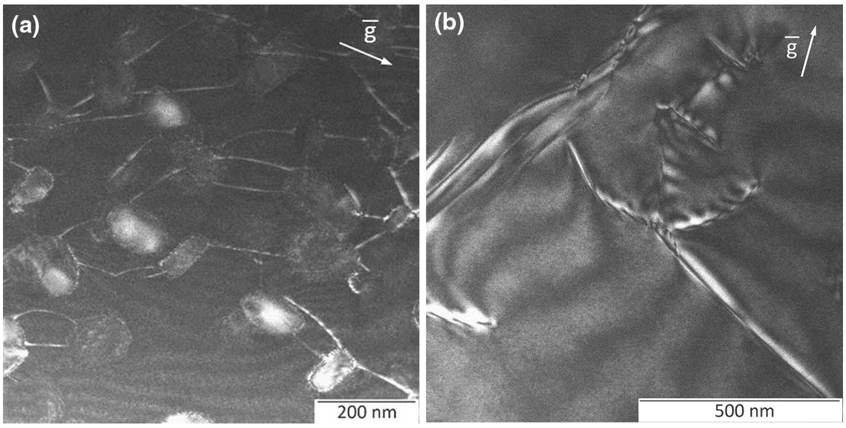

Fig. 7. TEM dark field images of (a) Mo solid solution and (b) A15 phase within alloy F crept at 1300°C and 200 MPa.

that these particles consist of $Ti_5Si_3$, which precipitate during processing. For the improvement of the creep resistance at higher temperatures, precipitation hardening is most likely more effective than solid solution strengthening by Ti. In addition, the higher strength of the particle-strengthened Mo solid solution phase could also be the reason for the observed participation of A15 on the creep deformation.

The strain rate versus stress representation (Norton plot) in Fig. 8 shows the lower minimum creep rate of alloy F, as compared to the Mo-12Si-8.5B alloy with comparable microstructure[31] and to the single crystalline Ni-base superalloy CMSX-4[3] at 1200°C. To illustrate the effect of density reduction, the applied creep stresses were normalized by 7.7 g/cm$^3$, 9.5 g/cm$^3$ and 8.7 g/cm$^3$ for the Mo-Si-B-Ti,[16] Mo-Si-B[32] and CMSX-4[33] alloys, respectively. Clearly the improvement of the creep resistance at the investigated temperature of 1200°C is demonstrated. The observed pinning effect of the $Ti_5Si_3$ precipitates on dislocation motion (Fig. 7a) is now believed to be the reason for the improved creep resistance of Ti-containing alloys compared to Ti-free Mo-Si-B alloys.

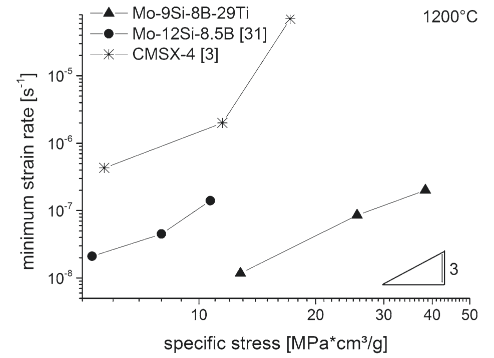

Fig. 8. Double logarithmic plot of minimum strain rate versus specific stress at 1200°C for alloy F compared to Ti-free Mo-Si-B alloy and single crystalline Ni-base superalloy CMSX-4.

Finally, we found that the A15 phase in the alloy F is not thermally stable at temperatures above 1250°C. Figure 9 compares the microstructure of an as-homogenized sample and after a heat treatment at 1300°C for 17 h. The A15 phase converts into $Mo_{ss}$ and $Ti_5Si_3$ by a eutectoid reaction of A15 ↔ $Mo_{ss}$ + $Ti_5Si_3$. Below 1250°C, the A15 phase seems to be stable due to the known sluggish diffusion in Mo-Si-B alloys.[26] Yang et al.[34] reported a Liq + A15 ↔ $Mo_{ss}$ + $Ti_5Si_3$ reaction for some of their investigated Mo-Si-Ti alloys. They found evidence for this reaction as part of their experiments and thermodynamic calculations. Considering our experimental observations, we believe that the liquid phase is not essential to convert A15 into $Mo_{ss}$ and $Ti_5Si_3$. Further investigations are necessary to examine the temperature range for this reaction and to explore the consequences for the high-temperature capability of the affected alloy systems.

## CONCLUSION AND OUTLOOK

Experimental results show that Ti additions improve both the oxidative properties and the mechanical behavior of Mo-Si-B-based alloys. This fact gives rise to the origination of new strategies in the alloy development in the Mo-Si-B system.

Ti additions to the T1 phase enormously improve the oxidation resistance in the temperature range from 750°C to 1360°C. The phase mixture of T2 with 19% T1 results in a fast and complete passivation of the material above 1100°C. As important consequences, (1) the initial evaporation of $MoO_3$ is decreased and (2) the oxidation rates during steady state oxidation are reduced due to a 30% increased $SiO_2$ content in the duplex layer.

The narrow phase field of $Mo_{ss}$-T1-T2, which impedes the manufacturing of the multiphase composite material, can be broadened by the addition of only 1–2% Fe.

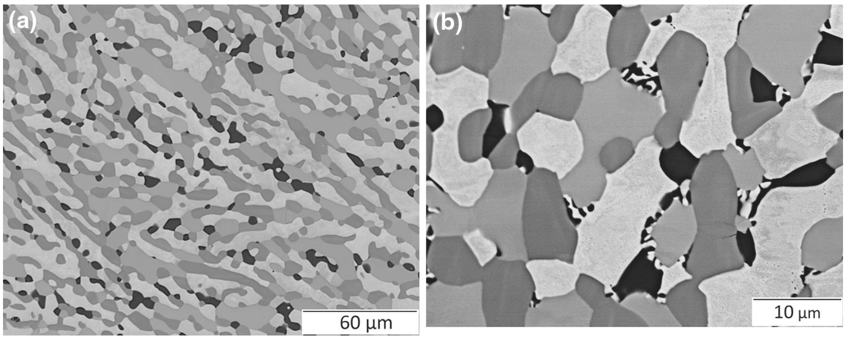

Fig. 9. SEM micrographs of alloy F in BSE mode (a) after homogenization treatment at 1600°C for 100 h and (b) after additional heat treatment at 1300°C for 17 h showing $Mo_{ss}$ (bright), T2 (darker gray), A15 (gray) and $Ti_5Si_3$ (dark).

Besides the density reduction of 7.7 g/cm$^3$, Ti alloying of Mo-Si-B alloys also leads to an improvement in creep resistance in terms of a decrease of the creep strain rate by more than two orders of magnitude compared to single crystalline CMSX-4 and by more than one order of magnitude compared to Ti-free Mo-Si-B. $Ti_5Si_3$ precipitates formed during processing are believed to be mainly responsible for this improvement. At temperatures higher than 1250°C, the A15 phase transforms into $Mo_{ss}$ and $Ti_5Si_3$ by a eutectoid reaction. This reaction needs to be clarified in further investigations to better understand and define the applicability to the Mo-Si-B-Ti alloy systems.

## ACKNOWLEDGEMENT

The financial support by Deutsche Forschungsgemeinschaft is gratefully acknowledged.

## REFERENCES

1. W.O. Soboyejo and T.S. Srivatsan, in *Advanced Structural Materials: Properties, Design Optimization, and Applications*, ed. W. O. Soboyejo and T. S. Srivatsan (CRC Press, Boca Raton, FL, 2007) pp. 475–493.
2. I.M. Wolff and P.J. Hill, *Platin. Met. Rev.* 44, 158 (2000).
3. M. Heilmaier, M. Krüger, H. Saage, J. Rösler, D. Mukherji, U. Glatzel, R. Völkl, R. Hüttner, G. Eggeler, C. Somsen, T. Depka, H.-J. Christ, B. Gorr, and S. Burk, *JOM* 61, 61 (2009).
4. J.H. Perepezko, R. Sakidja, and K.S. Kumar, in *Advanced Structural Materials : Properties, Design Optimization Applications,* ed. W.O. Soboyejo and T.S. Srivatsan (CRC Press, Boca Raton, FL, 2007), pp. 437–473.
5. R. Sakidja, J.H. Perepezko, S. Kim, and N. Sekido, *Acta Mater.* 56, 5223 (2008).
6. J.A. Lemberg and R.O. Ritchie, *Adv. Mater.* 24, 3445 (2012).
7. P. Jéhanno, M. Heilmaier, and H. Kestler, *Intermetallics* 12, 1005 (2004).
8. B. Gorr, L. Wang, S. Burk, M. Azim, S. Majumdar, H.-J. Christ, D. Mukherji, J. Rösler, D. Schliephake, and M. Heilmaier, *Intermetallics* 48, 34 (2014).
9. S. Majumdar, S. Burk, D. Schliephake, M. Krüger, H.-J. Christ, and M. Heilmaier, *Oxid. Met.* 80, 219 (2013).
10. J. Das, R. Mitra, and S.K. Roy, *Intermetallics* 19, 1 (2011).
11. S. Paswan, R. Mitra, and S.K. Roy, *Intermetallics* 15, 1217 (2007).
12. Y. Yang, H. Bei, S. Chen, E.P. George, J. Tiley, and Y.A. Chang, *Acta Mater.* 58, 541 (2010).
13. A. Yamauchi, K. Yoshimi, Y. Murakami, K. Kurokawa, and S. Hanada, *Solid State Phenom.* 127, 215 (2007).
14. K. Yanagihara, T. Maruyama, and K. Nagata, *Intermetallics* 4, 133 (1996).
15. S. Burk, B. Gorr, H.-J. Christ, D. Schliephake, M. Heilmaier, C. Hochmuth, and U. Glatzel, *Scr. Mater.* 66, 223 (2012).
16. D. Schliephake, M. Azim, K. von Klinski-Wetzel, B. Gorr, H.-J. Christ, H. Bei, E.P. George, and M. Heilmaier, *Metall. Mater. Trans. A* 45, 1102 (2013).
17. F.A. Rioult, S.D. Imhoff, R. Sakidja, and J.H. Perepezko, *Acta Mater.* 57, 4600 (2009).
18. M.K. Meyer and M. Akinc, *J. Am. Ceram. Soc.* 79, 938 (1996).
19. R. Mitra, *Int. Mater. Rev.* 51, 13 (2006).
20. Z. Tang, A.J. Thom, and M. Akinc, *Intermetallics* 14, 537 (2006).
21. J.J. Williams and M. Akinc, *Oxid. Met.* 58, 57 (2002).
22. M.A. Azim, S. Burk, B. Gorr, H.-J. Christ, D. Schliephake, M. Heilmaier, R. Bornemann, and P.H. Bolívar, *Oxid. Met.* 80, 231 (2013).
23. W.J.J. Wakelkamp, Diffusion and phase relations in the systems Ti-Si-C and Ti-Si-N, *Ph. D thesis Technische Universiteit Eindhoven* (Eindhoven, NL, 1991).
24. K. Yoshimi, S. Nakatani, T. Suda, S. Hanada, and H. Habazaki, *Intermetallics* 10, 407 (2002).
25. P. Jéhanno, M. Heilmaier, H. Saage, M. Böning, H. Kestler, J. Freudenberger, and S. Drawin, *Mater. Sci. Eng. A* 463, 216 (2007).
26. R. Sakidja, H. Sieber, and J.H. Perepezko, *Philos. Mag. Lett.* 79, 351 (1999).
27. M.K. Meyer, M.J. Kramer, and M. Akinca, *Intermetallics* 4, 273 (1996).
28. I. Rosales and J. Schneibel, *Intermetallics* 8, 885 (2000).
29. R. Rosenkranz, G. Frommeyer, and W. Smarsly, *Mater. Sci. Eng. A* A152, 288 (1992).
30. K. Ito, K. Ihara, K. Tanaka, M. Fujikura, and M. Yamaguchi, *Intermetallics* 9, 591 (2001).
31. J.H. Schneibel, P.F. Tortorelli, R.O. Ritchie, and J.J. Kruzic, *Metall. Mater. Trans. A* 36, 525 (2005).
32. D.M. Dimiduk and J.H. Perepezko, *MRS Bull.* 28, 639 (2003).
33. K. Harris, G.L. Erickson, S.L. Sikkenga, W.D. Brantnall, J.M. Aurrecoechea, and K.G. Kubarych, in *Superalloys 1992* (The Minerals, Metals & Materials Society, 1992), pp. 297–307.
34. Y. Yang, Y.A. Chang, L. Tan, and Y. Du, *Mater. Sci. Eng. A* 361, 281 (2003).

# Manuskript XIV

## Microstructure and mechanical properties at elevated temperatures of a new Al-containing refractory high-entropy alloy Nb-Mo-Cr-Ti-Al

H. Chen, A. Kauffmann, B. Gorr, D. Schliephake, C. Seemüller, J.N. Wagner, H.-J. Christ, M. Heilmaier

Journal of Alloys and Compounds, 661 (2016) 206-215

Journal of Alloys and Compounds 661 (2016)

Contents lists available at ScienceDirect

Journal of Alloys and Compounds

journal homepage: http://www.elsevier.com/locate/jalcom

# Microstructure and mechanical properties at elevated temperatures of a new Al-containing refractory high-entropy alloy Nb-Mo-Cr-Ti-Al

H. Chen [a, *], A. Kauffmann [a], B. Gorr [b], D. Schliephake [a], C. Seemüller [a], J.N. Wagner [a], H.-J. Christ [b], M. Heilmaier [a]

[a] *Institute for Applied Materials (IAM-WK), Karlsruhe Institute of Technology (KIT), Engelbert-Arnold-Str. 4, D-76131, Karlsruhe, Germany*
[b] *Institut für Werkstofftechnik, Universität Siegen, Paul-Bonatz-Str. 9-11, D-57068, Siegen, Germany*

## ARTICLE INFO

*Article history:*
Received 13 July 2015
Received in revised form
28 October 2015
Accepted 6 November 2015
Available online 17 November 2015

*Keywords:*
High-entropy alloys
Refractory metals
Homogenization
Deformation
Secondary phases

## ABSTRACT

In the present investigation, we provide results on the casting, homogenization, and deformation behavior of a new Al-containing refractory high-entropy alloy, namely the equiatomic Nb-Mo-Cr-Ti-Al. The alloy shows a dendritic microstructure after arc melting. The dendrites completely dissolve due to a heat treatment at 1300 °C for 20 h. Besides a major phase in the form of a solid solution of W prototype structure, identified by X-ray diffraction (XRD) measurements as well as electron backscatter diffraction (EBSD), additional phases of small volume fraction within the grains and at the grain boundaries were observed. Quasistatic compression tests, performed between room temperature and 1200 °C, reveal sustaining and high yield strength up to 800 °C and an increasing ductility with increasing test temperature. The dominant deformation mechanism for quasistatic compression loading between 800 °C and 1200 °C is the $\langle 111 \rangle$ pencil glide of dislocations within the solid solution which was proven by the according fiber texture components, evolving during deformation.

## 1. Introduction

Materials, combining excellent mechanical strength at ambient as well as elevated temperature with a suitable ductility and toughness, always are a reasonable optimization goal of modern materials science in order to facilitate new applications in mechanical engineering. In this respect, the recently proposed concept of suppression of intermetallic phases and stabilization of a solid solution of simple crystal structure by minimizing the configurational entropy term $-T\cdot\Delta S_{\mathrm{config}}$ in the Gibb's free energy [1–5] seems to provide an approach. For this purpose, equiatomic concentrations of mainly at least five alloying elements should be established in the solid solution in order to fulfill this concept. Due to the suppression of brittle intermetallic phases, ductility can in principle be improved. This is, of course, a rough assumption when the typical embrittlement of body-centered cubic (bcc) solid solutions with respect to the ductility and toughness of the base elements (for example Mo-Si or Mo-Re [6–8]) is taken into account. Nevertheless, Senkov & Semiatin [9] recently presented a bcc high entropy alloy which could be rolled up to a remarkable true strain of about 2.3 at room temperature indicating that a simple extrapolation from binary or ternary solid solutions to concentrated multicomponent systems with respect to ductility and toughness can be misleading. In addition to the suppression of intermetallic phases, choosing base elements with high melting points can lead to an enhanced melting point of the high-entropy alloy in comparison to currently used high temperature materials. Thus, operation at higher temperature is in principle possible. Moreover, adding alloying elements for improving properties other than pure mechanical ones is possible, too – for example, by utilizing elements facilitating the formation of a stable oxide scale for enhancing high temperature corrosion resistance.

Before adding Al, the focus has mainly been on the microstructure, mechanical properties and oxidation behavior of high-entropy alloys, solely based on elements with high melting points from group 4 to 6 (frequently named refractory metals) of the periodic table of elements [10–12]. Due to the high density of these alloys ranging up to 13.75 g/cm$^3$ for equiatomic W-Nb-Mo-Ta, heavy elements were replaced by lighter ones such as Hf, Zr, Cr and Ti [6,13–20]. The addition of Al to a high-entropy alloy changes its properties in different ways. With increasing Al content, the density of the alloy decreases. Comparing the alloys Ta-Nb-Hf-Zr-Ti and

---

[*] Corresponding author.
*E-mail address:* hans.chen@kit.edu (H. Chen).

http://dx.doi.org/10.1016/j.jallcom.2015.11.050
0925-8388/

$Al_{0.4}$-$Hf_{0.6}$-Nb-Ta-Ti-Zr which were introduced by Senkov et al. [20,21], the density drops from about 9.9 g/$cm^3$ to 9.0 g/$cm^3$. The mechanical properties, such as the yield strength and the ductility, depend on the amount of Al in the HEA, investigated on Nb-Ti-V-Ta-$Al_x$ [22] and $Al_x$-Hf-Nb-Ta-Ti-Zr [23]. Regarding high temperature oxidation, Al may form a stable and dense $Al_2O_3$ oxide scale. Oxidation tests of the high-entropy alloy W-Mo-Al-Cr-Ti reveal a scale growth following the parabolic growth law [24]. Having a similar atomic radius as refractory metals, it can be expected that Al-addition allows the formation of a solid solution in such an alloy, thus preventing the formation of intermetallic phases [21]. Never-theless, it has to be pointed out that several investigations already revealed various parameters other than the configurational entropy or atomic size difference to be more or less decisive, such as the mixing enthalpy $\Delta H_{mix}$, the mixing entropy $\Delta S_{mix}$ [25], the parameter $\Omega$ which describes the correlation between $\Delta H_{mix}$ and $\Delta S_{mix}$ [26], and the valence electron concentration VEC [27]. Hence, the stability of a solid solution with simple crystals structure has to be verified for each case.

In the present work, Nb-Mo-Cr-Ti-Al is investigated with respect to microstructural evolution during annealing as well as mechanical properties at various temperatures. For that, Nb, Mo and Ti are refractory metals for providing a suitable melting point for high temperature application. Ti, again, and Al are chosen in order to achieve low density, as shown by Senkov et al. [13,21], while Al and Cr are considered due to their ability to form stable oxide scales for good oxidation resistance. Nb-Mo-Cr-Ti-Al is expected to have similar properties as the W-containing counterpart, introduced above. CALPHAD calculations suggest that Nb-Mo-Cr-Ti-Al ("PanNb with V" database using Pandat; single phase, solid solution at 788—1712 °C) exhibits a similar melting temperature as W-Mo-Cr-Ti-Al (FactSage calculation; single phase, solid solution at 1077—1700 °C [24]). Considering the lower atomic mass of Nb, a lower density is to be expected when comparing Nb-Mo-Cr-Ti-Al with W-Mo-Cr-Ti-Al.

Generally, the investigated alloys show dendritic structure in the as-cast condition with significant differences in atomic concentration between dendritic and interdendritic regions [24,28]. An annealing step is typically performed after casting in order to homogenize the microstructure as well as to establish a single phase solid solution with simple crystal structure [13,14]. Despite the theory of stabilization of solid solutions by increasing the configurational entropy, a macro- and mesoscopically homogeneous microstructure cannot be reached in all cases of postulated high-entropy alloys. This is even more evident when investigations down to atomic scale are performed [29]. In addition to these local investigations, secondary phases are frequently found. XRD patterns of Ta-Nb-Hf-Zr-Ti show a presumably hexagonal second phase besides the main body-centered cubic structure (bcc) whereas Cr-Nb-Ti-(V-)Zr exhibits a Cr-rich face-centered cubic Laves phase [13,15].

In this publication, a detailed characterization of the alloy Nb-Mo-Cr-Ti-Al is presented, especially regarding microstructure, its evolution after heat treatment, and deformation at ambient and elevated temperature. Furthermore, the deformation mechanism by dislocation slip during compression loading at elevated temperatures is explicitly examined and identified by EBSD analysis.

## 2. Experimental

Nb-Mo-Cr-Ti-Al was melted from elemental bulk materials, mixed in equiatomic concentration, using an arc-melter AM/0.5, provided by Edmund Bühler GmbH. The purities of the starting materials Nb, Mo, Al, Cr and Ti were 99.9%, 99.96%, 99.9%, 99%, and 99.8%, respectively. The Ar base pressure for arc-melting was 0.6 bar following several alternating iterations of pumping and Ar flooding. A Zr lump in the vacuum chamber was used in order to reduce residual oxygen by liquefying prior to every melting step. The prepared buttons were flipped and remelted for at least five times for homogenization. After the final melting step, the alloy was cast into a rod-shaped Cu mold. The diameter and the length of the cast rod were 12 mm and 60 mm, respectively. The chemical alloy composition was analyzed using inductively coupled plasma optical emission spectrometry (ICP-OES) for the elements Nb, Mo, Cr, Ti and Al. O and N content were determined by means of carrier gas hot extraction analysis, using a TC500 by Leco. Heat treatments were performed using a Gero HTRH 70-600/18 resistance heating tube furnace under Ar flow at 1100, 1200, and 1300 °C for 20 h. The heating and cooling rate were 4.2 K/min. The platelet shaped samples with 12 mm in diameter were extracted from one and the same cast sample.

The cast as well as the heat-treated alloy conditions were investigated by means of SEM utilizing backscatter electron (BSE) imaging and energy dispersive X-ray spectroscopy (EDX) as well as EBSD for analytical purposes. All samples were prepared by a standard metallographic procedure finalized by a vibratory polishing step, using a non-crystallizing oxide polishing suspension with pH = 9.8, provided by Struers. Thereby, a combination of mechanical and chemical preparation was achieved. SEM investigations were performed on a Zeiss Auriga dual beam scanning electron and focused ion beam microscope equipped with an EDAX DigiView EBSD system and EDAX Octane silicon drift detector EDX system as well as a Zeiss EVO50 system equipped with a Thermo Scientific EDX system. X-ray diffraction analyses were carried out on a D2 Phaser system by Bruker equipped with a Lynxeye line detector. The Cu tube was operated at 30 kV and 10 mA. Quasistatic compression tests were performed utilizing a Zwick Z100 electromechanical universal testing machine equipped with a vacuum furnace by Maytec. After heating at a rate of 20 K/min, the test temperature was stabilized for 30 min before testing. The heat-treated samples (1300 °C/20 h) of $(3 \times 3 \times 4.5)$ $mm^3$ were tested under vacuum with an initial engineering strain rate of $10^{-3}$ $s^{-1}$. Strain was determined using strain gauges attached to the samples. The punches were made of SiC and hexagonal BN was used for lubrication. The specimens for compression tests shown in this article were extracted from the same cast sample as the specimens for heat-treatment experiments. For the reproduction of the deformation experiments, a second batch of material was produced and treated in the same way as described before.

## 3. Results and discussion

### 3.1. Casting and homogenization

Table 1 summarizes the chemical composition of the different materials conditions investigated in this article. For the as-cast state, wet chemical analysis by ICP-OES and EDX are in good agreement and the deviation from the equimolar composition does not exceed 0.75 at% for all elements. Hence, there is little evaporation during arc melting operations despite large differences in melting and boiling point of the alloying elements. The microstructure of the as-cast state, as it is shown in Fig. 1a, consists of dendritic and interdendritic regions within a polycrystalline matrix. Even at high resolution, no evidence for secondary phases was found. Previous investigations revealed that elements with high melting points tend to crystallize in the early stages of solidification [19,28]. In accordance to that, EDX of the dendrites reveals enrichment in Mo and Nb during primary solidification (Table 1). In contrast, the interdendritic regions are enriched in Cr, Ti and Al. By analyzing the compositions of the dendritic and inter-dendritic

**Table 1**

Composition of the investigated alloy in different conditions determined by EDX.† Composition determined by ICP-OES (unbalanced) for comparison. Dendritic and inter-dendritic regions are shown in the inset of Fig. 2a in detail. O content was determined to be 92 ppm in the as-cast state. N content was below the detection limit.* Phase located at the grain boundaries (see insets in Fig. 1c and d) and** located within the grains (see Fig. 1c).

| Condition | Temperature | Phase | Nb | Mo | Cr | Ti | Al |
|---|---|---|---|---|---|---|---|
| As-cast | – | Total† | 19.66 | 19.43 | 19.38 | 19.34 | 20.10 |
| | | Total | 19.8 ± 0.2 | 19.0 ± 0.2 | 20.3 ± 0.0 | 20.7 ± 0.0 | 20.2 ± 0.1 |
| | | Dendritic | 22.8 ± 0.3 | 28.7 ± 0.6 | 14.3 ± 0.3 | 18.4 ± 0.5 | 15.8 ± 0.7 |
| | | Inter-dendritic | 17.3 ± 0.4 | 10.9 ± 0.1 | 26.5 ± 0.7 | 22.5 ± 0.2 | 22.9 ± 0.9 |
| Annealed for 20 h | 1100 °C | Total | 20.2 ± 0.1 | 19.2 ± 0.1 | 20.4 ± 0.1 | 20.5 ± 0.2 | 19.8 ± 0.0 |
| | 1200 °C | Total | 19.9 ± 0.2 | 19.5 ± 0.2 | 19.9 ± 0.2 | 20.6 ± 0.1 | 20.1 ± 0.1 |
| | | Solid solution | 19.5 ± 0.1 | 19.6 ± 0.2 | 19.3 ± 0.2 | 21.4 ± 0.1 | 20.3 ± 0.2 |
| | | Laves | 24.8 ± 0.4 | 5.6 ± 0.9 | 40.3 ± 0.9 | 9.8 ± 0.6 | 19.4 ± 0.2 |
| | | Unknown* | 23.6 ± 3.6 | 22.3 ± 2.5 | 16.2 ± 3.6 | 17.0 ± 3.5 | 20.9 ± 0.5 |
| | | Unknown** | 21.4 ± 0.7 | 21.1 ± 0.9 | 18.1 ± 1.4 | 18.5 ± 1.2 | 20.9 ± 0.2 |
| | 1300 °C | Total | 20.5 ± 0.1 | 19.6 ± 0.1 | 19.7 ± 0.1 | 20.3 ± 0.2 | 19.9 ± 0.0 |
| | | Solid solution | 20.5 ± 0.1 | 19.5 ± 0.0 | 19.7 ± 0.1 | 20.5 ± 0.2 | 19.9 ± 0.1 |
| | | Unknown* | 21.7 ± 0.8 | 18.8 ± 0.3 | 21.2 ± 0.4 | 17.9 ± 1.1 | 20.3 ± 0.1 |
| Deformed | 1100 °C | Laves | 22.8 ± 0.8 | 17.6 ± 1.6 | 23.5 ± 2.6 | 17.8 ± 1.5 | 18.2 ± 0.4 |
| | | Unknown | 23.4 ± 0.7 | 20.1 ± 1.0 | 20.0 ± 1.7 | 17.0 ± 1.2 | 19.4 ± 0.3 |
| | 1200 °C | Laves | 24.4 ± 0.8 | 12.7 ± 3.5 | 30.6 ± 5.3 | 13.7 ± 0.8 | 18.5 ± 0.5 |
| | | Unknown | 24.0 ± 1.5 | 18.6 ± 4.6 | 21.3 ± 7.2 | 16.8 ± 3.0 | 19.3 ± 0.6 |

regions in comparison to the total composition, fractions of 46 at% dendritic as well as 54 at% inter-dendritic region can be calculated, respectively. The XRD analysis of the as-cast state is shown in Fig. 2. The major Bragg positions can be assigned to a bcc crystal structure of the W prototype with a broad variation of possible lattice constants ranging from about 0.312 nm up to 0.318 nm. The variation is most probably attributed to the inhomogeneous element distribution within the solid solution as it was assumed in previous investigations [24], too. This can be well described by assuming several bcc phases with different lattice parameters. The obtained

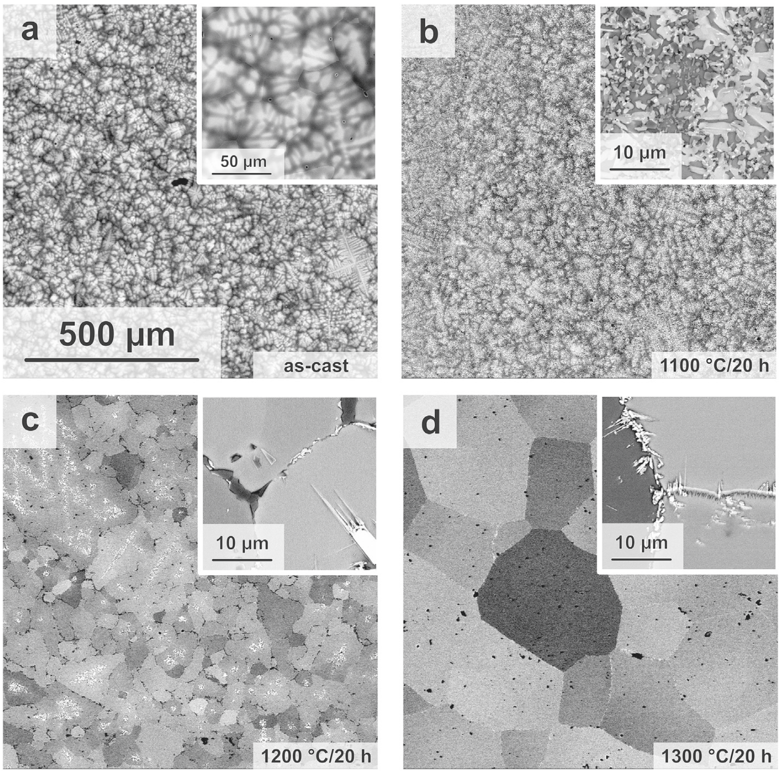

**Fig. 1.** SEM micrographs (BSE, orientation and composition contrast) of the microstructure of Nb-Mo-Cr-Ti-Al in the: a) as-cast and annealed conditions after heat treatment at b) 1100 °C, c) 1200 °C and d) 1300 °C for 20 h, respectively. All major micrographs are taken at the same magnification. Inset magnification is specified, respectively. The inset in (b) highlights the morphology of the at least three different phases at higher magnification. The insets in (c) and (d) show secondary phases with continuous as well as acicular morphology at the grain boundaries.

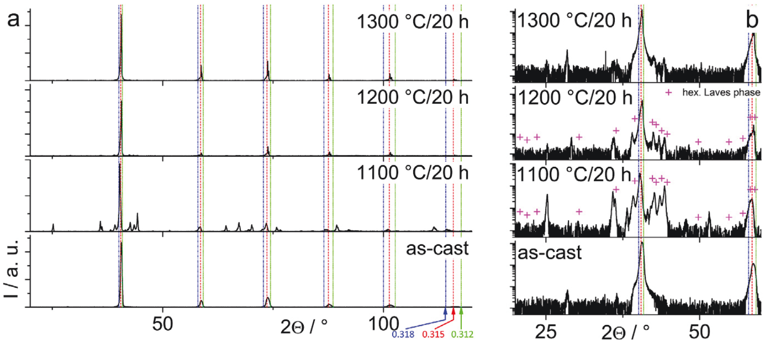

**Fig. 2.** Background subtracted XRD patterns of cross sections of Nb-Mo-Cr-Ti-Al in different conditions: a) full pattern and b) section of the pattern with logarithmic intensity scale. Bragg positions of bcc structures with varying lattice parameters (provided in nm) are indicated by dashed lines in (a). Bragg positions of the hexagonal Laves phase are highlighted according to the labels in (b) – positions with little intensity were excluded. Intensities may be influenced by limited number of grain orientations within the samples. The lines, indicating the lattice constant variation, are extended to the diffraction patterns of the annealed state in order to ease comparison.

values are slightly higher than those of the comparable W-Mo-Al-Cr-Ti alloy, which are between about 0.309 nm and 0.312 nm (for the as-cast as well as heat-treated condition) [24]. Considering the larger atomic radius of Nb (145 pm) compared to W (135 pm), an increase of the lattice parameter in Nb-Mo-Cr-Ti-Al is conceivable [30]. Local analysis of the crystal structure of dendritic and interdendritic regions within a single grain of the as-cast state (patterns are included in the online supplementary, similar pattern to that in Fig. 3d), respectively, support the global XRD analysis by patterns of bcc crystals with minor changes of the lattice constant (the determined variation of 0.312–0.318 nm is below the resolution of the EBSD camera system in use).

In order to homogenize the material as well as to establish a single phase solid solution, heat treatments of 20 h under Ar atmosphere were performed. The microstructure following an annealing at 1100 °C does not exhibit a significant homogenization effect which can be seen from microstructural imaging in Fig. 1b as well as global XRD analysis in Fig. 2. In Fig. 1b, a combination of composition and orientation contrast is visible. The local analysis of crystal structure reveals at least three different phases that can be identified as bcc (W prototype, Strukturbericht designation A2, pattern is included in the online supplementary, similar to the pattern in Fig. 3d), the hexagonal modification of the $Cr_2Nb$ Laves phase ($MgZn_2$ prototype, Strukturbericht designation C14, Fig. 3a) and an unknown phase (Fig. 3b). Due to the small length scale of the obtained microstructure, a detailed investigation of the local chemistry of the phases by SEM-EDX is not suitable, here. This is done for higher annealing temperatures in the following.

Subsequent to a heat treatment at 1200 °C, the volume fraction of dendritic microstructure was significantly reduced as visualized in Fig. 1c. Also, the number and intensity of Bragg positions, not correlating with those of the bcc crystal structure, are significantly reduced, as seen in the XRD pattern in Fig. 2a. The secondary phases are mainly located at the grain boundaries. The Laves phase, which was identified by electron diffraction (pattern is included in the online supplementary, similar to the pattern in Fig. 3a), appears dark-gray and an unknown phase (Fig. 3c) appears bright in the inset of Fig. 1c. The diffraction pattern of the unknown phase in Fig. 3c exhibits remarkable similarities to the pattern for the unknown phase obtained following the 1100 °C annealing step (Fig. 3b, indicated by arrows connecting similar zone axes). Thus, the unknown phase obtained subsequent to annealing at 1100 °C and 1200 °C seem to be the same. The grain size of the solid solution (W prototype, pattern is included in the online supplementary, similar pattern in Fig. 3d) has grown to 50–100 μm as it can be seen from the SEM image in Fig. 1c. According to Table 1, the solid solution approximately exhibits the equimolar composition with deviations less than 0.6 at%. By analyzing the compositions of the obtained phases in comparison to the total composition, the fraction of the solid solution can be calculated to about 87 at%, which is in good agreement with the SEM image in Fig. 1c. The hexagonal Laves phase is enriched in Cr. The presence of a Cr-rich Laves phase was already observed in the alloys Cr-Nb-Ta-Ti-Zr and Cr-Nb-Ti-V-Zr [13,19]. However, the reported Laves phases were identified as the face-centered cubic modification of $Cr_2Nb$ ($MgCu_2$ prototype, Strukturbericht designation C15). A possible substitution of lattice sites can be described by means of $(Cr,Al,Mo)_2(Nb,Ti)$ according to the overall composition of the phase: (i) ideal stoichiometry Cr:Nb = 66.6:33.3 and (ii) present sample (Cr,Al,Mo):(Nb,Ti) = 65.3:34.7 (see Table 1). Since the composition as well as crystallographic data suggest a derivation of the present Laves phase from the binary $Cr_2Nb$, the following discussion is based on the relation of these two elements to the others present in the HEA. Cr-Nb as well as Cr-Ti form Laves phases. Nb-Ti as well as Cr-Mo exhibit complete solubility (Cr-Mo with miscibility gap at low temperature). Al-Cr forms a $Cr_2Al$ compound but the prototype system is not related to a Laves phase ($MoSi_2$ prototype). It has to be emphasized, that Mo-Nb exhibit complete solubility in contrast to the proposed substitution. Thus, a certain amount of Mo on the Nb lattice site is to be expected, too. The XRD pattern shows a Bragg position at 25.22°, which can perhaps be assigned to the unknown phases (Fig. 3b and c). The EDX analysis does not provide indications for a suitable stoichiometric prototype structure since it exhibits a similar composition as the solid solution.

A further increase of homogenization temperature up to 1300 °C, as shown in Fig. 1d, results in a further reduction of secondary phases within the grains of the solid solution. The contrast of Fig. 1d is mainly attributed to different orientations of the chemically homogeneous grains. The chemical composition of the bcc solid solution (diffraction pattern in Fig. 3d) is shown in Table 1. The deviation from the equimolar composition is less than 0.5 at%. Residual intermetallic phases are found in the vicinity of the grain boundaries similar to observations on comparable Al-containing refractory high-entropy alloys in Ref. [21]. Hence, Bragg positions, not assignable to the bcc crystal structure, are still present as they are visualized in the logarithmic intensity plot in Fig. 2b. Evidence for the local appearance of any modification of the Laves phases was not found. The grain boundaries seem to be decorated by the

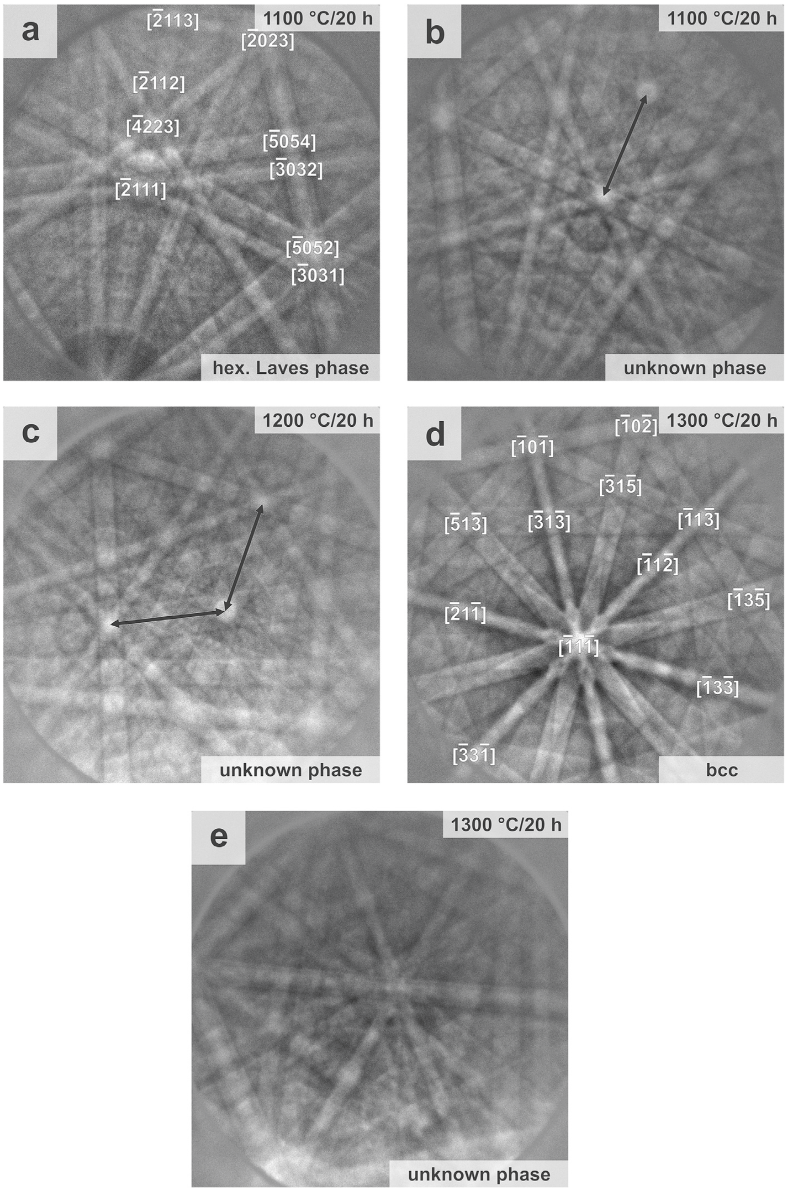

**Fig. 3.** EBSD patterns with corresponding zone axes of Nb-Mo-Cr-Ti-Al taken at 20 kV on samples in different conditions (a complete set of patterns for all phases is included in the online supplementary). The Laves phase is the hexagonal modification of $Cr_2Nb$ ($MgZn_2$ prototype, Strukturbericht designation C14).

unknown phase, exclusively. The pattern of the unknown phase in Fig. 3e differs from those observed for annealing at 1100 and 1200 °C (Fig. 3b and c). Based on image analysis the fraction of secondary phase at the grain boundary could be determined to be well below 0.5 vol% while the spread of the acicular morphology into the matrix grains is always below 10 μm (inset of Fig. 1d). The grain size of the bcc solid solution increased to about 250 μm. Abnormal grain growth has already started. A further increase of homogenization temperature to maximum 1400 °C does not lead to a full suppression of secondary phases but further rapid grain growth is observed (not shown here). In order to provide a reasonable orientation distribution during the following analysis of the microstructure subsequent to quasistatic compression tests, the following results were obtained on samples, homogenized at 1300 °C for 20 h.

### 3.2. *Deformation at ambient and elevated temperature*

In order to evaluate the potential of the present Nb-Mo-Cr-Ti-Al alloy regarding high temperature application, compression tests were performed at room temperature, 400 °C, 600 °C, 800 °C, 1000 °C and 1200 °C with a strain rate of $10^{-3}$ $s^{-1}$. Fig. 4 shows the

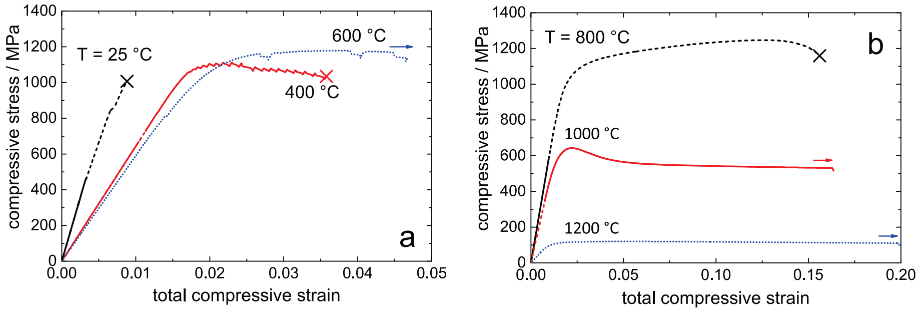

**Fig. 4.** Stress-strain dependence of quasistatic compression tests at: a) room temperature, 400 °C and 600 °C as well as b) 800 °C, 1000 °C and 1200 °C. Fracture is highlighted by X. Arrows indicate tests deliberately stopped.

according stress-strain dependence and Table 2 summarizes the mechanical properties determined by these tests.

At room temperature, there was no indication of plastic deformation. At elevated temperatures, plastic deformation was observed. A minimum fracture strain of 0.02 was reached at 400 °C. While strength remains stable, plastic deformability before failure rises up to 0.135 by increasing the temperature to 800 °C. Beside a significant drop of stress by 40% at 1000 °C, stress-strain dependence shows a characteristic curve shape with an inflection point after reaching maximum stress. At 1200 °C, a plastic strain of over 0.24 without indication of internal cracks was obtained.

Regarding room temperature compression test, onset of plasticity could not be determined unlike to comparable Al-containing high-entropy alloys, such as Al-$Nb_{1.5}$-$Ta_{0.5}$-$Ti_{1.5}$-$Zr_{0.5}$ which revealed a plastic strain of at least 0.035 at room temperature [21]. The maximum stresses during compression tests up to 800 °C are most probably determined by defects of the cast material as it can be exemplarily seen in the SEM micrographs in Fig. 1d. Thus, a large standard deviation of the characteristic stresses is observed at a test temperature of 800 °C (Table 2). As regularly seen in literature [14,16,21], temperature increase leads to higher plasticity. At 1000 °C, the investigated alloy shows a similar curve shape as high-entropy alloys by Senkov et al. [21], tested in the same temperature range. Dynamic recrystallization as a possible reason for the softening behavior [31] can be excluded since no evidence for microstructure restoration by nucleation at the grain boundary forming typical necklace structures or particle stimulated nucleation was found (Fig. 5d).

After performing the quasistatic compression tests, microstructure of the deformed samples was analyzed by means of EBSD. Therefore, orientation maps are shown in Fig. 5 as color-coded images according to the inverse pole figure (inset in Fig. 5b) of the compression direction (CD). Abnormal grain growth induced during the homogenization process is clearly indicated by grains with diameter of more than 500 μm in the as-homogenized state. Subsequent to deformation at 400 °C, cracks are observed with an orientation of about 45° with respect to the compression direction.

**Table 2**

: Yield stress $\sigma_{0.2}$, maximum strength $\sigma_{max}$ and obtained plastic strain before fracture $\varepsilon_p$ as a function of temperature during compression tests; (X) marks those compression tests which ended due to fracture of the respective sample.

| Testing temperature/°C | $\sigma_{0.2}$/MPa | $\sigma_{max}$/MPa | $\varepsilon_p$ | |
|---|---|---|---|---|
| 25 | – | 1010 | – | (X) |
| 400 | 1080 | 1100 | 0.020 | (X) |
| 600 | 1060 | 1170 | >0.025 | |
| 800 | 860 ± 110 | 1000 ± 195 | >0.020 | (X) |
| 1000 | 594 ± 5 | 630 ± 16 | >0.150 | |
| 1200 | 105 ± 14 | 116 ± 8 | >0.240 | |

Discontinuous stress-strain dependence during loading at 400 °C as well as 600 °C is caused by crack initiation within the material, which is exemplarily seen in Fig. 5b. In the vicinity of the crack, increased local misorientation is observed, revealing localized plastic deformation. In contrast, short cracks are oriented parallel to the compression direction and local misorientation is homogeneously distributed at 800 °C. In all cases, 400 °C, 600 °C and 800 °C, occurring cracks are transgranular, implying stable grain boundaries within the material. At 1000 °C as well as 1200 °C, cracks are absent, plastic deformation occurs uniformly, and grains become flattened as it is expected for ductile behavior during compression tests. In this temperature range, significant changes of the microstructure were observed during the solution annealing experiments. Thus, further analysis of changing microstructure and phases were performed after thermomechanical loading. In contrast to deformation tests at 800 °C and below, the phases at the grain boundaries of the as-homogenized microstructure tend to coarsen as can be seen by a comparison of Fig. 6a with Fig. 6b and c. Moreover, additional phase formation within the grains is observed at 1200 °C (Fig. 6c) within the deformed matrix (indicated by changes of orientation contrast by localized deformation). The hexagonal Laves phase (patterns are similar to that in Fig. 3a and are included in the online supplementary) and an unknown phase (electron patterns in Fig. 7) could be identified as the secondary phases developing and coarsening during deformation at 1000 °C as well as 1200 °C. The patterns of the unknown phase exhibit similar zone axes (indicated by arrows) to those of the unknown phase observed in the same temperature range during the solution annealing experiments. Nevertheless, the distances of zone axes in the case of Fig. 7b are slightly higher indicating changing lattice parameter ratios or lattice angles. This might be attributed to the different time scales for the compression tests at high temperature and for the solution annealing experiments. In accordance to the evaluation of the homogenized material, the Laves phase is enriched in Cr while the unknown phase exhibits a solute content similar to the solid solution. The local chemical analysis is included in Table 1.

Despite a comparatively low number of investigated grains, the orientation distribution plotted as contours in the inverse pole figure in Fig. 8 reveals an increase of orientation density between ⟨001⟩ and ⟨111⟩ crystallographic axes parallel to the compression direction as deformation temperature and, thus, plastic strain is increased. This can be explained by pencil glide being the predominant deformation mechanism. The ⟨111⟩ crystallographic axes seem to be the common slip directions. For the commonly observed slip systems of bcc metals, namely with a ⟨111⟩ slip direction and slip planes of type {110}, {121}, or {132}, a rotation of the compression direction under single slip from an arbitrary

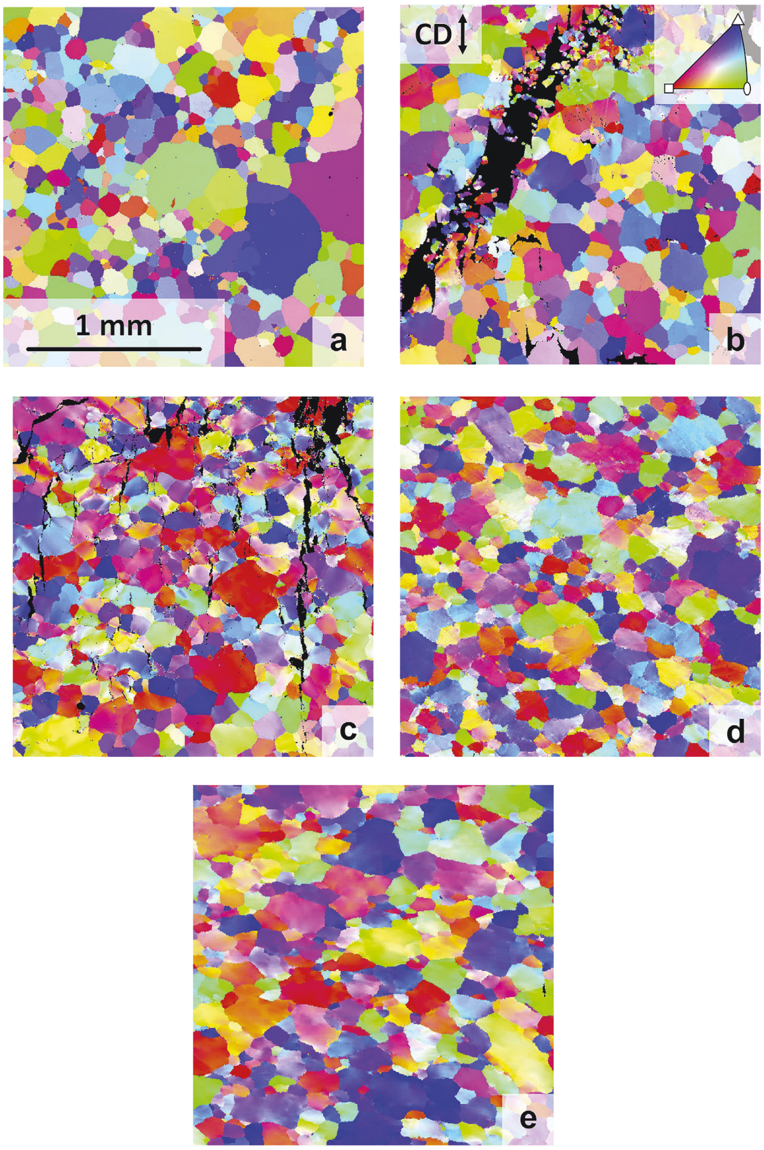

**Fig. 5.** Orientation imaging microscopy on longitudinal sections of Nb-Mo-Cr-Ti-Al quasistatically deformed in compression: a) initial condition and deformed at b) 400 °C, c) 800 °C, d) 1000 °C and e) 1200 °C. Compression direction is vertical and the color code corresponds to the inverse pole figure of the compression direction (inset in (b)). The maps are of the same size and observed using a step size of 5 µm.

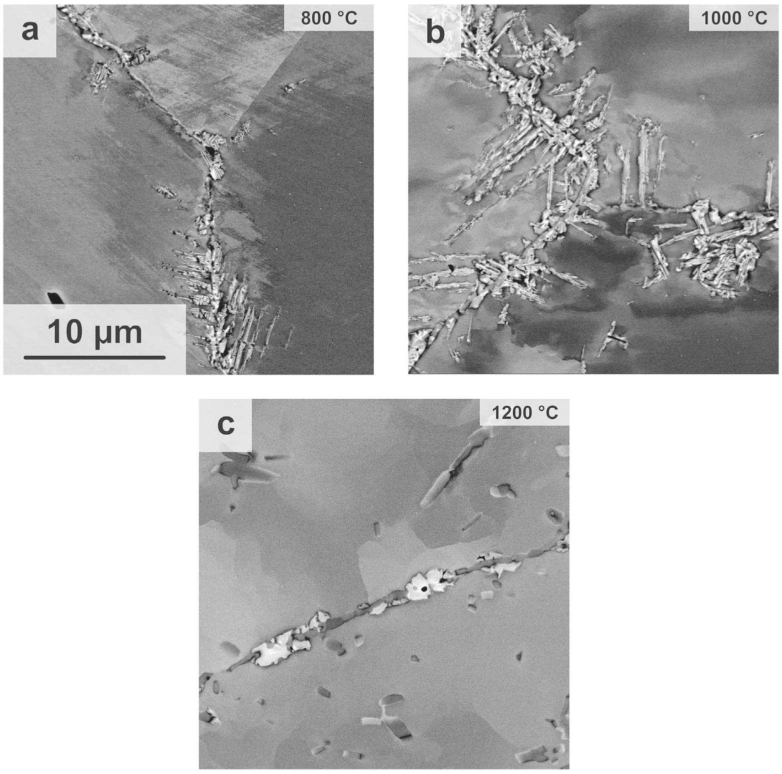

**Fig. 6.** Detailed SEM micrographs (BSE, orientation and composition contrast) of Nb-Mo-Cr-Ti-Al subsequent to deformation at: a) 800 °C, b) 1000 °C, and c) 1200 °C. All SEM micrographs are taken at the same magnification.

orientation within the standard triangle towards the trace between ⟨001⟩ and ⟨111⟩ is expected. The corresponding orientation changes are illustrated in Fig. 9.

## 4. Conclusions

This study provides the following main results regarding microstructure and deformation at elevated temperature of an equiatomic Nb-Mo-Cr-Ti-Al high-entropy alloy:

- The analysis of the microstructure of arc-melted Nb-Mo-Cr-Ti-Al subsequent to homogenization treatments reveals that the dendritic-like as-cast microstructure can be transformed into an equiaxed microstructure with minor secondary phases by annealing at 1300 °C under Ar atmosphere for 20 h. The formation of the hexagonal modification of the $Cr_2Nb$ Laves phase can be suppressed by a homogenization temperature of 1300 °C and above.
- Compression tests reveal a maximum strength of ≈ 1 GPa and increasing ductility up to a plastic strain of 24% with increasing

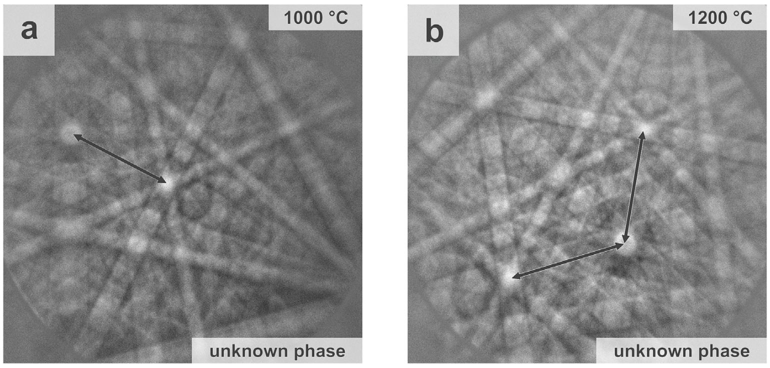

**Fig. 7.** EBSD patterns with corresponding zone axes of Nb-Mo-Cr-Ti-Al taken at 20 kV. A complete set of patterns for all phases is included in the online supplementary.

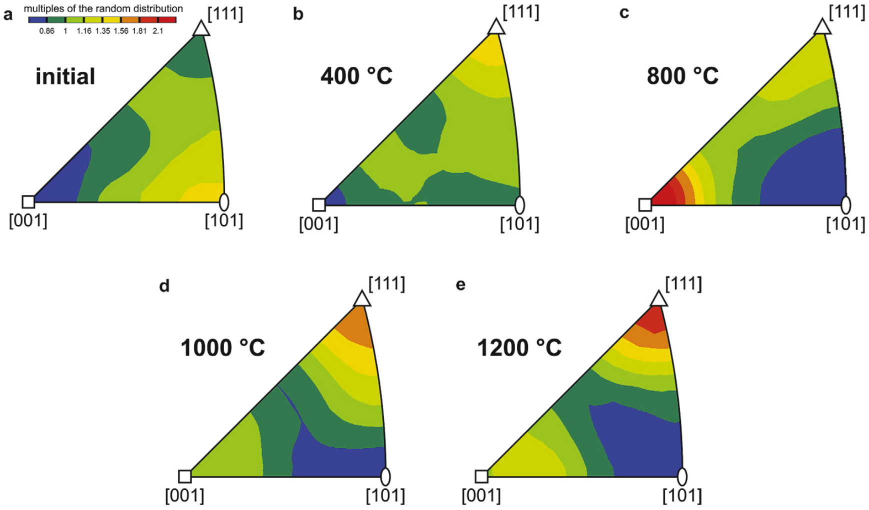

**Fig. 8.** Orientation distribution as contours in the inverse pole figures of the compression direction of Nb-Mo-Cr-Ti-Al quasistatically deformed in compression: a) initial condition, deformed at b) 400 °C, c) 800 °C, d) 1000 °C, and e) 1200 °C. Scale in multiples of the random distribution (inset in (a)) is kept constant.

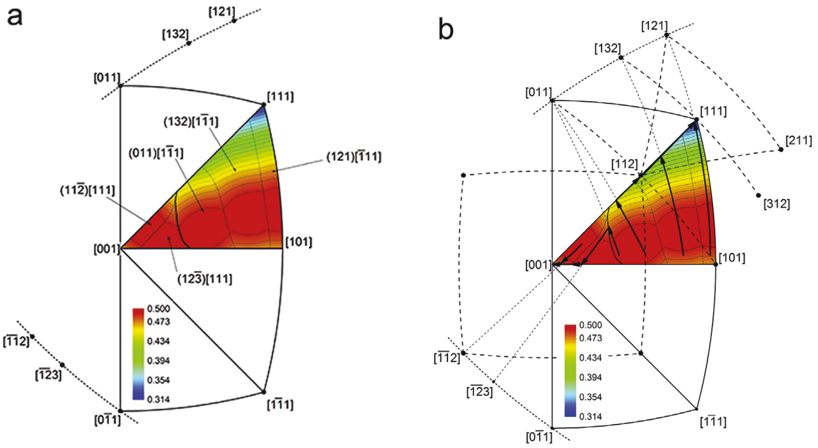

**Fig. 9.** a) Maximum Schmid factors (active slip system under single slip) of the pencil slip systems with common $\langle 1\bar{1}1\rangle$ slip direction and {110}, {121}, and {132} slip planes presented in the inverse pole figure of the compression direction. b) Rotation of the compression direction, indicated by arrows, in dependence of the initial orientation of a single crystal. Under compression load, the compression direction tends to rotate towards to slip plane normal. Dashed lines indicate the connection of slip plane normals when multiple slip is preferred.

test temperature up to 1200 °C. During compression testing at 1000 °C as well as 1200 °C, secondary phases are formed and coarsen, respectively.

- The analysis of fiber texture components subsequent to uniaxial compression testing at elevated temperatures suggests that Nb-Mo-Cr-Ti-Al deforms by dislocation slip, forming the common combined ⟨001⟩ and ⟨111⟩ fiber texture components along the compression direction. These can be explained in terms of the orientation change during slip deformation on slip systems with common ⟨111⟩ slip direction.

## Acknowledgments

The authors gratefully acknowledge the financial support by the Deutsche Forschungsgemeinschaft (DFG), grant no. HE 1872/31-1. AK thanks the Carl Zeiss Foundation for financial support by a postdoc grant. This work was partly carried out with the support of the Karlsruhe Nano Micro Facility (KNMF, www.knmf.kit.edu), a Helmholtz Research Infrastructure at Karlsruhe Institute of Technology (KIT, www.kit.edu). The authors acknowledge the chemical analysis by ICP-OES at the Institute for Applied Materials (IAM-AWP), Karlsruhe Institute of Technology (KIT). Furthermore, we would like to express our gratitude to S. Seils for experimental support.

## Appendix A. Supplementary data

Supplementary data related to this article can be found at http://dx.doi.org/10.1016/j.jallcom.2015.11.050.

## References

[1] J.-W. Yeh, S.-K. Chen, S.-J. Lin, J.-Y. Gan, T.-S. Chin, T.-T. Shun, C.-H. Tsau, S.-Y. Chang, Nanostructured high-entropy alloys with multiple principal elements: novel alloy design concepts and outcomes, Adv. Eng. Mater. 6 (2004) 299–303.

[2] J.-W. Yeh, Y.-L. Chen, S.-J. Lin, S.-K. Chen, High-entropy alloys - a new era of exploitation, Mater. Sci. Forum 560 (2007) 1–9.

[3] M.-H. Tsai, Physical properties of high entropy alloys, Entropy 15 (2013) 5338–5345.

[4] M.-H. Tsai, J.-W. Yeh, High-entropy alloys: a critical review", Mater. Res. Lett. 2 (2014) 107–123.

[5] Y. Zhang, T.T. Zuo, Z. Tang, M.C. Gao, K.A. Dahmen, P.K. Liaw, Z.P. Lu, Microstructures and properties of high-entropy alloys, Prog. Mater. Sci. 61 (2014) 1–93.

[6] L. Northcott, Molybdenum, Butterworths Scientific Publications, London, 1956.

[7] X. Yu, J. Yu, K.S. Kumar, The tensile response of Mo, Mo–Re and Mo–Si solid solutions", Int. J. Refract. Metals Hard Mater. 41 (2013) 329–338.

[8] D. Sturm, M. Heilmaier, J.H. Schneibel, P. Jéhanno, B. Skrotzki, H. Saage, The influence of silicon on the strength and fracture toughness of molybdenum, Mater. Sci. Eng. A 463 (2007) 107–114.

[9] O.N. Senkov, S.L. Semiatin, "Microstructure and properties of a refractory high-entropy alloy after cold working, J. Alloys Compd. 649 (2015) 1110–1123.

[10] O. Senkov, G. Wilks, D. Miracle, C. Chuang, P. Liaw, Refractory high-entropy alloys, Intermetallics 18 (2010) 1758–1765.

[11] O. Senkov, G. Wilks, J. Scott, D. Miracle, Mechanical properties of $Nb_{25}Mo_{25}Ta_{25}W_{25}$ and $V_{20}Nb_{20}Mo_{20}Ta_{20}W_{20}$ refractory high entropy alloys, Intermet. 19 (2011) 698–706.

[12] Zhang, B.; Gao, M. C.; Zhang, Y.; Yang, S.; Guo, SM. Senary Refractory High Entropy Alloy MoNbTaTiVW.

[13] O. Senkov, S. Senkova, C. Woodward, D.B. Miracle, Low-density, refractory multi-principal element alloys of the Cr–Nb–Ti–V–Zr system: microstructure and phase analysis, Acta Mater. 61 (2013) 1545–1557.

[14] O. Senkov, S. Senkova, D. Miracle, C. Woodward, Mechanical properties of low-density, refractory multi-principal element alloys of the Cr-Nb-Ti-V-Zr system", Mater. Sci. Eng. A 565 (2013) 51–62.

[15] O. Senkov, J. Scott, S. Senkova, D. Miracle, C. Woodward, Microstructure and room temperature properties of a high-entropy TaNbHfZrTi alloy, J. Alloys Compd. 509 (2011) 6043–6048.

[16] O. Senkov, J. Scott, S. Senkova, F. Meisenkothen, D. Miracle, C. Woodward, Microstructure and elevated temperature properties of a refractory TaNbHfZrTi alloy, J. Mater. Sci. 47 (2012) 4062–4074.

[17] O. Senkov, C. Woodward, Microstructure and properties of a refractory NbCrMo0.5Ta0.5TiZr alloy, Mater. Sci. Eng. A 529 (2011) 311–320.

[18] O.N. Senkov, F. Zhang, J.D. Miller, Phase composition of a CrMo0.5NbTa0.5TiZr high entropy alloy: comparison of experimental and simulated data, Entropy 15 (2013) 3796–3809.

[19] M.G. Poletti, G. Fiore, B.A. Szost, L. Battezzati, "Search for high entropy alloys in the X-NbTaTiZr systems (X= Al, Cr, V, Sn), J. Alloys Compd. 620 (2015) 283–288.

[20] J. Couzinié, G. Dirras, L. Perrière, T. Chauveau, E. Leroy, Y. Champion, I. Guillot, Microstructure of a near-equimolar refractory high-entropy alloy, Mater. Lett. 126 (2014) 285–287.

[21] O. Senkov, C. Woodward, D. Miracle, Microstructure and properties of aluminum-containing refractory high-entropy alloys, JOM 66 (2014) 2030–2042.

[22] X. Yang, Y. Zhang, P.K. Liaw, Microstructure and compressive properties of NbTiVTaAlx high entropy alloys, Procedia Eng. 36 (2012) 292–298.

[23] C.M. Lin, C.C. Juan, C.H. Chang, C.W. Tsai, J.W. Yeh, Effect of Al addition on mechanical properties and microstructure of refractory $Al_xHfNbTaTiZr$ alloys, J. Alloys Compd. (2015) 100–107.

[24] B. Gorr, M. Azim, H.-J. Christ, T. Mueller, D. Schliephake, M. Heilmaier, Phase equilibria, microstructure, and high temperature oxidation resistance of novel refractory high-entropy alloys, J. Alloys Compd. 624 (2014) 270–278.

[25] Y. Zhang, Y.J. Zhou, J.P. Lin, G.L. Chen, P.K. Liaw, Solid-solution phase transformation rules for multi-component alloys, Adv. Eng. Mater. 10 (2008) 534–538.

[26] Y. Zhang, X. Yang, P.K. Liaw, Alloy design and properties optimization of high-entropy alloys, JOM 64 (2012) 830–838.

[27] S. Guo, C. Ng, J. Lu, C.T. Liu, Effect of valence electron concentration on stability of fcc or bcc phase in high entropy alloys, J. Appl. Phys. 109 (2011) 103505.

[28] B. Gorr, M. Azim, H.-J. Christ, H. Chen, D.V. Szabo, M. Heilmaier, Microstructure Evolution in a New Refractory High-Entropy Alloy Mo-W-Al-Cr-Ti" in Metallurgical and Materials Transactions A, 2015 (submitted) for publication, http://dx.doi.org/10.1007/s11661-015-3246-0.

[29] M. Laurent-Brocq, A. Akhatova, L. Perrière, S. Chebini, X. Sauvage, E. Leroy, Y. Champion, Insights into the phase diagram of the CrMnFeCoNi high entropy alloy, Acta Mater. 88 (2015) 355–365.

[30] J.C. Slater, Atomic radii in crystals, J. Chem. Phys. 41 (1964) 3199–3204.

[31] F.J. Humphreys, M. Hatherly, Recrystallization and Related Annealing Phenomena, Elsevier, Oxford (, 2004.

# Manuskript XV

## Microstructure evolution in a new refractory high-entropy alloy W-Mo-Cr-Ti-Al

B. Gorr, M. Azim, H.-J. Christ, H. Chen, D.-V. Szaboo, A. Kauffmann, M. Heilmaier

Metallurgical and Materials Transactions A, 47A (2016) 961-970

# Microstructure Evolution in a New Refractory High-Entropy Alloy W-Mo-Cr-Ti-Al

BRONISLAVA GORR, MARIA AZIM, HANS-JUERGEN CHRIST, HANS CHEN,
DOROTHEE VINGA SZABO, ALEXANDER KAUFFMANN,
and MARTIN HEILMAIER

The microstructure of a body-centered cubic 20W-20Mo-20Cr-20Ti-20Al alloy in the as-cast condition as well as its microstructural evolution during heat treatment was investigated. Different characterization techniques, such as focused ion beam-scanning electron microscope, X-ray diffraction, and transmission electron microscope, were applied. Experimental observations were supported by thermodynamic calculations. The alloy exhibits a pronounced dendritic microstructure in the as-cast condition with the respective dendritic and interdendritic regions showing significant fluctuations of the element concentrations. Using thermodynamic calculations, it was possible to rationalize the measured element distribution in the dendritic and the interdendritic regions. Observations of the microstructure evolution reveal that during heat treatment, substantial homogenization takes place leading to the formation of a single-phase microstructure. Driving forces for the microstructural evolution were discussed from a thermodynamic point of view.

DOI: 10.1007/s11661-015-3246-0

## I. INTRODUCTION

METALLIC alloys with a beneficial combination of mechanical properties, easy formability, long-term stability, high-temperature corrosion resistance, and low manufacturing costs have always been in great demand for industry.[1,2] Some of the recently developed high-entropy alloys (HEAs) have been proposed as possible candidates for applications in structural components operated at high temperatures due to their potentially perspective properties, such as excellent long-term phase stability and strength.[3–7] Along the lines of aiming at development of novel high-temperature materials, a new equiatomic alloy system W-Mo-Cr-Ti-Al has been proposed by Gorr *et al.*[8] The alloy design concept supported by the thermodynamic analysis is generally based on the principle of HEAs. The microstructure and some properties of the first candidate from this new alloy family, namely the alloy W-Mo-Cr-Ti-Al, were screened and presented in Reference 8. First microstructural investigations showed that the alloy in the as-cast condition exhibits a relatively inhomogeneous microstructure with pronounced dendritic and interdendritic regions. XRD results indicated that either two body-centered cubic (bcc) phases with slightly different lattice parameters or one bcc phase with a lattice distortion form in the alloy in the as-cast condition. It was also found that the alloy possesses a high hardness of around 800 HV and a relatively good oxidation resistance at 1273 K (1000 °C).[8]

The identification of the phases present and investigation of their stability seem to be a general challenge in the exploration of the HEAs. For example, Cantor *et al.*[9] and later Otto *et al.*[10] reported that the equiatomic alloy Fe-Co-Ni-Cr-Mn consists of a single face-centered cubic (fcc) solid solution phase. However, recent TEM investigations carried out by Liu *et al.* reveal that a second fcc phase might be present in this alloy.[11] The recent study by Schuh *et al.* also highlights the decomposition tendency of the alloy CoCrFeMnNi upon annealing after severe plastic deformation.[12] It was found that the hardness increase to a maximum of about 910 HV after annealing at 723 K (450 °C) can be attributed to the formation of three additional phases, a NiMn-rich, Cr-rich, and FeCo-rich phase. Considering the fact that many HEAs containing additional phases often show beneficial properties compared to the truly single-phase materials, the HEA community discusses whether only single-phase materials should be classified as HEAs.

Since the combinations of compositions and processing routes of HEAs are numerous, each HEA usually possesses a unique microstructure and, consequently, different properties.[13–17] Hence, thorough knowledge of microstructure in the equilibrium state, the microstructure evolution from the as-manufactured state towards equilibrium as well as understanding of the driving forces and relevant mechanisms causing the resulting microstructure are indispensible for alloy development and possible future industrial

---

BRONISLAVA GORR, Group Leader of the Research Group "High Temperature Corrosion", MARIA AZIM, Ph.D. Student, and HANS-JUERGEN CHRIST, Professor, are with the Institut für Werkstofftechnik, Universität Siegen, Paul-Bonatz-Str. 9-11, 57068 Siegen, Germany. Contact e-mail: gorr@ifwt.mb.uni-siegen.de HANS CHEN, Ph.D. Student, DOROTHEE VINGA SZABO, Senior Researcher, ALEXANDER KAUFFMANN, Research Associate, and MARTIN HEILMAIER, Professor, are with the Institut für Angewandte Materialien - Werkstoffkunde (IAM-WK), Karlsruhe Institute of Technology (KIT), Engelbert-Arnold-Str. 4, 76131 Karlsruhe, Germany.

Manuscript submitted April 23, 2015.

applications. Thus, in the present work, further detailed microstructural investigations of the alloy W-Mo-Cr-Ti-Al, which has been introduced in Reference 8, were carried out for this alloy in the as-cast condition. Additionally, the microstructure evolution of the alloy during heat treatment processes was studied to gain a more comprehensive insight into the driving forces governing the formation of the alloy microstructure in the as-cast condition and during heat treatment.

## II. EXPERIMENTAL

The alloy 20W-2Mo-20Cr-20Ti-20Al was produced from elemental bulk materials by arc-melting in ~0.6 atm of argon utilizing an arc-melter AM 0.5 by Edmund Bühler GmbH. The purities of the starting materials Mo, W, Al, Cr, and Ti were 99.9, 99.96, 99.9, 99, and 99.8 pct, respectively. Gaseous impurities such as oxygen and nitrogen were generally found to be on a very low level. While nitrogen was found to be below the detection limit, between 50 and 100 wt ppm was measured for oxygen (see also Reference 18). The prepared buttons were flipped over and remelted more than five times in a water-chilled copper mold to facilitate alloy homogenization.

The alloy microstructure was analyzed by means of a FIB-SEM DualBeam system of type FEI Helios Nanolab 600. Utilizing this equipment, the TEM lamellae were prepared using a Ga ion beam. The crystal structure was identified using the Panalytical X́Pert pro MPD X-ray diffractometer applying Cu K$\alpha$ radiation. XRD *in situ* measurements were conducted in an Ar atmosphere to avoid severe oxidation of the sample. TEM investigations were conducted in a FEI Tecnai 20F ST, operated at 200 kV. Bright-field images and electron diffraction images were acquired using a Gatan ORIUS CCD camera (2688 pixel × 2672 pixel). The camera length for electron diffraction (150 mm) was calibrated with an Au grating. Electron diffraction images were evaluated using the PASAD-Software tool[19] in Digital Micrograph® with respect to lattice parameters. Energy dispersive X-ray spectroscopy (EDS) spectra were acquired in scanning transmission electron microscope (STEM)-mode using a Si-Li detector with ultrathin window (EDAX, Mahwah, NJ, USA).

To support experimental observation and to get fundamental knowledge of the alloy system, thermodynamic calculations were carried out using the software FactSage V6.4 in conjunction with a commercial database which includes elements constituting the alloy.

## III. RESULTS

### A. *Alloy Microstructure in the As-Cast Condition*

Figure 1(a) shows the microstructure of the alloy W-Mo-Cr-Ti-Al in the as-cast condition. The alloy exhibits a dendritic microstructure which is typical of

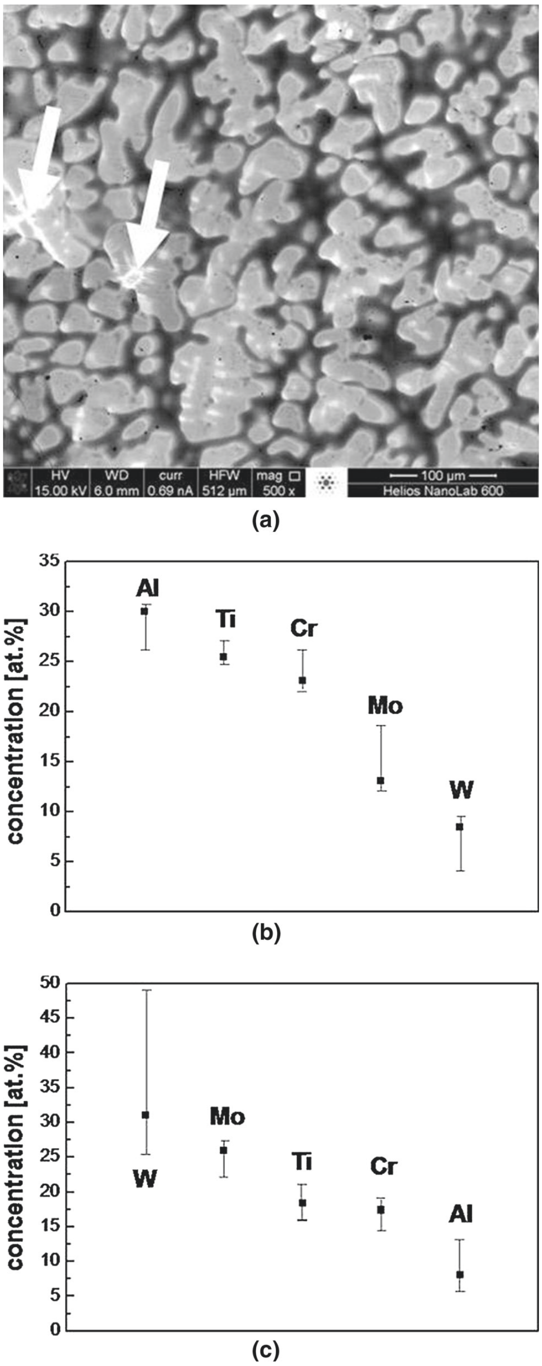

Fig. 1—(*a*) Alloy microstructure (BSE mode) in the as-cast condition, (*b*) average values and scatter of the element concentration in the interdendrites, (*c*) average values and scatters of the element concentration in the dendrites.

many HEAs after casting.[20] The chemical compositions of dendritic and interdendritic regions were derived from EDS analyses conducted in the SEM (Figures 1(b) and (c)). The results of EDS analyses show that predominantly W and Mo are enriched in the dendrites, while the interdendritic regions are rich in Al, Cr, and Ti. The data reveal, though, significant scatters of the element concentration values (see Figures 1(b) and (c)). This scatter is particularly pronounced for the element W within the dendrites. It is also noteworthy that even within the dendritic and interdendritic regions, contrast differences are visible indicating substantial variations of the element concentrations within the corresponding regions (see *e.g.*, the arrows pointing to local W enrichment in the dendrites in Figure 1(a)).

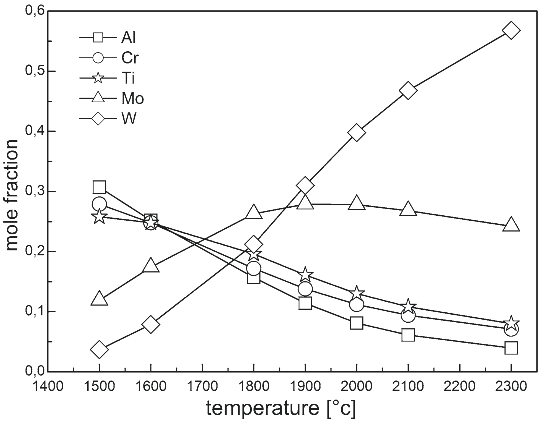

Fig. 2—Element distribution in the bcc phase (results of iterative thermodynamic calculations using FactSage).

It is likely to assume that the huge differences in the melting points of the alloy-constituting elements cause the formation of the observed as-cast microstructure. The high melting elements W and Mo preferably solidify first as dendrites, while the lower melting elements Cr, Ti, and Al are enriched in the interdendritic regions. In order to verify this assumption and to understand mechanisms leading (i) to the formation of the dendritic structure of the alloy W-Mo-Cr-Ti-Al in the as-cast condition and (ii) to the particular element distribution in respective areas, an iterative process of thermodynamic calculations was carried out. To simplify the iterative approach, calculation steps of 100 K (100 °C) were chosen within a temperature range of 1973 K and 2673 K (1700 °C and 2400 °C), where only the liquid and a solid bcc phase can coexist according to previous thermodynamic calculations.[8] Each calculation starts out with the concentration of the liquid phase of the previous calculation which was performed for a temperature being 100 K (100 °C) higher. The results of these calculations can be considered as a first approach of the alloy solidification process; they provide information on expected element concentration distribution between dendritic and interdendritic regions. It should be noted that the liquid phase, which is the only stable phase at 2673 K (2400 °C), is equiatomic. At 2573 K (2300 °C), the first step of the iterative thermodynamic calculations, element concentrations are obtained for the solid bcc phase which is formed from the equiatomic liquid phase. In the second step of the calculation, new element concentrations are calculated for the bcc phase that arises from the liquid phase with a new, *i.e.,* non-equiatomic, composition that was in equilibrium with the bcc phase in the first step of calculation. In this way, the calculations proceeded towards lower temperatures. Exemplary results of this iterative process of thermodynamic calculations are shown in Figure 2. It is evident that W plays the most important role in the bcc phase solidification at higher temperatures; however, its concentration decreases more rapidly compared to other elements. At lower temperatures, Al possesses the highest concentration in the bcc phase, but its fraction is significantly less pronounced compared to that of W at higher temperatures. In general, the left side of the diagram (at lower temperatures) can be considered being representative for the element distribution in the interdendrites, while the right side (higher temperatures) reflects the elemental distribution in the dendrites. Taking into account the calculation results presented in Figure 2, the scatter of the element concentrations shown in Figures 1(b) and (c) can be rationalized as follows: the rapid decrease of the W concentration in the bcc phase at higher temperature (right side of Figure 2) reflects the high scatter of the W concentration within the dendrites. In contrast, as the Mo concentration remains rather constant within a temperature interval ranging from 2073 K to 2573 K (1800 °C to 2300 °C), a rather small scatter of the Mo concentration within the dendrites results in Figure 1(c). However, at lower temperatures, a notable decrease of the Mo concentration is observed (left side of Figure 2) which readily explains the substantial scatter of Mo in the interdendrites (see Figure 1(b)). The same method to analyze element concentration distribution between and within the dendrites and interdendrites can be applied for other elements.

Earlier results of XRD measurements indicated that either two bcc phases with slightly different lattice parameters (3.103 and 3.116 Å) or one bcc phase with lattice distortion form in the alloy in the as-cast condition.[5] To get deeper insight into the microstructure of the alloy W-Mo-Cr-Ti-Al in the as-cast conditions, two TEM lamellae were prepared using FIB technique targeted (i) at a dendrite and (ii) at an interdendritic region. Figure 3 represents results of the TEM investigations. In order to verify EDS data obtained in SEM (Figure 1), additional EDS analyses were carried out in TEM. Figure 3(b) shows exemplarily the spectrum of a spot marked in the dendrite TEM-lamella (Figure 3(a)). The elements W, Mo, Ti, Cr, and Al were detected. This is in agreement with EDS results from SEM measurements shown in Figure 1(c). Furthermore, Cu stemming from the Cu-supporting TEM-grid, Pt stemming from the Pt protecting layer, and Ga stemming from the Ga ion source were found. In contrary to many other HEAs, nano-particles were detected neither in the dendritic nor in the interdendrite

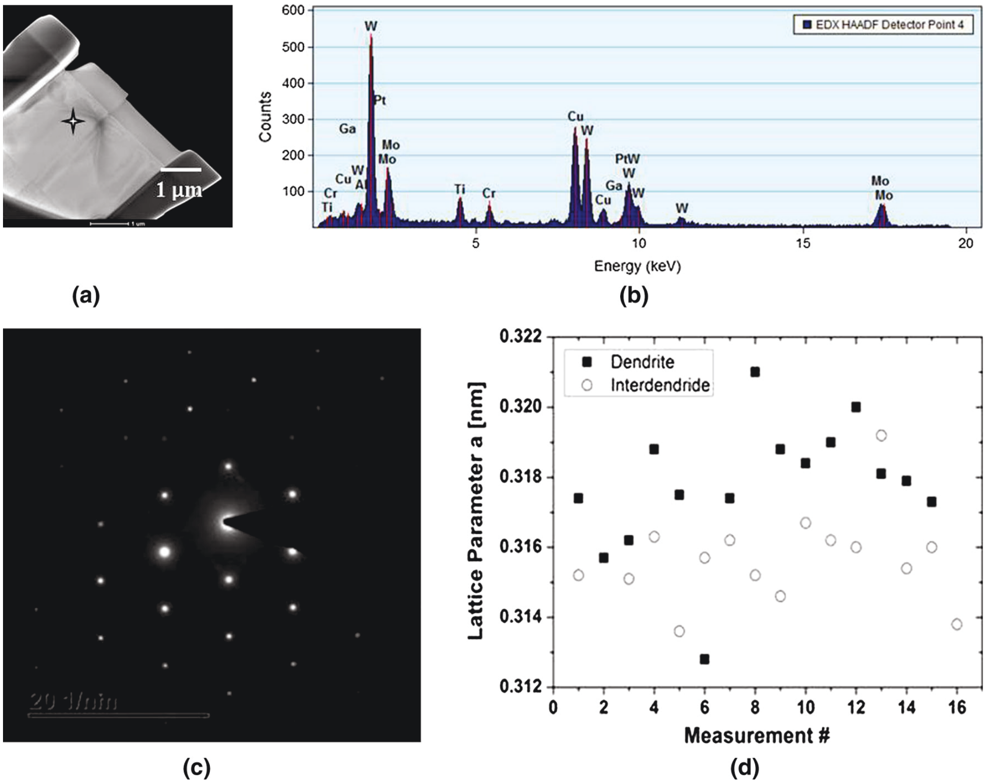

Fig. 3—TEM images of the alloy 20W-20Mo-20Cr-20Ti-20Al in the as-cast condition; (*a*) STEM image (overview) of the TEM lamella cut from a dendritic region, (*b*) EDS analysis of the spot marked in (a), (*c*) SAD pattern along [200] zone axis (sample tilt: $\alpha = -5.51$ deg, $\beta = -5.51$ deg) within the dendrite, (*d*) calculated lattice parameters in the dendritic and the interdendritic regions.

regions. Selected area diffraction (SAD) patterns were used to determine the lattice parameter of the relevant areas and to compare these values with the earlier XRD analysis. The lattice parameter values were calculated from measured d values of (110), (200), (210), (211), (220), (310), and (321) reflections. For each region, 15 values were obtained from 5 different diffraction images. The averaged values of the lattice parameters are 3.154 ± 0.002 and 3.178 ± 0.002 Å for the interdendritic and the dendritic regions, respectively. Thus, in tendency, the lattice parameter of the interdendritic region is slightly smaller than that of the dendritic region. However, the difference between two values is smaller than the accuracy of electron diffraction, since accuracy is usually in the region of 2 to 3 pct.[21] Interestingly, the lattice parameters determined by SAD are somewhat higher than those obtained from the XRD measurements. This difference can likely be attributed to the local concentration fluctuations within the respective dendritic and interdendritic regions which were observed in both, SEM and TEM (see Figures 1(b), (c) and 3(d)). Finally, Ga ions stemming from FIB preparation of the TEM lamellae may have an additional influence on the lattice parameter. Nevertheless, the tendency that the dendritic regions which contain more of the high melting and heavy elements possess a slightly larger lattice parameter is consistently confirmed by both measurement techniques.

### B. *Microstructural Evolution During Heat Treatment*

As outlined in the introduction, it is of paramount interest to explore the microstructure stability at elevated temperatures. To study the microstructure evolution at moderately high temperature, *in situ* XRD measurements were carried out. For this purpose, an as-cast alloy sample was heated stepwise in 200 K (200 °C) steps from room temperature up to 1273 K (1000 °C). XRD measurements were conducted at each step with the temperature kept constant for 2 hours at each step. The results show that two bcc phases could be identified at each temperature. The obtained values of the lattice parameters of both bcc phases at different temperatures are summarized in Table I. In agreement with the TEM investigations shown above, it can be stated again that the dendrite phase possesses higher lattice parameters of 3.118 Å and 3.148 Å, while the

**Table I. Lattice Parameters of the Two bcc Phases Obtained from *In Situ* XRD Measurements (bcc1: Dendrite, bcc2: Interdendrite)**

| Calculated Lattice Parameter *a* | 298 K (25 °C) | 473 K (200 °C) | 673 K (400 °C) | 873 K (600 °C) | 1073 K (800 °C) | 1273 K (1000 °C) | $a_{1273K} - a_{298K}$ (Å) |
|---|---|---|---|---|---|---|---|
| *a* (110) bcc1, (Å) | 3.106 | 3.112 | 3.116 | 3.124 | 3.137 | 3.142 | |
| *a* (110) bcc2, (Å) | 3.087 | 3.092 | 3.098 | 3.103 | 3.120 | 3.126 | |
| *a* (200) bcc1, (Å) | 3.132 | 3.122 | 3.132 | 3.133 | 3.143 | 3.160 | |
| *a* (200) bcc2, (Å) | 3.098 | 3.099 | 3.125 | 3.109 | 3.130 | 3.143 | |
| *a* (211) bcc1, (Å) | 3.115 | 3.121 | 3.141 | 3.133 | 3.134 | 3.137 | |
| *a* (211) bcc2, (Å) | 3.097 | 3.099 | 3.122 | 3.113 | 3.121 | 3.133 | |
| *a* (220) bcc1 (Å) | 3.127 | 3.132 | 3.137 | 3.142 | 3.145 | 3.152 | |
| *a* (220) bcc2, (Å) | 3.103 | 3.108 | 3.115 | 3.122 | 3.130 | 3.151 | |
| *a* (310) bcc1, (Å) | 3.110 | 3.125 | 3.126 | 3.131 | 3.136 | — | |
| *a* (310) bcc2, (Å) | 3.098 | 3.108 | 3.110 | 3.123 | 3.127 | — | |
| $a_{bcc1}$, (Å) | 3.118 | 3.122 | 3.130 | 3.133 | 3.139 | 3.148 | 0.030 |
| $a_{bcc2}$, (Å) | 3.096 | 3.101 | 3.114 | 3.114 | 3.126 | 3.138 | 0.042 |
| $a_{bcc1} - a_{bcc2}$, (Å) | 0.022 | 0.021 | 0.016 | 0.019 | 0.013 | 0.010 | |

interdendrite phase has lower lattice parameters of 3.096 Å and 3.138 Å at room temperature and at (1273 K) 1000 °C, respectively. It is obvious that the difference between the lattice parameters of dendrites and interdendrites decreases continuously with increasing temperature underpinning the results of earlier measurements.[8] At 1273 K (1000 °C), this difference is negligibly small yielding a value of 0.010 Å indicating the progressing homogenization process. This fact allows to state that the alloy 20W-20Mo-20Cr-20Ti-20Al possesses a single-phase microstructure. It should finally be mentioned that during the *in situ* XRD measurements, small amounts of pure W and a Ti-Al compound were detected at 1273 K (1000 °C). The formation of the last compound at 1273 K (1000 °C) is, in fact, not surprising, as it was predicted by thermodynamic calculations.[8] The appearance of pure W will be discussed later in this section.

Previous and current investigations reveal that the alloy 20W-20Mo-20Cr-20Ti-20Al shows a clear tendency to homogenize at high temperatures. After 40 hours annealing at 1473 K (1200 °C), a nearly fully homogeneous microstructure was observed in the alloy.[8] In order to examine the early stages of alloy homogenization as well as associated diffusion processes, heat treatments were carried out for 24 and 48 hours at 1273 K (1000 °C) and for 48 hours at 1373 K (1100 °C). Figure 4 shows a decrease of the dendrite volume fraction in the alloy during heat treatment at 1000 °C. By means of the software tool Image J, the changes of the dendrite volume fraction were quantified using the contrast differences between the interdendritic and the dendritic regions. The results are summarized in Table II. Obviously, the dendrite volume fraction decreases with increasing annealing time at 1273 K (1000 °C), indicating that the complete homogenization would occur if the annealing temperature and the annealing time were chosen sufficiently high and long, respectively.

Figure 5 shows the corresponding change of the element concentrations in the dendritic and interdendritic regions during heat treatment at 1273 K (1000 °C). In the interdendrites, no significant changes were observed, while element concentrations in the dendrites change substantially: a moderate decrease of Ti and Cr and a notable decline of the Mo concentration were detected, while the Al concentration seems to remain nearly constant. A peculiar behavior is noted for tungsten in this region. Based on the above findings, one would intuitively assume that the concentration of W would decrease in the dendrites and, consequently, increase in the interdendrites since the W content in the dendrites was found to be significantly higher than that in the interdendrites in the as-cast conditions (see Figures 1(b) and (c)). Instead, the tungsten content in the dendrites drastically increases, implying that W does not necessarily participate in the diffusion processes in the earlier stages of homogenization. Considering this very high W concentration in the dendrite as a result of the heat treatment, the lattice parameter of the dendrites obtained from the *in situ* XRD measurements (3.148 Å) at 1273 K (1000 °C) can be reinterpreted in that the dendrite lattice constant should approach the value of pure tungsten. Karabacak *et al*.[22] determined the lattice parameter of pure W at 1223 K (950 °C) yielding 3.157 Å which is very close to the value of the dendrite lattice parameter obtained in our XRD measurements at 1273 K (1000 °C). However, Figure 6 clearly shows that the outward diffusion of W takes place in the sample that was heat-treated for 48 hours at the higher temperature of 1373 K (1100 °C), indicating that W leaves the dendrites when a critical value of the W concentration is exceeded or when the diffusivity of W becomes significant. It should be kept in mind that the diffusion of W becomes significant at high temperatures. Mundy *et al.* reported on the self-diffusion coefficient in tungsten in the temperature range 1705 K to 3408 K (1432 °C to 3135 °C). At the lowest temperature, *i.e.,* at

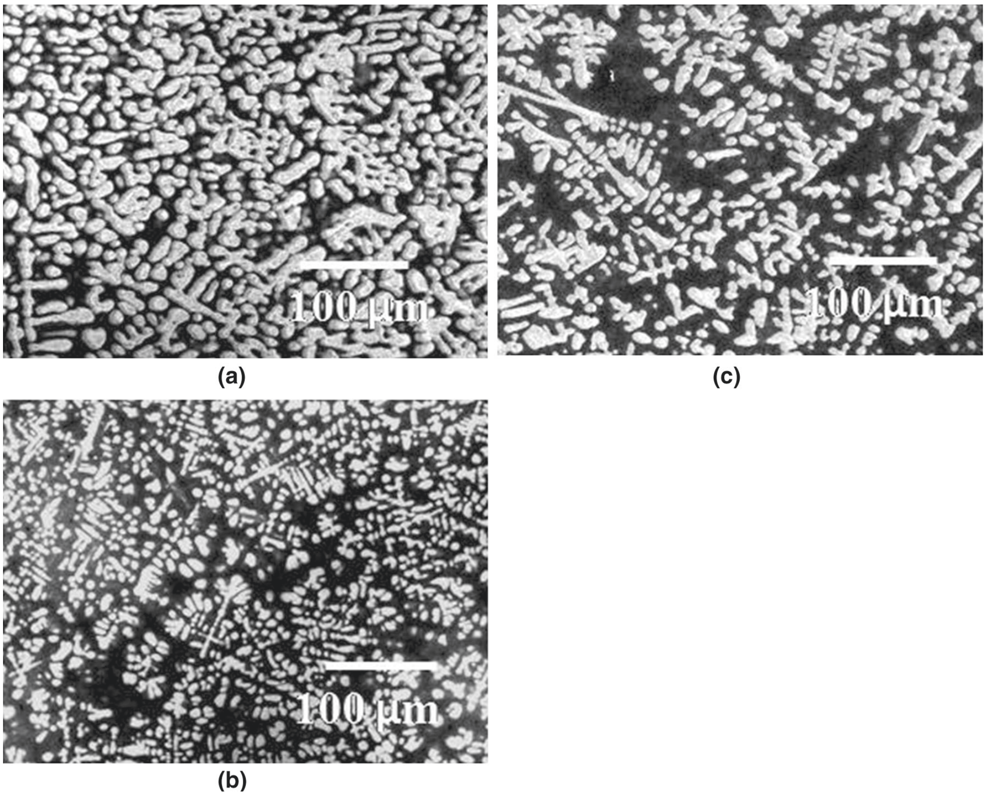

(a)
(c)
(b)

Fig. 4—Microstructure evolution of the alloy 20W-20Mo-20Cr-20Ti-20Al at 1273 K (1000 °C); (*a*) as-cast condition, (*b*) after 24 h at 1273 K (1000 °C), and (*c*) after 48 h at 1273 K (1000 °C).

**Table II. Volume Fraction of Dendrite During Heat Treatment at 1273 K (1000 °C)**

| Annealing duration (h) | 0 | 24 | 48 |
|---|---|---|---|
| Dendrite volume fraction (pct) | 54 | 47 | 41 |

1705 K (1432 °C), the value of $D = 3.17 \times 10^{-18}$ cm$^2$/s was obtained.[23] Considering the correlation between the element diffusivity and its melting temperature, it is obvious that the self-diffusion of tungsten is substantially slower than the self-diffusion of the other alloy elements at 1273 K (1000 °C).

## IV. DISCUSSION

The experimental results presented in the previous section clearly show that the alloy 20W-20Mo-20Cr-20-Ti-20Al forms a dendritic microstructure with significant chemical differences between dendritic and interdendritic regions in the as-cast condition. It should be pointed out that the values of the elemental concentration attainable with EDS in SEM must be considered critically as relative errors up to ±8 pct can generally be expected.[24] However, these concentration values were confirmed by very similar concentration values measured in the as-casted alloy using TEM. Therefore, element concentrations obtained for the alloy after heat treatment using SEM can be used to identify mechanisms causing the microstructure evolution. In addition, to obtain the average values of element concentrations, for example, in the dendrites, at least three dendrites were analyzed with at least three EDS measurements conducted in each of the dendrites. In other words, the average values and the connected scatter bars in Figures 1(b) and (c) represent at least 9 single measurements each. During heat treatment at high temperatures, the alloy tends to form a single bcc phase. To understand the mechanisms determining the microstructure evolution in the alloy, it is necessary to take a closer look at the driving forces governing the microstructural evolution.

In order to assess the kind of interaction prevailing between elements present in the alloy 20W-20Mo-20Cr-20Ti-20Al, enthalpies of mixing $\Delta H_{\text{mix}}$ in the bcc phase for all binary and ternary equiatomic alloys were calculated using the software FactSage. The majority of the equiatomic systems show positive enthalpy of mixing. Only Al-containing alloys apparently render negative enthalpy of mixing. Table III contains values for the four binary equiatomic systems containing Al at 1373 K (1100 °C). As expected, the strongest bond energy should exist between Al and Ti, followed by Mo, Cr, and W. Based on these results, it can be supposed that Al strongly bonds primarily Ti building stable interdendritic regions. It should be noted that Al exhibits a notable attractive bond to Mo, too. This strong attractive interaction between Al and Mo may force Mo to leave dendrites to join Al predominantly enriched in inderdendrites. This assumption is consistent with the experimental observation that Mo concentration in the dendrites substantially decreases during heat treatment (see Figure 5(b)).

Further, $\Delta H_{\mathrm{mix}}$ was calculated for all bcc ternary systems at 1373 K (1100 °C) in order to analyze the effect of the third element on the bond energy between two respective elements. The corresponding values are summarized in Table IV. Again, only for Al-containing systems, negative values of enthalpy of mixing were calculated. Also, the bond energy between Al and Ti seems to be still dominant since the systems containing both elements show the lowest values of $\Delta H_{\mathrm{mix}}$. Interestingly, the ternary system Al-Ti-Mo yields the strongest bond energy among all ternary systems reinforcing the assumption that Mo in the dendrites is probably attracted by Al towards the interdendrites. In general, it can be concluded that Al shows a clear tendency to build up extremely strong bonds with other

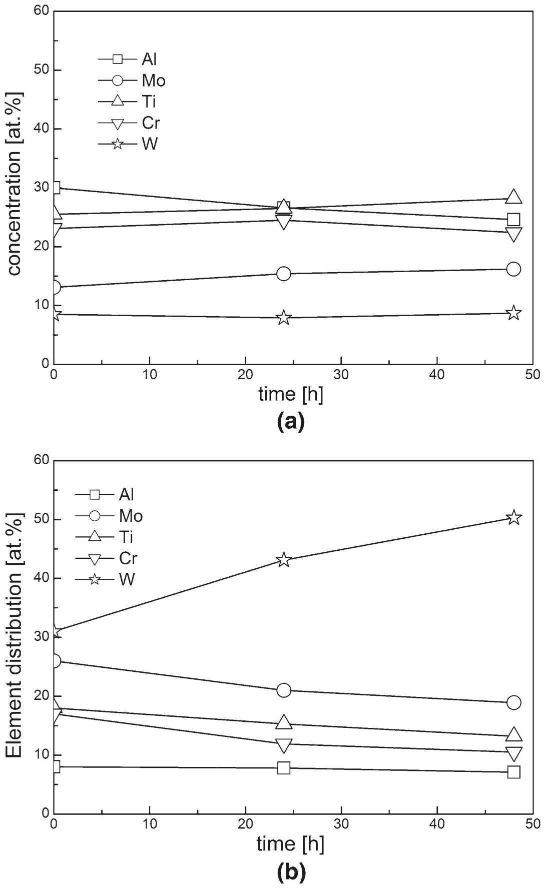

Fig. 5—Element concentration changes in the interdendrite (*a*) and dendrite (*b*) regions at 1273 K (1000 °C).

**Table III. Calculated Enthalpy of Mixing in Binary Systems at 1373 K (1100 °C)**

| System | Al-Ti | Al-Mo | Al-Cr | Al-W |
|---|---|---|---|---|
| $\Delta H_{\mathrm{mix}}$ (kJ/mol) | −30.8 | −18.9 | −13.9 | −6.9 |

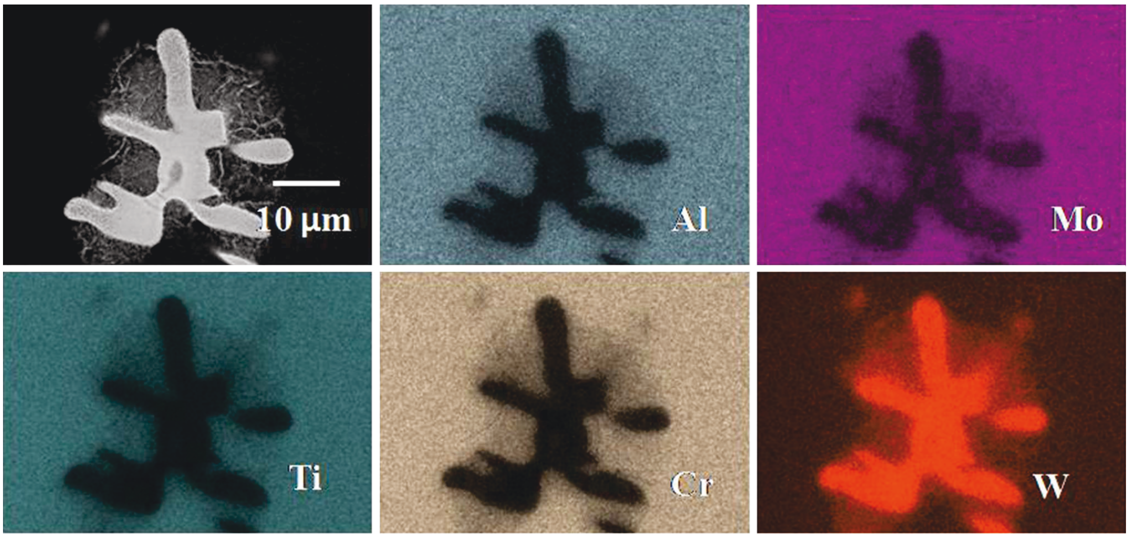

Fig. 6—Element distribution in the alloy 20W-20Mo-20Cr-20Ti-20Al after 48 h heat treatment at 1373 K (1100 °C).

**Table IV. Calculated Enthalpy of Mixing in Ternary Systems at 1373 K (1100 °C)**

| System | Al-Ti-Mo | Al-Ti-Cr | Al-Ti-W | Al-Mo-Cr | Al-Mo-W | Al-Cr-W |
|---|---|---|---|---|---|---|
| $\Delta H_{\mathrm{mix}}$ (kJ/mol) | −21.3 | −18.2 | −16.8 | −11.2 | −11.1 | −5.7 |

**Table V. Calculated Element Activities for the Dendritic and Interdendritic Regions**

| Element | Al | Ti | Cr | Mo | W |
|---|---|---|---|---|---|
| $a^{\mathrm{interdendrite}}$ | 0.031 | 0.11 | 0.357 | 0.127 | 0.59 |
| $a^{\mathrm{dendrite}}$ | 0.005 | 0.22 | 0.51 | 0.22 | 0.64 |

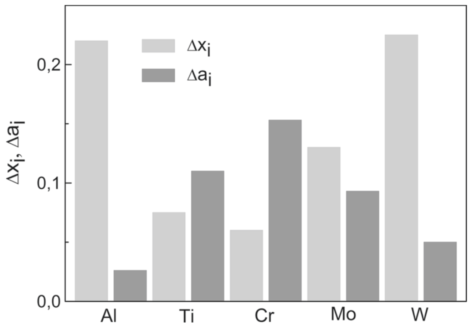

Fig. 7—Calculated concentration and activity differences of elements between dendritic and interdendritic regions.

elements. In contrary, W effectively weakens the bonds between elements (compare, for example, enthalpy of mixing in Al-Ti-Mo and Al-W-Mo or in Al-Mo-Cr and Al-Cr-W).

In order to understand the peculiar diffusion processes taking place during heat treatment as indicated in Figure 5 and described in the previous section, activities of the elements in the alloy were calculated for the respective dendritic and the interdendritic regions at 1373 K (1100 °C). The required chemical compositions for the dendrites and interdendrites were taken from Figures 1(b) and (c). The results are summarized in Table V. To understand the driving forces for diffusion of each element, the element activity differences $\Delta a_i$ between corresponding regions were calculated. For the sake of completeness, the element concentration differences $\Delta x_i$ were also determined. The results are shown in Figure 7. Al and W are correlated with the highest values of $\Delta x_i$. This means that if diffusion of these elements takes place during heat treatment, the concentration changes are easily detectable. However, no significant concentration changes were detected for Al, neither in the dendrites nor in the interdendrites. Taking the lowest value of the activity difference $\Delta a_i$ (see Figure 7) into account, it becomes clear that despite the fact that the concentration difference $\Delta x_i$ is very high, Al possesses the lowest driving force for diffusion in the alloy studied. Further, Ti and Cr exhibit significantly higher activity values in the dendrites than in the interdendritic regions creating a driving force for outward diffusion of these elements from dendrites into interdendrites as actually observed during heat treatment (see Figure 5(b)). Finally, considering the results shown in Figure 7, it can be explained why the Mo concentration in the dendrites decreases, while the W content notably increases during heat treatment despite the higher $\Delta x_i$ of W than that of Mo (see Figure 5(b)). Apparently, this can be attributed to the fact that the activity difference $\Delta a_i$ of Mo is substantially higher compared to that of W. The outward diffusion of Mo from the dendrites is, therefore, preferential from a thermodynamic point of view.

The results shown in Figure 7 raise further questions such as why the activity difference of W between dendritic and interdendritic regions was found unexpectedly small. or, in other words, how does each element influence the activity and, therefore, affect the driving force of concentration changes by diffusion of other elements in the alloy studied. Figure 8 shows results of thermodynamic calculations illustrating the effect of the element concentration on the activity of other elements constituting the alloy 20W-20Mo-20Cr-20Ti-20Al. Activities of four elements were calculated as a function of the concentration of the fifth element at 1273 K (1000 °C), assuming that the bcc phase is the only stable phase at this temperature. The concentrations of other elements were kept equal. It is obvious that both, Cr and W, have no significant effect on the activities of the other elements (see Figures 8(a) and (b)). Ti exhibits the same negligibly small impact (not shown here). Mo, in contrary, significantly diminishes the W activity (see Figure 8(c)). This implies that a high Mo content in the dendrites decreases the W activity in this region. In addition, the low content of Al in the dendrites decreases the W activity even further. The opposite effect occurs for W in the interdendrites: the low Mo and high Al concentrations cause an enhancement of the W activity. As a result, a low W activity difference results between the dendritic and interdendritic regions (see Figure 7). Interestingly, Al considerably influences the activities of all elements in the alloy. The Cr activity, for example, substantially decreases with increasing Al content. As a consequence, the low Al content in the dendrites results in a Cr activity being higher in the dendrite than in the interdendrite (see Table V). In turn, this leads to the outward diffusion of Cr from the dendritic into the

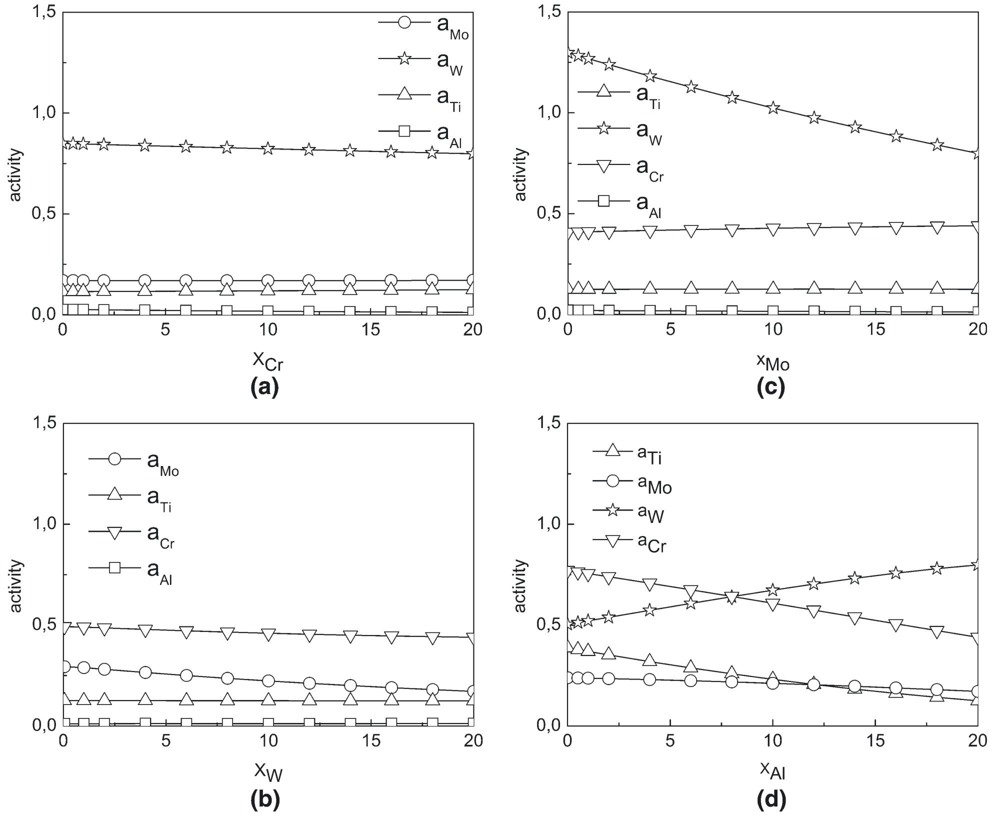

Fig. 8—Effect of element concentrations on the element activity.

interdendritic regions (see Figure 5(b)). The same observation holds true for Ti.

## V. CONCLUSIONS

The following main results were obtained in this study:

1. The microstructure of the alloy 20W-20Mo-20Cr-20Ti-20Al in the as-cast condition was investigated using various experimental techniques such as SEM, TEM, and XRD. It was found that primarily W and Mo are enriched in the dendrites, while interdendrites are rich in Al, Cr, and Ti. Within both regions, elemental distribution is not homogeneous as significant scatter of elemental concentrations was measured. W exhibits a particularly large concentration scatter from 26 to 49 at. pct in the dendrites. This feature was explained by an iterative of thermodynamic calculation procedure reflecting the element distribution in both relevant regions. Lattice parameters for the dendritic and interdendritic areas were determined as 3.178 and 3.154 Å, respectively, using TEM. These values confirm the trend observed earlier by XRD.
2. The homogenization process of the alloy 20W-20Mo-20Cr-20Ti-20Al was investigated by monitoring the microstructure evolution during and short-term annealings at moderate temperature [473 K to 1273 K (200 °C to 1000 °C)] as well as long-term treatments at elevated temperatures [1273 K to 1373 K (1000 °C to 1100 °C)]. It was observed that the difference in the lattice parameters becomes less pronounced with increasing annealing temperature and time [0.022 Å at 289 K (25 °C) and 0.010 Å at 1273 K (1000 °C)]. The alloy shows, therefore, a clear tendency to homogenize and possesses a single-phase microstructure. A significant decrease of the dendrite volume fraction from 53.9 to 41.1 vol pct was detected during annealing for up to 48 hours at 1273 K (1000 °C).
3. Thermodynamic calculations were conducted to assess the driving forces governing the alloy microstructure evolution. The calculations of the enthalpy of mixing for binary and ternary systems reveal that Al builds the strongest bonds with other elements, especially with Ti. In contrast, W seems to weaken the bonds between elements. The activity

differences between dendrites and interdendrites for corresponding elements were calculated. It was found that the experimentally observed microstructure evolution during heat treatment is in good agreement with these parameter values. The knowledge of the effect of element concentration on the element activity is important to understand the driving forces determining the alloy constitution.

## ACKNOWLEDGMENT

The financial support by the Deutsche Forschungsgemeinschaft (DFG) is gratefully acknowledged.

## REFERENCES

1. J.H. Perepezko: *Science*, 2009, vol. 326, pp. 1068–69.
2. J.-C. Zhao and J.H. Westbrook: *Mater. Res. Soc.*, 2003, vol. 28, pp. 622–30.
3. O.N. Senkov, J.M. Scott, S.V. Senkova, D.B. Miracle, and C.F. Woodward: *J. Alloy. Compd.*, 2011, vol. 509, pp. 6043–48.
4. Z. Tang, M.C. Gao, H. Diao, T. Yang, J. Liu, T. Zuo, Y. Zhang, Z. Lu, Y. Chen, Y. Zhang, K.A. Dahmen, P.K. Liaw, and T. Egami: *JOM*, 2013, vol. 65, pp. 1848–58.
5. Y. Zou, S. Maiti, W. Steurer, and R. Spolenak: *Acta Mater.*, 2014, vol. 65, pp. 85–97.
6. W.P. Huhn and M. Widom: *JOM*, 2013, vol. 65, pp. 1772–79.
7. J.W. Yeh: *JOM*, 2013, vol. 65, pp. 1759–71.
8. B. Gorr, M. Azim, H.-J. Christ, T. Mueller, D. Schliephake, and M. Heilmaier: *J. Alloy. Compd.*, 2015, vol. 624, pp. 270–78.
9. B. Cantor, I.T.H. Chang, P. Knight, and A.J.B. Vincent: *Mater. Sci. Eng. A*, 2004, vols. 375–377, pp. 213–18.
10. F. Otto, Y. Yang, H. Bei, and E.P. George: *Acta Mater.*, 2013, vol. 61, pp. 2628–38.
11. W.H. Liu, Y. Wu, J.Y. He, Y. Zhang, C.T. Kuz, and Z.P. Lu: *JOM*, 2014, vol. 66, pp. 1973–83.
12. B. Shuh, F. Mendez-Martin, B. Volker, E.P. George, H. Clemens, R. Pippan, and A. Hohenwarter: *Acta Mater.*, 2015, vol. 96, pp. 258–68.
13. M.R. Chen, S.J. Lin, J.W. Yeh, S.K. Chen, Y.S. Huang, and C.P. Tu: *Mater. Trans.*, 2006, vol. 47, pp. 1395–401.
14. Y.J. Zhou, Y. Zhang, Y.L. Wang, and G.L. Chen: *Mater. Sci. Eng., A*, 2007, vols. 454–455, pp. 260–65.
15. S. Guo and C.T. Liu: *Prog. Nat. Sci. Mater. Int.*, 2011, vol. 21, pp. 433–46.
16. F. Otto, A. Dlouhy, Ch. Somsen, H. Bei, G. Eggeler, and E.P. George: *Acta Mater.*, 2013, vol. 61, pp. 5743–55.
17. O.N. Senkov, C. Woodward, and D.B. Miracle: *JOM*, 2014, vol. 66, pp. 2030–40.
18. H. Chen, A. Kauffmann, B. Gorr, D. Schliephake, C. Seemüller, J.N. Wagner, H.-J. Christ, and M. Heilmaier: *J. Alloys Compd.* (submitted).
19. C. Gammer, C. Mangler, C. Rentenberger, and H.P. Karnthaler: *Scripta Mater.*, 2010, vol. 63, pp. 312–15.
20. J.W. Yeh, S.K. Chen, S.J. Lin, J.Y. Gan, T.S. Chin, T.T. Shun, C.H. Tsau, and S.Y. Chang: *Adv. Eng. Mater.*, 2004, vol. 6, pp. 299–303.
21. D.B. Williams and C.B. Carter: *Transmission Electron Microscopy: A Textbook for Materials Science*, Plenum Press, New York, 1996.
22. T. Karabacak, P.I. Wang, G.C. Wang, and T.M. Lu: *Thin Solid Films*, 2005, vol. 493, pp. 293–96.
23. J.N. Mundy, S.J. Rothman, N.Q. Lam, H.A. Hoff, and L.J. Nowiski: *Phys. Rev. B*, 1978, vol. 18, pp. 6566–75.
24. M. Miler and B. Mirtic: *Geologija*, 2013, vol. 56, pp. 5–17.

# Manuskript XVI

## High temperature oxidation behavior of an equimolar refractory metal-based alloy 20 Nb-20Mo-20Cr-20Ti-20Al with and without Si addition

B. Gorr, F. Mueller, H.-J. Christ, T. Mueller, H. Chen, A. Kauffmann, M. Heilmaier

Journal of Alloys and Compounds, 688 (2016) 487-477

Journal of Alloys and Compounds 688 (2016)

Contents lists available at ScienceDirect

Journal of Alloys and Compounds

journal homepage: http://www.elsevier.com/locate/jalcom

# High temperature oxidation behavior of an equimolar refractory metal-based alloy 20Nb–20Mo–20Cr–20Ti–20Al with and without Si addition

B. Gorr [a, *], F. Mueller [a], H.-J. Christ [a], T. Mueller [b], H. Chen [c], A. Kauffmann [c], M. Heilmaier [c]

[a] *Institut für Werkstofftechnik, Universität Siegen, Paul-Bonatz-Str. 9-11, 57068 Siegen, Germany*
[b] *Institut für Bau- und Werkstoffchemie, Universität Siegen, Paul-Bonatz-Str. 9-11, 57068 Siegen, Germany*
[c] *Institut für Angewandte Materialien – Werkstoffkunde (IAM-WK), Karlsruhe Institute of Technology (KIT), Engelbert-Arnold-Str. 4, D-76131 Karlsruhe, Germany*

ARTICLE INFO

*Article history:*
Received 15 January 2016
Received in revised form
15 July 2016
Accepted 20 July 2016
Available online 21 July 2016

*Keywords:*
High-entropy alloys
Refractory elements
High-temperature oxidation

ABSTRACT

The high temperature oxidation behavior of a refractory high-entropy alloy (HEA) 20Nb–20Mo–20Cr–20Ti–20Al at 900 °C, 1000 °C and 1100 °C was investigated. The oxidation kinetics of the alloy was found to be linear at all temperatures. Oxide scales formed are largely inhomogeneous showing regions with thick and porous layers as well areas with quite thin oxide scales due to formation of discontinuous chromium-rich oxide scales. However, the oxidation resistance can be moderately improved by the addition of 1 at.% Si. The thermogravimetric data obtained during oxidation of the Si-containing alloy at 1000 °C and 1100 °C reveal pronounced periods of parabolic oxidation that, however, change towards linear oxidation after prolonged exposure times. Microstructural investigations using scanning electron microscopy (SEM) and transmission electron microscopy (TEM) document that the Si addition gives rise to a nearly continuous alumina-rich layer which seems to be responsible for the good protection against further oxidation. Pronounced zones of internal corrosion attacks consisting of different oxides and nitrides were observed in both alloys. In order to determine the chemical composition of the corrosion products and their mass fraction, quantitative X-ray diffraction (XRD) analysis was performed on powdered oxide scales that formed on the alloys after different oxidation times. Rutile was identified as the major phase in the oxide scales rationalizing the relatively high mass gain during oxidation.

## 1. Introduction

Equiatomic multicomponent alloys have attracted great attention among material scientists worldwide in the last few years [1,2] due to their unique properties. Regarding the microstructure, HEAs stand out due to their tendency to possess simple, highly symmetric crystal structures, which often lead to single-phase microstructures [3], to nanoparticles in the matrix [4] and to sluggish diffusion of elements [5–7]. High temperature stability was reported by Hsieh et al. and Liu et al. for the alloy systems AlCrFeMnNi and FeCoNiCrMn, respectively [8,9]. With respect to mechanical properties, the so-called Cantor alloy sticks out in having simultaneously high strength and ductility, both of which increase with decreasing temperature [10,11]. Refractory HEAs exhibit extremely high strength at elevated temperatures exceeding even the levels provided by advanced Ni-based superalloys [12].

Characterization of the oxidation resistance of the alloy AlSiTiCrFeCoNiMo$_{0.5}$ and AlSiTiCrFeNiMo$_{0.5}$ was in part studied by Huang et al. who mainly focused on processing, microstructure, and wear resistance of the alloys [13]. It was concluded that the formation of the chromia-based layer underneath the outermost titanium oxide scale accounts for the good oxidation resistance of these materials. Daoud et al. characterized the oxidation behavior of three alloys based on the alloy system Al–Co–Cr–Cu–Fe–Ni [14]. Thin layers of α-$Al_2O_3$ and $Cr_2O_3$ were identified after 200 h of oxidation at 1000 °C, however severe spallation of oxide scales was also observed. High temperature oxidation behavior of multicomponent alloys of the system Al–Co–Cr–Ni-(Fe or Si) was investigated by Butler et al. [15]. They found that the formation of the

---

* Corresponding author.
*E-mail address:* gorr@ifwt.mb.uni-siegen.de (B. Gorr).

http://dx.doi.org/10.1016/j.jallcom.2016.07.219

external alumina is strongly dependent on the Al content in the alloys. The oxidation behavior of other transition metal-based HEAs has been frequently reported in the literature [16–21]. By contrast, there is a pronounced lack of studies dealing with high temperature oxidation behavior of refractory metal-based HEAS, despite the fact that these materials have been designed for high temperature applications. Senkov et al. investigated oxidation resistance of a refractory HEA NbCrMo$_{0.5}$ Ta$_{0.5}$TiZr in flowing air at 1000 °C [22]. A scale consisting of complex oxides was found on the alloy surface. Nevertheless, the alloy exhibits a much better combination of mechanical properties and oxidation resistance than commercial Nb alloys as well as NbSiAlTi and NbSiMo materials [22]. The study by Liu et al. revealed that the oxidation rates of refractory HEAs is significantly decreased by Ti and Si additions, while V additions cause on the contrary increased oxidation rates at 1300 °C [23]. The properties of HEAs as protective coating have also been investigated. The oxidation resistance of the alloy Ti−6Al−4V could be improved due to the laser clad TiVCrAlSi high entropy alloy coatings [24].

The equiatomic alloy 20W−20Mo−20Cr−20Ti−20Al is the first material from the recently proposed new alloy family that has been developed for high temperature structural applications [25]. Since W and Mo possess very high melting points, these elements were considered as prime candidates for the new alloy system. To possibly enable the formation of a protective oxide scale, Cr and Al were added to the alloy system, while Ti should reduce the alloy density. Further details regarding the alloy design concept can be found in Ref. [25]. Microstructure analysis of the alloy 20W−20Mo−20Cr−20Ti−20Al in the as-cast condition as well after annealing at high temperatures revealed that the alloy shows a clear tendency to homogenize yielding a simple single-phase body centered cubic (BCC) microstructure [26]. The microstructure and mechanical properties of the second alloy of this family, 20Nb−20Mo−20Cr−20Ti−20Al, were presented and discussed by Chen et al. [27] whereby tungsten has been replaced by niobium to further reduce density and to ease the fabrication by arc melting due to the lower melting point of Nb. The purpose of the present paper is twofold: (a) to assess the high temperature oxidation behavior of the equiatomic HEA 20Nb−20Mo−20Cr−20Ti−20Al and (b) to study the effect of 1 at.% of the Si addition aiming at enhancing the oxidation resistance following the recommendation by Ref. [23].

## 2. Experimental

The alloys were produced from elemental bulk materials by arc-melting in ~0.6 atm of argon (arc-melter AM 0.5 by Edmund Bühler GmbH). The purities of the starting materials Mo, Nb, Al, Cr, Ti, and Si were 99.9%, 99.9%, 99.9%, 99%, 99.8% and 99.9999%, respectively. Nitrogen impurities were found to be below the detection limit, oxygen content was measured being between 50 and 100 wt ppm. The prepared buttons were flipped over and remelted more than five times in a water-chilled copper mold to facilitate alloy homogenization. The alloys were heat-treated under Ar flow for 20 h at 1200 °C. For the oxidation tests, samples of dimension of approximately 10 mm × 10 mm × 2 mm were polished up to 1000 grit. The samples were ultrasonically cleaned in ethanol directly before testing in a Rubotherm thermogravimetric system. The oxide scale morphology was analyzed by means of a FIB-SEM DualBeam system of type FEI Helios Nanolab 600 equipped by the energy dispersive X-ray (EDX) detector. Before cross-section analysis, oxidized samples were Ni-plated to protect the oxide scales. A TEM-lamella was prepared applying ion milling in the FIB-SEM system. TEM analysis was performed in the TEM of type FEI Talos F200X. To analyze the composition of oxides formed on the alloys, XRD measurements were carried out using the X'Pert Pro MPD diffractometer (Cu-K$\alpha$ radiation) operating with Bragg-Brentano geometry. Divergence slits ½ degree and anti scatter slit 1° were used for XRD measurements. Oxide scales were removed from the oxidized samples and powdered into particle sizes smaller than 40 μm. Since the oxide scales were relatively thin, particularly after short oxidation experiments, background-free sample holders made of silicon single crystals (Panalytical PW 1817/32) were used. The measurements were carried out using $2\theta$ angles between 10 and 78°, the step size was adjusted to 0,017°, the scan time for a step was 30s. In order to quantify the amount of phases formed during oxidation, Rietveld analysis was performed using the cif-files (anatase (ICSD9852) [28], corundum (ICSD 160604 [29]), and rutile (ICSD 9161) [30]). The values of the standard free energy of formation of oxides and nitrides were calculated using the software FactSage V6.4 in conjunction with the SGPS database.

## 3. Results

### *3.1. Oxidation kinetics*

Fig. 1(a) shows thermogravimetric curves observed during exposure of the alloy Nb−Mo−Cr−Ti−Al to laboratory air at 900 °C, 1000 °C and 1100 °C. The curves obtained at 900 °C and 1000 °C obviously obey the linear oxidation kinetics, whereby the oxidation rate at 1000 °C is substantially higher compared to that at 900 °C indicating formation of non-protective oxide scales. Oxidation kinetics at 1100 °C shows a tendency to become decelerated after approximately 25 h of air exposure. The total mass gain after 48 h of oxidation at 1100 °C is slightly lower compared to that at 1000 °C. It can be assumed that the oxide scale formed on the alloy Nb−Mo−Cr−Ti−Al at 1100 °C becomes at least partially protective after prolonged oxidation times.

Thermogravimetric curves of the alloy Nb−Mo−Cr−Ti−Al−1Si obtained during oxidation at the same temperatures as for the Si-free alloy are shown in Fig. 1(b). The alloy oxidizes according to the linear rate law at 900 °C, while the thermogravimetric curves for 1000 °C and 1100 °C apparently show an initially parabolic weight gain which changes to the linear rate law after approximately 30 h. The oxidation kinetics at 1100 °C is only slightly higher compared to that at 1000 °C. The first few hours of transient oxidation are usually characterized by rapid oxidation of all elements present in the alloy. After a period of parabolic oxidation, an effect similar to breakaway oxidation, i.e. the oxidation rate increases markedly approaching the linear mass gain, is observed for the Si-containing alloy at 1000 °C and 1100 °C. This effect correlates with a change in the scale structure during oxidation towards formation of thick, porous oxide scales accompanied by enhanced ingress of gaseous species down to the metal phase. This will be discussed in more detail below. Given the high fraction of refractory elements contained in the HEAs studied, the weight gains found after nearly 50 h are relatively low (below 10 mg/cm$^2$).

### *3.2. Microstructural analysis of oxide scales*

#### *3.2.1. Alloy Nb−Mo−Cr−Ti−Al*

The oxide scale formed on the alloy Nb−Mo−Cr−Ti−Al at 900 °C after 48 h of oxidation is shown in Fig. 2(a). The scale is largely homogeneous and is approximately 4 μm thick. The EDX analysis of the oxide scale (not shown here) reveals that the scale consists of a mixture of Ti, Al, Cr, and Nb oxides. Such oxide layers are non-protective in nature and thus can explain the linear oxidation at 900 °C (see Fig. 1(a)). Fig. 2(b) shows the morphology of the oxide scale formed on the alloy Nb−Mo−Cr−Ti−Al after 48 h of oxidation at 1000 °C. Two different kinds of oxide morphology can be

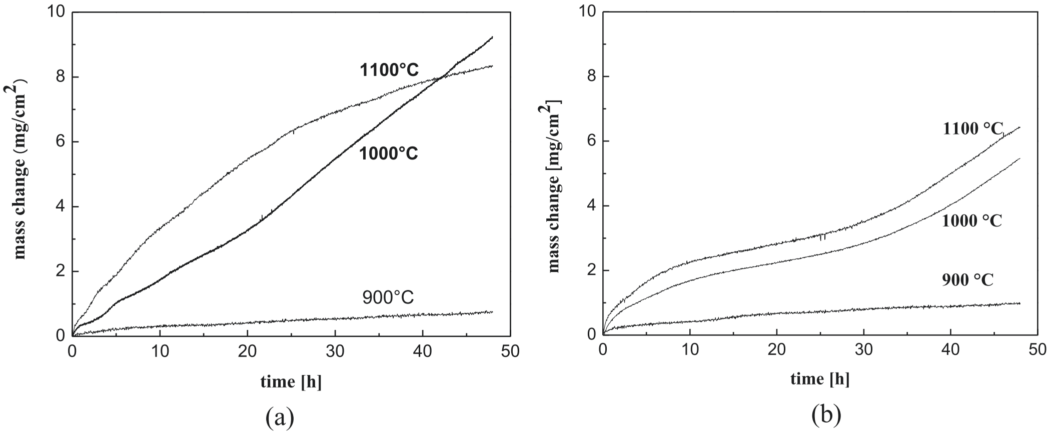

**Fig. 1.** Oxidation kinetics of alloys (a) Nb–Mo–Cr–Ti–Al and (b) Nb–Mo–Cr–Ti–Al–1Si.

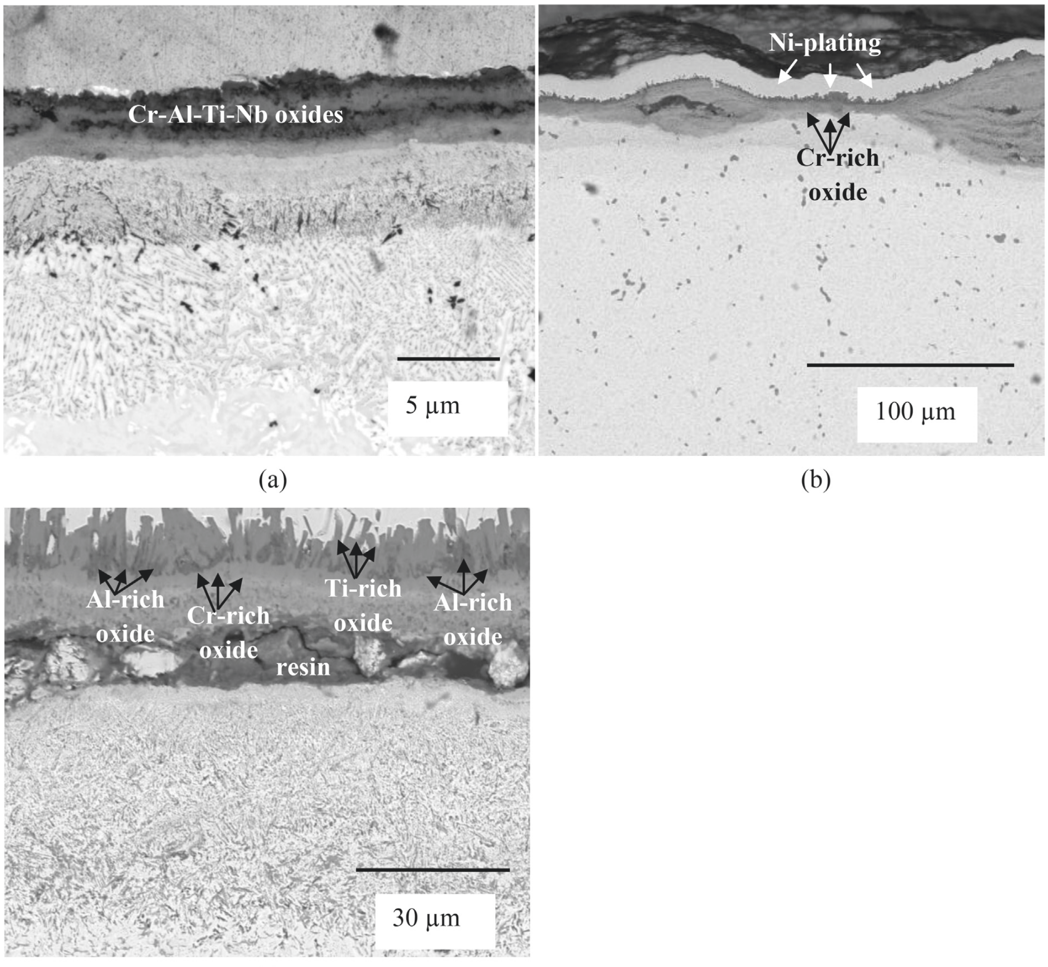

(a)

(b)

(c)

**Fig. 2.** Cross-section (BSE) of the alloy Nb–Mo–Cr–Ti–Al after 48 h oxidation at (a) 900 °C, (b) 1000 °C, and (c) at 1100 °C.

observed: (i) a thick (up to ~ 80 μm) and porous oxide mixture and (ii) a relatively thin (up to ~ 15 μm) and compact oxide layer. EDX analysis (not shown here) of these two distinctive regions revealed that Ti, Al, Cr and Nb, i.e. their oxides, are nearly homogeneously distributed in the thick oxide layers, while a discontinuous Cr oxide-rich layer was identified within the oxide scale in the case of the thin oxide layer. Interestingly, enrichment of Mo was found at the interface oxide/substrate indicating that evaporation of Mo oxides can be neglected. At 1100 °C, the microstructure of the oxide scale changes significantly compared to that formed at the lower temperatures. The oxide scale is mostly homogeneous and is about 25 μm thick (see Fig. 2(c)). Underneath the coarse crystals of Ti oxide clearly visible in the outermost part of the scale, a semi-continuous Al oxide-rich layer can be identified. The decelerated oxidation kinetics at 1100 °C can apparently be attributed to the formation of this Al oxide-rich layer. However, the microstructural analysis of the cross-sections after discontinuous oxidation tests revealed that the Al oxide-rich scale could only be detected after a prolonged oxidation time, i.e after at least 24 h. Further, a continuous Cr oxide-rich layer was observed underneath the Al oxide-rich scale that also contributes to slowing down the kinetics (see Fig. 2(c)). Underneath the Cr oxide-rich scale, Ti and Nb oxides were identified to prevail. It should also be mentioned that some areas with the thick scale similar to that formed at 1000 °C were pre-dominantly located on sample corners.

As shown in Fig. 2 (a)-(c), thick zones of internal precipitates were found underneath the oxide scales. In order to analyze these precipitates, the oxide scale was completely ground off from the sample oxidized for 48 h at 1000 °C, and a XRD measurement was carried out on the metallic substrate containing the internal precipitates. The results are shown in Fig. 3. The metallic substrate consists of the major solid solution BCC phase, the minor Laves phase ($Cr_2Nb$) as well as an unknown phase. These findings are in agreement with previous investigations of the alloy microstructure [27]. In addition to the very stable oxides, i.e. $Al_2O_3$ and $TiO_2$, three types of nitrides were detected: TiN, $Cr_2N$ and a $Nb_2N$. Considering the rather thick zone of internal precipitates, it can be concluded that the alloy Nb—Mo—Cr—Al—Ti is extremely susceptible to nitrogen ingress.

To identify the nature of corrosion products formed in the outermost scale and to estimate the amounts of different oxides as a function of the oxidation time, the oxide scales were removed from the samples oxidized for 8 h, 24 h and 48 h in air at 1000 °C, crushed into powders and quantitatively analyzed using XRD. Fig. 3 (b) and (c) shows the XRD patterns of the powdered oxide scales formed on the alloy Nb—Mo—Cr—Ti—Al at 1000 °C after 8 h and 48 h of exposure, respectively. The results are summarized in Table 1. Three crystal structures were identified, namely, rutile, corundum, and anatase. For all oxidation times, rutile seems to be the prevailing phase. The high amount of rutile can clearly be related to the formation of $TiO_2$ that was confirmed by the EDX analysis. How-ever, $Nb_2O_5$ exhibits polymorphism and can also crystallize in the rutile ($TiO_2$) structure [31]. Furthermore, Novotny reported that solubility of $Nb_2O_5$ in $TiO_2$ varies between 2 at.% and 41 at.% [32]. Besides, Nb oxide was identified by the EDX analysis of the oxide scale. Therefore, the two oxides $TiO_2$ and $Nb_2O_5$ can be responsible for the presence of rutile in the scale formed on the alloy Nb—⊖ Mo—Cr—Ti—Al. The negligibly small amount of anatase was only found after 8 h of oxidation. The two oxides $Al_2O_3$ and $Cr_2O_3$ that can form in this alloy during oxidation, possess the crystal structure of corundum. Bondioli et al. reported that below 950 °C a miscibility gap forms, where $Al_2O_3$ and $Cr_2O_3$ coexist, while above this temperature complete miscibility is present [33].

Results of the thermogravimetric analysis shown in Fig. 1(b) clearly demonstrate that Si has a beneficial effect on the oxidation behavior of the alloy Nb—Mo—Cr—Ti—Al. In literature, numerous studies exist suggesting several hypotheses on the positive effect of

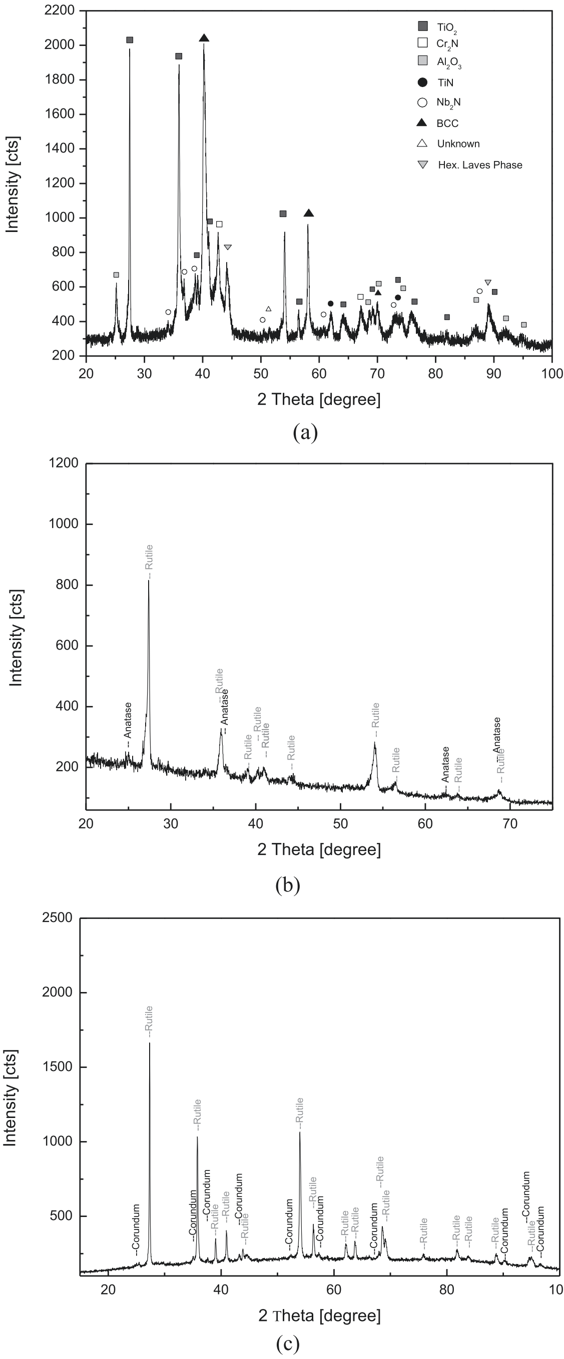

(a)

(b)

(c)

**Fig. 3.** XRD patterns of (a) the zone with internal precipitates formed underneath the oxide scale on the alloy Nb—Mo—Cr—Ti—Al after 48 h oxidation at 1000 °C, (b) powdered oxide scales formed on the alloy Nb—Mo—Cr—Ti—Al after 8 h oxidation at 1000 °C and (c) powdered oxide scales formed on the alloy Nb—Mo—Cr—Ti—Al after 48 h oxidation at 1000 °C.

**Table 1**
Phase fractions of corrosion products after oxidation of the alloy Nb−Mo−Cr−Ti−Al at 1000 °C.

| Oxidation time | 8 h | 24 h | 48 h |
|---|---|---|---|
| Rutile, % | 98.4 | 88.3 | 84.5 |
| Corundum, % | − | 11.7 | 15.5 |
| Anatase % | 1.6 | − | − |

Si with respect to high temperature oxidation resistance [34,35]. The two most commonly accepted ones are: (i) depending on the alloy system, Si favors the formation of either a protective external silica scale or of a silica layer on the phase boundary oxide/alloy [36] and (ii) $SiO_2$ acts as nucleation sites promoting the rapid formation of a continuous protective layer [37,38]. In order to proof hypothesis (ii), on one side of the samples of the alloy Nb−Mo−Cr−Ti−Al a thin (~20 nm) $SiO_2$ layer was sputter deposited, while the other side remained untreated. The sample was subsequently oxidized in air for 48 h at 1000 °C. As shown in Fig. 4, no difference can be identified between the sputtered and non-sputtered sides of the sample. It can, thus, be concluded that $SiO_2$ sputter deposition does not lead to a noticeable improvement of the oxidation resistance of the alloy Nb−Mo−Cr−Ti−Al. The fast growing oxide mixture clearly governs the entire oxidation process suppressing or even eliminating the possible positive Si effect from the formation of nucleation sites.

### 3.2.2. *Alloy Nb−Mo−Cr−Ti−Al−1Si*

Fig. 5(a)-(c) show the cross-sections of the alloy Nb−Mo−Cr−Ti−Al−1Si after 48 h of exposure to air at 900 °C, 1000 °C, and 1100 °C. Similar to the case of the Si-free alloy, the oxide scale formed on the Si-containing alloy at 900 °C is approximately 4 μm thick and represents a mixture of Ti, Al, Cr, and Nb oxides. The main parts of the oxide scales formed at 1000 °C and 1100 °C are 7 μm and 20 μm thick, respectively. Thicker and more porous oxide scales, if present, were occasionally observed on the sample corners (see Fig. 5(d)). Obviously, the dramatic increase in the oxidation rate after approximately 30 h of oxidation, Fig. 1(b), can be attributed to the formation of these thick layers on the sample corners.

In order to get a deeper insight into the morphology of the oxide scales formed at higher temperatures, a TEM lamella was prepared using ion milling in the SEM-FIB device from a sample oxidized at 1000 °C for 48 h. The morphology of the oxide layer and corresponding results of EDX analyses carried out in TEM are shown in Fig. 6. These results clearly reveal that nearly continuous Al oxide- and Cr oxide-rich scales are formed underneath coarse Ti oxide grains. The moderate mass gain during oxidation of the alloy Nb−Mo−Cr−Ti−Al−1Si at 1000 °C and 1100 °C for up to 30 h can be explained by the formation of these oxide layers. Still as for the base alloy described in the previous section, a significant amount of Nb and Ti oxides was also observed in the oxide scale. The distribution of Nb in the oxide scale indicates that the Al oxide-rich scale is the only efficient barrier against Nb diffusion since Niobium was detected exclusively underneath the Al-rich oxide layer. Another important positive finding is that Mo was only detected in the metallic substrate suggesting that the evaporation of Mo oxides can be largely excluded. Results of the EDX analysis of the zone marked in Fig. 6 as a black frame revealed that the small bright particles at the interface oxide/substrate consists of nearly pure Mo (see the magnified view of Fig. 6(a) in Fig. 7 together with the element specific mapping of molybdenum and oxygen). In addition, a pronounced zone of internal precipitates can clearly be seen in Figs. 5 and 6. These internally precipitated corrosion products are supposed to be the same as the ones identified in the previous section for alloy Nb−Mo−Cr−Ti−Al.

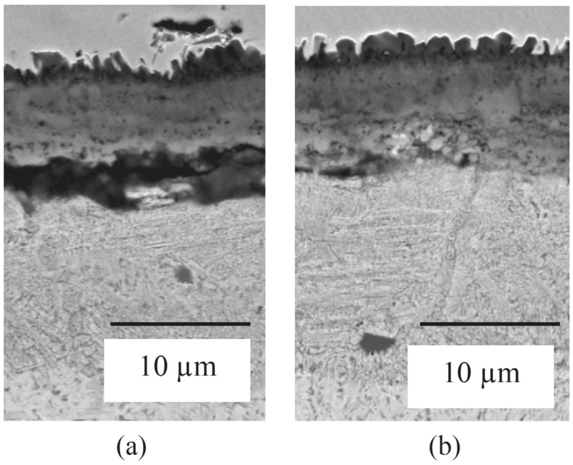

**Fig. 4.** Effect of $SiO_2$ sputter deposition on the oxidation behavior of the alloy Nb−Mo−Cr−Ti−Al after 48 h of oxidation at 1000 °C; (a) sputtered side of the oxidized samples, (b) non-sputtered side of the oxidized samples (BSE-images).

The results of the quantitative XRD analysis (prepared in the same way as described above for the Si-free alloy) of corrosion products after oxidation of the alloy Nb−Mo−Cr−Ti−Al−1Si at 1000 °C are summarized in Table 2. Fig. 8 shows exemplarily the XRD patterns of the powdered oxide scale formed during 24 h of oxidation at 1000 °C. It was found that only two crystal structures are present after both 24 h and 48 h air exposure, namely rutile and corundum. No anatase could be detected, though. Different to the Si-free alloy, the amount of the oxide powder available after 8 h of oxidation was too small to carry out XRD measurements. The rutile phase is again the major phase of the corrosion products formed on the alloy Nb−Mo−Cr−Ti−Al−1Si. The phase fraction of rutile increases slightly with oxidation time, while the percentage of corundum decreases correspondingly. The observed increase of the oxidation rate after 30 h of oxidation (see Fig. 1(b)) is an indication that the alumina and/or chromia scale loses its protectiveness, especially at the sample corners, causing the enhanced formation of fast growing and non-protective rutile.

## 4. Discussion

The experimental results presented in the previous section reveal a moderately beneficial effect of the Si addition on the oxidation behavior of the equiatomic alloy Nb−Mo−Cr−Ti−Al. Comparing the thermogravimetric curves of the Si-free and Si-containing alloy, it can be concluded that the better oxidation resistance at 1000 °C and 1100 °C of the alloy Nb−Mo−Cr−Ti−Al−1Si manifests itself (i) in a lower values of the total mass gain after 48 h of air exposure compared to the Si-free alloy and (ii) in an interim period of parabolic oxidation. However, at 900 °C, the thermogravimetric results of both alloys are rather similar. The microstructural analyses of the oxide scales formed on both alloys at 900 °C reveal this resemblance in the oxide thickness and the constitution of the oxide layers. These oxide scales represent a non-protective mixture of various oxides explaining the linear mass gain at 900 °C. At higher temperature, however, the constitution of the oxides scales formed on both alloys substantially differs. While the oxide scale of the Si-free alloy includes only a partly continuous Cr oxide-rich scale at 1000 °C and an additional semi-continuous Al oxide-rich scale that forms after a prolonged oxidation time at

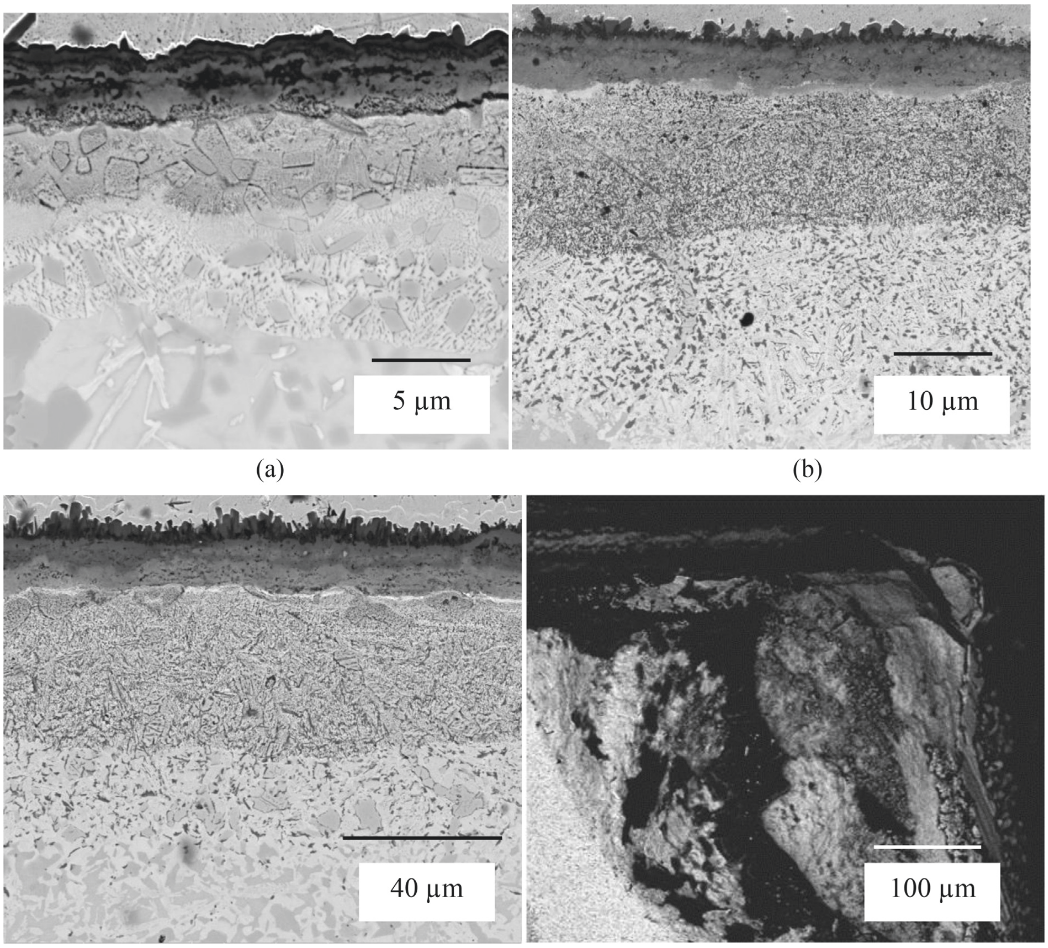

(a) (b) (c) (d)

**Fig. 5.** Cross-section (BSE) of the alloy Nb—Mo—Cr—Ti—1Si after 48 h oxidation at (a) 900 °C, (b) 1000 °C, and (c) at 1100 °C; (d) corner of the oxidized sample Nb—Mo—Cr—Ti—1Si at 1100 °C.

1100 °C, the alloy Nb—Mo—Cr—Ti—Al—1Si forms both, Cr oxide- and Al oxide-rich layers, at 1000 °C as well as at 1100 °C that are also noticeably more dense and compact compared to those formed on the Si-free alloy. Thus, it can be concluded that the formation of an Al oxide-rich scale in the alloy system Nb—Mo—Cr—Ti—Al is promoted by higher temperatures, prolonged oxidation time as well as Si additions. It should, however, be pointed out that the sample surfaces of both alloys after oxidation at 1000 °C and 1100 °C are covered by a non-uniform oxide scale showing regions of a thick, non-protective and quickly growing scale as well as regions with a relatively thin, to some extent protective oxide scale due to the formation of the Cr oxide-rich and Al oxide-rich layers mentioned above. The thick and non-protective scale seems to form at random on the alloy Nb—Mo—Cr—Ti—Al, while on the alloy Nb—Mo—⊖ Cr—Ti—Al—1Si it appears predominantly on the sample corners. It is well-known that oxide scales are less adherent on convex surfaces, e.g. corners of specimens, than on flat or concave surfaces because of the high tensile stresses developing in the growing scale [39]. As a consequence of these stresses, porosity and microchannels form in the scale resulting in the loss of protectiveness primarily on the specimen corners [39]. For the alloy Nb—Mo—Cr—Ti—Al—1Si it can, hence, be concluded that an effect similar to the breakaway oxidation, i.e. the local formation of thick and fast growing scales after a certain period of oxidation, takes place explaining the increase of the oxidation rate after 30 h of oxidation at 1000 °C and 1100 °C. The general reason why the Si-containing alloy shows a better oxidation behavior compared to that of the Si-free alloy is still unclear as the coverage of the alloy surfaces by a thin sputtered $SiO_2$ layer that should promote the formation of protective oxide scales did not show an appreciable effect on the oxide scale formation at least after longer oxidation times. A possible explanation of the positive effect of Si addition would be that Si favorably increases the activities of Cr and/or Al in the alloy, hence, leading to a higher driving force for the formation of the protective oxides $Cr_2O_3$ and $Al_2O_3$. The thermodynamic effect of Si in the alloy system studied will, thus, be explored in a future investigation in detail.

The mass fractions of oxides observed using XRD and their evolution during oxidation can be discussed only qualitatively, i.e. in terms of the major phase, minor phases and traces, and, therefore, cannot be unambiguously correlated with other experimental results, such as the thermogravimetric data. The reason for this restriction is that the phase fractions were determined assuming that rutile is represented by $TiO_2$ and corundum by $Al_2O_3$. The EDX results, however, show that other oxides are also extensively present in the oxide scales and possess the same crystal structures, which for instance holds true for $Cr_2O_3$ and $Al_2O_3$. A comparison of the oxide mass fraction differences between the alloy Nb–Mo–Cr–Ti–Al and the alloy Nb–Mo–Cr–Ti–Al–1Si is hardly possible because these two alloys seem to essentially form the same oxides and the differences of the oxide mass fractions are rather small and therefore not meaningful. Nevertheless, some important conclusions can be drawn from the quantitative XRD analysis. Fig. 9 shows the lattice parameters rutile identified using Rietveld analysis on powdered oxide scales formed on alloys Nb–Mo–Cr–Ti–Al (designated as “Nb” in Fig. 9) and Nb–Mo–Cr–Ti–Al–1Si (designated as “Nb1Si” in Fig. 9) after different oxidation times at 1000 °C. It is obvious that the lattice parameters determined from samples of both alloys oxidized for 24 h and 48 h are almost identical. A slight deviation was only observed for the Si-free alloy oxidized for 8 h at 1000 °C. This difference might be explained by the supposition that the initially formed rutile compound has not yet reached equilibrium. Further, Fig. 9 reviews literature data on lattice parameters of pure $TiO_2$ (designated as “TiO2”) [40–47], $TiO_2$ with Nb substituting Ti sites (designated as “Ti1-xNbxO2”) [48,49] as well as $TiO_2$ with Nb and Al substituting Ti (designated as “Ti0.6Al0.2Nb0.2”) [50]. Comparing the lattice parameter determined for rutile in this study with the literature data, it can be concluded that a certain amount of Nb may be dissolved in the rutile formed during oxidation of both alloys causing a significant cell distortion towards higher lattice parameters compared to pure $TiO_2$. Considering that both Nb and Al can occupy Ti sites in rutile, it cannot be excluded that Al may also be dissolved in the rutile formed on the HEAs studied.

As relatively thick oxide scales were observed on the surface of both alloys, the dominant contribution to the mass gain of the alloys studied can obviously be attributed to the oxygen uptake through the formation of external oxide scales. It is well-known that the growth rate of pure chromia and α-alumina forming a dense layer is very slow and consequently low values of the parabolic oxidation constants are reported in the literature, e.g. $2 \times 10^{-11}$ $mg^2cm^{-4}\,s^{-1}$ for chromia and $7 \times 10^{-12}$ $mg^2cm^{-4}s^{-1}$ for α-alumina [51] at 1000 °C. During exposure to air at temperatures above approximately 800 °C, pure Mo and Mo-based alloys form gaseous oxides that evaporate [52]. In case of the alloys investigated in this study, the evaporation of Mo oxides is presumably restricted to the initial transient oxidation stage, if it takes place at all. After a longer time of oxidation this effect can be neglected, since a clear Mo enrichment was observed at the interface oxide/substrate. It has been reported in the literature that both, Ti [53] and Nb [54], oxidize at 1000 °C according to the linear rate law that is usually typical of the growth of non-protective surface scales. The linear oxidation constants of Ti and Nb are 0.013 $mgcm^{-2}\,min^{-1}$ [53] and 1 $mgcm^{-2}\,min^{-1}$ [54], respectively. As oxides of these two elements may possess the same rutile structure (see above) that was identified as the predominant phase, the oxidation of Ti and Nb seem to primarily account for the formation of the thick oxide scales. However, the relatively high mass gain during oxidation in air can also be attributed to a nitrogen uptake forming the nitrides TiN, $Cr_2N$ and $Nb_2N$, which were

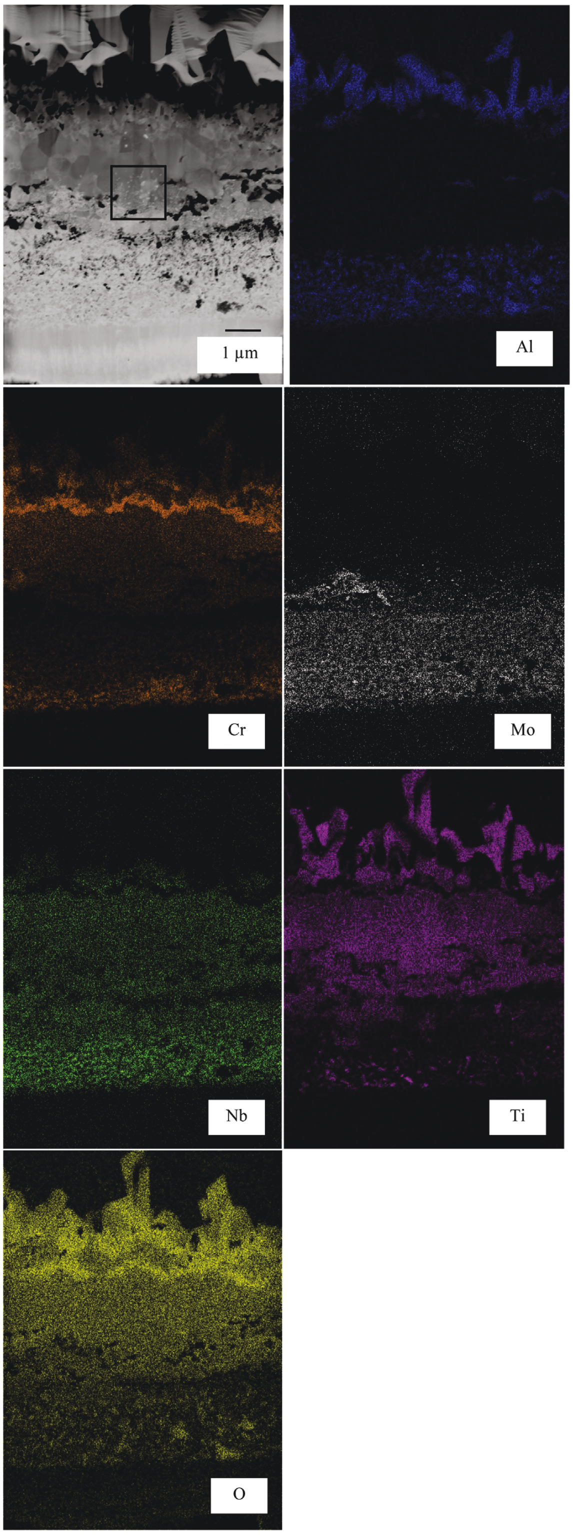

**Fig. 6.** TEM-bright field micrograph of a cross-section through the oxide scale of the alloy Nb–Mo–Cr–Ti–Al–1Si after 48 h oxidation at 1000 °C and the corresponding element-specific EDX mappings. The black box indicated in the bright field micrograph is presented as an enlarged view in Fig. 7.

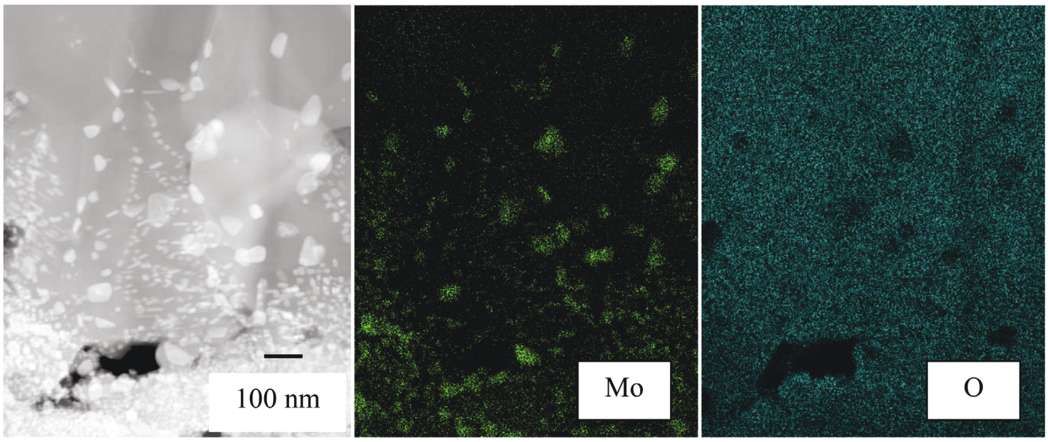

**Fig. 7.** EDX analysis of the zone marked in Fig. 6.

**Table 2**
Phase fraction of corrosion products after oxidation of the alloy Nb–Mo–Cr–Ti–Al–1Si.

| Oxidation time | 24 h | 48 h |
|---|---|---|
| Rutile, % | 89.7 | 93.2 |
| Corundum, % | 10.3 | 6.8 |

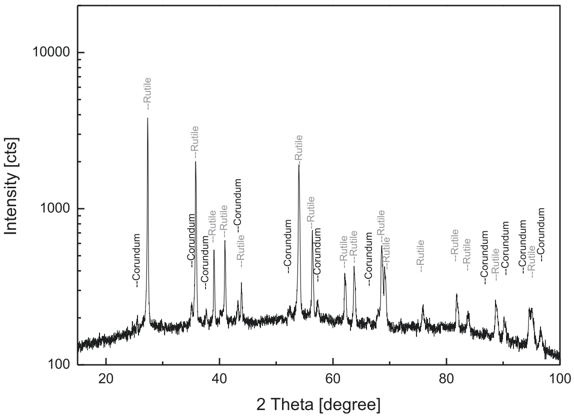

**Fig. 8.** XRD patterns of the powdered oxide scale formed on the alloy Nb–Mo–⊕Cr–Ti–Al–1Si after 24 h of oxidation at 1000 °C.

experimentally identified in the thick zone of internal corrosion in the alloy Nb–Mo–Cr–Ti–Al exposed to air for 48 h at 1000 °C. Similar findings hold true for the alloy Nb–Mo–Cr–Ti–Al–1Si. Thick and porous oxide mixtures can form on the alloy surface if the oxides constituting the scale possess similar thermodynamic stabilities, such as $Al_2O_3$ and $TiO_2$ [46]. In order to assess the thermodynamic stability of the most relevant oxides in this alloy system, the standard free energies of formation of the possible oxides at 1000 °C were calculated using the commercial software FactSage. The calculations were carried out assuming the element activities being equal unity. The calculated values of the standard free energy can however be considered since all elements in the alloys possess the same concentrations. The numbers are summarized in Table 3. In addition to the well-known similar thermodynamic affinity of oxygen to Al and Ti [55], almost identical values of the standard free energy of formation can be found for $Nb_2O_5$ and $Cr_2O_3$. It can be assumed that the formation of a pure alumina on the alloy surface is retarded because of similar thermodynamic stability of $Al_2O_3$ and $TiO_2$, while the formation of chromia is hampered because of the nearly equal values of the standard free energy for $Nb_2O_5$ and $Cr_2O_3$. Probably due to the slightly higher thermodynamic stability of $TiO_2$ in the rutile modification as compared to anatase, the latter was detected by the XRD analysis only after 8 h of oxidation as a transient phase. In terms of the thermodynamic stability of oxides listed in Table 3 it can be concluded that all oxides, except $MoO_3$, exhibit apparently high affinity to oxygen. Considering the very high oxidation rates of Ti and Nb discussed above, the predominant formation of the rutile phase consisting of $Nb_2O_5$ and $TiO_2$ becomes reasonable.

The values of standard free energies of formation of relevant nitrides at 1000 °C are summarized in Table 4. As described above, three types of nitrides, i. e. TiN, $Nb_2N$ and $Cr_2N$, were identified experimentally in the outer zone of internal corrosion of the alloy Nb–Mo–Cr–Ti–Al after air exposure for 48 h at 1000 °C. As shown in Table 4, Nb and Cr can form two corresponding types of nitrides, in each case the most stable one ($Nb_2N$, $Cr_2N$) was detected using XRD. It is also not surprising that TiN as the most stable nitride in this alloy system was identified in the inner zone of internal corrosion.

In terms of the high temperature oxidation resistance, the results presented here show the high potential of the new refractory HEAs. It is obvious that the oxidation behavior of these alloys can be moderately improved by micro-alloying, e.g. by Si, as was shown in this study. An increase of the Si concentration in the alloy Nb–⊕Mo–Cr–Ti–Al up to 2–3 at.% may lead to a further improvement of oxidation resistance. However, the strongest effect on the oxidation behavior can certainly be achieved by macro-alloying, i.e. by substituting of some elements, for example Nb, in the alloy's chemical composition. The development of the new refractory HEAs primarily aims at the definition of a core alloy system providing the best combination of mechanical properties, ductility, and oxidation resistance. Hence, in our further studies, the effect of macro-alloying will be investigated and discussed by comparing the oxidation behavior of the alloy systems Nb–Mo–Cr–Ti–Al, W–Mo–Cr–Ti–Al, and Ta–Mo–Cr–Ti–Al.

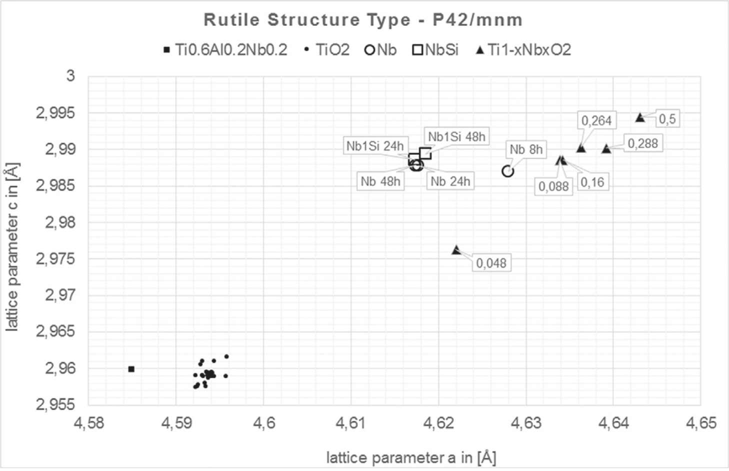

**Fig. 9.** Lattice parameters of the rutile lattice structure identified in powdered oxide scales formed on the alloys Nb–Mo–Cr–Ti–Al (marked as open circle) and Nb–Mo–Cr–⊕ Ti–Al–1Si (marked as open square) after different oxidation times at 1000 °C as well as literature data for pure $TiO_2$ (marked as point), Ti1-xNbxO2 (marked as filled triangle) and Ti0.6Al0.2Nb0.2 (marked as filled square). References are given in text.

**Table 3**
Standard free energies of formation of oxides at 1000 °C.

| Oxide | $Al_2O_3$ | $TiO_2$ (rutile) | $TiO_2$ (anatase) | $Nb_2O_5$ | $Cr_2O_3$ | $MoO_3$ |
|---|---|---|---|---|---|---|
| $\Delta G^0$ [kJ/mole $O_2$] | −853 | −713 | −702 | −540 | −538 | −293 |

**Table 4**
Standard free energies of formation of nitrides at 1000 °C.

| Nitrides | TiN | AlN | $Nb_2N$ | NbN | $Cr_2N$ | CrN |
|---|---|---|---|---|---|---|
| $\Delta G^0$ [kJ/mole $N_2$] | −434 | −359 | −251 | −229 | −64 | −41 |

## 5. Summary

In this study, high temperature oxidation behavior of the equiatomic refractory high-entropy alloy Nb–Mo–Cr–Ti–Al was investigated. The effect of 1 at.% of Si addition was also studied. The results can be summarized as follows.

1. Although the alloy 20Nb–20Mo–20Cr–20Ti–20Al contains a high amount of refractory elements, moderate mass gain was measured during oxidation in air. The oxidation kinetics follows the linear rate law at 900 °C and 1000 °C, while the decelerating oxidation rate was observed after approximately 30 h at 1100 °C. The metal surface was largely covered by thick, porous and non-protective oxide scales consisting of a mixture of various oxides. Localized, a relatively thin and more protective scale was observed containing an intermediate, semi-continuous Cr oxide-rich layer. At higher temperatures, an additional Al oxide-rich scale was identified after a prolonged oxidation time. A pronounced zone of internal corrosion was observed at all temperatures. The quantitative XRD analysis showed that rutile is the predominant phase in the oxide scale formed at 1000 °C.
2. The addition of 1 at.% Si to the alloy 20Nb–20Mo–20Cr–20-Ti–20Al improves the oxidation behavior moderately. The mass gain of the Si-containing alloy is by trend significantly lower compared to the Si-free alloy. The oxidation kinetics obeys the parabolic rate law up to approximately 30 h and changes subsequently towards a linear oxidation rate. The Si-containing alloy largely forms the quite thin and compact oxide scale at 1000 °C and 1100 °C that contains nearly continuous and compact Cr- and Al-rich oxide layers. Thick and rather porous scales were predominantly observed on the sample corners. The moderate mass gain during oxidation and formation of the relatively thin oxide scale is mainly attributed to the formation of an Al-rich oxide layer. However, zones of internal corrosion were observed in all oxidized samples.
3. Though the HEAs represent a new material class, they show a high potential in terms of possible high temperature applications. The results of this investigation indicate that the oxidation behavior of these materials can be substantially improved by macro- and micro-alloying.

## Acknowledgment

The financial support by the Deutsche Forschungsgemeinschaft (DFG) is gratefully acknowledged.

## References

[1] Y. Zhang, T.T. Zuo, Z. Tang, M. Gao, K.A. Dahmen, P.K. Liaw, Z.P. Lu, Microstructure and properties of high-entropy alloys, Prog. Mater. Sci. 61 (2014) 1–93.
[2] M.C. Gao, C.S. Carney, Ö.N. Dogan, P.D. Jablonski, J.A. Hawk, D.E. Alman, Design of refractory high-entropy alloys, JOM 67 (2015) 2653–2669.
[3] S. Guo, C.T. Liu, Phase stability in high entropy alloys: formation of solid-solution phase or amorphous phase, Prog. Nat. Sci. Mater. Int. 21 (2011) 433–446.
[4] C.J. Tong, M.R. Chen, S.K. Chen, J.W. Yeh, T.T. Shun, S.J. Lin, S.Y. Chang, Mechanical performance of the AlCoCrCuFeNi high-entropy alloy system with multiprincipal elements, Metallurgical Mater. Trans. A 36A (2005) 1263–1271.
[5] J.W. Yeh, Y.L. Chen, S.J. Lin, S.K. Chen, High-entropy alloys – a new era of exploitation, Mater. Sci. Forum 560 (2007) 1–9.
[6] K.Y. Tsai, M.H. Tsai, J.W. Yeh, Sluggish diffusion in Co-Cr-Fe-Mn-Ni high entropy alloys, Acta Mater. 61 (2013) 4887–4897.
[7] D.L. Beke, G. Erdelyi, On the diffusion in high-entropy alloys, Mater. Lett. 163 (2016) 111–113.
[8] K.C. Hsieh, C.F. Yu, W.T. Hsieh, W.R. Chiang, J.S. Ku, J.H. Lai, C.P. Tu, C.C. Yang, The microstructure and phase equilibrium of new high performance high-entropy alloys, J. Alloys Compd. 483 (2008) 209–212.
[9] W.H. Liu, Y. Wu, J.Y. He, J.Y. Zhang, C.T. Kuz, Z.P. Lu, The phase competition and stability of high-entropy alloys, JOM 66 (2014) 1973–1983.
[10] A.J. Zaddach, C. Niu, C.C. Koch, D.L. Irving, Mechanical properties and stacking

fault energies of NiFeCrCoMn high-entropy alloys, JOM 65 (2013) 1780–1789.

[11] B. Gludovatz, E.P. George, R. Ritchie, Processing, microstructure and mechanical properties of the CrMnFeCoNi high-entropy alloy, JOM 67 (2015) 2262–2270.

[12] O.N. Senkov, C. Woodward, D.B. Miracle, Microstructure and properties of aluminium-containing refractory high-entropy alloys, JOM 66 (2014) 2030–2042.

[13] P.K. Huang, J.W. Yeh, T.T. Shun, S.K. Chen, Multi-principal-element alloys with improved oxidation and wear resistance for thermal spray coating, Adv. Eng. Mater. 6 (2004) 74–78.

[14] H.M. Daoud, A.M. Manzoni, R. Völkl, N. Wanderka, U. Glatzel, Oxidation behavior of Al8Co17Cr17Cu8Fe17Ni33, Al23Co15Cr23Cu8Fe15Ni15, and Al17Co17Cr17Cu17Fe17Ni17 compositionally complex alloys (high-entropy alloys) at elevated temperature in air, Adv. Eng. Mater. 17 (2015) 1134–1141.

[15] T.M. Butler, J.P. Alfano, R.L. Martens, M.L. Weaver, High-temperature oxidation behavior of Al-Co-Cr-Ni-(Fe or Si) multicomponent high-entropy alloys, JOM 67 (2014) 246–259.

[16] S.T. Chen, W.Y. Tang, Y.F. Kuo, S.Y. Chen, C.H. Tsau, T.T. Shun, J.W. Yeh, Microstructure and properties of age-hardenable AlxCrFe1.5MnNi0.5 alloys, Mater. Sci. Eng. A Struct. Mater. Prop. Microstruct. Process. 527 (2010) 21–22.

[17] T.M. Butler, M.L. Weaver, Oxidation behavior of arc melted AlCoCrFeNi multi-component high-entropy alloys, J. Alloys Compd. 674 (2016) 229–244.

[18] M.H. Chuang, M.H. Tsai, W.R. Wang, S.J. Lin, J.W. Yeh, Microstructure and wear behavior of AlxCo1.5CrFeNi1.5Tiy high-entropy alloys, Acta Mater. 55 (2011) 6308–6317.

[19] J.C. Jiang, X.Y. Luo, High temperature oxidation behavior of AlCuTiFeNiCr high-entropy alloy, Adv. Mater. Res. 652 (654) (2013) 1115–1118.

[20] G.R. Holcomb, J. Tylczak, C. Carney, Oxidation of CoCrFrMnNi high entropy alloys, JOM 67 (2015) 2326–2339.

[21] H.H. Yang, W.T. Tsai, J.C. Kuo, Effecto of pre-oxidation on increasing resistance of Fe-Al-Ni-Cr-Co-Mn high entropy alloys to molten Al attack, Corros. Eng. Sci. Technol. 49 (2014) 124–129.

[22] O.N. Senkov, S.V. Senkova, D.M. Dimiduk, C. Woodward, D.B. Miracle, Oxidation behavior of a refractory NbCrMo0.5Ta0.5TiZr alloy, J. Material Sci. 47 (2012) 6522–6534.

[23] C.M. Liu, H.M. Wang, S.Q. Zhang, H.B. Tang, A.L. Zhang, Microstructure and oxidation behavior of new refractory high entropy alloys, J. Alloys Compd. 583 (2014) 162–169.

[24] C. Huang, Y. Zhang, J. Shen, R. Vilar, The stability and oxidation resistance of laser clad TiVCrAlSi high entropy alloy coating on Ti-6Al-4V alloy, Surf. Coat. Technol. 206 (2011) 1389–1395.

[25] B. Gorr, M. Azim, H.-J. Christ, T. Mueller, D. Schliephake, M. Heilmaier, Phase equilibria, microstructure, and high temperature oxidation resistance of novel refractory high-entropy alloys, J. Alloys Compd. 624 (2015) 270–278.

[26] B. Gorr, M. Azim, H.-J. Christ, H. Chen, D.V. Szabo, A. Kauffmann, M. Heilmaier, Microstructure evolution in a new refractory high-entropy alloy, Metallurgical Mater. Transaction 47A (2016) 961–970.

[27] H. Chen, A. Kauffmann, B. Gorr, D. Schliephake, C. Seemüller, J.N. Wagner, H.-J. Christ, M. Heilmaier, Mictrostructure and mechanical properties at elevated temperatures of a new Al-containing refractory high-entropy alloy Nb-Cr-Ti-Al, J. Alloys Compd. 661 (2016) 206–215.

[28] M. Horn, C.F. Schwerdtfeger, E.P. Meagher, Refinement of the structure of anatase at several temperatures, Z. für Kristallogr. 136 (1972) 273–281.

[29] S. Kondo, K. Tateishi, N. Ishizawa, Structural evolution of corundum at high temperatures, Jpn. J. Appl. Phys. 47 (2008) 616–619.

[30] W.H. Baur, A.A. Khan, Rutile-type compounds, IV. $SiO_2$, $GeO_2$ and a comparison with other rutile-type structures, Acta Crystallogr. Sect. B B27 (1971) 2133–2139.

[31] D.E. Sands, Introduction to Crystallography, Dover, New York, 1993.

[32] J. Novotny, Oxide Semiconductors for Solar Energy Conversion: Titanium Dioxide, CRC Press, 2011.

[33] F. Bondioli, A.M. Ferrari, C. Leonelli, Manfredini, L. Linati, P. Musterelli, Reaction mechanism in alumina/chrimia ($Al_2O_3$-$Cr_2O_3$) solid solution obtained by coprecipitation, J. Am. Ceram. Soc. 83 (2000) 2036–2040.

[34] Y. Liu, W. Weo, L. Benum, M. Oballa, M. Gyorffy, W. Chen, Oxidation behavior of Ni-Cr-Fe-based alloys: effect of alloy microstructure and silicon content, Oxid. Metals 73 (2010) 207–218.

[35] H.E. Evans, D.A. Hilton, R.A. Holm, S.J. Webster, Influence of silicon additions on the oxidation resistance of a stainless steel, Oxid. Metals 19 (1983) 1–18.

[36] M. Heilmaier, M. Krüger, H. Saage, J. Rösler, D. Mukherji, U. Glatzel, R. Völkl, R. Hüttner, G. Eggeler, Ch Somsen, T. Depka, H.-J. Christ, B. Gorr, S. Burk, Metallic materials for structural applications beyond nickel-based superalloys, JOM 61 (2009) 61–67.

[37] R. Durcham, B. Gleeson, D.J. Young, Silicon contamination effects in the oxidation of carbide-containing cobalt-chromium alloys, Mater. Corros. 49 (1998) 855–863.

[38] S. Wang, Y. Wu, F. Gesmundo, Y. Niu, The effect of Si additions on the high temperature oxidation of a ternary Ni-10Cr-4Al alloy in 1atm $O_2$ at 900-1000°C, Oxid. Metals 69 (2008) 299–315.

[39] M. Schuetze, Die Korrosionswirkung oxidischer Deckschichten unter thermisch-chemisch-mechanischer Werkstoffbeanspruchung, Gebrueder Borntraeger, Berlin, Stuttgart, 1991.

[40] W.H. Baur, A.A. Khan, Rutile-type compounds. VI. $SiO_2$, $GeO_2$ and a comparison with other rutile-type structures, Acta Crystallogr. B 27 (1971) 2133–2139 (24, 1968-38, 1982).

[41] W.H. Baur, Über die Verfeinerung der Kristallstrukturbestimmung einiger Vertreter des Rutiltyps: $TiO_2$, $SnO_2$, $GeO_2$ und $MgF_2$, Acta Crystallogr. 9 (1956) 515–520 (1, 1948-23, 1967).

[42] S.C. Abrahams, J.L. Bernstein, Rutile: normal probability plot analysis and accurate measurement of crystal structure, J. Chem. Phys. 55 (1971) 3206–3211.

[43] W.H. Baur, Atomabstände und Bindungswinkel im Rutil, Naturwissenschaften 42 (1955) 295–296.

[44] H. Seki, N. Ishizawa, N. Mizutani, M. Kato, High temperature structure of the rutile-type oxides, TiO2 and SnO2, J. Ceram. Assoc. Jpn. 92 (1984) 219–223.

[45] R. Restori, D. Schwarzenbach, J.R. Schneider, Charge density in rutile, $TiO_2$, Acta Crystallogr. Sect. B Struct. Sci. 43 (1987) 251–257.

[46] J.K. Burdett, T. Hughbanks, G.J. Miller, J.W. Richardson, J.V. Smith, Structural-electronic relationships in inorganic solids: powder neutron diffraction studies of the rutile and anatase, J. Am. Chem. Soc. 109 (1987) 3639–3646.

[47] D.M. Tobaldi, A. Tucci, A. Sever Skapin, L. Esposito, Effects of $SiO_2$ addition on $TiO_2$ structure and photocatalytic activity, J. Eur. Ceram. Soc. 30 (2010) 2481–2490.

[48] A. Peterson, H. Mueller-Buschmaum, Ein Beitrag über Oxide vom Typ AMO4 (A=Ti3+; M=Nb5+, Ta5+), Z. für Anorg. Allg. Chem. 609 (1992) 51–54.

[49] M. Okrusch, R. Hock, U. Schuessler, A. Brummer, M. Baier, H. Theisinger, Intergrown niobian rutile phases with Sc- and W-rich ferrocolumbite: an electron-microporbe and Rietveld study, Am. Mineralogist 88 (2003) 986–995.

[50] I. Abrahams, P.G. Bruce, W.I.F. David, A.R. West, Structure determination of substituted rutiles by time-of-flight neutron diffraction, Chem. Mater. 1 (1989) 237–240.

[51] C.S. Giggins, F.S. Pettit, Oxidation of Ni-Cr-Al alloys between 1000°C and 1200°C, J. Electrochem. Soc. 118 (1971) 1782–1790.

[52] E.A. Gulbransen, K.F. Andrew, F.A. Brassat, Oxidation of molybdenum 550° to 1700°C, J. Electrochem. Soc. 110 (1963) 110–119.

[53] P. Kofstad, P.B. Anderson, O.J. Krudtaa, Oxidation of Ti in the temperature range 800-1200°C, J. Less Common Metals 3 (1961) 89–97.

[54] P. Kofstad, H. Kjollesdal, Oxidation of niobium (columbium) in the temperature range 500 to 1200°C, Transaction Metallurgical Soc. AIME 221 (1961) 285.

[55] S. Becker, A. Rahmel, M. Schorr, M. Schütze, Mechanism of isothermal oxidation of the intermetallic TiAl and of TiAl alloys, Oxid. Metals 38 (1992) 425–464.

# Manuskript XVII

## Characterization of oxidation kinetics of Mo-Si-B-based materials

M. Azim, B. Gorr, H.-J. Christ, M. Heilmaier

Oxidation of Metals, 87 (2017) 89-108

Oxid Met (2017)
DOI 10.1007/s11085-016-9659-3

ORIGINAL PAPER

# Characterization of Oxidation Kinetics of Mo–Si–B-Based Materials

**M. A. Azim[1] · B. Gorr[1] · H.-J. Christ[1] · M. Heilmaier[2] · U. Koch[3] · M. Engelhard[3]**

Received: 9 August 2016 / Revised: 19 September 2016 / Published online: 20 October 2016

**Abstract** Characterization of oxidation kinetics of composites based on refractory metals like Mo by means of thermogravimetry is often very complex, because of the simultaneous formation of both volatile and stable oxides. Specifically, thermogravimetrically measured specific mass changes represent the sum of opposite mass change processes: (i) mass loss due to the formation of volatile oxide species and (ii) mass gain as a result of oxygen uptake due to the growth of solid, adherent oxide layers. In order to unambiguously assess the oxidation resistance of such alloys, a separation of these two opposing processes and their quantitative description are needed. In this study, a novel approach is proposed that enables determination of the amount of the material affected during oxidation using the measured oxide layer thickness. This approach also permits a quantitative separation of thermogravimetric data into mass loss (oxide evaporation) and mass gain (oxygen uptake). The advantage of splitting of the thermogravimetric curve into mass gain and mass loss is discussed on the basis of the multiphase material Mo–9Si–8B.

**Keywords** Refractory metal-based in situ composite · Thermogravimetric analysis · Oxidation kinetics · Volatile oxides

---

✉ M. A. Azim
maria.azim@uni-siegen.de

[1] Institut für Werkstofftechnik, Universität Siegen, Paul-Bonatz-Str.9-11, 57076 Siegen, Germany

[2] Institut für Angewandte Materialien, KIT, Engelbert-Arnold-Straße 4, 76131 Karlsruhe, Germany

[3] Department of Chemistry and Biology, Universität Siegen, Adolf-Reichwein-Str. 2, 57076 Siegen, Germany

## Introduction

Research activities of the last decades have shown that several material classes are currently being considered as ultra-high temperature materials for applications in advanced jet engines [1]. Amongst these, in situ composite materials based on refractory metals such as Mo–Si–B-based alloys do already show a good combination of mechanical properties and oxidation resistance. Additionally taking into account their inherently high melting points, these materials may pave the way for development of aeroengine parts with superior efficiency. As the main drawback, however, refractory metals such as W, Mo, and Nb form volatile oxides during oxidation. Thus, the thermogravimetric curves of alloys containing such elements often show the sum of opposite mass change effects, namely oxide evaporation (mass loss) and adherent oxide formation (mass gain).

This phenomenon is illustrated in Fig. 1 for novel Mo–Si–B-Ti alloys [2]. It can be seen that a horizontal oxidation curve (see Fig. 1a) does not necessarily indicate a complete passivation, but can also result from the interplay of a (nearly) equal mass loss by evaporation of oxides, such as $MoO_3$ and $B_2O_3$, and mass gain by the formation of adherent oxides, in this case $SiO_2$ and $TiO_2$, forming a non-protective porous oxide layer (see Fig. 1b).

There have already been different attempts to describe the oxidation kinetics of Mo–Si–B-based alloys. Rioult et al. developed a kinetic model based upon individual phase oxidation behavior considering the phase fraction [3]. The measured phase size distribution was taken into account to represent the mass change versus time for different microstructural size scales [3]. This model perfectly reflects the trends of the mass changes of the single phases $Mo_{ss}$, $Mo_3Si$, and $Mo_5SiB_2$ as well as of the multiphase alloy Mo–9Si–8B (unless denoted otherwise, all chemical compositions are given in at.%). However, the calculated mass change does not exactly match the oxidation kinetics and does not separate the mass change into mass loss due to the formation of evaporating oxides and mass gain due to the formation of solid oxides. Burk calculated the depth of the internal oxidation of Mo–Si–B alloys using a numerical approach by linking the FEM-software

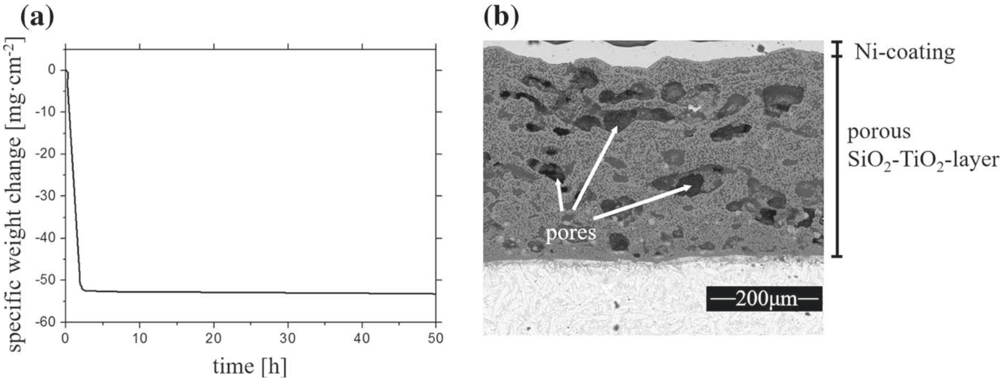

**Fig. 1** **a** Specific mass change versus time for a Mo-Si-B-Ti-based alloy oxidized in air at 1100 °C for 50 h, **b** the corresponding cross-section after exposure of 50 h

COMSOL with the thermodynamic library ChemApp [4]. He described the penetration depth of oxygen and predicted the oxide morphology verifying the results by cross-section analyses. However, he did not consider the oxidation kinetics in his calculations.

The aim of this study is the characterization of the oxidation kinetics of Mo–Si–B-based alloys by splitting the thermogravimetric curve into the mass loss resulting from the consumption of Mo and B by oxide evaporation and the mass gain due to the oxygen uptake by formation of adherent solid oxides. Application of this concept enables a better understanding of oxidation processes of the refractory metal-based alloys and is useful for the verification of the derived oxidation mechanisms. The new approach will be presented using the example of the composite alloy Mo–9Si–8B. The oxidation mechanisms of this alloy have extensively been explored by [4–7] and will only be summarized here. However, some data needed as input for the method used to quantitatively separate the thermogravimetric result into mass gain and mass loss, such as the amount of B dissolved in the silica scale, are missing in the literature. In this paper, experimental results on the oxidation behavior of the alloy Mo–9Si–8B at 1100 °C that are essential for the method proposed here will be shown, i.e., alloy microstructure characterization, thermogravimetric curves, cross-section analysis as well as results of the SIMS studies on the amount of B dissolved in the silica layer. FIB cutting technique is used in order to verify the concept. Through verification it will be shown that the concept applied allows the calculation of the material affected during oxidation and, therefore, the real damage depth of the cross section of an oxidized technical component.

## Experimental Procedures

### Alloy Preparation

Elemental Powder Mixtures of Mo, Si, and B of 99.95, 99.9, and 98 % Purity, respectively, were used to produce the multiphase Mo–9Si–8B composite alloy using a mechanical alloying route (MA). MA was carried out under Ar atmosphere in an attritor (ZoZ GmbH, Simoloyer CM01) at a speed of 1200 rpm and a powder to ball weight ratio of 1:12 for 10 h with an active cooling of the milling unit at −10 °C. Afterwards, the material was compacted by cold isostatic pressing at 200 MPa and sintered in hydrogen at 1600 °C to decrease the content of oxygen. Finally, the material was hot isostatically pressed at 1600 °C and 500 MPa to reduce the porosity of the material to a level below 1 %. For further details, see e.g., Krüger et al. [8].

### Alloy Characterization

To ensure reproducible experimental conditions, oxidation samples having a dimension of $\sim 4 \times 4 \times 3$ mm$^3$ were machined using a slow-cutting diamond saw and ground to a surface finish of 1200 grit. To avoid edge effects on oxidation, the edges of the samples were slightly rounded. Finally, the samples were ultrasonically cleaned in ethanol.

Samples utilized to verify the proposed calculation method had a specific geometry, i.e., two angles of 90° being placed adjacent to one another to assure a sufficiently high accuracy of the cross-section analysis. For this purpose, a specially designed right-angle grinder was used (see Fig. 2a) having a maximum deviation of less than 0.5° from the perpendicularity as inspected by optical microscopy. To obtain parallel opposite surfaces, the specimen had to be turned four times in the same direction. Then, two markers were placed by FIB technique near one of the two 90° edges to allow the precise measurement of the distance between the marker and the sample edge before oxidation and the distance between the marker and the front of the zone of internal oxidation after oxidation (see virtual model of the specimen in Fig. 2b). Two parallel planes and the 90° angle assure that the distance between the markers and the zone of internal oxidation does not change during cross-grinding because of sample asymmetry. The distance between the markers and the sample edge is chosen such that on the one hand, the markers are close enough to enable the comparison of images with a high magnification. On the other hand, the marker–edge distance should be sufficiently high to keep sufficient space between the marker and the zone of internal oxidation.

Two different marker geometries were tested—the circular- (Fig. 2c) and quadratic-shaped ones (Fig. 2d). The experiment shows that due to symmetry reasons, the center of the circular markers can be retrieved with a higher precision

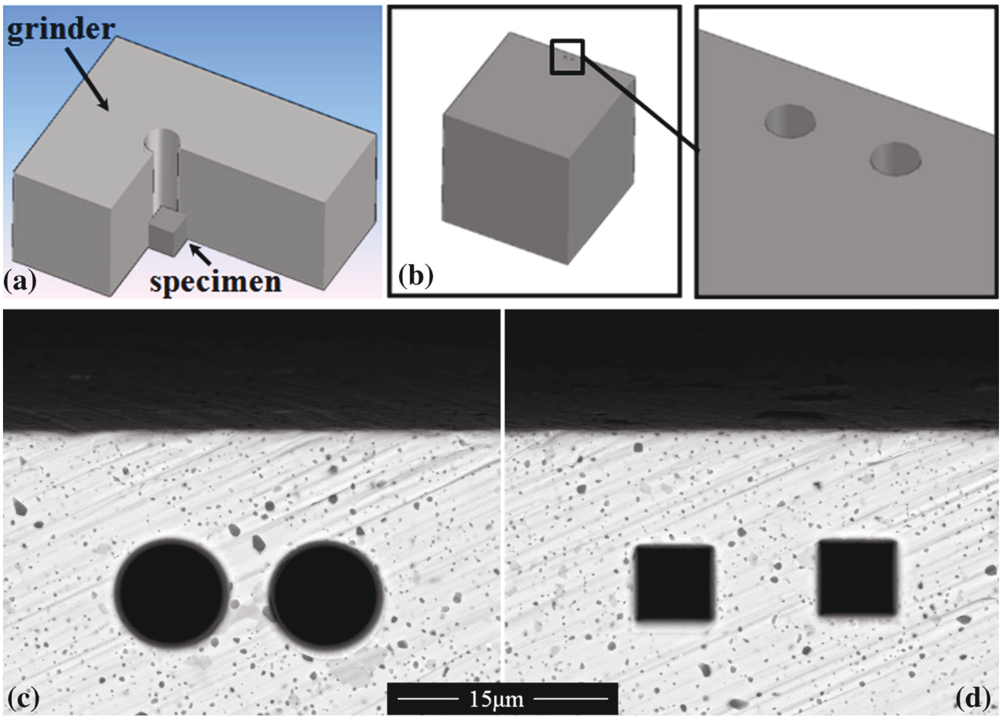

**Fig. 2** **a** Tailor-made right-angle grinder, **b** virtual model of the grinded specimen with FIB-cut markers in the near vicinity of a right-angle edge and SEM-BSE images of the edge-near FIB-made markers with **c** *circular* and **d** *quadratic shape*

than those of the squared markers. Edge effects, which play a significant role for samples experiencing longer oxidation times, can distort the squared marker and make it more difficult to retrieve its center.

For the characterization of the oxidation kinetics, multiphase Mo–9Si–8B was oxidized at 1100 °C in air for 1, 5, 10, 50, and 100 h. Oxidation kinetics was monitored under isothermal testing conditions in static laboratory air using a tailor-made Rubotherm magnetic suspension balance with a resolution of $10^{-5}$g equipped with automatic electronic drift compensation. For cross-section analyses, the oxidized samples were first nickel-coated to protect the oxide layer during sample preparation. Then the samples were embedded in epoxy and ground down to 4000 grit.

The microstructure and the corrosion products were characterized by scanning electron microscopy (Dual Beam FE-SEM of type FEI Helios Nanolab 600) in secondary-electron (SE) and backscattered-electron (BSE) mode. The SEM is equipped with a Si drift detector for energy-dispersive X-ray spectroscopy (EDS/Apollo XL) to qualitatively determine the elements present in the scale while ensuring high count rates even for light-weight elements. Additionally, X-ray powder diffraction analyses were performed using a Philips 3000 PTS X-ray generator equipped with the ultra-fast X-ray detector X'Celerator based on RTMS (Real Time Multiple Strip) technology. The X-ray diffraction (XRD) patterns were taken with Cu Kα-radiation operating at 45 kV and 40 mA at room temperature at $\lambda = 0.15406$ nm, a step size of 0.01°, and a count time of 100 s/step.

The presence of the light-weight element B was detected by an ION-TOF–SIMS IV-100 with a liquid metal ion gun generating a pulsed 25 kV $Bi_1^+$ beam and an electron impact gun to generate the 5 kV $O_2^-$ beam. The $Bi_1^+$ beam was scanned over a $150 \times 150\ \mu m^2$ area and centered inside the $500 \times 500\ \mu m^2$ $O_2^-$ crater hitting the target at an angle of 45°. Charge compensation was performed by a low-energy electron flood gun. The sputter beam current was 200nA.

The question about the modification of $SiO_2$ was studied using electron backscattered diffraction (EBSD/TSL-EDAX) integrated in the FIB system.

Rietveld analysis to determine the volume fraction of the different phases was performed using X́Pert High Score Plus. The amount of new phases formed during oxidation was determined using the image processing program ImageJ® based on the BSE cross sections. The calculation of the material affected during oxidation and the mass of the evaporated and the scale-forming oxides was performed with MATLAB®.

## Results and Discussion

### Characterization of the Alloy Microstructure and the Oxidation Behavior of Mo–9Si–8B

#### *Alloy Microstructure*

The in situ composite Mo–9Si–8B investigated in this study consists of molybdenum solid solution, $Mo_{ss}$, and the intermetallic phases $Mo_3Si$ and $Mo_5SiB_2$ (see

Fig. 3a). $Mo_{ss}$ serves as the phase, which provides adequate mechanical properties such as sufficient toughness at ambient temperature and plastic deformation capability at elevated temperatures [6, 9, 10]. The intermetallics are reservoirs for $SiO_2$ and $B_2O_3 \cdot SiO_2$ scale formation. The dots appearing black in the BSE contrast are segregations of $SiO_2$ which are known to form when residual oxygen due to the manufacturing is present in the alloy [11].

Two charges of Mo–9Si–8B were used to characterize the oxidation kinetics. Charge I was used for the verification of the applied concept, and charge II for the case study. The microstructure of both charges was very fine with an average phase size of <1 µm.

For the method to quantitatively separate the thermogravimetric result into mass gain and mass loss, the phase fractions in the alloy should be determined. As the difference in the BSE contrast between the $Mo_3Si$ and $Mo_5SiB_2$ phase is very low, the determination of the phase distribution was performed using two different methods: (i) the BSE contrast and (ii) Rietveld analyses of the XRD data. The phase fraction of $SiO_2$ in Charge I was calculated to be 1.4 % on the basis of 20 representative BSE images each covering an area of 100 $\mu m^2$. The volume fraction of $SiO_2$ was used as reference for the Rietveld analysis. For the Rietveld refinement the ICSD data codes 076279, 030640, and 044489 of $Mo_{ss}$, $Mo_3Si$, and $Mo_5SiB_2$ were used, respectively. Considering literature data [12, 13], the $SiO_2$ in the substrate is expected to be in the state of trigonal low-quartz. A careful investigation of the phase fraction of the phases was done for each sample separately, as the method is very sensitive to microstructural changes.

As the density is an important parameter in the Rietveld calculation and it varies in the case of $SiO_2$ up to 30 % depending on the modification

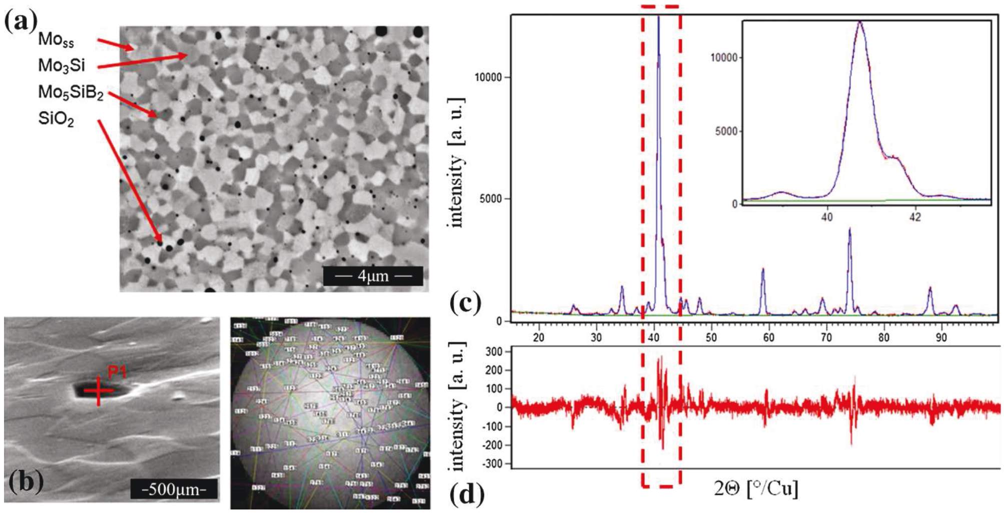

**Fig. 3** **a** BSE-SE image of the microstructure of Mo–9Si–8B, **b** area of EBSD investigation with corresponding Kikuchi pattern to prove the dark areas in the microstructure to be quartz in the low-temperature modification (*image on the left*) and **c** superposition of the recorded (*red curve*) as well as calculated (*blue curve*) room temperature X-ray diffraction profile for multiphase Mo–9Si–8B. The inset shows an enlarged view of the major diffraction peak. **d** Intensity difference between the experimental and the calculated scan

($\rho_{glass} = 2.2\frac{g}{cm_3};\rho_{l\_quartz} = 2.65\frac{g}{cm^3}$), EBSD investigation of the $SiO_2$ regions was performed. They revealed Kikuchi patterns which are characteristic for low-quartz (see Fig. 3b). This is in coincidence with the observations by Lima et al. who concluded that devitrification of borosilicate glass can be largely enhanced when powdered glass samples with high surface area were used [14]. Figure 3c shows the experimental (red) and calculated (blue) X-ray diffraction profile. As it is clearly visible in the difference plot (Fig. 3d), the optimization process under variation of the usual parameters utilized in Rietveld refinement results in an expected profile *R* value below 5, a weighted *R* value below 7, and a profile *R* value below 5 indicating high curve fitting quality.

Table 1 summarizes the phase fraction of the present phases as well as their densities that were determined by the Rietveld analyses of the XRD data.

### *Oxidation Behavior*

The oxidation kinetics of Mo–9Si–8B above 1000 °C can be divided into an initial severe mass loss due to the evaporation of $MoO_3$ and a steady-state stage of oxidation as soon as a continuous $B_2O_3{\cdot}SiO_2$ layer is formed on the surface [7, 15] (see Fig. 4). $B_2O_3$ formed during the oxidation of $Mo_5SiB_2$ reduces the viscosity of the silica layer facilitating a fast coverage of the substrate and sample passivation. However, even in the steady-state stage, a continuous mass loss is observed which can be attributed to the evaporation of $B_2O_3$ and $MoO_3$ [16].

To separate mass gain and mass loss of Mo–9Si–8B at different stages of oxidation, TGA was carried out at 1100 °C for 1, 10, 50, and 100 h in air. The curves of specific weight change versus time reveal a good reproducibility of the oxidation kinetics of this material.

Figure 5a–d show the cross sections of the corresponding samples after oxidation for 1, 10, 50, and 100 h at 1100 °C in air (Charge II). It becomes obvious that with increasing exposure time the formation of a continuous $MoO_2$ layer visible in Fig. 5 a is suppressed. No $MoO_2$ is visible after 10 h of oxidation. Mo particles are still located in the oxide layer. $MoO_2$ particles have been observed by Helmick in the outer oxide layer of the oxide scale of the arc-melted alloy Mo8.9Si7.7B after oxidation at 1100 °C for 3 and 20 h [16] and by Rioult et al. for Mo14,2Si9,6B (1100 °C/20 h) [3]. In this study, the powder metallurgically processed alloy Mo–9Si–8B shows lower oxidation rates as a result of the very fine-grained microstructure. That is why the oxide layer is more protective and after 10 h of

**Table 1** Crystal structure, space group number, density, and distribution of phases investigated and calculated by XRD for the in situ composite Mo–9Si–8B

| | $Mo_{ss}$ | $Mo_3Si$ | $Mo_5SiB_2$ | $SiO_2$ |
|---|---|---|---|---|
| Crystal structure | Im−3m | P m −3 n | I 4/m c m | P 32 2 1 |
| Space group number | 229 | 223 | 140 | 154 |
| Density | 10.21 | 8.98 | 8.86 | 2.65 |
| Phase fraction (Charge I) | 54.9 | 14.7 | 29.0 | 1.4 |

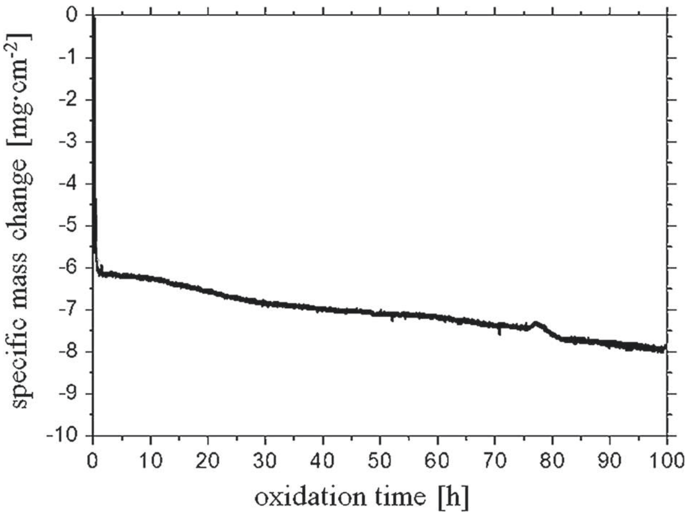

**Fig. 4** Specific weight change versus time for Mo–9Si–8B (Charge II) oxidized in air at 1100 °C for 100 h

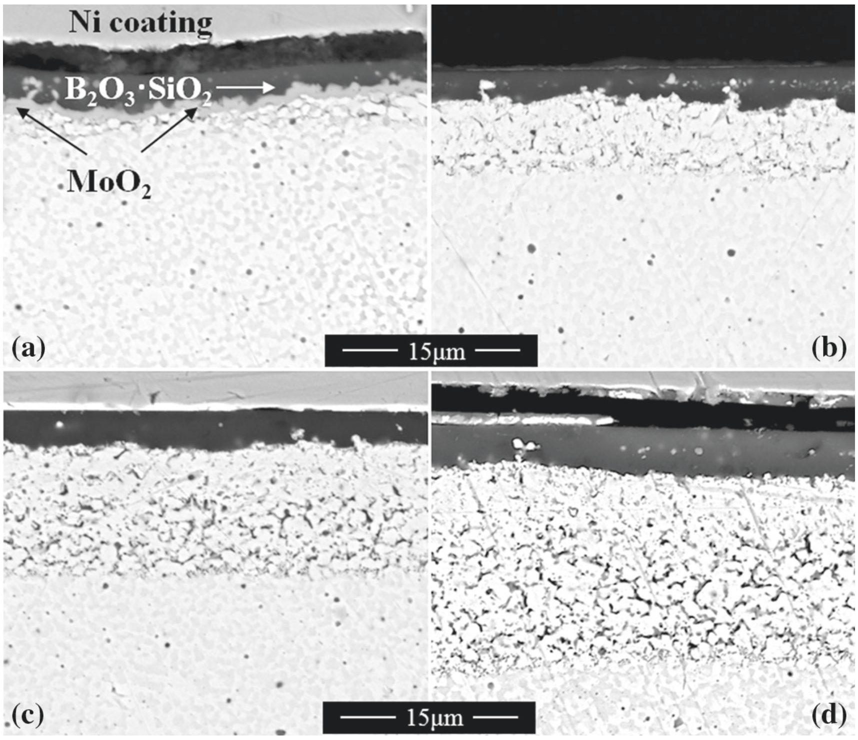

**Fig. 5** Cross sections of Mo–9Si–8B oxidized at 1100 °C for **a** 1 h, **b** 10 h, **c** 50 h, and **d** 100 h

oxidation Mo particles are trapped within the oxide scale according to the undergrowth mechanism proposed by [16]. Mo and $MoO_2$ can be well distinguished by the BSE-SEM phase contrast. The outer oxide layer does not change significantly, but grows with increasing exposure time to air, while the amount of

Mo particles decreases and the $MoO_2$ layer visible after 1 h (Fig. 5a) disappears. That is consistent with the observations of Helmick and Rioult et al. who reported $MoO_3$ and $B_2O_3$ evaporation in the steady-state stage of oxidation after the formation of a continuous oxide layer free of channels [3, 16]. That therefore supports the subsequent outward diffusion of Mo and B after the formation of a continuous oxide layer with no channels reported by [16]. Although no voids and channels are visible in the oxide layer in the BSE-SEM contrast, the disappearance of embedded Mo oxide and Mo particles and the growth of the outer silica layer indicate the presence of nanopores.

To prove that Mo and B are on the surface after 100 h of oxidation at 1100 °C, although no voids are visible in the BSE-SEM cross-section image (see Fig. 5a), TOF–SIMS maps have been collected (see Fig. 6). The maps show that B-Ions and Mo-Ions are concentrated in bubbles located at the surface. Further, the ion intensities normalized to the total ion intensity decrease for $^{10}B^+$, $^{11}B^+$, $^{95}Mo^+$, $BO^-$, and $BO_2^-$ from the sputter time of 5 and 10 s indicating their increased surface concentration.

The thickness of the zone of internal oxidation increases even in the advanced stage of oxidation. In this zone, no pores are visible by SEM, but they are present as has been shown by TEM analyses conducted by Burk [4].

At 1100 °C, the volatilization rate of $B_2O_3$ is 1 $mg \cdot cm^{-2} \cdot h^{-1}$ [17]. Thus, the silica scale is expected to have a very low $B_2O_3$ content. Consequently, the fluidity of the silica scale decreases and kinetics is mainly controlled by oxygen diffusion through the silica scale and outward diffusion of Mo. As already demonstrated by Burk et al. [18] and Rioult et al. [3], the microstructure has a significant effect both on the transient behavior and the steady-state stage of oxidation. Due to the fine microstructure, the transient stage is negligibly short so that the diffusion-controlled oxidation starts after only 1 h and the total specific mass loss after 100 h at 1100 °C is $<8\ mg \cdot cm^{-2}$. The SEM analysis of the oxide morphology reveals the formation of an outer borosilicate/silica layer of <10 μm thickness with a pronounced zone of internal oxidation which forms just below the oxide scale and comprises $Mo_{ss}$ and $SiO_2$ (see Fig. 5). Due to the low oxygen partial pressure under the scale, $MoO_2$ can additionally form at the interface between the oxide layer and the zone of internal oxidation (see Fig. 5a). This issue has been reported in [18].

The room temperature crystal structure of $SiO_2$ and the amount of $B_2O_3$ dissolved in the glass significantly influence the density which is relevant for the calculation. According to the calculated $B_2O_3$–$SiO_2$ phase diagram taking into consideration the re-evaluated and re-optimized phase diagram by Decterov et al.[13] (see Fig. 7), no intermediate compounds are formed. This diagram was calculated using FactSage® and coincides with the one experimentally assessed by Gupta et al. [12].

It can be concluded that $B_2O_3$ as well as $SiO_2$ in the modification of low-temperature quartz are expected to be present at room temperature. However, amorphous silica can form after quenching [12, 13] and was also observed by Burk after oxidation of Mo–9Si–8B in air at 1100 °C and subsequent cooling in air [4]. Likewise, XRD as well as TEM (EDS and diffraction) analyses by Yoshimi et al. detected amorphous silica on monolithic $Mo_5SiB_2$ exposed at 1200 °C for 24 h [19].

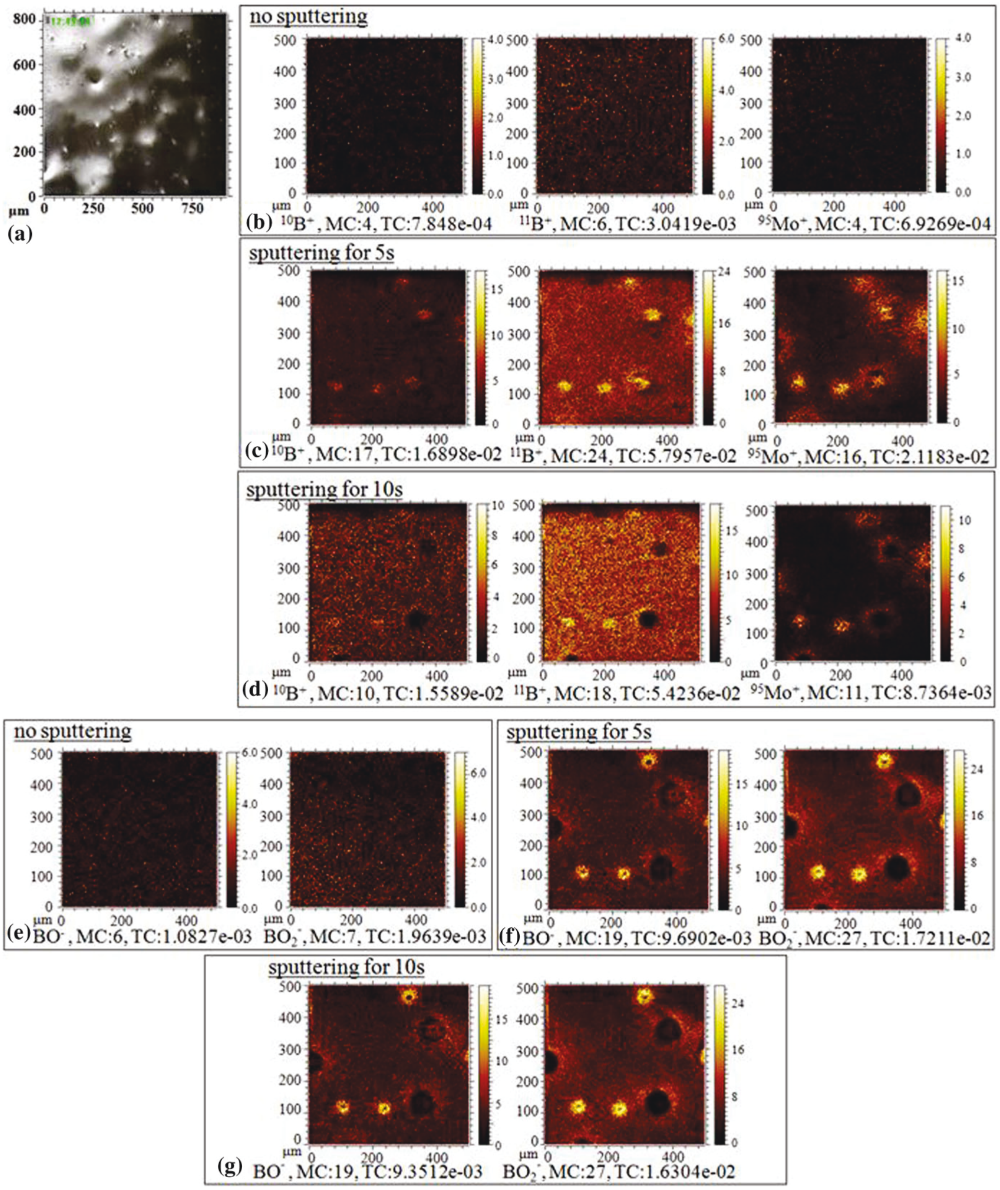

**Fig. 6** **a** Video Snapshot at start of the TOF–SIMS measurement of Mo–9Si–8B oxidized for 100 h at 1100 °C, **b–f** TOF–SIMS maps together with the $^{10}B^+$, $B^+$, $Mo^+$, $BO^-$, and $BO_2^-$ intensities normalized to the total ion intensity after different prior sputtering times for 3D reconstruction of the ion distribution. TC is the total ion count, MC denotes the ion count in the brightest pixel

EBSD analyses in this study confirmed that cooling in air is sufficiently fast to form vitreous silica. No Kikuchi patterns could be observed in the silica scale, while distinct patterns for $MoO_2$ and the substrate could be detected. Only at a few isolated positions, Kikuchi bands of low-quartz could be identified indicating that the low-quartz from the substrate did not transform into vitreous silica and led to the development of crystalline silica regions. As the crystalline regions are rare, the calculation presumes that the silica formed during the oxidation process is

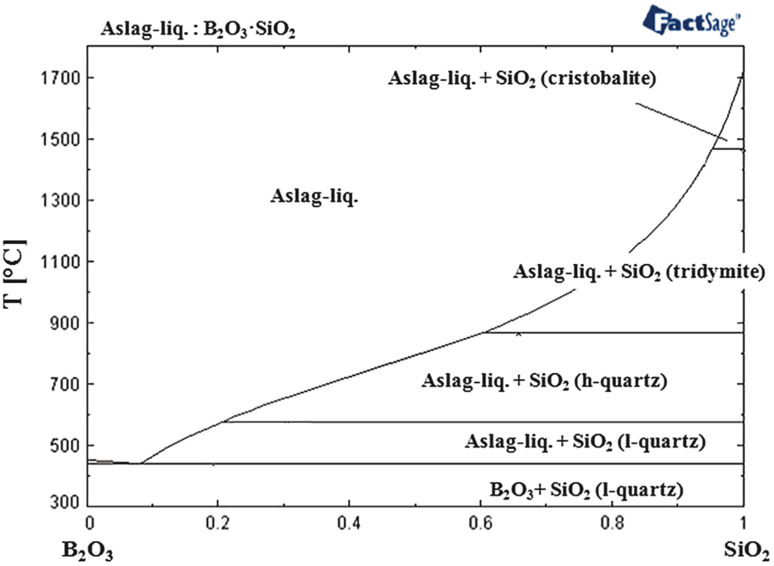

**Fig. 7** $B_2O_3$–$SiO_2$ phase diagram calculated with the data optimized by [13] using FactSage®

amorphous silica and quartz in the substrate remains in the trigonal state after cooling to room temperature. Due to the large atomic size difference between B and Si, no substitution of Si by B in $SiO_2$ was observed in XRD studies by Rockett and Foster [20]. Later studies by Vortmann et al. [21] and Elomari et al. [22] indicated that B substitutes Si with a probability of only 4 %. Thus, $B_2O_3$ and $SiO_2$ can be treated as two different phases in the upcoming calculation. As the addition of 30.5 mol % $B_2O_3$ to $SiO_2$ causes a density reduction of only 7.18 % [23], the density reduction caused by the substitution of Si by B is neglected in this study.

The amount of $B_2O_3$ remaining in the oxide layer after different oxidation times was investigated by SIMS comparing the concentration of the B isotopes with increasing exposure time.

Figure 8 exemplifies that B isotopes are well-visible in the positive spectrum as is described in [24]. Due to the natural isotope ratios, the intensity for the $^{11}B^+$ is higher than for $^{10}B^+$. Further, the intensity of $^{11}B^+$ and $^{10}B^+$ in the positive spectrum of a sample not oxidized is very low when the measurement is performed without sputtering the sample surface (see Fig. 8). A sputter time of 5 s enhances the intensity of the $^{11}B^+$ peak (see Fig. 8). A sputter time of 160 s increases the intensity of the $^{11}B^+$ peak to a stable level. It is obvious that due to the large differences in the hardness of the phases present in the composite, even the polished sample surface exhibits an appreciable topography (see Fig. 3b). Sputtering of the surface is, thus, needed to determine the correct B content for the samples before oxidation.

Figure 9 compares the intensities of the $^{11}B^+$ and $^{10}B^+$ surface ion concentration (normalized to the total ion intensity) of Mo–9Si–8B before oxidation and after oxidation at 1100 °C for 1, 10, and 100 h. It becomes obvious that the surface concentration of B decreases with increasing exposure time and reaches a stable low level after 10 h (see Fig. 9). It can be concluded that severe $B_2O_3$ evaporation takes

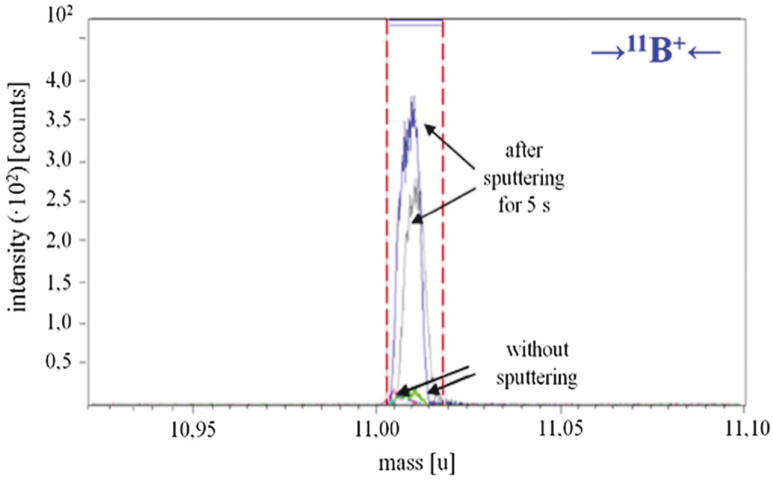

**Fig. 8** TOF-SIMS spectra showing the abundance of $^{11}B^+$ detected on an unoxidized sample that was directly probed without sputtering the sample surface (*bottom*) and after sputtering the surface for 5 s (*top*), respectively

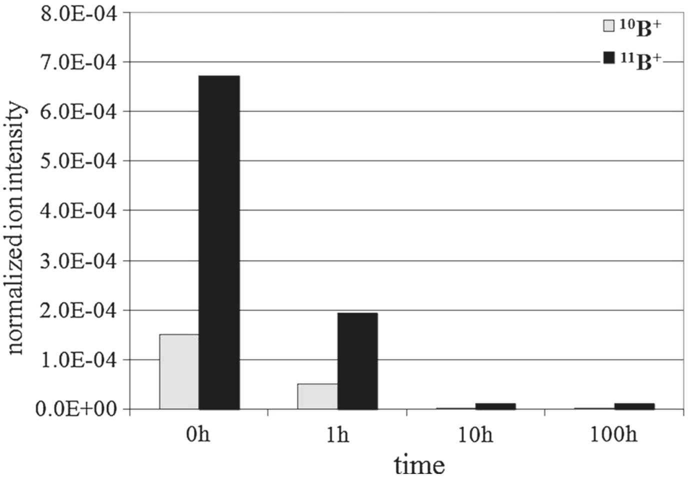

**Fig. 9** Overview of the measured $^{10}B^+$-peak and $^{11}B^+$-peak intensity (normalized to the total ion intensity) of the sample before oxidation (corresponds to 0 h of oxidation time) and oxidized samples after 0 h, 1 h, 10 h, and 100 h exposure time

place during proceeding oxidation, especially in the initial stage of oxidation. After 10 h, the amount of B present in the scale is highly reduced.

## Application and Verification of the Method Applied to Separate Mass Gain and Mass Loss

### *Calculation Method: Prerequisites and Input Parameters*

The calculation method used in this study is based on easily accessible data gained from the cross sections of the oxidized sample, e. g., the volume fraction of the

$SiO_2$, $MoO_2$, and $Mo_{ss}$ formed during the oxidation process. As $SiO_2$ forms at the surface as adherent solid oxide and has a very low Gibbs free energy change, the thickness of $SiO_2$ can be representative for the substrate material which was affected during the oxidation process. The calculation of the affected material depth is important as it provides information about the "true" damage depth of the cross section of technical components exposed to oxidizing environments at elevated temperatures and, therefore, represents an important parameter for the aviation and aerospace industry. As a significant amount of refractory metal-based materials can evaporate due to the formation of volatile $MoO_3$ and $B_2O_3$, the real damage depth can be much higher than the thickness of the oxide formed on the material. Likewise, the evaluation of the material affected enables the calculation of the mass loss due to the evaporating oxide and mass gain due to the formation of solid oxides. Prerequisites for the high calculation accuracy are:

- Knowledge about the microstructure (composition of the different phases etc.) and oxide nature, i.e., crystallography and stoichiometry, as well as the oxide scale morphology;
- The formation of a continuous and adherent protective oxide which presumes the formation of a continuous, preferably straight oxidation front;
- Negligible or homogenously distributed porosity in the oxide layer formed;
- Possibility to quantify the amount of outward diffusing elements by quantitative EDX analyses in the case of affected zones with the depleted elements;
- Possibility to distinguish oxides formed during the oxidation process using the BSE contrast if several oxides are formed;
- High measuring accuracy of the microbalance or TGA and precise measurement of the sample surface.

The calculation method is presented in detail in "Appendix A" section. Table 2 summarizes the input parameters as well as the corresponding data sources for Mo–9Si–8B.

### *Characterization of the Oxidations Kinetics*

Figure 10 summarizes the results calculated on the basis of the thickness of the $SiO_2$ layer and the zone of internal oxidation. Figure 10a shows (i) the changes of the

**Table 2** Input and reference parameters required for the calculation as well as the corresponding data sources

| Composite material forming one adherent solid oxide scale | | |
|---|---|---|
| | Input parameters | Reference parameters |
| Values | Thickness of the layer of the adherent oxide | Mass change |
| | Thickness of the internal oxidation zone | |
| | Sample surface | |
| Source | Cross sections | TGA or sensitive microbalance |

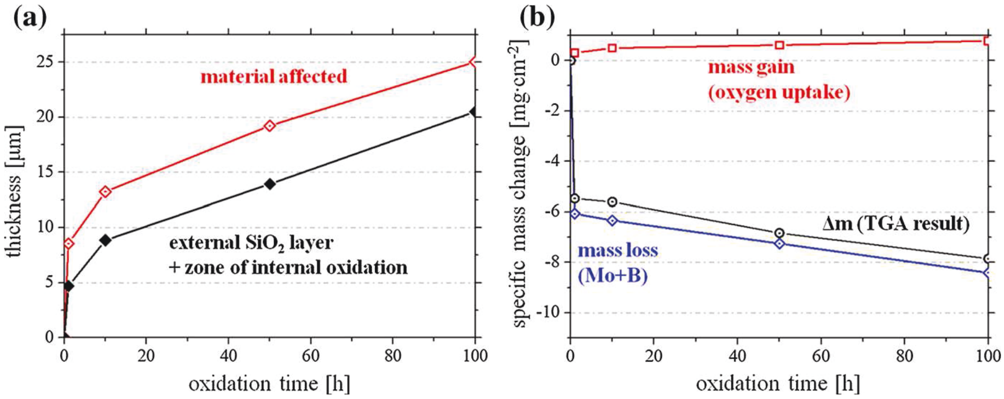

**Fig. 10** Time-dependent development of **a** the thicknesses of the material affected and the sum of the outer $SiO_2$-layer and the internal oxidation zone formed during oxidation of Mo–9Si–8B at 1100 °C and **b** the mass gain due to the oxygen uptake by the growth of adherent oxides and mass loss due to the loss of Mo and B by the formation of volatile oxides

time-depending thicknesses of the material affected (distance from the original surface to the internal oxidation front, for details see next chapter) and (ii) the sum of the external oxide layer and the zone of internal oxidation. It becomes obvious that the thickness of the oxide layer plus the zone internal oxidation is lower than the thickness of the material affected during corrosion. Both values increase with increasing exposure time.

Figure 10b shows the mass gain due to oxygen uptake during the corrosion process and the mass loss of Mo and B lost due to the formation of volatile $MoO_3$ and $B_2O_3$. The black curve represents the TGA-measured weight change. It becomes obvious that the mass loss of the metal Mo and the metalloid B exceeds the mass gain due to oxygen uptake. This effect is confirmed by the TGA curves which show overall mass loss and continuous, negative oxidation rates (see Fig. 4).

### *Verification of the Approach by FIB-Marker Insertion*

The validity of this concept was verified. For this reason, FIB markers with a radius of 11 µm and a depth of 30 µm were set at a distance of 127 µm from the original surface as the depth of the corrosion attack was estimated to be about 60 µm after 100 h of oxidation at 1100 °C (see Fig. 11).

The mass change $\Delta m$ was interpreted as the difference between (i) the "positive contributions" (abbreviation $\Delta m_{\text{positive}}$) resulting from the remaining $Mo_{\text{ss\_i.O}}$. in the zone of internal oxidation as well as the corrosion products $MoO_2$, $SiO_2$, and $B_2O_3$ and (ii) the "negative contributions" (abbreviation $\Delta m_{\text{negative}}$) caused by the material affected during the oxidation (see Fig. 12; Eq. (15) in "Appendix A" section). In the calculation the actual oxide morphology is considered. Using the calculation scheme presented in Fig. 12, it is not necessary to distinguish between $Mo_{ss}$ from the substrate and $Mo_{ss}$ formed by the reaction equation. Only the net volume of $Mo_{ss}$ is needed which is visible in the BSE-SEM image. The evaluation of the cross sections of Mo–9Si–8B oxidized for 100 h at 1100 °C was carried out

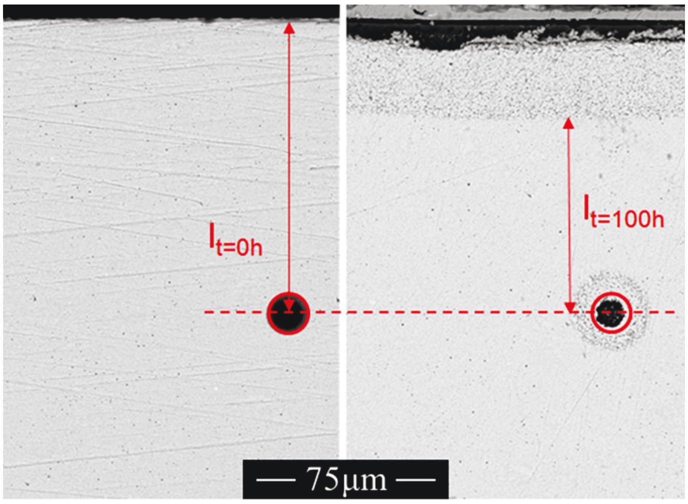

**Fig. 11** Direct comparison of the circular marker before (*left image*) and after oxidation (*right image*) with the measured distance between sample edge and marker center point $l_t$

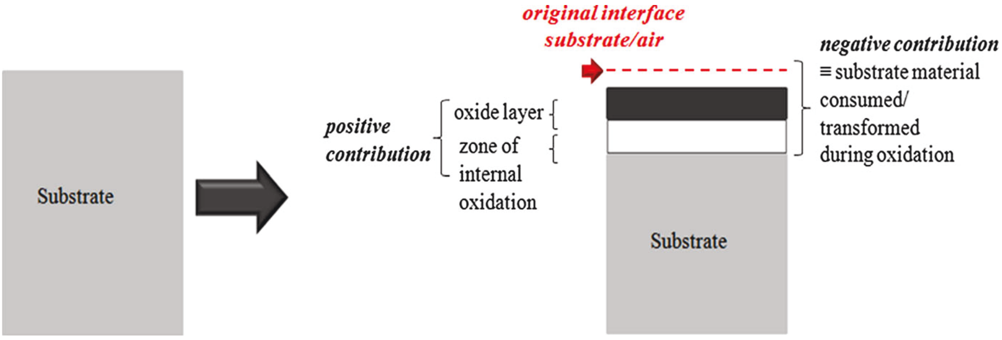

**Fig. 12** Scheme of calculation of the net mass change and definition of positive and negative contributions

yielding a thickness of the affected material $l_{\mathrm{Mc}} = l_{t=100h} - l_{t=0h} = 42.2\,\mu\mathrm{m}$. Based on this value, the volume of the affected material is calculated with respect to a unit cell with a depth and width of 1 µm. The number of unit cells $N$ in the volume element of phase φ is given by Eq. (2) in the "Appendix A" section.

The expected silica thickness $d_{\mathrm{SiO_2,calc}}$ of the volume unit $V_{\mathrm{SiO_2}}$ of $SiO_2$ formed during the oxidation was computed using Eq. (1) with $m_{\mathrm{SiO_2}}$ denoting the mass of $V_{\mathrm{SiO_2}}$ with the density $\rho_{\mathrm{SiO_2}}$ and $a$ being the atomic weight of the component named in the subscript, and the atomic mass unit $u$:.

$$d_{\mathrm{SiO_2,calc}} = \frac{V_{\mathrm{SiO_2}}}{1 \cdot 1} = \frac{m_{\mathrm{SiO_2}}}{\rho_{\mathrm{SiO_2}}} = \frac{N_{\mathrm{SiO_2}} \cdot (1a_{\mathrm{Si}} + 2a_{\mathrm{O}}) \cdot u}{\rho_{\mathrm{SiO_2}}} \tag{1}$$

The experimental value of the silica layer which was determined using the BSE contrast is $d_{\mathrm{SiO_2,calc}} = 11.04\,\mu\mathrm{m}$. The calculated value is $d_{\mathrm{SiO_2,calc}} = 11.00\,\mu\mathrm{m}$ resulting in a relative error of $f < 1\ \%$. The relative error $f$ amounts to 5.2/4.2/–2.9/–

2.8 for the samples analyzed in the case study (see Fig. 5) oxidized for 1/10/50, and 100 h, respectively. The relative error *f* indicates that the calculation accuracy of the method proposed increases when less $B_2O_3$ is dissolved in the amorphous oxide layer. The highest value of *f* is reached for the sample oxidized for 1 h, as the calculated mass change overestimates the mass loss because a certain amount of $B_2O_3$ is still dissolved in the oxide layer as was verified by SIMS measurements (see Fig. 6). After 10 h of exposure the relative measuring error is less than 5 % and remains below 3 % after 50 h of exposure. If we assume that $B_2O_3$ does not evaporate, the calculation yields an oxide thickness of $d_{SiO_2B_2O_3,\mathrm{exp}} = 15.30\,\mu\mathrm{m}$ for the sample oxidized for 100 h. The error rises to 39 % and the calculation heavily overestimates the expected oxide thickness indicating that the $B_2O_3$ evaporates nearly completely from the oxide layer and the B content left in the oxide layer is sufficiently low to be neglected.

In order to verify the method proposed here, experimental mass change was compared with the calculated values. The calculation of the mass change takes into account the thickness of the $MoO_2$ region as well as the thickness of the $Mo_{ss}$ region formed in the zone of internal oxidation. The fractions of both phases can be clearly distinguished using the BSE contrast of the cross-section images. The deviation between the calculation of the mass change on the basis of the material which was consumed during the oxidation which we observe by TGA and the experimental result yields a value of $f = 3\ \%$ ($\Delta m_{\mathrm{exp}} = -13.31\mathrm{mg};\ \Delta m_{\mathrm{calc}} = -13.15\,\mathrm{mg}$) for the sample oxidized for 100 h at 1100 °C. This deviation can be explained by edge effects and inhomogeneities in the microstructure. Furthermore, micropores at the interface of $B_2O_3{\cdot}SiO_2$/substrate, which were observed by Burk in TEM analyses [4], are not taken into account. However, the high accuracy in the calculation of the $SiO_2$ layer thickness indicates that this assumption is durable. Thus, the thickness of the $SiO_2$ layer is representative for the material affected and, therefore, for the depth of the material damaged during the oxidation process.

## Conclusions

The mass change of refractory metal-based alloys measured by TGA is a result of (i) mass gain due to oxygen uptake (ii) mass loss due to the loss of Mo and B by formation of volatile oxides. To separate both opposed mass effects and determine the real material damage in a more accurate way, a new concept was applied. The calculation accuracy was verified by specific FIB markers and the calculated mass change values were compared with the experimental values for the multiphase material Mo–9Si–8B. The deviation between theory and experiment is very low. Thus, the method can be applied for the alloy Mo–9Si–8B without FIB markers. This method enables (i) the characterization of the oxidation kinetics of refractory metal-based alloys with components forming volatile oxides in a more accurate way and (ii) the determination of the real damage depth of the material cross section.

**Acknowledgments** Financial support of Deutsche Forschungsgemeinschaft (DFG) is gratefully acknowledged.

## Appendix A

The verification of the method applied (see Chapter 3) shows that the thickness of the silica layer is representative for the material affected during oxidation. The correlation between the thickness of the material affected (M_A) and the thickness of the $SiO_2$ layer ($d_{SiO_2}$) is linear and can be described by first degree polynomial function of the form M_A = $a_0 \cdot d_{SiO_2}$ with the coefficient $a_0$, if there is no change of the microstructure. Thus, the thickness of the material affected can be calculated on the basis of the $d_{SiO2}$ estimated by the BSE contrast in the SEM image using an image processing program.

For the beginning, all calculations are made for the volume of the affected material with the respect to a unit cell with height, width, and length of 1 μm each. The number of unit cells $N$ of the phase φ in the volume element of the material affected is given by Eq. (2) where $a_k$ describes the atomic weight of the $j = 3$ basic components $k = \{Mo, B, Si\}$ of the unit cell, $n_k$ is the number of atoms of each element in the unit cell, $m_\varphi$ is the mass of phase φ, and $u$ denotes the atomic mass of the unit.

$$N_\phi = \frac{m_\phi}{\left(\sum_{k=1}^{j} a_k \cdot n_k\right) \cdot u} \tag{2}$$

Which corrosion products are formed depends on the oxygen partial pressure. The mass of the oxides $SiO_2$ and $B_2O_3$ formed during the oxidation process is assessed applying the silicide/oxide ratio given in the reaction Eqs. (3–4), valid at higher oxygen partial pressures and in the transient stage of oxidation:

$$Mo_3Si + 5.5 \cdot O_2 \rightarrow 3 \cdot MoO_3 + SiO_2 \tag{3}$$

$$Mo_5\ SiB_2 + 10O_2 \rightarrow 5MoO_3 + SiO_2 + B_2O_3 \tag{4}$$

$$Mo + 1.5O_2 \rightarrow MoO_3 \tag{5}$$

After formation of a continuous $B_2O_3 \cdot SiO_2$ scale, lower oxygen partial pressures are estimated at the oxide/substrate interface which result in the formation of corrosion products according Eqs. (6–8).

$$Mo_3\ Si + 4O_2 \rightarrow 3MoO_2 + SiO_2 \tag{6}$$

$$Mo_5\,SiB_2 + 7.5O_2 \rightarrow 5MoO_2 + SiO_2 + B_2O_3 \tag{7}$$

$$Mo + O_2 \rightarrow MoO_2 \tag{8}$$

As soon as the oxygen partial pressure at the oxide/substrate interface reaches values $\leq 10^{-21}$bar, corrosion products are formed according to Eqs. (9–10).

$$Mo_3Si + O_2 \rightarrow 3Mo_{ss} + SiO_2 \tag{9}$$

$$2Mo_5\,SiB_2 + 5O_2 \rightarrow 10Mo_{ss} + 2SiO_2 + 2B_2O_3 \qquad (10)$$

The mass of the oxides $Me_zO_y$ (here: $SiO_{2,}$ $MoO_2$ and $B_2O_3$) formed was calculated by eq. (11).

$$m_{\mathrm{oxide}} = N_{\mathrm{oxide}} \cdot a_{\mathrm{oxide}} \cdot u \qquad (11)$$

The reaction equations are based on thermodynamics and show which corrosion products are formed at which oxygen partial pressures. But as the oxidation process is a sum of thermodynamics and kinetics which depend on time, the oxygen distribution along the oxide layer changes with different annealing times. That is why Mo and $MoO_2$ can transform to $MoO_3$ with time when the oxygen concentration increases.

In the model, only the amounts of solid oxides are used as input parameters. As we cannot quantify the amount of gaseous oxides, the amount of Mo and B which evaporates in the form of volatile oxides is the output value. That is an advantage, because considering of volatile oxides by reaction equations is not needed.

For the calculation of the mass gain due to oxygen uptake, the conversion factor *c* is calculated by Eq. (12) for the oxide $Me_zO_y$ with M as the molar mass.

$$c = \frac{y \cdot M_{\mathrm{O}}}{M_{\mathrm{MezOy}}} \qquad (12)$$

Then, the mass gain due to oxygen uptake is given by (8.12):

$$mass\_gain\,(\mathrm{O} - \ \mathrm{uptake}) = c_{\mathrm{SiO_2}} \cdot m_{\mathrm{SiO_2}} + c_{\mathrm{MoO_2}} \cdot m_{\mathrm{MoO_2}} \qquad (13)$$

The specific mass change *Δm(calculated)* (for comparison with the specific mass change *Δm(TGA)* measured by TGA) can be calculated as the sum of the mass gain due to oxygen uptake by formation of adherent oxides (*mass_gain(O-uptake)*) and the mass loss due to the loss of Mo and B by the formation of volatile $MoO_3$ and $B_2O_3$ (*mass_loss(Mo + B)*):

$$\Delta m(calculated) = mass\_gain(O - uptake) + mass\_loss(Mo + B) \qquad (14)$$

The value *mass_loss(Mo + B)* cannot be used as input into model because there is no possibility of quantitative and time resolved measurement of evaporated oxides. That is why this value must be calculated using the net mass change Δm which is interpreted as the difference between (i) “positive contributions” (abbreviation $\Delta m_{\mathrm{positive}}$) resulting from the remaining $Mo_{ss\_i.O}$. in the zone of internal oxidation as well as the corrosion products $MoO_2$, $SiO_2$, and $B_2O_3$ and (ii) “negative contributions” (abbreviation $\Delta m_{\mathrm{negative}}$) resulting from the mass reduction caused by the material affected during the oxidation as presented in Fig. 12.

$$\begin{aligned}\Delta m &= \Delta m_{\mathrm{positive}} \ - \Delta m_{\mathrm{negative}} \\ &= \left(m_{\mathrm{Mo_{SS}\_i.O.}} + m_{\mathrm{SiO_2}} + m_{\mathrm{MoO_2}}\right) \ - \left(m_{\mathrm{Mo_{SS}}} + m_{\mathrm{Mo_3Si}} + m_{\mathrm{Mo_5SiB_2}}\right)\end{aligned} \qquad (15)$$

The mass change gained by TGA is used as reference to estimate the quality of the calculation accuracy.

The mass loss as the material affected by oxidation consisting of the phases $Mo_{ss}$, $Mo_3Si$, and $Mo_5SiB_2$ results from Eq. (16) with the number of phases $\varphi = 1,\ldots,i$ and the volume fraction x of phase $\varphi$:

$$\Delta m_{\text{negative}} = \sum_{\phi=1}^{i} x_\phi \cdot V_{\text{MC}} \cdot \rho_\phi \tag{16}$$

The measuring accuracy was calculated by the accuracy value *f* given in %:

$$f = \frac{\Delta m\,(\text{TGA}) - \Delta \text{m}\,(\text{calculated}))}{\Delta m\,(\text{TGA})} \bigstar 100$$

## References

1. J. C. Zhao and J. H. Westbrook, *MRS Bulletin* **28**, 2003 (622–630).
2. M. Azim, S. Burk, B. Gorr, H.-J. Christ, D. Schliephake, M. Heilmaier, R. Bornemann and P. H. Bolivar, *Oxidation of Metals* **80**, (3–4), 2013 (231–242).
3. F. A. Rioult, S. D. Imhoff, R. Sakidja and J. H. Perepezko, *Acta Materialia* **57**, 2009 (4600–4613).
4. S. Burk, Hochtemperaturoxidation Molybdän-basierter Legierungen unter Berücksichtigung von Einflüssen aus Umgebungsatmosphäre und legierungstechnischen Maßnahmen, Doctoral Thesis, Universität Siegen, ed. Siegener werkstoffkundliche Berichte, Vol. 1, Siegen, 2011.
5. D. M. Berczik, Method for enhancing the oxidation resistance of a molybdenum alloy, and a method of making a molybdenum alloy, United States Patent 5.595.616.
6. J. H. Perepezko, R. Sakidja, K. S. Kumar, in Advanced Structural Materials: Properties, Design Optimization, and Applications, ed. W. O. Soboyejo and T. S. Srivatsan (CRC Press, Boca Raton, FL, 2007) pp. 437–473.
7. V. Supataravanich, D. R. Johnson and C. T. Liu, *Materials Science and Engineering A* **344**, 2005 (328–339).
8. M. Krüger, P. Jain, K. S. Kumar and M. Heilmaier, *Intermetallics* **48**, 2014 (10–18).
9. M. Krüger, Pulvermetallurgische Herstellung und Charakterisierung von oxidationsbeständigen Molybdänbasislegierungen für Hochtemperaturanwendungen, Doctoral Thesis, Otto-von-Guericke-Universität Magdeburg, ed. Logos Verlag Berlin, 2010.
10. J. H. Schneibel, R. O. Ritchie, J. J. Kruzic and P. F. Tortorelli, *Metallurgical and Materials Transactions A* **36A**, 2005 (525–531).
11. P. Jehanno, M. Heilmaier, H. Saage, M. Böning, H. Kestler, J. Freudenberger and S. Drawin, *Materials Science and Engineering A* **463**, 2007 (216–223).
12. T. K. Gupta and J. H. Jean, *Journal of Materials Science* **9**, 1994 (999–1009).
13. S. A. Decterov, V. Swamy and I.-H. Jung, *International Journal of Materials Research* **98**, 2007 (987–994).
14. M. M. Lima and R. Monteiro, *Thermochimica Acta* **373**, 2001 (69–74).
15. S. Burk, B. Gorr, V. B. Trindade, U. Krupp and H.-J. Christ, *Corrosion and Engineering Science and Technology* **44**, 2009 (168–175).
16. D. A. Helmick, High Temperature Oxidation Behavior of Mo-Si-B based alloys, Doctoral Thesis, University of Pittsburgh, Pittsburgh, 2003.
17. C. G. Cofer and J. Economy, *Carbon* **33**, 1995 (389–395).
18. S. Burk, B. Gorr, V. B. Trindade and H.-J. Christ, *Oxidation of Metals* **73**, 2009 (163–181).
19. K. Yoshimi, S. Nakatani, T. Suda, S. Hanada and H. Habazaki, *Intermetallics* **10**, 2002 (407–411).
20. T. J. Rockett and W. R. Foster, *Journal of the American Ceramic Society* **48**, 1965 (75–80).
21. S. Vortman, B. Marler, H. Gies and P. Daniels, *Microporous Materials* **4**, 1995 (111–121).

22. S. Elomari, A. W. Burton, K. Ong, A. R. Pradhan and I. Y. Chan, *Chemistry of Materials* **19**, 2007 (5485–5492).
23. A. Abd, *Physica B* **325**, 2003 (319–322).
24. C. Dubois, G. Prudon, B. Gautier and J. C. Dupuy, *Applied Surface Science* **255**, (4), 2008 (1377–1380).

# Manuskript XVIII

## High temperature oxidation behavior of refractory high entropy alloys: Effect of alloy composition

B. Gorr, F. Müller, M. Azim, H.-J. Christ, T. Müller, H. Chen, A. Kauffmann, M. Heilmaier

Oxidation of Metals, 88 (2017) 339-349

Oxid Met (2017)
DOI 10.1007/s11085-016-9696-y

ORIGINAL PAPER

# High-Temperature Oxidation Behavior of Refractory High-Entropy Alloys: Effect of Alloy Composition

**Bronislava Gorr[1] · Franz Müller[1] · Maria Azim[1] · Hans-Jürgen Christ[1] · Torsten Müller[2] · Hans Chen[3] · Alexander Kauffmann[3] · Martin Heilmaier[3]**

Received: 21 December 2016 / Published online: 5 January 2017

**bstract** The high-temperature oxidation behavior of a new family of refractory igh-entropy alloys (HEAs) with compositions of W–Mo–Cr–Ti–Al, Nb–Mo–Cr–i–Al and Ta–Mo–Cr–Ti–Al was studied at 1000 and 1100 °C. Based on these quimolar starting compositions, the main incentive of this study was to select the ost promising alloy system whose properties may then be successively improved. espite the high amount of refractory elements, Ta–Mo–Cr–Ti–Al showed good xidation resistance at 1000 and 1100 °C. Moderate values of mass gain and

---

Bronislava Gorr
gorr@ifwt.mb.uni-siegen.de

Franz Müller
franz.mueller@uni-siegen.de

Maria Azim
maria.azim@uni-siegen.de

Hans-Jürgen Christ
christ@ifwt.mb.uni-siegen.de

Torsten Müller
t.mueller@chemie.uni-siegen.de

Hans Chen
hans.chen@kit.edu

Alexander Kauffmann
alexander.kauffmann@kit.edu

Martin Heilmaier
martin.heilmaier@kit.edu

Institut für Werkstofftechnik, Universität Siegen, Paul-Bonatz Str. 9-11, 57068 Siegen, Germany

Institut für Bau- und Werkstoffchemie, Paul-Bonatz Str. 9-11, 57068 Siegen, Germany

Institut für Angewandte Materialien-Werkstoffkunde, Karlsruhe Institute of Technology, Engelbert-Arnold-Str. 4, 76131 Karlsruhe, Germany

complex oxidation kinetics were observed for the W- and Nb-containing HEAs. These alloys formed inhomogeneous oxide scales possessing regions with thick and porous layers as well as areas revealing quite thin oxide scales due to the formation of discontinuous Cr- and Al-rich scales. The most promising behavior was shown by the alloy Ta–Mo–Cr–Ti–Al which followed the parabolic rate law for oxide growth due to the formation of a thin and compact Al-rich layer.

**Keywords** High-entropy alloys · Refractory metals · Oxidation kinetics · Oxide scale morphology · Oxide evaporation

## Introduction

Alloys based on refractory metals are potentially very attractive for high-temperature applications primarily because of their high melting points [1]. Extended explorations of refractory-based materials aiming at a practical use of these materials in ambient environment at high temperatures were undertaken during the 1950s and 1960s of the twentieth century [2]. However, the commercial implementation of these alloys as structural materials has largely been prohibited since they suffered from severe drawbacks such as insufficient ductility at low temperatures and poor oxidation resistance. Currently, refractory elements, such as Mo, W, and Re, are added in only moderate concentrations to conventional high-temperature materials such as Fe- and Ni-based alloys, to enhance their strength [3]. Nevertheless, some refractory-based alloy systems are still intensively investigated, and their properties have been significantly improved. For example, Bewlay et al. reported on the excellent balance between room- and high-temperature mechanical properties and oxidation behavior of advanced Nb-based composites consisting of a Nb-based solid solution with $Nb_3Si$ and $Nb_5Si_3$-type silicides [4]. Significant improvements in high-temperature oxidation behavior of Mo-based alloys have been recently achieved due to macroalloying with Ti [5].

In the recent years, the so-called high-entropy alloys (HEAs) and particularly refractory HEAs have attracted steadily increasing attention among the scientists worldwide [6–9]. In HEAs, elements possess equal or nearly equal concentrations. From the thermodynamic point of view, such alloys exhibit high entropy of mixing; the formation of simple solid solution is, therefore, favored, while the appearance of intermetallic phases is suppressed because of their ordered structure and, consequently, much lower entropy of mixing [6]. However, experimental studies on the microstructure of HEAs show that most of the HEAs contain more than one phase [6, 7]. Some new refractory HEAs show extremely high strength at elevated temperature and have, thus, been considered as prospective materials for high-temperature application [7]. Recently, a new equimolar refractory alloy system X–Mo–Cr–Ti–Al was proposed by Gorr et al. [10]. Extensive microstructural analyses were carried out for W–Mo–Cr–Ti–Al and Nb–Mo–Cr–Ti–Al alloys, and mechanical properties at room and elevated temperatures were investigated for the Nb-containing alloy [10–12]. The oxidation resistance has been studied in detail for the alloy Nb–Mo–Cr–Ti–Al [13], while oxidation behavior of the

W-containing HEA was only briefly assessed [10]. Novel experimental results on the oxidation behavior of the alloy Ta–Mo–Cr–Ti–Al have meanwhile been obtained.

Hence, this paper represents a comparative study of a refractory-based HEA family of type X–Mo–Cr–Ti–Al (with X = W, Nb, Ta) in terms of high-temperature oxidation resistance aiming at selecting the most promising equimolar alloy systems properties of which might be further improved by microalloying in future work.

## Experimental Procedures

All alloys were produced from elemental bulk materials by arc-melting process in ~0.6 atm of argon (arc-melter AM 0.5 by Edmund Bühler GmbH). The purities of the starting materials Ta, Mo, Nb, Al were all 99.9%, W was available in 99.96% purity, whereas Cr and Ti had purities of only 99 and 99.8%, respectively. In the alloys, nitrogen impurities were found to be below the detection limit of 5–10 wt ppm, oxygen content was measured to be between 50 and 100 wt ppm. The prepared buttons were flipped over and remelted more than five times in a water-chilled copper mold to facilitate alloy homogenization. The analyses of nitrogen and oxygen impurities were carried out after the remelting. Oxidation tests of the alloy W–Mo–Cr–Ti–Al were performed on samples in the as-cast condition, while Nb- and Ta-containing alloys were heat treated (1200 °C for 20 h) before oxidation. The samples having the dimension of 6 × 6 × 2 mm were ground to the 1200 grit and cleaned in ethanol before oxidation tests. Thermogravimetric experiments were carried out in static laboratory air at 1000 and 1100 °C. Detailed sample preparation procedures as well as detailed description of oxidation tests can be found elsewhere [13]. The oxide scale morphology was analyzed by means of a FIB-SEM DualBeam system of type FEI Helios Nanolab 600 equipped with an energy dispersive X-ray (EDX) detector. To analyze the composition of oxides formed on the alloys, X-ray diffraction (XRD) measurements were carried out using the X'Pert Pro MPD diffractometer operating in Bragg–Brentano geometry. Oxide scales formed on W- and Nb-containing alloys were removed from the oxidized samples, powdered into particle sizes smaller than 40 μm, and analyzed as described in Ref. [13]. Since the oxide scales formed on the alloy Ta–Mo–Cr–Ti–Al were extremely thin, XRD measurements were conducted directly on oxidized samples, i.e. without removing the oxide layers. To support experimental observation and to get a more fundamental knowledge of the alloy systems, thermodynamic calculations were carried out using the software FactSage V6.4 in conjunction with a commercial database FRAN.

## Results

Figure 1a, b compares the oxidation kinetics of the alloys W–Mo–Cr–Ti–Al, Nb–Mo–Cr–Ti–Al, and Ta–Mo–Cr–Ti–Al at 1000 and 1100 °C. The alloy Nb–Mo–Cr–Ti–Al exhibits a relatively high mass gain at both temperatures, while the curve at 1100 °C shows clearly decelerating oxidation kinetics. The oxidation kinetics of the

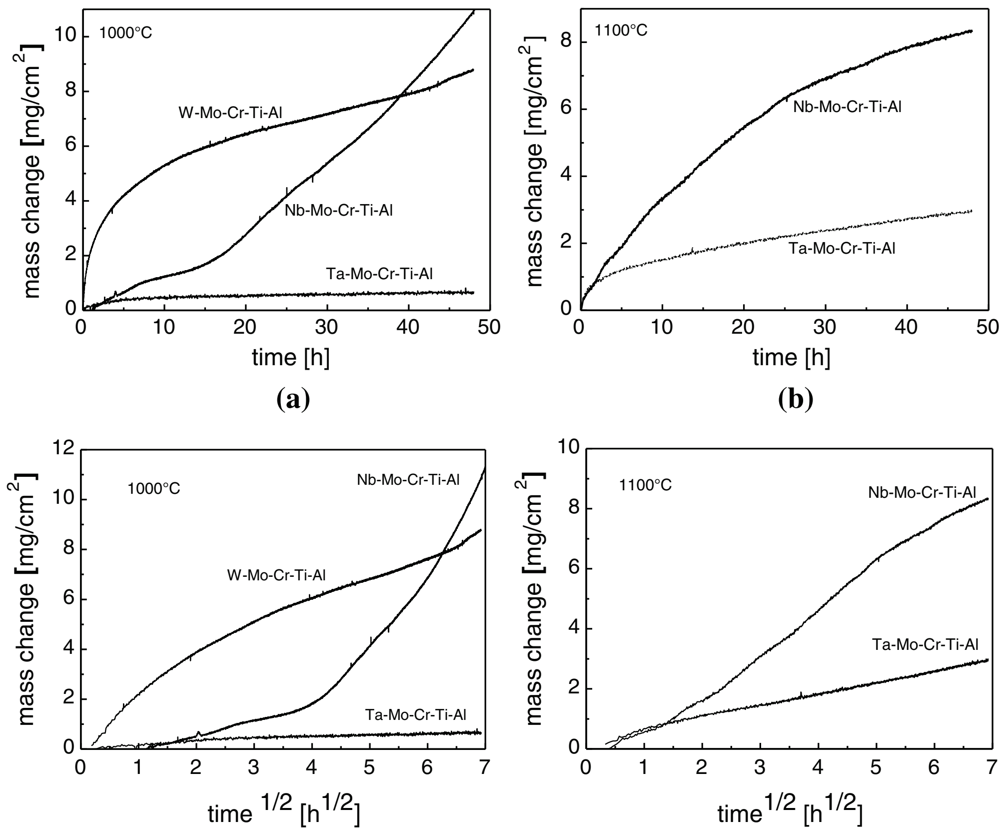

(a) (b)

(c) (d)

**Fig. 1** Thermogravimetric curves of HEAs W–Mo–Cr–Ti–Al, Nb–Mo–Cr–Ti–Al, and Ta–Mo–Cr–Ti–Al at **a** 1000 °C and **b** 1100 °C; plot of the mass change versus square root of the oxidation time at **c** 1000 °C and **d** 1100 °C

alloys W–Mo–Cr–Ti–Al and Nb–Mo–Cr–Ti–Al seem to be complex, while the oxidation curves of the alloy Ta–Mo–Cr–Ti–Al may follow the parabolic rate law. In order to understand, whether the oxidation curves of alloys studied obey the parabolic or linear rate law, the mass change is plotted versus square root of the oxidation time (Fig. 1c, d). Obviously, the oxidation behaviors of the alloys W–Mo–Cr–Ti–Al and Nb–Mo–Cr–Ti–Al do not obey the parabolic rate law. As opposed to this, the oxidation curves of the alloy Ta–Mo–Cr–Ti–Al follow the parabolic rate law after a short period of oxidation at both temperatures indicating the formation of a protective oxide scale.

Figure 2a, b shows the nonuniform oxide scale formed on the alloy W–Mo–Cr–Ti–Al after 48 h of oxidation at 1000 °C. Two different kinds of oxide morphology can be observed: (i) thick (up to ∼180 μm) and porous oxide mixture, and (ii) a relatively thin (up to ∼20 μm) and compact oxide layer. EDX analysis (not shown here) of these two distinctive regions revealed that Ti, Al, Cr, W, and O are nearly homogeneously distributed in the thick oxide, while a discontinuous layer of a Cr-rich oxide was identified at the interface oxide/substrate in the case of the thin oxide

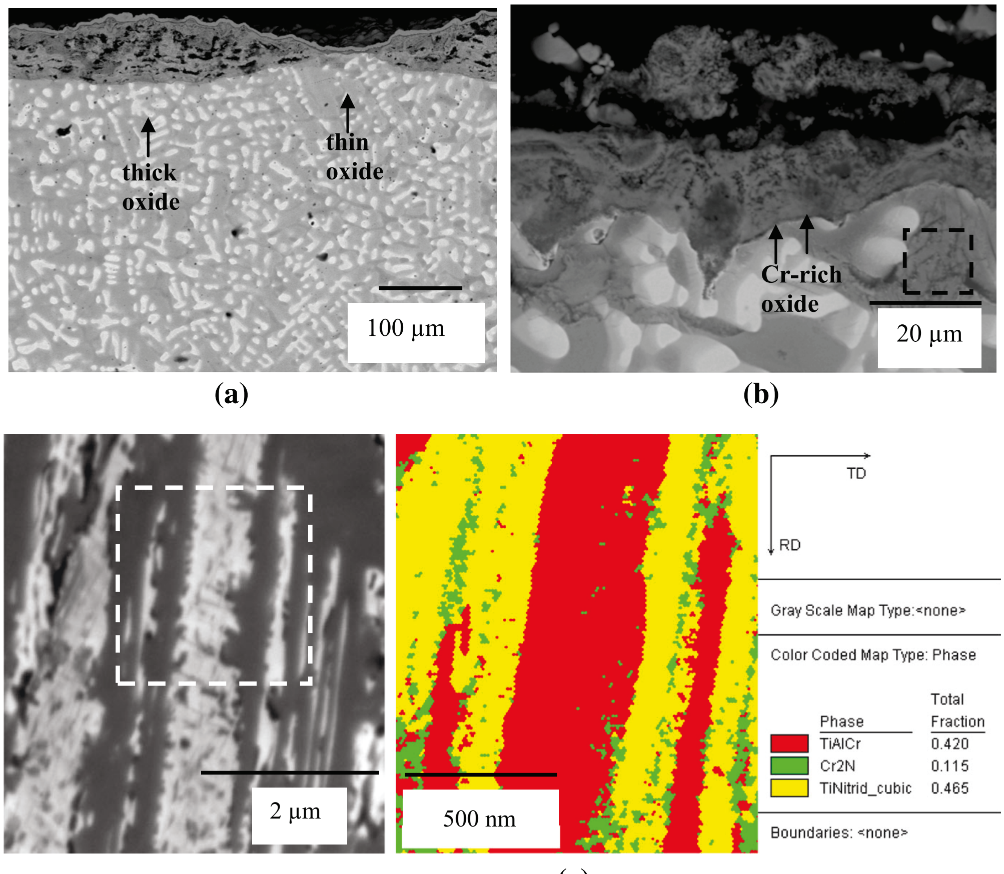

(a) (b)

(c)

**Fig. 2** Corrosion products formed on the alloy W–Mo-Cr–Ti–Al after 48 h of oxidation at 1000 °C; **a** cross section (BSE-mode) of the oxidized sample, **b** high magnification of the thin oxide scale region, and **c** formation of $Cr_2N$ and TiN as internal precipitates

layer [10]. Interestingly, enrichment of Mo was found at the interface oxide/substrate underneath the thin oxide layers. A closer look at this interface (see Fig. 2b) reveals some additional particular features: (i) the W- and Mo-rich dendrites (bright phase in the BSE contrast) possess a poorer oxidation resistance compared with the matrix and (ii) underneath the relatively thin oxide layer, internally formed precipitates (marked in Fig. 2b) are observed. To determine the nature of these precipitates, EBSD analysis was performed. Figure 2c shows that these precipitates are rich in Ti, Al, and Cr. Two types of nitrides were identified, namely, $Cr_2N$ and TiN. It should be mentioned that the alloy W–Mo–Cr–Ti–Al in the as-cast condition consists of two BCC phases with very close lattice parameter; for details, see Ref. [10, 12].

To identify the nature of the corrosion products formed on the alloy W–Mo–Cr–Ti–Al depending on the oxidation time, the oxide scales were removed from the samples oxidized for 8, 24, and 48 h in air at 1000 °C, powdered, and then analyzed using XRD. The results of this analysis reveal that three types of lattice structures were present, namely, rutile, corundum, and aluminum tungstate $Al_2(WO_4)_3$. Rutile was detected after all oxidation times, and can clearly be related to the formation of $TiO_2$ as confirmed by the EDX analysis. With respect to corundum, two oxides that can form in this alloy during oxidation, i.e. $Al_2O_3$ and $Cr_2O_3$, possess this crystal structure. Bondioli et al. reported that above 950 °C, a solid solution exists between alumina-rich and chromia-rich crystalline phases [14]. In the alloy W–Mo–Cr–Ti–Al, corundum was detected after 8 and 48 h of oxidation, while after 24 and 48 h, the formation of aluminum tungstate $Al_2(WO_4)_3$ that results from the reaction of $Al_2O_3$ with $WO_3$ was found. According to Waring, this compound may form in a wide concentration range and remains stable at temperatures up to 1200 °C [15]. The formation of aluminum tungstate was also observed during heat treatment of plasma-sprayed $Al_2O_3$ and $Al_2O_3$–$WO_3$ coatings above 700 °C [16, 17]. As aluminum tungstate was only detected after prolonged oxidation time in the alloy W–Mo–Cr–Ti–Al, and the kinetics of $Al_2(WO_4)_3$ formation is obviously slow.

The detailed description of the microstructure analyses of the metallic substrate as well as oxide scales formed on the alloy Nb–Mo–Cr–Ti–Al can be found elsewhere [11, 13]. In summary, the alloy consists of three phases, BCC solid solution, hexagonal Laves phase, and one unknown phase. Oxide scales formed on this alloy after air exposure at 1000 and 1100 °C are rather inhomogeneous exhibiting regions with thick layers as well as areas showing quite thin oxide layers due to the formation of discontinuous chromium- and aluminum-rich scales (see Fig. 3). XRD analysis revealed that two crystal structures, rutile and corundum are present as corrosion products in the outer oxide scale after 24 and 48 h air exposure at 1000 °C. After short oxidation time, i.e. 8 h, anatase, $TiO_2$ in the tetragonal structure, was additionally found in the oxide scale. Underneath the thin layers, Mo enrichments were identified using EDX. In contrast to the W-containing alloy, a thick zone (up to 30 μm) of internal oxidation was observed beneath the thin oxide scales [13].

As opposed to the W- and Nb-containing alloys, a homogeneously thin (up to 7 μm) and continuous oxide scale was observed on the alloy Ta–Mo–Cr–Ti–Al after 48 h of oxidation at 1000 °C. Figure 4 shows the microstructure of the oxide scale: beneath the coarse Ti oxide particles, an Al oxide layer can be identified that obviously provides a high oxidation resistance (see also the weight gain curves in

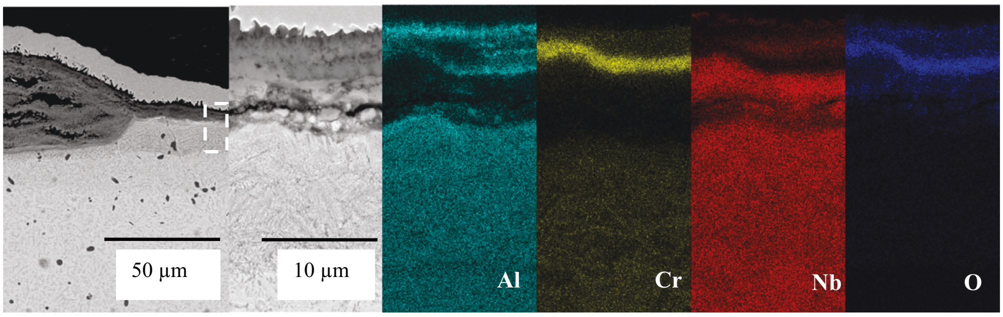

**Fig. 3** Oxide scales formed on the alloy Nb–Mo–Cr–Ti–Al after air exposure at 1000 °C for 48 h; the *white box* on the farthest *left micrograph* indicates the area chosen for EDX analysis (*right color-coded micrographs*)

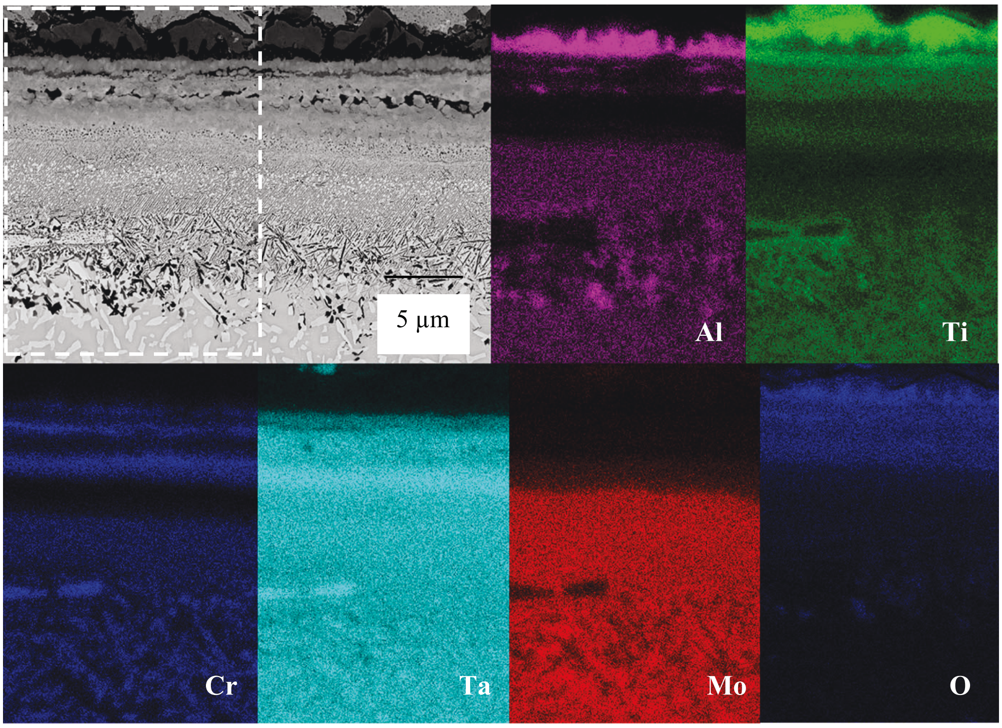

**Fig. 4** Oxide scale formed on the alloy Ta–Mo–Cr–Ti–Al after air exposure at 1000 °C for 48 h; again the *white box* on the *left upper micrograph* indicates the area chosen for EDX analysis

Fig. 1). Underneath the Al oxide layer, Cr, Ti and Nb were detected using EDX. However, a pronounced zone (up to 15 µm) of internal corrosion was also identified. Results of the XRD analysis reveal that $TiO_2$, $Al_2O_3$, $Cr_2O_3$ and probably $CrTaO_4$ are present in the oxide scale after 48 h of air exposure at 1000 °C, while some $Cr_2N$ seems to have been internally precipitated. It should, however, be mentioned that these microstructural investigations of oxide scales and internal precipitates are of preliminary nature and need to be intensified in future work.

## Discussion

Considering the high amount of refractory elements in all HEAs studied, it can be stated that the alloys show acceptable or even good oxidation resistance at least during the 48 h of air exposure at high temperatures. Figure 5a compares the parabolic oxidation constants of the alloy Ta–Mo–Cr–Ti–Al investigated in this study with those of Ni-based alloys, i.e. $Cr_2O_3$- and $Al_2O_3$-formers. Figure 5a reveals that the alloy Ta–Mo–Cr–Ti–Al reaches the level of the $Cr_2O_3$-former Ni-based alloys. However, the oxidation resistance of the $Al_2O_3$-former Ni-based alloys is clearly better as compared to the alloy Ta–Mo–Cr–Ti–Al.

The dominant contribution to the mass gain during oxidation can obviously be attributed to the oxygen uptake as relatively thick oxide scales were observed on the alloys W–Mo–Cr–Ti–Al and Nb–Mo–Cr–Ti–Al. Refractory metals, however,

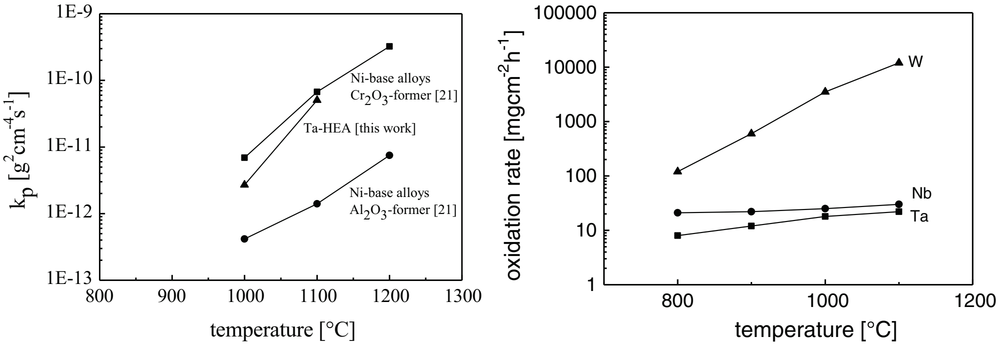

**(a)** **(b)**

**Fig. 5** **a** Parabolic oxidation constants of Ta-HEA and Ni-based alloys [21] and **b** linear oxidation rates of pure refractory metals W, Nb, and Ta [18]

exhibit very poor oxidation resistance. Geyer studied oxidation resistance of pure refractory metals at high temperatures [18]. In order to understand the role of refractory elements in the alloys studied in this paper, linear oxidation constants of the pure refractory metals W, Nb, and Ta calculated by Geyer [18] are summarized in Fig. 5b. Apparently, oxidation rates of W, Nb, and Ta are very high at these temperatures. It is well known that pure Mo forms gaseous oxides above 800 °C that evaporate extremely fast [19]. By contrast, W, Nb, and Ta oxidize to form solid oxides at temperatures of interest. In fact, W also forms gaseous $WO_3$, however, Gulbransen et al. observed severe evaporation of tungsten trioxide only at temperatures well above 1150 °C [20]. Figure 5b clearly shows that W yields the highest oxidation rate at temperatures between 900 and 1100 °C. This seems to be the probable reason for the high mass gain of the alloy W–Mo–Cr–Ti–Al during air exposure at 1000 °C, especially of the dendritic regions that have a very high W content (see Fig. 2b). In the temperature range between 900 and 1100 °C, pure Ta and Nb possess similar oxidation resistance, where Ta exhibits only a slightly lower oxidation rate as compared to Nb.

Weight gain curves of HEAs observed during oxidation in air can be ascribed not only to oxygen but also to nitrogen uptake as nitrides were experimentally identified in the zones of internal corrosion observed in all alloys. It should be pointed out that the zone of internal corrosion is the most pronounced for the Nb-containing alloy, while the thinnest one was observed in the alloy W–Mo–Cr–Ti–Al. In order to understand this experimental finding and to assess the effect of each element in the alloy W–Mo–Cr–Al–Ti on the ability of the metallic matrix to dissolve nitrogen, the mole fraction of dissolved nitrogen in the BCC phase was calculated as a function of alloy element concentrations (Fig. 6). It was assumed that the BCC phase is the only stable phase in the alloy system that is in equilibrium with the atmosphere 20Ar–80 N at 1000 °C. The concentration of one element was changed, while the contents of the other elements were kept “equimolar”. The results shown in Fig. 6 represent the solubility limit of nitrogen in the BCC phase at 1000 °C. It seems that W in this alloy plays a crucial role in terms of nitrogen solubility decreasing the amount of dissolved nitrogen in the BCC phase extremely efficiently. It can, therefore, be

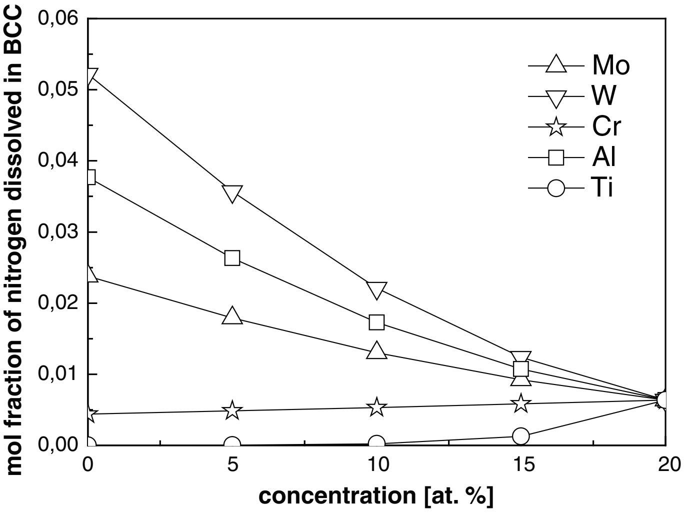

**Fig. 6** Nitrogen dissolved in the BCC phase of the alloy W–Mo–Cr–Ti–Al versus elemental concentration

concluded that the decreased concentration of W may lead to the enhanced formation of various nitrides in the considered alloy system. In contrary, Cr additions do not influence the nitrogen solubility notably. Further, decreasing the Ti content up to 15 at.% may cause substantial lowering of the nitrogen solubility in the alloy (see Fig. 6). Ti concentrations below this critical value, however, do not affect the nitrogen solubility significantly.

Table 1 summarizes the literature values of oxygen and nitrogen solubilities in those elements being present in the alloys studied. It is apparent that W, Mo, Cr, and Al do not support gas solubility in HEAs, while Nb, Ta, and Ti may contribute to oxygen and/or nitrogen solubility in the alloys. The extremely low values of oxygen and nitrogen solubilities in pure W support the above suggestion that W seems to counteract the gas solubility. Comparing the corresponding values of oxygen and nitrogen solubilities in pure W, Ta, and Nb, it can be concluded that Nb-containing alloys, compared with Ta- and especially W-containing ones, may be intrinsically prone to dissolve notable amounts of oxygen and nitrogen which cause substantial internal corrosion. Taking into account that all the alloys in this study contain the same concentration of Ti, which possesses an extremely high ability to dissolve gases, and considering the rather thin zone of internal corrosion in the W-containing HEAs, it seems that the deleterious effect of Ti in terms of gas solubility may be largely excluded.

**Table 1** Oxygen and nitrogen solubilities in pure elements at 1000 °C

| Elements | W | Nb | Ta | Mo | α-Ti | Cr | Al |
|---|---|---|---|---|---|---|---|
| O solubility (at.%) | 0.03 [22] | 2.5 [23] | 3 [24] | 0.03 [22] | 33 [25] | 0.0006 [22] | ~0 |
| N solubility | 0.4 ppm [26] | 14.5 at.% [27] | 4 at.% [28] | 20 ppm [29] | 17 at.% [30] | 0.08 at.% [22] | ~0 |

Results of the XRD measurements are useful to indicate tendencies in the oxidation behavior of HEAs. Comparing the development of oxides formed on the alloys W–Mo–Cr–Ti–Al and Nb–Mo–Cr–Ti–Al, it becomes clear that despite the slightly less mass gain after 48-h oxidation at 1000 ° C, the alloy W–Mo–Cr–Ti–Al shows a significantly lower potential in terms of high-temperature oxidation resistance. This is because of the disadvantageous reaction between $Al_2O_3$ and $WO_3$, which results in the formation of aluminum tungstate $Al_2(WO_4)_3$. Obviously, this reaction reduces the probability to form a continuous and protective $Al_2O_3$ layer. Although corundum could be detected in the oxide scale of the W-containing alloy after 48 h of oxidation at 1000 °C, it is likely attributed to $Cr_2O_3$ rather than to $Al_2O_3$ formation, as a thin and discontinuous Cr-rich oxide layer was identified at the interface oxide/substrate. Despite the high oxidation rates during oxidation, the alloy Nb–Mo–Cr–Ti–Al shows a higher potential to form a protective alumina scale. The formation of a protective alumina in this alloy can successfully be facilitated by higher temperatures, prolonged oxidation times, and microalloying, e.g. with Si [13]. The alloy Ta–Mo–Cr–Ti–Al forms a protective alumina scale after 48 h of air exposure at 1000 and 1100 °C and seems to be the most promising system. The mechanisms of alumina scale formation, the protective properties of $CrTaO_4$, as well as the role of $TiO_2$ in oxidation mechanisms are, however, not clear and should be thoroughly studied in future work.

## Conclusions

The comparative study of oxidation resistances of three HEAs at 1000 and 1100 °C revealed that the alloy W–Mo–Cr–Ti–Al possesses the lowest ability to form a protective alumina scale because of the disadvantageous reaction between $Al_2O_3$ and $WO_3$, which results in the formation of fast growing aluminum tungstate $Al_2(WO_4)_3$. Even though the HEA Nb–Mo–Cr–Ti–Al exhibits rather high oxidation rates, this alloy possesses a clear potential to form an alumina scale. However, this alloy system shows a particular tendency to dissolve high amounts of oxygen and nitrogen, as a thick zone of internal corrosion was observed. The alloy Ta–Mo–Cr–Ti–Al exhibits a superior oxidation resistance comparable to those of its counterparts. Due to the formation of a continuous and dense alumina scale underneath the rutile layer, oxidation kinetics obeys the parabolic rate law and low mass gain. Apparently, the oxidation mechanisms of this alloy need to be investigated in more detail to exploit its full potential.

**Acknowledgements** The financial support by Deutsche Forschungsgemeinschaft (DFG) is gratefully acknowledged.

## References

1. J. H. Perepezko, *Science* **326**, 1068 (2009).
2. R. Syre, *Niobium, Molybdenum, Tantalum and Tungsten: A Summary of Their Properties with Recommendation for Research and Development* (North Atlantic Treaty Organization, Advisory Group For Aeronautical Research and Development, 1961).

3. L. Huang, X. F. Sun, H. R. Guang, and Z. Q. Hu, *Oxidation of Metals* **65**, 391 (2006).
4. B. P. Bewlay, M. R. Jackson, and H. A. Lipsitt, *Metallurgical and Materials Transactions A* **27A**, 3801 (1996).
5. M. Azim, D. Schliephake, C. Hochmuth, B. Gorr, H.-J. Christ, U. Glatzel, and M. Heilmaier, *Journal of Minerals* **57**, 2621 (2015).
6. J. W. Yeh, Y. L. Chen, S. J. Lin, and S. K. Chen, *Materials Science Forum* **560**, 1 (2007).
7. O. N. Senkov, C. Woodward, and D. B. Miracle, *Journal of Minerals* **66**, 2030 (2014).
8. O. N. Senkov, S. V. Senkova, D. M. Dimiduk, C. Woodward, and D. B. Miracle, *Journal of Materials Science* **47**, 6522 (2012).
9. C. M. Liu, H. M. Wang, S. Q. Zhang, H. B. Tang, and A. L. Zhang, *Journal of Alloys and Compounds* **583**, 162 (2014).
10. B. Gorr, M. Azim, H.-J. Christ, T. Mueller, D. Schliephake, and M. Heilmaier, *Journal of Alloys and Compounds* **624**, 270 (2015).
11. H. Chen, A. Kauffmann, B. Gorr, D. Schliephake, C. Seemüller, J. N. Wagner, H.-J. Christ, and M. Heilmaier, *Journal of Alloys and Compounds* **661**, 206 (2016).
12. B. Gorr, M. Azim, H.-J. Christ, H. Chen, D. V. Szabo, A. Kauffmann, and M. Heilmaier, *Metallurgical and Materials Transactions A* **47A**, 961 (2016).
13. B. Gorr, F. Mueller, H.-J. Christ, T. Mueller, H. Chen, A. Kauffmann, and M. Heilmaier, *Journal of Alloys and Compounds* **688**, 468 (2016).
14. F. Bondioli, A. M. Ferrari, C. Leonelli, L. Manfredini, L. Linati, and P. Musterelli, *Journal of the American Ceramic Society* **83**, 2036 (2000).
15. J. L. Waring, *Journal of the American Ceramic Society—Discussion and Notes* **48**, 493 (1965).
16. S. Matthews, F. Taliana, and B. James, *Surface & Coatings Technology* **212**, 109 (2012).
17. S. Matthews, *Surface & Coatings Technology* **206**, 3323 (2012).
18. N. M. Geyer, Protection of Refractory Metals Against Atmospheric Environments, http://contrails.iit.edu/DigitalCollection/1961/ASDTR61-322article07.pdf. Assessed 1 March 2016.
19. E. A. Gulbransen, K. F. Andrew, and F. A. Brassant, *Journal of the Electrochemical Society* **110**, 952 (1963).
20. E. A. Gulbransen, K. F. Andrew, and F. A. Brassant, *Journal of the Electrochemical Society* **111**, 103 (1961).
21. C. S. Giggins and F. S. Pettit, *Journal of Electrochemical Society* **118**, 1782 (1971).
22. W. D. Klopp, *Recent Developments in Chromium and Chromium Alloys*, NASA-Report TM X-1867 (1969).
23. R. P. Elliot, *Transaction of the ASM* **52**, 900 (1960).
24. H. Jehn and E. Olzi, *Journal of the Less Common Metals* **27**, 297 (1972).
25. J. L. Murray and H. A. Wriedt, *Journal of Phase Equilibria* **8**, 148 (1987).
26. R. L. Wagner, *Metallurgical Transactions* **1**, 3365 (1970).
27. A. Taylor, Research for Solubility of Interstitials in Columbium Part III. A Study of Columbium-Rich Alloys in the Ternary Systems Cb-Mo-O, Cb-Mo-N and Cb-Mo-C, Technical Report, Westinghouse Research Labs Pittsburgh (1966).
28. F. E. Bacon and P. M. Moanfeldt, *Reaction with common gases, Columbium and Tantalum* (Wiley, New York, 1963).
29. D. E. Weaver, The diffusivity and Solubility of Nitrogen in Molybdenum and Trapping of Nitrogen by Carbon in Molybdenum, PhD Thesis, Lawrence Livermore Laboratory, University of California (1972).
30. B. Holmberg, *Acta Chemica Scandinavica* **16**, 1255 (1992).